MIO-PLIOCENE GEOLOGY OF THE SOUTHERN PUNA PLATEAU MARGIN, ARGENTINA

by

Scott Anthony Hynek

A dissertation submitted to the faculty of
The University of Utah
in partial fulfillment of the requirements for the degree of

Doctor of Philosophy

in

Geology

Department of Geology and Geophysics

The University of Utah

August 2011

The University of Utah Graduate School

STATEMENT OF DISSERTATION APPROVAL

The dissertation of **Scott Anthony Hynek**

has been approved by the following supervisory committee members:

Francis H. Brown	, Chair	**April 6, 2011** Date Approved
Ronald L. Bruhn	, Member	**April 11, 2011** Date Approved
Thure E. Cerling	, Member	**April 7, 2011** Date Approved
Barbara P. Nash	, Member	**April 11, 2011** Date Approved
W. James Steenburgh	, Member	**April 6, 2011** Date Approved

and by **D. Kip Solomon** , Chair of

the Department of **Geology and Geophysics**

and by Charles A. Wight, Dean of The Graduate School.

ABSTRACT

The Mio-Pliocene geologic record is investigated along the southeastern margin of the Puna plateau in northwestern Argentina. The Puna plateau is the southernmost extension of the high elevation, internally drained, Central Andean plateau. A series of intermontane basins at the plateau margin preserve thick stratigraphic sections spanning ~10–3 Ma. The strata in these basins were investigated between 25°30′S and 28°S latitude, with geochronological and paleoenvironmental objectives. The stratigraphy, composition, and age of volcanic ash beds provide age control. Fossil vertebrates and soils interbedded with these volcanic ash beds provide material for stable isotopic proxies of environment. This approach permits analysis of spatial and temporal patterns in the tectonic and climatic evolution of the landscape at the Puna margin.

Stable isotope analysis of fossil tooth enamel from the 2.5 km thick section at Puerta de Corral Quemado documents the late Miocene expansion of plants using the C_4 photosynthetic pathway. Tooth enamel was analyzed by conventional methods, and by laser ablation which incorporates small bodied taxa in the study. These results indicate the presence of C_4 plants in the region by at least 8.5 Ma and a shift to C_4 diets among fossil notoungulates between 7–5.5 Ma. Fossil rodents exhibit a less dramatic diet change across this interval, and all taxa document transient enrichment in ^{13}C and ^{18}O approximately coincident with the Miocene-Pliocene boundary.

Interbasin correlation of ash beds demonstrate that conglomeratic deposits are conformable with stratified sections and initiated between 4–3 Ma. These deposits lag uplift of basin margin mountain blocks by several million years and precede contractional deformation of Mio-Pliocene strata. This sequence is characteristic, but diachronous between basins. This Mio-Pliocene pulse of deformation typifies the evolution of a broken foreland at the plateau margin.

Interbasin comparison of isotopic proxy data from fossil soils identifies regional ^{18}O enrichment concurrent with topographic growth at the plateau margin. Carbon isotope data from fossil soils demonstrate strong ecological gradients at the landscape-scale and at local scales. The record of C_4 expansion in fossil soils is significantly influenced by the growth of complex topography and possibly by regional reorganization of precipitation systems.

TABLE OF CONTENTS

LIST OF TABLES

TABLE

ACKNOWLEDGMENTS

This research was initiated with support from the Packard Foundation, and the University of Utah, Vice President of Research. In 2002, field assistance was provided by Graciela Esteban, Rafael Herbst, Claudia Muruaga, Norma Nasif (Universidad Nacional de Tucumán), Gustavo Gómez and Pamela Steffan (Universidad Nacional del Centro), and is gratefully acknowledged. Thure Cerling, Ben Passey, Pepe Prado, and Jay Quade were instrumental in the early stages of the project. In 2007, exceptional field assistance was provided by Lars Battle.

In the laboratory numerous people provided advice and assistance. Most notably: Frank Brown taught me to process volcanic ash samples efficiently and effectively, Barb Nash expertly maintains the Cameca SX50 electron microprobe and works to provide the highest quality data, and Diego Fernandez spent considerable effort developing a method for the digestion and trace element analysis of volcanic glass separates by ICP-MS.

My committee is thanked for their support, flexibility, and collective wisdom. Frank Brown must be singled out as a patient, hardworking and thoughtful advisor and as a collaborator of immense value. Jim Steenburgh provided an opportunity to get involved with mountain meteorology. Senior faculty at the University of Utah are thanked for friendship and mentoring, especially Thure Cerling, Dave Chapman, Jim Ehleringer, and Bill Parry. My parents, my wife, and my friends all contributed to keeping me on the straight and narrow path forward.

CHAPTER 1

INTRODUCTION: TECTONIC AND GEOLOGIC SETTING OF THE PUNA PLATEAU MARGIN, NORTHWESTERN ARGENTINA

Purpose of the dissertation

The data collected for this dissertation, and the themes discussed herein relate to the late Miocene and Pliocene geologic history at the southeasternmost margin of Central Andean plateau. In northwestern Argentina, modern interactions between climate and topography are striking features of the landscape and profoundly influence geological processes. The evolution of this system before, during, and after a strong Pliocene pulse of uplift in the region is investigated.

Several lines of inquiry are followed. A stable isotope proxy approach to environmental change during this period addresses questions of landscape scale ecology and its relationship with growing topography and global ecological change. Stratigraphic study of volcanic ash beds provides chronological control for stable isotope data and permits analysis of the locus and timing of plateau margin uplift. Integration of volcanic ash and stable isotope stratigraphies is a means of addressing local and regional variations in environmental change. A composite record of climate and ecology in the region permits analysis of the relative importance of global and regional events on the evolution of Central Andean plateau and its environment.

This chapter provides an introduction to the region of study, formulates the questions addressed, and describes the methods employed. A general tectonic framework for the Andes is followed by a description of the study area and a summary of hypothesized mechanisms for plateau uplift. The methods employed are then discussed, highlighting the assumptions and realistic limits of data interpretation. Having established the scientific approach, the organization of the dissertation is presented.

Tectonic setting

The Andes mountains span ~7500 km along the western margin of the South American continent (Figure 1.1). In places, the Andes are a single narrow spine; in others, a broad amalgamation of ranges, with each range having its own structure and morphology. It has been hypothesized that at the continental scale, the Andes owe their morphological variation to climatic patterns of zonal atmospheric circulation (Montgomery *et al*., 2001). The focus of this dissertation is the southern terminus of the broad, high elevation Puna-Altiplano plateau which is well developed in the subtropical belt of deserts (~15–33°S).

As the type example of subduction related continental mountain building, cordilleran fold-thrust belt tectonics, and volcanic arc processes, the Andes remain atypical in many respects. Subduction zones are common geologic features known from many locations on Earth, but only along the western margin of South America does subduction of oceanic lithosphere beneath a continent result in topography and crustal thickness comparable to the Himalaya. The Central Andes in particular, have a variable but thick (up to 75 km) continental crust underlying the plateau portion of the mountain belt (Beck *et al*., 1996; Yuan *et al*., 2002).

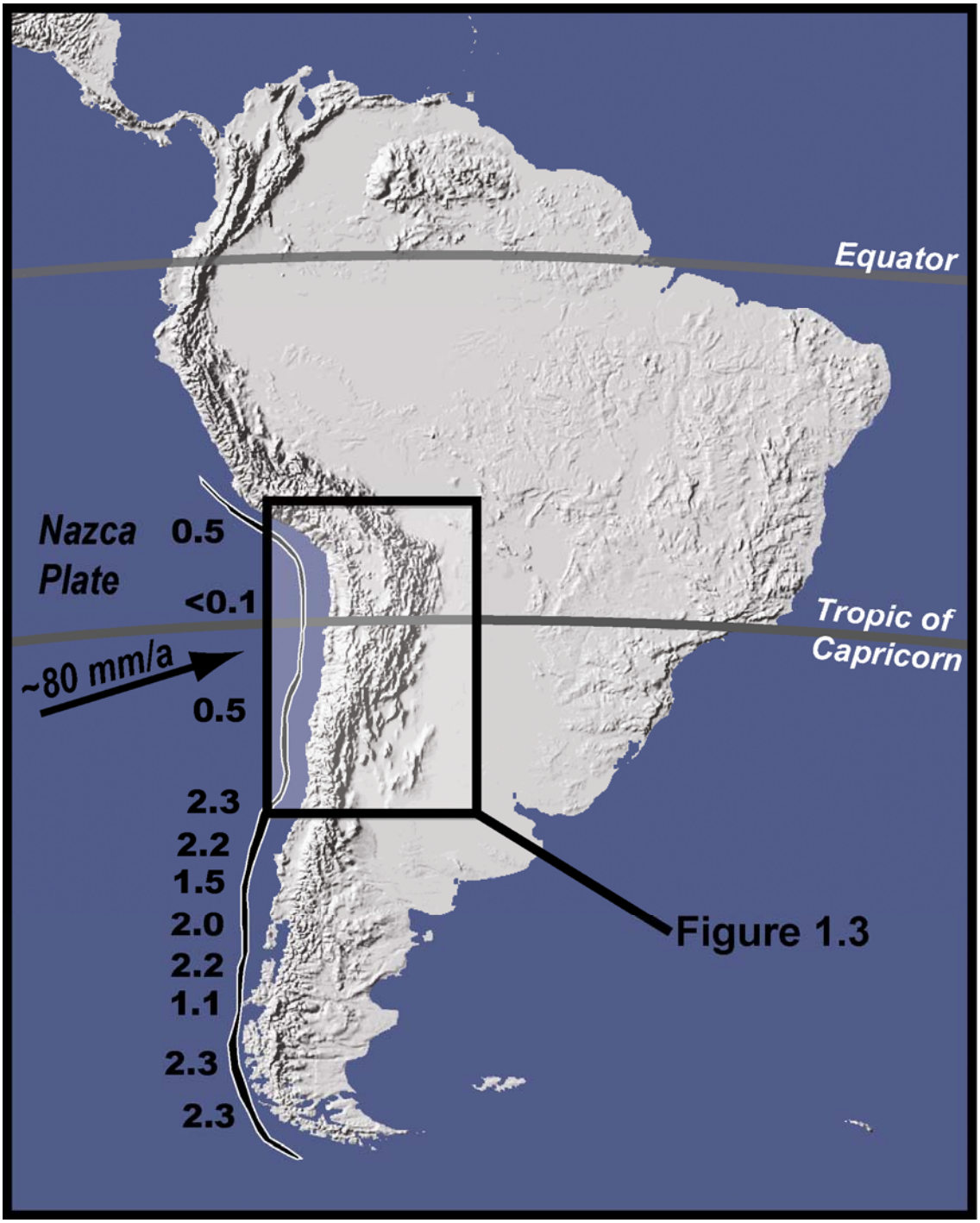

Figure 1.1: Shaded relief map of South America from GTOPO30 data. The Central Andean plateau, highlighted in the box, corresponds to the area of Figure 1.3. The approximate location of subduction is indicated by the trench. Kilometers of sediment-fill thickness (from Bangs and Cande, 1997) are denoted along the length of the trench.

Except at the northernmost and southernmost ends, the subduction zone is comprised of the oceanic Nazca plate moving to the northeast at 3–4 cm/year and the overriding South American plate moving to the west at comparable rates (Marret and Strecker, 2000). Sediment supply to the oceanic trench demarcating the Nazca-South America plate boundary varies greatly along strike (Bangs and Cande, 1997). This results in dramatic differences in sediment-fill thickness and potentially important differences in the coupling between the two plates. Lamb and Davis (2003) have proposed that arid climates reduce sediment supply to the trench resulting in stronger plate coupling, more efficient transfer of shear stress to the mountain belt, and ultimately enhanced uplift.

The geometry of the subducting Nazca plate beneath South America changes along strike. Some segments of the Nazca plate dip eastward at ~30°; whereas other segments dip much more shallowly. Among other factors, the flat-subducting sections of the Nazca plate have been correlated to aseismic ridges, seamount chains, and associated seafloor topography (Pilger, 1981; von Huene and Ranero, 2009). Regardless of cause, flat-subducting segments are associated with notable changes in continental tectonics (Jordan *et al*., 1983). Cessation of arc volcanism and changes in the style of continental deformation are spatially related to flat-subducting segments. The study area of this thesis, ~26.5–28°S, overlies a gradual transition zone in the dip of the subducting Nazca plate. To the north of the study area lies the Altiplano, bounded on the east by a thin-skinned fold-thrust belt and underlain by a slab subducting at a dip of 30° (Figure 1.2a). To the south, inland topography is dominated by the thick-skinned deformation of the Sierras Pampeanas and a flat-subducting slab is present (Figure 1.2b).

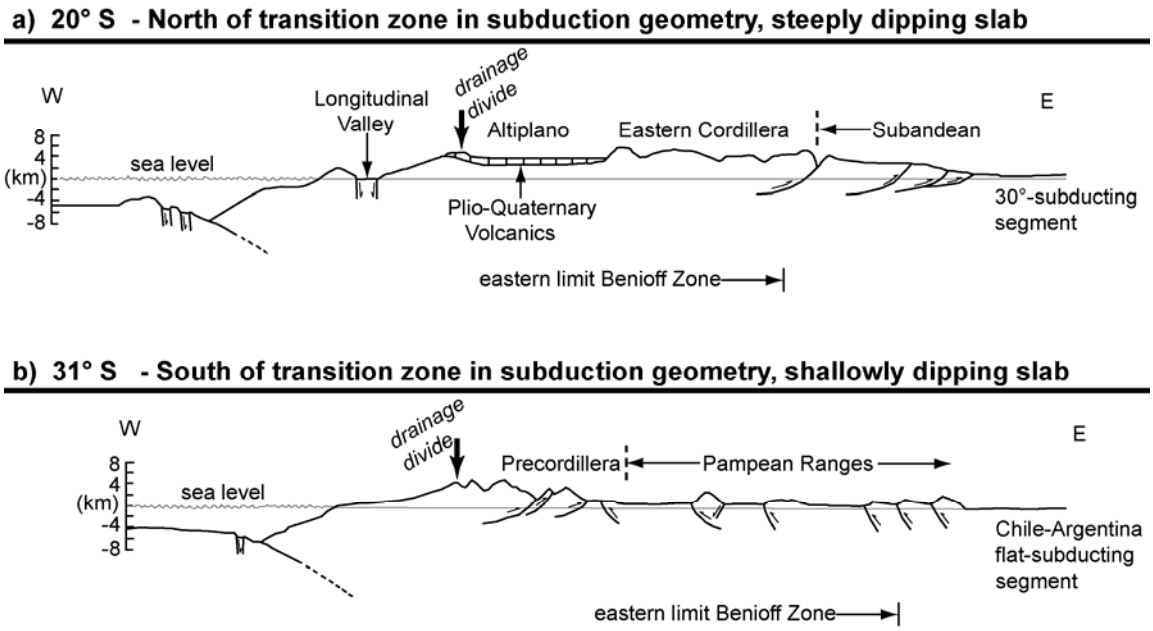

Figure 1.2: Topographic profiles and structural cross sections, reprinted with permission from Jordan *et al*. (1983).

What is the Puna plateau?

The Puna is a high volcanically active plateau in northwestern Argentina whose topography is characterized by basins and ranges (Figure 1.3). Volcanism on the Central Andean plateau is extensive and diverse, being dominated on the west by stratovolcanoes of the frontal magmatic arc. Young back-arc mafic rocks are widely distributed throughout the plateau (Kay *et al*., 1994). Both large and small silicic calderas are also present (de Silva and Francis, 1991). One of the world's largest silicic calderas, Cerro Galán, is an important feature of the southern Puna plateau that was first recognized with spacecraft imagery (Francis *et al*., 1978, 1983, 1989). An accurate geochronology of the most recent explosive silicic volcanism at Cerro Galan and associated mafic flows is just emerging (Kay *et al*., in press; Risse *et al*., 2008). The youngest silicic ignimbrite from this volcanic center is very precisely dated at 2.06 Ma (Hynek *et al*., 2011).

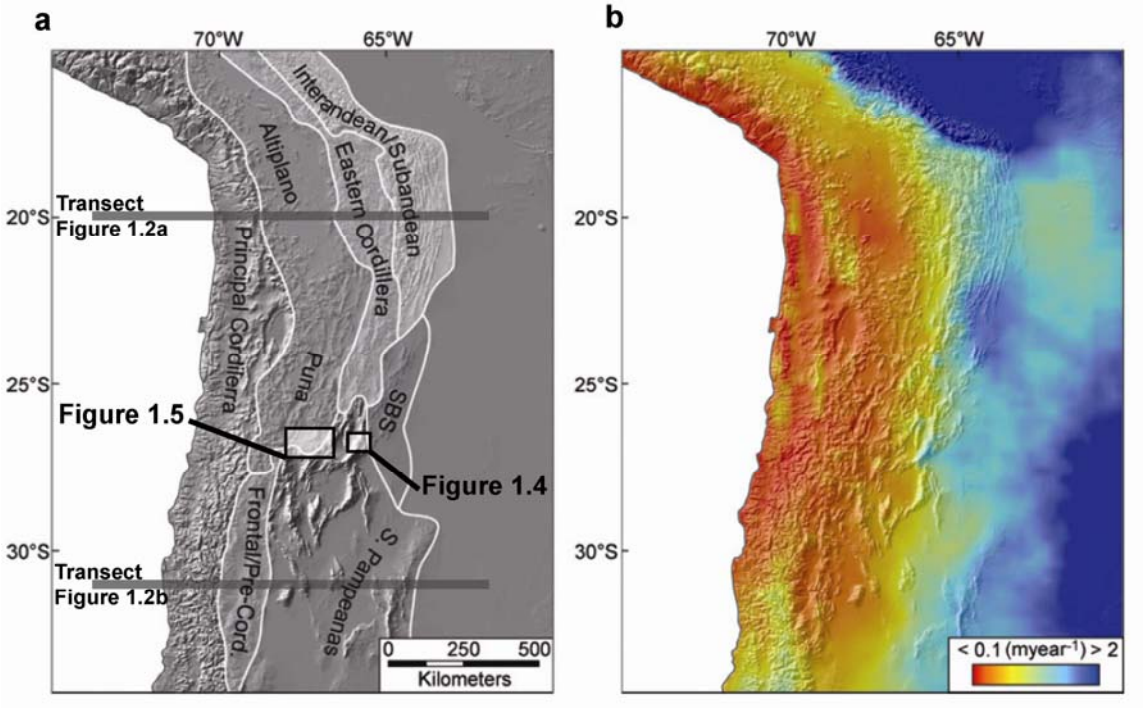

Figure 1.3: Tectonic and climatic setting of the study area reprinted with permission from Strecker *et al*. (2007a); **a)** shaded relief map and principal morphotectonic provinces (after Jordan *et al*., 1983), **b)** Mean annual rainfall distribution from the Tropical Rainfall Measurement Mission (TRMM) satellite, calibration of rainfall amounts described in Strecker *et al*. (2007a). Transects highlighted in **a)** correspond to those presented in Figure 1.2 of this dissertation, and boxes shown in **a)** denote the locations depicted in the following two figures of this chapter.

The basins and ranges of the Puna create high relief which is in marked contrast to the Altiplano of Bolivia. The basins commonly contain volcanic, clastic, and evaporite deposits 3–5 km thick (Alonso *et al*., 1991). Internally drained, evaporite depositional centers have existed in the region since ~15 Ma (Vandervoort *et al*., 1995). This dissertation focuses on the geologic record contained in structurally similar intermontane basins along the plateau margin, which are currently externally drained. These basins are associated with contractional deformation during the late Miocene and Pliocene, and may represent an early stage of plateau growth (Coughlin *et al*., 1998).

Concentration of precipitation along the eastern flanks of the plateau is documented by climatological data (WMO, 1975), and by more recent Tropical Rainfall Measurement Mission (TRMM) satellite observations (Figure 1.3b; Bookhagen and Strecker, 2008). Most of this precipitation falls during the summer months, and is believed to originate in the Amazon lowland, being advected southward by the South American low-level jet (Strecker *et al*., 2007a). The localization of precipitation on the eastern flanks of a topographic barrier is especially obvious across the Sierra Aconquija at ~26°S latitude where vegetative cover responds strongly to precipitation (Figure 1.4). Stable isotope proxy data from the leeward side of the Sierra Aconquija (Kleinert and Strecker, 2001) and apatite fission track thermochronology of the Sierra Aconquija bedrock (Sobel and Strecker, 2003) are both believed to record initial uplift at ~6 Ma and the development of this orographic rainshadow by ~3 Ma. This example of topographic control on climatic and ecologic gradients is extreme, yet characteristic of the region.

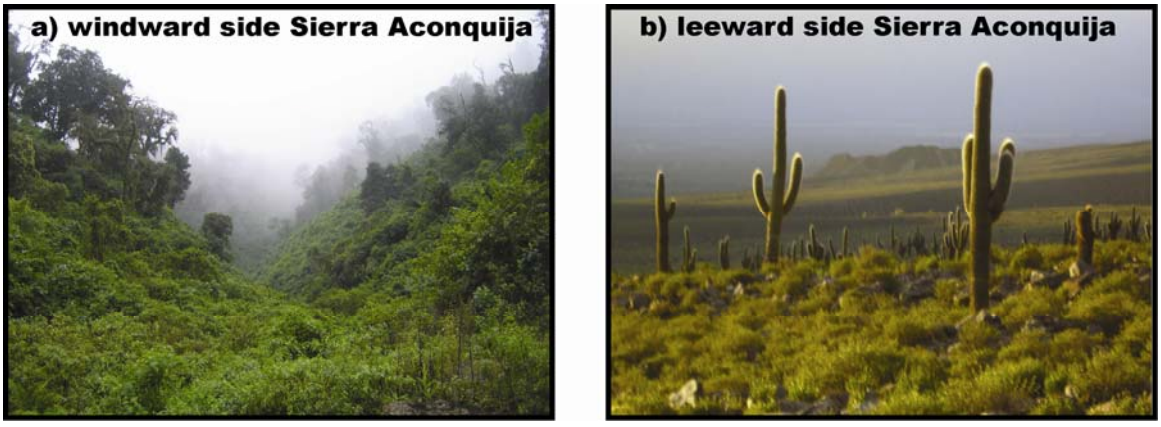

Figure 1.4: Representative vegetation on the windward and leeward side of the Sierra Aconquija; **a)** subtropical rainforest at ~1,300 m elevation along the east facing (windward) flank of the range, **b)** semi-arid intermontane basin at ~1,800 m elevation on the west facing (leeward) side of the range. These two sites are separated by less than 50 km along an east to west transect which corresponds to an approximately 3–4 fold decrease in mean annual rainfall.

Thus, tropical moisture drawn to the latitude of the southern Puna is effectively blocked from the interior of the plateau by the series of orographic barriers on its eastern margin. Moisture flux to the plateau appears to be funneled through topographic lows and to respond to short term climatic variations (Bookhagen and Strecker, 2008). However, sedimentary and geomorphic records of lake type and lake level indicate that the Puna remained relatively arid during the last glacial cycle compared to the Chilean Atacama Desert or the Bolivian Altiplano (Godfrey *et al*., 2003; Placzek *et al*., 2006). A glacial chronology for the region is essentially nonexistent; however, during Pleistocene glaciations moisture flux to the plateau appears to have increased. Glacial landforms and the modern snowline document westward increases in elevation, suggesting that easterly moisture sources have remained important at this latitude throughout the recent past (Haselton *et al*., 2002). In the plateau interior and along its western margin, evidence for glaciation is lacking for many peaks attaining elevations between 5,500–6,000 m.

The general east to west aridity gradient continues to the hyper-arid climate of northern Chile which has existed intermittently for the last 10–15 Ma (Houston and Hartley, 2003). Westerly circulation over the plateau is unlikely to be moisture bearing, but its influence on the plateau is profound nonetheless. Wind sculpted features in ignimbrite sheets of the southern Puna indicate strong northwesterly oriented wind regimes since at least 2 Ma (Greene, 1995). In some localities the wind sculpted ignimbrites are associated with the largest known wind ripples on Earth (Milana, 2009). These extreme geomorphic features have been explored as terrestrial analogs to Martian geomorphic features (de Silva *et al*., 2010; de Silva, 2010; Milana *et al*., 2010). This strong westerly circulation is manifested as dune fields in intermontane basins at the

plateau margin, further afield as loess deposits, and possibly as significant dust contributions to South Atlantic sediments and East Antarctic ice (Gaiero, 2007).

The modern tectonic and geomorphic setting of the southern Puna margin is particularly well exemplified by the Cerro Blanco volcanic complex (Figure 1.5). The Cerro Blanco volcanic complex, is characterized by at least two young collapse calderas and several lava domes (Arnosio *et al*., 2005). The Cerro Blanco caldera was observed to subside rapidly (2.5 cm/year) during the 1990s and is the only subsiding volcano of more than 900 Central Andean volcanic centers studied (Pritchard and Simons, 2002). Pritchard and Simons (2004) suggest that the subsidence is caused by a cooling magma chamber (9–14 km depth) and associated hydrothermal systems. Recent volcanic activity is attested to by the Campo de la Piedra Pómez ignimbrite, and younger unconsolidated ignimbrites to the south and west of the volcanic center (Arnosio *et al*., 2008).

High rates of eolian erosion on the Puna are documented by the Campo de la Piedra Pómez ignimbrite (Figure 1.5b), which is dated at 44.1 ± 2.2 ka by $^{40}Ar/^{39}Ar$ analysis of sanidine (Appendix A). This young, moderately welded, ignimbrite is extensively exposed on the southernmost Puna plateau where it is dissected into northwest-southeast oriented yardangs. Erosional relief of 10 m is observed for mature yardangs and an estimated 5 m of thickness has been removed from the ignimbrite since eruption (de Silva *et al*., 2010). If this erosion is averaged over the 44 ka since emplacement, minimum long-term eolian erosion rates of >10 cm/ka are implied.

The influence of northwesterly atmospheric circulation over the Puna plateau and resulting erosion and sediment evacuation is well documented in the Corral Quemado basin (Figure 1.5c, d). Extensive dune fields are present in hanging valleys of the plateau

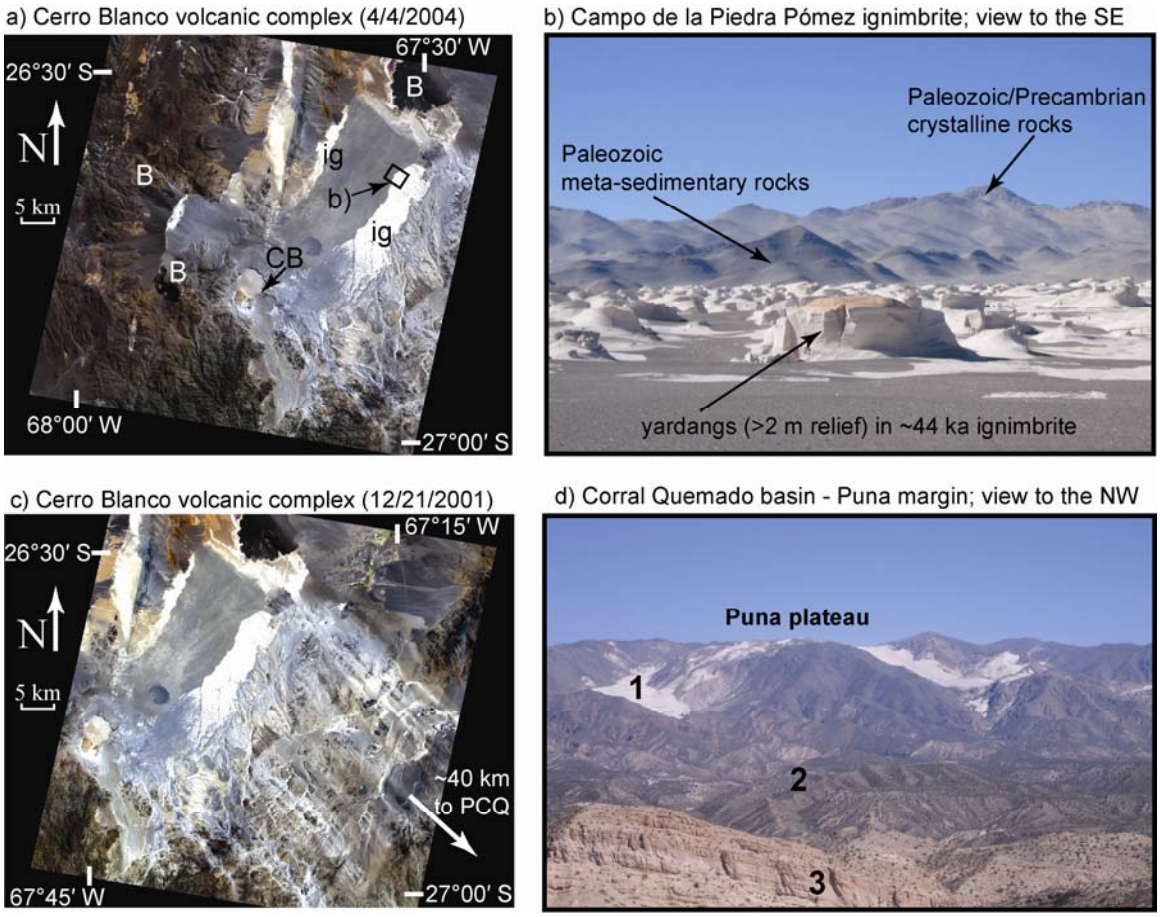

Figure 1.5: Field photographs and ASTER (http://ava/jpl.nasa.gov/) images of the southern Puna plateau margin: **a)** image depicting the Cerro Blanco volcanic complex (CB), the Campo de la Piedra Pómez ignimbrite (ig), and Quaternary basaltic and basaltic-andesite flows (B), **b)** photograph of the ignimbrite illustrating wind erosion into elongated swales (yardangs), **c)** image depicting transport of wind eroded material to the southeast, **d)** the intermontane Corral Quemado basin at the Puna margin, *1)* eolian deposits derived from the Puna, *2)* Quaternary range front gravels and terraces disconformably overlying *3)* Miocene and Pliocene continental strata.

margin and eolian deposits are found throughout the modern basin. Quaternary pediments and fluvial terraces host soils with extremely thick Av horizons, indicating high rates of eolian deposition (cf. McFadden *et al*., 1987). The modern and recent eolian systems of the region provide an important analog for the ~2.5 km thick Puerta de Corral Quemado stratigraphic section, which records Mio-Pliocene eolian deposition, with extensive dune fields present from ~7–6 Ma (cf. Chapter 2).

How did the Puna plateau form?

Along the margins of the southern Puna plateau, vigorous Pliocene deformation of the upper crust is documented by deposition of syntectonic conglomerates, as well as folding and faulting of Mio-Pliocene deposits. This surficial expression of tectonic activity is broadly synchronous along the plateau margin throughout the study area encompassed by this dissertation (~28–26.5°S). In contrast to the plateau margins, relatively minor deformation is observed within the plateau after 10 Ma, although abundant evidence exists for surface uplift on the order of 2 km between 10–6 Ma (Hoke and Garzione, 2008). Most data regarding plateau uplift pertain to the Altiplano; substantially less information exists regarding the uplift of the Puna. Therefore much of the following discussion is comparative. The Puna and Altiplano share many similarities, including a dramatic Mio-Pliocene uplift history; however, their paths to the present state differed (cf. Allmendinger *et al*., 1997).

Several processes have been implicated in formation of the Puna-Altiplano plateau. These processes, by no means mutually exclusive, have been put forward as general models to explain the genesis of this enigmatic geologic province. The mechanics of building and supporting a vast high altitude plateau are poorly understood and simple models are useful for conceptualizing relevant processes. Regarding the southern Puna, Allmendinger (1986) summarized potential plateau uplift mechanisms (Figure 1.6). Observations of upper crustal fault geometries in this study, favor a structural model of distributed shortening leading to crustal thickening rather than underthrusting of the stable craton beneath the orogenic belt.

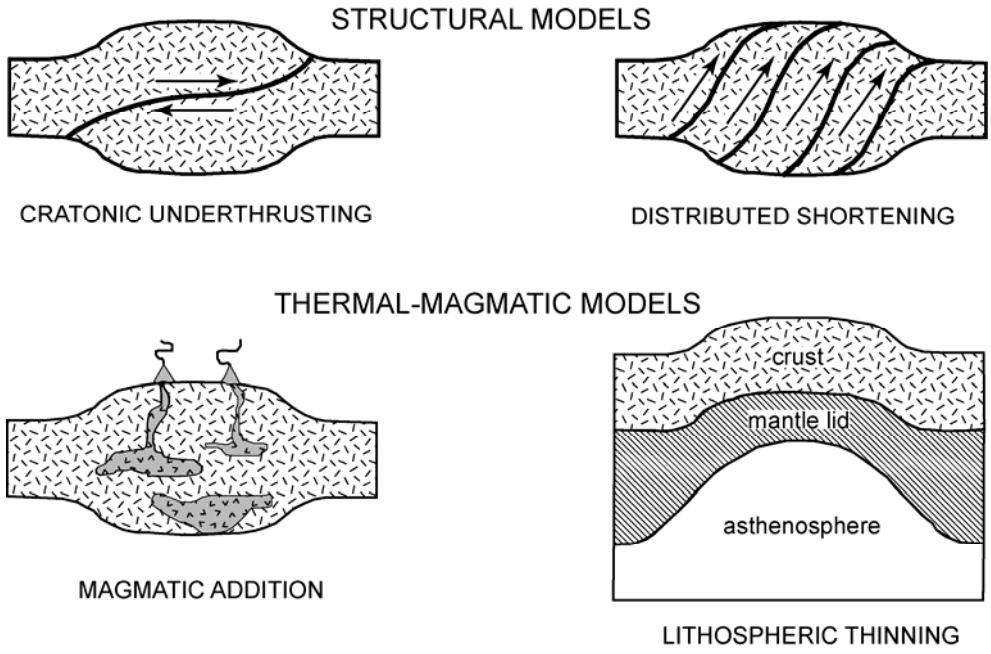

Figure 1.6: Cartoon models of continental plateau uplift (reprinted with permission from Allmendinger, 1986.)

Comprehensive models for deformation within the Central Andes and uplift of the Puna-Altiplano plateau rely on a combination of crustal thickening and lithospheric thinning (Isacks, 1988). A majority of crustal thickening (70–90%) is attributed to shortening, leaving a minor role for magmatic addition in supporting the expansive topography of the plateau (Allmendinger *et al*., 1997). Isacks (1988) proposed a two-stage model for crustal thickening, the first stage dominated by distributed shortening and the second characterized by underthrusting of the foreland beneath the plateau by shortening of the ductile lower crust. This two-stage model is attractive because it produces recent uplift of a low relief, internally drained plateau with minor surface deformation of the plateau interior. This two-stage model has been shown to be viable for the Altiplano (Gubbels *et al*., 1993), but unlikely for the Puna, which exhibits little evidence of underthrusting (Allmendinger and Gubbels, 1996).

Recent geophysical data also suggest that the two-stage model, which relies on underthrusting of the craton beneath the plateau, is viable for the Altiplano. Of particular interest is a regionally extensive, rheologically weak layer observed as a thin horizon at ~20 km depth below the Altiplano (Chmielowski *et al*., 1999; Beck and Zandt, 2002; Oncken *et al*., 2003). This weak mid-crustal layer may serve to decouple the upper and lower crust, effectively permitting underthrusting from the east and geodynamically isolating the brittle upper crust. Beck and Zandt (2002) indicate that the crust underlying high topography is thick and has a felsic to intermediate bulk composition. They further suggest that the lower crust is ductile, and that underthrusting from the east has penetrated beneath the plateau margin, but does not penetrate beneath the entire Altiplano. It is also suggested that dense sub-crustal lithosphere is delaminating beneath the Altiplano, thereby reducing lithospheric thickness, accommodating inflow of upper and mid-crustal material beneath the plateau and resulting in the "felsification" of continental crust (Beck and Zandt, 2002).

In a recent review of evidence for the rapid Mio-Pliocene uplift of the Altiplano, Hoke and Garzione (2008) provide an updated conceptual review of the possible geodynamic processes responsible for plateau formation (Figure 1.7). This analysis was aimed at determining which geophysical models are capable of producing a hypothesized 2.5 km of surface uplift between 10–6 Ma. In this instance, proposed models of plateau uplift are essentially constrained by the rate at which they proceed. Crustal shortening alone appears incapable of producing plateau uplift. As proposed by Hoke and Garzione (2008), the second, underthrusting, stage of Isacks' (1988) model represents a combination of crustal thickening (Figure 1.7a) and mass redistribution by

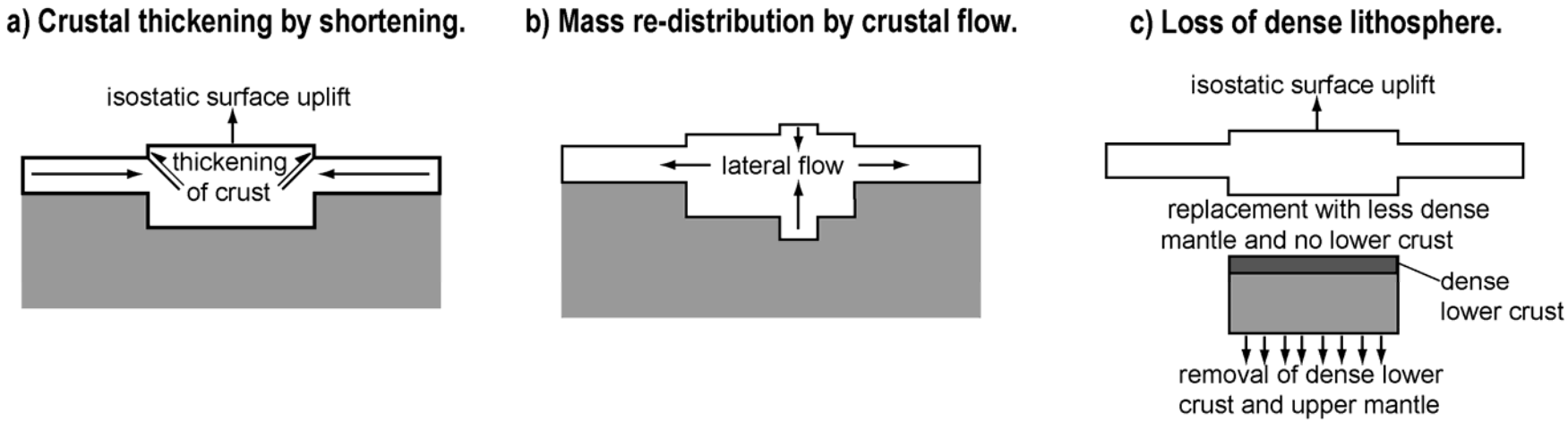

Figure 1.7: Conceptual models for rapid, large magnitude, surface uplift of the Altiplano plateau (reprinted with permission from Hoke and Garzione, 2008).

crustal flow (Figure 1.7b). Various modes of mass redistribution by crustal flow have been proposed for the Altiplano (Husson and Sempere, 2003; Hindle *et al*., 2005), but Hoke and Garzione (2008) prefer to implicate removal of the lower lithosphere (lower crust and upper mantle; Figure 1.7c) in the late Miocene uplift of the Altiplano. In discussing mechanisms of lower lithosphere removal, they disregard ablative subduction (e.g., Pope and Willett, 1998) and focus instead on mechanisms driven by gravitational instability (Kay and Kay, 1993; Molnar and Houseman, 2004). Removal of dense lower lithosphere and influx of hot, buoyant, asthenospheric mantle is equivalent to lithospheric thinning (Figure 1.6). Lithospheric thinning and thermal isostatic effects are smaller than those of lithological density variations, but conform well to geologic observations for the plateau (Froidevaux and Isacks, 1984).

Disentangling the various geodynamic models of plateau formation is not an especially tractable problem given the data presented in this dissertation; however, an interesting paradox presents itself. The Altiplano portion of the Central Andean plateau is hypothesized to have uplifted rapidly by isostatic adjustment to removal of dense lower lithosphere, but the strongest evidence for removal of the lower lithosphere is documented in the southern Puna portion of the Central Andean plateau.

It has been suggested that magmatic rocks provide the most enduring and unequivocal evidence for delamination (Kay and Kay, 1993). Mafic lavas in particular have been explored as a proxy for lithospheric delamination and influx of fresh asthenospheric mantle. Basaltic rocks of intraplate type are found in a zone overlying the proposed lower lithospheric delamination of the southern Puna. This zone is ringed by

mafic rocks of calc-alkaline affinity, and north of approximately 24°S, mafic lavas are shoshonitic (Kay *et al*., 1994). These high potassium basaltic rocks continue across the Altiplano (Davidson and de Silva, 1992) to its northernmost termination, where mafic rocks of ultra-potassic composition are described (Carlier *et al*., 2005). It has been argued, that the zone of basaltic and silicic volcanic rocks centered about 26°S is a signal of lithospheric delamination (Drew *et al*., 2009; Kay, 2010).

Approximately 1/3 of the available age estimates for volcanic rocks in the Central Andes are samples from the southern Puna between 25–27°S (cf. Trumbull *et al*., 2006). These radiometric data provide a first approximation of the most recent volcanic history in the region (Figure 1.8). Several observations relevant to delamination, volcanism, and regional geology over the last 10 Ma can be made: 1) the age distribution of rhyolitic and dacitic rocks associated with the volcanic arc is approximately constant, 2) eruption of basaltic and andesitic rocks in the volcanic arc may document a transient increase between 6–5 Ma, and 3) mafic back-arc volcanism and the Cerro Galán caldera commenced eruption at ~6 Ma. This period also produced intraplate volcanic rocks 300 km west of the main arc, and 170 km west of the plateau margin (Gioncada *et al*., 2010).

While excellent age control exists for volcanic rocks in the southern Puna plateau, geophysical data are sparse by comparison. Existing geophysical data demonstrate that the southern Puna is the region of thinnest crust beneath the plateau, perhaps as little as 40 km thick (Yuan *et al*., 2002; Tassara *et al*., 2006; McGlashan *et al*., 2008). This is consistent with a lower crustal delamination event as an important mechanism for the generation of widespread back-arc mafic volcanism on the plateau since 7 Ma.

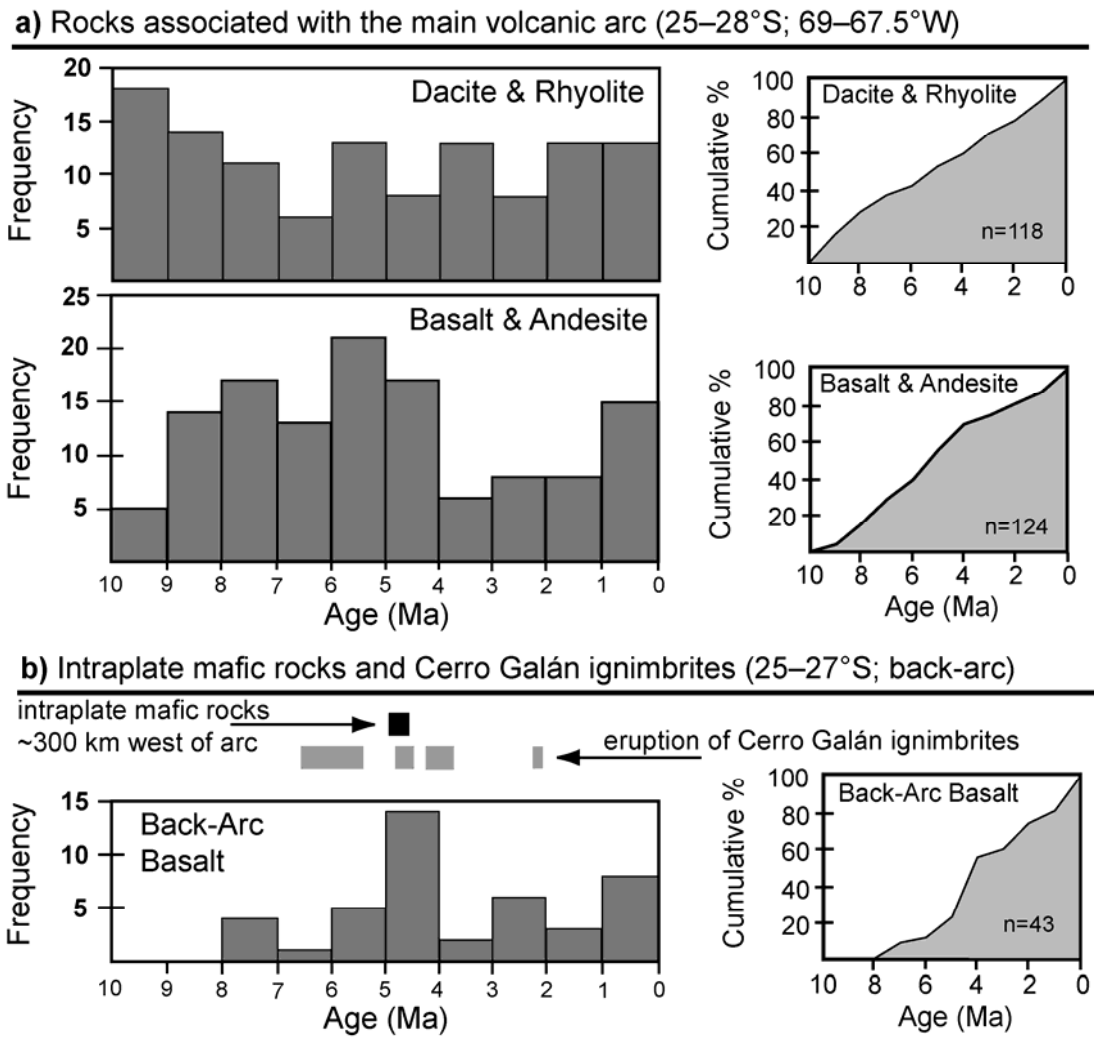

Figure 1.8: Frequency-age histograms and cumulative percentages plots for volcanic rocks <10 Ma in the study area; **a)** data from Trumbull *et al*. (2006), **b)** data from Risse *et al*. (2008), Kay *et al*. (2010 and *in press*), and Gioncada *et al*. (2010).

The back-arc magmatic pulse documented by mafic lavas between 25–27°S, and by volcanic history at Cerro Galan caldera currently provides the strongest evidence for lower lithospheric delamination of any locality in the region (Kay and Coira, 2009). This is ~750 km removed from the observations indicating rapid surface uplift of the Altiplano, and any mechanistic link between the two is precluded. Geophysical understanding of the Altiplano is significantly greater, as is the direct evidence of plateau

uplift; however, the evidence for large scale delamination events beneath the Altiplano is not strong (Beck and Zandt, 2002; Hoke and Garzione, 2008). Conversely, the magmatic understanding of the southern Puna is significantly more advanced. The age data shown in Figure 1.8 provide an opportunity to compare surficial geologic data directly with the proposed tectonic models for plateau formation, by using volcanic rocks as a proxy for tectonic processes. Constraining the timing of geological proxy records for surficial tectonic and climatic events will yield more meaningful comparisons with the magmatic record of the southern Puna and with the paleoenvironmental record of the Altiplano. Developing a high resolution paleoenvironmental record for the southern Puna margin and facilitating its comparison with other data is the primary goal of this dissertation.

Geologic record of the southeastern Puna plateau margin

This dissertation is guided by the principle that models and theories must not violate geological observations. Extensively exposed and exceptionally thick sedimentary records preserved along the southern and eastern margins of the Puna plateau are investigated. These sedimentary records contain continental deposits commonly in excess of 1 km thick and generally span much of the late Miocene and Pliocene epochs (~10–3 Ma).

As discussed, this temporal interval includes the proposed rapid uplift of the Central Andean orogenic plateau (Garzione *et al*., 2008) and is also a period of global ecologic change (Cerling *et al*., 1997). Utilizing the geologic record of continental sedimentation, two primary types of information are documented; 1) paleoenvironmental proxy data relating to climate, depositional environment, and the ecology of plants and

herbivores, and 2) geochronology of volcanic ash beds intercalated with paleoenvironmental proxy data.

Paleoenvironmental proxy data

Stable isotope proxies for climate and ecology provide the most widespread, abundant, and high resolution data available for the region. Materials studied include soil carbonate, tooth enamel, snail shell, diagenetic carbonate, and water. The isotopic composition of carbonate was measured in CO_2 liberated by phosphoric acid digestion. A subset of tooth enamel samples were analyzed by laser ablation, which, unlike acid digestion,samples both the carbonate and phosphate components of the enamel.

Temporal intervals sampled. Three temporal intervals are represented by stable isotope data. Wherever possible, paleosols and fossil tooth enamel were sampled from localities with interstratified volcanic ash beds. In the absence of absolute age estimates, these data still provide a temporal record of climate and ecology based upon the principle of stratigraphic superposition. The extent of these data is over the interval from 9–3 Ma. The second temporal interval investigated is from ~2 Ma–present; these samples are associated with geomorphic features interpreted as relict land surfaces. These features are pediments or fluvial terraces high above modern river level, comprising a veneer of coarse-grained sediments disconformably overlying Mio-Pliocene strata (cf. Figure 1.5d). In most cases the ages of these geomorphic surfaces are poorly known at best, so assembling a precise time-series of stable isotope data is precluded. The third group of samples presents modern isotopic data for a variety of materials. Samples of water, terrestrial gastropods, and tooth enamel can reliably be assumed to represent the modern

environment. Soil carbonate on modern land surfaces can not be strictly interpreted as modern, but most likely represents the Holocene (<10 ka).

Stable isotopes in soil carbonate. Soil and paleosol carbonate are interpreted in the framework put forth by Cerling (Cerling; 1984; Cerling *et al*., 1989; Cerling and Quade, 1993). The carbon isotopic composition of soil carbonate is interpreted in terms of the proportion of C_3 and C_4 vegetation present at a location, recognizing that formation depth of soil carbonate and soil respiration rates are extremely important considerations. A first order assumption is that C_4 plant ecosystems are dominated by tropical grasses, and are most successful under conditions of water stress, low elevation, low concentrations of atmospheric CO_2, and warm growing season (Ehleringer *et al*., 1997). The oxygen isotope composition of soil carbonate relates to the isotopic composition of soil water *and* the temperature of carbonate formation. These confounding variables are further complicated by processes that modify the composition of soil from that of meteoric water (i.e., evaporation). Thus, oxygen isotopic data must be interpreted as a balance between precipitation input and soil water evaporation in which the signal is modified by the temperature of carbonate formation. The isotopic composition of soil water is, at best, difficult to reconstruct and reconstructing the isotopic composition of meteoric water is one step further removed.

Spatial scale represented by soil carbonate data. A distinct advantage of isotope proxy data from paleosol carbonates is that the signal is integrated over a relatively small land area, probably 10–100 m^2 (Quade *et al*., 2007). The estimated proportion of C_3 to C_4 vegetation is a function of the below ground biomass at this scale, and landscape variations in ecosystem composition can be recorded by carbon isotopic

data (cf. Behrensmeyer *et al*., 2007). Input to the soil water oxygen isotope system is at a similar spatial scale, assuming precipitation as the dominant isotopic contribution.

Age of soil carbonate on abandoned geomorphic surfaces. Interpreting soil carbonate formed on long-lived geomorphic surfaces presents its own set of challenges. The age of the surface and the age of the carbonate are two different parameters, which do not have a strict relationship. Soil formation continues from the inception of these land surfaces to present, and isotopic data may realistically integrate this whole period, or some unknown portion of it. Given the age of many of theses surfaces, soil carbonate can record 0.1–1.0 Ma of time. This is a period long enough to record long-term ecological change as well as incorporate several glacial-interglacial transitions in plant communities. Often, the soil carbonate on these surfaces is in the form of laminated pendants which underlie cobbles or boulders. These laminations have measurable isotopic differences, and may provide an internal stratigraphic record of carbonate formation. Temporal control on isotopic records derived from ancient geomorphic surfaces in northwestern Argentina is poorly established, but given the internal lamination of many soil carbonates and accounting for the relative height of a geomorphic surface above the modern river level, a crude time series can be constructed. Concerted effort to establish ages for geomorphic surfaces and associated carbonate would improve this situation.

Lack of age control on geomorphic surfaces does not present the biggest problem with extending the isotopic record from ~3 Ma–present. The soils formed on relict land surfaces are fundamentally different from those in the stratigraphic record (Figure 1.9). These two types of soil carbonate form in different landscape positions. Paleosols in the stratigraphic record are generally interpreted to have formed on floodplains or alluvial

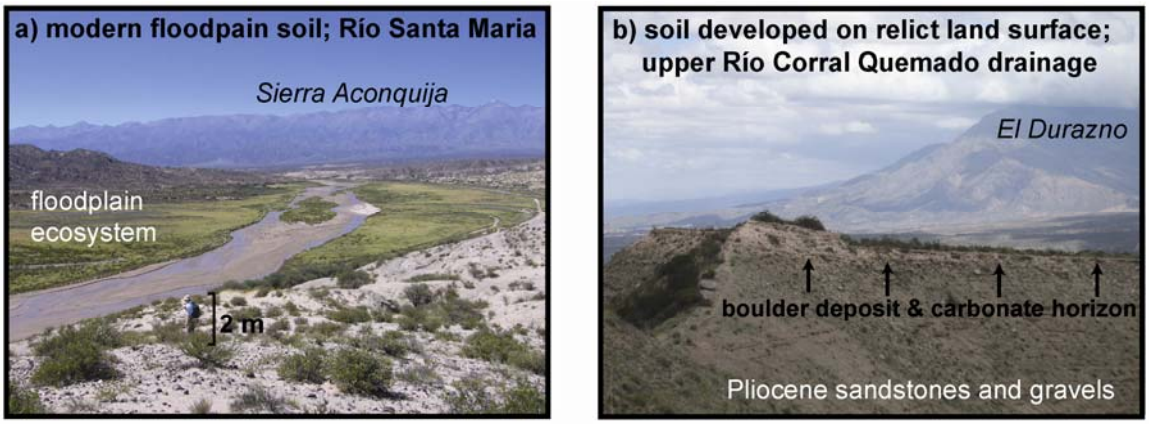

Figure 1.9: Modern soil forming environments in northwestern Argentina; **a)** floodplain soil in which water availability results in a riparian ecosystem, **b)** soil on a relict land surface, isolated from the modern depositional system and from range-front topography, resulting in protracted soil formation under water limiting conditions. The surface in **b)** is composed of basalt boulders unconformably overlying Pliocene (~3.5 Ma) sandstones.

plains. These soils form in aggradational sedimentary settings during periods of reduced sedimentation. Eventually a sedimentary event(s) buries the soil and largely quenches formation processes. In this manner, paleosols represent a discrete period of formation that is associated with fluvial or alluvial sedimentary systems at topographically low points in the landscape. These sedimentary systems implicate a nearby water source, at least intermittently, and exert some control over vegetation. This is quite distinct from soil formation on abandoned geomorphic surfaces, which is protracted and occurs on local topographic highs isolated from modern hydrological catchments. The ecology of these surfaces is different than that on adjacent floodplains.

Isotopic interpretation of soil carbonate on geomorphic surfaces. As discussed, the interpretation of carbonate isotopic data from soils on long-lived geomorphic surfaces is hampered by problems of age control and landscape ecology. Two specific issues related to the isotopic composition of soil carbonate can be identified. Firstly, the ecology of high geomorphic surfaces can be quite different from that of

nearby environments; this is particularly notable in the Santa Maria valley where the cactus *Trichocereus atacamensis* (pasacana) is limited to upland hillslopes, pediments, and terraces (cf. Figure 1.4b). This large cactus employs Crassulacean Acid Metabolism (CAM) photosynthesis. All cacti use this photosynthetic pathway to acquire atmospheric CO_2 for growth, yet the specific implications of CAM photosynthesis for carbon isotope studies of plant tissue are still being delineated (Dodd *et al*., 2002; Black and Osmond, 2003; Griffiths *et al*., 2007; English, 2008). Carbon isotope discrimination of CAM plants is intermediate to that of C_3 and C_4 plants, thus, soil carbonates with significant CAM contributions are not interpretable with a C_3/C_4 mixing model. Practically speaking, humid C_3 ecosystems can be positively identified, but the isotopic signatures of water-stressed C_3 plants, CAM plants, and C_3/C_4 mixtures are very similar.

Trichocereus atacamensis is a particularly drought tolerant species which prefers well drained soils. The surfaces which host *T. atacamensis* are covered by coarse alluvium and consequently well drained. This soil physical property raises two difficulties in interpreting isotopic data: 1) these high permeability soils are much more susceptible to soil water evaporation (oxygen isotopic effect), and 2) the combination of high permeability and low soil respiration rate raises concerns of atmospheric CO_2 contributions to soil carbonate (carbon isotopic effect).

Stable isotopes in tooth enamel. Both observational (Cerling and Harris, 1999) and experimental data (Passey *et al*., 2005a) document a predictable carbon isotope relationship between diet and tooth enamel. This implies that tooth enamel is a faithful recorder of diet in modern environment. Fossil tooth enamel retains a robust record of dietary composition, even under strong diagenetic influence (Wang and Cerling, 1994).

As such, a number of ecological and paleoecological questions can be generated and addressed. Dietary specialization is commonly documented, and it is shown that grazing animals such as horses were among the first herbivores to adapt to the ecological expansion of C_4 grasses in the late Miocene (Wang *et al.*, 1994; Passey *et al*., 2002). By selective feeding, herbivores can document the presence of C_4 vegetation when soil carbonate data are difficult to interpret. Behavioral differences among herbivores provide a proxy for mixed C_3/C_4 ecosystems that is also unambiguous. Comparison of tooth enamel and soil carbonate data yields complementary information on the landscape scale distribution of plants using different photosynthetic pathways. This approach is necessary to understand local and regional paleoecologic complexities, cast them in a global context, and to address the influence of growing topography on the late Miocene and Pliocene ecology of northwestern Argentina.

Isotopic time series in tooth enamel. Serial analysis of modern and fossil teeth provides valuable insights into short term temporal changes in the diet and body water composition of herbivores (Passey and Cerling, 2002; Passey *et al*., 2005b). The ability to recover a high resolution time series from a single tooth presents several opportunities for understanding paleoclimate and paleoecology. Temporal variation within a tooth may record ancient seasonality, though with larger mammals migration is a confounding variable. Analysis of small mammal fossils can increase confidence that the dietary signal is locally derived and that migration is a secondary concern. The home range of a small mammal is greater than the land area typically integrated by soil carbonate isotopic data and significantly less than that for large mammals. Given the richness of the South

American fossil rodent record (Simpson, 1980), and their under-representation in isotopic datasets, an effort was undertaken to incorporate small mammals into the study.

Laser ablation isotopic analysis of tooth enamel. Small teeth can be difficult to analyze by common phosphoric acid digestion methods, which typically require in excess of 500 µg of tooth enamel. Careful analysis by laser ablation produces carbon isotope results in agreement with conventional analyses and permits high spatial resolution sampling of small teeth (Passey and Cerling, 2006). More than 1/3 of the fossil teeth in this dissertation were analyzed by laser ablation. This has reduced the bias of the isotopic record towards large mammals and successfully identified high resolution variation is the diet of small mammals (Figure 1.10). These data have also filled in the stratigraphic record, enabling higher temporal resolution across >5 Ma of geologic time.

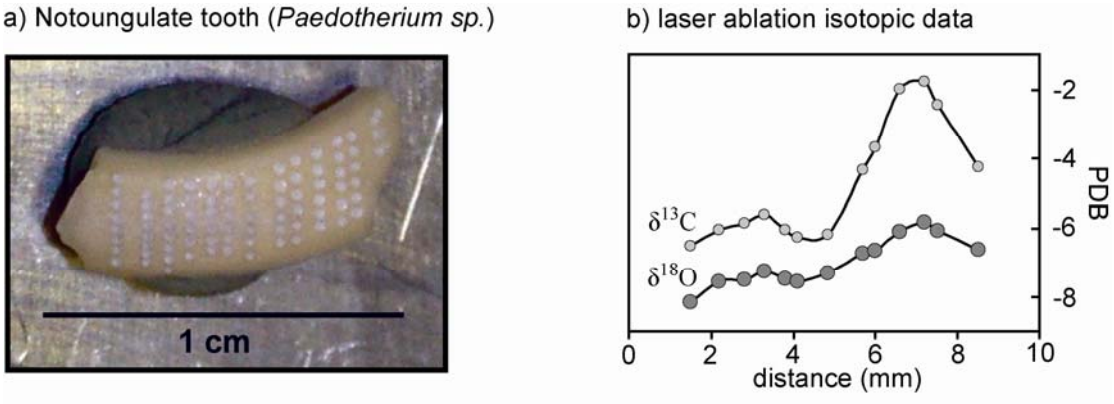

Figure 1.10: Laser ablation of small teeth: **a)** sample Arg-246, ~3.5 Ma hegetothere notoungulate tooth, each row of ablation craters corresponds to an isotopic analysis, and **b)** resultant isotopic profile, size of symbols approximates precision.

Geochronology of volcanic ash beds

Volcanic ash beds are common in the late Miocene and Pliocene continental deposits along the southern margin of the Puna plateau. Age data for volcanic ash beds are not as numerous as for volcanic rocks on the Puna, but radiometric age estimates for the eruption and deposition of high silica volcanic ashes are available. This constrains the age of deposits and fossils in the region, but few studies have undertaken a systematic approach to dating strata in the region. At Puerta de Corral Quemado, 2 km of strata with a magnetic polarity stratigraphy and multiple dated ash beds (via the K-Ar and $^{40}Ar/^{39}Ar$ methods) is the principal section of this dissertation (Butler *et al*., 1984; Latorre *et al*., 1997). To the south, in the Fiambalá basin, recent stratigraphic work has been undertaken with U-Pb zircon geochronology; these results constrain the age of the strata (Carrapa *et al*., 2008), and have improved chronological control of formation boundaries (McPherson, 2008). To the north, in the Angastaco basin, U-Pb zircon geochronology has also successfully improved age control of Mio-Pliocene strata and documents time-transgressive formation boundaries (Bywater-Reyes *et al*., 2010).

Integration of this age data into a coherent framework for the region is the principal aim of the geochronological efforts in this dissertation. When possible, stratigraphic sequences of volcanic ash beds have been collected and geochemically analyzed. Sequences of ash beds which contain one or more absolute ages can provide chronological control at other localities via identification and correlation of chemically similar ash beds. Volcanic glass has been separated and analyzed for its major, minor, and trace element composition to accomplish this. In concert, selected ash beds have been dated by $^{40}Ar/^{39}Ar$ geochronology.

$^{40}Ar/^{39}Ar$ geochronology. When the strata of interest are of unknown or poorly constrained age, minerals have been separated for $^{40}Ar/^{39}Ar$ geochronology from intercalated tuffs. Mineral separates were analyzed by single crystal laser fusion at the Rare Gas Geochronology Laboratory, University of Wisconsin-Madison. When possible sanidine was used, and provided excellent results. In the age range between 2.0–5.5 Ma, fully propagated external uncertainty at the 2σ level is ~0.2% of the measured age. A sanidine dated at 9.1 Ma is slightly less precise, yielding an uncertainty > 0.3%. Sanidine from a young ignimbrite (44 ka) exposed on the Puna plateau yielded an uncertainty of ~5%. For $^{40}Ar/^{39}Ar$ work, the precision and accuracy of sanidine is unsurpassed.

Unfortunately, sanidine is not always present, and other minerals must be employed for age dating. Coeval biotite-sanidine ages provide a basis for testing the fidelity of biotite $^{40}Ar/^{39}Ar$ geochronology in the region. The oldest age measured was a 9.4 Ma biotite age from the same sample that yielded a 9.1 Ma sanidine age. The biotite age is nearly as precise, but its accuracy is in question. The > 300 ka discrepancy is similar to bioitite-sanidine age discordances identified throughout the region (Hora *et al*., 2010) and suggests that $^{40}Ar/^{39}Ar$ analysis of biotite should be avoided if possible.

Plagioclase feldspar is an alternative to sanidine; however, $^{40}Ar/^{39}Ar$ ages are an order of magnitude less precise, yielding external 2σ uncertainties of 2–3% at 4 Ma. The uncertainty obtained for plagioclase (±100 ka) is equivalent to that obtained by U-Pb zircon results, and the two methods are in excellent agreement within the study area. Plagioclase is the most common and abundant mineral in the volcanic ash beds sampled; therefore, its inherent precision may dictate the temporal resolution of the geologic record in unfavorable circumstances.

Major element composition of volcanic glass. Broad patterns are discernable in the chemical composition of volcanic glass separated from ash beds (Figure 1.11). Nearly all analyzed samples are rhyolites or dacites following the total alkalis vs. silica classification of Le Bas *et al*. (1986). Dacitic ash beds are characterized by the highest Fe_2O_3 and CaO values, in addition to high Al_2O_3, TiO_2, and MgO concentrations. Rhyolitic ash beds have the lowest Fe_2O_3 and CaO values, and the highest SiO_2 content. Ash beds of intermediate composition and character are termed rhyodacites in this dissertation. The average composition and the mineralogy of ash beds are valuable descriptors, but microanalysis is imperative to document and account for shard-to-shard variation in composition. The intershard pattern of Fe_2O_3 and CaO, as determined by electron probe microanalysis, can be characteristic for a given ash bed, and is especially useful for identifying multiple compositional modes (Figure 1.11).

Rhyolite ash beds. Typically, rhyolite ash beds contain only a single compositional mode and can be differentiated from one another on the basis on Fe_2O_3 and CaO alone. In some instances, ash beds with nearly identical patterns in Fe_2O_3-CaO space can be differentiated by minor element concentrations (cf. Figure 1.11a). In this dissertation TiO_2, MnO, MgO, BaO, Cl, and F are shown to be sufficient to successfully distinguish rhyolitic ash beds. Most rhyolite ash beds fall within a limited range of Fe_2O_3 and CaO contents (~0.4–1.0 weight %), so positively identifying unique compositions in this field requires as much information as possible. Some ash beds have truly unique chemistry. In the Fiambalá basin, a low CaO composition has the highest measured MnO content and in the Santa Maria valley a sequence of high Fe_2O_3 rhyolites have the highest measured F contents (Figure 1.11d,f).

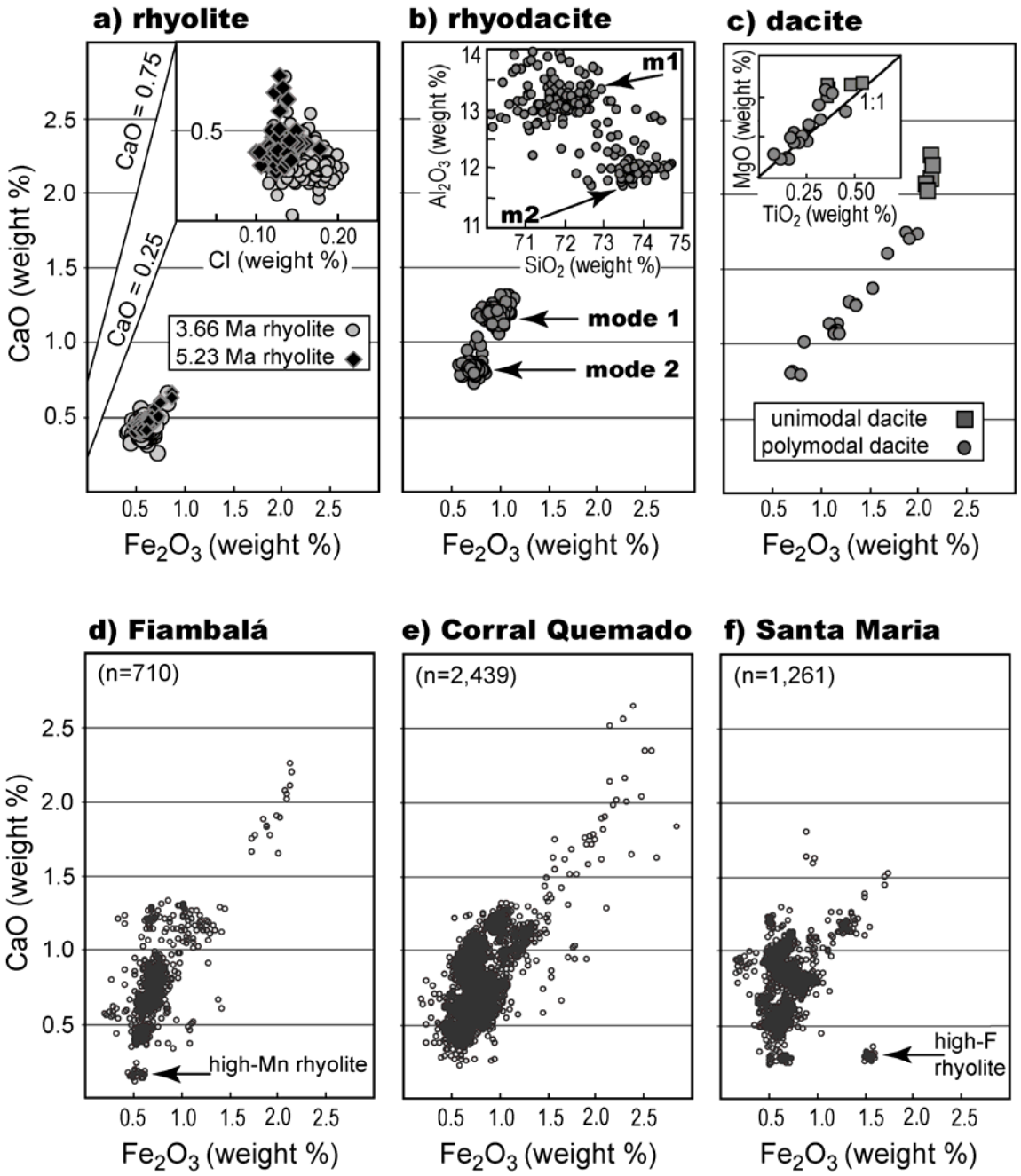

Figure 1.11: Intershard variation of volcanic glass as documented by electron probe microanalysis; **a)** two rhyolitic ashes indistinguishable by patterns of Fe_2O_3 and CaO variation, but differentiable by Cl and slightly different CaO content, **b)** rhyodacite ash bed with bimodal composition, **c)** dacite ash beds illustrating polymodal composition, less common unimodal composition, and typical TiO_2/MgO covariance, **d)** all shards from the Fiambalá basin, predominantly rhyolite and dacite compositions, **e)** all shards from the Corral Quemado basin demonstrating numerous occurrences of all three types of ash beds, and **f)** all shards from Santa Maria valley illustrating predominatly rhyodacite and rhyolite compositions and the absence of dacite ash beds.

Rhyodacite ash beds. Although not strictly defined, the term rhyodacite as used herein is a useful descriptor for ash beds which have compositions intermediate to those strictly defined as rhyolites or dacites. Glass of rhyodacitic composition has higher Fe_2O_3 and CaO values than rhyolite glass. Several patterns of shard-to-shard variation also serve to distinguish these ash beds. Rhyodacite ash beds may contain glass composition characterized by two discrete compositional modes (Figure 1.11b). These compositional modes are generally apparent on the basis of SiO_2, Al_2O_3, Fe_2O_3 and CaO. TiO_2 or MgO may also identify the compositional modes, but this is not always the case and variation of these elements is greatly reduced relative to true dacites. It is hypothesized that strongly bimodal rhyodacite ash beds are the products of zoned, perhaps stratified, magma chambers. Another common pattern of rhyodacite ash beds is strong intershard variation in Fe_2O_3 and/or CaO, such that the range could easily encompass several compositional modes, but none are identified. For these ash beds, intershard patterns in Fe_2O_3-CaO space can have a distinctive orientation, which may reflect processes of mineral growth in the evolving magma.

Dacite ash beds. The low SiO_2 content (often <70 weight %) of dacitic volcanic glass is inversely correlated with Al_2O_3, Fe_2O_3, CaO, TiO_2, and MgO contents. These variations are strong, and can span more than one weight % in Fe_2O_3-CaO space. This variation is often manifested in a series of compositional modes, such that some of these ash beds are termed polymodal (Figure 1.11c). Insufficient analyses have been obtained to adequately define these ‘modes’. Such patterns may emerge with additional data; however, some dacite ash beds have unimodal compositions. High, and covarying, TiO_2 and MgO values may be the most universal characteristic of dacite glass.

Regional patterns in ash bed composition. Several simple observations regarding the geographic distribution of volcanic ash beds are instructive. Firstly, the majority of ash beds are of rhyolitic composition. Rhyodacite and dacite ash beds are subordinate. Of these, rhyodacite ash beds are thicker and more widespread in their distribution. Dacite ash beds are typically preserved as thin lenses and no long distance correlations have been established. Based upon these observations, it is suggested that dacite eruptions are typically smaller, and perhaps less explosive.

Dacite volcanoes may be restricted to the volcanic arc or to isolated back-arc centers; their distribution appears to reflect this. The Santa Maria valley is furthest from the volcanic arc and no dacite ash beds are documented there (Figure 1.11f). The Santa Maria valley is characterized by the highest proportion of rhyodacite ash beds, and by the presence of a short sequence of distal rhyolite ashfall deposits characterized by high Fe_2O_3 and F contents. Most ash beds in Santa Maria valley are assumed to have derived from large silicic eruptive centers on the Puna plateau. Ash beds preserved in the Fiambalá basin are mostly rhyolites, with rhyodacite and dacite ash beds approximately equivalent in abundance. Fiambalá is the closest locality to the volcanic arc and therefore interpreted as indicative of ashes derived from the arc. Geographically, the Corral Quemado basin is intermediate between Fiambalá and Santa Maria, and the record of explosive volcanism there reflects this. Ash beds at Corral Quemado yield correlations to both Fiambalá and Santa Maria, but no direct correlations have yet been identified between Fiambalá and Santa Maria. Each basin appears to yield a record of explosive volcanism which is dominantly local; these changes are observed at a spatial scale of ~100 km.

Trace element composition of volcanic glass. Some trends in trace element composition of volcanic glass are observed, but data are not nearly as extensive as for major elemental composition. Glass data confirm the basic compositional patterns determined from analysis of ignimbrite samples in the region (Schnurr *et al*., 2007; Kay *et al*., 2010). Comparison to data from whole rock ignimbrite samples is not equivalent because the samples are fundamentally different material, but some potential correlations from distal ash beds to proximal ignimbrites have been identified on this basis. In the future this may become more tractable as additional source regions are identified and trace element concentrations in glass can be used predictively.

Ash beds with similar major element composition often have similar trace element chemistry. For this reason, differentiating ash beds on trace element data is not always straightforward, though small differences in trace element content appear to reliably distinguish ash beds. Building confidence in the robustness of small trace element variations within and between ash beds is crucial. Importantly, trace elemental compositional variation, laterally or vertically, within a volcanic ash bed is observed to be small, even for ash beds which are zoned in major element composition. Trace element data have proven very useful, but the methodology employed relies on samples with well characterized intershard variation. This is because 30 mg aliquots of volcanic glass concentrates are digested and analyzed as a bulk sample. Trace element analysis of individual shards by laser ablation might be employed when several compositional modes are documented in an important sample, but this still relies on abundant electron probe data to characterize the population of glass shards. Electron probe analysis must be used to understand how data are being averaged and which samples carry a primary signal.

Sedimentary mixing of volcanic glass. Most of the volcanic ash beds in northwestern Argentina display some evidence of sedimentary reworking. That is, very few ash beds are primary ashfall deposits. Fluvial and eolian processes mix foreign material, volcanic or otherwise, with primary eruptive material. These processes can be assessed by analysis of individual glass shards and the resultant data can be used to determine whether the measured compositions are petrologically related, or the result of sedimentary mixing. These interpretations influence potential correlations, and determine which samples are promising for trace element work. With broad petrologic patterns of volcanic glass chemistry established, several examples are drawn upon here to illustrate the situation (Figure 1.12). These examples reinforce the need for careful sample selection, analysis of large glass shard populations, and detailed analysis of data.

At the principal section in the Corral Quemado basin, there is a ~300 m thick interval of laterally extensive coarse sandstone bodies. This interval is interpreted as strata of a braided river system, and numerous volcanic ash beds are present. The stratigraphic relationships between many of these ash beds are difficult to document because they are exposed for only several hundred meters along strike in an almost 5 km wide panel of coarse sandstone. A 2 km long lateral transect in this interval, assumed to be the same ash bed, yielded at least three distinct compositions (Figure 1.12a). The first two samples are unimodal, but their Fe_2O_3, TiO_2, and MgO contents are distinct. The third sample yields a composition equivalent to the second sample, and another population of glass shards that appears to derive from an unrelated polymodal dacite. This is interpreted as resulting from sedimentary mixing. This interpretation is supported by the fourth sample, which contains only a few shards similar to the first sample.

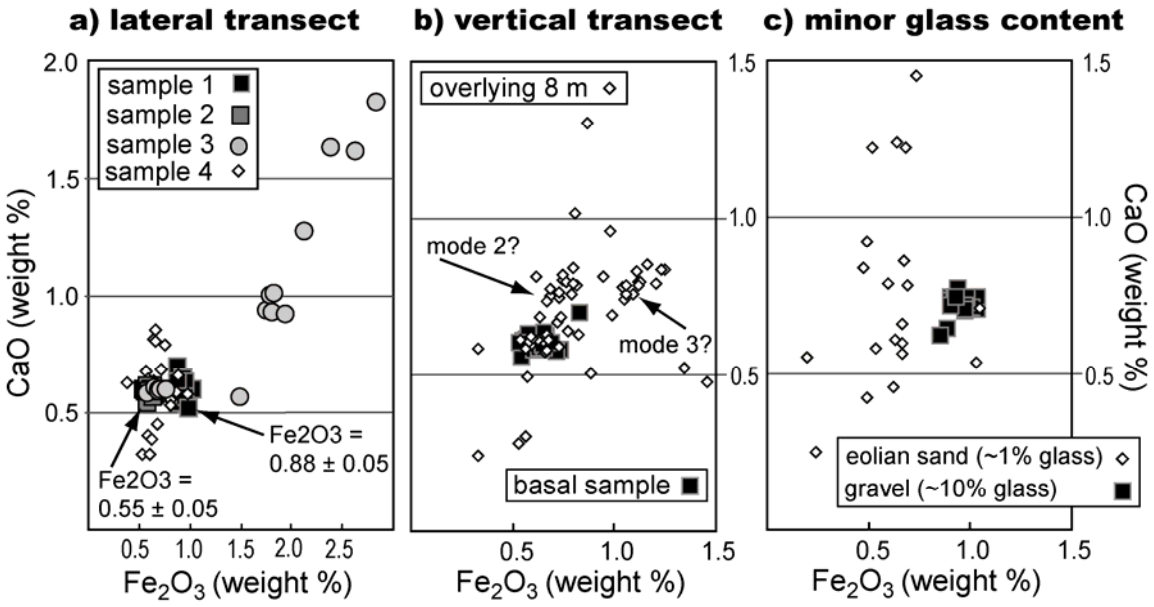

Figure 1.12: Compositional populations within volcanic ash beds resulting from sedimentary mixing, **a)** samples evenly spaced along a 2 km lateral transect assumed to be the same ash bed, **b)** vertical transect through an ash bed containing finely laminated sediment and paludal carbonate, **c)** samples with low initial glass concentration.

Similarly, a vertical transect through an ash bed yields at least one definite compositional mode and some ambiguous compositional groups (Figure 1.12b). The basal sample constitutes a well defined population, but four samples in the 8 m above it have minimal overlap with this population. The upper samples may define additional compositional modes associated with the base of the ash bed, but sedimentary processes have clearly also mixed in a number of apparently unrelated compositions.

Samples of ash beds containing >50% volcanic glass are generally less likely to yield complicated results, but this is not always the case. Alternatively, some samples with a minor volcanic glass component can yield robust and interpretable results. One such example is a thin tuffaceous horizon in Pliocene gravels which was essentially unimodal and can be correlated to other localities (Figure 1.12c). This stands in contrast to a Miocene eolian sandstone with ~1% glass, which appears to be a complex mixture.

Volcanic ash beds as structural datums. Volcanic ash beds provide chronological horizons for stratigraphic studies; however, once their age has been established the attitude (strike and dip) of the ash bed provides valuable structural information as well (Figure 1.13). Assuming that deposition was close to horizontal, inferences made from current orientation can be used to constrain the location, timing, and magnitude of upper crustal deformation. This is the most promising approach to study deposition and deformation of poorly bedded conglomerates in the region.

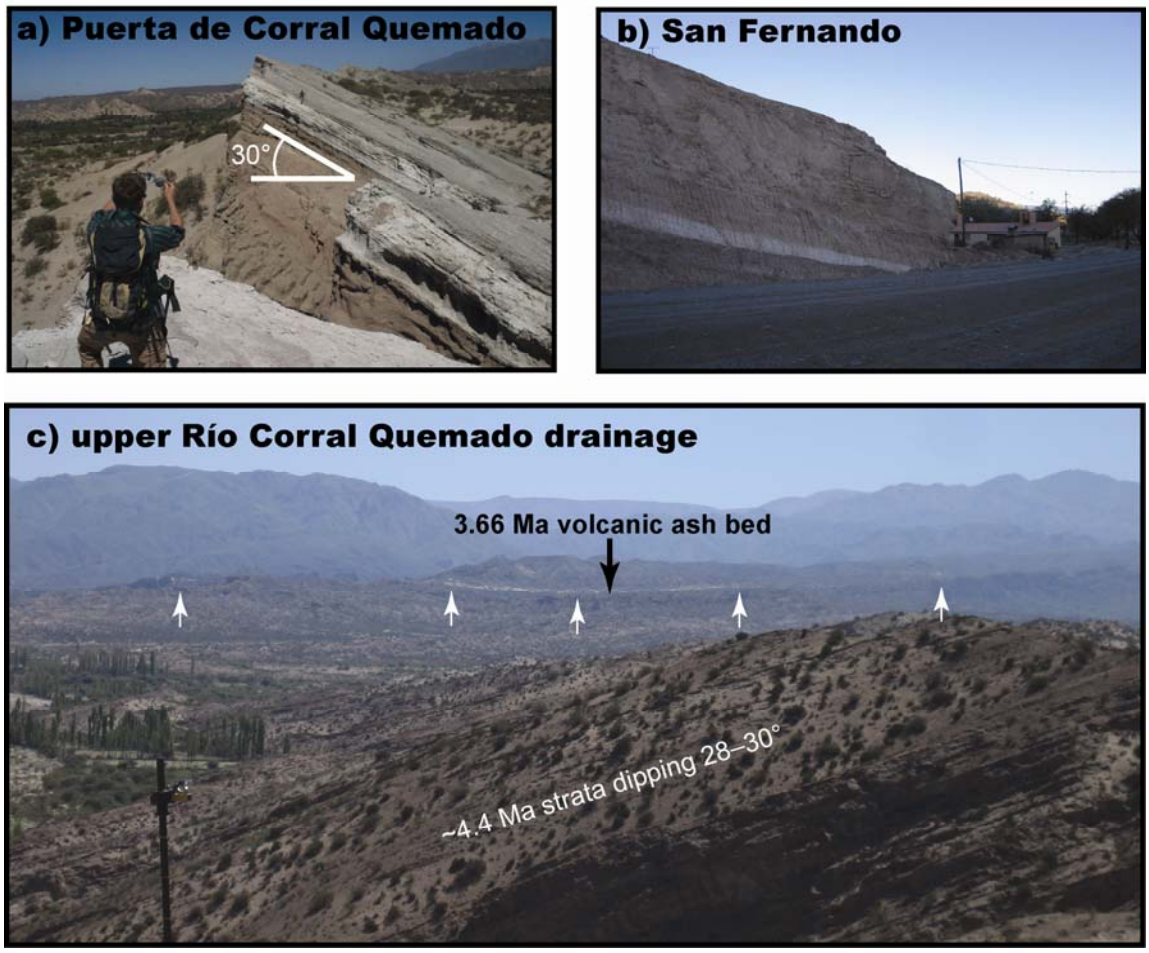

Figure 1.13: Volcanic ash beds in the Corral Quemado basin, illustrating their utility as structural datums; **a)** prominent ash bed at the 482 m level in the Puerta de Corral Quemado (PCQ) stratigraphic section, **b)** latest Miocene ash bed, dipping ~15° to the SSW at San Fernando, **c)** view from the upper PCQ section to the prominent Toba Corral Quemado (8 km), which delineates a syncline in coarse sandstones and conglomerates.

Structure of the dissertation

This dissertation is organized into three principal chapters, each focused on a different set of questions relating to the Miocene-Pliocene development of the southeastern Puna plateau margin. Data collected during the course of this dissertation are fully documented in the appendices, but not necessarily discussed in the text. Data are drawn upon as needed in each chapter. As a whole, the goal of this dissertation is to provide geological constraints on the tectonic, climatic, and ecologic evolution of the southeastern Puna plateau margin during the late Miocene and Pliocene epochs.

Chapter 2 develops a synoptic paleoecologic reconstruction in the region between 9–3.5 Ma. This work is undertaken in the 2.5 km thick stratigraphic section exposed at Puerta de Corral Quemado. This was the location of early biostratigraphic studies (cf. Marshall and Patterson, 1981), in addition to the most detailed chronostratigraphic study in the region (Butler *et al*., 1984) and a long paleosol carbonate record with the highest resolution in the region (Latorre *et al*., 1997). For these reasons, a detailed paleoecologic analysis was pursued at this locality. Stable isotope data from diagenetic, paleosol, and fossil tooth enamel carbonate are compared throughout the section with the following questions in mind: 1) is the late Miocene expansion of C_4 grasslands in northwestern Argentina synchronous with the global record?, 2) how was this ecological expansion modulated by growing orographic barriers?, and 3) what landscape-scale ecological patterns existed in the region during the late Miocene and early Pliocene?

Chapter 3 puts forth a regional geochronological framework for the latest Miocene and early Pliocene. This framework is based upon isotopic dating and

geochemical characterization of volcanic ash beds. A composite tephrostratigraphy is developed for the upper section at Puerta de Corral Quemado and correlations to volcanic ash beds in the Fiambalá basin are proposed. Identification of widespread ash beds permits their use as both stratigraphic and structural datums. When each datum is considered within a coherent geochronological framework, analysis of spatial and temporal variation in tectonic and sedimentary processes becomes tractable. Following this approach several questions are addressed at Puerta de Corral Quemado and Fiambalá. The timing and style of the Plio-Pleistocene contractional deformation that exposed the study sections is addressed, as is the timing of deposition for coarse conglomeratic deposits capping most stratigraphic sections in the region. Both of these are interpreted as proxies for plateau margin uplift; and thereby constrain the recent tectonic history of the southeastern Puna.

Chapter 4 extends the geochronological framework northward to Vallé Santa Maria, and explores regional variations in paleosol carbonate isotopic data within this framework. Short sequences of paleosol carbonate data from Fiambalá are compared to the Puerta de Corral Quemado record. The longer paleosol carbonate record from Vallé Santa Maria is also assessed, with emphasis on the portions of the record that can be confidently correlated to Puerta de Corral Quemado. In total, data spanning ~200 km kilometers from north to south are incorporated into a regional stable isotope record spanning 10 Ma–present. This regionally integrated record is most robust between 8.5–3.5 Ma, a period of time coincident with global change in terrestrial ecosystems (Cerling *et al*., 1997) and with the hypothesized rapid uplift of the Altiplano plateau (Hoke and Garzione, 2008).

Chapter 5 summarizes the results of Chapters 2, 3, and 4. These results are contextualized with respect to the geologic and tectonic setting as laid forth in this chapter. Major conclusions derived from the late Miocene and Pliocene geological record of the southern Puna plateau margin are synthesized. Outstanding problems are identified, and exciting questions are formulated.

Appendix A hosts the background stratigraphic and geochemical framework of the dissertation. The location, identity, composition, and age of important stratigraphic markers are documented. Electron probe microanalysis (EPMA) data for volcanic glass are presented in a stratigraphic framework. Trace element data for volcanic glass, measured by Inductively coupled plasma mass spectrometry (ICP-MS), and $^{40}Ar/^{39}Ar$ age estimates for minerals are reported by sample number and can be referenced to the stratigraphic framework in this way.

Appendix B contains all stable isotope data gathered from northwestern Argentina. This includes analysis of a variety of materials (water, carbonate, and tooth enamel) ranging in age from Miocene to modern. Geographic coordinates, and stratigraphic placement where appropriate, are linked to each sample.

CHAPTER 2

STABLE ISOTOPE ECOLOGY ACROSS THE MIOCENE-PLIOCENE BOUNDARY; PUERTA DE CORRAL QUEMADO

Introduction

The late Miocene hosts a rich record of environmental change in terrestrial environments. The global nature of the environmental change is evidenced, in part, by stable isotope proxies from most continents. Late Miocene expansion of plants using the C_4 photosynthetic pathway is frequently documented in locales where these plants currently comprise an important proportion of modern ecosystems (Cerling *et al*., 1997; Latorre *et al*., 1997; Passey *et al*., 2009). C_4 plants are particularly successful in tropical and temperate latitudes where monsoonal climates (abundant summer rainfall) dominate. A high proportion of plant cover in grassland and savanna environments is attributable to the C_4 pathway. The late Miocene expansion of C_4 ecosystems is a global phenomenon; yet potential differences in the timing, magnitude and rate of ecologic change raise questions regarding regional and local response to global change (Fox and Koch, 2004).

Having established a detailed stratigraphic framework through a section in northwestern Argentina it is possible to compare stable isotope proxies for plant cover and mammalian diet across the Miocene-Pliocene boundary (cf. Koch, 1998). The stratigraphy is based on volcanic ash beds collected from a 2.3 km thick section at Puerta de Corral Quemado (PCQ) in Catamarca Province, northwestern Argentina (Figure 2.1).

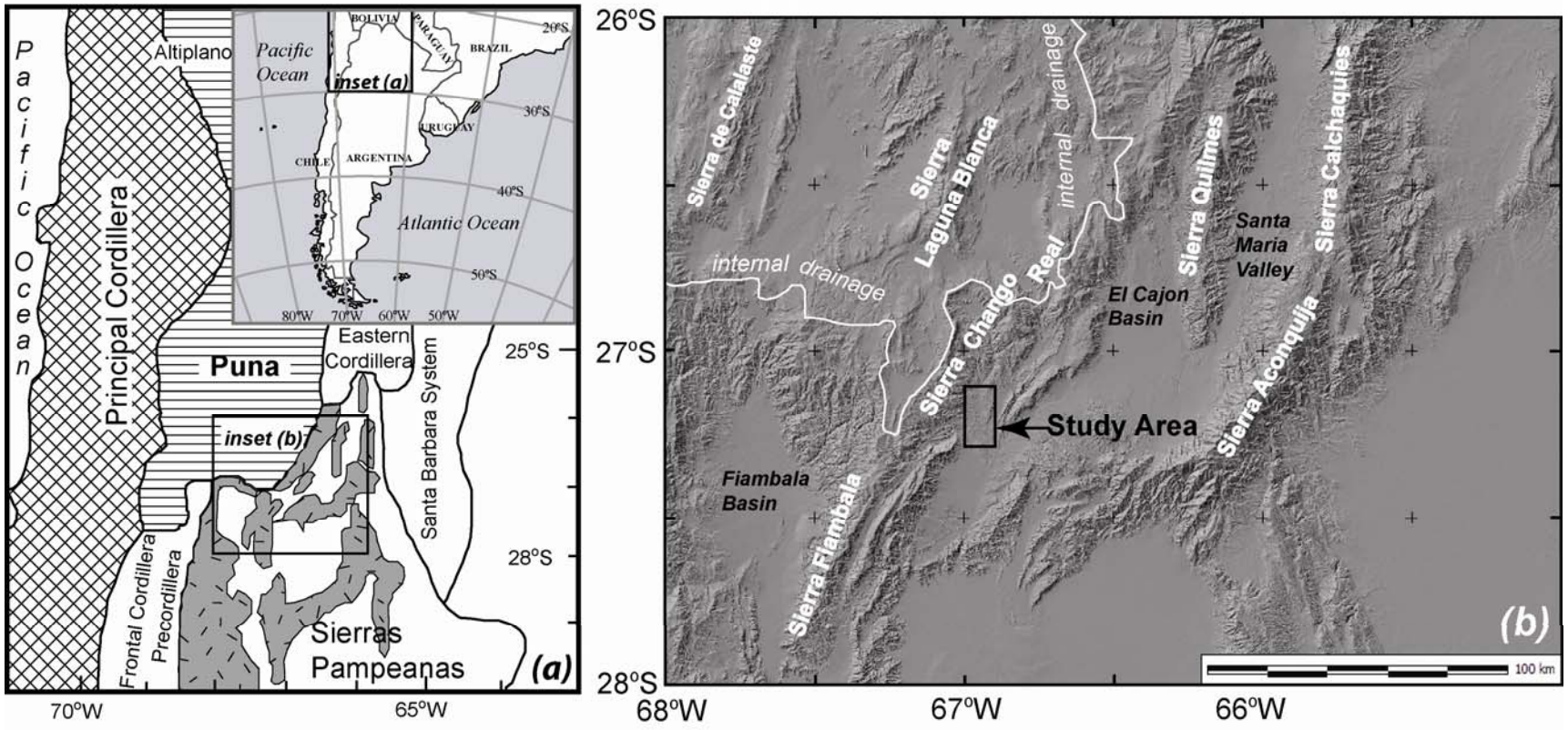

Figure 2.1: Study area and geologic setting; **a)** Location map denoting morphotectonic provinces of the southern Central Andes (after Jordan *et al*., 1983), **b)** Shaded relief map (from Shuttle Radar Topography Mission 3 arc second data).

Volcanic ash beds and sandstone marker beds which have known relations with the paleosol carbonate record from PCQ (Latorre *et al*., 1997) permit analysis at high stratigraphic resolution. Within this framework, the nature of Miocene-Pliocene ecological change in the region is addressed through analyses of $\delta^{13}C$ and $\delta^{18}O$ in enamel of fossil teeth collected from the PCQ section. Stable isotope ratios were analyzed by conventional methods, and also by laser ablation. Laser ablation enables analysis of small and delicate teeth, thereby removing some of the sampling bias inherent to stable isotope studies of fossil collections.

The presence of plants using the C_4 photosynthetic pathway, as detected by the carbon isotope ratio of paleosol carbonate or fossil tooth enamel, is a proxy for environmental conditions in which C_4 plants are ecologically successful. These parameters include low mean annual precipitation, low atmospheric CO_2 concentrations and warm growing season (Ehleringer *et al*., 1997). Warm growing seasons are a result of numerous factors including low latitude, low elevation, and monsoonal precipitation. The modern geographic and climatic setting of the studied section is favorable for recording the Miocene-Pliocene history of C_4 biomass in the region. Regional studies indicate a strong elevational gradient in modern C_4 plant abundance, and PCQ is currently near the upper limit for C_4 dominated ecosystems (Cabido *et al*., 1997). At present, C_4 plants comprise a small proportion of subsurface biomass locally. Regionally, paleosol carbonate studies have documented a complex ecological history over the last 10 Ma; possibly modulated by the growth of orographic barriers during the Pliocene (Kleinert and Strecker, 2001; Latorre *et al*., 1997). Comparison of stable

isotope proxies for C_4 vegetation within discrete stratigraphic intervals is an opportunity to evaluate the spatial and temporal dynamics of ecologic change.

The goals of this study are to: 1) assess the proliferation of C_4 ecosystems in the southern Central Andes as a means of constraining Miocene-Pliocene climate and ecology in the region, 2) compare this to the global record of C_4 expansion and evaluate possible local or regional controls on C_4 plant distribution , and 3) provide a coherent and accessible chronostratigraphic framework, based upon the geochemical characterization of volcanic ash beds, for use in studies by other workers concerning tectonic, climatic, or ecologic questions.

Materials and methods

Geochemical characterization of volcanic ash beds

Volcanic ash beds were characterized and correlated based upon the elemental composition of volcanic glass. Glass separates were prepared for electron probe microanalysis (EPMA) by ultrasonic treatment of the 125–250 μm fraction in 10% HNO_3, 5% HF, and distilled water. When necessary, the glass fraction was concentrated by standard magnetic and density methods prior to being mounted in epoxy, polished, and carbon coated. Analysis of major and minor elements was carried out on a Cameca SX-50 microprobe using methods described by Nash (1992). Typically, 20 glass shards per sample were analyzed and incorporated into average values (Appendix A).

Stable isotope analysis of carbonate by acid digestion

Paleosol, diagenetic, and tooth enamel carbonate were analyzed using an online carbonate device, the Finnigan Carboflo. Samples were reacted in 100% H_3PO_4 at 90°C

and the evolved CO_2 was cryogenically purified prior to analysis via a dual inlet and micro-volume coldfinger on a Finnigan MAT 252 at the University of Utah. Internal carbonate and tooth enamel standards, calibrated to NBS-19, were used to correct measured values relative to the PDB scale. This correction is small for carbon isotope ratios and indicates comparable results irrespective of analytical session. Apparent acid fractionation factors for the oxygen isotope ratio of CO_2 liberated from tooth enamel apatite were calculated separately for modern and fossil enamel using equations presented in Passey *et al*. (2007). Tooth enamel standards analyzed during the study had a 1σ standard deviation of 0.09‰ for $\delta^{13}C$ and 0.16‰ for $\delta^{18}O$. This estimate of precision is in agreement with the average absolute difference between duplicate analyses of unknowns ($\delta^{13}C$ = 0.07‰, $\delta^{18}O$ = 0.31‰, n = 7).

A subset of tooth enamel powders was chemically pretreated in ~3% H_2O_2 for 15 minutes and 0.1 M glacial acetic acid for 15 minutes. Pretreatment is intended to remove organic material and non-enamel carbonate, but in many cases has little effect on the $\delta^{13}C$ values (Levin *et al*., 2008; Passey *et al*., 2002). In this study, treated enamel is depleted in ^{13}C by ~0.13 ± 0.20 ‰ and enriched in ^{18}O by ~0.39 ± 1.00 ‰ relative to untreated enamel (n = 20). Comparison between untreated enamel and various organic materials demonstrates an opposite relationship. Enrichment in ^{13}C (1.05 ± 0.71‰) and depletion in ^{18}O (1.77 ± 1.58 ‰) is observed in dentin, cementum, and the red coating on rodent incisors relative to adjoining tooth enamel (n = 11). Non-enamel tooth materials may have different isotopic compositions initially, or they may be diagenetically altered. Fossil enamel is less affected by treatment than modern enamel, suggesting that contamination by organic tooth material may be a more important consideration than

non-structural carbonate. Our effort to sample as many teeth as possible resulted in most analyses deriving from untreated tooth powders. When a tooth was too small or delicate to physically isolate tooth enamel from the adjoining organic material laser ablation methods were employed.

Stable isotope analysis of tooth enamel by laser ablation

A subset of fossil tooth enamel samples was analyzed using thermal laser ablation methods. Analysis by laser ablation allows incorporation of small mammals into the study, and additionally permits intratooth analysis of these specimens. Of the 43 samples analyzed for this study, 9 individuals were previously reported in a publication detailing the analytical method (Passey and Cerling, 2006). These data showed that laser $\delta^{13}C$ values are comparable to conventional phosphoric acid digestion within 0.5‰ and sufficient for the reconstruction of the fraction of C_3 vs. C_4 plants in the diet.

Later work on the same system observed a 1.9 ± 0.4 depletion in ^{13}C relative to acid digestion (Podlesak *et al*., 2008). A similar depletion in laser $\delta^{13}C$ values is noted for some samples analyzed herein (Arg-103, Arg-106; Appendix B). Passey and Cerling (2006) clearly show that quantitative CO_2 yield is not achieved during ablation and that depletion of ^{13}C occurs at low laser power. Fractionation of ^{12}C into the CO_2 analyte and ^{13}C into melt-forming condensate may occur during ablation, particularly at low laser power. The analytical strategy was to utilize laser power near the low end of optimal analytical conditions (~5 W) and to increase the number of ablation events as needed to achieve sufficient CO_2 for analysis. Primarily, this strategy compromises spatial (temporal) resolution. Any fractionation during ablation should lead to systematically depleted $\delta^{13}C$ values and thus does not jeopardize conservative identification of fossil

taxa consuming C_4 plants. Laser ablation $\delta^{13}C$ data are reported relative to the PDB standard and these results are discussed together with those from acid digestion.

$\delta^{18}O$ laser values are measured in CO_2 deriving O from the phosphate, carbonate, and potentially the hydroxyl components of tooth enamel. The mixing of these components and the nonstochiometric yield of oxygen in the CO_2 analyte obfuscates the relationship between laser values and conventional acid digestion data. The majority of the O analyzed is from the phosphate component of enamel (Passey and Cerling, 2006). In general, the phosphate oxygen is believed to be more resistant to diagenetic alteration than either the carbonate or hydroxyl oxygen (Zazzo *et al*., 2004). Deviation from the predicted $\delta^{18}O$ offset between laser and acid digestion values may result from incomplete mixing of phases or isotopic fractionation during ablation. Further, the observed difference between fossil and modern enamel analyzed by laser ablation may result from isotopic exchange of carbonate oxygen or replacement of OH^- by F^- in fossil enamel (Passey *et al*., 2007). Laser ablation $\delta^{18}O$ values are reported on the PDB scale and are discussed briefly alongside the acid digestion analyses.

Stratigraphic framework

Lithostratigraphic framework

Strata of interest belong to the Neogene Santa Maria Group, which also crops out extensively in the Santa Maria Valley 100 km NNE of the study area (cf. Figure 2.1). A historical summary and revision of the lithostratigraphic nomenclature is presented by Muruaga (2001). Stratigraphic correlations to the earliest paleontologic work are possible, though currently supported by only a few marker beds (Butler *et al*., 1984;

Marshall and Patterson, 1981). Magnetostratigraphic and ^{40}K-^{40}Ar data firmly place the PCQ section across the Miocene-Pliocene boundary (Butler *et al*., 1984). This 2300 m thick section was sampled on the north side of Río Corral Quemado. Subsequently, a 2300 m section south of Río Corral Quemado (Figure 2.2) was sampled for paleosol carbonate and correlated to the magnetostratigraphy by identification and redating of two prominent tuffs by $^{40}Ar/^{39}Ar$ (Latorre *et al*., 1997). Together, the paleomagnetic and radiometric age contraints on the strata at Puerta de Corral Quemado provide an integrated geochronology which bears on biostratigraphic, paleontologic, and stable isotopic data.

Latorre *et al*. (1997) recorded the stratigraphy of part of the section at PCQ; geographic coordinates are established for some of their stratigraphic layers (Table 2.1). Ten of these layers are numbered sandstone marker beds; three are prominent tuffs. To ensure proper correlation, samples of eight volcanic ash beds from the study of Latorre *et al*. (1997) were also analyzed. These establish four additional stratigraphic correlations, and provide the basis for the tephrostratigraphy reported here and in Chapter 3.

Tephrostratigraphic framework

Compositionally, all analyzed glasses are dacite or rhyolite considering their SiO_2, Al_2O_3, and alkali content. The ash beds at PCQ preserve a rich record of volcanism through the late Miocene and early Pliocene, and are especially numerous in the upper 1,000 m of the section. Analyses of ash beds reported here are only a skeletal framework of the potential record, but they all relate directly to previous stable isotope work.

Electron probe microanalyses of volcanic glass improve correlation of this study to Latorre *et al*. (1997), by providing compositional information for stratigraphically

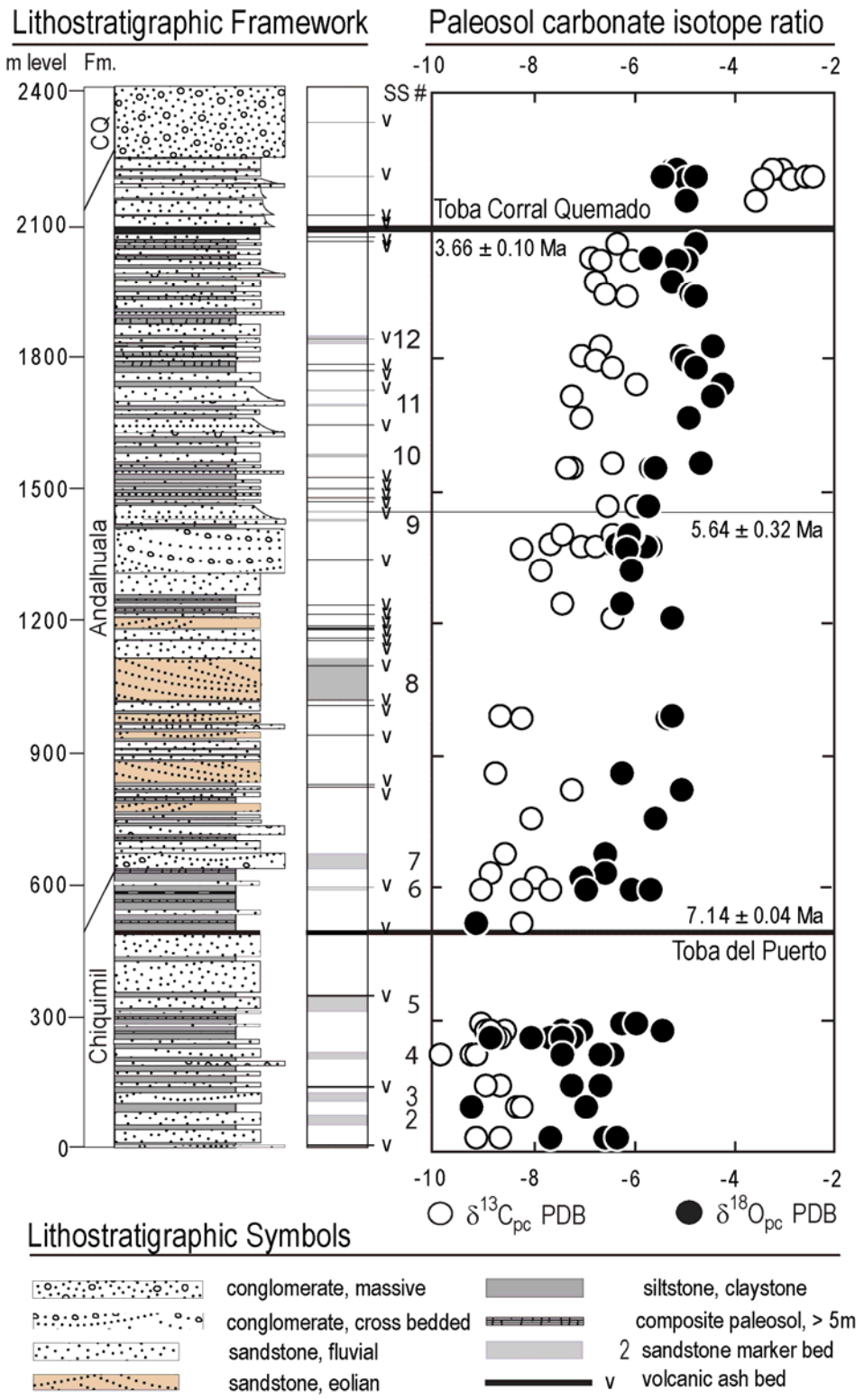

Figure 2.2: Stratigraphic section at Puerta de Corral Quemado. Lithologic column, sandstone marker beds, volcanic ash beds, and paleosol carbonate data from Latorre *et al*. (1997). Formation names and ash bed names are after Muruaga (2001).

Table 2.1: Stratigraphic framework at Puerta de Corral Quemado.

Unit[a]	Sample ID	Thickness (m)	Age (Ma)	Latitude[b] (°S)	Longitude (°W)	Correlative sample	EPMA
tuff[d]	Arg 267	2320		27.2210	66.9643	PCQ 806	y
tuff[c]	Arg 244	2198		27.2213	66.9631	PCQ 578, 805	y
Toba Corral Quemado[c, d]	Arg 241	2072	3.66 ± 0.10	27.2227	66.9608	PCQ 109, 511, 582-584	y
Sandstone #12[c]		1838		27.2224	66.9548		
tuff of sandstone #12[d]	Arg 227	1832		27.2226	66.9548	PCQ 573-575, 793-795	y
tuff[d]	Arg 215	1715		27.2239	66.9529	PCQ 570	y
Sandstone #11[c]		1682		27.2236	66.9514		
Sandstone #10[c]		1565		27.2263	66.9494		
tuff[d]	Arg 196	1440	5.64 ± 0.32	27.2278	66.9488	PCQ 560	y
Sandstone #9[c]		1417		27.2280	66.9484		
tuff	Arg 167	1180					y
tuff	Arg 168	1176					
tuff	Arg 166	1092					

[a]Unit, sample ID, thickness, and age (2σ) from Latorre *et al*. (1997).
[b]Geographic coordinates, correlative samples, and electron probe microanalysis (EPMA) this study.
[c]Coordinates established using photographs and field notes of J. Quade (see Appendix A; Figure A.1).
[d]Geographic coordinates from volcanic ash samples correlated to those of Latorre *et al*. (1997).

Table 2.1 (*continued*): Stratigraphic framework at Puerta de Corral Quemado.

Unit[a]	Sample ID	Thickness (m)	Age (Ma)	Latitude[b] (°S)	Longitude (°W)	Correlative sample	EPMA
Sandstone #8		1015					
lateral tuff	Arg 164	1005					
tuff	Arg 155	821					
Sandstone #7[c]		630		27.2425	66.9436		
tuff	Arg 131	595					y
Sandstone #6[c]		588		27.2479	66.9398		
Toba del Puerto[c]	Arg 101	486		27.241	66.931		
Toba del Puerto[c]	Arg 100	482	7.14 ± 0.04	27.241	66.931		
Sandstone #5[c]		309		27.2420	66.9267		
Sandstone #4[c]		202		27.2425	66.9241		
Sandstone #3[c]		102		27.2431	66.9214		
Sandstone #2[c]		48		27.2442	66.9203		

[a]Unit, sample ID, thickness, and age (2σ) from Latorre *et al*. (1997).
[b]Geographic coordinates, correlative samples, and electron probe microanalysis (EPMA) this study.
[c]Coordinates established using photographs and field notes of J. Quade (see Appendix A; Figure A.1).
[d]Geographic coordinates from volcanic ash samples correlated to those of Latorre *et al*. (1997).

important ash beds. Four samples analyzed in duplicate confirm analytical reproducibility capable of uniquely identifying ash beds. Populations of glass shards within an individual ash bed are unimodal with two exceptions. A dacitic ash bed 595 m above the base of the section contains at least five compositional modes, identified by discrete TiO_2, Fe_2O_3, MgO, and CaO contents. A rhyodacitic ash bed 1832 m above the base has two compositional modes. All correlations are supported by calculation of the statistical distance between analyses using the concentrations of TiO_2, Fe_2O_3, MnO, MgO, CaO, and Cl (Perkins *et al*., 1995; Appendix B). Full analyses are provided in Appendix A.

The ultimate goal is to examine stable isotope data at high stratigraphic resolution; therefore all data are referenced to their stratigraphic level. The three $^{40}Ar/^{39}Ar$ dates on volcanic ash beds reported in Latorre *et al*. (1997) are known to their exact stratigraphic level. Two of these ages also have a known relationship with the magnetostratigraphy presented in Butler *et al*. (1984). We refrain from calculating ages for intermediate stratigraphic levels because such age estimates are subject to revision as new data become available, but the stratigraphic level of each fossil remains constant. The only stratigraphic level subject to revision is our estimate of the Miocene-Pliocene boundary (1555 m) based upon linear interpolation between two dated ash beds and a boundary age of 5.33 Ma (Van Couvering *et al*., 2000). In the ensuing text all stratigraphic levels are given in meters above the base of the section.

Soil carbonate record

Several salient features of the paleosol record frame our analysis of tooth enamel data (Figure 2). The first $\delta^{13}C$ pedogenic carbonate ($\delta^{13}C_{pc}$) values > -8.0‰ indicating

the presence of C_4 vegetation in a fossiliferous paleosol at 591 m. Several meters above the paleosol, a dacitic ash layer is preserved as a thin discontinuous bed (Arg 131; Table 2.1). $\delta^{13}C_{pc}$ values higher than -7.5‰ further confirm the presence of C_4 plants at 816 m. Latorre *et al*. (1997) highlight the interval between 591 and 816 m as recording minor contributions of C_4 biomass to paleosol carbonate, and we adopt this interpretation terming it the $\delta^{13}C_{pc}$ C_4 first appearance interval. The largest range in $\delta^{13}C_{pc}$ values (2.6‰) is observed between 1300 and 1400 m, coinciding with the first major conglomerates in the section. A series of paleosols beginning at 2149 m record a rapid increase in C_4 vegetation. This sharp positive excursion in $\delta^{13}C_{pc}$ values lies above the 3.66 Ma Toba Corral Quemado (Table 2.1).

Paleosol carbonate is an *in situ* proxy for local environmental conditions at a relatively small spatial scale (10–100 m^2). As such, sedimentary and stratigraphic observations provide complementary information to stable isotope data. At PCQ, Muruaga (2001) uses the two most prominent ash beds to demarcate formation boundaries. This approach is convenient, chronostratigraphically robust, and broadly approximates important changes in the sedimentary system. Strata of the Chiquimil Formation below Toba del Puerto record an alluvial environment characterized by sandy channels, broad floodplains, and preservation of fossil wood. Above the Toba del Puerto (~ base Andalhuala Formation) sediments deposited on a broad floodplain continue for more than 300 m upsection before grading into fining upwards gravel beds. Only a little higher in the section, eolian cross-strata and marlstones indicative of sand dunes and shallow standing water become intercalated (Muruaga, 2001). The upper Andalhuala Formation contains extensive bodies of coarse sand indicative of deposition in the distal

reaches of a braided river. Above the Toba Corral Quemado (~ base Corral Quemado Formation) cobble sized clasts become more common and give way upward to massive, disorganized conglomerates characteristic of the top of the section. The stratigraphic record of environmental change at PCQ is broadly similar to other localities in the central Andes (Strecker *et al*., 2007a).

Stable isotope results

Tooth enamel isotope ratios were obtained for 141 individual specimens; 21 modern and 120 fossil. Rodents and notoungulates comprise ~85% of the fossil teeth sampled. Many specimens were sampled multiple times to assess the isotopic variation within individuals. To mitigate the bias toward specimens sampled multiple times an average value can be assigned to each individual. However, this approach masks potentially important ecological variation within individuals. The use of maximum and minimum values to represent specimens sampled three or more times is explored as an effort to capture individual variation while limiting the importance of multiply sampled individuals in stratigraphic and numerical analyses (Table 2.2). This approach is also attractive because analysis of the data includes measured values, a criterion not satisfied by individual averages. Each stratigraphic interval is further characterized by the 20^{th} and 80^{th} percentile for each population of isotopic data. Unless otherwise noted, data presented and discussed are the max-min subset of the full data (Appendix B).

Table 2.2. Summary of stable isotope data grouped by stratigraphic interval and data filtering method.

Stratigraphic interval		**Tooth enamel (all data)**			**Tooth enamel (individual average)**			**Tooth enamel (max-min filter)**			**Paleosol carbonate (all data)**	
m level		$\delta^{13}C$ PDB	$\delta^{18}Ocvn$[a] PDB	$\delta^{18}Olas$ PDB	$\delta^{13}C$ PDB	$\delta^{18}Ocvn$ PDB	$\delta^{18}Olas$ PDB	$\delta^{13}C$ PDB	$\delta^{18}Ocvn$ PDB	$\delta^{18}Olas$ PDB	$\delta^{13}C$ PDB	$\delta^{18}O$ PDB
Modern	n[b]	44	44	0	21	21	0	28	28	0	0	0
	avg	**-8.2**	**0.7**	-	**-8.4**	**0.3**	-	**-8.5**	**0.3**	-	-	-
	1σ	*2.7*	*3.3*	-	*2.8*	*3.1*	-	*2.8*	*3.1*	-	-	-
	20%	*-10.6*	*-2.7*	-	*-10.7*	*-2.9*	-	*-10.7*	*-2.8*	-	-	-
	80%	*-6.0*	*3.6*	-	*-6.0*	*3.4*	-	*-6.1*	*3.0*	-	-	-
1555-2215 m	n	99	31	68	23	13	15	40	17	29	24	24
	avg	**-6.2**	**-2.3**	**-7.9**	**-7.2**	**-1.0**	**-8.2**	**-7.6**	**-1.3**	**-8.2**	**-5.7**	**-5.0**
	1σ	*4.4*	*2.2*	*2.4*	*4.1*	*2.3*	*2.4*	*4.3*	*2.3*	*2.5*	*1.7*	*0.4*
	20%	*-10.3*	*-4.2*	*-9.7*	*-10.2*	*-2.5*	*-9.7*	*-10.4*	*-3.2*	*-10.1*	*-7.0*	*-5.3*
	80%	*-1.7*	*-0.4*	*-6.7*	*-4.1*	*0.0*	*-7.4*	*-4.3*	*-0.2*	*-6.6*	*-3.4*	*-4.8*
591-1555 m	n	124	58	66	41	32	15	62	41	30	26	26
	avg	**-8.0**	**-2.0**	**-8.8**	**-8.1**	**-2.1**	**-8.6**	**-8.1**	**-2.0**	**-8.6**	**-7.5**	**-6.0**
	1σ	*3.0*	*2.0*	*2.2*	*2.7*	*2.3*	*2.2*	*2.8*	*2.2*	*2.3*	*1.0*	*0.5*
	20%	*-10.7*	*-3.7*	*-10.6*	*-10.2*	*-3.9*	*-10.4*	*-10.2*	*-3.9*	*-10.6*	*-8.3*	*-6.3*
	80%	*-5.9*	*-0.2*	*-6.7*	*-6.3*	*-0.2*	*-7.2*	*-6.1*	*-0.1*	*-6.5*	*-6.5*	*-5.7*
0-591 m	n	234	186	48	55	46	13	85	68	26	22	22
	avg	**-9.6**	**-4.2**	**-8.5**	**-9.2**	**-3.2**	**-8.1**	**-9.3**	**-3.4**	**-8.1**	**-8.9**	**-7.3**
	1σ	*1.5*	*2.3*	*3.5*	*1.5*	*2.2*	*3.7*	*1.7*	*2.4*	*3.7*	*0.4*	*1.0*
	20%	*-10.6*	*-5.9*	*-10.8*	*-10.1*	*-4.9*	*-10.5*	*-10.5*	*-5.1*	*-10.3*	*-9.1*	*-7.7*
	80%	*-8.7*	*-2.7*	*-6.8*	*-8.1*	*-1.4*	*-6.8*	*-8.2*	*-1.7*	*-6.3*	*-8.7*	*-6.5*

[a] cvn=conventional phosphoric acid digestion method (cf. Passey *et al*., 2007), las=laser ablation method (cf. Passey and Cerling, 2006).

[b] n=number of measurements, avg=average, 1σ =standard deviation, 20%=20th percentile of the population, 80%=80th percentile of the population.

$\delta^{18}O$ composition of tooth enamel and diagenetic carbonate

Paleoclimatic and paleoecologic reconstructions based upon tooth enamel necessitate that the primary stable isotope signature be recovered. Tooth enamel has low porosity and structural carbonate is expected to retain a primary carbon isotope signature in most diagenetic environments, whereas oxygen isotope signatures are more vulnerable to diagenetic alteration (Wang and Cerling, 1994). This is consistent with diagenetic studies of carbonate rocks and is believed to result from significantly higher molar water/rock ratios for oxygen than for carbon (Banner and Hanson, 1990). Paleosol carbonate often preserves primary carbon isotope signatures, but oxygen isotope alteration is demonstrated from samples which nonetheless retain a micritic texture (Leier *et al*., 2009). To address the potential for alteration of the primary isotopic signal, diagenetic calcite veins and disseminated carbonate were studied in addition to paleosol and fossil tooth enamel carbonate.

$\delta^{18}O$ is more variable in tooth enamel ($\delta^{18}O_{en}$) than in paleosol carbonate ($\delta^{18}O_{pc}$), but the two records exhibit similar stratigraphic patterns (Figure 2.3). Paleosol and tooth enamel carbonate both record ^{18}O enrichment from the late Miocene to the early Pliocene of at least 2‰ (Table 2.2). Diagenetic calcite veins are consistently depleted in ^{18}O relative to paleosol and fossil tooth enamel carbonate; whereas disseminated carbonate is of similar isotopic composition to paleosol carbonate (Appendix B).

Based upon paleosol carbonate $\delta^{18}O$ values and the isotopic composition of modern water in the region, we choose -4‰ (SMOW) as a conservative initial value for diagenetic water (Appendix B). Choosing initial water values < -5‰ (SMOW) or surface temperature of 25°C both move the depth dependent $\delta^{18}O$ calcite projections to the left

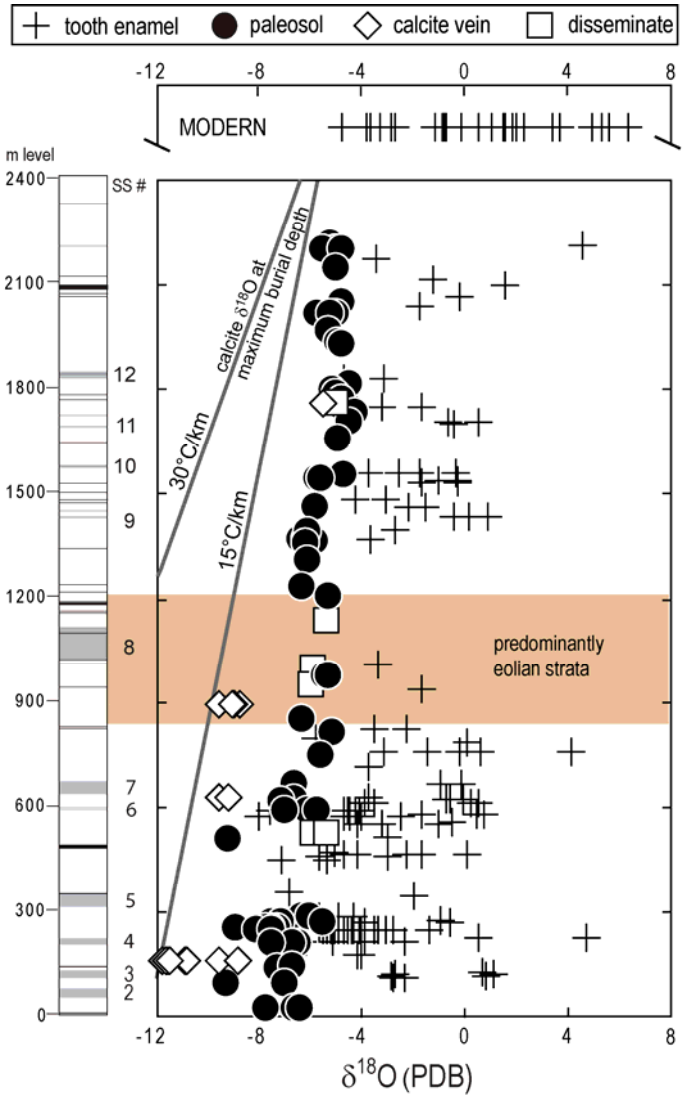

Figure 2.3: Oxygen isotope composition of carbonate phases at Puerta de Corral Quemado. The isotopic composition of diagenetic calcite is depicted as a function of temperature using fractionation factors from Friedman and O'Neil (1977) where surface temperature is 20°C and diagenetic fluids are assumed to have a homogenous isotopic composition of -4‰ (SMOW).

approximately the same amount. Either of these changes precludes calcite precipitation at maximum burial depth.

Diagenetic calcite veins sampled from strata buried more than 2 km have $\delta^{18}O_{cv}$ values of -10.4 ± 1.9 ‰ (n=12). The oxygen isotope ratio of this diagenetic calcite is easily distinguished from $\delta^{18}O_{en}$ values observed in fossil teeth buried to an equivalent depth (-3.4 ± 2.6 ‰; n=30). A more convincing test of the fidelity of $\delta^{18}O_{en}$ values is afforded by a rodent tooth and adjoining maxillary bone buried to ~1,700 m (Arg 148; 629 m level). Diagenetic calcite crystals ($\delta^{18}O_{cv}$ = -9.4‰) growing in porous bone adjacent to the tooth are distinct from $\delta^{18}O_{en}$ values (-3.7‰).

$\delta^{18}O_{cv}$ data provides constraints on possible deep burial diagenesis because isotopic fractionation of oxygen between calcite and water is a function of temperature (depth). Thus, a deep burial diagenetic event with an isotopically homogenous fluid could produce the observed stratigraphic trend in $\delta^{18}O$. To produce $\delta^{18}O$ vs. depth slopes equivalent to those observed for both paleosol and tooth enamel carbonate would require a geothermal gradient as low as 7°C/km. Use of a more realistic range of geothermal gradients (e.g., 15–30°C/km; see Figure 2.3) indicates that calcite veins probably did not precipitate at maximum burial depth. Disseminated carbonate content in sandstones and volcanic ash beds ranges between 1–65% and yields $\delta^{18}O$ values consistent with paleosol carbonate, indicating early diagenetic precipitation rather than deep burial diagenesis.

Modern tooth enamel is enriched ~1.5–2.0‰ relative to Pliocene $\delta^{18}O_{en}$ values and the standard deviation of the modern data is significantly larger (Table 2.2). Modern data were derived from samples within a 10 km radius of PCQ with two exceptions. A horse sampled on the windward flank of the northernmost Sierra Aconquija (~125 km

northeast of PCQ) yields $\delta^{18}O_{en}$ values of -4.0 ± 0.7‰, whereas a vicuña sampled ~90 km northwest of PCQ on the Puna plateau has a $\delta^{18}O_{en}$ of 3.5 ± 0.2‰. Excluding the aforementioned data from the modern PCQ subset does not significantly change $\delta^{18}O_{en}$ (0.4 ± 2.9‰; n = 24). Vicuña are believed to be obligate drinkers (Vila and Roig, 1992); but the physiological considerations of strong environmental aridity and the possibility of evaporatively enriched drinking water preclude strict comparisons with horse data. However, it remains clear that PCQ occupies an intermediate position both geographically and isotopically.

$\delta^{13}C$ composition of tooth enamel

Endmember C_3 and C_4 diets are calculated using the strategy of Passey *et al*. (2002; 2009), which accounts for changing isotopic composition of the atmosphere through time. This calculation utilizes the enrichment factor between enamel and diet ($\varepsilon^*_{en\text{-}diet}$ = 14.1 ± 0.5 ‰) estimated by Cerling and Harris (1999). Taxon-specific experimental estimates demonstrate that this enrichment factor is applicable to domestic cows, ~ 1‰ high for domestic pigs, and at least 2‰ greater than observed for rabbits and voles (Passey *et al*., 2005a). The latter estimates agree with an $\varepsilon^*_{en\text{-}diet}$ value of 11.0±0.1‰ calculated for woodrats on a controlled diet (Podlesak *et al*., 2008). This calculation thus employs a conservative approach to identifying fossil specimens with a C_4 component in their diet. Many South American fossils have few extant relatives, so little can be inferred about their digestive physiology. Some fossil rodents distributed throughout the section have $\delta^{13}C_{en}$ values more negative than estimates for a pure C_3 diet and likely indicate a digestive physiology characterized by $\varepsilon^*_{en\text{-}diet}$ <14.1‰.

Fossil tooth enamel data record C_4 resource availability not observed in soil carbonate (Figure 2.4). This is notable for the extensive fossil collection older than ~7 Ma, in which 7 of the 59 individuals analyzed, provide positive evidence for the presence of C_4 plants. These fossil specimens (Rodentia and Notoungulata), may have acquired C_4 plants in their diet either by selective grazing of limited C_4 plants locally or by consumption of potentially more abundant C_4 resources at other localities. Relative to the paleosol carbonate record these fossils push the first appearance of C_4 plants at PCQ back from the 591 m level nearly to the base of the section with $\delta^{13}C_{en}$ >-6.0‰ at the 123, 250, 253, and 350 m levels.

In the first appearance interval defined by the $\delta^{13}C_{pc}$ record (591–816 m), 4 of the 20 individuals analyzed record a C_4 dietary component. Again, these specimens are both rodents and notoungulates. The fossil record is especially sparse between 830 and 1200 m, a long interval of eolian strata. In total 16 specimens above the $\delta^{13}C_{pc}$ first appearance interval and below the inferred level of the Miocene-Pliocene boundary (1555 m) were analyzed; all but 4 specimens have $\delta^{13}C_{en}$ values indicating C_4 plants in their diet. Taken together, 44% of the fossils between 591 and 1555 m consumed C_4 plants; though most have $\delta^{13}C_{en}$ values consistent with a minor C_4 dietary component. One fossil tooth at 1462 m (a mesothere notoungulate) has values approximating a C_4 endmember diet.

Of Pliocene fossils, 13 of 23 indicate C_4 plants in their diet. As a percentage this is not markedly greater than for the latest Miocene. Of these, 5 have $\delta^{13}C_{en}$ > -2.0‰, consistent with interpretation as predominantly C_4 grazers (MacFadden, 2005). The range of values for Pliocene samples far exceeds that observed for the Miocene. The

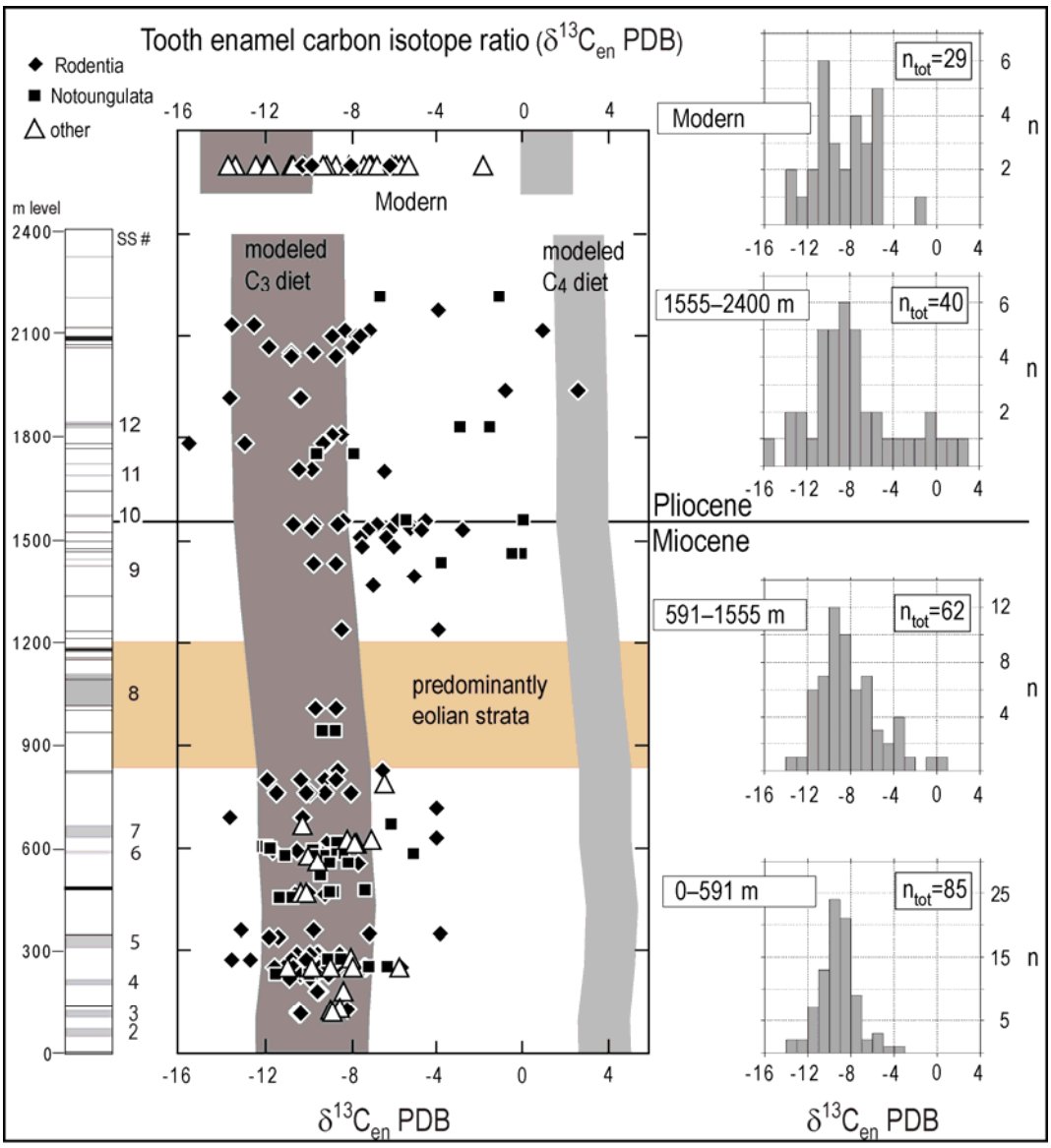

Figure 2.4: Tooth enamel carbon isotope composition from Puerta de Corral Quemado. Estimates of $\delta^{13}C_{en}$ for taxa consuming C_3 and C_4 diets follow the strategy of Passey *et al*. (2002, 2009). Histograms represent the stratigraphic intervals identified in Table 2.2

distribution of $\delta^{13}C_{en}$ values also records some C_3 and mixed feeders. The enriched $\delta^{13}C_{en}$ values may represent a group of specialized C_4 feeders.

Modern tooth enamel identifies predominantly C_3 and mixed feeders. All modern samples were collected within ~10 km of PCQ, with two exceptions: a horse sampled 125 km to the northeast (~2750 m elevation), which yields an average $\delta^{13}C_{en}$ value of -12.2 ± 0.2‰, and a vicuña 90 km to the northwest (~3100 m elevation), which yields an average $\delta^{13}C_{en}$ value of -9.2 ± 0.1‰. Both of these are assumed to represent pure C_3 diets owing to their elevations. Most modern taxa sampled at PCQ, i.e., horses and goats, are recent arrivals to South America. Perhaps the best analog to the PCQ fossil record are the modern rodents. Assuming $\varepsilon^*_{en\text{-}diet}$ = 14.1‰ the data indicate a mixed diet dominated by C_3 plants. Probably more realistic is an $\varepsilon^*_{en\text{-}diet}$ closer to 11‰, which implies that modern rodents have available and consume a mixture of C_3 and C_4 plants locally.

Intratooth profiles of $\delta^{13}C$ and $\delta^{18}O$

The South American record contains numerous taxa, especially within the Rodentia and Notoungulata, with high-crowned (including ever-growing) teeth (Simpson, 1980). Along its length a high-crowned tooth preserves an isotopic record of change experienced by the animal while the tooth was being formed (Balasse, 2002; Koch *et al*., 1989; Passey and Cerling, 2002). Thus, sample profiles along the length of fossil teeth record temporal variations in diet and body water composition (Figure 2.5).

For this study, intra-tooth profiles of large teeth were drilled at a spatial resolution of ~1 mm, and the resulting powder was analyzed for $\delta^{13}C$ and $\delta^{18}O$ using conventional phosphoric acid digestion. Smaller teeth were sampled serially by laser ablation at a spatial resolution of 0.4–0.8 mm. This spatial resolution is approximately equivalent to

Figure 2.5: Intra-tooth profiles for selected samples. Laser $\delta^{18}O$ data have been shifted +5‰ for purposes of visual comparison (cf. Passey and Cerling, 2006). Taxon, stratigraphic height, and analytical method are noted in each panel. Full data are available in Supplementary data 2. Sample numbers are as follows: a) Arg2002-1, b) Arg2002-17, c) Arg2002-22, d) Arg-246, e) Arg2001-50, f) Arg-200, g) Arg2002-5, h) Arg2002-2, i) Arg-121, j) Arg-133n, k) Arg2002-19, l) Arg2002-25.

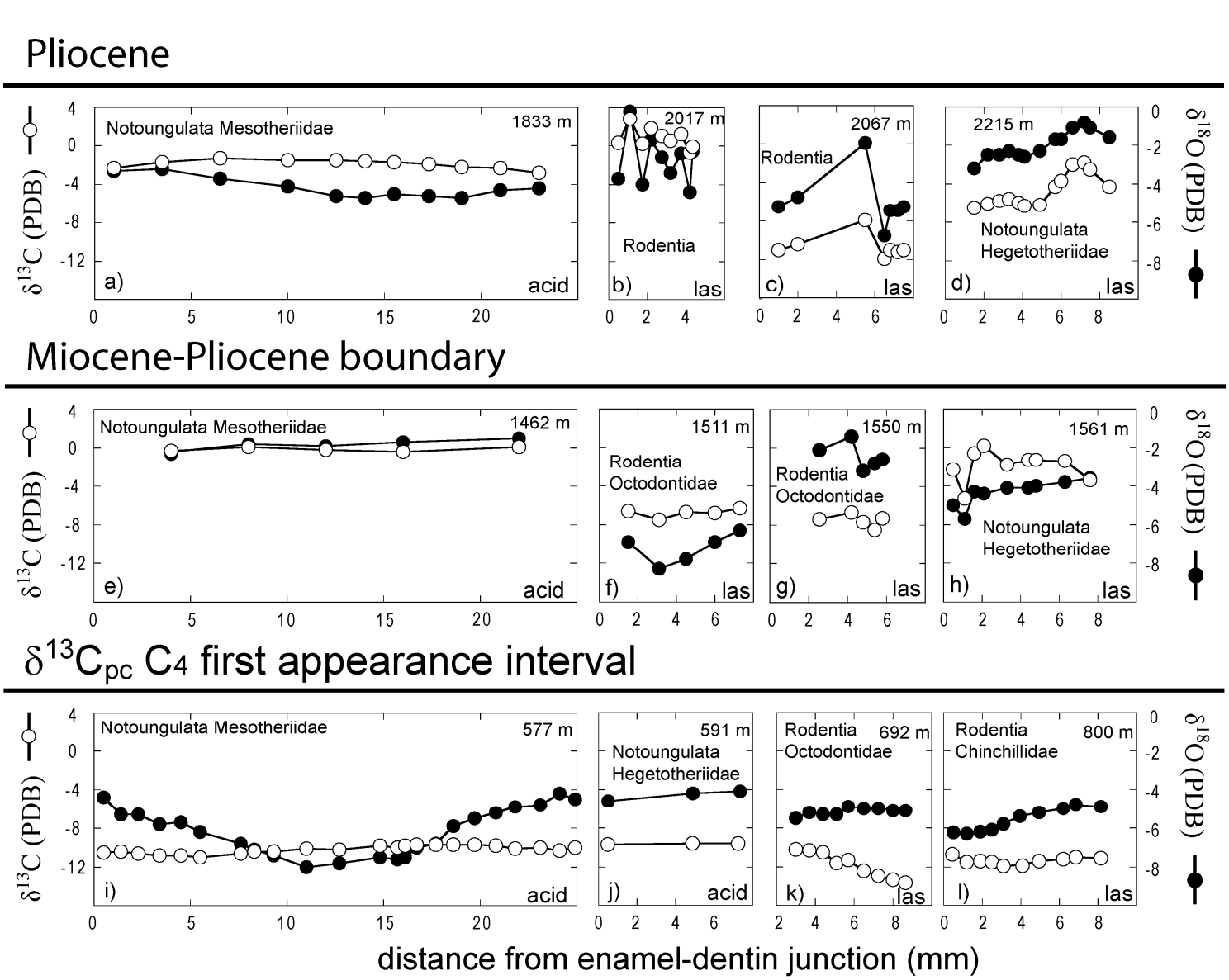
Pliocene
Miocene-Pliocene boundary
δ13Cpc C4 first appearance interval
δ13C (PDB)
δ18O (PDB)
Notoungulata Mesotheriidae
1833 m
a)
acid
2017 m
Rodentia
b)
las
2067 m
Rodentia
c)
las
2215 m
Notoungulata
Hegetotheriidae
d)
las
1462 m
e)
acid
1511 m
Rodentia
Octodontidae
f)
las
1550 m
Rodentia
Octodontidae
g)
las
1561 m
Notoungulata
Hegetotheriidae
h)
las
577 m
i)
acid
591 m
Notoungulata
Hegetotheriidae
j)
acid
692 m
Rodentia
Octodontidae
k)
las
800 m
Rodentia
Chinchillidae
l)
las
distance from enamel-dentin junction (mm)

1–3 days for ever-growing incisors of small mammals (Passey *et al*., 2005a; Podelsak *et al*., 2008). Laser profiles reported here may record as little as a few weeks, and should be interpreted as capturing short-term changes in diet and body water, likely on sub-seasonal timescales for many taxa. Profiles of larger teeth analyzed by conventional acid digestion methods probably represent annual or greater timescales.

$\delta^{13}C_{en}$ values varied little within any tooth of larger bodied mammals. Intra-tooth 1σ standard deviations rarely exceeded 0.5‰, and in every instance near endmember diets are indicated. In the lowest 500 m of the section, dinomyid rodents have average $\delta^{13}C_{en}$ values of -9.9 ± 0.6 ‰ and -10.0 ± 0.3 ‰ respectively, while a typothere notoungulate has a value of -10.9 ± 0.2‰ (Appendix B). Mesotheres record a change from pure C_3 to pure C_4 diets between 577 and 1462 m (Figure 2.5). A Pliocene mesothere (1833 m) also has a near endmember C_4 diet and confirms an abundance of C_4 plants locally from the latest Miocene through the early Pliocene.

Smaller bodied mammals, including hegetotheres and rodents, document more variable diets (Figure 2.5). Specifically, teeth analyzed from the hegetothere subfamily Pachyrukhinae have the largest ranges in $\delta^{13}C_{en}$. A specimen from near the Miocene-Pliocene boundary has a range of 5.5‰ and one from near the top of the section (*Paedotherium sp.*) has a range of 4.7‰. Both have mixed diets with substantial C_4 components.

Rodents from the $\delta^{13}C_{pc}$ first appearance interval at 692 and 800 m have isotopically variable, but endmember C_3 diets. Octodontid rodents from the Miocene-Pliocene boundary have stable diets with a minor C_4 component. Pliocene rodent incisors collected immediately below the Toba Corral Quemado (3.66 Ma) appear to record

strong short-term variation in diet. One incisor indicates a C_3 diet and the other a C_4 diet, both have large intra-tooth ranges (4.0‰ and 3.4‰, respectively).

Oxygen isotope compositions vary widely between individuals. Two octodontid rodents of similar age and similar diet have $\delta^{18}O_{en}$ values that differ by nearly 5‰ (Figure 2.5, panel f,g). Intra-tooth variation greater than 2‰ is unusual in rodents, but hegetotheres have slightly larger ranges. Oxygen isotope variation in excess of 4‰ is noted for Pliocene rodents with large carbon isotope variations. For these fossils a strong correlation between the carbon and oxygen isotope composition of tooth enamel exists. A broad 4‰ excursion observed in the mesothere at 577 m presumably formed on annual or longer timescales. This range in $\delta^{18}O_{en}$ values may record either migration or local seasonality.

Discussion of stable isotope results

The faunal record at Puerta de Corral Quemado

The PCQ fossil record contains some of the earliest North American participants in the Great American Biotic Interchange (GABI; sensu Webb, 1991). At PCQ Procyonidae are known from below the Toba del Puerto (7.14±0.04 Ma) as well as in several higher stratigraphic levels (Butler *et al*., 1984). This dispersal represents an early wave of North American immigrants prior to the closure of an interoceanic seaway at the isthmus of Panama. Additionally, fossil assemblages of the Huayaquerian and Montehermosan South American Land Mammal Ages (SALMA) are in conformable superposition at PCQ. Butler *et al*. (1984) place this boundary very near the top of the eolian interval locally and suggest an age of 6.0 Ma for Argentina. An estimate of 6.8

Ma for the Huayaquerian/Montehermosan boundary in the Bolivian Altiplano highlights potential regional differences in the boundary (Flynn and Swisher, 1995). At PCQ this timespan (6.8–6.0 Ma) encompasses ~600 m of section that correspond to the poorly fossiliferous interval including and immediately overlying eolian strata. Thus, the PCQ section is not ideal for establishing this boundary.

Several observations of the fossil record indicate environmental change through the section. The absolute abundance of fossil teeth decreases upsection (Figure 2.4). The proportion of rodent teeth also increases from 46% in the lowest 590 m of the section to 68% between 591–1555 m, and 83% for the early Pliocene. Larger bodied fossil mammals including dinomyid rodents, toxodont notoungulates, and litoptern ungulates are not known above the base of the $\delta^{13}C_{pc}$ C_4 first appearance interval (591–816 m). The fossil lineages providing the most continuous records at PCQ, hegetothere and mesothere notoungulates and octodontid and chinchillid rodents, are among the taxa that never dispersed to North America. This fact attests to the sub-tropical/temperate affinities of the PCQ fauna (Webb, 1991).

Estimation of C_4 dietary component identifies family level differences in the timing and extent of diet change among rodents and notoungulates (Figure 2.6). The estimates of C_4 dietary component presented are conservative by design; nonetheless, strict interpretation of the calculated C_4 dietary component is not pursued. Since relative comparisons are always the most robust (given $\delta^{13}C_{en}$ variation due to diagenesis, digestive physiology, plant physiology, and changes in the $\delta^{13}C$ of atmospheric CO_2) calculated diets between 0–25% C_4 as considered probable signs of a C_4 dietary component and those >25% as confirmation of a C_4 dietary component. Comparatively,

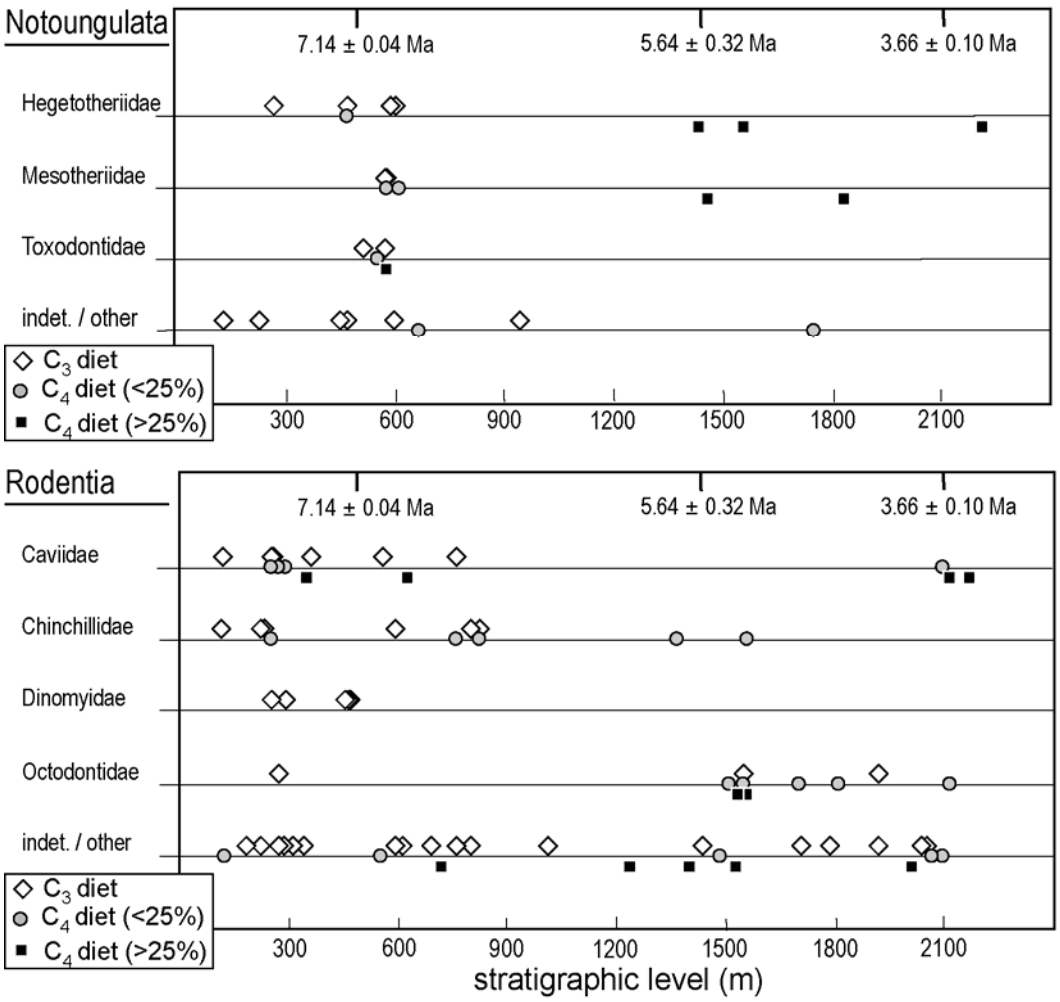

Figure 2.6: Family level diet changes for rodents and notoungulates as a function of stratigraphic level. The C_4 dietary component is calculated using the strategy of Passey *et al*. (2002, 2009).

the absolute range in $\delta^{13}C_{en}$ values observed for the early Pliocene is strong evidence for abundant C_4 plants and a stark contrast to the base of the section. However, to assess family-level stratigraphic patterns, estimation of diet composition is advantageous.

Fossils of the notoungulate family Toxodontidae were among the earliest taxa to consume C_4 plants, but no specimens have been collected above the 580 m level. Mesothere notoungulates (3 specimens) below 614 m had C_3 diets, one at 1462 m had a

consistent diet of 70–75% C_4 plants and one at 1833 m had a diet between 50–60% C_4. Based upon dietary composition and estimated body size of mesothere notoungulates (20–60 kg; Croft *et al*., 2004); abundant C_4 grasses during the latest Miocene and Pliocene are inferred. Hegetothere notoungulates (5 specimens) below 604 m exclusively consumed C_3, one at 1437 m records ~40% C_4 vegetation in its diet, one at 1561 m ranges between 25–75% C_4 and one at 2215 m ranges from 20–65% C_4. Hegetothere notoungulates are smaller bodied than mesotheres and are characterized by isotopically variable diets relative to mesotheres (Figure 2.5). Both families consume a greater proportion of C_4 plants near the Miocene-Pliocene boundary than they do higher in the section.

The largest bodied rodents sampled (Dinomyidae) record C_3 diets in the lowest 500 m of the section and are not known from higher in the section. Rodent fossils of the family Caviidae are the first specimens recording consumption of C_4 plants. Four caviid rodents record 20–40% C_4 dietary component at the 250, 350, 629, and 729 m levels, whereas nine specimens below 760 m may have consumed pure C_3 diets. Fossils caviids are not known from the middle part of the section, but three specimens above the 2100 m level consumed 10–80% C_4 plants and give no indication of pure C_3 diets. Octodontid rodents are poorly represented in the lower part of the section, but the record from 1500–2120 m shows that 7 of 9 specimens consumed C_4 vegetation. These octodontid rodents indicate a diet containing 0–35% C_4 plants, and, as with the notoungulates, maximum C_4 consumption is observed near the Miocene-Pliocene boundary. In contrast to octodontids, the Chinchillidae rodent record is richer for the lower section; 3 of 7 specimens below 860 m record minor C_4 components to their diet (5–20%). Maximum

C_4 consumption is again documented near the Miocene-Pliocene boundary; a chinchillid at 1370 m records ~15% C_4 and one at 1561 m records ~25% C_4.

For Rodentia the dietary estimates should be viewed as extremely conservative for two additional reasons: 1) the enamel-diet isotopic enrichment factor ($\varepsilon^*_{en\text{-}diet}$ = 14.1 ‰) employed may overestimate that for rodents by as much as 3‰ and therefore underestimate C_4 dietary component by as much as 25%, 2) laser ablation methods may bias $\delta^{13}C_{en}$ values by as much as -2‰ and consequently underestimate C_4 consumption by >15%. Based upon the consistent occurrence of rodent $\delta^{13}C_{en}$ values depleted beyond estimates for C_3 diets (Figure 2.4) it is inferred that an enamel-diet isotopic enrichment factor less than ~14‰ is most reasonable. The evidence for ^{13}C depletion associated with laser ablation of fossil enamel is minimal and in our view a minor consideration for this data (cf. Passey and Cerling, 2006).

In the absence of additional tooth enamel records in the region, it is difficult to determine if the fossil record at PCQ effectively captures the adaptation of fossil taxa to C_4 food resources or merely the local arrival of these taxa. A shift in notoungulate diet to predominantly C_4 food sources is documented to occur between the 600 and 1400 m levels at PCQ. The precise nature and timing of this change is not well documented, but volcanic ash beds constrain it to 7.1–5.6 Ma on the basis of $^{40}Ar/^{39}Ar$ age estimates. Notoungulate fossils with pure C_3 diets have not been identified after 5.6 Ma suggesting a true shift in diet. Rodents are among the first to consume C_4 plants, but an obvious shift in diet is not observed. Several Pliocene rodents appear to have had nearly pure C_4 diets, though most indicate mixed diets dominated by C_3 plants. Due to their limited home ranges, rodents provide isotopic proxies that are more likely to sample an environment

similar to that in which they were preserved (taphonomic considerations excluded). As such Pliocene rodents indicate an abundance of both C_3 and C_4 plants.

Understanding small scale spatial patterns in plant communities is aided by laser ablation methods. The small volume sampled by laser ablation, coupled with the high growth rates of small mammal teeth, resolves isotopic heterogeneity resulting from short-term variations in diet and body water composition. For small mammals, such intra-tooth variations can be constrained to a limited home range and thereby remove taphonomic concerns of a mixed assemblage representing two separate environments. The most convincing evidence for mixed C_3/C_4 environments comes from intra-tooth laser ablation of the smallest notoungulates (hegetotheres). Hegetotheres have isotopically variable (mixed) diets and also suggest a landscape with both plant types locally available.

At many scales, small teeth analyzed by laser ablation methods exhibit a relationship between $\delta^{13}C$ and $\delta^{18}O$. Rodent teeth analyzed from the $\delta^{13}C_{pc}$ C_4 first appearance interval are systematically depleted in ^{13}C and ^{18}O relative to those near the Miocene-Pliocene boundary (Figure 2.7). These two intervals represent the most fossiliferous strata above and below the C_4 expansion at PCQ, and correspondingly afford the best opportunity to compare ecological variation as a function of time. Increased inter-tooth isotopic variation is coincident with enrichment for both $\delta^{13}C$ and $\delta^{18}O$. Ecological expansion of C_4 plants is expected to increase inter-tooth variation in $\delta^{13}C$ as a new, isotopically distinct, food source becomes available. Increased inter-tooth variation in $\delta^{18}O$ among rodents may result from increased aridity, new ecological strategies, or both (Levin *et al*., 2006). The observation of increased inter-tooth variation is consistent with the opening of new, isotopically varied, ecological niches between 7.0–5.5 Ma.

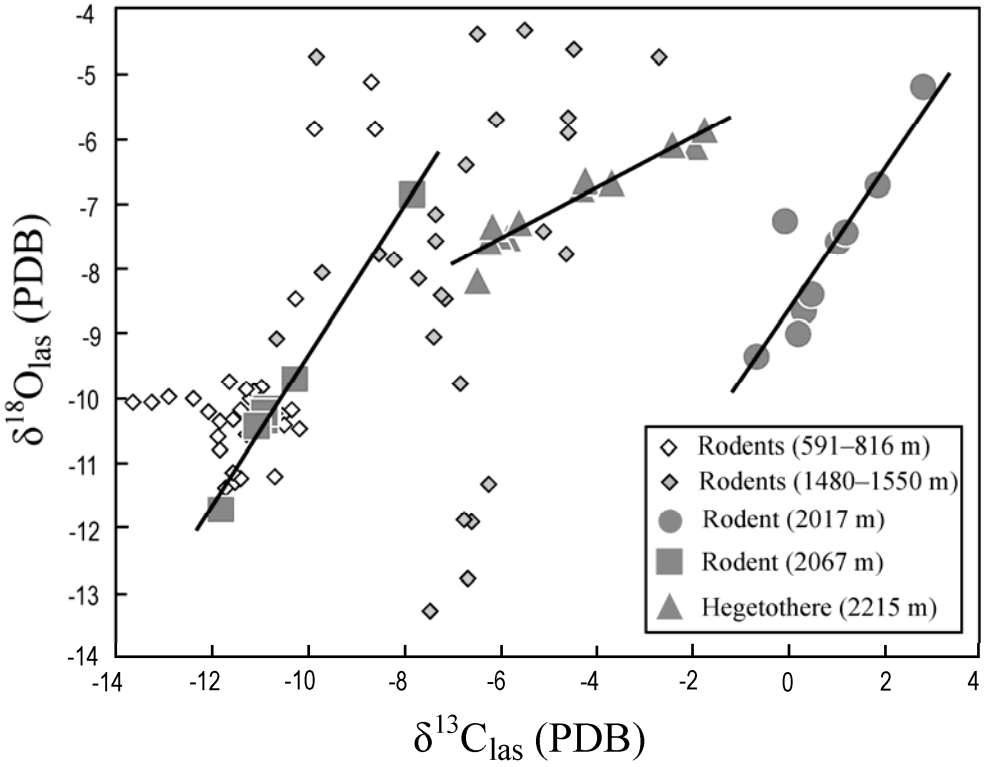

Figure 2.7: Inter-and intra-tooth isotopic variability measured by laser ablation. Data from 591–816 m represent all analyses of rodents (4 multiply sampled specimens) within the $\delta^{13}C_{pc}$ C_4 first appearance interval. Data from 1480–1550 m represent all analyses of rodents (7 multiply sampled specimens) from the fossil rich interval immediately below the inferred level of the Miocene-Pliocene boundary. The intra-tooth variation of three Pliocene fossils is plotted along with a linear least squares regression through the data for each individual; these three specimens correspond to panels b, c, and d in Figure 2.5.

Intra-tooth isotopic variation, as measured by the variance, standard deviation and range of values from a single tooth, does not increase significantly across this interval. Rodents from the base of the section exhibit the least intra-tooth variation and no marked differences are noted from 591–2000 m. However, a subset of rodents between 2000–2100 m exhibits strong intra-tooth variation in $\delta^{13}C$ and $\delta^{18}O$ characterized by positive linear correlations (Figure 2.7). In total, four rodents from this interval yield linear relationships with consistent slopes where the range of $\delta^{18}O$ values is greater than $\delta^{13}C$.

A positive linear correlation is also noted for a hegetothere (*Paedotherium sp.*) at 2215 m, though the slope is significantly different (Figure 2.7). A hegetothere from the 1561 m level yields a similar slope and in both cases the range in $\delta^{13}C$ is much greater than the range in $\delta^{18}O$. These observations suggest that under some circumstances a strong relationship exists between diet and body water isotopic composition for small mammals. This relationship is especially strong for fossil rodents from the upper part of the section.

A host of climatic, ecological, and physiological factors can be invoked to explain the relationship between a ^{13}C enriched diet and ^{18}O enriched body water. The $\delta^{18}O$ enrichment of warm season precipitation should correspond to maximum C_4 abundance and result in a positive correlation between diet and body water at seasonal timescales. The growth rates of rodent incisors are probably too high to record seasonal changes, though the intra-tooth profiles of hegetotheres may do so. Leaf water of grasses is known to be more evaporatively enriched in ^{18}O than dicotyledonous species (Helliker and Ehleringer, 2000). Short term dietary changes might explain the inferred diet-body water relationships by providing ^{18}O enriched leaf water during periods of increased C_4 consumption. This mechanism relies on a large percentage of body water deriving from plant water (at least during consumption of C_4 plants) and is most attractive for small mammals with rapid body water turnover. This is supported by $\delta^{18}O$ enrichment of a C_4 rodent incisor relative to a contemporaneous C_3 rodent incisor (Figure 2.7). The C_4 incisor has an average $\delta^{18}O_{las}$ of -7.7 ± 1.3 ‰ (Arg2002-17; 2017 m) whereas the C_3 incisor has an average $\delta^{18}O_{las}$ of -9.9 ± 1.5 ‰ (Arg2002-22; 2067 m).

The strong intra-tooth relationship between $\delta^{13}C$ and $\delta^{18}O$ ($r^2 > 0.9$ in many cases) raises some analytical concerns. This is particularly true for rodent incisors with thin

enamel, where lower laser power is required for analysis. The possibility of simultaneous fractionation of ^{13}C and ^{18}O during ablation events exists, though the range of values far exceeds the anticipated effect due to changes in laser power (Passey and Cerling, 2006). The teeth exhibiting $\delta^{13}C/\delta^{18}O$ correlation were not analyzed at lower laser power than other teeth. Further, the $\delta^{13}C/\delta^{18}O$ correlation was observed for teeth in several analytical sessions during which many teeth do not exhibit such a correlation. The fact that these teeth are confined to a specific stratigraphic interval suggests an ecological rather than analytical signal.

The distinctly different, though equally robust, $\delta^{13}C/\delta^{18}O$ correlation for the *Paedotherium sp.* from 2215 m also supports an ecological interpretation of this correlation. Larger body size, lower metabolism, and slower turnover of body water combined with different tooth growth rate and ecological strategy could explain the much shallower slope in $\delta^{13}C/\delta^{18}O$ space. The *Paedotherium sp.* tooth is characterized by thick enamel and high CO_2 yield per ablation event. These characteristics make similar samples attractive for future laser ablation work. If tooth growth is slow enough such samples may be ideal for addressing Pliocene seasonality. Larger bodied notoungulates (e.g., mesotheres) are also attractive targets for assessing seasonality based on potentially slower tooth growth rates. However these specimens may be less likely to record $\delta^{13}C/\delta^{18}O$ relationships due to body size and feeding ecology (not mixed feeders).

The ecological implications of the $\delta^{13}C/\delta^{18}O$ correlations observed for laser ablation data are approached with caution. Analytical concerns are considerable and may prove difficult to control when analyzing rodent incisors with extremely thin enamel. Nonetheless, small Pliocene mammals from PCQ provide evidence that diet and body

water isotopic composition are positively correlated. This may prove useful for investigating physiology, environmental aridity, and seasonality. Fossils of the subfamily Pachyrukhinae (Notoungulate, Hegetotheriidae) appear to be especially well suited for intra-tooth studies using laser ablation.

Climate and environment at Puerta de Corral Quemado

Stable isotope data from paleosol and fossil tooth carbonate document climatic and environmental change. These two proxies record $\delta^{18}O$ enrichment > 2‰ through the section. Globally, paleosol carbonate data document enrichments in ^{18}O in South Asia and East Africa during the late Miocene and early Pliocene (Cerling, 1992; Quade and Cerling, 1995; Quade *et al*., 1995). General correlations between $\delta^{13}C_{pc}$ and $\delta^{18}O_{pc}$ in these records led to the hypothesis that the oxygen isotope record was dominated by increased evaporation of soil water as C_4 grasslands expanded. Recent studies in South Asia have concluded instead that the ^{18}O enrichment in paleosol carbonate documents decreasing rainfall via the "amount effect" (Behrensmeyer *et al*., 2007; Dettman *et al*., 2001). Plant wax δD values from the Bengal Fan indicate that both decreased precipitation and increased evaporation between 10 and 5.5 Ma contributed to the ^{18}O enrichment (Huang *et al*., 2007).

The $\delta^{18}O$ enrichment at PCQ can be constrained to the same interval as observed for East Africa and South Asia. Whether this enrichment records a globally significant shift in the hydrologic cycle remains an important question. Several potential global causes have been suggested; including increasing continental aridity and ecological disturbance worldwide (Tipple and Pagani, 2007). If earth's hydrologic cycle is a closed system at the temporal scale of 10 Ma, an increase in aridity must be balanced by similar

increases in precipitation. Changes in the distribution of precipitation may have been spatial, temporal, or both. Increased seasonality of precipitation is an attractive explanation for two reasons; 1) precipitation during warmer months would result in systematically enriched ^{18}O input to the landscape (Kohn and Welker, 2005; Rozanski *et al*., 1993), and 2) enhanced evaporation during the dry season would lead to ^{18}O enriched soil water (Gat, 1996). Both of these factors are likely to be recorded in paleosol carbonate isotope ratios if carbonate formation is seasonally biased towards dry periods following a rainy season (Breecker *et al*., 2009).

Paleosol carbonate data from the Bolivian Altiplano record depletion in ^{18}O across the same time interval (Garzione *et al*., 2006). These $\delta^{18}O_{pc}$ data, supported by other proxy data, have been interpreted to document rapid uplift of the northern Altiplano between 10–6 Ma (Bershaw *et al*., 2010; Garzione *et al*., 2008). Rapid uplift of the Bolivian Altiplano is a viable cause for the inititation of the South American monsoon by increasing moisture transport from the tropics to higher latitudes via the South American low-level jet (Insel *et al*., 2009). However, it is possible that slow topographic growth of the Andean plateau may have triggered similar climatic changes when a topographic threshold was crossed (Ehlers and Poulsen, 2009). In either case, the strong divergence in $\delta^{18}O$ proxy records between PCQ and the Altiplano points to major reorganization of precipitation patterns during the late Miocene.

Regional differences in $\delta^{18}O$ proxy records may be further explained by differential uplift histories and local orographic effects. An orographic rainshadow related to growth of the Sierra Aconquija may have formed as early 6–5 Ma (Kleinert and Strecker, 2001; Sobel and Strecker, 2003), and a pulse of Pliocene uplift is well

documented in northwestern Argentina (Strecker *et al*., 2007a). By definition, orographic controls on climate and environment predict strong spatial gradients. Consequently, our ability to test the influence of local orographic barriers on the Miocene-Pliocene climate and ecology of PCQ is currently limited by the spatial density and temporal control of proxy records.

Modern climatic gradients in the region are striking (Bookhagen and Strecker, 2008). A strong gradient from the easternmost Sierras Pampeanas to the Puna plateau is documented with modern isotope data. Two modern $\delta^{18}O_{en}$ values from high elevation samples record a 7.5‰ westward enrichment at a spatial scale of 150 km. Both of these samples are from obligate drinkers; yet, the complexity of variables influencing $\delta^{18}O_{en}$ values in an individual precludes straightforward interpretations (cf. Levin *et al*., 2006). The corresponding 3‰ enrichment in $\delta^{13}C_{en}$ provides more convincing evidence of a strong climatic gradient. We assume that both specimens sampled environments of pure C_3 plants owing to their elevation (>2.7 km). The 3‰ difference in $\delta^{13}C_{en}$ is attributable to differences in carbon isotope discrimination between C_3 plants in wet environments and C_3 plants in water-stressed environments (Farquhar *et al*., 1989). Documenting Miocene-Pliocene climatic and environmental gradients in northwestern Argentina at similar spatial scales should be possible using isotope proxy data, and doing so will provide a test of local/regional modulation of a global ecological event.

With regard to the vegetative history at PCQ, carbon isotope ratios of fossil and modern teeth complement the paleosol carbonate isotopic record. $\delta^{13}C_{en}$ values indicate that C_4 plants were present at PCQ from 9.0–3.5 Ma, and remain there today. C_4 plants were consumed by herbivores in minor amounts prior 7 Ma; during this time many of the

largest herbivores have $\delta^{13}C_{en}$ values (-8 to -11‰) indicative of C_3 vegetation in mesic to xeric environments. The environment was probably not humid or densely forested, but rather a mosaic of forested and grassland environments. Substantial C_3 grassland may have existed and some C_4 grasses were certainly present.

For plant and herbivore communities, the period from 7.0–5.5 Ma was one of transition. Locally eolian environments were present for ~ 0.5 Ma. The proportion of herbivores consuming C_4 plants increases markedly across this interval, but due to the poorly fossiliferous nature of the strata details are scarce.

The Pliocene fossil record strongly indicates a mixed or patchy environment with sufficient C_4 vegetation to support specialized feeders. This reconstruction informs interpretation of the uppermost paleosol carbonate in the section. Between 2149 and 2219 soil carbonate nodules at 4 different levels record a dramatic positive shift in $\delta^{13}C$ values to a maximum of -2.5‰. This entire zone is above Toba Corral Quemado (2072 m, 3.66 Ma). A prominent ash bed occurs within this interval (Arg-244, 2198 m) and another (Arg-267, 2320 m) overlies this positive shift in $\delta^{13}C_{pc}$ values. Radioisotopic ages for these ash beds will be an important constraint on the rate of this change.

The present interpretation is that this occurred relatively rapidly and probably represents a shift across ecotone boundaries present throughout the early Pliocene as opposed to an ecological expansion of C_4 grasslands. An elevational shift in ecotone boundaries due to glacial-interglacial type climate changes is plausible (cf. Amundson *et al*., 1996); however the absence of a synchronous $\delta^{18}O_{pc}$ shift argues against this hypothesis. Similarly, the lack of a $\delta^{18}O_{pc}$ shift also argues against a C_4 expansion resulting from the development of orographic rainshadows (Kleinert and Strecker, 2001).

Instead an explanation invoking lateral shifts in ecotone boundaries that were locally present throughout the Pliocene, but poorly sampled by the $\delta^{13}C_{pc}$ record, is preferred. The increase in C_4 vegetation is approximately coincident with the appearance of coarse gravels which also document spatial shifts in the landscape. Progradation of gravel may be suitably explained by either autocyclic fluvial processes or renewed uplift of nearby mountain blocks. It is noted that high variance in $\delta^{13}C_{pc}$ values between 1300 and 1400 m correlates with a gravel rich interval. Landscape scale isotopic variation is well documented by detailed studies of laterally extensive paleosols (Levin *et al*., 2004; Behrensmeyer *et al*., 2007). In the absence of additional data it is difficult to properly assess the significance of the post 3.6 Ma $\delta^{13}C_{pc}$ shift at PCQ.

No information is currently available about the climate or environment at PCQ between ~3 Ma and present. Modern tooth enamel identifies predominantly C_3 and mixed feeders. Based upon these results it appears that C_4 plants were more abundant during the Pliocene than they are today, even though modern aridity and summer precipitation tend to favor C_4 plants. This decrease in C_4 abundance at PCQ since the Pliocene may be explained by surface uplift to modern elevations of ~ 2 km. Modern high elevation samples provide no evidence of C_4 plants in their diet and PCQ is currently near the upper elevation limit for C_4 plants (Cabido *et al*., 1997), so it is surmised that during the late Pliocene the study area may have been at a lower elevation.

Timing and nature of C_4 expansion

The timing of the C_4 expansion recorded at Puerta de Corral Quemado is broadly synchronous with the global tooth enamel record (Passey *et al*., 2009). A dramatic diet change is observed in notoungulates between 7.0–5.5 Ma. The rodent record is more

ambiguous as many taxa are characterized by mixed C_3/C_4 diets; however, an increase in C_4 consumption is still documented across the same temporal interval. The paleosol carbonate isotopic record at PCQ confirms this timing (Latorre *et al*., 1997). Collectively these records indicate that C_4 plants were present in minor amounts during the interval between 9–7 Ma, but an ecosystem with abundant C_4 grasses existed during the early Pliocene—the intervening time is the period of ecological change.

At PCQ, all data derive from a single stratigraphic section and great care has been taken to ensure high resolution stratigraphic control. This affords an important opportunity to directly compare multiple isotopic proxies. Direct comparison of paleosol carbonate and fossil tooth enamel proxy records greatly increases confidence in the timing and structure of C_4 expansion. While it is common to find isotopic evidence for C_4 plants in paleosol carbonate records prior to the late Miocene (Clyde *et al*., 2001; Fox and Koch, 2004), the global tooth enamel record is quite distinct. Some fossil tooth enamel indicates consumption of C_4 plants as early as 10 Ma in low latitudes, but the ecological event recorded by this proxy appears to be approximately synchronous globally (Cerling *et al*., 1997; Passey *et al*., 2009). Stratigraphic analysis of both proxy records at PCQ confirms the estimate that major ecological change took place between 7.0–5.5 Ma, and extends the interval of major ecologic change to ~5 Ma (Figure 2.8).

The most notable feature of these stratigraphic analyses is that all proxies record change during two intervals. The first interval of change is approximately coincident with the $\delta^{13}C_{pc}$ C_4 first appearance interval (~600 m level). This period of change is defined by the carbon isotope record, but its best expression is found in $\delta^{18}O$ proxy records. A second period of change is observed near the Miocene-Pliocene boundary.

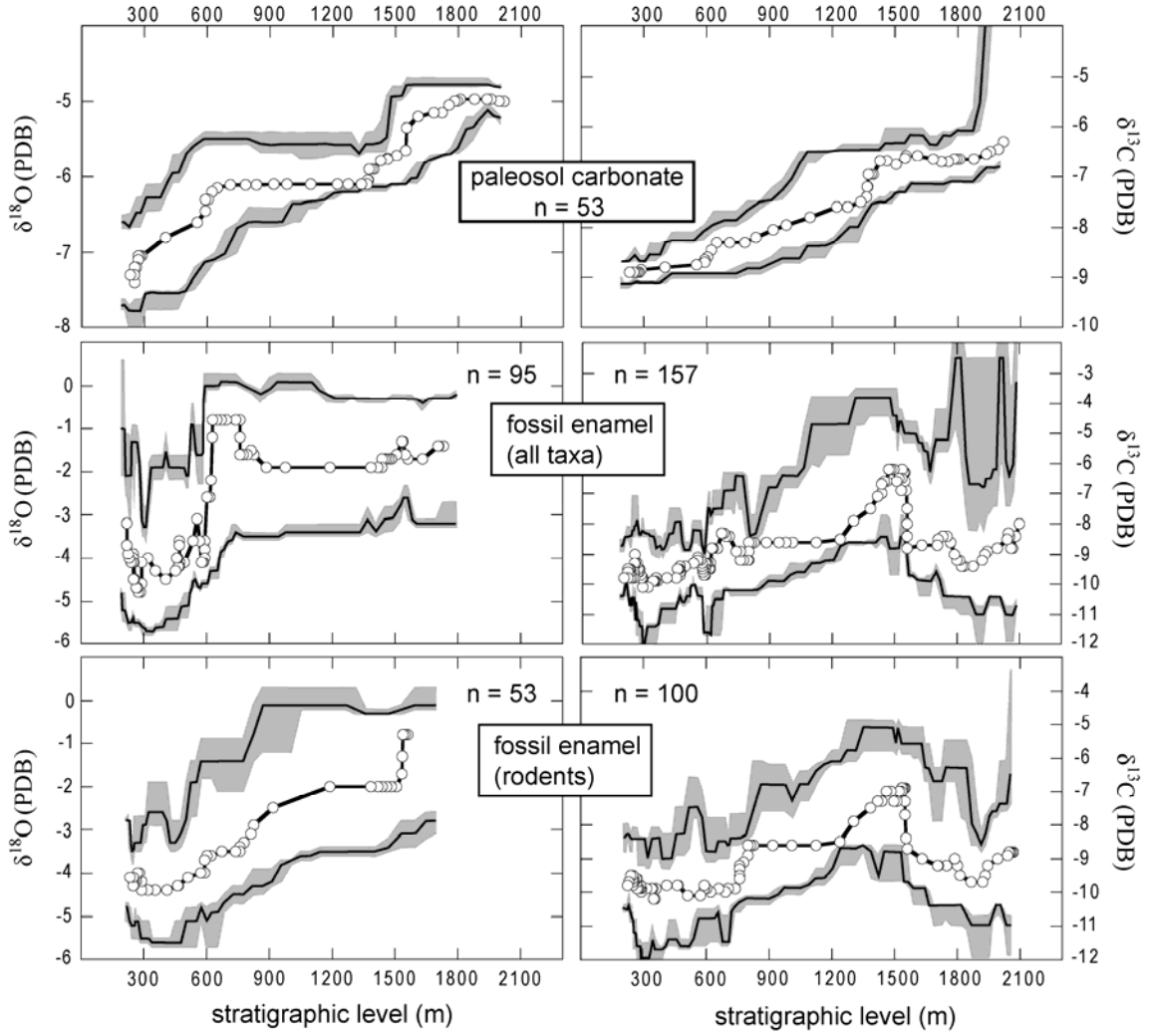

Figure 2.8: Twenty point moving window of tooth enamel and paleosol carbonate stable isotope data. The upper bounds represent the 80th (± 5) percentile of the population and the lower bounds represent the 20th (± 5) percentile of the population. Percentiles are plotted against the mean stratigraphic height of each successive 20 point window. Median isotopic value versus median stratigraphic height for each 20 point window is also plotted. For paleosol carbonates all data are used and for fossil tooth enamel the max-min filtered subset is used. Tooth enamel $\delta^{13}C$ values include laser ablation and acid digestion measurements. Tooth enamel $\delta^{18}O$ values include only those measured by acid digestion.

This Mio-Pliocene feature is also present in all proxy records, but is best expressed in the $\delta^{13}C_{en}$ record. Tooth enamel demonstrates a transient $\delta^{13}C$ enrichment of > 2‰ at ~ 1500 m; whereas the paleosol carbonate $\delta^{13}C$ record is stepwise and appears to precede the tooth enamel enrichment. $\delta^{18}O_{en}$ data also suggest a transient event, though conventional acid digestion data are too sparse in the upper part of the section to robustly document this. If all laser $\delta^{18}O$ data are used a similar enrichment is noted near the Miocene-Pliocene data. This supports the interpretation of a transient ^{18}O enrichment in tooth enamel and suggests that laser $\delta^{18}O$ data may prove useful for environmental reconstruction given sufficient data. Again, the paleosol carbonate data contrast with the tooth enamel data in that they record a stepwise enrichment in ^{18}O during this interval.

Currently, the only multiproxy record of comparable length and fidelity is that of the Siwalik Hills, Pakistan (Cerling *et al*., 1997; Quade and Cerling, 1995). The C_4 expansion there is believed to have been an ecological transition on a broad flood plain (Behrensmeyer *et al.*, 2007). The timing is constrained to 8.0–5.0 Ma and the rates appear to be steady across this interval. The record at PCQ demonstrates ecological change across the same temporal interval, but the structure of the C_4 expansion in northwestern Argentina is clearly different. Growing concern exists that single vertical sampling profiles of paleosol carbonate may not appropriately characterize landscape scale vegetation structure (Behrensmeyer *et al*., 2007). The relatively poorly developed paleosols at PCQ preclude extensive studies of lateral variation within individual soil horizons. Assessment of landscape scale vegetation patterns from paleosol carbonate stable isotope data will have to proceed by sampling contemporaneous strata at nearby localities. Instead the $\delta^{13}C_{en}$ of small mammals is used to assess spatial variability in

plant communities, and demonstrates mixed C_3/C_4 ecosystems during the Pliocene. Based upon $\delta^{13}C$ and $\delta^{18}O$ data from paleosol carbonate and fossil tooth enamel it is inferred that the C_4 expansion at PCQ was pulsed.

A complex array of factors, ranging from global to regional and local drivers of climatic and ecologic change, may be implicated in contributing to the C_4 expansion at PCQ. The initial C_4 expansion is documented at ~7.0 Ma and clearly precedes the pulse of Pliocene uplift in the region (Strecker *et al*., 2007a). Specifically, an orographic rainshadow related to growth of the Sierra Aconquija is not expected until nearly 5 Ma (Kleinert and Strecker, 2001; Sobel and Strecker, 2003), and plateau margin deformation and uplift is not documented locally until after 3.5 Ma. It is therefore difficult to attribute the initial C_4 expansion to local aridification resulting from development of orographic barriers. Global causes such as increased seasonality of precipitation and ecological disturbance remain attractive explanations (Tipple and Pagani, 2007). This initial expansion may also be related to development of the South American monsoon (Uba *et al*., 2007; Strecker *et al*., 2007b; Mulch *et al*., 2010), but its timing is also broadly synchronous with the global tooth enamel record.

The second period of ecological change occurs near the Miocene-Pliocene boundary. Several other stable isotope records from the region also document ecological change at approximately the same time. In the Santa María Valley a transient increase in the $\delta^{13}C$ values of paleosol carbonate occurs between 6–5 Ma (Kleinert and Strecker, 2001). Nearly 200 km north of PCQ, strata in the Angastaco basin record enrichment in $\delta^{13}C$ and $\delta^{18}O$ values of both paleosol and fossil tooth enamel carbonate (Bywater-Reyes *et al*., 2010). This shift occurs at ~5 Ma and is interpreted to reflect regional

aridification. Taken together these three records argue strongly for the regional significance of C_4 expansion near the Miocene-Pliocene boundary, possibly related to aridification or to the intensification of the South American monsoon.

A clearer understanding of regional synchroneity and spatial variation during the expansion of C_4 grasses at PCQ is critical to elucidating potential drivers of ecological change. It has been hypothesized that uplift of the Puna-Altiplano plateau was integral to development of the South American monsoon (Strecker *et al*., 2007a) and several tectonic models have been proposed for plateau uplift leading to monsoonal intensification (cf. Ehlers and Poulsen, 2009). If monsoonal intensification is interpreted to be the primary driver of C_4 expansion at PCQ then modulation of monsoonal dynamics by drivers other than plateau uplift will likely be needed to explain the pulsed nature of the expansion. If regional aridification linked to the expansion of the West Antarctic Ice Sheet is interpreted as the primary driver of C_4 expansion at PCQ the pulsed nature of the proxy records is more easily explained (Lamb and Davis, 2003; Bywater-Reyes *et al*., 2010). However, attributing the C_4 expansion to any single regional climatic driver may be fundamentally flawed and ignores the potentially dramatic influence of growing topographic barriers (Kleinert and Strecker, 2001). Further, interpretation of C_4 expansion resulting from regional climatic drivers ignores the global nature of this ecological event (see Tipple and Pagani, 2007). Any effort to disentangle these potential drivers of climatic and ecological change must be based upon increased spatial density of isotopic proxy records and dramatically improved temporal control.

Conclusions

Detailed stratigraphic work, including geochemical correlation of volcanic ash beds provides a high resolution framework for analysis of stable isotope proxy data. Fossil tooth enamel carbonate $\delta^{13}C$ and $\delta^{18}O$ analyzed by conventional acid digestion methods and by laser ablation are compared to the paleosol carbonate record. Together these proxy data document $\delta^{18}O$ enrichment of >2‰ across the late Miocene and early Pliocene. Both proxies additionally document $\delta^{13}C$ enrichment across the same interval indicating late Miocene expansion of C_4 plants in northwestern Argentina. The timing of the C_4 expansion at Puerta de Corral Quemado is synchronous with the global tooth enamel $\delta^{13}C$ record.

C_4 plants were present and consumed by herbivores as early as 9 Ma, but the ecosystem was dominated by C_3 plants in a mesic to xeric environment. A period of major ecological change occurs between 7.0–5.0 Ma. Notoungulate fossils indicate a shift from C_3 to C_4 diets between 7.0–5.5 Ma. Pliocene hegetothere notoungulates consumed mixed diets with a substantial C_4 component that varied temporally (seasonally?). Rodent fossils of Pliocene age have diets dominated by both C_3 and C_4 plants, in addition to some mixed diets. Both the mixed and specialized diets of small mammals during the Pliocene are interpreted to indicate a landscape in which C_3 and C_4 plants were abundant locally.

Stratigraphic analysis of this multiproxy record identifies two prominent intervals of ecological change. The first interval occurs at ~7 Ma and predates a pulse of Pliocene uplift. It is suggested that this interval of change is related to the global expansion of C_4 plants and not a result of aridification associated with the uplift of orographic barriers. A

second interval of change at approximately the Miocene-Pliocene boundary is observed in other stable isotope records from the region. While precise synchroneity can not yet be demonstrated, there appears to be a regionally significant period of climatic and ecological change between 5.5 and 5.0 Ma. This may be related to regional aridification, or to changes in South American monsoon precipitation patterns both of which should produce ^{18}O enriched soil carbonate.

Modern tooth enamel stable isotope data are difficult to interpret because many of the taxa sampled are domestic. Most of the taxa are also recent arrivals to South America and only distantly related to the Miocene and Pliocene faunal assemblages. Nonetheless these data serve to identify strong modern climatic gradients present from the windward eastern flanks of the Sierra Aconquija to the interior of the Puna plateau. The $\delta^{18}O$ values of modern tooth enamel are enriched relative to Pliocene tooth enamel and the range of values is also significantly larger, indicating that the region has become more arid between ~3.5 Ma and present. Modern herbivores consume C_4 plants but not to the degree that Pliocene herbivores did; this provides modest evidence for surface uplift in the intervening time as well.

CHAPTER 3

MIO-PLIOCENE SEDIMENTATION AND DEFORMATION CONSTRAINED BY IDENTIFICATION OF WIDESPREAD VOLCANIC ASH BEDS

Introduction

High altitude plateaux are increasingly understood as topographic features of global significance. These massive protrusions into the atmosphere modify zonal atmospheric circulation, play an important role in the surface heat budget of the earth, and generate regionally important precipitation systems (Ehlers and Poulsen, 2009; Insel *et al*., 2009.). Such plateaux, due to their size, elevation, and location in the center of orogenic systems are characterized by arid climates with unique ecological, geomorphic, and geodynamic systems. The link between arid climates and plateau growth presents a fundamental geodynamic problem of broad interest (Molnar and England, 1990; Masek *et al*., 1994). This study constrains the Miocene-Pliocene geologic history along the southernmost margins of the South American Puna-Altiplano plateau by using widespread volcanic ash beds to date tectonic and sedimentary events (Figure 3.1). Accurate and precise chronologic horizons of regional import address two questions relating to the Miocene-Pliocene growth of the plateau: 1) What is the timing and style of surface deformation along the plateau margin? 2) What is the timing and significance of extensive conglomeratic units that cap stratigraphic sequences in the region?

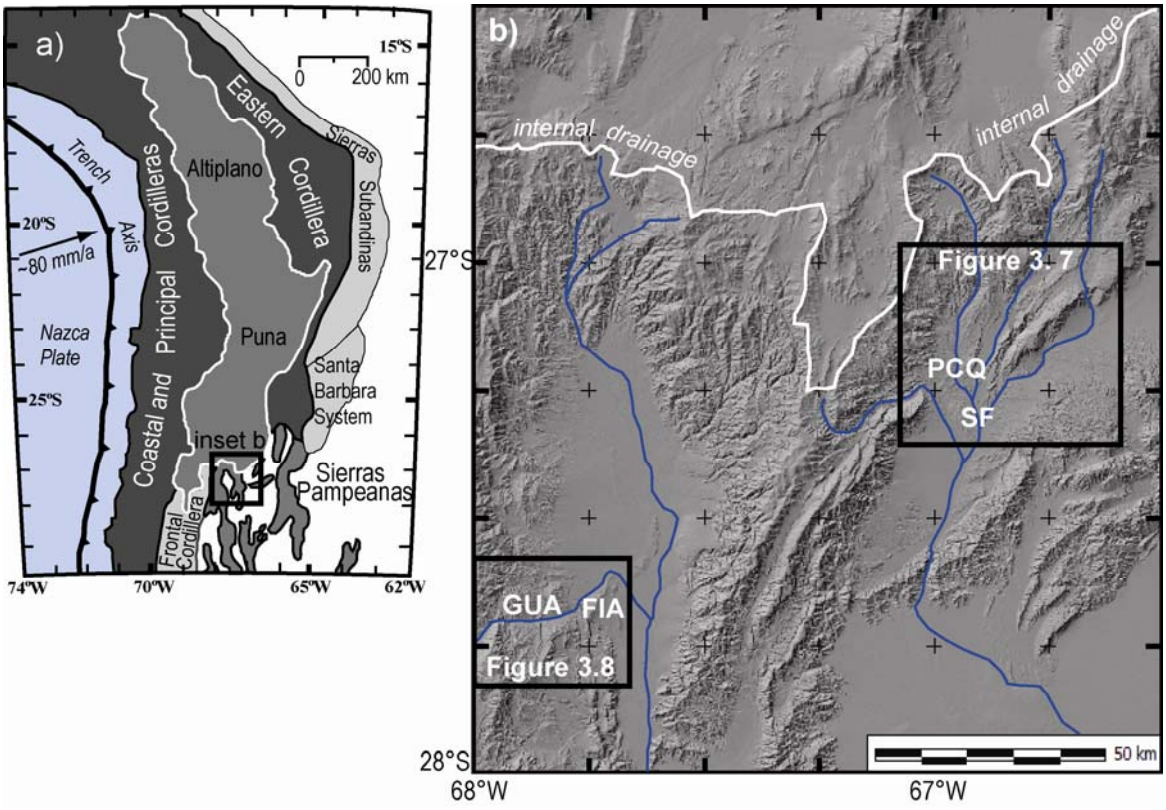

Figure 3.1: Tectonic and topographic setting of the study area: **a)** morphotectonic provinces of the Central Andes after Jordan *et al*. (1983), Nazca-South America convergence vector from Marrett and Strecker (2000), **b)** DEM of study area from Shuttle Radar Topography Mission 3 arc second data, modern drainages highlighted in blue, GUA = Río Guanchin section, FIA = Fiambalá section, SF = San Fernando sections, and PCQ = Puerta de Corral Quemado section.

In northwestern Argentina between 26–28°S latitude the Sierras Pampeanas morphotectonic province, at its northernmost termination, is characterized by basement cored, reverse fault bounded uplifts on the periphery of the southern Puna plateau (Jordan *et al*., 1983). The Sierras Pampeanas correspond geographically with an amagmatic zone of shallow-dipping subduction and have been described as analogous to Laramide uplifts of the western United States (Jordan and Allmendinger, 1986).

The Puna-Altiplano plateau is the second highest and largest such feature in the world, second only to the Tibetan plateau. The Puna-Altiplano system is notable in that it

corresponds spatially with Neogene volcanism and that it attained its current height and extent in the absence of continental collision or terrane accretion. If the plateau is defined as the notable broadening of the area above the 3 km elevation contour (*sensu* Isacks, 1988), it spans ~1,800 km latitudinally and ranges between 350 and 400 km in width. The area of the plateau that is internally drained is roughly coincident with the 3 km contour, yet considerably smaller in extent. The complex history of the plateau is reviewed by Allmendinger *et al*. (1997) and geologic descriptions of intra-plateau differences are available therein; several salient points are highlighted here. The Puna is that part of the plateau mostly in northwestern Argentina which is characterized by higher average elevation, more relief, some of the youngest ignimbrite centers on the plateau, and active tectonic shortening until 1–2 Ma. The Altiplano, by contrast is older, broader, and flatter; intense volcanism and active shortening appear to have terminated earlier.

The present study is concerned with constraining the timing and style of the most recent tectonism at the southern margin of the plateau. A recent body of work has advanced understanding of tectonic and climatic controls on uplift, deformation and sedimentation in the region (cf. Strecker *et al*., 2007a). Critically, the Sierras Pampeanas are effective barriers to easterly moisture transport and create a series of semi-arid intermontane basins along the margin of the Puna plateau (Bookhagen and Strecker, 2008). The development of arid intermontane basins can lead to storage of large volumes of coarse grained sediment. In cases where aridity is pronounced and resistant bedrock is exposed by uplift, fluvial systems can become isolated from the foreland and from global base level (Sobel *et al*., 2003).

Intermontane sedimentary basins along the Puna margin may be repeatedly filled and excavated within a period of ~10 Ma (Hilley and Strecker, 2005). Alternatively, sedimentary basins may become permanently isolated from the foreland (internally drained); storing sediment indefinitely and ultimately coalescing with adjacent basins (cf. Sobel *et al*., 2003). Development and coalescence of arid intermontane basins is thus a potential mechanism for outward growth of the Puna plateau. Within this framework, the questions posed regarding timing of deformation and coarse grained sedimentation at the plateau margin are relevant to the Miocene-Pliocene development of the Puna plateau.

Scientific approach, material studied, and analytical methods

Aside from the well known Cerro Galán volcanic complex (Francis *et al*., 1983; Francis *et al*., 1989), explosive silicic volcanism on the southern Puna plateau produced numerous small to medium volume ignimbrites between 25 Ma and present. These ignimbrites are characterized as metaluminous, crystal-poor rhyolites which are often chemically zoned (Schnurr *et al*., 2007). Volcanic ash from these eruptions is preserved in sedimentary basins at the plateau margin and exploited as a means of constraining the geologic history of these basins.

During eruption, explosive silicic eruptions produce large amounts of fragmental material (tephra). Deposition of tephra, generally within days to years following an eruption, results in volcanic ash beds. Upon deposition and burial, volcanic ash beds become stratigraphic horizons with chronological significance. Volcanic ash beds in northwestern Argentina often contain detrital material of uncertain origin, but are predominantly composed of volcanic glass and comagmatic mineral phases. Eruptive minerals such as sanidine, biotite, plagioclase, and zircon provide material for

radioisotopic dating and volcanic glass provides a proxy for the composition of the liquid part of the magma. Magma composition is unique for nearly every eruption and compositional analysis of volcanic glass is a proven method for identification and correlation of volcanic ash beds from widespread localities (e.g., Izett, 1981; Sarna-Wojcicki *et al*., 1987; Perkins *et al*., 1998). Because the timescale of deposition for a volcanic ash bed is orders of magnitude less than the uncertainty associated with radioisotopic age estimates, geochemical correlation of ash beds creates chronostratigraphic horizons with extremely high precision. Thus volcanic ash beds are markers capable of providing age control for a variety of geologic records associated with the encasing strata. Moreover, when chronostratigraphic information is combined with strike and dip an individual ash bed becomes a structural datum, enabling constraints to be placed on the timing, magnitude, and locus of deformation.

The term tuff, and its Spanish equivalent 'toba', referring to consolidated volcanic ash are employed occasionally. When discussing an individual deposit, the term ash bed is used to denote the specific occurrence. Tuff and toba are used in conjunction with formal or informal unit names to discuss well described ash beds which have been correlated between stratigraphic sections and do not refer to a specific occurrence or sample of a volcanic ash bed.

Volcanic ash samples were disaggregated, sieved, and washed in an ultrasonic bath with 10% HNO_3 to remove any adhering carbonate and 5% HF to remove clay minerals and birefringent rims from glass. Optical inspection of the 125–250 μm fraction commonly revealed >50% glass shards, and in many instances glass was sufficiently concentrated for electron probe microanalysis (EPMA). Glass separates for bulk analysis

were further concentrated by standard magnetic and density techniques. Final density separation with tribromomethane was conducted in a differential specific gravity tube and subtle gradients permitted separation of glass with feldspar inclusions from the bulk sample. Purity of each sample was checked with a petrographic microscope. Samples exceeding 99.9% glass were handpicked to remove remaining contaminants under a binocular microscope until 30–60 mg was available for solution nebulization Inductively Coupled Plasma - Mass Spectrometry (ICP-MS).

EPMA of major and minor element concentrations in glass and minerals were determined with a Cameca SX 50 using methods described by Nash (1992). Analyses were made at 15 keV accelerating voltage, a beam current of 25 nA, and a beam diameter of 10 μm. To minimize Na mobility and associated analytical errors, Na K_α X-rays were counted for only 5 seconds at the beginning of each analysis (Nielsen and Sigurdsson, 1981; Hunt and Hill, 2001). Additionally, beam diameter was maximized to reduce Na mobility; 10 μm generally being the largest possible diameter for which all samples could be analyzed under identical operating conditions. Estimates of water content for glass shards were calculated from the difference between measured and stoichiometric oxygen contents assuming all Fe as Fe_2O_3 (cf. Nash, 1992). Analysis of individual volcanic glass shards is critical to establish shard to shard variability, often a robust characteristic of individual eruptions. Typically 20 shards were analyzed for each sample; important samples were often analyzed in duplicate during different analytical sessions. Potentially correlative samples were identified using the statistical distance function (Perkins *et al.*, 1995; Appendix B) based on EPMA values for Ca, Cl, Fe, Mg, Mn, and Ti.

Once potential correlations were identified by EPMA they were further tested by analysis of trace element concentration in volcanic glass. Purified glass separates were analyzed for trace element concentrations by ICP-MS methods. The analytical approach is a modification of that of Willbold and Jochum (2005). 30 mg aliquots were digested in ultra-pure acid (2.4 % HNO_3 with 100 µl additions of concentrated HF). After digestion, sequential dilutions were carried out with 2.4% HNO_3 prior to standard addition and isotopic spiking. Ba and Sr were measured by isotope dilution and all other elements were measured by standard addition, using Ba as an internal standard. Analysis of reference material confirms the accuracy and precision of the method (Hynek *et al*., 2010). Data are within 10% of the preferred value, and repeat analysis of unknowns and internal standards indicate that precision is ≤ 5% of the measured value for all elements.

Major volcanic ash beds of the southern Puna plateau

Four stratigraphic sequences of latest Miocene and Pliocene age are reported from the southeastern margin of the Puna plateau (Figure 2.1). Three of these sequences are from the ~2.8 km thick stratigraphic section at Puerta de Corral Quemado and one is from a ~1 km thick section along the western margin of the Fiambalá basin. As estimated by the density of stratigraphically and geochemically unique ash beds, each of the sequences likely represents a period of higher than average eruption rates. Consequently, many volcanic ash beds which have been sampled and analyzed from parallel sections are not presented within a composite stratigraphic sequence. Because stratigraphic order (homotaxy) is one of the most important criteria when correlating ash beds, only those with secure stratigraphic placement are presented in the following. Many thinner, less extensive ash beds have known stratigraphic relationships with one of the reported

samples, but cannot be firmly placed in a composite sequence. When sufficient data exists to geochemically characterize these samples it is given in Appendix A along with a conservative range of stratigraphic heights.

Each sequence is developed principally at one locality, but local and regional correlation of ash beds between localities are established in three of the four instances. Correlation of volcanic ash beds and construction of composite tephrostratigraphies is guided by field mapping, $^{40}Ar/^{39}Ar$ and U-Pb geochronology of eruptive minerals, and the chemical composition volcanic glass. Three of the sequences of volcanic ash beds contain at least one sample for which glass composition and radioisotopic age estimates have been determined on splits of the same sample. One sequence has no absolute age estimate; its age is estimated by interpolation between ash beds of known age. Hence, correlation to an ash bed in one of these sequences leverages as much geochronological information as possible. To aid this endeavor, the age, stratigraphic relationships, and chemical composition of important samples are discussed below.

Late Miocene sequence at Puerta de Corral Quemado (<5.6 Ma)

The base of this sequence is defined by a thin (10–20 cm thick) ash bed from the 1440 m level at Puerta de Corral Quemado. $^{40}Ar/^{39}Ar$ analyses of sanidine from the basal 1 cm of this ash bed yield an age of 5.64 ± 0.32 Ma (Latorre *et al*., 1997). This places the base of sequence in the late Miocene. At PCQ, thick or laterally extensive ash beds in this interval are uncommon. Short sequences of stratigraphically distinct, but geochemically similar ash beds complicate interpretation. However, ash beds are numerous and a composite tephrostratigraphy is developed from six stratigraphic sections sampled along strike (Figure 2.2a). The ~100 m thick composite tephrostratigraphy

yields correlations at two additional localities within the Corral Quemado basin, and can be extended to the Fiambalá basin from one of these localities (Figure 2.2b).

The generally fine-grained nature, and presumably distal origin, of many ash beds in the latest Miocene interval presents several problems. Strata interbedded with the ash beds are generally indicative of a braided fluvial system transporting coarse sand and minor gravel. As a result, detrital contamination is common. Abundant detrital contamination and the fine grain size of tephra combine to make preparation of samples difficult and preclude trace element analysis for many samples. Moreover, sedimentary mixing of volcanic glass from different eruptions is a concern.

For the latest Miocene ash beds at PCQ, intrasample populations of glass shards are not explicitly considered. For convenience, EPMA data given are average values presented without standard deviation (available in Appendix A). Data plotted are also average values for each sample. In discussion of other sequences of volcanic ash beds, standard deviations are presented in tables, individual glass shards are plotted, and intra-sample variability is considered. In general, populations of glass shards provide valuable information which should be drawn upon; however, doing so here does not facilitate communication of salient chronostratigraphic details. For this discussion glass compositions are grouped by Ca/Fe ratios. Absolute CaO and Fe_2O_3 values reasonably split glass compositions within these groups, and grouping glass composition by Ca/Fe ratio may identify systematically related groups (eruptive sources) and help to identify stratigraphic trends within a group.

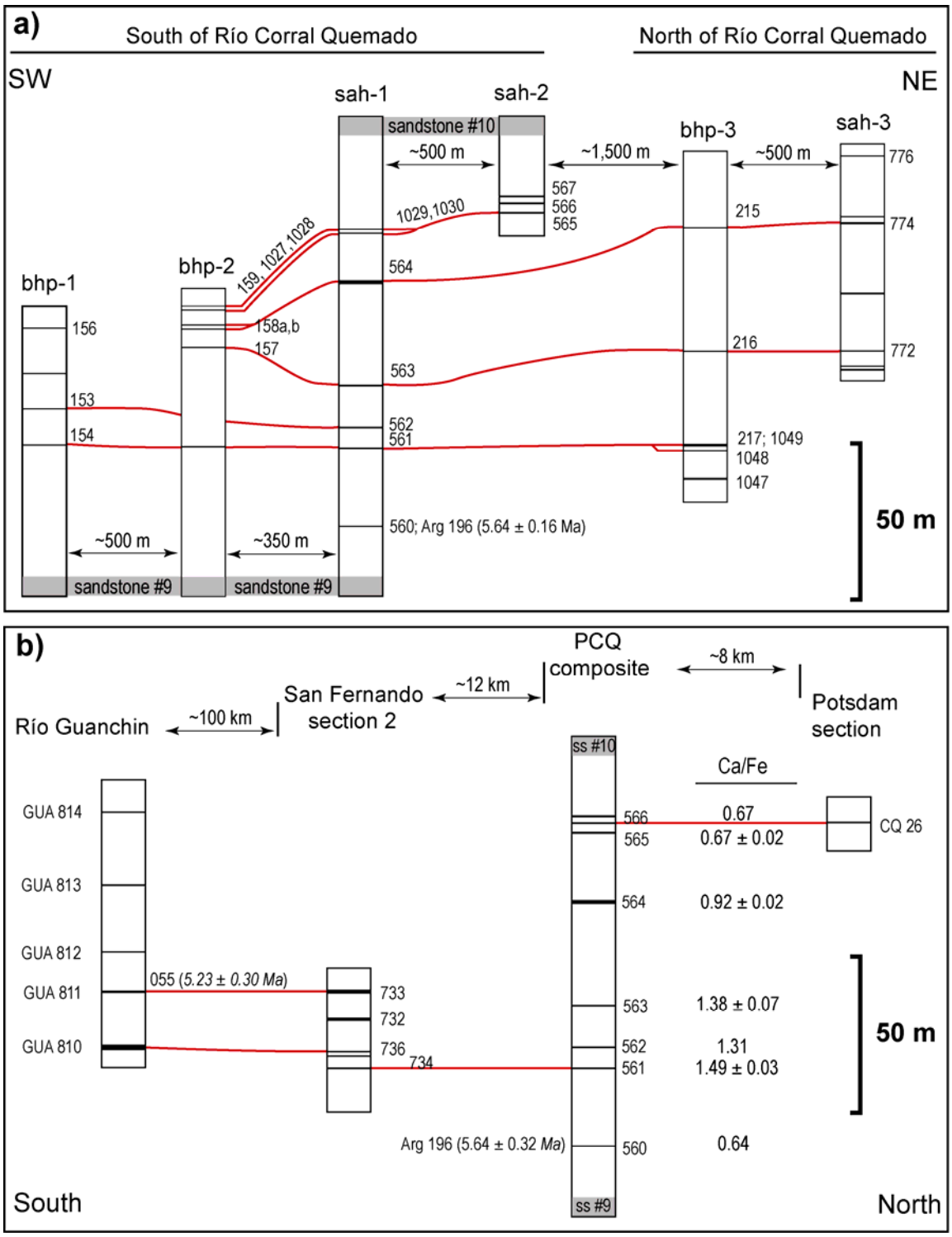

Figure 3.2: Late Miocence tephrostratigraphic framework: **a)** construction of a composite sequence of ash beds from six individual sections sampled along strike at Puerta de Corral Quemado, **b)** correlation of the composite stratigraphy to additional localities in the Corral Quemado basin and to the Fiambalá basin. Sample Arg 196 was dated by Latorre *et al*. (1997) and 055 was dated by Carrapa *et al*. (2008).

The most persistent stratigraphic marker in the latest Miocene sequence at PCQ is a fine-grained ash bed 25 m above the base. This ash bed is an important marker which is correlated locally across Río Corral Quemado and also to the San Fernando section; six samples are assigned to the 1465 m level on the basis of EPMA data (Table 3.1).

The glass composition of this ash bed has the highest Ca/Fe ratio of any in the sequence, and is the stratigraphically lowest of three ash beds between 1465–1485 m with Ca/Fe > 1 (Figure 3.3). The ash beds at 1465 and 1472 m are characterized by high BaO values, but can be differentiated by Cl (Figure 3.3). The uppermost ash bed in this group (1485 m level) has the highest CaO and MgO values of the group. The three glass compositions identified within this group may have originated from the same source volcano. If true, the close stratigraphic association of these ash beds implies that the source volcano was very active at this time and that undocumented ash beds of similar composition are likely to be found in late Miocene strata of the region.

A group of samples at ~1518 m is clearly delineated by Ca/Fe values between 0.88–0.92. Section *bhp-2* documents two samples with similar composition in very close stratigraphic proximity (Figure 3.2a). Sample PCQ 158a is pumiceous; PCQ 158b is 1 m upsection and devoid of pumice. Although EPMA data provide no basis for distinguishing between the two samples, a similar stratigraphic pattern is observed in section *sah-3*. There sample PCQ 774 is a 40 cm thick ash bed with pumice and a 10 cm thick ash bed (PCQ 775) is present 1.4 m upsection. No data exist for PCQ 775, but it might be expected to be of similar composition to PCQ 158. Ash beds of similar composition and stratigraphic placement are also observed in sections *sah-1* and *bhp-3*.

Table 3.1: EPMA data for latest Miocene sequence at Puerta de Corral Quemado.

Sample	n[a]	SiO_2	TiO_2	Al_2O_3	Fe_2O_3	MnO	MgO	CaO	BaO	Na_2O	K_2O	Cl	H_2O	Total	D[b]
1542 m level															
PCQ 566	**12**	71.8	0.15	12.3	0.93	0.08	0.15	0.57	0.07	2.4	6.1	0.14	4.7	99.5	0.0
CQ 26	**19**	72.0	0.14	12.5	0.91	0.09	0.16	0.61	0.06	2.9	5.4	0.13	6.6	101.5	2.8
CQ 26[c]	**22**	72.5	0.16	12.5	0.92	0.08	0.16	0.62	0.06	2.8	5.6	0.14	6.4	102.0	2.2
1540 m level															
PCQ 565	**10**	72.3	0.13	12.4	0.82	0.09	0.12	0.53	0.07	2.4	6.1	0.13	4.4	99.5	0.0
PCQ 159	**12**	71.9	0.11	12.6	0.85	0.07	0.13	0.53	0.07	2.6	6.1	0.13	5.1	100.1	4.3
PCQ 1027	**10**	71.4	0.14	12.8	0.81	0.08	0.13	0.51	0.08	2.6	5.8	0.14	5.5	100.0	2.6
PCQ 1028	**10**	71.3	0.12	12.7	0.83	0.08	0.15	0.56	0.07	2.7	5.7	0.12	6.0	100.4	3.9
PCQ 1029	**10**	70.6	0.12	12.6	0.77	0.09	0.13	0.50	0.09	2.6	5.7	0.12	6.6	100.0	3.3
PCQ 1030	**4**	71.6	0.16	12.5	0.85	0.09	0.12	0.58	0.05	2.4	6.2	0.14	5.7	100.4	3.2
1518 m level															
PCQ 564	**12**	71.5	0.13	12.8	0.82	0.08	0.12	0.73	0.09	2.5	5.8	0.14	4.8	99.5	0.0
PCQ 158a	**16**	71.0	0.13	13.1	0.83	0.07	0.13	0.74	0.07	2.8	5.7	0.14	5.5	100.2	1.7
PCQ 158b	**16**	71.0	0.11	13.0	0.82	0.07	0.11	0.74	0.07	2.9	5.6	0.14	5.6	100.1	1.8
PCQ 215	**7**	73.1	0.12	13.0	0.80	0.07	0.13	0.73	0.05	2.0	6.0	0.13	4.6	100.8	1.4
PCQ 774	**19**	72.4	0.12	13.0	0.86	0.07	0.13	0.75	0.08	3.0	5.4	0.14	5.7	101.7	2.1
1485 m level															
PCQ 563	**10**	71.7	0.11	12.9	0.78	0.04	0.11	1.06	0.08	2.6	5.6	0.09	4.3	99.4	0.0
PCQ 157	**13**	71.6	0.11	13.0	0.75	0.05	0.11	1.03	0.08	2.6	5.9	0.08	4.7	100.3	2.9
PCQ 216	**25**	73.1	0.11	12.9	0.74	0.04	0.11	1.05	0.08	2.4	5.2	0.08	4.6	100.5	2.7
PCQ 772	**9**	71.8	0.09	12.8	0.80	0.04	0.10	1.00	0.06	2.5	5.5	0.08	5.4	100.3	3.6
1472 m level															
PCQ 562	**9**	72.3	0.07	12.0	0.61	0.03	0.07	0.81	0.11	2.3	6.3	0.09	5.0	101.0	0.0
PCQ 153	**14**	71.3	0.09	12.6	0.66	0.03	0.08	0.82	0.11	2.2	6.3	0.10	5.5	99.8	2.4
1465 m level															
PCQ 561	**11**	72.5	0.11	12.0	0.67	0.06	0.07	0.96	0.09	2.0	6.2	0.12	4.3	99.3	0.0
PCQ 154	**14**	71.9	0.10	12.2	0.66	0.07	0.06	0.95	0.11	2.1	6.2	0.13	5.3	99.7	2.5
PCQ 217	**9**	73.9	0.08	12.2	0.66	0.06	0.07	0.97	0.10	1.9	5.9	0.12	4.7	100.6	2.5
PCQ 734[d]	**12**	73.2	0.09	12.4	0.66	0.07	0.07	1.00	0.11	1.2	5.0	0.11	6.4	100.5	2.8
PCQ 1048	**15**	72.3	0.09	12.0	0.63	0.07	0.07	0.92	0.09	2.1	6.1	0.12	5.5	100.0	2.4
PCQ 1049	**18**	72.3	0.10	12.4	0.66	0.07	0.08	0.95	0.09	2.1	6.0	0.12	5.5	100.3	0.8
1440 m level															
PCQ 560	**13**	72.7	0.07	12.0	0.81	0.07	0.04	0.49	0.03	2.2	6.4	0.11	4.3	99.3	0.0
Arg 196[e]	**19**	73.6	0.07	11.9	0.80	0.06	0.05	0.52	0.02	2.0	6.4	0.12	6.6	102.1	2.2
Arg 196[c]	**21**	73.0	0.07	12.0	0.81	0.05	0.04	0.51	0.03	2.2	6.4	0.12	6.6	101.9	2.4

[a] n=number of analyzed shards; all oxides and elements reported in weight %, total Fe as Fe_2O_3; H_2O calculated from the difference between measured and stoichiometric oxygen (Nash, 1992).

[b] Statistical distance (Perkins *et al*., 1995; Appendix B) calculated using the concentrations of TiO_2, Fe_2O_3, MnO, MgO, CaO and Cl; $D \leq 3.5$ indicate analyses are identical at 95% confidence level.

[c] Replicate analysis.

[d] Analyses combined or excluded; see Appendix A for more information.

[e] Sample dated by Latorre *et al*. (1997).

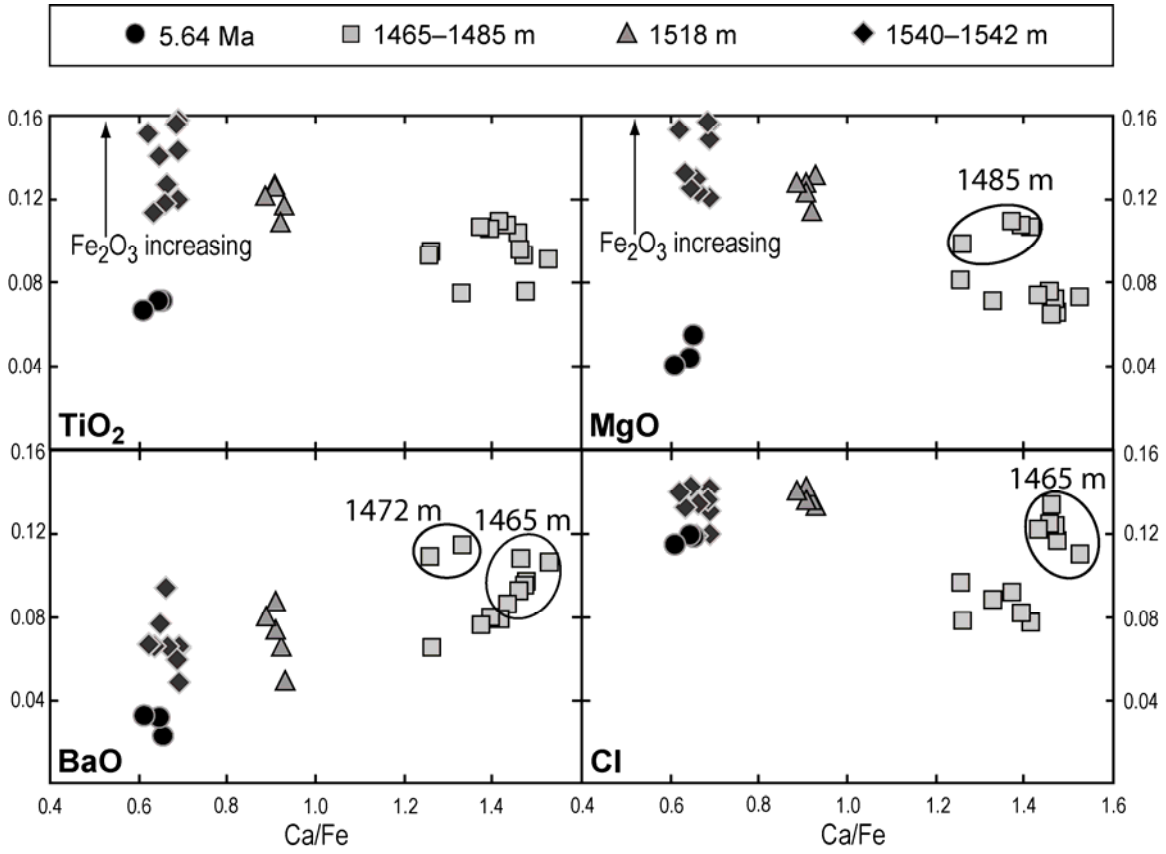

Figure 3.3: EPMA data for ash beds between 1440–1542 m at Puerta de Corral Quemado. Three groups are identified based upon Ca/Fe ratio (x-axis) and can be subdivided using average TiO_2, MgO, BaO, and Cl values (y-axis of respective panel).

Sample PCQ 564 is a 1m thick tuff with detrital medium sand, no pumice is observed and no other ash bed is known within close stratigraphic proximity. Taken together these five samples from four stratigraphic sections provide no basis for differentiating between at least two stratigraphic occurrences. If there are two or more closely spaced ash beds at ~1518 m level from different eruptive events, it is not documented by EPMA data.

In addition to documenting two unique stratigraphic occurrences of the ~1518 m tuff, section *bhp-2* is important in that it documents the stratigraphic relationship between PCQ 564 and PCQ 565 which is not known *a priori*. Sample PCQ 159 correlates to PCQ 565, both of which represent the base of a short sequence of ash beds characterized by

Ca/Fe between 0.60–0.68. This group of ash beds has Ca/Fe values identical to the 5.64 Ma ash bed which defines the base of the latest Miocene sequence, but significantly higher TiO_2, MgO, and BaO contents.

Construction of the composite sequence at Puerta de Corral Quemado provides an important point of comparison for late Miocene volcanic ash beds younger than ~5.6 Ma. Upper age bounds for this sequence at PCQ are not well established, but rather determined by interpolation from which an age of ~5.3 Ma is suggested (cf. Chapter 2). Correlation to additional localities within the Corral Quemado basin is established by comparison with the composite sequence. Sample PCQ 566 is correlated to a sample along strike ~8 km northeast of the nearest locality. This sample (CQ 26; Table 3.1) is from a stratigraphic section sampled by Isabelle Coutand in 2002 (then at Universität Potsdam, Germany). Two other samples from this Universität Potsdam stratigraphic section are correlated to younger ash beds described later in this chapter.

Correlation to a short stratigraphic sequence at San Fernando is also established. In San Fernando section #2, the lowermost ash bed correlates to the 1465 m level of the composite section (PCQ 734; Table 3.1). Section #2 at San Fernando is comprised of ash beds dipping ~15° to the south which are exposed in recent road cuts. Two ash beds appear to be correlative to the Río Guanchin section in the Fiambalá basin (Table 3.2). A prominent 1.2 m thick ash bed at the base of the Río Guanchin section yields a tentative correlation to San Fernando. GUA 810 and PCQ 736 are indistinguishable on the basis of EPMA analysis; however, this correlation is considered tentative because PCQ 736 contains two compositional modes. GUA 810 is correlated to the secondary mode (5 of 18 shards) found in PCQ 736. This correlation is further supported by

Table 3.2: EPMA data for latest Miocene sequence at Río Guanchin.

Sample	n[a]	SiO_2	TiO_2	Al_2O_3	Fe_2O_3	MnO	MgO	CaO	BaO	Na_2O	K_2O	Cl	H_2O	Total	m[b]
GUA 814	**18**	**73.3**	**0.09**	**11.9**	**0.69**	**0.06**	**0.07**	**0.63**	**0.06**	**2.9**	**4.7**	**0.13**	**5.4**	**100.0**	**81.8**
1σ		0.6	0.04	0.1	0.07	0.03	0.02	0.02	0.03	0.3	0.3	0.02	1.1	0.3	
GUA 813	**13**	**73.2**	**0.12**	**12.4**	**1.07**	**0.03**	**0.13**	**1.03**	**0.05**	**2.8**	**4.9**	**0.08**	**4.5**	**100.3**	**58.6**
1σ		0.7	0.06	0.4	0.15	0.03	0.05	0.10	0.03	0.2	0.2	0.02	0.5	0.3	
GUA 812	**12**	**72.5**	**0.14**	**12.6**	**0.75**	**0.04**	**0.07**	**0.87**	**0.09**	**2.9**	**5.0**	**0.11**	**4.9**	**100.0**	**37.4**
1σ		0.7	0.03	0.3	0.07	0.02	0.02	0.05	0.04	0.2	0.1	0.01	0.4	0.7	
GUA 811	**15**	**72.9**	**0.08**	**12.4**	**0.61**	**0.05**	**0.06**	**0.47**	**0.05**	**3.0**	**5.0**	**0.12**	**4.9**	**99.7**	**24.2**
1σ		0.5	0.04	0.3	0.08	0.03	0.03	0.06	0.05	0.1	0.1	0.01	0.5	0.3	
055[c]	**34**	**73.0**	**0.09**	**12.7**	**0.58**	**0.08**	**0.07**	**0.44**	**0.02**	**2.0**	**4.8**	**0.13**	**5.8**	**99.7**	**-**
1σ		0.9	0.03	0.1	0.04	0.02	0.02	0.02	0.03	0.3	0.2	0.01	0.9	0.6	
055[c, d]	***25***	**72.9**	**0.10**	**12.7**	**0.60**	**0.07**	**0.07**	**0.46**	**0.02**	**1.6**	**4.9**	**0.14**	**5.9**	**99.5**	**-**
1σ		0.7	0.03	0.1	0.04	0.02	0.01	0.02	0.02	0.2	0.2	0.01	0.7	0.5	
PCQ 733[e]	**20**	**72.8**	**0.10**	**12.4**	**0.65**	**0.07**	**0.07**	**0.48**	**0.05**	**2.4**	**6.2**	**0.13**	**6.1**	**101.6**	**-**
1σ		0.5	0.03	0.2	0.10	0.02	0.02	0.07	0.06	0.3	0.3	0.01	0.6	0.3	
GUA 810	**15**	**71.9**	**0.11**	**12.6**	**0.71**	**0.05**	**0.12**	**0.86**	**0.06**	**2.9**	**4.4**	**0.10**	**6.0**	**99.8**	**6.0**
1σ		0.4	0.04	0.1	0.06	0.02	0.02	0.03	0.03	0.2	0.2	0.01	0.6	0.3	
PCQ 736[e, f]	**5**	**72.0**	**0.10**	**12.4**	**0.74**	**0.05**	**0.12**	**0.87**	**0.04**	**2.5**	**5.5**	**0.10**	**6.2**	**100.8**	**-**
1σ		0.5	0.02	0.1	0.02	0.02	0.02	0.04	0.05	0.4	0.3	0.01	0.6	0.3	

[a] n=number of analyzed shards; all data in weight %, 1σ=standard deviation; total Fe as Fe_2O_3; H_2O calculated from the difference between measured and stoichiometric oxygen (Nash, 1992).
[b] meter level in Río Guanchin section; total thickness ~250 meters; additional data in Appendix A.
[c] Sample dated by Carrapa *et al*. (2008).
[d] Replicate analysis.
[e] Proposed correlation to a sample from San Fernando section #2.
[f] Analyses combined or excluded; see Appendix A for more information.

correlation of the uppermost ash bed at San Fernando (PCQ 733) to sample GUA 811. Sample GUA 811 is important because it establishes correlation to a dated sample (055; Table 3.2) from the same locality. The age estimate for 055 is established by the youngest single zircon U-Pb age of five (5.23 ± 0.30 Ma; Carrapa *et al*., 2008). Direct correlation is not yet achieved between Río Guanchin and PCQ, but the balance of information suggests that Río Guanchin is approximately correlative to sandstone #10 at PCQ and likely encompasses the Miocene-Pliocene boundary. A 5.51 ± 0.14 U-Pb zircon age from Río Guanchin strongly supports this, but its stratigraphic position is not known relative to the Río Guanchin section presented here (cf. sample 029, Appendix A).

Sandstone #12 sequence at Puerta de Corral Quemado (~4.4 Ma)

A complex sequence of ash beds crops out from 1775–1860 m at Puerta de Corral Quemado. These ash beds encompass sandstone #12, a marker bed at 1832 m, which ranges between 5–20 m thick along strike for ~5 km. On the basis of EPMA data, samples along this transect document many ash beds present at only one or two localities. Fewer, more laterally continuous, ash beds are present at numerous localities. The ash bed most clearly associated with sandstone #12 has a characteristic microstratigraphy and glass composition (Figure 3.4). Due to its lateral persistence and unique geochemical signal the informal term, tuff of sandstone #12, is adopted for convenience.

The tuff of sandstone #12 can be subdivided stratigraphically and geochemically. The lower two samples (PCQ 573/574) of this sequence are easily differentiated by the higher Al_2O_3, Fe_2O_3, CaO, TiO_2, and MgO content of volcanic glass; however, they also contain a minor compositional mode indistinguishable from the upper sample (PCQ 575). The upper sample contains no glass shards from the lower samples, suggesting that in this instance sedimentary mixing is not the reason for multiple compositional modes within the bed. Instead, magma mixing prior to and during eruption is invoked to explain the occurrence of the minor compositional modes of PCQ 573/574.

In general, these observations are corroborated by other samples (Table 3.3). Lower samples of the tuff of sandstone #12 (PCQ 793 and 794) both contain ~10% glass shards similar to the upper part of the ash bed; whereas, samples Arg 227 and PCQ 795 are unimodal. The upper tuff of sandstone #12 is unimodal in samples PCQ 118 and 575, but PCQ 585 contains <10% glass shards that are similar in composition to the lower part

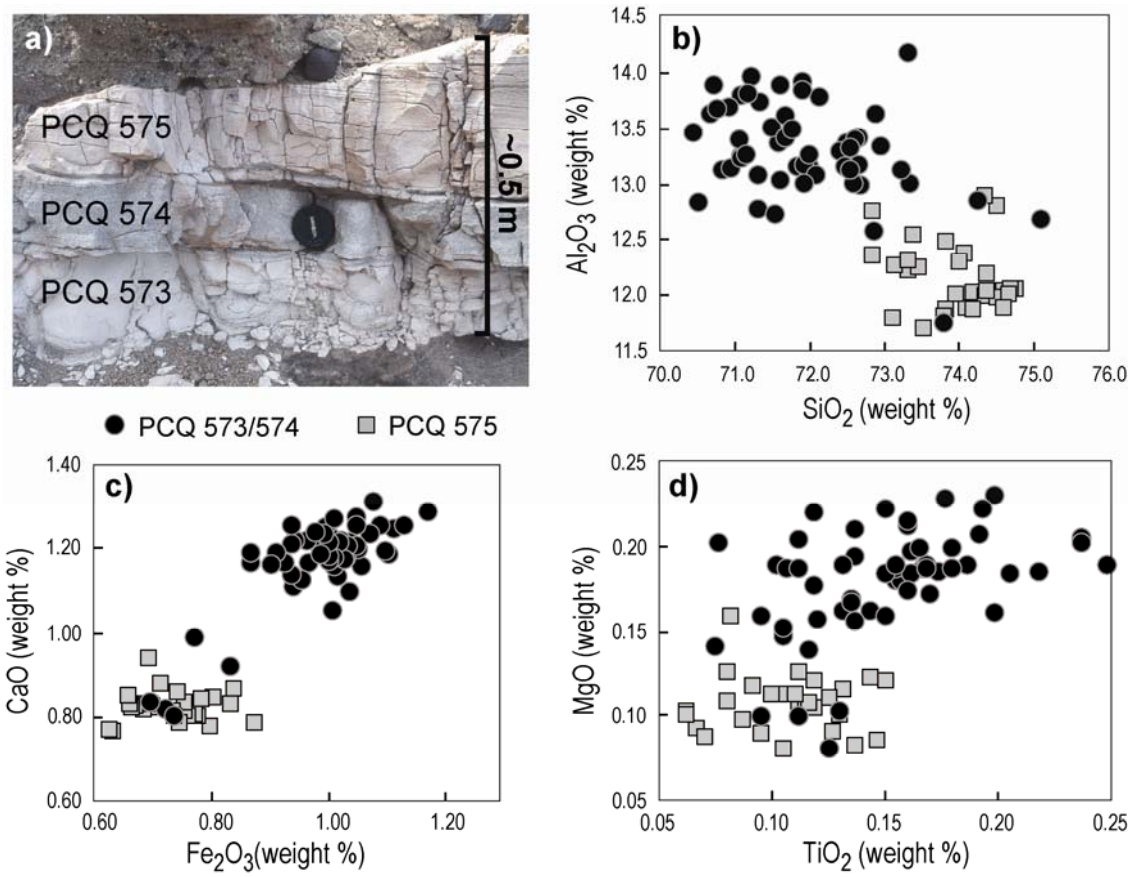

Figure 3.4: Tuff of sandstone #12: **a)** field photograph of sampled micro-stratigraphy; panels **b)**, **c)**, and **d)** distinguish upper and lower tuff of sandstone #12 compositions using EPMA data. On this basis a chemically zoned magma chamber is inferred.

of the ash bed. Because PCQ 585 is a tuffaceous sandstone, the bimodal glass composition is interpreted to result from sedimentary mixing in this instance.

Considering all field observations and EPMA data, the two glass compositions observed in the tuff of sandstone #12 are inferred to be sourced from the same magma chamber. There may have been a hiatus between eruption of the lower and upper ash bed, but the persistent internal stratigraphic pattern of this ash bed suggests that such a hiatus was likely brief. A zoned rhyodacite magma chamber is proposed to be the source. A less evolved portion of this magma chamber appears to have been erupted and

Table 3.3: EPMA data for tuff of sandstone #12 sequence at Puerta de Corral Quemado.

Sample	n[a]	SiO_2	TiO_2	Al_2O_3	Fe_2O_3	MnO	MgO	CaO	BaO	Na_2O	K_2O	Cl	H_2O	Total	D[b]
tuff at 1852 m level															
PCQ 503	**15**	**72.7**	**0.13**	**13.0**	**0.86**	**0.08**	**0.12**	**0.73**	**0.06**	**3.0**	**5.4**	**0.13**	**5.3**	**101.6**	**0.0**
1σ		1.1	0.06	0.4	0.08	0.03	0.03	0.1	0.04	0.4	0.6	0.03	0.9	0.5	
PCQ 796	**20**	**72.1**	**0.12**	**13.3**	**0.85**	**0.08**	**0.13**	**0.77**	**0.06**	**3.3**	**4.7**	**0.14**	**4.8**	**100.6**	**2.0**
1σ		0.3	0.04	0.2	0.04	0.03	0.02	0.03	0.04	0.2	0.4	0.02	0.7	0.3	
upper tuff of sandstone #12 (1832.3 m level)															
PCQ 118	**19**	**74.2**	**0.12**	**12.2**	**0.77**	**0.05**	**0.12**	**0.83**	**0.06**	**3.1**	**4.7**	**0.11**	**4.3**	**100.5**	**0.0**
1σ		0.6	0.03	0.3	0.05	0.02	0.01	0.05	0.03	0.3	0.5	0.02	0.6	0.5	
PCQ 575	**29**	**73.9**	**0.11**	**12.2**	**0.72**	**0.04**	**0.11**	**0.83**	**0.05**	**2.9**	**4.8**	**0.11**	**4.5**	**100.3**	**1.5**
1σ		0.6	0.04	0.3	0.07	0.03	0.02	0.03	0.04	0.3	0.5	0.01	0.6	0.4	
PCQ 585[c]	**28**	**73.5**	**0.13**	**12.0**	**0.77**	**0.05**	**0.10**	**0.81**	**0.07**	**3.0**	**4.6**	**0.10**	**5.4**	**100.5**	**1.7**
1σ		0.6	0.05	0.1	0.05	0.03	0.02	0.05	0.04	0.3	0.4	0.02	0.7	0.3	
CQ 22	**25**	**73.6**	**0.13**	**12.0**	**0.76**	**0.05**	**0.11**	**0.84**	**0.06**	**3.0**	**4.7**	**0.11**	**5.8**	**101.2**	**0.8**
1σ		0.6	0.02	0.1	0.03	0.02	0.02	0.03	0.03	0.3	0.5	0.01	0.5	0.3	
lower tuff of sandstone #12 (1832 m level)															
Arg 227	**19**	**71.6**	**0.19**	**12.9**	**1.03**	**0.05**	**0.19**	**1.22**	**0.05**	**2.9**	**4.3**	**0.12**	**6.5**	**101.1**	**0.0**
1σ		1.1	0.03	0.3	0.06	0.01	0.03	0.06	0.03	0.4	0.5	0.01	1.1	0.9	
PCQ 573[c]	**26**	**71.9**	**0.16**	**13.5**	**1.02**	**0.05**	**0.19**	**1.20**	**0.06**	**3.4**	**4.1**	**0.12**	**4.9**	**100.4**	**2.6**
1σ		0.8	0.04	0.4	0.05	0.03	0.02	0.06	0.03	0.2	0.3	0.01	0.6	0.3	
PCQ 574[c]	**25**	**71.7**	**0.15**	**13.3**	**0.99**	**0.05**	**0.18**	**1.20**	**0.05**	**3.1**	**4.5**	**0.12**	**5.0**	**100.3**	**2.8**
1σ		0.7	0.03	0.2	0.07	0.02	0.02	0.04	0.04	0.4	0.5	0.02	0.7	0.5	
PCQ 725	**16**	**72.1**	**0.16**	**13.1**	**0.95**	**0.06**	**0.19**	**1.17**	**0.04**	**3.0**	**4.5**	**0.12**	**5.2**	**100.6**	**3.2**
1σ		0.4	0.04	0.2	0.08	0.03	0.03	0.04	0.03	0.5	0.4	0.01	0.6	0.2	

[a] n=number of analyzed shards; all oxides and elements reported in weight %, total Fe as Fe_2O_3; H_2O calculated from the difference between measured and stoichiometric oxygen (Nash, 1992).

[b] Statistical distance (Perkins *et al.*, 1995; Appendix B) calculated using the concentrations of TiO_2, Fe_2O_3, MnO, MgO, CaO and Cl; $D \leq 3.5$ indicate analyses are identical at 95% confidence level.

[c] Analyses combined or excluded; see Appendix A for more information.

Table 3.3 (*continued*): EPMA data for tuff of sandstone #12 sequence at Puerta de Corral Quemado.

Sample	n[a]	SiO_2	TiO_2	Al_2O_3	Fe_2O_3	MnO	MgO	CaO	BaO	Na_2O	K_2O	Cl	H_2O	Total	D[b]
lower tuff of sandstone #12 (1832 m level)															
PCQ 793[c]	**11**	**72.1**	**0.18**	**13.2**	**1.02**	**0.04**	**0.19**	**1.19**	**0.05**	**3.3**	**3.9**	**0.12**	**5.8**	**101.1**	**1.7**
1σ		0.3	0.06	0.2	0.06	0.02	0.02	0.05	0.04	0.2	0.2	0.01	0.5	0.3	
PCQ 794[c]	**17**	**72.1**	**0.16**	**13.2**	**0.97**	**0.06**	**0.18**	**1.19**	**0.06**	**3.3**	**4.1**	**0.12**	**5.0**	**100.4**	**2.8**
1σ		0.3	0.05	0.2	0.06	0.03	0.02	0.03	0.04	0.2	0.4	0.01	0.4	0.4	
PCQ 795	**10**	**71.3**	**0.18**	**12.9**	**0.98**	**0.05**	**0.18**	**1.17**	**0.06**	**3.0**	**4.3**	**0.11**	**5.6**	**99.9**	**2.7**
1σ		0.3	0.05	0.2	0.05	0.04	0.02	0.04	0.04	0.7	0.5	0.01	0.6	0.4	
tuff at 1828 m level															
PCQ 500	**17**	**74.3**	**0.12**	**12.1**	**0.69**	**0.04**	**0.09**	**0.85**	**0.07**	**2.8**	**5.0**	**0.09**	**5.3**	**101.5**	**0.0**
1σ		0.3	0.04	0.2	0.08	0.03	0.02	0.03	0.04	0.3	0.4	0.01	0.5	0.2	
PCQ 502	**15**	**74.1**	**0.10**	**12.1**	**0.71**	**0.04**	**0.10**	**0.85**	**0.05**	**2.7**	**5.1**	**0.10**	**5.2**	**101.3**	**1.8**
1σ		0.6	0.05	0.2	0.05	0.03	0.02	0.03	0.04	0.2	0.3	0.01	0.5	0.4	
PCQ 792	**20**	**74.1**	**0.11**	**12.2**	**0.72**	**0.04**	**0.10**	**0.85**	**0.06**	**2.8**	**4.8**	**0.10**	**5.4**	**101.3**	**1.6**
1σ		0.4	0.02	0.5	0.04	0.02	0.01	0.03	0.03	0.2	0.4	0.01	1.0	0.7	
PCQ 1024	**18**	**73.6**	**0.11**	**12.1**	**0.72**	**0.05**	**0.11**	**0.83**	**0.05**	**3.0**	**4.6**	**0.10**	**5.0**	**100.3**	**2.2**
1σ		0.5	0.04	0.3	0.04	0.02	0.01	0.05	0.03	0.2	0.3	0.01	0.6	0.4	
tuff 11C (1775 m level)															
PCQ 115	**18**	**72.5**	**0.11**	**12.9**	**0.66**	**0.07**	**0.11**	**0.61**	**0.06**	**2.6**	**5.8**	**0.12**	**5.2**	**100.8**	**0.0**
1σ		0.4	0.03	0.2	0.05	0.02	0.01	0.02	0.03	0.5	0.5	0.01	0.6	0.3	
PCQ 572	**14**	**71.6**	**0.11**	**12.7**	**0.66**	**0.08**	**0.10**	**0.62**	**0.06**	**2.2**	**6.5**	**0.12**	**4.5**	**99.2**	**1.4**
1σ		0.4	0.03	0.2	0.04	0.03	0.02	0.02	0.05	0.4	0.3	0.02	1.0	0.4	
PCQ 791	**15**	**72.3**	**0.11**	**12.6**	**0.69**	**0.07**	**0.09**	**0.61**	**0.06**	**2.6**	**5.6**	**0.12**	**5.3**	**100.3**	**1.6**
1σ		0.8	0.05	0.2	0.07	0.02	0.02	0.03	0.03	0.3	0.4	0.02	0.6	0.4	

[a] n=number of analyzed shards; all oxides and elements reported in weight %, total Fe as Fe_2O_3; H_2O calculated from the difference between measured and stoichiometric oxygen (Nash, 1992).

[b] Statistical distance (Perkins *et al*., 1995; Appendix B) calculated using the concentrations of TiO_2, Fe_2O_3, MnO, MgO, CaO and Cl; $D \leq 3.5$ indicate analyses are identical at 95% confidence level.

[c] Analyses combined or excluded; see Appendix A for more information.

deposited first. To reconcile this observation with the expectation that the top of the magma chamber is the most evolved, a complex eruptive mechanism is suggested.

Numerous ash beds are intimately associated with sandstone #12; small ash beds generally continue along strike for <500 m of the 5 km wide panel investigated. This precludes establishing stratigraphic relationships between many of the smaller ash beds. On the basis of homotaxy and glass composition, four individual ash beds can be reliably characterized and placed in stratigraphic order (Table 3.3). The tuff of sandstone #12 has two compositional modes, thus a total of five glass compositions are reported between 1775–1860 m at PCQ. This is a small fraction of the unique glass compositions identified within this interval.

Data from San Fernando section #1, ~15 km SSE of PCQ, also identify numerous closely spaced and compositionally unique ash beds; seven stratigraphically distinct ash beds exist within a 20 m of gently dipping strata. The basal sample (PCQ 725) correlates to the tuff of sandstone #12 (Table 3.3). Data from San Fernando section #1, suggest several additional correlations with ash beds at PCQ. These tentative correlations are not regarded with a high degree of confidence, but are briefly noted in Appendix A because of their stratigraphic proximity to tuff of sandstone #12 at San Fernando.

Given the potential of the tuff of sandstone #12 as a regional marker bed, accurate and precise age estimates are desirable. $^{40}Ar/^{39}Ar$ sanidine ages bracketing this interval at PCQ; 5.64 ± 0.32 Ma (1440 m) and 3.66 ± 0.10 Ma (2076 m) respectively, yield an age of 4.4 Ma by linear interpolation. Sanidine is not known from the tuff of sandstone #12 and plagioclase K/Ca ratios ($An_{37–65}$ $Ab_{34–61}$ $Or_{1–3}$) are not favorable for precise $^{40}Ar/^{39}Ar$ age estimates. Plagioclase $^{40}Ar/^{39}Ar$ would still be valuable, as the accuracy of direct

determination is preferred to interpolation over 600 m and 2 Ma. Ultimately, the age estimate for the tuff of sandstone #12 might be improved upon by U-Pb zircon analysis.

4.0 Ma sequence at Fiambalá

Along the western margin of the Fiambalá basin, a sequence of numerous stratigraphically distinct ash beds crops out within a 90 m interval of westward dipping sandstones and siltstones (Figure 3.5). This sequence occurs in the lower half of an 800–1000 m thick section immediately to the west of Fiambalá (town). Plagioclase separates ($An_{26–46}$ $Ab_{58–70}$ $Or_{2–5}$) from two ash beds in the middle of this 90 m sequence yield indistinguishable $^{40}Ar/^{39}Ar$ ages of 4.0 Ma (Figure 3.5; Appendix A). Rapid deposition and high rates of explosive volcanism are inferred based upon these age estimates.

Although these ash beds are compositionally quite similar, most of them are distinguishable (Table 3.4). The compositional differences between ash beds are small, but so is the compositional variation within an individual ash bed. The largest compositional variation within ash beds can be confined to three samples (Figure 3.5). A sample at the 261 m level (FIA 832) is compositionally similar to an ash bed 1.7 m upsection, but exhibits a notably larger compositional range for most elements. Whether this represents sedimentary mixing of multiple eruptive events or a compositionally variable magma is unclear. At ~275 m, a thick pumiceous sandstone (FIA 834) yields a much less variable population of glass shards suggesting that in some cases sedimentary mixing is not a primary concern. The upper two ash beds are also more compositionally variable than the others in this sequence. These ash beds (FIA 845, 846) have higher CaO, Fe_2O_3, MgO, and TiO_2 contents and accordingly are interpreted as deriving from rhyodacite magmas.

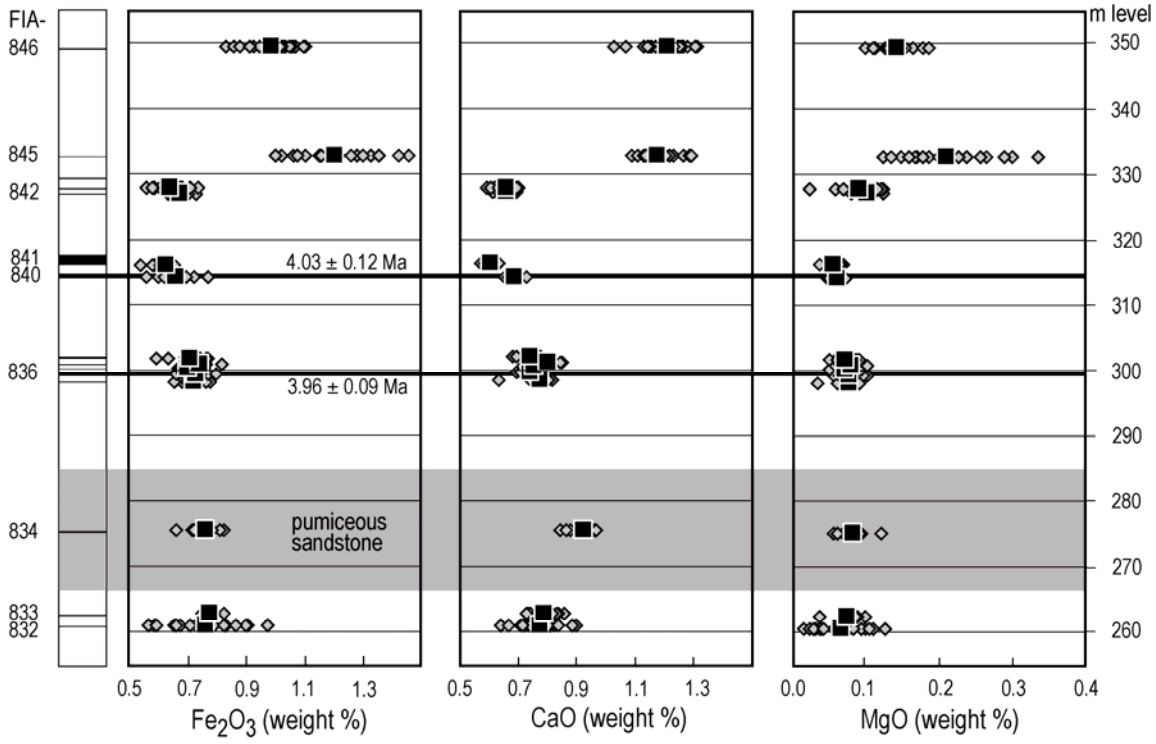

Figure 3.5: Sequence of ~4 Ma tuffs at Fiambalá. Sample numbers and a tephrostratigraphic column are presented in the left hand y-axis; dated ash beds and a thick pumiceous sandstone are carried across all panels. The three panels depict the respective oxide concentrations for glass from each sample; small grey diamonds represent individual shards and black squares represent the average value of all shards. The stratigraphic level is presented on the right hand y-axis; additional volcanic glass data from the full section are presented in Appendix A, as are details of the $^{40}Ar/^{39}Ar$ plagioclase laser fusion experiments, which yield a weighted mean age of 4.0 ± 0.1 Ma.

Three closely spaced groups of ash beds in the middle of the sequence have small but significant compositional differences. As is typical of silicic tephra in the region, the Fe_2O_3 variance is 1.5–3.0 higher than for CaO. The lowermost sequence contains five stratigraphically unique ash beds at ~300 m level (FIA 835–839). Fe_2O_3, CaO, and Cl contents identify subtle differences between these ash beds, suggesting that each ash bed derived from a unique eruption. FIA 836 and FIA 837 are not measurably different and may result from either sedimentary reworking of the same eruptive material or two closely spaced eruptions from the same source. Two closely spaced ash beds at ~315 m

Table 3.4: EPMA data for the 4.0 Ma sequence at Fiambalá.

Sample	n[a]	SiO_2	TiO_2	Al_2O_3	Fe_2O_3	MnO	MgO	CaO	BaO	Na_2O	K_2O	Cl	H_2O	Total	m[b]
FIA 846	**23**	**70.5**	**0.16**	**13.5**	**0.99**	**0.03**	**0.14**	**1.21**	**0.08**	**2.7**	**5.5**	**0.12**	**5.2**	**100.2**	**349.4**
1σ		0.7	0.05	0.5	0.08	0.03	0.02	0.08	0.03	0.3	0.3	0.02	0.9	0.5	
FIA 845	**23**	**72.3**	**0.23**	**13.2**	**1.21**	**0.05**	**0.21**	**1.18**	**0.07**	**2.2**	**5.0**	**0.12**	**6.1**	**101.9**	**332.7**
1σ		0.7	0.11	0.2	0.12	0.05	0.05	0.05	0.07	0.2	0.3	0.03	0.7	0.7	
FIA 843	**20**	**72.3**	**0.10**	**12.1**	**0.64**	**0.05**	**0.09**	**0.66**	**0.05**	**2.3**	**5.2**	**0.07**	**6.3**	**100.0**	**327.9**
1σ		0.3	0.04	0.1	0.04	0.03	0.02	0.03	0.04	0.1	0.1	0.01	0.5	0.2	
FIA 842	**11**	**72.9**	**0.10**	**12.2**	**0.68**	**0.06**	**0.11**	**0.66**	**0.06**	**2.4**	**5.4**	**0.06**	**6.1**	**100.8**	**327.1**
1σ		0.3	0.02	0.1	0.03	0.02	0.01	0.03	0.02	0.2	0.1	0.01	0.7	0.2	
FIA 841	**15**	**73.3**	**0.09**	**12.0**	**0.63**	**0.06**	**0.06**	**0.61**	**0.06**	**2.4**	**5.5**	**0.13**	**5.9**	**100.7**	**316.3**
1σ		0.3	0.02	0.1	0.04	0.02	0.01	0.02	0.02	0.2	0.1	0.01	0.7	0.4	
FIA 840[c]	**15**	**73.1**	**0.09**	**12.1**	**0.66**	**0.05**	**0.06**	**0.69**	**0.06**	**2.5**	**5.5**	**0.13**	**5.4**	**100.3**	**314.3**
1σ		0.4	0.03	0.1	0.05	0.02	0.01	0.02	0.03	0.2	0.2	0.01	0.9	0.4	

[a] n=number of analyzed shards; all data in weight %, 1σ=standard deviation; total Fe as Fe_2O_3; H_2O calculated from the difference between measured and stoichiometric oxygen (Nash, 1992).

[b] meter level in Fiambalá section; total thickness ~700 meters; additional data in Appendix A.

[c] Sample dated by $^{40}Ar/^{39}Ar$ single crystal laser fusion of plagioclase (Appendix A).

Table 3.4 (*continued*): EPMA data for the 4.0 Ma sequence at Fiambalá.

Sample	n[a]	SiO_2	TiO_2	Al_2O_3	Fe_2O_3	MnO	MgO	CaO	BaO	Na_2O	K_2O	Cl	H_2O	Total	m[b]
FIA 839	**15**	**72.9**	**0.11**	**12.3**	**0.71**	**0.04**	**0.08**	**0.74**	**0.05**	**2.7**	**5.3**	**0.12**	**5.4**	**100.5**	**302.0**
1σ		0.3	0.02	0.1	0.05	0.02	0.01	0.02	0.03	0.2	0.2	0.01	0.4	0.3	
FIA 838	**14**	**73.2**	**0.10**	**12.5**	**0.74**	**0.05**	**0.08**	**0.80**	**0.05**	**2.9**	**5.2**	**0.10**	**4.5**	**100.4**	**301.1**
1σ		0.2	0.03	0.1	0.03	0.02	0.01	0.02	0.03	0.3	0.2	0.01	0.3	0.3	
FIA 837	**15**	**72.6**	**0.12**	**12.3**	**0.70**	**0.05**	**0.07**	**0.76**	**0.05**	**2.6**	**5.4**	**0.13**	**5.6**	**100.4**	**300.4**
1σ		0.3	0.03	0.1	0.03	0.02	0.01	0.02	0.02	0.2	0.1	0.01	0.6	0.2	
FIA 836[c]	**15**	**72.6**	**0.10**	**12.2**	**0.73**	**0.06**	**0.08**	**0.75**	**0.06**	**2.5**	**5.4**	**0.12**	**6.2**	**100.8**	**299.5**
1σ		0.3	0.04	0.1	0.04	0.02	0.02	0.02	0.02	0.3	0.2	0.01	0.7	0.4	
FIA 835	**11**	**73.4**	**0.11**	**12.5**	**0.72**	**0.04**	**0.08**	**0.78**	**0.07**	**3.1**	**5.2**	**0.09**	**4.3**	**100.4**	**298.4**
1σ		0.3	0.03	0.1	0.04	0.02	0.02	0.05	0.03	0.3	0.3	0.01	0.3	0.2	
FIA 834	**13**	**72.6**	**0.10**	**12.5**	**0.77**	**0.05**	**0.09**	**0.93**	**0.06**	**2.9**	**5.1**	**0.12**	**4.9**	**100.3**	**275.4**
1σ		0.3	0.03	0.2	0.04	0.02	0.02	0.04	0.02	0.2	0.3	0.01	0.6	0.3	
FIA 833	**10**	**73.9**	**0.12**	**11.9**	**0.78**	**0.04**	**0.08**	**0.79**	**0.03**	**2.6**	**5.4**	**0.15**	**4.5**	**100.4**	**262.7**
1σ		0.4	0.02	0.2	0.02	0.02	0.02	0.05	0.02	0.2	0.2	0.02	0.4	0.2	
FIA 832	**24**	**74.9**	**0.09**	**12.1**	**0.76**	**0.05**	**0.07**	**0.78**	**0.08**	**2.0**	**5.3**	**0.14**	**5.5**	**101.9**	**261.0**
1σ		0.7	0.08	0.2	0.11	0.05	0.03	0.07	0.07	0.2	0.2	0.05	0.8	0.6	

[a] n=number of analyzed shards; all data in weight %, 1σ=standard deviation; total Fe as Fe_2O_3; H_2O calculated from the difference between measured and stoichiometric oxygen (Nash, 1992).

[b] meter level in Fiambalá section; total thickness ~700 meters; additional data in Appendix A.

[c] Sample dated by $^{40}Ar/^{39}Ar$ single crystal laser fusion of plagioclase (Appendix A).

level are distinguished by CaO (FIA 840, 841). Two closely spaced ash beds at ~327 m level may be distinguished by Fe_2O_3 and MgO (FIA 842, 843). Each of these groups is easily distinguished from the other; for example the group of ash beds at ~300 m has higher Fe_2O_3 and CaO values than the group at ~315 m, and the group at ~327 m can be confidently discerned from the other two groups by Cl content.

The fourteen ash beds documented in the 4.0 Ma sequence at Fiambalá are not yet identified at other localities. These ash beds are a traceable unit for ~5 km to the north and ~10 km to the south; focused study of this interval might yield a composite tephrostratigraphy with high potential for local and regional correlations. In fact, recent U-Pb age estimates from the Fiambalá basin identify a number of potentially correlative ash beds. Six ash beds sampled to constrain a formational boundary yield ages of 3.90, 3.93, 3.99, 4.08, 4.11, and 4.12 Ma; pooling zircon grains for all six samples yields a weighted mean of 4.02 ± 0.04 Ma (McPherson, 2008). These ash beds were sampled on a north-south transect as far as 60 km north of the 4.0 Ma sequence described here. The U-Pb ages indicate that several different ash beds were sampled and likely correlate to those between 298–328 m level at Fiambalá, further suggesting that this sequence may contain important regional marker beds.

The uppermost ash bed reported for this sequence (FIA 846) is compositionally similar to the lower tuff of sandstone #12 at PCQ, being distinguished by only by SiO_2 and MgO content and stratigraphic age constraints. The composition of these ash beds is uncommon in the region, suggesting a common source volcano for both. If FIA 846 is from the same source as the tuff of sandstone #12, it might be reasonably expected to be deposited and preserved in the Puerta de Corral Quemado section. At PCQ, the interval

between 1850–1950 m is poorly sampled at present, but ash beds which are correlative to the 4.0 Ma Fiambalá sequence may be identified given further study.

Toba Corral Quemado sequence (<3.8 Ma)

At Puerta de Corral Quemado (PCQ), a 10–15 m thick ash bed provides a widespread and continuous chronostratigraphic datum at the 2072 m level (Latorre *et al*., 1997). This ash bed is an important marker bed and was termed Toba Corral Quemado by Muruaga (2001). Toba Corral Quemado crops out in a sequence of ash beds between 1998–2340 m that yield important local and regional correlations. Four major ash beds found within this interval at PCQ can be clearly differentiated by their Fe_2O_3 and CaO contents; populations of glass shards provide clear criteria for establishing these differences (Figure 3.6). These populations are unimodal, with occasional outliers. A high Fe_2O_3 ash bed, at the 2198 m level (Arg 244) may contain a minor mode with lower Fe_2O_3 and CaO contents but more analyses are required to rigorously define this. The primary sample of Toba Corral Quemado, dated at 3.66 ± 0.10 Ma (Latorre *et al*., 1997), contains three shards which were excluded from the average value of one analysis.

A pumiceous ash bed (samples PCQ 1032/1034) ~75 m below Toba Corral Quemado is not prominent at PCQ, but yields important correlations to the Fiambalá basin (samples 001 and 074; Table 3.5). At Fiambalá these two samples yield U-Pb zircon ages, 3.69 ± 0.12 Ma (001) and 3.74 ± 0.10 Ma (074), in agreement with their stratigraphic position (Carrapa *et al*., 2008). A third ash bed dated at 3.77 Ma ± 0.10 Ma (003) stratigraphically underlies the other two by <20 m (Carrapa *et al*., 2008). Fiambalá sample 003 has unique glass chemistry owing to its low CaO and Cl contents as well as its high MnO content (Table 3.5). This sample (003) is not known from PCQ, but its

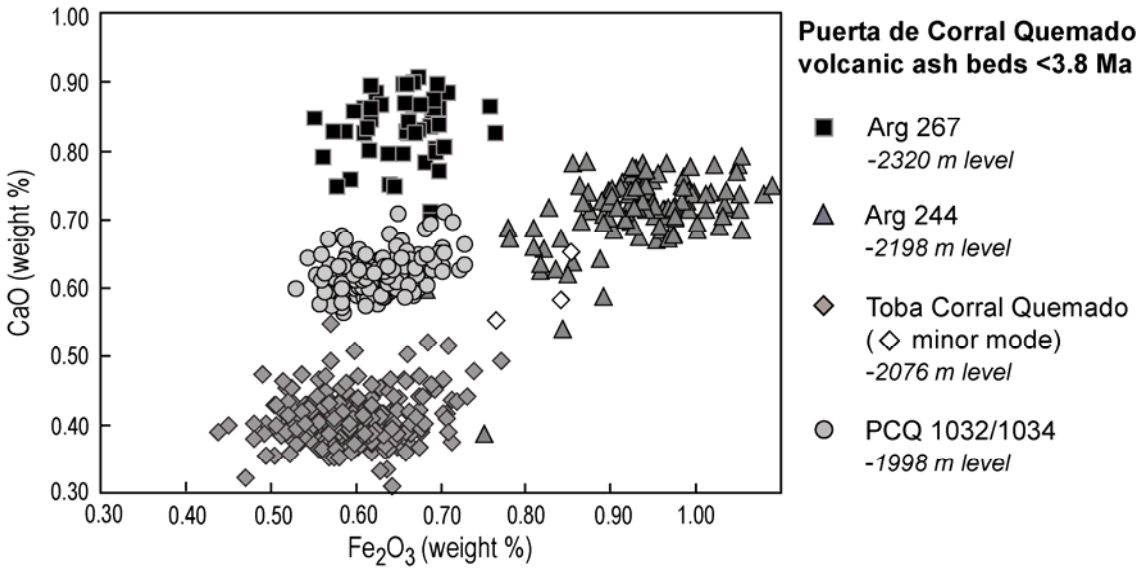

Figure 3.6: EPMA data depicting the composition of four major tuffs <3.8 Ma at Puerta de Corral Quemado. Populations of glass shards demonstrate unique compositions; Toba Corral Quemado has characteristically low CaO and Fe_2O_3 values.

chemistry and age data are reported along with a stratigraphic position of < 1998 m. Together these three samples, their zircon U-Pb ages, and their glass composition define the base of the sequence beginning at ~3.8 Ma and encompassing Toba Corral Quemado.

Fiambalá samples 001 and 074 are very close stratigraphically, their ages overlap, and EPMA data provides no criteria for distinguishing them (Table 3.5). The apparent correlation of these two samples with PCQ 1032 and 1034 is consistent with the $^{40}Ar/^{39}Ar$ sanidine age of Toba Corral Quemado (Arg 241; Latorre *et al*., 1997). Initial data indicated that the PCQ samples had lower Fe_2O_3 and CaO contents than the Fiambalá samples. Reanalysis of PCQ 1034 and Fiambalá 001 during the same analytical session resolved this issue and suggests that the higher Fe_2O_3 and CaO values are correct. At PCQ the stratigraphic relationship between samples 1032 and 1034 is not known; both samples are from the pumice rich upper portions of a 30–75 cm thick ash bed. It is possible that these four samples represent two temporally resolved but geochemically

Table 3.5: EPMA data for the Toba Corral Quemado sequence (<3.8 Ma).

Sample	n[a]	SiO_2	TiO_2	Al_2O_3	Fe_2O_3	MnO	MgO	CaO	BaO	Na_2O	K_2O	Cl	H_2O	Total	D[b]
tuff at 2320 m level															
Arg 267	**18**	**74.2**	**0.07**	**12.2**	**0.65**	**0.06**	**0.07**	**0.84**	**0.03**	**3.0**	**5.1**	**0.09**	**4.3**	**100.7**	**0.0**
1σ		0.3	0.04	0.2	0.04	0.04	0.02	0.06	0.03	0.1	0.2	0.01	0.4	0.3	
Arg 267[c, d]	**14**	**73.9**	**0.07**	**12.1**	**0.65**	**0.07**	**0.07**	**0.81**	**0.03**	**2.7**	**5.1**	**0.10**	**3.8**	**99.4**	**2.1**
1σ		0.5	0.04	0.3	0.05	0.03	0.02	0.03	0.03	0.1	0.2	0.02	0.7	0.4	
PCQ 806	**18**	**73.9**	**0.09**	**12.4**	**0.66**	**0.05**	**0.07**	**0.84**	**0.03**	**3.0**	**5.1**	**0.10**	**4.0**	**100.3**	**2.3**
1σ		0.3	0.05	0.2	0.05	0.03	0.02	0.04	0.03	0.1	0.2	0.02	0.5	0.4	
tuff at 2198 m level															
Arg 244	**19**	**72.5**	**0.18**	**12.1**	**0.93**	**0.04**	**0.12**	**0.73**	**0.03**	**2.7**	**5.5**	**0.17**	**5.9**	**100.8**	**0.0**
1σ		0.6	0.04	0.1	0.06	0.02	0.02	0.09	0.02	0.2	0.4	0.01	0.9	0.8	
Arg 244[c]	**30**	**73.4**	**0.18**	**12.1**	**0.92**	**0.05**	**0.12**	**0.69**	**0.04**	**2.6**	**5.7**	**0.18**	**5.7**	**101.7**	**2.4**
1σ		0.6	0.06	0.2	0.09	0.03	0.02	0.04	0.03	0.4	0.3	0.02	0.4	0.4	
PCQ 578	**24**	**72.8**	**0.17**	**12.1**	**0.97**	**0.04**	**0.12**	**0.72**	**0.04**	**2.7**	**5.6**	**0.18**	**5.4**	**100.9**	**1.5**
1σ		0.6	0.04	0.1	0.07	0.03	0.02	0.04	0.03	0.2	0.4	0.02	0.8	0.4	
PCQ 715[e]	**20**	**73.2**	**0.19**	**11.9**	**0.95**	**0.04**	**0.12**	**0.72**	**0.02**	**2.8**	**5.3**	**0.18**	**5.5**	**100.6**	**1.1**
1σ		0.3	0.04	0.1	0.05	0.01	0.02	0.03	0.02	0.1	0.2	0.01	0.4	0.2	
PCQ 805	**18**	**73.2**	**0.18**	**12.2**	**0.91**	**0.04**	**0.12**	**0.71**	**0.04**	**2.8**	**5.4**	**0.17**	**4.3**	**100.2**	**1.3**
1σ		0.3	0.05	0.1	0.07	0.02	0.02	0.03	0.04	0.1	0.2	0.01	0.5	0.4	

[a] n=number of analyzed shards; all oxides and elements reported in weight %, total Fe as Fe_2O_3; H_2O calculated from the difference between measured and stoichiometric oxygen (Nash, 1992).

[b] Statistical distance (Perkins *et al*., 1995; Appendix B) calculated using the concentrations of TiO_2, Fe_2O_3, MnO, MgO, CaO and Cl; D≤3.5 indicate analyses are identical at 95% confidence level.

[c] Replicate analysis.

[d] Analyses combined or excluded; see Appendix A for more information.

[e] Correlation to flat lying section ~12 km NNE of the principal PCQ section.

Table 3.5 (*continued*): EPMA data for the Toba Corral Quemado sequence (<3.8 Ma).

Sample	n[a]	SiO_2	TiO_2	Al_2O_3	Fe_2O_3	MnO	MgO	CaO	BaO	Na_2O	K_2O	Cl	H_2O	Total	D[b]
Toba Corral Quemado samples from the principal section (3.66 Ma; 2072–2084 m level)															
Arg 241[d, f, g]	**17**	**72.8**	**0.09**	**11.9**	**0.60**	**0.07**	**0.06**	**0.42**	**0.00**	**2.6**	**6.0**	**0.16**	**6.5**	**101.1**	**0.0**
1σ		0.4	0.03	0.1	0.04	0.02	0.02	0.02	0.01	0.3	0.6	0.01	0.6	0.5	
Arg 241[c]	**20**	**73.7**	**0.11**	**11.8**	**0.59**	**0.07**	**0.06**	**0.41**	**0.01**	**2.6**	**5.5**	**0.16**	**6.2**	**101.3**	**1.4**
1σ		0.3	0.03	0.1	0.05	0.02	0.01	0.02	0.02	0.3	0.4	0.01	1.0	0.9	
Arg 241[c]	**15**	**73.7**	**0.11**	**12.1**	**0.61**	**0.08**	**0.06**	**0.41**	**0.01**	**2.8**	**5.6**	**0.15**	**4.7**	**100.4**	**3.0**
1σ		0.4	0.05	0.2	0.05	0.02	0.02	0.03	0.02	0.2	0.5	0.02	0.6	0.5	
PCQ 109a[f]	**20**	**74.2**	**0.09**	**12.2**	**0.59**	**0.07**	**0.07**	**0.39**	**0.00**	**3.1**	**5.2**	**0.17**	**4.6**	**100.6**	**1.8**
1σ		0.4	0.02	0.2	0.04	0.02	0.01	0.02	0.01	0.3	0.4	0.01	0.5	0.3	
PCQ 109b[f]	**16**	**74.4**	**0.10**	**12.1**	**0.57**	**0.08**	**0.07**	**0.39**	**0.01**	**3.3**	**5.1**	**0.16**	**4.6**	**101.0**	**1.7**
1σ		0.6	0.03	0.1	0.06	0.02	0.01	0.01	0.01	0.3	0.4	0.01	0.7	0.3	
PCQ 511[f]	**19**	**74.4**	**0.10**	**12.1**	**0.60**	**0.07**	**0.06**	**0.40**	**0.01**	**2.9**	**5.5**	**0.17**	**5.1**	**101.5**	**1.6**
1σ		0.5	0.04	0.2	0.05	0.04	0.02	0.02	0.02	0.4	0.5	0.02	0.7	0.3	
PCQ 582[f]	**30**	**73.4**	**0.09**	**12.0**	**0.60**	**0.08**	**0.06**	**0.41**	**0.03**	**3.0**	**5.3**	**0.16**	**5.4**	**100.5**	**1.1**
1σ		0.6	0.06	0.2	0.06	0.03	0.02	0.04	0.03	0.3	0.5	0.02	0.9	0.5	

[a] n=number of analyzed shards; all oxides and elements reported in weight %, total Fe as Fe_2O_3; H_2O calculated from the difference between measured and stoichiometric oxygen (Nash, 1992).

[b] Statistical distance (Perkins *et al*., 1995; Appendix B) calculated using the concentrations of TiO_2, Fe_2O_3, MnO, MgO, CaO and Cl; D≤3.5 indicate analyses are identical at 95% confidence level.

[c] Replicate analysis.

[d] Analyses combined or excluded; see Appendix A for more information.

[e] Correlation to flat lying section ~12 km NNE of the principal PCQ section.

[f] Sample from the basal 2 m of Toba Corral Quemado at the principal section.

[g] Sample dated by Latorre *et al*. (1997).

Table 3.5 (*continued*): EPMA data for the Toba Corral Quemado sequence (<3.8 Ma).

Sample	n[a]	SiO_2	TiO_2	Al_2O_3	Fe_2O_3	MnO	MgO	CaO	BaO	Na_2O	K_2O	Cl	H_2O	Total	D[b]
Toba Corral Quemado samples from the principal section (3.66 Ma; 2072–2084 m level)															
PCQ 583	**30**	**73.5**	**0.09**	**12.0**	**0.59**	**0.09**	**0.06**	**0.40**	**0.01**	**2.9**	**5.3**	**0.17**	**5.7**	**100.9**	**2.5**
1σ		0.7	0.04	0.2	0.05	0.03	0.01	0.03	0.02	0.4	0.4	0.02	0.8	0.4	
PCQ 584	**28**	**73.4**	**0.11**	**11.9**	**0.61**	**0.08**	**0.06**	**0.40**	**0.02**	**3.1**	**5.1**	**0.16**	**5.4**	**100.5**	**2.3**
1σ		0.8	0.04	0.1	0.06	0.03	0.02	0.04	0.02	0.3	0.3	0.02	0.9	0.4	
Samples correlated to Toba Corral Quemado at the principal section (3.66 Ma; 2072 m level)															
TCQ[h]	**195**	**73.7**	**0.11**	**11.9**	**0.62**	**0.08**	**0.07**	**0.40**	**0.01**	**3.1**	**5.1**	**0.16**	**5.5**	**100.5**	**0.0**
1σ		0.7	0.04	0.2	0.05	0.03	0.02	0.03	0.02	0.3	0.3	0.02	1.0	0.3	
CQ 38[e]	**25**	**74.4**	**0.11**	**12.1**	**0.61**	**0.08**	**0.06**	**0.43**	**0.01**	**3.1**	**5.1**	**0.16**	**5.0**	**101.4**	**2.0**
1σ		0.9	0.04	0.2	0.07	0.02	0.01	0.05	0.02	0.4	0.5	0.02	1.6	0.7	
PCQ 210[e]	**16**	**74.8**	**0.10**	**12.0**	**0.59**	**0.07**	**0.06**	**0.41**	**0.03**	**2.5**	**5.0**	**0.16**	**5.3**	**101.0**	**1.5**
1σ		0.6	0.05	0.2	0.07	0.03	0.02	0.03	0.02	0.4	0.4	0.02	1.0	0.4	
PCQ 519[e]	**29**	**74.6**	**0.10**	**12.1**	**0.59**	**0.07**	**0.07**	**0.41**	**0.02**	**3.1**	**5.1**	**0.16**	**5.6**	**102.0**	**2.2**
1σ		0.7	0.05	0.2	0.06	0.04	0.02	0.04	0.02	0.4	0.4	0.02	1.0	0.5	

[a] n=number of analyzed shards; all oxides and elements reported in weight %, total Fe as Fe_2O_3; H_2O calculated from the difference between measured and stoichiometric oxygen (Nash, 1992).

[b] Statistical distance (Perkins *et al*., 1995; Appendix B) calculated using the concentrations of TiO_2, Fe_2O_3, MnO, MgO, CaO and Cl; D≤3.5 indicate analyses are identical at 95% confidence level.

[c] Replicate analysis.

[d] Analyses combined or excluded; see Appendix A for more information.

[e] Correlation to flat lying section ~12 km NNE of the principal PCQ section.

[f] Sample from the basal 2 m of Toba Corral Quemado at the principal section.

[g] Sample dated by Latorre *et al*. (1997).

[h] Weighted average of all Toba Corral Quemado samples from the principal section as reported above.

Table 3.5 (*continued*): EPMA data for the Toba Corral Quemado sequence (<3.8 Ma).

Sample	n[a]	SiO_2	TiO_2	Al_2O_3	Fe_2O_3	MnO	MgO	CaO	BaO	Na_2O	K_2O	Cl	H_2O	Total	D[b]
Samples correlated to Toba Corral Quemado at the principal section (3.66 Ma; 2072 m level)															
FIA 847[i]	**19**	**73.2**	**0.12**	**11.8**	**0.62**	**0.09**	**0.06**	**0.40**	**0.01**	**2.7**	**5.3**	**0.17**	**5.3**	**99.8**	**1.6**
1σ		0.5	0.04	0.1	0.04	0.03	0.01	0.03	0.01	0.2	0.2	0.02	0.7	0.3	
tuff at 1998 m level (~3.7 Ma)															
001[j, k]	**25**	**73.4**	**0.11**	**11.9**	**0.65**	**0.05**	**0.06**	**0.63**	**0.06**	**2.7**	**5.4**	**0.13**	**5.8**	**101.0**	**0.0**
1σ		0.4	0.03	0.1	0.04	0.02	0.01	0.02	0.03	0.2	0.2	0.01	0.8	0.3	
001[c]	**20**	**73.2**	**0.11**	**12.2**	**0.64**	**0.05**	**0.05**	**0.62**	**0.07**	**2.8**	**5.5**	**0.12**	**5.2**	**100.7**	**1.6**
1σ		0.6	0.05	0.2	0.04	0.03	0.02	0.02	0.04	0.2	0.2	0.01	0.7	0.3	
074[j]	**20**	**73.4**	**0.12**	**12.1**	**0.63**	**0.06**	**0.06**	**0.63**	**0.05**	**3.1**	**5.1**	**0.12**	**5.3**	**100.7**	**1.5**
1σ		0.4	0.05	0.2	0.05	0.04	0.02	0.02	0.03	0.2	0.3	0.01	0.6	0.3	
PCQ 1032	**19**	**72.7**	**0.09**	**12.0**	**0.61**	**0.05**	**0.06**	**0.60**	**0.06**	**2.6**	**5.8**	**0.12**	**5.6**	**100.3**	**2.8**
1σ		0.4	0.03	0.1	0.03	0.02	0.01	0.02	0.02	0.2	0.3	0.01	0.6	0.3	

[a] n=number of analyzed shards; all oxides and elements reported in weight %, total Fe as Fe_2O_3; H_2O calculated from the difference between measured and stoichiometric oxygen (Nash, 1992).

[b] Statistical distance (Perkins *et al*., 1995; Appendix B) calculated using the concentrations of TiO_2, Fe_2O_3, MnO, MgO, CaO and Cl; D≤3.5 indicate analyses are identical at 95% confidence level.

[c] Replicate analysis.

[d] Analyses combined or excluded; see Appendix A for more information.

[e] Correlation to flat lying section ~12 km NNE of the principal PCQ section.

[f] Sample from the basal 2 m of Toba Corral Quemado at the principal section.

[g] Sample dated by Latorre *et al*. (1997).

[h] Weighted average of all Toba Corral Quemado samples from the principal section as reported above.

[i] Correlation to Fiambalá section at 431 m level.

[j] Sample dated by Carrapa *et al*. (2008).

[k] Analyzed during the same analytical session.

Table 3.5 (*continued*): EPMA data for the Toba Corral Quemado sequence (<3.8 Ma).

Sample	n[a]	SiO_2	TiO_2	Al_2O_3	Fe_2O_3	MnO	MgO	CaO	BaO	Na_2O	K_2O	Cl	H_2O	Total	D[b]
tuff at 1998 m level (~3.7 Ma)															
PCQ 1034	**18**	**72.8**	**0.11**	**12.2**	**0.61**	**0.05**	**0.06**	**0.61**	**0.05**	**2.7**	**5.5**	**0.12**	**5.5**	**100.3**	**2.4**
1σ		0.5	0.03	0.2	0.05	0.02	0.01	0.04	0.03	0.3	0.5	0.01	0.6	0.3	
PCQ 1034[k]	**25**	**73.4**	**0.11**	**12.0**	**0.64**	**0.05**	**0.06**	**0.63**	**0.05**	**2.6**	**5.5**	**0.13**	**5.6**	**100.8**	**1.2**
1σ		0.4	0.03	0.2	0.04	0.02	0.02	0.03	0.03	0.3	0.5	0.01	0.6	0.3	
tuff <1998 m level (3.77 Ma)															
003[j]	**19**	**73.9**	**0.06**	**14.2**	**0.54**	**0.24**	**0.08**	**0.16**	**0.00**	**4.0**	**4.4**	**0.05**	**3.0**	**100.6**	**-**
1σ		0.3	0.04	0.2	0.05	0.04	0.02	0.03	0.01	0.1	0.1	0.01	0.3	0.2	

[a] n=number of analyzed shards; all oxides and elements reported in weight %, total Fe as Fe_2O_3; H_2O calculated from the difference between measured and stoichiometric oxygen (Nash, 1992).

[b] Statistical distance (Perkins *et al*., 1995; Appendix B) calculated using the concentrations of TiO_2, Fe_2O_3, MnO, MgO, CaO and Cl; D≤3.5 indicate analyses are identical at 95% confidence level.

[c] Replicate analysis.

[d] Analyses combined or excluded; see Appendix A for more information.

[e] Correlation to flat lying section ~12 km NNE of the principal PCQ section.

[f] Sample from the basal 2 m of Toba Corral Quemado at the principal section.

[g] Sample dated by Latorre *et al*. (1997).

[h] Weighted average of all Toba Corral Quemado samples from the principal section as reported above.

[i] Correlation to Fiambalá section at 431 m level.

[j] Sample dated by Carrapa *et al*. (2008).

[k] Analyzed during the same analytical session.

similar eruptions. Presently these ash beds are assumed to be a single chronostratigraphic horizon of identical age and to represent the 1998 m level at PCQ.

Toba Corral Quemado, the thickest and most widespread ash bed, was investigated systematically throughout its ~15 m thickness at PCQ. Major element compositional variation within volcanic glass is minor and internal stratigraphic variation is not documented. However, statistical distance estimates suggest that samples from the middle (PCQ 583) and upper (PCQ 584) portions of the ash bed may have slightly different compositions than the other samples, all of which were taken in the basal 2 m. The original analysis of sample Arg 241 identified a small population of glass shards with higher Fe_2O_3 and CaO content (Figure 3.6). Subsequent analyses of this sample failed to document additional shards of similar composition; therefore, this minor compositional mode is noted, but excluded from the average when considering correlation to other samples (Table 3.5; Appendix A).

The extensive data for Toba Corral Quemado build confidence in proposed local and regional correlations. Three samples from the upper Río Corral Quemado drainage ~12 km NNE of the PCQ section are correlated to Toba Corral Quemado based upon the appearance and thickness of the ash bed as well as glass composition (Table 3.5). This correlation is further supported by a zircon U-Pb age of 3.66 ± 0.12 Ma for sample CQ 38 (Coutand, I. and Sobel, E.R. pers. comm.). This agrees with the sanidine $^{40}Ar/^{39}Ar$ age of 3.66 ± 0.10 Ma reported by Latorre *et al*. (1997). An additional correlation is developed from these localities in the Corral Quemado basin to an ash bed (FIA 847) sampled in the Fiambalá basin (Table 3.5). Sample FIA 847 was taken from the base of a prominent 0.8 m thick lenticular tuff with soft-sediment deformation at the 431 m level of the Fiambalá

section. This sample is ~80 m above the top of the 4.0 Ma sequence, lending further support to the proposed correlation.

In addition to the two volcanic glass compositions below Toba Corral Quemado; two compositions are reported above it. The compositions, based upon multiple samples exhibit more variable composition in Fe_2O_3-CaO space (Arg 244, Arg 267; Figure 3.6). Several other compositions are known above Toba Corral Quemado from ash beds at the 2114 and 2340 m levels. These are documented by single samples, but have explicit stratigraphic relationships with the reported sequence (PCQ 804, PCQ 807; Appendix A).

Samples Arg 244, PCQ 578, and PCQ 805 are all sampled from the basal meter of a prominent cross-bedded 5 m thick tuff ~115 m above Toba Corral Quemado. The basal meter of this tuff is massive and has less detrital contamination than the higher part of the tuff. These three samples provide confidence in correlation to an ash bed ~90 m above Toba Corral Quemado in the upper Río Corral Quemado drainage (PCQ 715; Table 3.5). At this locality PCQ 715 exists as an impure but laterally persistent tuffaceous horizon in the base of a pebble conglomerate. Prior to concentration, volcanic glass comprises <20% of the 125–250 μm fraction; however, the glass is easily purified and all of the shards analyzed by EPMA were consistent with the composition defined by samples from the 2198 m level at PCQ.

Samples Arg 267 and PCQ 806 are from the base of a 1.5 m thick ash bed at the 2320 m level. Above 30 cm this ash bed contain significant detrital contamination including coarse sand and gravel with abundant lithic fragments. The same sedimentary pattern and similar glass chemistry is observed for a 5 m thick ash bed just upsection (PCQ 807; Appendix A). The composition of PCQ 807 is similar to that of the ash bed

below it, being distinguishable only by slightly higher Fe_2O_3 and CaO and notably higher TiO_2. These ash beds are interbedded with significantly coarser strata than the ash bed at 2198 m and provide the closest approximation to the top of the PCQ section.

Of all the late Miocene and Pliocene volcanic ash beds presented in this study, Toba Corral Quemado is the thickest and most widespread. Toba Corral Quemado has high potential as a regional chronostratigraphic horizon along the southeastern margin of the Puna plateau. This prompts speculation regarding the volcanic source of this deposit.

Notably, a series of ignimbrites dated at ~3.6 Ma crop out 150 km NW of the PCQ section (Schnurr *et al*., 2007). These ignimbrites appear to have erupted from calderas near the Argentina-Chile border and flowed eastward. Especially promising is the Vallecito ignimbrite, feldspar separates from which are dated at 3.61 ± 0.01 Ma by $^{40}Ar/^{39}Ar$ (Kraemer *et al*., 1999) and 3.6 ± 0.1 Ma by K-Ar (Siebel *et al*., 2001). The age reported by Kraemer *et al*. (1999) was obtained from the upper unit of two pumice-poor flow units attaining maximum thickness of ~20 m along the western border of Salar de Antofalla. The dispersal of tephra from this region to the Corral Quemado basin is considered likely, and conforms very well to the observations laid out in Figure 1.5 of this dissertation. The proposed source area and dispersal pattern are also supported by the greatly diminished thickness of Toba Corral Quemado in the Fiambalá basin. Geochemical data supporting correlation of Toba Corral Quemado to the Vallecito ignimbrite is presented in the following section.

Proposed tephrostratigraphic correlations

Correlation of volcanic ash beds is proposed on the basis of homotaxy and EPMA of volcanic glass. Confidence in this approach was established through repeated

sampling of major ash beds both laterally and vertically throughout their exposures. This effort is especially well developed for Toba Corral Quemado and the tuff of sandstone #12, both exposed extensively in the upper PCQ section. Mapping these volcanic ash beds develops *a priori* correlation of individual samples which can be further tested by EPMA. These data demonstrate that intra-sample compositional differences within a single ash bed resulting from sample variability and analytical reproducibility are minor. Correlations are also supported by patterns of shard to shard compositional variation and by isotopic age dating of eruptive minerals.

The regional chronological framework built upon these observations is internally consistent; however, tephrostratigraphic correlations may never be proven, they may only be supported or refuted. In the interest of rigorously developing this framework, additional effort was undertaken to further test proposed correlations. This was undertaken with the aim of: 1) carefully evaluating chronostratigraphic correlations and, 2) improving the utility of important tephrostratigraphic horizons in the region. Correlations proposed in the preceding sections were identified and evaluated using the Statistical Distance function of Perkins *et al*. (1998; Appendix A). However, sequences of volcanic ash beds with similar chemistry may lead to spurious correlation. This is of concern particularly when short sequences are compared and when the ash beds in question are not closely constrained by isotopic age estimates. Ash beds with similar major element chemistry may often be distinguished by trace element concentrations. Trace element concentrations measured by ICP-MS have proven useful in supporting correlations, deciding between two or more possible correlations, refuting potential

correlations, and further characterizing ash beds. The results of this work are presented in Table 3.6 and discussed in the following pages.

Toba Corral Quemado sequence (<3.8 Ma)

At Puerta de Corral Quemado, the tuff at the 2198 m level is notable for its high concentrations of Ce, Cs, Hf, La, Nd, Rb, Sm, Th, and U, whereas Toba Corral Quemado is noted for low Ba, Ce, La, Nd, and Sr concentrations, and relatively high U and Th concentrations. Fiambalá samples 001 and 074, dated at 3.69 ± 0.12 and 3.74 ± 0.10 Ma respectively are correlated on the basis on EPMA data and cannot be distinguished by trace element data. Fiambalá sample 003 dated at 3.77 ± 0.10 has unique trace element compositions, in particular extremely low concentrations of Ba, Ce, La, Nd, and Sr coupled with Cs, Rb, Ta, and U concentrations among the highest measured.

Toba Corral Quemado correlations to the upper Río Corral Quemado drainage and to Fiambalá are confirmed and minor compositional zoning is identified. The dated sample of Toba Corral Quemado from the principal section (Arg 241; Latorre *et al*., 1997) was analyzed using five individual digestions in four different analytical sessions. These data document high Ba and Sr contents relative to many other samples of Toba Corral Quemado. Sample PCQ 582 was sampled at the base of the ash bed and exhibits Ba and Sr contents similar to Arg 241, and different from PCQ 583 and 584 which were sampled higher in the ash bed. As was suggested by the Statistical Distance function applied to EPMA data, minor compositional zoning of the ash bed is likely, and trace element data support this. The compositional range exhibited by Ba (204–107 μg/g) and Sr (27–13 μg/g) in volcanic glass significantly exceeds the analytical precision as estimated by replicate analyses of an internal standard or by the standard deviation on the

Table 3.6: ICP-MS data for volcanic glass in widespread ash beds.

Sample	Age (Ma)	Ba[a]	Ce	Cs	Hf	La	Lu	Nd	Rb	Sm	Sr	Ta	Th	U	Y
		µg/g	µg/g	µg/g	µg/g	µg/g	µg/g	µg/g	µg/g	µg/g	µg/g	µg/g	µg/g	µg/g	µg/g
2198 m level; Puerta de Corral Quemado															
Arg 244	<3.6	483	106	19	3.4	54	0.34	32	276	4.6	84	2.5	61	19	20
Arg 244		453		19	3.7				258	6.0	74	2.5		19	15
PCQ 578	<3.6	481	109	18	3.0	52	0.35	30	298	5.8	76	2.4	63	19	18
PCQ 805	<3.6	483	105	18	3.0	53	0.36	32	272	5.1	84	2.5	60	19	20
PCQ 805		484	114	18		55	0.35	30	300	5.7	80	2.4	64	18	19
Vallecito Ignimbrite[b] *(proximal Toba Corral Quemado?)*															
Sia92/3a	3.6 ± 0.1	390	30	12		15	0.36	14	232	3.4	63	2.1	30	11	22
Sia92/3a		390	30	12		15	0.36	14	232	3.4	63	2.1	30	11	13
Sia83b8	3.61 ± 0.01	340	48	14		25	0.26	18	248	3.4	46	1.9	28	11	14
Toba Corral Quemado[c] *(principal section at PCQ)*															
Arg 241[d]	3.66 ± 0.05	**202**	**48**	**12**	**1.9**	**21**	**0.28**	**12**	**234**	**3.3**	**27**	**2.2**	**26**	**12**	**16**
1σ		12	2	1	*0.1*	1	*0.004*	1	13	0.1	2	0.5	1	*0.2*	0.4
PCQ 582	3.66	204	38		2.0	18		11	234		27	2.4	23	11	
PCQ 511	3.66	125	35	11	1.4	16		11	242		17	2.2	22	11	
PCQ 583	3.66	124	33		1.4	15		10	230		18	1.1	19	9	
Toba Corral Quemado (correlation to principal section at PCQ)															
PCQ 210	3.66	107	33	14	1.7	15		10	227		15	2.3	22	11	
PCQ 519	3.66	114	38	12	1.9	15	0.27	10	250	3.0	15	3.4	24	12	17
CQ 38	3.66 ± 0.12	159	39	13	2.0	16	0.29	10	252	3.2	18	2.7	24	12	17
CQ 38		152	36			16			240	3.0	19	1.7	23		16

[a]Values in micrograms/gram; Ba and Sr by isotope dilution, other elements by standard addition.

[b]Age and chemical data from Kraemer *et al*. (1999), Siebel *et al*. (2001), and Schnurr *et al*. (2007).

[c]Arg 241 = Average and standard deviation for 5 digestions, asterisk indicates only 3 values included.

[d]Samples from Latorre *et al*. (1997); dated by $^{40}Ar/^{39}Ar$ analysis of sanidine.

[e]Samples from Carrapa *et al*. (2008); dated by U-Pb analysis of zircon.

Table 3.6 (*continued*): ICP-MS data for volcanic glass in widespread ash beds.

Sample	Age (Ma)	Ba[a]	Ce	Cs	Hf	La	Lu	Nd	Rb	Sm	Sr	Ta	Th	U	Y
		µg/g	µg/g	µg/g	µg/g	µg/g	µg/g	µg/g	µg/g	µg/g	µg/g	µg/g	µg/g	µg/g	µg/g
Toba Corral Quemado (correlation to principal section at PCQ)															
FIA 847	3.66	114	39	13	1.8	15	0.29	9	249	3.1	13	2.2	23	12	17
FIA 847		109	31			13			232		15	2.1	22		14
Fiambalá ash beds defining base of Toba Corral Quemado sequence[e]															
001	3.69 ± 0.12	642	66	6	2.0	30	0.22	19	192	4.1	101	3.2	23	8	14
074	3.74 ± 0.10	634	71	6	1.9	33	0.23	20	208	4.1	98	3.4	25	8	15
074		609		7	2.2			17	175	4.3	91	1.6	22	9	11
003	3.77 ± 0.10	19	18	31	1.3	4	0.37	7	511	4.5	2	5.1	17	20	26
003		16		26					374		2	8.2		17	
~4.0 Ma sequence at Fiambalá															
FIA 846	3.7–4.0	783	69	6	2.8	35		19	160	3.8	254	0.7	19	5	4
FIA 846		802	76	6	3.0	38		21	173	3.8	262	0.7	21	5	5
FIA 843	~4.0	533	26	8	1.9	11	0.19	7	160	2.9	88	1.5	9	7	13
FIA 842	~4.0	549	10	9	2.2	3	0.20	2	127	3.1	85	1.4	4	8	4
FIA 841	~4.0	637	63	6	1.7	29	0.22	17	190	4.0	94	1.3	23	8	13
FIA 841		609	53	6	2.2	23		14	172	4.3	87	1.5	20	9	10
FIA 840[f]	4.03 ± 0.12	654	66	6	1.8	31	0.22	19	182	4.1	113	1.4	24	8	13
FIA 840		662	58			30		19	175	3.9	117	1.3	22		13
FIA 839	~4.0	660	76	6	2.0	38	0.20	21	183	4.0	131	1.4	24	9	12
FIA 838	~4.0	665	75	6	1.9	36	0.21	19	183	4.0	143	1.5	23	9	11

[a]Values in micrograms/gram; Ba and Sr by isotope dilution, other elements by standard addition.

[b]Age and chemical data from Kraemer *et al*. (1999), Siebel *et al*. (2001), and Schnurr *et al*. (2007).

[c]Arg 241 = Average and standard deviation for 5 digestions, asterisk indicates only 3 values included.

[d]Samples from Latorre *et al*. (1997); dated by $^{40}Ar/^{39}Ar$ analysis of sanidine.

[e]Samples from Carrapa *et al*. (2008); dated by U-Pb analysis of zircon.

[f]Age data from this study, see Appendix A for full details.

Table 3.6 (*continued*): ICP-MS data for volcanic glass in widespread ash beds.

Sample	Age (Ma)	Ba[a] µg/g	Ce µg/g	Cs µg/g	Hf µg/g	La µg/g	Lu µg/g	Nd µg/g	Rb µg/g	Sm µg/g	Sr µg/g	Ta µg/g	Th µg/g	U µg/g	Y µg/g
upper tuff of sandstone #12															
PCQ 575	~4.4	612	74	8	1.6	38	0.23	17	177	3.6	117	1.3	21	7	13
CQ 22	~4.4	609	75	8	1.9	39	0.25	19	183	3.8	114	1.7	22	8	13
lower tuff of sandstone #12															
Arg 227	~4.4	631	65			35		14	140	3.4	244		17	8	11
Arg 227		596		6	2.6			14	120	3.6	193	1.2	15	5	
Arg 227		598		6	2.3			11	107	3.3	233	1.1	12	5	
PCQ 573	~4.4	615	75	7	1.9	38	0.23	19	167	3.7	159	1.3	21	7	13
PCQ 574	~4.4	649	75	6	2.1	39	0.22	18	156	3.7	191	1.1	17	5	12
PCQ 793	~4.4	666	75	6	2.2	37	0.23	18	156	3.6	179	1.2	19	6	10
PCQ 793		660	65			31		17	136		183		16		10
PCQ 794	~4.4	687	77	6	2.3	38	0.24	20	164	3.8	197	1.2	20	6	10
PCQ 794		648	71			37		18	146		195		17		11
lower tuff of sandstone #12 (correlated to principal section at PCQ)															
PCQ 725[g]	~4.4	658	80	6.2	2.5	40		20	159	3.4	185	1.1	20	5	12
1828 m level; Puerta de Corral Quemado															
PCQ 502	~4.4	629	72	10	1.8	35	0.25	18	204	3.9	113	2.1	24	9	14
PCQ 792	~4.4	610	75	10	1.8	37	0.25	18	203	3.8	124	1.9	24	9	13

[a]Values in micrograms/gram; Ba and Sr by isotope dilution, other elements by standard addition.

[b]Age and chemical data from Kraemer *et al*. (1999), Siebel *et al*. (2001), and Schnurr *et al*. (2007).

[c]Arg 241 = Average and standard deviation for 5 digestions, asterisk indicates only 3 values included.

[d]Samples from Latorre *et al*. (1997); dated by $^{40}Ar/^{39}Ar$ analysis of sanidine.

[e]Samples from Carrapa *et al*. (2008); dated by U-Pb analysis of zircon.

[f]Age data from this study, see Appendix A for full details.

[g]Correlation to San Fernando section #2.

Table 3.6 (*continued*): ICP-MS data for volcanic glass in widespread ash beds.

Sample	Age (Ma)	Ba[a]	Ce	Cs	Hf	La	Lu	Nd	Rb	Sm	Sr	Ta	Th	U	Y
		µg/g	µg/g	µg/g	µg/g	µg/g	µg/g	µg/g	µg/g	µg/g	µg/g	µg/g	µg/g	µg/g	µg/g
late Miocene sequence at Río Guanchín															
GUA 814	<5.2	640	62	6	1.7	30	0.18	15	172	3.2	85	1.7	20	6	9
055[e]	5.23 ± 0.30	316	32	10	1.7	10	0.43	10	230	4.1	21	2.4	16	9	31
055		319	28			11			221	4.0	22		14		28
GUA 811	~5.2	433	38	10	1.8	13	0.44	12	229	4.6	27	2.1	16	9	31
GUA 811		431	32	10		13		12	213		27	2.0	15	8	
PCQ 733	~5.2	429	37	9	1.9	13	0.47	12	222	4.7	26	2.2	16	9	30
PCQ 733		414	31			12			210	4.2	26		14		28
GUA 810	5.2–5.6	727	65	4	1.7	31	0.18	17	158	3.8	139	1.3	17	4	12
GUA 810		731	58			30		17	153	3.7	142	1.1	17		12
late Miocene sequence at Puerta de Corral Quemado															
PCQ 566	5.2–5.6	763	63	3	2.2	27	0.23	18	158	4.4	81	1.4	14	3	15
CQ 26	5.2–5.6	791	58	3	2.1	25	0.23	16	162	4.2	87	1.4	14	4	14
PCQ 565	5.2–5.6	801	50	3	1.9	21	0.22	14	166	3.9	81	1.5	13	4	14
PCQ 564	5.2–5.6	799	66	3	1.7	30	0.20	19	154	4.3	121	1.2	14	3	13
Arg 196	5.64 ± 0.16	327	49	13	1.6	23	0.29	17	244	2.8	41	1.5	14	7	22
Arg 196		327	55	13	1.9	23	0.34	16	259		39	1.7	14	8	
PCQ 560	5.6	324	51	12	1.8	24	0.29	18	247	3.0	43	1.6	14	7	
PCQ 560		338	50	13	1.8	23		16	241	2.9	42	1.4	14	7	

[a]Values in micrograms/gram; Ba and Sr by isotope dilution, other elements by standard addition.

[b]Age and chemical data from Kraemer *et al*. (1999), Siebel *et al*. (2001), and Schnurr *et al*. (2007).

[c]Arg 241 = Average and standard deviation for 5 digestions, asterisk indicates only 3 values included.

[d]Samples from Latorre *et al*. (1997); dated by $^{40}Ar/^{39}Ar$ analysis of sanidine.

[e]Samples from Carrapa *et al*. (2008); dated by U-Pb analysis of zircon.

[f]Age data from this study, see Appendix A for full details.

[g]Correlation to San Fernando section #2.

five analyses of Arg 241. If the early erupted material is inferred to be the first deposited, Ba and Sr were enriched at the beginning of the eruptive sequence relative to the end.

The potential correlation to the Vallecito ignimbrite as a proximal equivalent of Toba Corral Quemado is also supported by trace element data. Data for three whole rock samples of the Vallecito ignimbrite are consistent with this correlation excepting a few elements. The Vallecito ignimbrite is characterized by higher Ba, Nd, Sr, and Th values, of these Ba and Sr are the most discrepant. EPMA of a single plagioclase crystal from sample Arg 241 measured >1,000 μg/g Ba, well in excess of that measured in volcanic glass. Samples of the Vallecito ignimbrite likely contained feldspars; the Ba and Sr values are suspected to record this and therefore do not refute the proposed correlation.

4.0 Ma Fiambalá sequence

The sequence of closely spaced ash beds dated at 4.0 Ma exhibits very similar trace element chemistry throughout, in accord with observations from EPMA data. The rhyodacitic ash bed FIA 846 is distinguished from the other ash beds in the sequence by high Ba, Hf, and Sr and by low Ta, U, and Y contents. The same characteristics are the only measureable differences between FIA 846 and tuff of sandstone #12 samples from Puerta de Corral Quemado. Sample Arg 227 shares more similarities with FIA 846 including relatively lower concentrations of Cs and U and higher Sr concentration relative to samples of other tuffs sandstone #12. Measureable differences in major, minor, and trace element composition exist between FIA 846 and the tuff of sandstone #12, but the strong similarities in their respective chemistries imply a common volcanic source and perhaps temporal affinity. Direct age measurements of tuff of sandstone #12 will be valuable in addressing this possibility.

As documented by EPMA data, the ash beds between the 300–330 m level at Fiambalá exhibit similar, but distinguishable, chemistries. Relative to the other ash beds in this interval those at the ~327 m level (FIA 842, 843) have high Cs and lower concentrations of Ba, Ce. La, Nd, Rb, Th, and Sm. Fe_2O_3 and MgO contents suggest that ash bed FIA 842 contains different volcanic glass than FIA 843; this is further supported by its distinctly lower Ce, La, Nd, Rb, Th, and Y contents. The two thick ash beds at ~315 m level (FIA 840, 841) have Ce, La, and Sr contents intermediate to the ash beds above and below them; they can be distinguished by their CaO and Sr contents which have positive covariance. Of the ash beds at the ~300 m level, only two (FIA 838, 839) were analyzed for trace element concentrations. These two samples have higher Ce, La, and Sr contents than those at the ~315 or ~327 m levels. While FIA 838 and 839 can be differentiated on the basis of Fe_2O_3, CaO, and Cl, they cannot be differentiated by trace element data. In the 300–330 m interval at Fiambalá, numerous closely spaced and chemically similar ash beds likely derived from one or more similar volcanic centers which were highly active at 4.0 Ma. Apparent stratigraphic patterns in Ce, La, and Sr may prove useful in subdividing this sequence of ash beds and in understanding the short-term evolution of the volcanic center(s).

Tuff of sandstone #12 sequence (~4.4 Ma)

Numerous analyses of the tuff of sandstone #12 confirm correlations proposed by EPMA and document significant trace element variation. Variation in the elements Ba, Cs, Nd, Rb, Sr, and Th greatly exceeds the expected analytical precision and indicates that the source magma chamber was likely zoned with respect to these elements. Within the lower tuff of sandstone #12, sample Arg 227 (Latorre *et al*., 1997) has lower Nd and

Rb concentrations and higher Sr concentrations than most other samples. Sample PCQ 725 (San Fernando section #1) has the highest Ce and La concentrations of any lower tuff of sandstone #12 sample, but trace element data provide strong support for the proposed correlation. Collectively, samples of the lower tuff of sandstone #12 have lower Cs, Rb, Ta, and Th and higher Sr contents than ash beds immediately above and below it.

A stratigraphically distinct ash bed (1828 m level) directly underlying the tuff of sandstone #12 has major and minor element chemistry very similar to that of the upper tuff of sandstone #12 (cf. Table 3.3). Correlation of Universität Potsdam sample CQ 22 can be made to either of the two ash beds on the basis of EPMA and trace element data. Subtle differences in Cs, Rb, Th, and U and slightly lower statistical distance values relative to upper tuff of sandstone #12 samples (D = 0.8, 1.6, 1.7) than to the samples of the ash bed at 1828 m level (D = 2.3, 2.9, 3.3, 3.8) support correlation of CQ 22 with the former. Nonetheless, the ash bed at 1828 m level probably has a genetic relationship with the tuff of sandstone #12 and the age difference is not likely to be measurable.

Late Miocene sequence

Within ~75 m of the late Miocene sequence at Río Guanchin the largest measured range of Lu contents is present. Ash beds at the 6 m level (GUA 810) and the ~80 m level (GUA 814) have the lowest Lu of any sample (0.18 μg/g). The ash bed from the ~24 m level (GUA 811) has the highest Lu content of any sample (0.43–0.47 μg/g).

On the basis of EPMA data, GUA 811 is correlated to a Río Guanchin sample dated to ~5.2 Ma by U-Pb zircon analysis (055) and to San Fernando section #2 (PCQ 733). Relative to other ash beds in the late Miocene sequence these ~5.2 Ma samples have low Ce, La, Nd, and Sr and high Lu, Ta, U, and Y. All trace element values are consistent

with correlation between Río Guanchin and San Fernando, but notable differences in Ba and Sr content exist between the dated sample (055) and the other two samples. Similar variation of Ba and Sr within an eruption is documented by Toba Corral Quemado and the tuff of sandstone #12, and much more extreme variations in these elements are known from eruptive products of large silicic magma chambers (e.g., Bishop Tuff; Wilson and Hildreth, 1997). Sample GUA 811 is a 0.7 m thick lenticular ash bed with soft sediment deformation and is replaced laterally by coarse sand. GUA 811 was sampled close to 055, but it is probable that due to lateral discontinuity of the ash bed, these two samples represent different portions of the eruptive sequence. The correlation between the two samples at Río Guanchin and to the sample at San Fernando is strongly supported by the unique (highest measured in NW Argentina) Lu and Y values that they share.

The late Miocene sequence at Puerta de Corral Quemado is a complicated interval with closely spaced ash beds of similar chemistry, data in Table 3.6 represent only those ash beds having Ca/Fe <1.0. Ash beds at ~1540 m level (PCQ 565, 566) have Ca/Fe ratios between 0.60–0.68 and can be most easily differentiated from ash beds at ~1518 m (PCQ 564) on this basis and by Sr content. PCQ 564 also has slightly higher Ce and La contents and lower Lu than ash beds from ~1540 m level. Samples PCQ 565 and 566 are not easily differentiated by trace element chemistry and can be more confidently discerned by their Fe_2O_3, TiO_2, and MgO contents (cf. Table 3.1). Correlation of Universität Potsdam sample CQ 26 to a tuff at the ~1540 m level at PCQ is supported by strong trace element similarities with PCQ 565 and 566. Excellent correspondence in trace element composition between Arg 196 and PCQ 560 provides valuable data for the

dated ash bed defining the base of the late Miocene sequence at Puerta de Corral Quemado.

Accuracy and precision of the chronological framework

The chronological framework developed herein is based upon radioisotopic dating of volcanic ash beds; both the U-Pb and $^{40}Ar/^{39}Ar$ systems are utilized. A primary goal of tephrostratigraphic studies is to extend age estimates from dated samples to new localities where material for dating may be scarce or absent. To this end, major and trace element data are presented for volcanic glass from each dated sample. If a split of a dated sample could not be obtained and analyzed, the age information is not drawn upon in this study. Two samples dated by Latorre *et al*. (1997) provide sanidine $^{40}Ar/^{39}Ar$ age constraints at Puerta de Corral Quemado. Four splits of samples dated by ion probe U-Pb analysis of zircon (Carrapa *et al*., 2008) have also been analyzed and produce important correlations between PCQ and Fiamabalá. A sample from the upper Río Corral Quemado drainage was dated using the methodology described in Carrapa *et al*. (2008) and is presented here for the first time. Two samples from this study have been dated by $^{40}Ar/^{39}Ar$ analysis of plagioclase; compositional data for volcanic glass is presented in this chapter and $^{40}Ar/^{39}Ar$ data are presented in Appendix A.

These absolute age estimates are consistent with stratigraphic information, and the correspondence between the two isotopic systems is excellent. Some debate exists as to the agreement between the U-Pb and $^{40}Ar/^{39}Ar$ geochronometers, particularly regarding the decay constants used for $^{40}Ar/^{39}Ar$ dating (e.g., Min *et al*., 2000; Mundil *et al*., 2006). Although the accuracy of the decay constants recommended by Steiger and Jäger (1977) is the matter of discussion, research has proceeded by attempts to calibrate the age of

standards commonly used as neutron fluence monitors (cf. Jourdan and Renne, 2007). Recent efforts have shifted the age of the Fish Canyon sanidine (FCs) standard older by 0.6–0.7% (Kuiper *et al*., 2008) and now by >1.0% (Renne *et al*., 2010) relative to the 28.02 Ma age proposed by Renne *et al*. (1998).

Recent studies of Cretaceous (Siewert *et al*., 2010) and Eocene (Smith *et al*., 2010), volcanic ash beds have preferred a 28.201 Ma age for the FCs (Kuiper *et al*., 2008). Data presented in this chapter and in Appendix A provide no evidence that adopting an age >28.02 Ma for FCs is necessary or even favorable for Pliocene volcanic ash beds in northwestern Argentina. All ages in Appendix A are relative to the FCs (28.02) or Taylor Creek sanidine (28.34) ages reported by Renne *et al*. (1998). The $^{40}Ar/^{39}Ar$ ages reported by Latorre *et al*. (1997) are relative to a FCs age of 27.84 Ma. Both of these ages for FCs provide reasonable agreement with the U-Pb zircon ages.

Several opportunities exist to assess the accuracy of absolute ages drawn upon here. Importantly, age estimates throughout fall in the correct stratigraphic order. The latest Miocene sequence of ash beds contains two dated samples whose stratigraphic position is consistent with their age estimates. This builds confidence in the 5.23 Ma U-Pb age based on a single zircon grain from the Río Guanchin section (Carrapa *et al*., 2008). Two closely spaced ash beds in the Fiambalá section provide the only instance in which age estimates violate stratigraphic position. These ash beds, dated by $^{40}Ar/^{39}Ar$ analysis of plagioclase, are within 15 m stratigraphically and their age estimates are indistinguishable within uncertainty. While out of stratigraphic order, the similarity of these ages establishes confidence in the 4.0 Ma estimate for the sequence of ash beds centered on the 300 m level at Fiambalá. An ash bed that is considered correlative of Toba Corral

Quemado (3.66 Ma) crops out 125 m upsection, further confirming the accuracy of the 4.0 Ma ages. If a weighted mean of 4.0 ± 0.1 Ma (derived from the two plagioclase $^{40}Ar/^{39}Ar$ age estimates at Fiambalá) is assumed to represent the age of this closely spaced and geochemically similar group of volcanic ash beds it is in excellent agreement with the U-Pb system. McPherson (2008) obtained six U-Pb zircon ages from ash beds in the Fiambalá basin, which are presumably the same group of ash beds, and reported a weighted mean of 4.02 ± 0.04 Ma. Glass chemistry of the ash beds dated by the U-Pb method will be crucial to assessing the appropriateness of calculating a mean age from all samples; yet, existing data indicate that the 4.0 Ma sequence represents a short temporal interval so that resolving ages of individual ash beds by U-Pb age is unlikely.

The most stringent test of accuracy is afforded by Toba Corral Quemado and closely associated ash beds. In the Fiambalá basin, along the Río Guanchin, three closely spaced ash beds yield U-Pb zircon ages which define the base of the Toba Corral Quemado sequence. Ages estimates of these samples are stratigraphically consistent and define a mean age of 3.7 ± 0.1 Ma (Carrapa *et al*., 2008). The upper two ash beds are correlative with two samples at PCQ which are ~75 m below Toba Corral Quemado. The close agreement of the U-Pb and $^{40}Ar/^{39}Ar$ systems at the <100 ka level is encouraging and further supported by a U-Pb zircon age of 3.66 ± 0.12 Ma for Toba Corral Quemado. This age is identical to the 3.66 ± 0.10 Ma $^{40}Ar/^{39}Ar$ sanidine age (Latorre *et al*., 1997).

Recalculating the Latorre *et al*. (1997) age with FCs ages of 28.02 Ma (Renne *et al*., 1998) or 28.10 Ma (Spell and McDougall, 2003) shifts the age to 3.68 Ma and 3.69 Ma respectively. These ages are younger than or equivalent to the uppermost U-Pb age of 3.69 ± 0.12 Ma reported by Carrapa *et al*. (2008). These shifts are small relative to the

reported 2σ uncertainty and all ages are technically indistinguishable; nevertheless, a $^{40}Ar/^{39}Ar$ age for Toba Corral Quemado that does not violate stratigraphic order is preferred. Because the 3.69 Ma U-Pb age is correlative to an ash bed ~75 m below Toba Corral Quemado, the 28.10 Ma FCs age (Spell and McDougall, 2003) is considered the oldest for which stratigraphic order is not violated by isotopic age estimates. Following this reasoning, and prioritizing agreement between the two radioisotopic systems in question, the Toba Corral Quemado ages calculated using the FCs ages proposed by Kuiper *et al*. (2008) or Renne *et al*. (2010) yield much less favorable ages (3.71 Ma and 3.72 Ma, respectively). Accounting for the possibility that zircon crystals may have significant pre-eruption magmatic histories and therefore be systematically older, an older age limit of ~3.7 Ma is suggested for Toba Corral Quemado.

A younger age limit can also be placed on Toba Corral Quemado because of its paleomagnetic polarity. In 2007, three oriented blocks were sampled from the fine grained base of the tuff at the locality where Latorre *et al*. (1997) sampled. Two of these blocks were measured for NRM, demagnetized using alternating field methods, and found to have reversed polarity. This places Toba Corral Quemado in the Gilbert Reversed Chron because Gradstein *et al*. (2004) place the boundary between the Gilbert and Gauss Chrons at 3.596 Ma. This supports the 3.66 Ma age estimate and an earlier K-Ar age (3.53 ± 0.04 Ma; Butler *et al*., 1984) appears to be slightly too young, which may result from incomplete degassing of radiogenic argon from the sample. This has been shown to be the case with other feldspar samples (cf. McDougall *et al*., 1980; McDowell *et al*., 1983). The paleomagnetic sampling of Butler *et al*. (1984) did not extend high enough in the section to establish a polarity for Toba Corral Quemado or the position for

the boundary between the Gauss and Gilbert Chrons; doing so would extend chronological control upsection and establish a precise, globally recognized, age datum.

The accuracy of the reported Toba Corral Quemado ages is indicated by agreement between $^{40}Ar/^{39}Ar$, U-Pb, and paleomagnetic data. Confidence in the 3.66 Ma age is high, and the reported 2σ uncertainties for the $^{40}Ar/^{39}Ar$ (0.10 Ma) and U-Pb (0.12 Ma) systems are demonstrated to be reasonable. Three U-Pb zircon ages delineate an older age bound of 3.7 Ma and a paleomagnetic reversal establishes a younger age bound of 3.6 Ma. In the absence of additional, concerted radioisotopic work, accuracy and precision at the sub-100 ka level should be considered likely, but not proven.

Correlation of tephrostratigraphic horizons leads to highly precise age control, but accurate ages of correlated horizons rely on primary radioisotopic data. Because eruption and deposition of tephra associated with explosive silicic volcanism generally occurs on the timescale of 1–100 years, correlated horizons can be considered ~1,000 times more precise than age control provided by two independently dated samples of identical age. Considering correlated horizons closely constrained by absolute age estimates as the ultimate goal, several intervals of the reported chronological framework can be identified for further investigation.

The latest Miocene sequence has a detailed stratigraphy and inter-basin correlations, but relatively imprecise absolute ages. Additional $^{40}Ar/^{39}Ar$ or U-Pb ages would be valuable in determining the stratigraphic level of the Miocene-Pliocene boundary. This would reduce somewhat the ~2 Ma undated early Pliocene interval for which no inter-basin correlations exist; however, establishing new ages in the >300 m of strata at PCQ which are younger than 3.6 Ma is more critical. Extrapolation of ages to the top of the

section is undesireable, therefore, ash beds above the 2198 level, as well as those in younger disconformable gravel deposits should be regarded as higher priority for dating.

Regional lithostratigraphic framework

Application of the tephrostratigraphy developed herein presents opportunities for comparing strata in widely separated and previously uncorrelated localities (Figure 3.7). Combining age control with stratigraphic observations of depositional environment elucidates spatial variation and permits reconstruction of depositional systems. The period of time studied (~5.6–3.0 Ma) includes the latest Miocene, all of the early Pliocene, and a good portion of the late Pliocene, even though the upper age bounds are poorly known at present. This Mio-Pliocene sedimentary system is very different than its precursor and thought to result from segmentation of a regionally continuous foreland basin (26–32°S) at ~6 Ma (Carrapa *et al*., 2008).

On the western margin of the Fiambalá basin, the Guanchin Formation (~5.5–4.3 Ma) is composed of mudstones, siltstones, and sandstones interbedded with conglomerates which coarsen and thicken upwards. Along the Río Guanchin, it is overlain by coarse grained conglomerates that are clast-supported and poorly sorted. These conglomerates have both transitional and unconformable relationships with the underlying Guanchin Formation (Carrapa *et al*., 2008). The exact nature of this stratigraphic relationship is not documented along the Río Guanchin. Deposition of conglomerates in the vicinity continued until at least 3.7 Ma, however the stratigraphic record may be discontinuous.

The lower half of the Fiambalá section, ~15 km to the east, is coeval with of the Río Guanchin section. Extrapolation through two dated ash beds (4.0 Ma) and Toba Corral

Figure 3.7: Integrated tephrostratigraphy and lithostratigraphy of latest Miocene and Pliocene deposits in the Corral Quemado and Fiambalá basins. Ages estimates (all 2σ) in the framework are derived from the following; **a** – Carrapa *et al*. (2008), 3.7 Ma age is the weighted mean of three ages and 5.23 Ma is the youngest single zircon in the sample, **b** – McPherson (2008), ash said to be ~100 m above the base of the Punaschotter Formation, **c**- Latorre *et al*. (1997), **d** – weighted mean of two $^{40}Ar/^{39}Ar$ plagioclase ages from this study (see Appendix A), **e** – interpolation between 5.64 Ma and 3.66 Ma, using stratigraphic heights of Latorre *et al*. (1997).

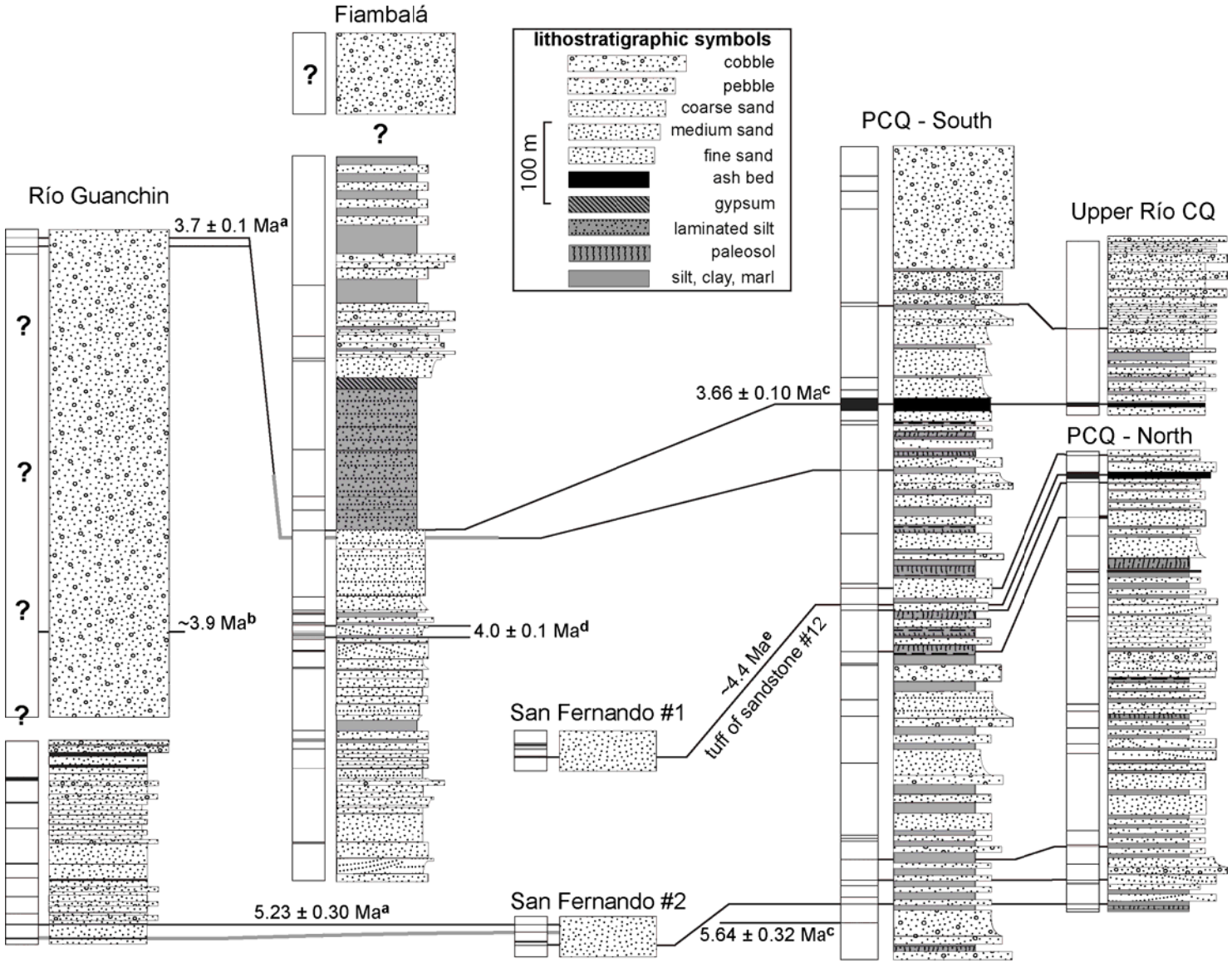
Fiambalá
Río Guanchin
PCQ - South
Upper Río CQ
PCQ - North
lithostratigraphic symbols
cobble
pebble
coarse sand
medium sand
fine sand
ash bed
gypsum
laminated silt
paleosol
silt, clay, marl
100 m
3.7 ± 0.1 Ma[a]
~3.9 Ma[b]
3.66 ± 0.10 Ma[c]
4.0 ± 0.1 Ma[d]
~4.4 Ma[e]
tuff of sandstone #12
San Fernando #1
San Fernando #2
5.23 ± 0.30 Ma[a]
5.64 ± 0.32 Ma[c]

Quemado (3.66 Ma) predict an age of 4.8 Ma for the base of the section and 2.2 Ma for the top of the section. The upper Fiambalá section is younger than Río Guanchin strata and lacks coarse gravel deposits except for a 30 m interval. This coarse grained interval, estimated to be ~3.0 Ma, is directly underlain by evaporite deposits in mudstone and a 200 m thick interval of laminated siltstones. Above the gravel deposits at Fiambalá are interbedded tuffaceous sandstones and siltstone interbeds which become thicker and more common upsection. These uppermost siltstones are characteristically orange relative to other deposits in the section and continue upsection to very coarse grained and poorly sorted gravel deposits. It is unknown whether this contact with the upper gravel deposits is structural or stratigraphic in nature.

At Puerta de Corral Quemado a transition from eolian strata to coarse sandstone and occasional conglomerate is recorded in the interval immediately below the 1440 m level (5.64 Ma). From ~1440 m, strata of the Andalhuala Formation continue upwards as medium and coarse grained sandstones with occasional gravel or cobble conglomerates which define the base of fining upwards fluvial cycles, characteristic of a braided fluvial system (Muruaga, 2001). The finer grained intervals of these cycles consist of overbank sandstones and occasional eolian sandstones with paleosol horizons commonly preserved at the top of the fining upward sequence. Nearly 1 km of such Andalhuala Formation deposits exist before grading conformably into cobble and boulder sized conglomerates which are clast supported and moderately to poorly sorted.

Two chronostratigraphic intervals can be correlated between the Corral Quemado and Fiambalá basins. The late Miocene sequence of volcanic ash beds yields a robust correlation from the Río Guanchin section to San Fernando section #2. This correlation

is supported by major and trace element data for volcanic glass and by isotopic dating of the correlated ash bed (~5.2 Ma). Directly underlying this ash bed, a tentative correlation between Río Guanchin and San Fernando is also proposed. These correlations establish a stratigraphic relationship with the principal PCQ section via an ash bed at San Fernando.

The second chronostratigraphic interval that yields interbasin correlations is the Toba Corral Quemado sequence. Within this sequence, two correlated inter-basin horizons exist. Samples near the top of the thick gravel section at Río Guanchin have been dated to 3.7 ± 0.1 Ma by Carrapa *et al*. (2008); two of the ash beds have glass chemistry indistinguishable by EPMA and ICP-MS and are correlated to the 1998 m level at Puerta de Corral Quemado. This correlation is further supported by its stratigraphic relationship with Toba Corral Quemado (3.66 Ma). Toba Corral Quemado overlies these ash beds by ~75 m at PCQ, but is not observed at Río Guanchin. However, Toba Corral Quemado is observed in the Fiambalá section 80 m above the 4.0 Ma sequence. This second inter-basin correlation provides important constraints on the temporal relationships between the Río Guanchin and Fiambalá sections.

The temporal interval from ~5.2–3.8 Ma is extensively studied, but inter-basin correlations are yet to be discovered. The 4.0 Ma sequence of ash beds at Fiambalá probably represents a short temporal interval. Multiple $^{40}Ar/^{39}Ar$ dates from this sequence indicate high rates of sediment accumulation, and help bracket the age of ash beds between 4.0–3.7 Ma. This sequence of ash beds is believed to lie above the tuff of sandstone #12 sequence at Puerta de Corral Quemado on the basis of age estimates derived from interpolation. The interpolated age for the tuff of sandstone #12 (~4.4 Ma) is the only evidence supporting the hypothesized stratigraphic relationship. The strong

geochemical similarity observed between the tuff of sandstone #12 and the uppermost ash bed of the 4.0 Ma sequence (FIA 846) may implicate a closer temporal affinity. Direct age determinations for additional ash beds will be important to resolving this question. Ultimately, inter-basin correlation of these chronostratigraphic intervals will directly document the stratigraphic relationship. Inter-basin correlation seems probable as these ash beds are known to be widespread within their individual basins. The 4.0 Ma sequence extends more 60 km from north to south in the Fiambalá basin (McPherson, 2008), and the sandstone #12 sequence is observed for ~25 km from north to south in the Corral Quemado basin.

Sediment accumulation rates are similar across both basins. A range of 300–600 m/Ma encompasses the rates estimated between most of the dated intervals. This is consistent with long term average rates for the late Miocene and Pliocene elsewhere in the Central Andes (Bywater-Reyes *et al*., 2010). One notable departure from this sediment accumulation rate is observed. The coarse gravel deposits along the Rio Guanchin are calculated to have accumulated at a rate of ~2,500 m/Ma.

This estimate is based upon the following three pieces of information: 1) an ash bed dated at 3.9 ± 0.12 Ma is "approximately 100 m above the contact with the Guanchin Formation" (McPherson, 2008), 2) three ashes at the top of these gravel deposits yielded a weighted mean age of 3.7 ± 0.1 Ma (Carrapa *et al*., 2008), and 3) "The thickness of this unit is ~600 m" (Carrapa *et al*., 2008). Accounting for potential errors in thickness and age, it is possible to reduce this value to 1,200 m/Ma in the most extreme case. It should also be considered that the finer-grained, and more deeply buried, strata may have undergone significantly more compaction; however, this would decrease calculated

sediment accumulation rates by 10–20% (Allen and Allen, 2005). It thus seems that in the Fiambalá basin at least rates of conglomerate deposition were anomalously high.

Deposition of conglomeratic units

Widespread conglomerate units at the plateau margin have long drawn the interest of geologists. Penck (1920) is commonly cited as first describing these boulder conglomerates in the Fiambalá basin, where he named them "Punaschotter" – Puna gravel(s). Punaschotter was adopted by Allmendinger (1986) as a unit name and extended ~120 km northward along the plateau margin. His description can be summarized as a boulder conglomerate comprised of rounded granitic clasts and minor metasedimentary clasts, locally interbedded with medium to coarse sandstone. These characteristics are attributed to the unit throughout its extent and are considered to encompass both the Corral Quemado and Fiambalá localities documented in this study.

In the Corral Quemado basin, Allmendinger estimated that the Punashotter may be as old as 2.35 Ma based upon the work of Butler *et al*. (1984). Extrapolation through the upper two $^{40}Ar/^{39}Ar$ dated ash beds from Latorre *et al*. (1997) yields an age of ~2.7 Ma for the onset of Punaschotter deposition at Corral Quemado. Much of the discrepancy between these estimates is due to differences in the assumed stratigraphic relationship between Toba Corral Quemado (3.66 Ma) and the Punaschotter. Allmendinger (1986) stated that there is ~660 m of conformable section above the highest dated tuff; yet this study has been able to document no more than ~300 m.

The uppermost PCQ strata and overlying disconformable Punaschotter contain ash beds with material appropriate for $^{40}Ar/^{39}Ar$ or U-Pb geochronology; yet this goal remains unrealized. Such data will provide direct constraints on the initiation of

Punaschotter deposition in the Corral Quemado basin. Nonetheless, correlation between the two localities containing Toba Corral Quemado and overlying coarse grained strata advances understanding of the Punaschotter locally. Importantly, Punaschotter are observed to be conformable with underlying Pliocene sediments at PCQ.

In the upper Río Corral Quemado drainage, Toba Corral Quemado overlies a medium grained sandstone in a gently deformed syncline. Overlying strata are interbedded mudstones, fine to medium grained sandstones, and pebble to granule conglomerates capped by a 1–2 m veneer of basaltic boulders. The basaltic boulders are coated with carbonate rinds and in places they coalesce into a well developed pedogenic carbonate horizon. The boulder deposit capping the section is interpreted as a long-lived geomorphic surface which has an unconformable relationship with the underlying strata. Evidence for Punaschotter deposits in the upper Río Corral Quemado is currently lacking; instead, the Punaschotter are confined to the plateau-margin range front due west of the upper PCQ section. This documents strong spatial variation in Punaschotter deposition along strike. All evidence of Punschotter deposition in the Corral Quemado basin significantly postdates Toba Corral Quemado (3.66 Ma) and is assumed to be late Pliocene and Quaternary.

In the Fiambalá basin, Toba Corral Quemado (TCQ) also provides important constraints on deposition of the Punaschotter. The TCQ sequence of volcanic ash beds establishes proximal-distal relationships in Punaschotter deposition within the basin. The ash beds at the base of the TCQ sequence are defined, and isotopically dated, at the Río Guanchin section where they overlie ~600 m of Punaschotter. Conservative estimates suggest that this entire thickness of gravel was deposited during the early Pliocene. This

documents a diachronous onset of deposition for the Punaschotter between the Fiambalá and Corral Quemado basins.

Identification of Toba Corral Quemado in the Fiambalá section clearly identifies strongly diachronous deposition within the Fiambalá basin. Based upon lithostratigraphic relationships, the Fiambalá section is proposed to be a distal equivalent of the Río Guanchin section. Detailed work is required to establish the nature of this relationship, but fluvial, floodplain, and alluvial plain depositional environments in the distal basin can be clearly identified as coeval with Punaschotter deposition on the western margin of the basin. A brief interval of conglomerate deposition is recorded at ~3.0 Ma in the distal portion of the basin, but this rapidly returns to deposition of fine-grained material. This brief interval of cobble conglomerates is bedded and well-sorted, characteristics which set it apart from classic "Punaschotter" conglomerates. It is suggested that the conglomerates may represent the distal reaches of a Punaschotter alluvial fan, and that lenses of similarly thin conglomeratic intervals might be found at different stratigraphic levels along strike.

In summary, tephrostratigraphic constraints on spatio-temporal deposition of the Punaschotter document strong diachroneity. Deposition in the Fiambalá basin precedes that in the Corral Quemado basin by a minimum of 0.6 Ma, and possibly as much as 1.6 Ma. Some of the uncertainty in this estimate could be eliminated by additional numerical age determinations on volcanic ash beds; however, much of the uncertainty is a result of the diachronous nature of conglomerate deposition within individual basins. Estimates are minimum ages because initiation of deposition is time-transgressive, initiating at a source and prograding basinward. Likewise, initiation of deposition could propagate

along strike as uplift migrates along a fault zone. The specific source of the Punaschotter is inferred to be uplift of resistant bedrock along basin margins.

Specifically, it is suggested that deposition of the conglomerates, referred to in a regional context as Punaschotter, is directly related to exposure of Paleozoic crystalline and metasedimentary rocks along active faults. This implicates two factors in the formation of the Punaschotter: 1) relief generation resulting from uplift along a fault zone, and 2) exposure of erosion resistant bedrock lithologies along active fault zones. As uplift commenced at the margin of basins, overlying sedimentary cover and less resistant sedimentary rocks would have been stripped without generating coarse clastic debris (e.g., Carroll *et al*., 2006). When more resistant bedrock types became exposed, deposition of Punaschotter would have initiated. Arid climates, in particular, should be particularly sensitive to development of coarse grained deposits during episodes of high uplift rates (Sobel *et al*., 2003). The geometry of the resulting conglomeratic deposit should be influenced by structural style, uplift rate, rock strength and resistance to weathering, as well as geomorphic and climatic controls on weathering and transport.

Structural and stratigraphic relationships in the Corral Quemado basin

Two parallel sections at PCQ expose more than 2.5 km of late Miocene and early Pliocene strata along the northwest dipping flank of a plunging anticline (Figure 3.8). On the north side of Río Corral Quemado, Butler *et al*. (1984) measured a magnetostratigraphic section. The upper 1,200 m of this section has been sampled extensively, and volcanic ash beds from the late Miocene sequence as well as those from the sandstone #12 interval can be correlated to south of the river. This section is truncated by Rio Corral Quemado before it reaches the stratigraphic level of Toba Corral

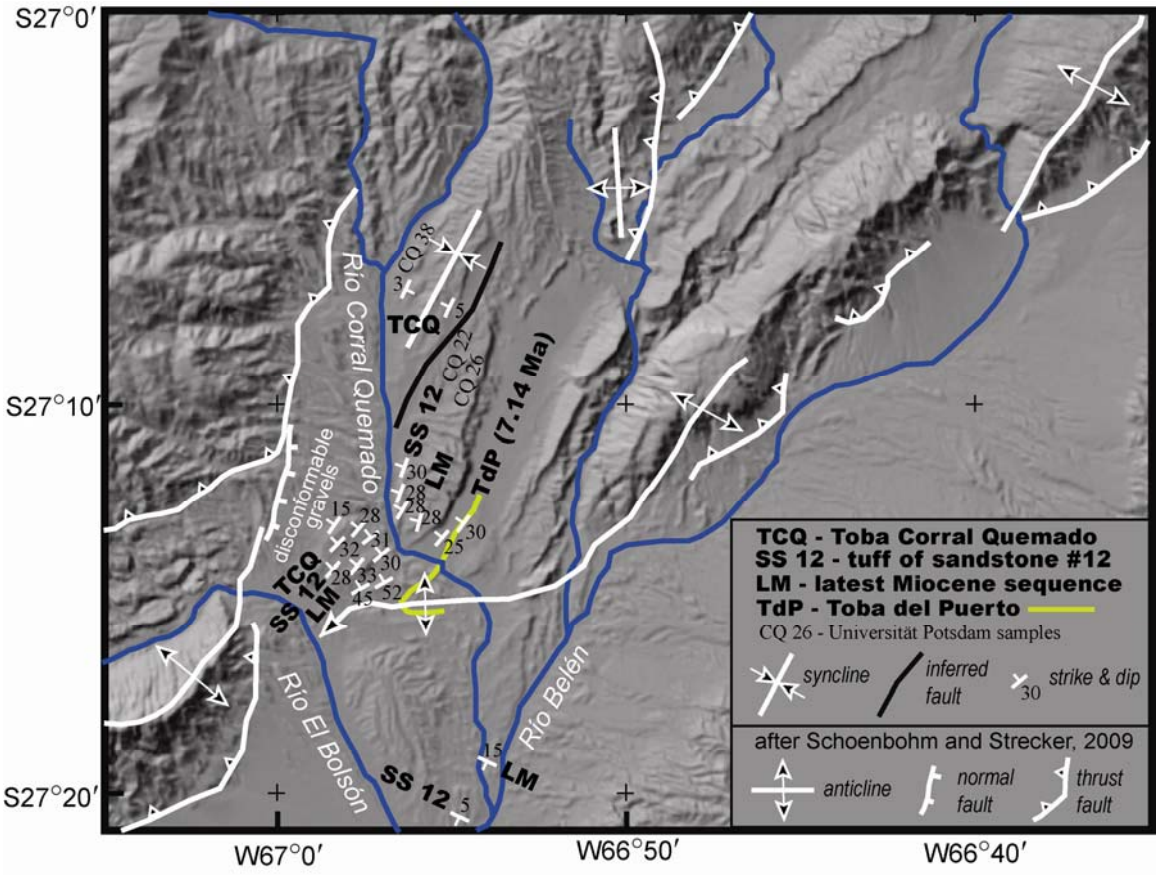

Figure 3.8: Structral and stratigraphic map of the Corral Quemado basin.

Quemado. However, Toba Corral Quemado is identified on this side of the river ~10 km to the north in a gently warped syncline. A thick tuff, Toba del Puerto, crops out ~1 km below the late Miocene sequence of ash beds and is an important marker bed locally (Muruaga, 2001). Toba del Puerto can be traced across the river where it has been dated at 7.14 ± 0.04 (Latorre *et al*., 1997).

On the south side of Río Corral Quemado, Toba del Puerto is tightly folded in the hinge of a plunging anticline (Figure 3.8). Toba del Puerto is an important stratigraphic and structural datum, but the interval between it and the late Miocene sequence of ash beds remains poorly understood. This ~1 km thick stratigraphic interval contains abundant eolian sandstone and is poorly fossiliferous compared to the strata above and

below it. Volcanic ash beds have been sampled from this interval, but a coherent tephrostratigraphy has not yet been achieved in these eolian strata.

The upper section on the north side of Río Corral Quemado contains laterally extensive exposures of the late Miocene, sandstone #12, and Toba Corral Quemado volcanic ash sequences. In contrast to the lower part of the section, strata in these intervals have remarkably constant attitude (Strike = N50E ± 10°; Dip = NW30 ± 3°). The highest ash bed in the TCQ sequence (2340 m level) is still dipping at ~30°. Upsection and toward the range front from this sample, volcanic ash beds in gravel dip progressively more shallowly. Neither stratigraphic height nor age estimates presently exist for these ash beds, but these strata are interpreted to record proximal sedimentation during uplift of the range to the west, and later, concurrent growth of the anticline to the east. Disconformable surfaces have not been identified within these gravel deposits, but interbedded ash layers provide evidence that they may exist. Based upon these observations it is suggested that surface deformation associated with growth of the anticline did not begin until well after 3.6 Ma. This is constrained only by the youngest ash bed in the section with an absolute age. Dating of ash beds from the upper TCQ sequence and from the disconformable gravels will provide significantly improved constraints on the timing of this deformation.

Correlation with ash beds at two additional localities in the Corral Quemado basin do not provide further information on timing, but they do constrain the geometry of deformation. The primary structural feature exposing Miocene-Pliocene strata at PCQ is the south-vergent plunging anticline, presumed to be active after 3.6 Ma, and possibly much later. Exposures of ash beds at San Fernando, ~12 km SSE of the main section dip

shallowly to the SW. A late Miocene ash bed dated at 5.23 Ma dips 15°; whereas the tuff of sandstone #12 (4.4 Ma) dips ~5°.

In summary, the range front gravels at the top of the PCQ section provide a minimum age estimate for the uplift of the range to the west. The gravels (Punaschotter) are conformable with the underlying Pliocene strata, and were deposited at least 5 km distal from their inferred source. These gravels were subsequently tilted to the northwest, and deformation continued during deposition of younger gravel deposits. This deformation is associated with the growth of the anticlinal structure to the east. The relationship between the growing anticline and the range front fault system is unknown. One possibility is that the fault inferred to separate Toba Corral Quemado from older strata on the north side of Rio Corral Quemado continues across the river to the top of the PCQ section. Together, these observations support a strong pulse of Pliocene deformation beginning at the range front and later involving anticlinal growth to the east.

Structural and stratigraphic relationships in the Fiambalá basin

Two stratigraphic sections in the Fiambalá basin document dramatically different depositional environments. A simple model of the early Pliocene depositional system is proposed, based on observations summarized in Figure 3.6 and discussed briefly here. The section measured along Río Guanchin is suggested to represent the proximal to medial portions of a sedimentary system originating on the western margin of the basin. The Fiambalá section, 15 km to the east, is assumed to be the distal portion of this sedimentary system (Figure 3.9). Bedrock exposures immediately to the west are suggested to be an important sediment source for strata at both sections. The distal

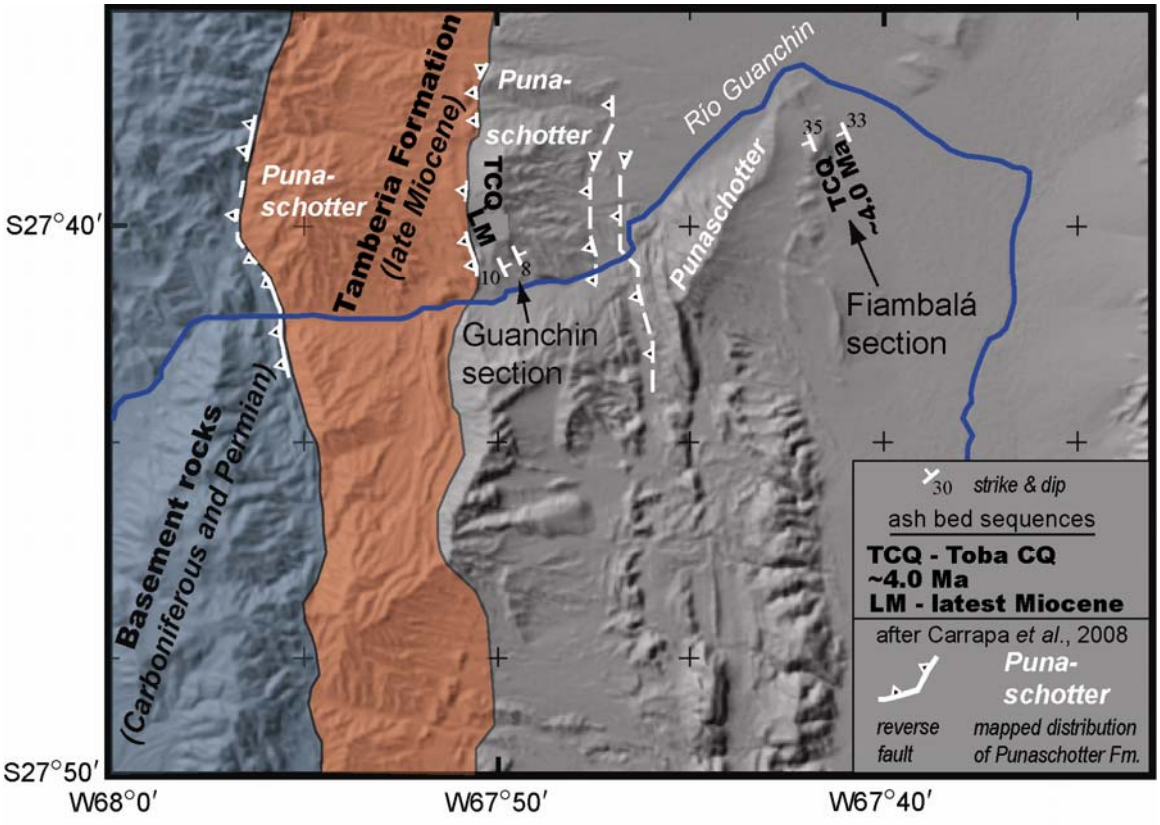

Figure 3.9: Structural and stratigraphic map of Fiambalá basin, geologic units and faults from Carrapa *et al*. (2008), with mapped anticlinal and synclinal structures excluded.

(Fiambalá) strata probably also received sediment input from an axial fluvial system originating in the north and draining towards the south (Carrapa *et al*., 2008).

At Fiambalá, the base of the section (4.8–4.3 Ma) is characterized by blue-gray cross-bedded sandstones interbedded with pale brown sandstones. The blue-gray sandstones become less abundant upsection. The interval between 4.3–3.7 Ma contains carbonate bearing paleosol horizons, fossil wood, and numerous volcanic ash beds. Above this, Toba Corral Quemado (3.66 Ma) is interstratified in the base of laminated siltstones ~200 m thick. The top of the laminated siltstones is capped by bedded gypsum and claystone. These intervals comprise the lower Fiambalá section and document a general fining upwards trend. In the absence of robust paleocurrent estimates this trend is

interpreted as displacement of an axial fluvial system flowing N-S by a margin alluvial fan system growing on the western margin of the basin.

This fining upwards sequence is truncated abruptly at the 640 m level (3.0 Ma) by the first true gravels in the section. The gravels are interbedded with coarse gray, occasionally tuffaceous, sandstones for ~120 m. Above this level (760 m), the grey sandstones become finer and are interbedded with pink siltstones and red claystones. Exposure is poor at the top of the section, but eventually the pink siltstones and gray sandstones come into contact with very coarse conglomerates of unknown age. The nature of this contact is also unknown, but no evidence exists to suggest that the contact is structural. If this contact is stratigraphic, conformable or otherwise, it represents the youngest and most basinward deposition of the Punashotter.

Clast counts from the Punaschotter support the general depositional model proposed (Carrapa *et al*., 2008). Based on this depositional model and the stratigraphic observations from Fiambalá, several additional hypotheses can be put forward. Firstly, the gray and pale brown sands at the base of the Fiambalá section might represent at least two individual source lithologies, one derived from the west and the other representing an axial fluvial system. Secondly, the pink silts and red clays which become increasingly abundant above the Fiambalá gravel interval (~3.1 Ma) may represent the growing importance of the Miocene Tamberia Formation as a source for sediment in the late Pliocene. Deformation of Tamberia Formation strata to the west is a probable cause of this change. The petrology of the sand, silt, and clay portions of these strata would provide a valuable comparison to that of the Punaschotter and be an appropriate test of the hypothesized relationships.

Strata of the Fiambalá section dip westward at 30–35°, and there do not appear to be any significant changes in dip within the section. The age at the top of the section is poorly constrained, but extrapolation through the three horizons of known age suggests that the top of the section may be younger than 2.5 Ma. In the absence of obvious upsection decreases in dip, it is suggested that the investigated strata were deformed after ~2.5 Ma. This is the youngest phase of deformation recorded by Miocene-Pliocene strata. Deformation to the west began at least 5.5 Ma and continued to at least 3.7 Ma immediately to the west of the Río Guanchin section (Carrapa *et al*., 2008). Back tilting of the Fiambalá strata is younger, and further documents eastward progressing deformation throughout the Pliocene.

Timing, style, and locus of plateau-margin deformation

Several unifying characteristics can be ascribed to plateau-margin deformation as observed in the Fiambalá and Corral Quemado basins. Onset of Punaschotter deposition can be considered Pliocene in the regional sense, but the record is shown to be diachronous both within and between basins. Gravels document relief generation, which should lag deformation and exhumation. This coupled with along strike and proximal-distal differences in the timing of gravel deposition, ensures that deposition of the Punaschotter Formation yields only minimum age estimates for initiation of deformation at the margin. In the Fiambalá basin, Punaschotter deposition spans at least 4–3 Ma. At Corral Quemado it can only be said to be significantly younger than 3.6 Ma, perhaps 3–2.5 Ma.

Structural deformation of Miocene-Pliocene strata provides another constraint on plateau margin deformation. At both Corral Quemado and Fiambalá, deformation toward

the center of the basin significantly post-dates the initiation of uplift at the basin margin. Within an individual basin, deformation appears to migrate eastward with time. In the Fiambalá basin, this began to the west of the basin margin by at least 5.5 Ma (Carrapa *et al*., 2008). No such age control exists for basin margin deformation at Corral Quemado.

As a first approximation, it can be stated that plateau margin deformation probably began 6–5 Ma in the region (cf. Sobel and Strecker, 2003). This deformation was contractional in nature, and may have continued until 2 Ma or later. The timing of the youngest contractional deformation remains a fundamental problem which will require further integration of geochronology with the Punaschotter and with the geomorphic record of landscape evolution in the region. By 2–1 Ma, a neutral to extensional stress regime existed within the plateau and along its margins (Schoenbohm and Strecker, 2009). Documenting the change from a contractional to extensional stress regime at the plateau margin is an interesting problem, for the time being it can be said that a strong pulse of contractional deformation occurred during the Pliocene and may have lasted no more than 2–3 Ma.

CHAPTER 4

PALEOSOL CARBONATE RECORDS OF CLIMATE AND ENVIRONMENT: REGIONAL SYNTHESIS

Introduction

Having developed a long paleoenvironmental record at Puerta de Corral Quemado (Chapter 2) and some understanding of surface deformation along the southeastern margin of the Puna plateau (Chapter 3), this chapter addresses Miocene-Pliocene climate and environment in a regional context. Stable isotope proxy records are compared across 2° of latitude at the plateau margin. Four sedimentary basins are discussed (from south to north): Fiambalá, Corral Quemado, Vallé Santa Maria, and Angastaco (Figure 4.1). New pedogenic carbonate stable isotope data and additional chronological control are established for the three southernmost localities, and compared with recently published data from Angastaco. Three periods of marked ^{13}C enrichment beginning at ~5.6, 4.3, and 3.6 Ma are noted, as is a long-term enrichment in ^{18}O between 7and 4 Ma.

The fundamental question is whether these isotopic enrichments actually record regional ecologic (climatic?) events. Paleosol carbonate $\delta^{18}O$ data are affected by numerous confounding variables, including temperature, precipitation source, precipitation season, precipitation amount, and soil water evaporation. Disentangling

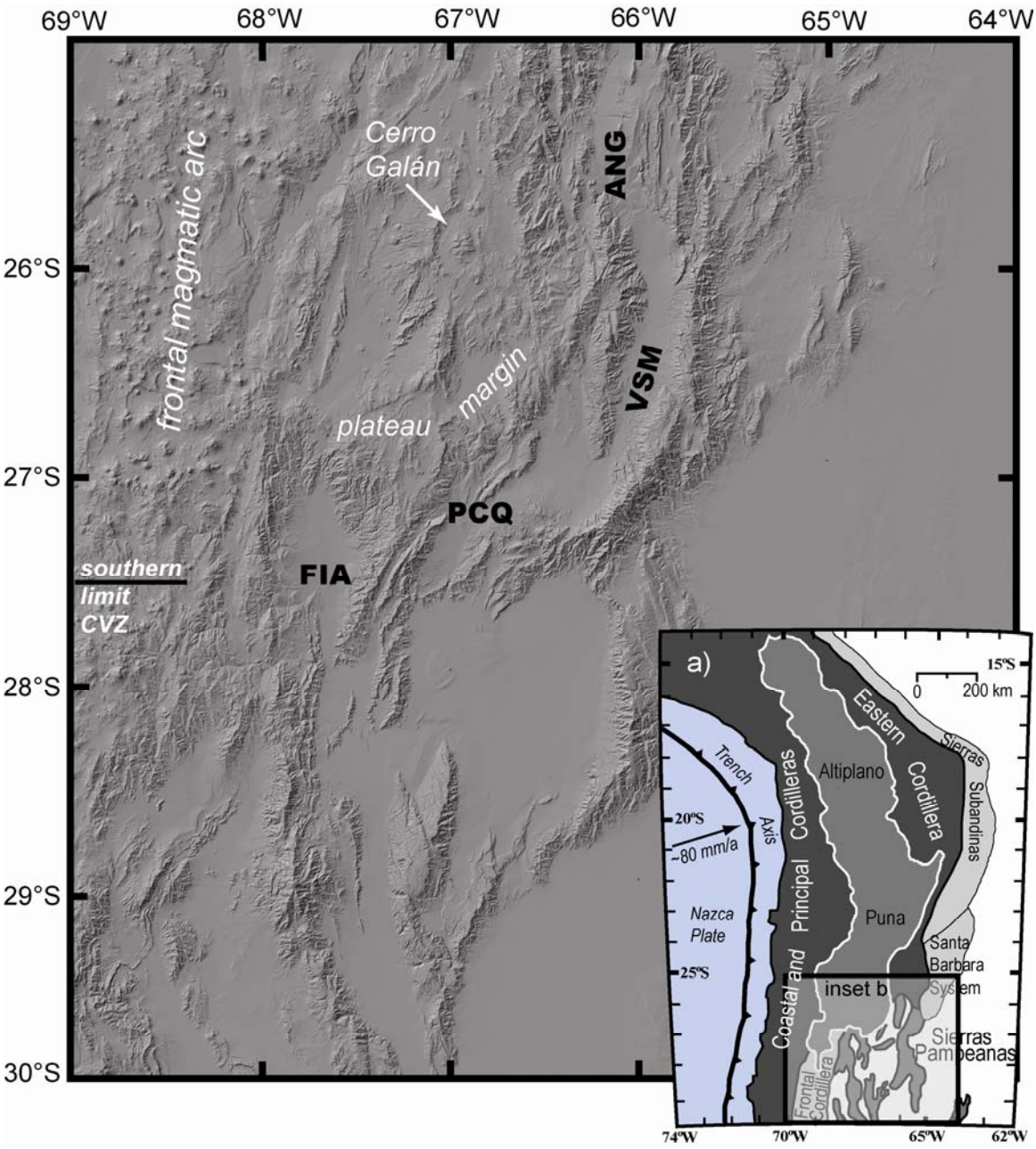

Figure 4.1: Location map for Miocene-Pliocene stable isotope proxy records in the southern Central Andes; **a)** major morphotectonic provinces (after Jordan *et al*., 1983), **b)** shaded relief map on the southern Puna plateau and surrounding regions (using Shuttle Radar Topograpy Mission 3 arc second data), the termination of the Central Volcanic Zone (CVZ) and beginning of the Sierras Pampeanas magmatic gap is approximately coincident with the southern margin of the plateau. FIA denotes the Fiambalá basin, PCQ the Puerta de Corral Quemado basin, VSM, the Vallé Santa Maria basin, and ANG, the Angastaco basin.

these factors is not generally tractable. Paleosol carbonate $\delta^{13}C$ values are more easily interpreted, but in a landscape that contains a mixture of C_3 and C_4 plants major climatic and ecologic events are not necessary to generate rapid shifts in paleosol carbonate $\delta^{13}C$. Thus an alternate hypothesis is that many $\delta^{13}C$ enrichments in the region merely result from the vagaries of the geologic record.

It has been demonstrated that the latest Miocene and Pliocene landscape contained a mixture of C_3 and C_4 plants, and paleosol carbonate proxies may record spatial distribution of plant types. It thus follows that a stratigraphic change in paleosol carbonate $\delta^{13}C$ may result from either temporally or spatially related changes at that location. If closely spaced and coeval stratigraphic sections record different depositional environments, it may suggest that plant distribution varied similarly. Stratigraphic changes in depositional environment can indicate a shifting landscape and isotopic variation coincident with changes in depositional environment cannot *a priori* be interpreted to reflect extra-local forcing. This is particularly true in low latitude settings where the ancient environment was relatively arid. In such settings, C_3 plants may dominate the riparian ecosystem, and in turn the geologic record if the deposits of interest are fluvial or alluvial in nature (cf. Behrensmeyer *et al*., 2007; Levin *et al*., 2004, *in review*). Rapid landscape shifts in plant communities may be caused by relatively common geomorphic phenomena; e.g., avulsion of the active channel in alluvial fans depositional systems or avulsion of fluvial channels in tributary systems. A less rapid, but equally probable process for shifts in vegetative communities is progradation of coarse alluvial deposits associated with basin margin uplift (cf. Chapter 3).

The difficulty, then, in constructing a regionally relevant record of climate and ecology from paleosol carbonate $\delta^{13}C$, is demonstrating that the isotopic signal is indeed regional. Demonstrating regional patterns of paleosol carbonate $\delta^{18}O$ can be less difficult, but the ultimate causes of trends or shifts are elusive.

To make a rigorous comparison of stable isotope proxy data across distances of 100 km, chronological control is essential. Numerical age estimates and inter-basin correlations of volcanic ash beds provide a basic framework for the Fiambalá basin (Chapter 3), and a new framework for Vallé Santa Maria is developed in this chapter.

Material sampled and methods employed

Volcanic ash beds were sampled extensively at seven sections within and adjacent to Vallé Santa Maria. Those data are discussed briefly in this chapter as they apply to new and existing stable isotope data from pedogenic carbonate. Volcanic glass was analyzed by electron probe microanalysis (EPMA) and inductively coupled plasma–mass spectrometry (ICP-MS) methods, as described in Chapter 3. Four $^{40}Ar/^{39}Ar$ ages from Vallé Santa Maria are drawn upon; complete data is given in Appendix A.

Pedogenic carbonate was sampled in three geologic settings: 1) nodular and disseminated carbonate from paleosol horizons, 2) carbonate crusts and disseminated carbonate from boulder and gravel terraces high above modern river level, and 3) disseminated and nodular carbonate in modern soils. Stable isotope analysis of carbonate was carried out in a common acid bath autosampler coupled to an Isotope Ratio Mass Spectrometer (IRMS) in continuous flow mode. Details of the methodology, including an assessment of accuracy and precision are available in Chapter 2. In general, the external reproducibility for $\delta^{13}C$ is on the order of 0.1‰ and $\delta^{18}O$ is ~0.2‰.

Fiambalá basin

Paleosol horizons are described from Fiambalá ~ 100 m below the 4.0 Ma sequence of volcanic ash beds. Paleosol carbonate nodules were sampled from a closely spaced series of paleosols between the 170 and 190 m levels (Figure 4.2). Parent material is very pale reddish brown silty clayey sandstone interbedded with tuffs, sandstones, and fossil wood. The matrix of the paleosols is leached of $CaCO_3$. Pedogenic nodules sampled were 5–10 mm in diameter and range from 40–75% carbonate. The thickness of paleosol horizons is ~2 m and all nodules were taken from near the top of the carbonate bearing horizons, or ~40–70 cm below the top of the paleosol. A fourth paleosol, at ~220 m level, also contained authigenic carbonate. This soil horizon contains flat, platy chips of carbonate throughout its thickness and is considered a poorly developed soil. Carbonate was not sampled from this horizon.

The stable isotope data obtained from paleosol carbonate documents a ~4‰ shift in $\delta^{13}C$ values through 15 m of strata (Figure 4.2; data available in Appendix A). This dramatic shift towards ^{13}C enriched values is interpreted to document an increase in the proportion of C_4 plants. Once it became evident that such a shift might exist, a second—more detailed—sampling was undertaken. Paleosol carbonate nodules were cut in half and one half was subsampled using a hand held drill. If the nodule was devoid of sparry calcite veins the other half was amalgated with other nodules from the horizon and the <125 μm fraction was analyzed in replicate. The stable isotope data from this amalgamated powder correspond well to the median values derived from samples and subsamples of individual nodules. In each case the bulk powder represents four to five nodules, whereas the median is based upon data from seven nodules. The percent

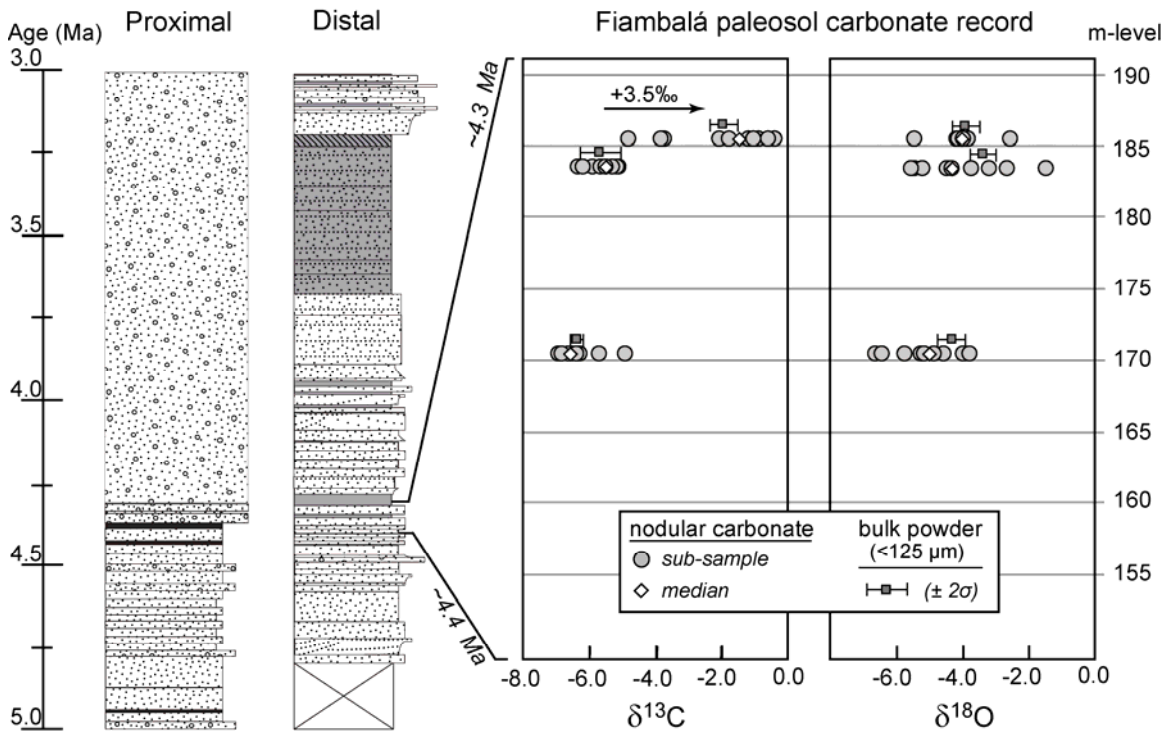

Figure 4.2: Stable isotope data for pedogenic carbonate in the lower Fiambalá section. Age constraints for the Guanchin (Proximal) section are taken from Carrapa *et al*. (2008) and McPherson (2008). Age constraints for the Fiambalá (Distal) section are from Chapter 3 of this dissertation. Full isotopic data are given in Appendix B.

carbonate is notably higher for the bulk powder, likely due to the exclusion of matrix (predominantly quartz/feldspar) from the <125 µm fraction.

These data record a $\delta^{13}C$ enrichment of 0.8‰ between the 171 and 184 m levels, and a further enrichment of >3.5‰ between 184 and 186 m. No evidence is found for a $\delta^{18}O$ shift across this interval. Several mechanisms can be invoked to explain the rapid (~40 ka) $\delta^{13}C$ shift in paleosol carbonate. Ecological expansion of plants using C_4 photosynthesis is possible, though the most comprehensive isotopic records from the region do not document any event synchronous with the Fiambalá shift (4.4–4.3 Ma). Local or regional climatic forcing might reasonably cause an increase in C_4 vegetation.

One such possibility is aridification, but evidence of climatic change is not provided by $\delta^{18}O$ data. A decrease in soil respiration rates might also cause a rapid positive shift in $\delta^{13}C$, but this effect should be most pronounced at shallow depths and increased soil water evaporation (and ^{18}O enrichment) should be attendant on such changes.

Alternatively, a rapid $\delta^{13}C$ shift without a corresponding shift in $\delta^{18}O$ values can be explained by a shift in landscape position across a mixed C_3/C_4 ecosystem. In the Fiambalá basin a landscape-scale shift might reasonably be controlled by depositional systems. In particular, displacement of an axial fluvial system and associated riparian vegetation by marginal alluvial fan ecosystems and more open vegetative environments might explain the $\delta^{13}C$ shift in paleosol carbonate (cf. Chapter 3). Similarly, shifting of the active channel in a large alluvial fan could also rapidly shift vegetative communities on the landscape. Thus, the $\delta^{13}C$ data in distal strata (Fiambalá section) is hypothesized to record the onset of coarse gravel deposition (Punaschotter Formation) along the western margin of the basin.

The timing of these two events is approximately coeval. The age of the paleosols is established by linear extrapolation from Toba Corral Quemado (3.66 Ma) downsection through the ~4.0 Ma sequence of ash beds. The age of the base of the Punaschotter Formation along the western margin of the Fiambalá basin is shown to vary locally, but on the basis of U-Pb zircon ages it began at least by 4.2 Ma (McPherson, 2008). Ultimately additional field mapping combined with tephrostratigraphic and isotopic studies will provide the most robust test of the proposed sedimentation driven ^{13}C enrichment at Fiambalá.

Puerta de Corral Quemado

In addition to the detailed paleosol carbonate record of Latorre *et al.* (1997), other isotopic data are contributed here. A fossil bearing paleosol was sampled from the 1462 m level, this was established by correlation of an ash bed immediately overlying the paleosol (PCQ 217; Table 3.1). The sampled paleosol is over 2 m thick, and carbonate nodules were taken from greater than 1 m depth. Isotope data from this paleosol carbonate help to fill a 175 m thick stratigraphic gap in the published record (Latorre *et al*., 1997). Measured $\delta^{13}C$ values (Table 4.1) are slightly enriched relative to the paleosol carbonate in the 200 m above and below this level which average -7.1 ± 0.7‰ (n=14). Similarly, fossil teeth sampled from this paleosol have some of the highest $\delta^{13}C$ values of all fossils at Puerta de Corral Quemado (cf. Figure 2.5e).

Soil carbonates from Quaternary geomorphic features along the Río Corral Quemado also contribute data to a large gap in the existing isotope record (Table 4.1). A carbonate pendant was sampled east of upper Río Corral Quemado ~240 m above the modern river level. This laminated carbonate was sampled from 50 cm below the modern surface, and subsampling through its 2 cm thickness revealed measureable isotopic differences.

A second terrace was sampled at Puerta de Corral Quemado along the southern side of Río Corral Quemado ~60 m above modern river level. This terrace is characterized by a well developed desert pavement and 3 cm thick vesicular A (Av) horizon. Disseminated carbonate in the Av horizon is relatively enriched in ^{13}C and ^{18}O indicating potential influences from detrital marine rocks of Paleozoic age, atmospheric CO_2, and soil water evaporation. A sample of loess from 25 cm depth also contains

disseminated carbonate, and its isotopic composition suggests contribution from soil respired CO_2 and reduced degrees of soil water evaporation (PCQ 1039; Table 4.1). These data are consistent with those reported for a Holocene age soil in the region , where a strong soil water evaporation signal is documented (McFadden *et al*., 1998).

Vallé Santa Maria

Approximately 2 km of continental Neogene strata are exposed along the eastern margin of Vallé Santa Maria. The upper 500–800 m of these strata belong to the Andalhuala Formation, and are equivalent to the upper section at Puerta de Corral Quemado. Kleinert and Strecker (2001) have constructed a paleosol carbonate record in Vallé Santa Maria spanning 12 Ma–present. The geochronological control on these strata and the age model applied to the paleosol carbonate are not explicit, and comparison with Puerta de Corral Quemado is currently not possible at high temporal resolution. However, samples of paleosol carbonate and volcanic ash beds from Vallé Santa Maria have produced the first direct tie with Puerta de Corral Quemado. The results of this work are presented here as a first step toward integration of these two records.

Stable isotope stratigraphy of Vallé Santa Maria

Two paleosol horizons of Kleinert and Strecker (2001) have been identified in the field and the stable isotope composition of their carbonate has been determined. Field and laboratory data both support correlation of these horizons with published data. Kleinert and Strecker (2001) describe two paleosols developed on volcanic ash beds separated by ~50 m stratigraphically. These paleosols, and associated carbonate, were sampled from section #1 at Entre Ríos (Appendix A).

Table 4.1: Stable isotope data for pedogenic carbonates in the Corral Quemado basin.

Sample ID	Material	Age[a] (Ma)	n[b]	$\delta^{13}C$ (PDB)	±1σ	$\delta^{18}O$ (PDB)	±1σ
Puerta de Corral Quemado terrace (lower)							
PCQ 1038	vesicular A, 5 cm depth	0.0–0.5	1	-0.1	-	2.6	-
PCQ 1039	loess, 25 cm depth	0.0–0.5	3	-4.5	0.6	-0.7	0.4
upper Río Corral Quemado terrace							
PCQ 716a-1	pendant; outermost lamination	0–1.0	1	-2.7	-	-2.3	-
PCQ 716a-2	pendant; outer lamination	0–1.0	2	-2.5	0.0	-2.4	0.1
PCQ 716a-3	pendant; outer tan lamination	0–1.0	2	-1.9	0.1	-2.6	0.1
PCQ 716a-4	pendant; inner tan lamination	0–1.0	1	-2.1	-	-2.4	-
PCQ 716a-5	pendant; powdery white coat	0–1.0	1	-2.5	-	-1.9	-
paleosol (1462 m)							
PCQ 219	nodules; 1.0–1.6 m depth	~5.5	3	-6.2	0.3	-5.8	0.1

[a]Age established by linear interpolation between dated ash beds or by estimating conservatively.
[b]n= number of analyses included in average; complete data available in Appendix B.

The most prominent paleosol is developed on a 1–1.5 m thick volcanic ash bed (Figure 4.3a). Sample ENTR 535, taken from the upper portion of this paleosol, contains poorly preserved volcanic glass shards and is devoid of carbonate. Sample ENTR 534, taken from the lower portion of the paleosol, contains nodular and disseminated carbonate in addition to well preserved volcanic glass. Isotopic analysis of disseminated carbonate in ENTR 534 produces values similar to previous measurements, though the $\delta^{18}O$ values reported here are 1.5–2.0‰ more negative (Table 4.2). This (upper) tuffaceous paleosol is exposed 10 m below the thickest and most prominent ash bed in Vallé Santa Maria. This ash bed contains a thin yellow horizon in some exposures. Due to its utility as a stratigraphic marker it has been informally termed, toba rayita amarilla (TRA, herein). Taken together, TRA and the tuffaceous paleosol below it, provide the most prominent stratigraphic interval in Vallé Santa Maria and the most confident correlation with previous work (Figure 4.3b).

The second correlated paleosol horizon is less secure, but probable nonetheless. This tuffaceous paleosol is reported to contain rhizoliths and crops out ~50 m

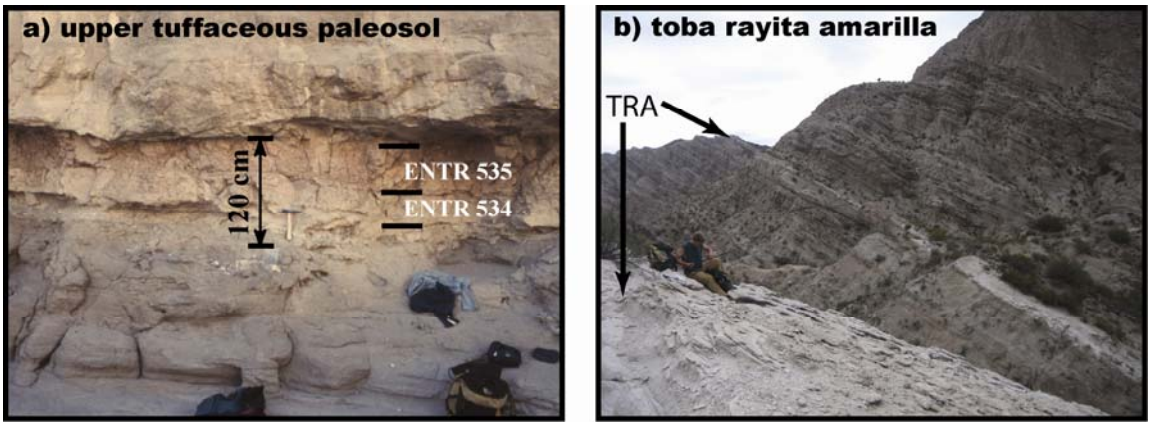

Figure 4.3: Field photographs of the tuffaceous paleosol interval at Entre Rios: **a)** upper tuffaeous paleosol sampled in section ENTR #1, **b)** TRA at the base of section ENTR #2.

downsection from the upper tuffaceous paleosol (Kleinert and Strecker, 2001). A similar occurrence was sampled ~100 m below the upper tuffaceous paleosol; these two estimates of stratigraphic thickness are considered within error given the rough terrain, and the two samples may represent the same paleosol. This incipient paleosol was observed to form on top of a 0.5–1.2 m thick volcanic ash bed. This ash bed, sampled in three localities along strike in Vallé Santa Maria overlies another ash bed by 1–4 m. At Entre Ríos the lower bed contains no carbonate, while the upper bed is bioturbated at the top and contains carbonate. This pedogenically modified ash bed also yields stable isotope data in agreement with previously reported values (Table 4.2).

Table 4.2: Stable isotope data comparative with that of Kleinert and Strecker (2001).

Sample ID	Material	Age[a] (Ma)	n[b]	$\delta^{13}C$ (PDB)	±1σ	$\delta^{18}O$ (PDB)	±1σ
modern-recent surficial carbonate							
Recent[c]	pebble coating	0.00–0.01	2	-5.5	0.1	-2.3	0.1
TUC 908[d]	carbonate nodule	0.00–0.01	3	-7.4	0.4	-2.2	0.2
ENTR 538[d]	disseminated carbonate	0.00–0.005	2	-3.9	0.5	-2.6	0.2
pediment (~0.9 Ma)							
Ped-III[c]	Calcrete	0.9	3	-3.3	1.0	-4.9	0.4
ENTR 527[d]	carbonate pendant; inner tan	0.3–1.2	2	-2.8	0.0	-0.3	0.0
ENTR 527[d]	carbonate pendant; outer white	0.3–1.2	1	-2.0	-	2.8	-
upper tuffaceous paleosol							
ER-19/4A[c]	Calcrete/tephra	5.2	1	-1.2	-	-6.0	-
19/4-N[c]	Nodules/tephra	5.2	3	-3.3	0.3	-6.4	0.1
ENTR 534[d]	disseminated carbonate	5.2	6	-2.8	0.3	-8.0	0.2
lower tuffaceous paleosol							
ER-R[c]	Rhizoliths/tephra	5.2–5.6	7	-1.1	1.0	-6.2	0.4
ENTR 525/533[d]	disseminated carbonate	5.2–5.6	4	-2.9	0.4	-6.7	0.4

[a]Ages established as follows: Recent and TUC 908 (Holocene?); ENTR 538 carbonate in Buey Muerto/Alemania ash (~5 ka, cf. Hermanns and Schellenberger, 2008); ENTR 527 = pediment III of Strecker *et al.* (1989); tuffaceous paleosols shifted younger as discussed in the following sections
[b]n= number of analyses included in average; complete data available in Appendix B.
[c]Data from Kleinert and Strecker (2001).
[d]Data from this dissertation.

This short sequence of tuffaceous paleosols is a unique interval in VSM, where only two paleosols developed on volcanic ash beds are known to exist (Kleinert and Strecker, 2001). Stable isotope data for carbonate in these tuffaceous paleosols document the most $\delta^{13}C$ enriched values in Vallé Santa Maria strata (Figure 4.4). These characteristics provide strong confidence in the proposed correlation of this interval.

Importantly, this correlation allows the stable isotope data reported by Kleinert and Strecker (2001) to be integrated with tephrostratigraphic work in Vallé Santa Maria. This is accomplished by relating the uppermost tuffaceous paleosol with the highest paleosol carbonate $\delta^{13}C$ values in the basin to TRA which is the thickest and most extensive volcanic ash bed in the basin. TRA is positively identified in every section sampled over a distance of 20 km from south to north. This ash bed may be Chiquimil unit XIX, dated at 6.02 Ma by Marshall *et al*. (1979), or it may lie above unit XIX.

Tephrostratigraphy of Vallé Santa Maria

Seven sequences of volcanic ash beds have been sampled in Vallé Santa Maria, four of these are depicted in Figure 4.4. Data from the other sections are reported in Appendix A, but mentioned only briefly here. At Entre Ríos the youngest sequence of ash beds (ENTR section #3) can be tentatively correlated to the top of other sections, but absolute age control is lacking. At El Infiernillo, a short sequence of volcanic ash beds of multi-modal rhyolitic composition (INF section #2) was sampled and $^{40}Ar/^{39}Ar$ data for one of these ash beds yields an age of 9.1 Ma (Appendix A). Kleinert and Strecker (2001) report paleosol carbonate isotopic data from El Infiernillo that are assigned ages between 3.7–3.3 Ma. An unconformity has been proposed to exist at El Infiernillo (Bossi

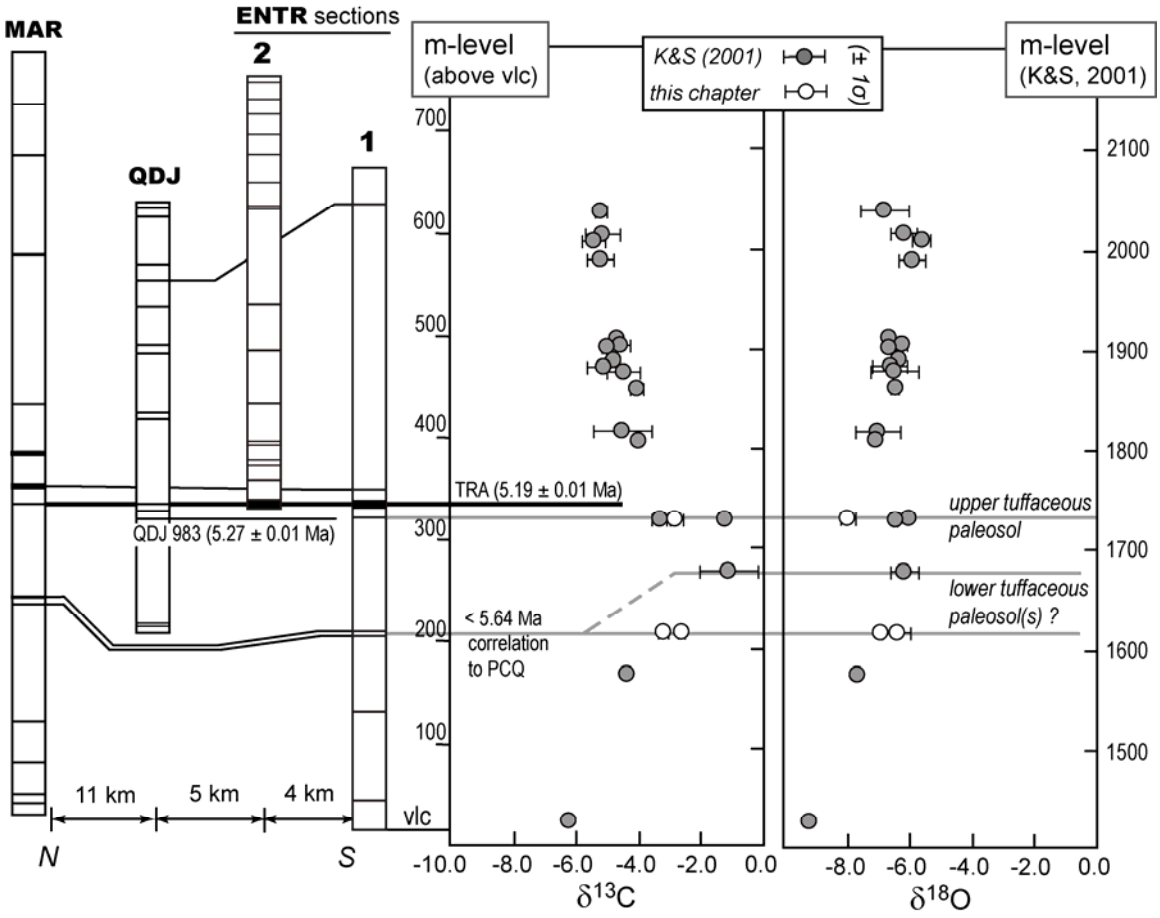

Figure 4.4: Stable isotope stratigraphy from Entre Ríos correlated to the sampled tephrostratigraphy at section ENTR #1, as measured relative to a volcanic lithic conglomerate (vlc) which is traceable for several km (Appendix A). The tephrostratigraphic interval associated with TRA and the tuffaceous paleosols are confidently correlated to La Maravilla at the northern end of Vallé Santa Maria. A full tephrostratigraphic interpretation for Vallé Santa Maria is available in Appendix A.

et al., 1984), but until the occurrence of a ~5 Ma disconformity can be confirmed, stable isotope proxy data and tephrostratigraphic results have limited context for discussion.

The tephrostratigraphic interval associated with the TRA can be identified for ~20 km from south to north in Vallé Santa Maria (Figure 4.4). This stratigraphic interval is relatively continuous along strike, and temporally it spans the Miocene-Pliocene boundary. To relate stable isotope data to other localities, a basic tephrostratigraphic

framework is established for ENTR section #1 (Table 4.3). Glass chemistry as determined by EPMA provides sufficient criteria to identify TRA when present. In Vallé Santa Maria TRA is notable for its relatively high Ca/Fe ratio (~1.5), MnO content > 0.1 weight %, and Cl content < 0.1 weight %. This widespread stratigraphic marker directly overlies the interval of tuffaceous paleosols and is dated at 5.19 ± 0.01 Ma (Appendix A). The base of the tuffaceous paleosol interval is directly underlain by another widespread and important tephrostratigraphic marker. This lower ash bed is indistinguishable from the tuffaceous paleosol above it on the basis of major, minor, and trace element chemistry (Table 4.4). These two ash beds correlate with two closely spaced ash beds at Puerta de Corral Quemado (1518 m level; Table 3.1). At most localities in the region, these two ash beds are observed to be separated by 1–4 m of non tuffaceous strata. That this pattern persists at both PCQ and VSM, supports the interpretation that two closely spaced but individual eruptions produced two ash beds for which compositional differences have not yet been measured. At Puerta de Corral Quemado these two ash beds are ~80 m above one dated at 5.64 Ma. Thus the paleosol carbonate ^{13}C enrichment in Vallé Santa Maria is constrained between 5.6–5.2 Ma. Direct dating of the ash beds associated with the lower tuffaceous paleosol would considerably improve these constraints. Stratigraphic placement of the 5.235 Ma base of the Gilbert paleomagnetic chron would further refine age control (Gradstein *et al*., 2004).

Table 4.3: EPMA data for Entre Ríos section #1 ash beds and correlative samples.

Sample	n[a]	SiO_2	TiO_2	Al_2O_3	Fe_2O_3	MnO	MgO	CaO	BaO	Na_2O	K_2O	Cl	H_2O	Total	D[b]
tuff at ~600 m level															
ENTR 539	**14**	**73.3**	**0.08**	**12.5**	**0.64**	**0.07**	**0.07**	**0.47**	**0.02**	**2.0**	**6.2**	**0.13**	**6.5**	**101.8**	**0.0**
1σ		0.3	0.02	0.1	0.04	0.02	0.02	0.03	0.03	0.1	0.2	0.01	0.8	0.6	
QDJ 992	**21**	**73.3**	**0.09**	**12.5**	**0.59**	**0.08**	**0.06**	**0.44**	**0.03**	**1.5**	**7.6**	**0.13**	**4.2**	**100.6**	**2.3**
1σ		1.1	0.04	0.2	0.04	0.03	0.01	0.03	0.02	0.3	0.3	0.02	0.6	0.9	
tuff at 343 m level															
ENTR 537	**31**	**73.7**	**0.10**	**12.3**	**0.72**	**0.08**	**0.07**	**1.04**	**0.05**	**2.0**	**5.0**	**0.11**	**7.8**	**103.0**	**0.0**
1σ		0.5	0.03	0.1	0.04	0.02	0.01	0.04	0.04	0.2	0.3	0.01	0.8	0.5	
MAR 863	**12**	**73.1**	**0.09**	**11.7**	**0.67**	**0.08**	**0.07**	**1.00**	**0.02**	**1.9**	**6.4**	**0.11**	**5.0**	**100.2**	**2.1**
1σ		0.4	0.03	0.4	0.02	0.02	0.02	0.02	0.02	0.2	0.2	0.01	1.1	0.6	
TRA - toba rayita amarilla (5.19 Ma; 325 m level)															
ENTR 909[c]	**5**	**74.3**	**0.07**	**12.4**	**0.60**	**0.11**	**0.06**	**0.92**	**0.00**	**1.4**	**5.0**	**0.09**	**5.8**	**100.9**	**0.0**
1σ		0.1	0.03	0.0	0.02	0.01	0.00	0.03	0.01	0.1	0.1	0.01	0.4	0.5	
ENTR 524	**14**	**73.0**	**0.08**	**12.3**	**0.63**	**0.12**	**0.07**	**0.96**	**0.01**	**2.1**	**5.0**	**0.09**	**8.1**	**102.4**	**2.1**
1σ		0.7	0.03	0.2	0.04	0.02	0.01	0.03	0.03	0.2	0.2	0.01	0.7	0.4	
ENTR 536	**18**	**73.0**	**0.07**	**12.3**	**0.60**	**0.10**	**0.06**	**0.93**	**0.01**	**2.3**	**5.0**	**0.08**	**8.0**	**102.5**	**1.5**
1σ		0.6	0.03	0.2	0.03	0.03	0.01	0.03	0.02	0.1	0.2	0.01	1.3	0.9	
ENTR 588	**31**	**73.3**	**0.07**	**12.3**	**0.61**	**0.11**	**0.06**	**0.95**	**0.01**	**2.4**	**3.8**	**0.09**	**8.0**	**101.8**	**1.6**
1σ		0.6	0.02	0.2	0.04	0.02	0.01	0.03	0.02	0.6	0.3	0.01	1.6	1.1	
ENTR 589	**31**	**72.8**	**0.09**	**12.1**	**0.62**	**0.11**	**0.06**	**0.94**	**0.01**	**2.6**	**3.9**	**0.09**	**7.5**	**100.9**	**1.9**
1σ		1.0	0.03	0.2	0.05	0.03	0.02	0.03	0.01	0.5	0.2	0.01	1.7	1.5	
ER-Q1	**13**	**72.8**	**0.07**	**12.2**	**0.60**	**0.11**	**0.06**	**0.93**	**0.01**	**2.0**	**5.5**	**0.09**	**6.9**	**101.3**	**1.3**
1σ		0.9	0.03	0.2	0.05	0.02	0.02	0.03	0.01	0.6	0.5	0.01	0.9	0.6	

[a] n=number of analyzed shards; all data in weight %, 1σ=standard deviation; total Fe as Fe_2O_3; H_2O calculated from the difference between measured and stochiometric oxygen (Nash, 1992).

[b] Statistical distance (Perkins *et al*., 1995; Appendix B) calculated using the concentrations of TiO_2, Fe_2O_3, MnO, MgO, CaO and Cl; D≤3.5 indicate analyses are identical at 95% confidence level.

[c] Sample dated by $^{40}Ar/^{39}Ar$ single crystal laser fusion of sanidine (Appendix A).

[d] Analyses combined or excluded; see Appendix A for more information.

Table 4.3 (*continued*) : EPMA data for Entre Ríos section #1 ash beds and correlative samples.

Sample	n[a]	SiO_2	TiO_2	Al_2O_3	Fe_2O_3	MnO	MgO	CaO	BaO	Na_2O	K_2O	Cl	H_2O	Total	D[b]
TRA - toba rayita amarilla (5.19 Ma; 325 m level)															
QDJ 985	**15**	**71.3**	**0.06**	**12.9**	**0.59**	**0.10**	**0.05**	**0.90**	**0.02**	**1.9**	**6.6**	**0.09**	**6.3**	**100.8**	**1.7**
1σ		1.2	0.05	0.3	0.05	0.03	0.02	0.03	0.02	0.1	0.2	0.02	0.8	0.7	
MAR 862	**8**	**72.6**	**0.09**	**12.1**	**0.61**	**0.11**	**0.06**	**0.88**	**0.01**	**1.8**	**6.3**	**0.09**	**6.2**	**100.8**	**2.4**
1σ		0.6	0.02	0.1	0.04	0.02	0.01	0.04	0.01	0.1	0.2	0.01	0.3	0.8	
upper tuffaceous paleosol (~314 m level)															
ENTR 534	**34**	**74.1**	**0.08**	**12.2**	**0.70**	**0.03**	**0.05**	**0.56**	**-**	**2.2**	**4.2**	**0.12**	**7.8**	**102.0**	**-**
1σ		0.6	0.03	0.2	0.08	0.02	0.02	0.05	-	0.7	0.8	0.02	0.8	1.3	
lower tuffaceous paleosol (~200 m level)															
ENTR 533[d]	**36**	**72.8**	**0.13**	**13.0**	**0.86**	**0.08**	**0.13**	**0.78**	**-**	**2.3**	**3.8**	**0.15**	**7.0**	**101.2**	**0.0**
1σ		0.6	0.03	0.2	0.04	0.03	0.02	0.06	-	0.2	0.4	0.01	1.0	1.1	
MAR 861	**18**	**71.7**	**0.13**	**11.9**	**0.82**	**0.07**	**0.13**	**0.75**	**0.07**	**2.8**	**4.8**	**0.14**	**7.1**	**100.5**	**2.3**
1σ		0.3	0.02	0.6	0.04	0.02	0.02	0.02	0.04	0.2	0.2	0.01	0.6	0.4	
PCQ 158b	**16**	**71.0**	**0.11**	**13.0**	**0.82**	**0.07**	**0.11**	**0.74**	**0.07**	**2.9**	**5.6**	**0.14**	**5.6**	**100.1**	**3.5**
1σ		0.5	0.04	0.5	0.07	0.03	0.02	0.03	0.03	0.3	0.4	0.02	0.7	0.6	
tuff at 195 m level															
ENTR 532	**29**	**73.3**	**0.12**	**12.9**	**0.84**	**0.08**	**0.13**	**0.76**	**-**	**2.6**	**3.6**	**0.13**	**7.5**	**102.1**	**0.0**
1σ		0.5	0.04	0.1	0.04	0.02	0.02	0.02	-	0.2	0.3	0.01	0.9	0.6	
PCQ 158a	**16**	**71.0**	**0.13**	**13.1**	**0.83**	**0.07**	**0.13**	**0.74**	**0.07**	**2.8**	**5.7**	**0.14**	**5.5**	**100.2**	**2.0**
1σ		0.4	0.05	0.5	0.06	0.03	0.02	0.03	0.04	0.4	0.4	0.02	0.5	0.5	
PCQ 774	**19**	**72.4**	**0.12**	**13.0**	**0.86**	**0.07**	**0.13**	**0.75**	**0.08**	**3.0**	**5.4**	**0.14**	**5.8**	**101.7**	**1.9**
1σ		0.4	0.04	0.1	0.03	0.02	0.02	0.02	0.03	0.4	0.7	0.01	0.4	0.3	

[a] n=number of analyzed shards; all data in weight %, 1σ=standard deviation; total Fe as Fe_2O_3; H_2O calculated from the difference between measured and stochiometric oxygen (Nash, 1992).

[b] Statistical distance (Perkins *et al*., 1995; Appendix B) calculated using the concentrations of TiO_2, Fe_2O_3, MnO, MgO, CaO and Cl; D≤3.5 indicate analyses are identical at 95% confidence level.

[c] Sample dated by $^{40}Ar/^{39}Ar$ single crystal laser fusion of sanidine (Appendix A).

[d] Analyses combined or excluded; see Appendix A for more information.

Table 4.4: ICP-MS data for volcanic glass in correlated and dated ash beds in VSM.

Sample	Age (Ma)	Ba[a] µg/g	Ce µg/g	Cs µg/g	Hf µg/g	La µg/g	Lu µg/g	Nd µg/g	Rb µg/g	Sm µg/g	Sr µg/g	Ta µg/g	Th µg/g	U µg/g	Y µg/g
top of ENTR section #1 (~600 m level)															
ENTR 539		362	32	10	1.8	11	0.44	11	233	4.3	28	2.5	15	9	29
QDJ 992		391	36	10	1.8	12	0.43	11	246	4.5	29	2.0	15	9	29
TRA- toba rayita amarilla (325 m level)															
ENTR 909[b]	5.19 ± 0.01	60	30	26	1.4	14	0.45	7	307	1.8	97	3.0	16	10	18
ER-Q1		49	30	29	1.5	14	0.49	6	310	1.8	76	3.2	17	12	19
QDJ 985		66	29	26	1.1	14	0.43	6	313	1.7	92	3.0	16	10	18
QJ-4[c]	5.20 ± 0.06	66	31	27	1.4	15	0.48	7	298	2.0	94	3.1	16	10	19
coarse pumice tuff (~20 m below TRA)															
QDJ 983[b]	5.27 ± 0.01	14	24	20	0.9	9	0.60	7	265	3.7	27	3.6	10	8	41
lower tuffaceous paleosol; doublet (195–200 m level)															
PCQ 564	<5.6	799	66	3	1.7	30	0.20	19	154	4.3	121	1.2	14	3	13
ENTR 532	<5.6	785	63	3	1.8	27	0.22	18	153	4.4	105	1.8	14	4	12
ENTR 533	<5.6	734	62	4	1.7	27	0.23	17	166	4.3	111	1.3	14	4	15

[a]Values in micrograms/gram; Ba and Sr by isotope dilution, other elements by standard addition.
[b]Sample dated by $^{40}Ar/^{39}Ar$ single crystal laser fusion of sanidine (Appendix A).
[c]Sample dated by $^{40}Ar/^{39}Ar$ analysis of biotite (Ed Sobel, Universität Potsdam, pers.comm.).

Revised chronology of the Vallé Santa Maria paleosol carbonate record

Based upon $^{40}Ar/^{39}Ar$ age dating and stratigraphic constraints, an age of 5.2 Ma is proposed for the upper tuffaceous paleosol in VSM. This is 300 ka younger than the age used by Kleinert and Strecker (2001). To conform with new tephrostratigraphic constraints the age of the lower tuffaceous paleosol must also be shifted at least 200 ka younger. The impact of these chronological revisions on the age of other paleosol carbonate data is not clear.

Table 1 of Kleinert and Strecker (2001) implies a linear sediment accumulation rate of ~230 m/Ma for all formations investigated in VSM. This is in agreement with a rate derived over the interval from 5.27–5.19 Ma at Quebrada de Jujuy (QDJ; Figure 4.4). This stratigraphic interval yields an accumulation rate between 185 and 225 m/Ma. Although this interval is short, both of the ages are high precision $^{40}Ar/^{39}Ar$ sanidine dates. The accuracy of the sediment accumulation rate is not a primary concern, but the applicability of the rate from this short interval to all strata is questionable. Interpolation from the lower tuffaceous paleosol through TRA at section ENTR #1 requires a minimum sediment accumulation rate of 300 m/Ma. These estimates cannot be improved upon without acquiring new age dates, and the sediment accumulation estimate of Kleinert and Strecker (2001) is a reasonable compromise for the Andalhuala Formation. This means shifting the age of these pedogenic carbonate data younger by 300 ka, and this is done for the Andalhuala Formation at Entre Ríos and Quebrada de Jujuy.

The youngest paleosol carbonate data are constrained in age by a zircon fission track determination of 3.4 ± 0.5 Ma near the top of the section at La Maravilla (Strecker *et al*., 1989). The dated volcanic ash bed overlies the paleosols that were studied at this

locality, and does not permit shifting the age of these samples 300 ka younger. Stable isotope data from La Maravilla are included in the composite record, but their age is not shifted and they are assumed to be equivalent in age to the youngest paleosols from Entre Ríos. Given the uncertainty associated with the age of the strata at El Infiernillo, the paleosol carbonate data from there are excluded from further discussion. The ages of pedogenic carbonate on ancient pediments are adopted from Kleinert and Strecker with conservative estimates of the age range (Table 4.2).

The age of pedogenic carbonate from the underlying Chiquimil Formation is based upon lithostratigraphic correlations to Puerta de Corral Quemado (Strecker *et al*., 1989; Bossi *et al*., 1998). The inferred chronological relationships between the two localities are not predicated on any new information, and the ages assigned to the stable isotope data are not impacted. Isotopic data from the underlying Las Arcas Formation are excluded from further analysis based upon the suggestion of Kleinert and Strecker (2001) that, "the possibility of a diagenetic origin should not be excluded".

Miocene-Pliocene ^{13}C enrichments

Several intervals of paleosol carbonate ^{13}C enrichment are identified in the region, but the timing of these signals does not support a regional interpretation. Four periods of potential enrichment are noted between 27° and 28°S (Figure 4.5a). The first such feature is estimated to occur at ~5.75 Ma; these paleosol carbonates are from a conglomeratic interval overlying the eolian strata at PCQ. This ^{13}C enrichment has previously been interpreted to result from the greater landscape variability associated with a braided fluvial depositional system (Chapter 2). The next possible feature also

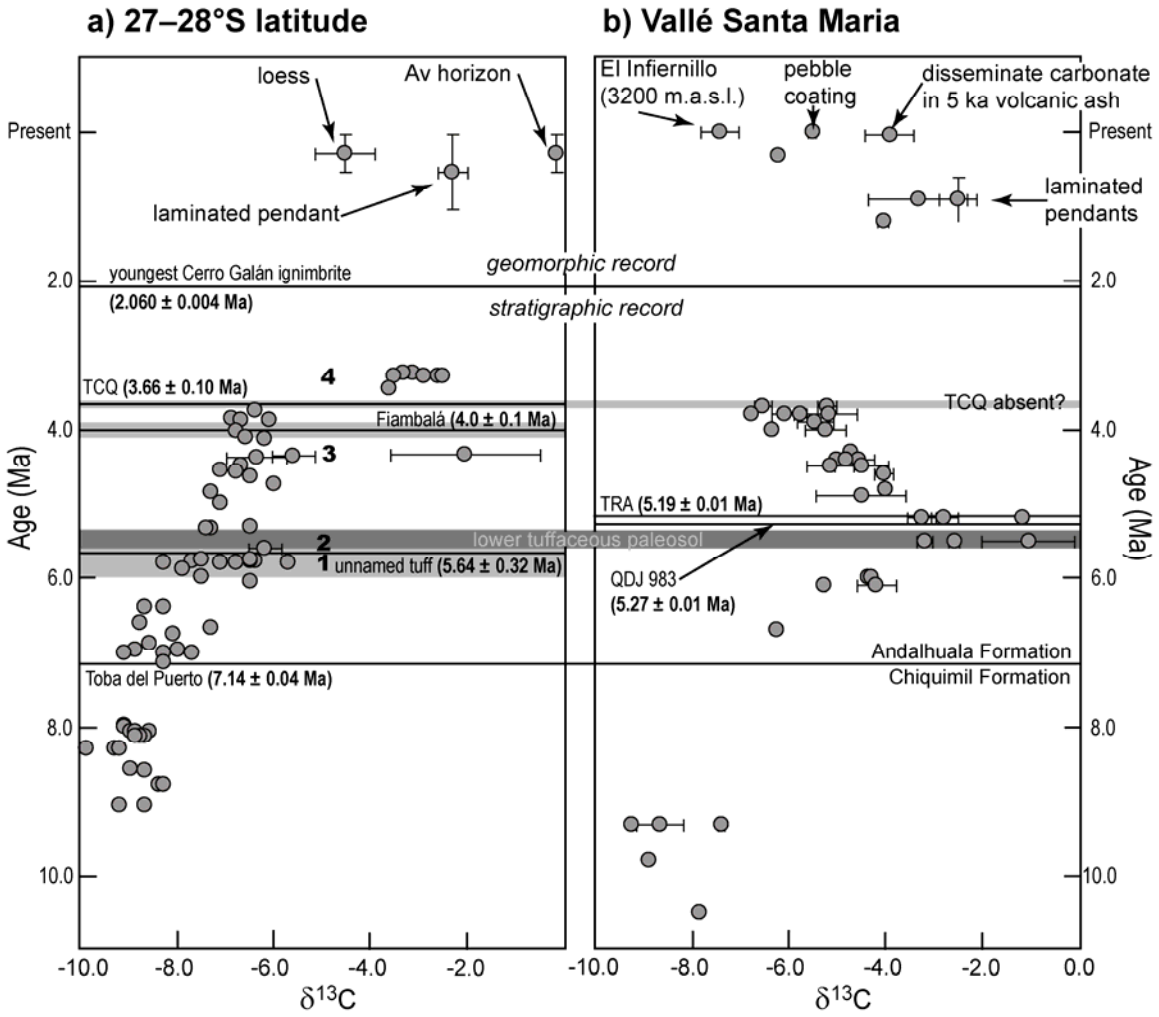

Figure 4.5: Soil carbonate $\delta^{13}C$ from the southern Puna margin with important tephrostratigraphic horizons; **a)** bold numbers indicate ^{13}C enrichments discussed in the text, **b)** the ^{13}C enrichment at VSM overlies enrichments 1 and 2 from panel a.

occurs at PCQ, just above the ash bed dated at 5.64 Ma. This ^{13}C enrichment is associated with ^{13}C enriched fossil teeth, but limited to a single paleosol. The third feature is the rapid $\delta^{13}C$ shift observed in paleosol carbonate at ~4.3 Ma in the Fiambalá basin. This sharp ^{13}C enrichment has been hypothesized to result from a shifting landscape driven by progradation of alluvial fans and associated ecosystems. A similar isotopic enrichment at PCQ occurs at ~3.6 Ma, and may also result from progradation of coarse grained basin margin depositional systems (Chapter 2).

The strongest possibility for a regional $\delta^{13}C$ signal is the transient positive shift in paleosol carbonate in VSM. This isotopic feature is documented by the interval of tuffaceous paleosols which are constrained to 5.6–5.2 Ma in age (Figure 4.5b). If the minor enrichments in paleosol carbonate at PCQ are part of this signal, they may represent the base of the enrichment. These minor enrichments are PCQ are not particularly notable except that they correspond with ^{13}C enrichment in tooth enamel across the same interval.

The best evidence for transient ^{13}C enrichment at the Miocene-Pliocene boundary is from the tooth enamel record at PCQ (Figure 2.8). The bulk of this positive $\delta^{13}C$ excursion is represented by fossil tooth enamel between the 1400–1560 m levels. Current estimates place the age of these fossils between 5.7–5.2 Ma, or broadly coincident with the tuffaceous paleosols in VSM. This interval includes the minor paleosol ^{13}C enrichments noted at PCQ (Figure 4.5a). From 27–28°S, the lower two ^{13}C enrichments are muted relative to the upper two. These lower two enrichments may be part of a 300–400 ka $\delta^{13}C$ excursion prior to and spanning the Miocene-Pliocene boundary, but sampling density and chronological control need improvement to test this.

Overall, poor evidence exists for a transient $\delta^{13}C$ excursion about the Miocene-Pliocene boundary. This is particularly true in VSM where the highest $\delta^{13}C$ values are directly related to a specific lithology (volcanic ash beds). The paleosol carbonate $\delta^{13}C$ record in the region is interpreted in terms of landscape control on plant communities. It is possible that C_4 plants preferentially colonize landscapes dominated by volcanic ash, and until these relatively positive $\delta^{13}C$ values can be documented in paleosols developed on a different substrate the significance of the data will remain unclear.

Several approaches to testing for a transient Miocene-Pliocene ^{13}C enrichment exist. Firstly, attempts to spatially extend the 5.6–5.2 Ma paleosol carbonate record can be guided by additional sampling carried out beneath the TRA tuff. Extension of the ^{13}C enrichment to paleosols developed on a different substrate would discount the potential influence of the volcanic ash on the plant communities contributing to the $\delta^{13}C$ of pedogenic carbonate. Secondly, a chronological approach to testing for synchroneity between PCQ and VSM is advocated. Obtaining a radioisotopic date for the ash bed correlated between the two basins would provide greatly improved chronological control for the Miocene-Pliocene boundary at PCQ and provide a precise lower age bound for the ^{13}C enrichment in VSM. Paleomagnetic sampling would also provide a precise temporal horizon by identifying the reversed to normal transition at the base of the Gilbert Chron. This boundary is estimated to be 5.235 Ma (Gradstein *et al*., 2004) and should fall directly between the TRA tuff (5.19 Ma) and the ash bed dated at 5.27 Ma (QDJ 983; Appendix A). A similar transition has been identified ~30 m below Chiquimil unit XIX (Marshall *et al*., 1979). If unit XIX is correlative to TRA, identification of this reversal would constrain the upper tuffaceous paleosol to a temporal interval of less than 45 ka.

When each of these disparate paleosol carbonate $\delta^{13}C$ features is amalgamated into a regional record, it is difficult to make a case for a synchronous ecological event driven by global or regional climatic events. The growth of orographic barriers and resultant rain shadows has been suggested to control the distribution of late Miocene and Pliocene plant communities in Vallé Santa Maria (Kleinert and Strecker, 2001). This remains a potential driver of the 4.3 Ma Fiambalá shift and the 3.6 Ma PCQ shift. However, if one considers that the spatial and temporal scale of isotopic changes in the

paleosol carbonate record should match that of the driver, some doubt is cast on the orographic rain shadow hypothesis. At PCQ and Fiambalá it appears that the spatial scale of the positive $\delta^{13}C$ shifts was small and the temporal scale was short. The scaling of the features in the isotopic proxy record may more closely match the sedimentation driven hypothesis proposed in this dissertation. Additionally, these rapid $\delta^{13}C$ shifts occur in the absence of a $\delta^{18}O$ shift. Strong changes in precipitation distribution that result from development of an orographic rain shadow should also impart a $\delta^{18}O$ signal, though this is not always the case (Galewsky, 2009b).

For these reasons, the late Miocene and Pliocene are interpreted as times when a patchy mixture of C_3 and C_4 plants characterized the landscape. Following from this, the $\delta^{13}C$ paleosol carbonate record is suggested to be a sensitive recorder of landscape variability in plant communities. If this is true, the late Miocene expansion of C_4 plants in northwestern Argentina should be documented in the paleosol carbonate record by an increase in the range of $\delta^{13}C$ values rather than a regionally coherent positive $\delta^{13}C$ shift. This seems to be the case for proxy records along the southern margin of the Puna plateau, where the range of $\delta^{13}C$ values increases significantly after ~6 Ma (Figure 4.6a). Meaningful spatio-temporal patterns of Mio-Pliocene climate may eventually emerge, but a significant increase in data density and improvements in age control will be necessary to resolve such patterns. Improved conceptual models of landscape ecology derived from modern and ancient systems will be important as well. In the interim, it seems reasonable to assume a patchy C_3-C_4 mixture of plants at spatial scales ranging from 10 m to 100 km that is sampled randomly by the geologic record.

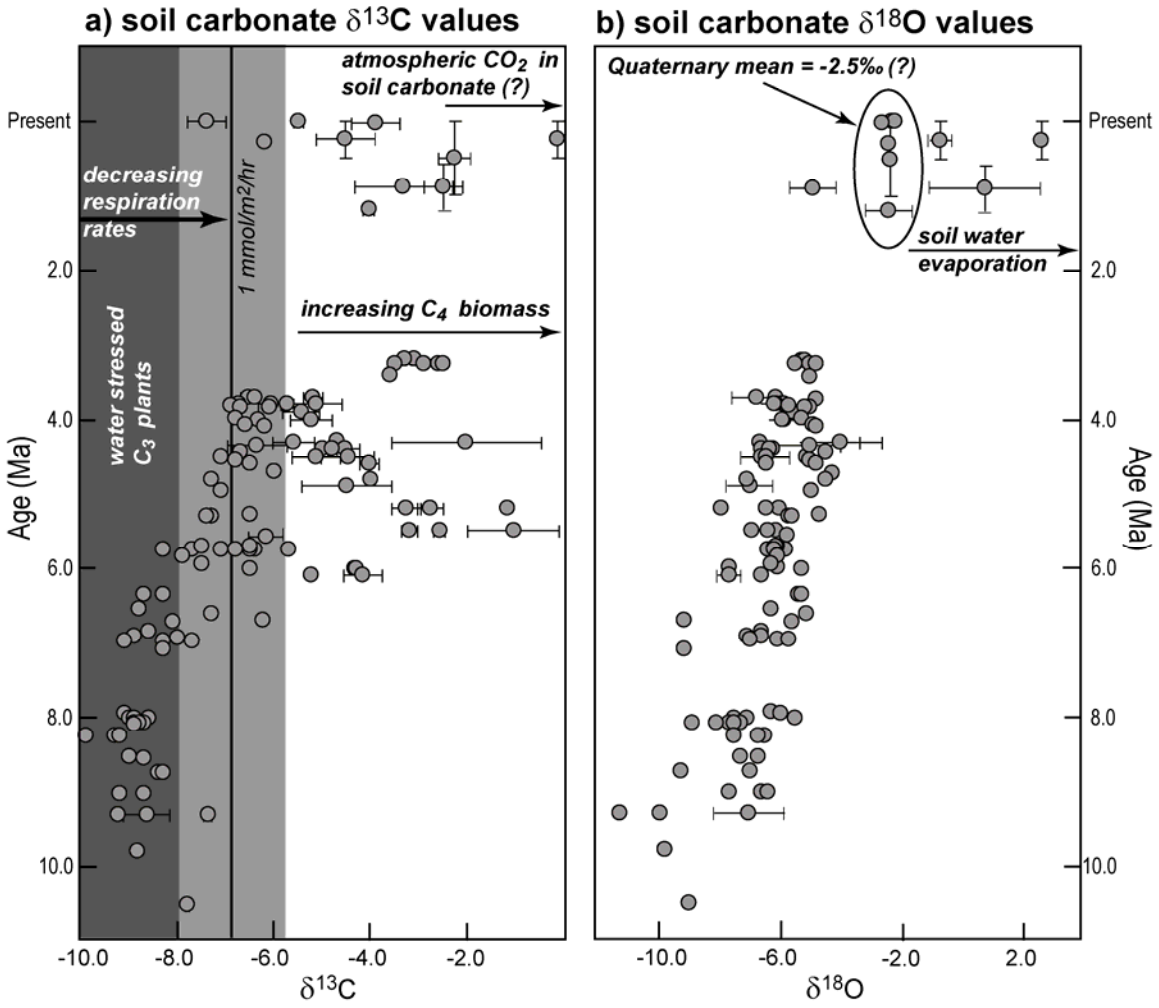

Figure 4.6: The isotopic composition of soil carbonate from 26–28°S; **a)** measured and modeled carbon isotopic composition indicating positive identification of C_4 biomass at ~6 Ma, **b)** oxygen isotopic composition demonstrating long term ^{18}O enrichment and the strong effects of soil water evaporation on the isotopic composition of carbonate sampled from geomorphic surfaces. Primary references for the soil CO_2 model are Cerling (1984); Quade *et al*. (1989); Cerling *et al*. (1991); Romanek *et al*. (1992); Cerling and Quade (1993); Davidson (1995). Invariant parameters include $\delta^{13}C$ value of -23 ‰ for water stressed C_3 plants, soil porosity of 0.35, mean rooting depth of 10 cm, and soil temperature of 25°C. C_3 plant isotopic composition is based upon the likely maximum value recommended by Kohn (2010). Soil temperature is based upon the mean monthly growing season temperatures at La Rioja, Santiago del Estero, and Salta from the period 1961–1990 (Servicio Meterológico Nacional de Argentina; http://www.smn.gov.ar). The gray envelope about a respiration rate of 1 mmol/m^2/hour includes the isotopic effects of Miocene-Pliocene variations in atmospheric CO_2 content and its carbon isotopic composition. The range of atmospheric CO_2 contents employed is 180–400 ppmv (cf. Pagani *et al*., 1999; Tripati *et al*., 2009; Pagani *et al*., 2010; Seki *et al*., 2010). The $\delta^{13}C$ value of atmospheric CO_2 during this time is estimated to range between -5‰ and -7‰ (cf. Passey *et al*., 2002, 2009; Cerling *et al*., 2010; Tipple *et al*., 2010).

Miocene-Pliocene ^{18}O enrichment

Paleosol carbonate from both PCQ and VSM reveals a long-term change in $\delta^{18}O$ values between 7 and 4 Ma (Figure 4.7). VSM data are ~1.5‰ more negative than PCQ data. The clear trend of both records is towards ^{18}O enriched carbonate in the Pliocene. Conversely this could be viewed as ^{18}O depletion with depth. Such a pattern might reasonably be produced by burial diagenesis. Isotopic exchange between carbonate and diagenetic fluids would produce a similar effect due to changes in calcite-water isotopic fractionation. If an isotopically homogenous water source was circulated to a depth of 2 km, strong depth dependent differences in $\delta^{18}O$ would be produced by the increasing temperature of calcite-water isotopic exchange. As previously discussed, this simple model requires an unrealistically low geothermal gradient for PCQ (Figure 2.3). However, VSM data fall within the range of reasonable model parameters (Figure 4.7a). Careful textural analysis was undertaken for the VSM paleosol samples (Kleinert and Strecker, 2001); however, even micritic carbonate can have undergone isotopic exchange with little or no textural evidence (Leier *et al*., 2009). Consequently, both the PCQ and SMV data are interpreted in a climatic framework with extreme caution.

Both PCQ and VSM exhibit an isotopic enrichment of ~0.6‰/Ma between 7 and 4 Ma (Figure 4.7b). The difficulty in ascribing a climatic forcing to this signal arises for two reasons. Firstly, a secular and transient climatic change which was protracted over ~3 Ma must be invoked. Secondly, specific mechanisms for a positive shift in paleosol carbonate $\delta^{18}O$ values are highly conjectural. Some combination of changes in precipitation source, amount, and seasonality can be constructed to produce the observed trend, but disentangling these factors remains a considerable challenge. Increasing

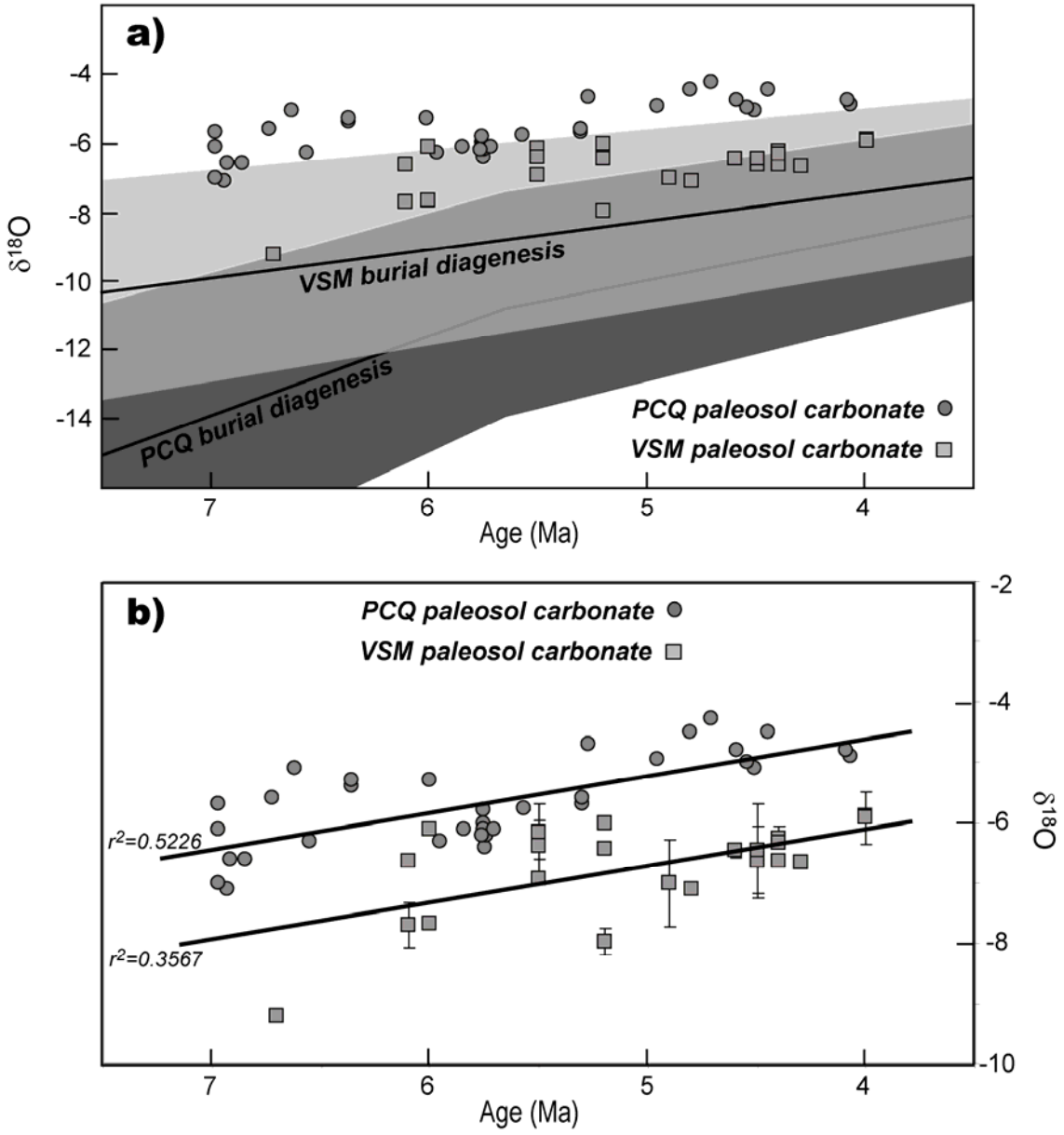

Figure 4.7: Paleosol carbonate $\delta^{18}O$ between 7–4 Ma at PCQ and VSM; **a)** isotopic data relative to models of burial diagenesis, **b)** isotopic data (1σ standard deviation for n>2), and linear least squares regression for each basin. The model of burial diagenesis is based on an isotopically homogenous diagenetic fluid (-4 ± 1‰), a surface temperature between 20–30°C, and a geothermal gradient between 15–30°C/km (cf. Figure 2.3).

dominance of precipitation derived from low latitudes via the South American low-level jet might cause an ^{18}O enrichment (Rozanski *et al*., 1993). Such a shift in precipitation source would presumably be associated with development of the South American Monsoon (Strecker *et al*., 2007a). Development of the South American Monsoon would result in warmer precipitation and soil temperatures in addition to greater amounts of rainout from air masses, all of which would mitigate the ^{18}O enrichment associated with low-latitude moisture sources. If the ^{18}O enrichment between 26–28°S is ascribed to development of the South American Monsoon, the change in the isotopic composition of the precipitation source may be significantly larger than the ~2‰ recorded by paleosol carbonate.

In southern Bolivia (20–22°S), an abrupt enrichment in paleosol carbonate ^{18}O of ~3‰ is interpreted to reflect the onset of monsoon precipitation (Mulch *et al*., 2010). This shift is coincident with the hypothesized 9–8 Ma onset of the South American Monsoon at this latitude (Strecker *et al.,* 2007b; Mulch *et al*., 2010). These data raise concerns with the interpretation of stable isotope data from the Altiplano (Garzione *et al*., 2006), and support models of reorganization of precipitation source and seasonality when topographic thresholds are crossed in the Bolivian Andes (Ehlers and Poulsen, 2009; Insel *et al.*, 2009). Additionally, tectonic and sedimentary changes in the Bolivian Andes during the late Miocene have been interpreted to result from changes in precipitation regimes (Uba *et al*., 2007; Mosolf *et al*., in press). If the PCQ and VSM paleosol records are interpreted in this framework, the onset of the South American Monsoon along the southern Puna plateau differs in timing and nature from that of the Bolivian Altiplano and adjacent low elevation Subandean Zone.

The development of orographic rainshadows is another mechanism by which paleosol carbonate $\delta^{18}O$ values might increase gradually through time, though the relationships between growing orographic barriers and precipitation distribution are complex (Galewsky, 2009a). Broader patterns of landscape development and climatic change can influence precipitation isotopic ratios, and relating isotopic proxies to the uplift of a specific orographic barrier is fraught with complications (Galewsky, 2009b). In the simplest sense, the growth of an orographic rainshadow should cause a redistribution of precipitation towards the windward flanks and the isotopic composition of precipitation on the lee of the barrier should be ^{18}O depleted relative to pre-barrier scenarios. Such a scenario appears to be applicable to major orographic rainshadows in both the northern and southern hemispheres where a marine vapor source is likely and >40–50% of incoming water vapor is rained out over the orographic barrier (Smith *et al*., 2005; Smith and Evans, 2007).

Thus, if enrichment of ^{18}O in paleosol carbonate records results from the formation of a rainshadow, it is not the result of primary changes in the isotopic composition of precipitation. Enrichment in ^{18}O of soil water (and paleosol carbonate) might however, result from two factors related to arid climates resulting from establishment of an orographic rainshadow. Increased evaporation or isotopic exchange of hydrometeors below cloud base, falling through a warm dry atmosphere should result in ^{18}O enriched precipitation and positive $\delta^{18}O$ shifts in soil water (Dansgaard, 1964; Gat, 1996). Soil water evaporation in strongly arid environments should lead to further soil water ^{18}O enrichment and positive $\delta^{18}O$ shifts in paleosol carbonate. The magnitude of these effects is difficult to estimate, but soil water evaporation can strongly influence

isotopic values. This is observed for Quaternary soils in the region (Figure 4.6). Holocene soils in the region document intra-soil isotopic variation exceeding 10‰ in the upper 10 cm, and 3–4‰ between 20–100 cm depth (McFadden *et al*., 1998). If increased soil water evaporation is the primary driver of the 7–4 Ma ^{18}O enrichment, an increase in the range of isotopic composition might reflect a strong and variable evaporative influence. Current data do not obviously document such a pattern during the late Miocene or early Pliocene (Figure 4.6b).

Mio-Pliocene ecological gradients in northwestern Argentina

The isotopic record of that emerges from chronological integration of paleosol data between 26–28°S (Fiambalá, PCQ, and VSM) illustrates strong spatial gradients in climate and environment. These gradients are documented by both carbon and oxygen isotopic systems. Given the complexities of atmospheric dynamics, precipitation, and the resulting meteoric water $\delta^{18}O$ values, interpretation of paleosol carbonate $\delta^{18}O$ is not pursued further. A strong linkage exists between precipitation and vegetation in the study area (cf. Chapter 1). It is therefore possible to use the $\delta^{13}C$ values of paleosol carbonate as an ecological indicator which is closely linked to local climate. This line of reasoning is pursued with respect to the late Miocene and early Pliocene in northwestern Argentina.

A case has been made for complex distribution of C_3 and C_4 plants at 10–100 m spatial scales, based upon tooth enamel (Chapter 2) and paleosol (this Chapter) carbonate $\delta^{13}C$ data from 27–28°S. These data, when compared to VSM, present a case for environmental gradients at the 100 km scale as well (Figure 4.5). The potential for strong ecological gradients at this scale is further highlighted by comparison with paleosol carbonate data from the Angastaco basin (Figure 4.1).

Sedimentary history of the Angastaco basin

The stratigraphic record in the Angastaco basin is one of the longest in South America, yielding more than 6 km of continental deposits during the middle and late Miocene (Coutand *et al.*, 2006). Miocene exhumation of ranges to the west began about 20 Ma, and the deposition rate of continental strata increased at ~15 Ma (Deeken *et al.*, 2006). The observations of Coutand *et al.* (2006) indicate that the majority of the sedimentary section (>4 km) is the Angastaco Formation, composed of conglomerates, sandstones, and siltstones organized in fining-upwards fluvial cycles. The overlying Palo Pintado Formation consists of fluvial-lacustrine strata interpreted to reflect a period of increased humidity beginning at ~9 Ma (Starck and Anzotegui, 2001). These strata transition to conglomerates deposited by braided stream and alluvial fan depositional system beginning after ~5.3 Ma (San Felipe Formation; Coutand *et al.*, 2006). This transition to conglomeratic deposits is hypothesized to result from regional aridification on the basis of stable isotope proxy data (Bywater-Reyes *et al.*, 2010). This aridification appears to precede uplift of a mountain block to the east, Sierra de Los Colorados, which is estimated to have commenced 3.4–2.4 Ma (Coutand *et al.*, 2006).

Geochronology of the Angastaco basin

Miocene-Pliocene deposits of the Angastaco basin are exposed in a series of north-south trending folds in a modern intramontane basin. The strata of interest are ~60 km west of the Puna plateau margin, and ~80 km from the Cerro Galán caldera. Volcanic glass from three samples of Coutand *et al.* (2006) has been analyzed (Appendix A), but ash beds from this basin have not been systematically investigated. Recent U-Pb zircon geochronology of ash beds between 7–3 Ma provides excellent age control (Bywater-

Reyes *et al.*, 2010). The instrumentation and methodology are the same as for zircon ages drawn upon in Chapter 3, where an internally consistent chronological framework demonstrated the compatibility of the U-Pb and $^{40}Ar/^{39}Ar$ systems in the region. Stable isotope proxy data spanning the late Miocene and Pliocene are assigned ages by interpolation between dated ash beds (using Bywater-Reyes, 2009). These ages should be equivalent to ages presented in this dissertation within <100 ka (cf. Chapter 3); the exact age of stable isotope proxy data may be less precise due to errors associated with interpolation/extrapolation of age relative to dated horizons.

Stable isotope data from the Angastaco basin

Based upon $\delta^{13}C$ and $\delta^{18}O$ paleosol carbonate data, Bywater-Reyes *et al.* (2010) interpret increasing aridity from at least 6 Ma through 5 Ma. They attribute this signal to increasing aridity regionally, and not to uplift of the Sierra de los Colorados east of the Angastaco basin. Enrichment in both ^{13}C and ^{18}O through time at Angastaco is consistent with the record compiled from 26–28°S (Figure 4.6). The ^{18}O enrichment appears to correspond with that at VSM and PCQ, suggesting a regional signal. The ^{13}C enrichment corroborates the general trend observed to the south, but unambiguous evidence for C_4 plants is lacking. This is the most striking feature of the Angastaco record, and it indicates strong environmental gradients in the region (Figure 4.8).

Paleosol carbonates from the Palo Pintado Formation have some of the most negative $\delta^{13}C$ values known. Two paleosol have average $\delta^{13}C$ values between -13.5 and -14‰, and another sample has values ranging from -13.8 to -15.5‰ (Bywater-Reyes *et al.*, 2010). In fact, only a handful of paleosol carbonates sampled across the Paleocene-Eocene Thermal Maximum (PETM) have $\delta^{13}C$ values below -15‰ (Koch *et al.*, 2003).

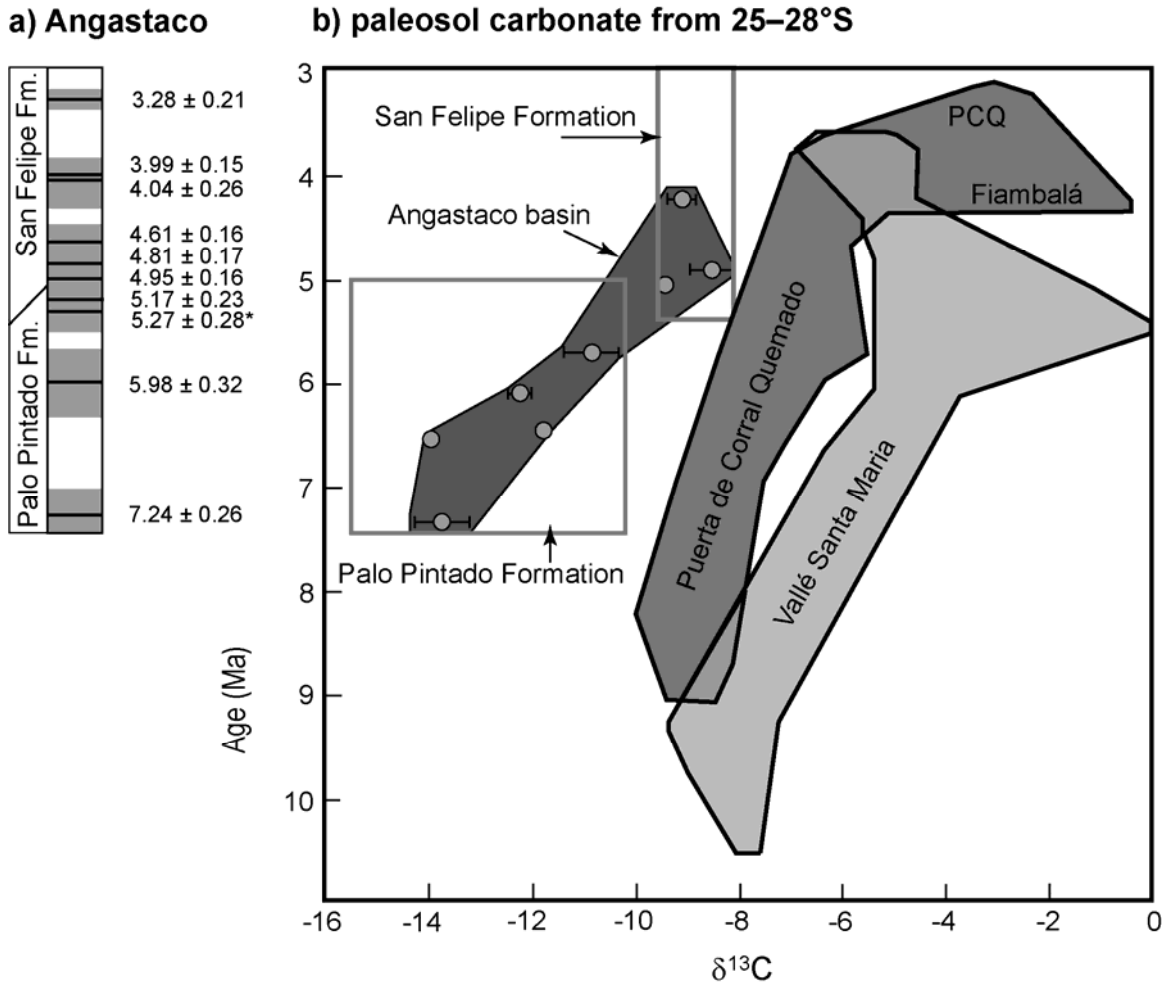

Figure 4.8: Carbon isotopic composition of paleosol carbonate; **a)** U-Pb zircon geochronology from Angastaco, **b)** comparison of paleosol carbonate records between 25–28°S. Geochronology from Bywater-Reyes *et al*. (2010), except *, which is from Coutand *et al*. (2006). Grey envelopes about ash beds represent the 2σ uncertainty of the weighted mean. Paleosol carbonate data from Angastaco represented as follows; individual points and error bars represent the average and 1σ standard deviation of individual paleosols whose age could be estimated by interpolation between or extrapolation from dated horizons using Bywater-Reyes (2009), this excludes data from section 8. Gray boxes representing the Palo Pintado and San Felipe Formations encompass the full range of $\delta^{13}C$ values reported in Bywater-Reyes *et al*. (2010). The polygons representing Vallé Santa Maria and Puerta de Corral Quemado/Fiambalá were constructed as shown for Angastaco using the data in Figure 4.5.

The ^{13}C depletion during the PETM has been attributed, in part, to increased continental humidity resulting in more negative $\delta^{13}C$ plants values (Bowen *et al.*, 2005). Carbonate $\delta^{13}C$ values for the most negative Palo Pintado paleosols can not be easily achieved using the commonly cited average C_3 plant value of -26 to -27‰ (cf. Cerling and Quade, 1993; Koch, 1998). At respiration rates in excess of 8 mmol/m^2/hour, a carbonate formation temperature of 40°C is required to produce $\delta^{13}C$ values of -15.5‰ (other parameters as described in Figure 4.6). If -28.5‰ is used for an average C_3 value (Kohn, 2010), more moderate carbonate forming conditions of 30°C at a soil respiration rate of 4 mmol/m^2/hour are permissible. These results suggest that a C_3 ecosystem in a humid setting is capable of producing the unusually negative $\delta^{13}C$ paleosol carbonate values. Further, these isotopic constraints agree with interpretations of the fossil plants and mammals from the Palo Pintado Formation (Starck and Anzótegui, 2001).

That the Palo Pintado $\delta^{13}C$ data are unusually negative may result in part from a preservational and scientific bias towards arid environments (Kohn, 2010). In any case, the potential for formation and preservation of soil carbonate in humid environments is greatly reduced relative to arid environments. However, to form a soil carbonate net evaporation is the only requirement (Cerling and Quade, 1993). By analogy to the modern Sierra Aconquija (Figure 1.4), strong topographic control on precipitation may present situations where local hydrologic systems allow evaporation in depositional settings adjacent to a hillslope that maintains a positive soilwater balance. Generation of highly negative $\delta^{13}C$ soil carbonate would be enhanced by contributions to soil organic matter from plants growing in the adjacent (humid) upland. This physiographic model approximates the situation proposed by Coutand *et al.* (2006) where the uplifts on the

western margin of the Angastaco basin were orographic barriers that prevented moisture penentration to the Puna by 9 Ma. The windward flanks of these barriers would presumably be the source for moisture and low $\delta^{13}C$ soil organic matter essential for precipitation of low $\delta^{13}C$ carbonate in the Angastaco basin.

Taken together, sedimentary indicators, fossil assemblages, and paleosol carbonate $\delta^{13}C$ values from the Angastaco basin indicate a humid, wooded environment from 9–5 Ma. Fossil rodent $\delta^{13}C$ tooth enamel data from Angastaco are sparse, but they tell a more complex story (Bywater-Reyes *et al.*, 2010). These data are surprisingly ^{13}C enriched relative to paleosol carbonate. For the Palo Pintado Formation tooth enamel data constrained diet composition between -21 and -23‰, and for the San Felipe Formation diet composition is estimated to range from -13.5 to -18.5‰ (Passey *et al.*, 2005a; Podlesak *et al.*, 2008). With respect to the Palo Pintado Formation, plants of this carbon isotope composition cannot create paleosol carbonate $\delta^{13}C$ values below -9.5‰. This discrepancy can be reconciled somewhat by the fact that the rodent fossils analyzed are estimated to be between 5.8 and 5.2 Ma, while the most negative paleosol carbonates are significantly older. For the San Felipe Formation, the situation is clarified somewhat. A comparison can be made between fossil tooth enamel and pedogenic carbonate from the same paleosol, which is constrained to between 4.8 and 5.0 Ma by two dated ash beds. Using the rodent diet to estimate plant composition yields a range of modeled paleosol carbonate $\delta^{13}C$ composition ranging from 1 to -5‰. These estimated paleosol carbonate values encompass the range of atmospheric CO_2 values from Figure 4.6 and soil respiration rates between 1 and 8 mmol/m^2/hour, and are clearly discrepant with the measured $\delta^{13}C$ of -8.4 ± 0.4‰.

While the rodent tooth enamel data are few, they facilitate understanding of the environment in the Angastaco basin during the late Miocene and early Pliocene. Importantly, rodent diets include C_4 plants and are isotopically distinct from the soil-respired CO_2 assumed to be in equilibrium with soil carbonate. Several possibilities exist. Rodent diets may have been acquired by selective grazing. This would indicate that C_4 plants were present as a minor component of the landscape, but not recorded by paleosol carbonate. This may arise simply as a consequence of the limited samples available, or it may result from C_3 dominance of soil-respired CO_2. C_3 dominance of soil-respired CO_2 does not preclude C_4 biomass in the soil, particularly if soil organic matter is transported from upland slopes to depositional settings which preserve pedogenic carbonate. Clearly more data are needed to address these questions.

Conclusions

Strong gradients in ecosystems during the late Miocene and early Pliocene are documented by paleosol carbonate $\delta^{13}C$ data. These gradients may be similar to modern, and by analogy it is reasoned that growing topography at the Puna plateau margin between 25–28°S created localized climates. In climatic settings prone to expansion of C_4 plants this ecologic event was documented and is concomitant with other records from the region (7.0–5.5 Ma; Chapter 2).

The regional compilation of paleosol carbonate data in this chapter suggests an increase in C_4 vegetation at ~6 Ma (Figure 4.6a). This is reflected as an increase in the range of $\delta^{13}C$ values, and supports the interpretation of the latest Miocene and Pliocene landscape as one with a patchy distribution of C_3 and C_4 plants at spatial scales of 100 m to 1 km. Consequently, rapid $\delta^{13}C$ shifts in paleosol carbonate are not interpreted to

result from global, regional, or local climatic forcing. Unless a regionally persistent isotopic signal is documented, ^{13}C enrichments in paleosol carbonate are just as easily interpreted to result from random sampling of a diverse landscape variably affected by common tectonic and geomorphic processes.

A practical implication of the proposed landscape-based paleoecological model is that regional or global climatic and ecological events cannot be inferred from a single stratigraphic section. The subtropical setting of the study area and its complex topographic evolution during the Mio-Pliocene should be assumed to produce a complicated isotopic proxy record.

The oxygen isotopic record documents ^{18}O enrichment in paleosol carbonate across the interval of C_4 expansion. Diagenetic influence on this record cannot be ruled out, and the gradual nature of the isotopic shift remains a concern. If the oxygen isotopic record is primary, it appears to be a regional signal from the late Miocene and early Pliocene. Both the growth of orographic barriers and increasing influence of the South American Monsoon remain possible causes of the climatic change inferred from $\delta^{18}O$ data. A shift towards warm season precipitation via strengthening of the South American Monsoon would likely result in more ^{18}O enriched precipitation. If the $\delta^{18}O$ data do indeed capture the onset of this precipitation system at 26–28°S, it can be said to lag monsoon development in Bolivia by ~1.5 Ma and to develop over a protracted period spanning the Miocene and Pliocene. Alternatively, the growth of orographic barriers or regional atmospheric circulation changes that result in increased aridity remain possible causes of climatic change. Aridification leads to enhanced evaporation in atmospheric and soil environments, ultimately producing ^{18}O enriched soil carbonate.

CHAPTER 5

DISCUSSION AND CONCLUSIONS

Paleoenvironmental observations

The climates and environments along the southern Puna plateau were a complex mosaic across the Miocene-Pliocene boundary. The relative distributions of C_3 and C_4 plants responded to climate and environment at a variety of scales. Long range (100 km) differences in plant communities persist throughout the interval from 9 to 3.5 Ma. Local plant communities themselves became more diverse after ~6 Ma, displaying a patchy distribution of C_3 and C_4 plants at scales ranging from 100 m to ~1 km. The diet of some mammalian herbivores shifted to include substantial quantities of C_4 plants at approximately the same time (7–5.5 Ma). The fossil record also documents immigrant taxa from North America by 7 Ma, and fossils of large Miocene mammals are notably absent from the Pliocene record.

Together, these observations suggest a shift to drier climates and increasing presence of C_4 plants through time. The enrichment of ^{18}O in soil carbonate between 7 and 4 Ma might record this climatic shift, and provides evidence that this trend could be regional. These events result from a number of potential drivers, so that identifying a truly regional paleoenvironmental signal is difficult.

Observations of sedimentation and deformation at the plateau margin

A dramatic change in sedimentary systems along the eastern Puna margin occurred about 6 Ma and may be attributed to the transition from thin-skinned to thick-skinned deformation (Carrapa *et al*., 2008). During the Pliocene, deposition of the Punaschotter Formation along the plateau margin was protracted and diachronous. These coarse, poorly sorted, plateau margin gravels are associated with uplift of resistant bedrock and provide a proxy for relief generation. Growth of basement-cored anticlinal structures within sedimentary basins postdates deposition of the Punaschotter and is the culmination of contractional deformation in the region. This deformation may have continued into the Quaternary, but by 2–1 Ma the southern Puna plateau margin was in a neutral to extensional state (Schoenbohm and Strecker, 2009). Range front pediments and high fluvial terraces suggest that during the Quaternary, intermontane basins were aggradational, at least intermittently. The late Quaternary is characterized by excavation of sediment from these basins. Multiple aggradation/excavation cycles are known from basins in the region (cf. Hilley and Strecker, 2005; Strecker *et al*., 2009), and it is possible that some plateau margin basins were internally drained at times during the late Pliocene or Quaternary.

The stratigraphic record of volcanism (observations)

The stratigraphy, age, and composition of volcanic ash beds deposited in sedimentary basins at the Puna margin contain a detailed volcanic history. Several reasons prevent this volcanic history from being interpreted more rigorously. Additional age control for the youngest ash beds is needed for proper interpretation of late Pliocene volcanism. Also, sampling and analysis of Miocene ash beds older than ~7 Ma is limited

and this period can not be accurately evaluated. The lack of information for pre-7 Ma ash beds is partly due to poor preservation, but it appears that ash beds are less common during this interval. At Puerta de Corral Quemado, a detailed stratigraphic record can be constructed from 7–3.5 Ma (Figure 5.1). This record indicates that volcanism increased dramatically at ~7 Ma, and further identifies pulses of volcanism between 5.5–5.0 Ma and 4.5–4.0 Ma. These observations corroborate the suggestion that stratigraphic intervals identified and reported in Chapter 3 might represent periods of higher than average eruption rates. Exhaustive sampling and analysis of ash beds in the interval from 5.6 Ma to 3.5 Ma clearly delineates these eruptive pulses (Figure 5.1b).

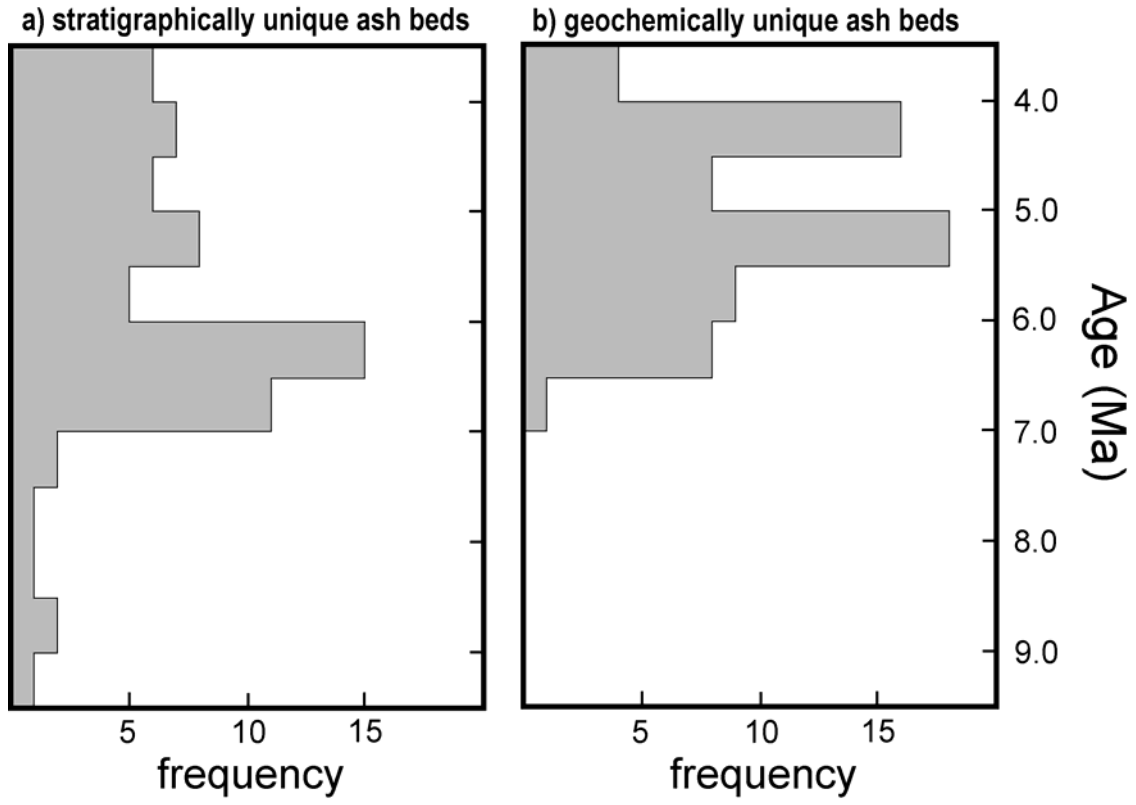

Figure 5.1: Stratigraphic record of explosive volcanism at Puerta de Corral Quemado in 0.5 Ma intervals, using linear interpolation between ash beds and an age of 9.14 Ma for the base of the section (cf. Latorre *et al.*, 1997). Volcanic ash beds in **a)** are taken from Table A.5, and those in **b)** are from Tables A.3 through A.7.

Tectonics, climate, and the origin of the Puna plateau

The topographic expression of the Puna plateau has been hypothesized to result from a combination of climatic and tectonic processes. Late Miocene initiation of broken foreland topography is coincident with several hypothesized tectonic events including delamination of lower crust and mantle lithosphere beneath the Puna (Kay *et al*. 1994) steepening of the subduction zone (Coira *et al*., 1993), or vertical thickening of orogenic crust past threshold values (Riller *et al*., 2001).. During this time, several regional climatic events are also proposed to have affected the plateau margin. Late Miocene onset or intensification of the South American Monsoon in Bolivia (Uba *et al*., 2007; Strecker *et al*., 2007b; Mulch *et al*., 2010) appears to have preceded a period of aridification (Bywater-Reyes *et al*., 2010) along the Puna plateau margin by 2 to 3 Ma.

These events are pertinent because a strong coupling between climate, topography and geomorphology is documented along the plateau margin at a variety of spatial and temporal scales (Strecker *et al*., 2007a; Bookhagen and Strecker, 2008). It has been suggested that the high elevation of the plateau results primarily from deep-seated phenomena (e.g., variations in crustal thickness and density), but that the low relief of the plateau results from aridity and sediment storage within the plateau (Strecker *et al*., 2009). Given the complexity of topographic growth at the plateau margin and interaction with a dynamic Mio-Pliocene climate, the primary contribution of this dissertation is improved constraints on the geological history of the plateau margin. The timing of tectonic and climatic events in the southern Puna appears to lag similar events in the Bolivian Altiplano, and some consistent patterns exist in the study area.

Tectonic evolution of the Puna plateau

The study area at the margin of the Puna plateau is a geologically diverse collection of tectonic provinces, and many important structural features in the region may be inherited from previous tectonic episodes (Allmendinger *et al*., 1983; Grier *et al*., 1991; Kley and Monaldi, 2002). The Puna is composed of ranges that were uplifted in the Oligocene, and basins which accumulated sediment from the Eocene through the Pliocene (Kraemer *et al*., 1999; Carrapa *et al*., 2005). Many plateau margin and intra-plateau ranges were exhumed during the Oligocene, but development of high topography may have occurred much later (e.g., Carrapa *et al*., 2006).

While most of the mountain blocks in the region were exhumed by ~20 Ma, Mio-Pliocene deformation has been expressed by reactivation of some uplifts and incipient exhumation of others (Strecker *et al*., 2007a; Figure 7). This Mio-Pliocene deformation was complex, and its spatiotemporal distribution does not yield simple patterns. Rather it can be said that fragmentation of the foreland and creation of localized depocenters occurred in the late Miocene (Carrapa *et al*., 2008). The sequence of events during the Mio-Pliocene includes several styles of upper crustal deformation as well as major volcanic and sedimentary events (Figure 5.2). The interrelationships among these events and their relevance to development of the Puna plateau can be evaluated to a first order by comparing the timing of events.

In Vallé Santa Maria, deposits of the San José Formation record marginal marine environments which presumably document the ~12 Ma highstand of the Paraná sea (Ramos and Alonso, 1995). There are no deposits related to younger marine incursions (see Hernandez *et al.*, 2005 and Uba *et al.*, 2009) that have been recorded in Vallé Santa

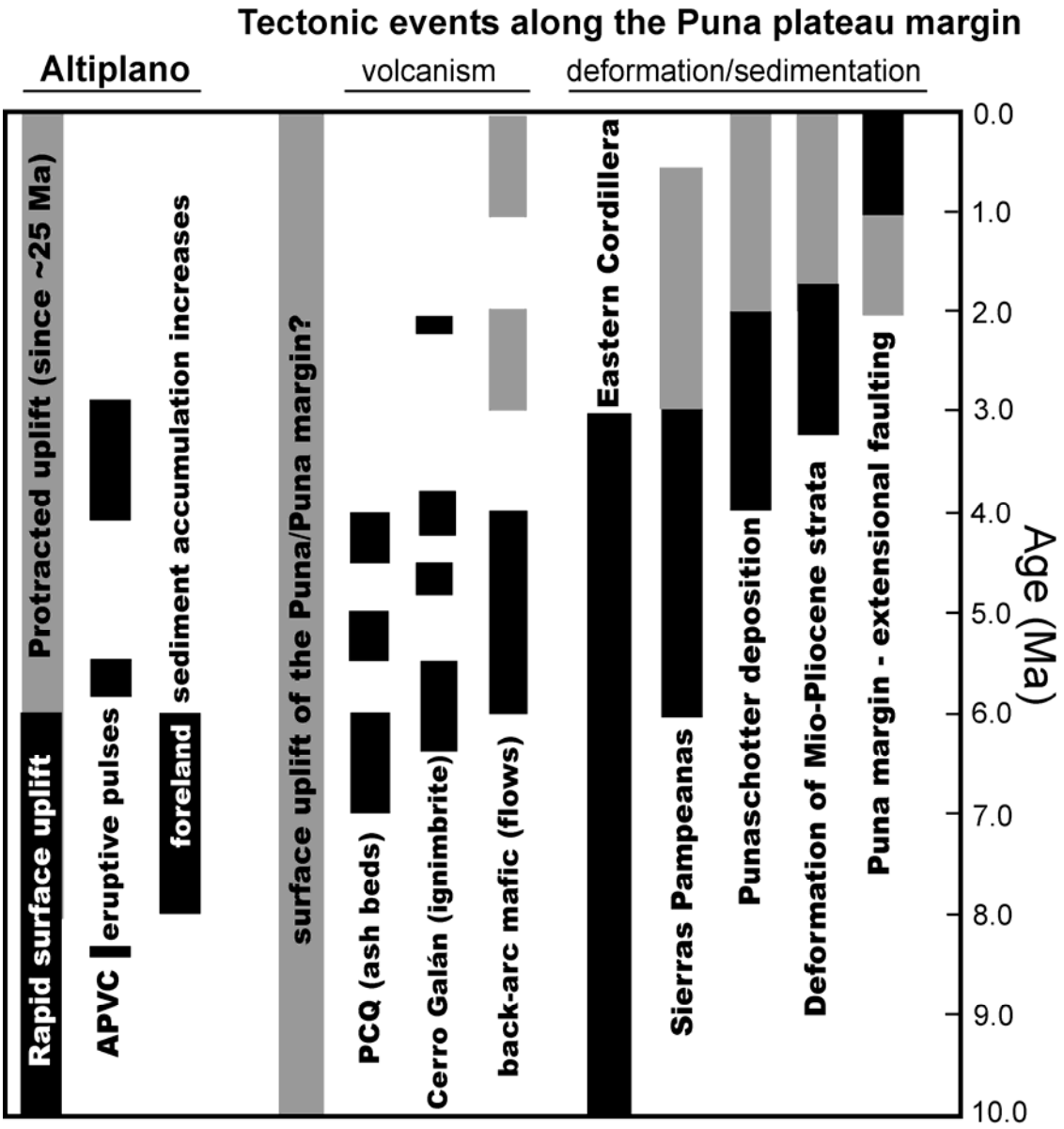

Figure 5.2: Timing of tectonic events in the Altiplano and along the southern Puna plateau margin. Intervals highlighted in black indicate well constrained events, those is gray have less certain age control or interpretation. Rapid uplift of the Altiplano after Garzione *et al*. (2008), protracted uplift of the Altiplano after Barnes and Ehlers (2009), volcanic pulses in the Altiplano-Puna Volcanic Complex (APVC) after Salisbury *et al*. (2011, Figure 10), and sediment accumulation history in the Bolivian foreland after Uba *et al*. (2007). Volcanic pulses on the Puna plateau are delineated using data from Figure 5.1, Kay *et al*. (2010), and Risse *et al*. (2008). Deformation of the Eastern Cordillera (~26°S) is after Carrapa *et al*. (in press) and constraints on uplift of the Sierras Pampeanas are from (Sobel and Strecker, 2003). Deposition of the Punashotter and deformation of Mio-Pliocene strata is from Chapter 3, with reference to Carrapa *et al*. (2008), McPherson (2008), Mortimer *et al*. (2007), and Strecker *et al*. (1989). Extension at the Puna margin is after Schoenbohm and Strecker (2009).

Maria, providing circumstantial evidence that some surface uplift occurred there between 12 and 7 Ma. Moreover, the presence of marginal marine deposits in Vallé Santa Maria at elevations close to 2,000 m above sea level indicate surface uplift of ~2 km since 12 Ma. This is consistent with the magnitude of uplift for the Altiplano over this interval. No firm constraints can be placed on the rate of surface uplift in Vallé Santa Maria and it may well have been protracted relative to that proposed for the Altiplano (Figure 5.2).

Turning to the Mio-Pliocene geologic record developed herein, a relatively richer picture emerges for the tectonic evolution of the Puna plateau margin from ~7 Ma to present. In general, the tectonic and volcanic pulse registered in the southern Puna appears to lag similar events in the Altiplano. This is consistent with southward younging trends in arc volcanism (Trumbull *et al.*, 2006). Using the distal record of volcanic ash beds, current data from 27–28°S identify probable eruptive pulses at 7–6 Ma, 5.5–5.0, and 4.5–4.0. This volcanic history indicates that rhyolite and rhyodacite eruptions in the region increased approximately coincidently with or slightly before caldera forming ignimbrites and mafic flows increased on the plateau.

If these volcanic records do indeed provide a proxy for tectonic processes on the plateau, these processes (slab steepening, delamination, regional contraction) appear to be coincident with initiation of exhumation and uplift in the foreland (Figure 5.2). It has been inferred that exhumation (and deformation) in the Eastern Cordillera progressed sequentially eastward from 14 Ma to 3 Ma (Carrapa *et al.*, in press). This overlaps with, but largely precedes, uplift of the Sierras Pampeanas that resulted in a broken foreland at the plateau margin. Uplift of individual mountain blocks in the foreland was diachronous and spatially complex, but initiated at the same time or slightly after increased volcanism

on the Puna. Thus, increased volcanism on the plateau and deformation in a broken foreland province may have resulted from the same large scale tectonic forcing.

The post 3.0 Ma record of volcanism is poorly known due to deformation within sedimentary basins beginning at this time and the resulting lack of a continuous sedimentary record. This deformation continued until the late Quaternary and overlaps in time with an extensional stress regime at the plateau margin. However, most of the deformation within sedimentary basins probably occurred in a short pulse between 3–2 Ma as evidenced by terraces and pediments approaching 2–1 Ma which are cut into deformed Mio-Pliocene strata. In general these geomorphic surfaces and younger features display minimal deformation relative to the Mio-Pliocene strata they rest on. The temporal relationships between sedimentation and deformation are the same throughout the study area, though variation in timing between basins is significant.

The essential features of this relationship, largely confined to the Pliocene, are characterized by the following sequence of events: 1) uplift of basin margin mountain blocks, 2) deposition of coarse, poorly sorted, gravel to boulder conglomerates (Punaschotter), and 3) deformation of Mio-Pliocene strata within sedimentary basins. Deposition of the Punaschotter is conformable with Mio-Pliocene strata, but likely continues during intra-basin deformation. If, as suggested in Chapter 3, deposition of Punaschotter lags uplift and exhumation of basin margin mountain blocks, then these coarse gravel deposits may be a proxy for exposure of resistant bedrock lithologies and acceleration of surface uplift. Exposure of resistant bedrock and creation of orographic barriers resulting from surface uplift both serve to reduce rates of mountain block exhumation (Sobel and Strecker, 2003).

This pattern of deformation and sedimentation is self-consistent across the region, and provides a model which can be further tested. Of particular interest is the timing of transition between the stratigraphic and geomorphic records in intermontane basins which record the culmination of deformation. Similarly, the initiation of Mio-Pliocene contractional deformation and uplift is poorly constrained in the region. It has been suggested that a number of mountain blocks began to be exhumed from beneath sedimentary cover in a contiguous foreland basin at ~6 Ma (Sobel and Strecker, 2003; Carrapa *et al*., 2008). This scenario may be similar to the modern Santa Barbara System (cf. Figure 1.3) where incipient ranges are being exhumed from sedimentary cover in a previously unbroken foreland (Hain *et al.*, in press).

Climatic evolution of the Puna plateau

Mio-Pliocene climate and environment has not been studied as intensively as the tectonic history in the region. Further, many proxy records cannot be unambiguously interpreted and chronologic control is evolving. The vertebrate fossil record provides the most widespread proxy for environment; however, it can be temporally correlated with events that are not directly related to climate (Figure 5.3). The interhemispheric exchange of terrestrial vertebrate taxa, known as the Great American Biotic Interchange (GABI; Webb, 1991, 2006), was facilitated by tectonic forces and by climatic forcing of savanna environments during the Plio-Pleistocene (Webb, 1991). The boundary between the Huayaquerian and Montehermosan South American Land Mammal Ages (SALMA) is present at Puerta de Corral Quemado, but is not tightly constrained and may be time-transgressive in the region (Flynn and Swisher, 1995).

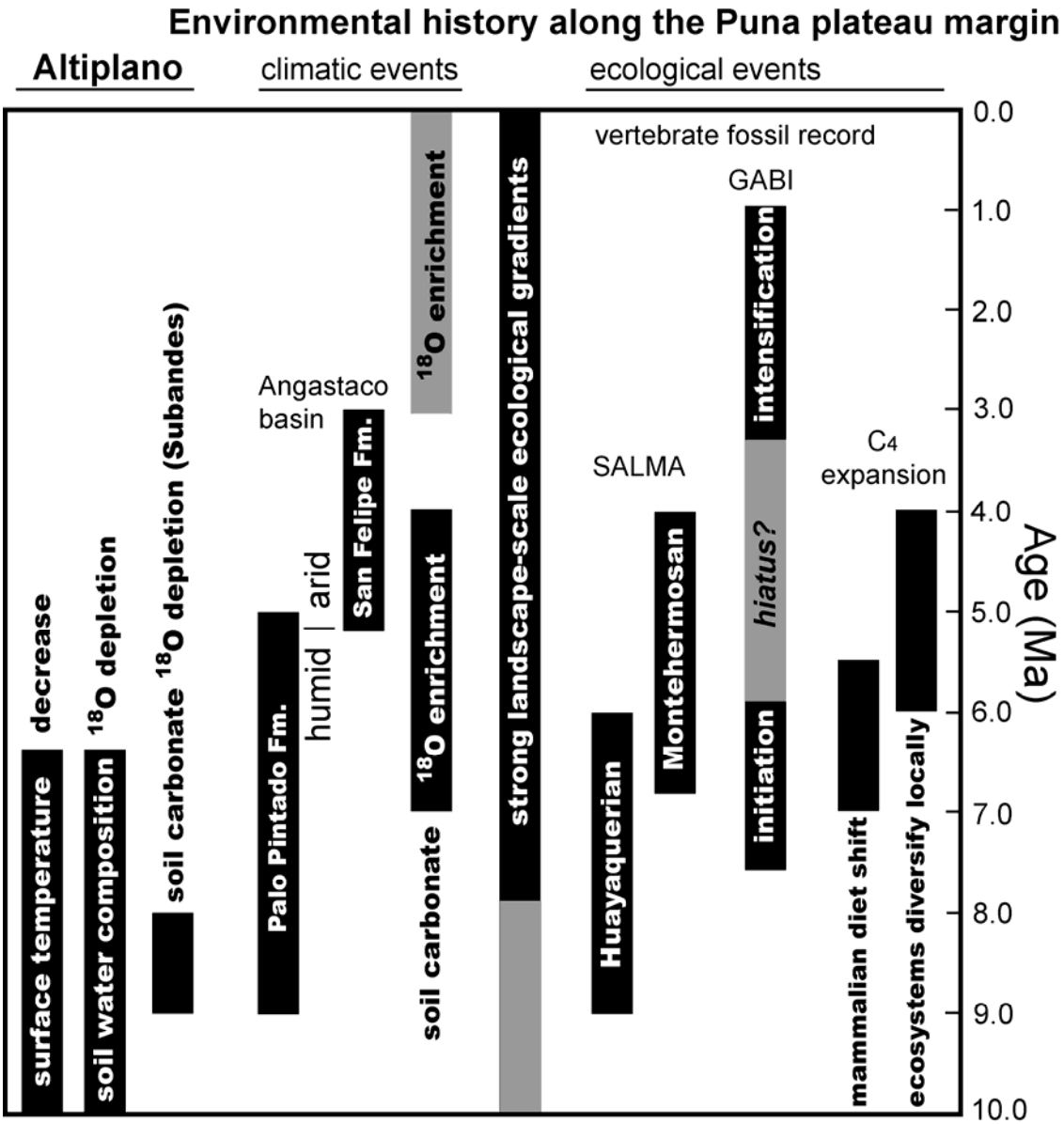

Figure 5.3: Timing of climatic and ecologic events along the Central Andean plateau. Intervals in black indicate well constrained events, those in gray have less certain age control or interpretation. In the Altiplano, surface temperature and soil water isotopic composition are documented by the Δ_{47} carbonate thermometer (Ghosh *et al*., 2006). Paleosol carbonate ^{18}O enrichment in the Subandes is from Mulch *et al*. (2010). In the Angastaco basin climatic interpretation of the Palo Pintado Formation is based on Starck and Anzotegui (2001). The climatic significance of the San Felipe Formation is after Bywater-Reyes *et al*. (2010). Paleosol carbonate ^{18}O enrichment along the Puna margin is based upon Figure 4.6, Figure 4.7, and Bywater-Reyes *et al*. (2010). Timing of SALMAs is from Butler *et al*. (1984), Flynn and Swisher (1995), and Chapter 2. Details of the GABI are from Webb (1991, 2006), Butler *et al*. (1984), and Chapter 2. Inferences regarding the timing and nature of C_4 expansion and landscape-scale ecological gradients are made explicit in Chapter 2 and Chapter 4 (see Figure 2.6 and Figure 4.6).

At present, it can be stated that the expansion of C_4 plants in the region is approximately coincident with the arrival of the earliest participants in the GABI and with the Huayaquerian/Montehermosan SALMA boundary. The nature of these relationships is not certain, but it is possible that the transition to the Montehermosan SALMA follows a regional shift to more open environments with an increasing abundance of plants using the C_4 photosynthetic pathway. This transition is first registered in the tooth enamel $\delta^{13}C$ values of herbivores, and later by paleosol carbonate $\delta^{13}C$ data (Figure 5.3). Mammalian herbivores document C_4 plants in their diet as early as 8 Ma, but a true shift to C_4 dominated diets among some taxa occured between 7 Ma and 5.5 Ma. Paleosol carbonate $\delta^{13}C$ values indicate that C_4 plants were becoming an increasingly important component of plant ecosystems at the local scale between 6 Ma and 4 Ma. Given the climatic affinities of C_4 plants this can be interpreted to result from increased aridity, development of the South American Monsoon, or perhaps a combination of the two.

While it is tempting to interpret the increase of C_4 plants in terms of climatic patterns, this is not an equivocal interpretation. The late Miocene expansion of plants using the C_4 photosynthetic pathway is a global phenomenon with uncertain and complex origins (see Tipple and Pagani, 2007). As discussed in the previous paragraphs, interpretation of ecological events (e.g., SALMA boundaries or the GABI) does not lend itself to correlation with any single variable. The late Miocene C_4 expansion in northwestern Argentina is approximately synchronous with the global record of fossil tooth enamel $\delta^{13}C$ from low latitudes (Cerling *et al*., 1997; see also Passey *et al*., 2009).

In northwestern Argentina, plants using the C_4 photosynthetic pathway underwent an ecological expansion during a period of growing topography and changing climate. The spatial density and temporal control of proxy records are not sufficient to make strong arguments about how regional and sub-regional climatic patterns may have influenced this ecological event. C_4 plants might serve as a proxy for climatic conditions favorable to their growth, namely aridity and monsoonal precipitation.

During the late Miocene and early Pliocene both monsoon intensification and aridity are invoked as climatic events. Based on vertebrate and plant fossils, depositional environments, and stratigraphic patterns of the Palo Pintado Formation, Starck and Anzotegui (2001) provide a strong case for the onset of humid conditions in the Angastaco basin beginning ~9 Ma. Subsequent deposition of the San Felipe Formation beginning ~5 Ma has been interpreted to result from increasing aridity in the region (Bywater-Reyes *et al*., 2010). In light of the strong ecological and climatic gradients that were shown to exist throughout the Mio-Pliocene geologic record (see Figure 4.8), ascribing these climatic patterns to regional changes is not tenable.

The most probable regional climatic signal is the ^{18}O enrichment documented in paleosol carbonate from Puerta de Corral Quemado and Vallé Santa Maria between 7 Ma and 4 Ma (Figure 4.7). This broad isotopic pattern can be extended to the Angastaco basin (cf. Bywater-Reyes *et al.*, 2010); thereby encompassing 2° of latitude. When compared to paleosol carbonate data from Bolivia several critical differences are noted (Figure 5.3). A very rapid ^{18}O enrichment is documented in the Subandes between 9 Ma and 8 Ma; this contrasts with the later more protracted isotopic signal along the southern Puna margin. Both of these records contrast with late Miocene data from the Altiplano

which document not only ^{18}O depletion in pedogenic carbonate, but also very strong secular changes in soil temperature and soil water isotopic composition (Ghosh *et al*., 2006). Between 10.4 Ma and 6.7 Ma, soil water $\delta^{18}O$ values decreased ~4‰ (Ghosh *et al*., 2006; Quade *et al*., 2007). This has been commonly interpreted as evidence for rapid uplift of the Altiplano during this interval, but others have proposed that threshold elevations were attained for large scale reorganization of precipitation by modest elevation gain in the Eastern Cordillera and Altiplano (Ehlers and Poulsen, 2009).

Evidence for late Miocene intensification of the South American Monsoon is nascent (Strecker *et al*., 2007a, 2007b), but strongly divergent $\delta^{18}O$ data from coeveal paleosol carbonates support spatial, and perhaps seasonal, redistribution of precipitation. Extending this pattern to the study area at the southernmost extent of the Central Andean plateau supports large scale changes in precipitation systems and further calls into question the need for rapid surface uplift of the Bolivian Altiplano to produce the paleosol proxy record observed on the Altiplano (see Mulch *et al*., 2010).

If the South American Monsoon intensified or migrated southward during the late Miocene, it did so on a substrate of growing topography and evolving orographic rainshadows. To best understand the climatic and ecological changes that took place along the southern Puna margin during the Mio-Pliocene, each stratigraphic record must be interpreted with as much geological context as possible. In some instances proxy records are divergent between stratigraphic sections, suggesting local control on climate and environment. However, individual stratigraphic sections have to be interpreted cautiously because locally heterogenous environments may be recorded more or less randomly in any single section, this is especially true for paleosol carbonate $\delta^{13}C$ data.

Conclusions

In the late Miocene, volcanism increased on the Puna plateau and intense deformation commenced along the plateau margin. These were synchronous and might result from tectonic processes at the plate margin or in deep-crustal levels beneath the plateau. Deformation at the plateau margin was manifested as out-of-sequence uplift of mountain blocks along preexisting zones of structural weakness. In some cases this resulted in uplift of existing mountain blocks that were exhumed during the Oligocene; in other cases new mountain blocks were exhumed from beneath Mesozoic and Cenozoic sedimentary cover in the foreland. By the Quaternary, Mio-Pliocene sedimentary basins had been deformed and the plateau margin was in a neutral to extensional stress regime.

The climatic and ecological record during this period is complex, and strong landscape-scale environmental gradients existed from 10 Ma to present. The early part of the Mio-Pliocene record might be influenced by intensification or southward migration of the South American Monsoon, whereas the later part of the record is characterized by local aridification and shifting environments related to complex topographic growth. During these events the global expansion of C_4 plants proceeded in NW Argentina.

In favorable circumstances, the Mio-Pliocene geologic record along the Puna margin can be interpreted with sub-100 ka temporal resolution. This is most easily achieved through a combination of geochronological methods (magnetic polarity, radioisotopic dating, tephrostratigraphy). Correlation of volcanic ash beds provides a precise and accurate method for comparison of widely separated stratigraphic sections. Tephrostratigraphic work is not only an integrative geochronological method, but is also one approach to deciphering crustal-scale tectonic processes.

Outstanding questions

Volcanic history of the southern Puna

The volcanic history of the southern Puna plateau is well constrained. Robust new age data are now available for both Cerro Galán and back-arc basaltic lavas in the region (Kay *et al*., in press; Risse *et al*., 2008), in addition to detailed geochemical and petrological models (Kay *et al*., 2010; Drew *et al*., 2009). These data, and many other indicate that at the latitude of the southern Puna both arc magmatism and intra-plateau magmatism increased since ~10 Ma and likely provide a record of tectonic processes (Trumbull *et al.*, 2006).

The distal record of explosive volcanism has been exploited to enrich the understanding of unique volcanic provinces (cf. Perkins and Nash, 2002; Nash *et al.*, 2006), and might prove fruitful for the southern Puna. Volcanic ash beds in sedimentary basins at the plateau margin provide a rich record of silicic volcanism from 5.6 Ma to 3.5 Ma (Chapter 3). This could be extended to 7–3Ma, and to the Quaternary record with targeted sampling. Such efforts would appropriately test the suggestion of pulsed magmatism between 10 Ma and present (Figures 5.1 and 5.2). Preservation and exposure of volcanic ash beds is better in marginal basins than on the plateau, resulting in a more detailed record. A detailed record of volcanism would characterize individual eruptive centers more accurately, and highlight possible crustal-scale tectonic events.

The significance of eolian strata at Puerta de Corral Quemado

In the interval from ~7 Ma to 5.5 Ma, thick eolian deposits accumulated at PCQ. The environmental significance of these deposits is highlighted by reference to modern eolian systems which erode material on the Puna plateau and deposit it at the plateau

margin (cf. Figure 1.5). Eolian deposits are not described prior to this interval; however, lenses of eolian deposits can be found in the strata overlying this interval, in Quaternary deposits, and modern environments. The onset of eolian deposition in the basin may record a fundamental and permanent change. The thick sequence of eolian sandstones in the late Miocene accumulated very rapidly and is laterally extensive, suggesting that a true change in sedimentary processes occurred rather than a lateral shift in depositional environments. Late Miocene eolian deposition may result from topographic enhancement at the plateau margin such that sediment began accumulating in the leeside of the plateau from dominant northwesterly winds.

Detailed study of this stratigraphic interval would address this hypothesis and serve several other objectives. Volcanic ash beds in the eolian interval are common and well-preserved; focused tephrostratigraphic work in this interval would extend the record of explosive volcanism. Improved geochronology and stratigraphy of this interval would also be beneficial to constraining the mammalian diet shifts that occurred concurrently.

The geologic record from 3.5 Ma to present

The upper age bounds on many sections, including Fiambalá, Puerta de Corral Quemado, and Vallé Santa Maria are poorly constrained. The best age control for the transition between the stratigraphic record and the geomorphic record is the collection of fission-track ages for ash beds in Vallé Santa Maria (Strecker *et al*. 1989). Constraining this transition more tightly will provide valuable information on the spatio-temporal pattern of deformation. Importantly, when did contractional deformation migrate to sedimentary basins and when did it culminate. Combining geochronological controls on

stratigraphic and geomorphic records in the basins at the plateau margin should also be beneficial to understanding environmental change during this poorly sampled interval.

APPENDIX A

STRATIGRAPHIC AND GEOCHEMICAL DATA FOR VOLCANIC ASH BEDS

Introduction

The location, stratigraphic position, and major elemental composition of volcanic ash beds is presented in Tables A.1 through A.19, organized by stratigraphic section from south to north. Table A.20 provides the major elemental composition of Quaternary ash beds, and Table A.21 provides compositional data for volcanic ash samples originating from researchers associated with Universität Potsdam, Germany. Table A.22 provides trace element concentrations of volcanic glass separates from all analyzed samples. Table A.23 is a summary of $^{40}Ar/^{39}Ar$ results for eruptive minerals in volcanic ash beds, and the details of these experiments are presented in Table A.24.

Two figures are also included. Figure A.1 provides field photographs that were used to match the primary section at Puerta de Corral Quemado (Table A.5) with the previous work of Latorre *et al*. (1997). Figure A.2 is a preliminary tephrostratigraphic panel for Vallé Santa Maria. This provides a fuller framework than was presented in Chapter 4, highlighting potential correlations to Puerta de Corral Quemado, Angastaco and to Universität Potsdam samples from Vallé Santa Maria.

Table A.1: Stratigraphy and composition of volcanic ash beds from Fiambalá section
(base of section = 27.6346°S, 67.6871°W; total thickness ~1 km)

Sample	Lat	Lon	strat	n*	SiO2	TiO2	ZrO2	Al2O3	Fe2O3	MnO	MgO	CaO	BaO	Na2O	K2O	F	Cl	H2O	Total	Comment
	(°S)	(°W)	m																	thickness (m), lithology
FIA 823	27.6346	67.6874	47.1		*not analyzed*															*0.005, blue/gray ss*
FIA 824	27.6346	67.6874	47.2		*not analyzed*															*0.005, blue/gray ss*
FIA 825	27.6362	67.6889	139.7		*not analyzed*															*0.3, blue/gray interbeds ss*
FIA 826	27.6362	67.6892	162.3	12	73.8	0.10	0.07	12.6	0.59	0.08	0.08	0.62	0.06	2.9	5.2		0.11	3.3	99.6	*0.1, tuffaceous ss*
					1.3	*0.03*	*0.07*	*0.5*	*0.23*	*0.05*	*0.03*	*0.17*	*0.04*	*0.2*	*0.3*		*0.06*	*1.0*	*0.3*	
FIA 826	*mode 2*			5	70.9	0.11	0.10	12.9	1.10	0.11	0.09	0.47	0.00	3.2	5.7		0.23	5.0	99.8	
					0.3	*0.09*	*0.09*	*0.2*	*0.02*	*0.02*	*0.03*	*0.06*	*0.00*	*0.2*	*0.1*		*0.01*	*0.4*	*0.1*	
FIA 826	*mode 3*			1	68.4	0.29	0.19	13.9	1.38	0.10	0.19	0.66	0.05	3.5	5.8	0.00	0.20	5.3	99.9	
FIA 826	*mode 3*			1	70.1	0.32	0.00	13.7	1.42	0.05	0.10	0.60	0.00	3.5	5.8	0.00	0.23	4.5	100.2	
FIA 827	27.6363	67.6894	171.1		*carbonate nodule; see appendix B for stable isotope data*															*1.5, paleosol*
FIA 828	27.6364	67.6893	174.1		*not analyzed*															*0.1, green tuff, fossil wood*
FIA 829	27.6365	67.6894	184.0		*carbonate nodule; see appendix B for stable isotope data*															*2, paleosol*
FIA 830	27.6365	67.6894	186.1		*not analyzed*															*0.1, tuff in bedded ss*
FIA 831	27.6365	67.6894	186.2		*carbonate nodule; see appendix B for stable isotope data*															*2, paleosol*
FIA 832	27.6367	67.6908	261.0	24	74.9	0.09	0.07	12.1	0.76	0.05	0.07	0.78	0.08	2.0	5.3	0.03	0.14	5.5	101.9	*0.1; fine white tuff*
					0.7	*0.08*	*0.08*	*0.2*	*0.11*	*0.05*	*0.03*	*0.07*	*0.07*	*0.2*	*0.2*	*0.03*	*0.05*	*0.8*	*0.6*	
FIA 833	27.6367	67.6907	262.7	10	73.9	0.12	0.11	11.9	0.78	0.0	0.1	0.79	0.03	2.6	5.4	0.01	0.15	4.5	100.4	*0.2, pale gray tuff*
					0.4	*0.02*	*0.05*	*0.2*	*0.02*	*0.0*	*0.0*	*0.05*	*0.02*	*0.2*	*0.2*	*0.02*	*0.02*	*0.4*	*0.2*	
FIA 834	27.6369	67.6910	275.4	13	72.6	0.10	0.08	12.5	0.77	0.05	0.09	0.93	0.06	2.9	5.1	0.02	0.12	4.9	100.3	*18.5, gray ss w/ pumice*
					0.3	*0.03*	*0.05*	*0.2*	*0.04*	*0.02*	*0.02*	*0.04*	*0.02*	*0.2*	*0.3*	*0.02*	*0.01*	*0.6*	*0.3*	
FIA 835	27.6370	67.6913	298.4	11	73.4	0.11	0.08	12.5	0.72	0.04	0.08	0.78	0.07	3.1	5.2	0.01	0.09	4.3	100.4	*0.1, tuff*
					0.3	*0.03*	*0.05*	*0.1*	*0.04*	*0.02*	*0.02*	*0.05*	*0.03*	*0.3*	*0.3*	*0.01*	*0.01*	*0.4*	*0.2*	
FIA 836	27.6370	67.6913	299.5	15	72.6	0.10	0.07	12.2	0.73	0.06	0.08	0.75	0.06	2.5	5.4	0.02	0.12	6.2	100.8	*0.5, tuff*
					0.3	*0.04*	*0.04*	*0.1*	*0.04*	*0.02*	*0.02*	*0.02*	*0.02*	*0.3*	*0.2*	*0.02*	*0.01*	*0.7*	*0.4*	
FIA 837	27.6373	67.6914	300.4	15	72.6	0.12	0.05	12.3	0.70	0.05	0.07	0.76	0.05	2.6	5.4	0.02	0.13	5.6	100.4	*0.05, tuff in med-coarse ss*
					0.3	*0.03*	*0.05*	*0.1*	*0.03*	*0.02*	*0.01*	*0.02*	*0.02*	*0.2*	*0.1*	*0.03*	*0.01*	*0.6*	*0.2*	
FIA 838	27.6373	67.6914	301.1	14	73.2	0.10	0.05	12.5	0.74	0.05	0.08	0.80	0.05	2.9	5.2	0.02	0.10	4.5	100.4	*0.1, tuff*
					0.2	*0.03*	*0.04*	*0.1*	*0.03*	*0.02*	*0.01*	*0.02*	*0.03*	*0.3*	*0.2*	*0.02*	*0.01*	*0.3*	*0.3*	

Table A.1 (*continued*)

Sample	Lat	Lon	strat	n*	SiO2	TiO2	ZrO2	Al2O3	Fe2O3	MnO	MgO	CaO	BaO	Na2O	K2O	F	Cl	H2O	Total	Comment
	(°S)	(°W)	m																	thickness (m), lithology
FIA 839	27.6373	67.6914	302.0	15	72.9	0.11	0.06	12.3	0.71	0.04	0.08	0.74	0.05	2.7	5.3	0.03	0.12	5.4	100.5	*0.3, tuff*
					0.3	*0.02*	*0.05*	*0.1*	*0.05*	*0.02*	*0.01*	*0.02*	*0.03*	*0.2*	*0.2*	*0.03*	*0.01*	*0.4*	*0.3*	
Pumiceous sandstone			302.3		*not sampled*															*12, pumice throughout*
FIA 840	27.6374	67.6916	314.3	15	73.1	0.09	0.04	12.1	0.66	0.05	0.06	0.69	0.06	2.5	5.5	0.03	0.13	5.4	100.3	*0.4–0.7, tuff*
					0.4	*0.03*	*0.04*	*0.1*	*0.05*	*0.02*	*0.01*	*0.02*	*0.03*	*0.2*	*0.2*	*0.03*	*0.01*	*0.9*	*0.4*	
FIA 841	27.6374	67.6916	316.3	15	73.3	0.09	0.06	12.0	0.63	0.06	0.06	0.61	0.06	2.4	5.5	0.02	0.13	5.9	100.7	*1.4–1.7, tuff*
					0.3	*0.02*	*0.04*	*0.1*	*0.04*	*0.02*	*0.01*	*0.02*	*0.02*	*0.2*	*0.1*	*0.02*	*0.01*	*0.7*	*0.4*	
Pumiceous sandstone			317.4		*not sampled*															*6.2, soft-sed. deformation*
FIA 842	27.6374	67.6918	327.1	11	72.9	0.10	0.06	12.2	0.68	0.06	0.11	0.66	0.06	2.4	5.4	0.03	0.06	6.1	100.8	*0.05, tuff w/ crystal base*
					0.3	*0.02*	*0.05*	*0.1*	*0.03*	*0.02*	*0.01*	*0.03*	*0.02*	*0.2*	*0.1*	*0.02*	*0.01*	*0.7*	*0.2*	
FIA 843	27.6374	67.6918	327.9	20	72.3	0.10	0.07	12.1	0.64	0.05	0.09	0.66	0.05	2.3	5.2		0.07	6.3	100.0	*tuff*
					0.3	*0.04*	*0.05*	*0.1*	*0.04*	*0.03*	*0.02*	*0.03*	*0.04*	*0.1*	*0.1*		*0.01*	*0.5*	*0.2*	
FIA 844	27.6374	67.6918	329.4		*not analyzed*															*0.2, tuff*
Pumiceous sandstone			329.6		*not sampled*															*3–4, soft sed. deformation*
FIA 845	27.6373	67.6920	332.7	23	72.3	0.23	0.09	13.2	1.21	0.05	0.21	1.18	0.07	2.2	5.0	0.04	0.12	6.1	101.9	*tuff*
					0.7	*0.11*	*0.11*	*0.2*	*0.12*	*0.05*	*0.05*	*0.05*	*0.07*	*0.2*	*0.3*	*0.06*	*0.03*	*0.7*	*0.7*	
Pumiceous sandstone					*not sampled*															
FIA 846	27.6373	67.6923	349.2	23	70.5	0.16	0.06	13.5	0.99	0.04	0.14	1.21	0.08	2.7	5.5	0.03	0.12	5.2	100.2	*0.2, tuff*
					0.7	*0.05*	*0.04*	*0.5*	*0.08*	*0.03*	*0.02*	*0.08*	*0.03*	*0.3*	*0.3*	*0.03*	*0.02*	*0.9*	*0.5*	
FIA 847	27.6376	67.6937	431.1	20	73.2	0.12	0.08	11.8	0.62	0.08	0.06	0.41	0.01	2.7	5.3		0.17	5.3	99.8	*0.8, white lenticular tuff*
					0.5	*0.04*	*0.07*	*0.1*	*0.05*	*0.03*	*0.01*	*0.03*	*0.02*	*0.2*	*0.2*		*0.02*	*0.7*	*0.3*	
Approximate base silts			431.9																	*~185, bedded siltstone*
FIA 848	27.6374	67.6941	456.2		*not analyzed*															*0.1, laminated tuff*
FIA 849	27.6373	67.6943	472.7		*not analyzed*															*0.1, laminated tuff*
FIA 850	27.6370	67.6949	529.3	16	73.1	0.07	0.07	12.0	0.76	0.05	0.06	0.76	0.07	2.5	5.4		0.12	4.7	99.7	*0.1, white tuff*
					0.4	*0.05*	*0.07*	*0.1*	*0.05*	*0.03*	*0.02*	*0.03*	*0.05*	*0.1*	*0.2*		*0.01*	*0.3*	*0.4*	
FIA 850	*mode 2*			1	73.6	0.11	0.12	11.9	0.99	0.09	0.10	0.97	0.09	2.8	4.8	0.00	0.10	4.5	100.0	
FIA 850	*mode 2*			1	72.5	0.19	0.00	12.2	1.12	0.04	0.14	1.08	0.04	2.7	4.5	0.00	0.10	5.3	99.9	

Table A.1 (*continued*)

Sample	Lat	Lon	strat	n*	SiO2	TiO2	ZrO2	Al2O3	Fe2O3	MnO	MgO	CaO	BaO	Na2O	K2O	F	Cl	H2O	Total	Comment
	(°S)	(°W)	m																	thickness (m), lithology
Bedded gypsum in clays			605																	*>10, oxidized Fe in clay*
FIA 851	27.6384	67.6979	639.4		*not analyzed*															*tuff in coarse pebbly ss*
FIA 852	27.6384	67.6979	643.4	30	75.2	0.09	0.08	12.2	0.69	0.06	0.07	0.77	0.06	2.3	5.2	0.06	0.12	4.9	101.7	*0.1, lenticular tuff*
					0.5	*0.10*	*0.10*	*0.2*	*0.11*	*0.05*	*0.04*	*0.07*	*0.05*	*0.3*	*0.3*	*0.12*	*0.03*	*0.6*	*0.5*	
Base of gravel			643.5																	*~50, conglomerate & ss*
FIA 853			670.8	16	72.8	0.12	0.06	12.1	0.70	0.07	0.08	0.86	0.04	2.6	5.3		0.10	4.8	99.5	*tuffaceous lens in ss*
					1.2	*0.05*	*0.06*	*0.4*	*0.08*	*0.04*	*0.04*	*0.09*	*0.03*	*0.3*	*0.2*		*0.02*	*1.3*	*0.4*	
Cobble	27.6387	67.6994	703.8																	*<1, ~top of gravel unit*
Orange/pink silts interbedded with gravels and sands																				*~200 m*

*Elemental composition of volcanic glass by Electron Probe Microanalysis (cf. Nash, 1992), n=number of shards, for n≥4 average and 1σ standard deviation are reported.

Table A.2: Stratigraphy and composition of volcanic ash beds from Guanchin section
(base of section = 27.6874°S, 67.8203°W; total thickness ~250 m)

Sample	Lat	Lon	strat	n*	SiO2	TiO2	ZrO2	Al2O3	Fe2O3	MnO	MgO	CaO	BaO	Na2O	K2O	F	Cl	H2O	Total	Comment
	(°S)	(°W)	m																	thickness (m), lithology
GUA 810	27.6874	67.8203	6	15	71.9	0.11	0.05	12.6	0.71	0.05	0.12	0.86	0.06	2.9	4.4		0.10	6.0	99.8	*1.7, tuff, sandy upper 0.5 m*
					0.4	*0.04*	*0.05*	*0.1*	*0.06*	*0.02*	*0.02*	*0.03*	*0.03*	*0.2*	*0.2*		*0.01*	*0.6*	*0.3*	
GUA 811	27.6853	67.8193	24	15	72.9	0.08	0.06	12.4	0.61	0.05	0.06	0.47	0.05	3.0	5.0		0.12	4.9	99.7	*0.7, lenticular tuff, bedded*
					0.5	*0.04*	*0.06*	*0.3*	*0.08*	*0.03*	*0.03*	*0.06*	*0.05*	*0.1*	*0.1*		*0.01*	*0.5*	*0.3*	
GUA 812	27.6857	67.8187	37	12	72.5	0.14	0.07	12.6	0.75	0.04	0.07	0.87	0.09	2.9	5.0		0.11	4.9	100.0	*0.2, massive tuff*
					0.7	*0.03*	*0.06*	*0.3*	*0.07*	*0.02*	*0.02*	*0.05*	*0.04*	*0.2*	*0.1*		*0.01*	*0.4*	*0.7*	
GUA 813	27.6857	67.8184	59	13	73.2	0.12	0.08	12.4	1.07	0.03	0.13	1.03	0.05	2.8	4.9	0.01	0.08	4.5	100.3	*0.02, tuff*
					0.7	*0.06*	*0.05*	*0.4*	*0.15*	*0.03*	*0.05*	*0.10*	*0.03*	*0.2*	*0.2*	*0.02*	*0.02*	*0.5*	*0.3*	
GUA 813	*mode 2*			1	73.7	0.11	0.00	12.4	0.52	0.07	0.08	0.41	0.03	3.2	5.1	0.11	0.15	4.9	100.7	
GUA 813	*mode 2*			1	73.5	0.16	0.07	12.3	0.52	0.14	0.03	0.39	0.02	2.7	5.3	0.08	0.11	5.2	100.4	
Gravel			63																	*6, pebble to cobble*
GUA 814	27.6875	67.8156	82	18	73.3	0.09	0.08	11.9	0.69	0.06	0.07	0.63	0.06	2.9	4.7		0.13	5.4	100.0	*2, tuff, upper 1.5 m sandy*
					0.6	*0.04*	*0.07*	*0.1*	*0.07*	*0.03*	*0.02*	*0.02*	*0.03*	*0.3*	*0.3*		*0.02*	*1.1*	*0.3*	
GUA 815	27.6879	67.8151	100	5	67.1	0.43	0.04	14.7	2.12	0.08	0.55	2.14	0.04	3.4	3.8		0.11	5.3	99.9	*1.5, pumiceous base (0.2 m)*
					0.8	*0.09*	*0.05*	*0.1*	*0.03*	*0.03*	*0.03*	*0.10*	*0.04*	*0.2*	*0.1*		*0.02*	*0.5*	*0.4*	
Gravel			127																	*3-5, occassional cobble*
GUA 816	27.6867	67.8147	143	15	74.5	0.15	0.06	12.0	0.73	0.03	0.10	0.61	0.05	2.8	5.1		0.13	4.2	100.4	*0.01, tuff in med.-coarse ss*
					0.8	*0.06*	*0.07*	*0.5*	*0.14*	*0.04*	*0.03*	*0.04*	*0.05*	*0.3*	*0.2*		*0.01*	*0.8*	*0.8*	
GUA 816	*mode 2*			1	71.9	0.15	0.15	14.1	0.79	0.01	0.10	1.73	0.00	3.6	4.3		0.09	4.2	101.1	
GUA 816	*mode 2*			1	71.1	0.08	0.00	14.5	0.73	0.00	0.08	1.99	0.06	3.6	4.1		0.09	3.8	100.1	
Gray band	27.6862	67.8136	175																	*1.5, gray band (slumped?)*
GUA 817	27.6861	67.8147	185	11	68.0	0.37	0.11	14.2	1.90	0.05	0.53	1.82	0.06	3.4	4.1	0.02	0.07	5.6	100.2	*> 2, gray tuffaceous band*
					0.6	*0.06*	*0.09*	*0.2*	*0.12*	*0.03*	*0.06*	*0.12*	*0.03*	*0.2*	*0.2*	*0.03*	*0.02*	*0.6*	*0.4*	
GUA 818	27.6856	67.8147	192		*not analyzed*															*3, pumiceous base (0.3 m)*
GUA 819			206	15	74.0	0.14	0.09	11.8	0.69	0.03	0.09	0.80	0.07	2.8	4.7	0.00	0.08	4.9	100.1	*4.5, white pumiceceous base*
					0.5	*0.04*	*0.07*	*0.2*	*0.04*	*0.02*	*0.02*	*0.05*	*0.03*	*0.2*	*0.2*	*0.00*	*0.01*	*0.6*	*0.5*	
GUA 819	*mode 2*			1	73.1	0.15	0.17	11.9	0.71	0.07	0.09	0.47	0.05	3.1	4.9	0.02	0.13	5.1	99.9	
GUA 819	*mode 2*			1	73.4	0.06	0.00	12.2	0.65	0.00	0.04	0.46	0.06	2.4	4.7	0.04	0.14	5.2	99.3	

Table A.2 (*continued*)

Sample	Lat	Lon	strat	n	SiO2	TiO2	ZrO2	Al2O3	Fe2O3	MnO	MgO	CaO	BaO	Na2O	K2O	F	Cl	H2O	Total	Comment
	(°S)	(°W)	m																	thickness (m), lithology
GUA 820			210		*not analyzed*															*4.5, dark gray tuffaceous ss*
GUA 821			223	13	74.6	0.11	0.04	12.2	0.72	0.05	0.11	0.81	0.05	3.0	4.6		0.11	4.0	100.3	*2, blue/gray ss below congl.*
					0.7	*0.04*	*0.05*	*0.2*	*0.05*	*0.03*	*0.02*	*0.04*	*0.03*	*0.2*	*0.2*		*0.01*	*0.9*	*0.3*	

*Elemental composition of volcanic glass by Electron Probe Microanalysis (cf. Nash, 1992), n=number of shards, for n≥4 average and 1σ standard deviation are reported.

Table A.3: Stratigraphy and composition of volcanic ash beds from San Fernando section #1
(base of section = 27.3421°S, 66.9076°W; total thickness ~20 m, ash beds dip ~5° SSW)

Sample	Lat	Lon	strat	n*	SiO2	TiO2	ZrO2	Al2O3	Fe2O3	MnO	MgO	CaO	BaO	Na2O	K2O	F	Cl	H2O	Total	Comment
	(°S)	(°W)	m																	thickness (m), lithology
PCQ 725	27.3421	66.9076	0.0	16	72.1	0.16	0.06	13.1	0.95	0.06	0.19	1.17	0.04	3.0	4.5	0.00	0.12	5.2	100.6	*2, tuff with biotite rich base*
					0.4	*0.04*	*0.05*	*0.2*	*0.08*	*0.03*	*0.03*	*0.04*	*0.03*	*0.5*	*0.4*	*0.01*	*0.01*	*0.6*	*0.2*	
PCQ 726			13	20	72.1	0.09	0.06	12.9	0.87	0.07	0.13	0.73	0.07	3.0	4.9	0.00	0.15	5.4	100.5	*0.5, sampled base of tuff*
					0.2	*0.03*	*0.05*	*0.4*	*0.04*	*0.02*	*0.01*	*0.03*	*0.03*	*0.3*	*0.4*	*0.00*	*0.01*	*0.3*	*0.4*	
PCQ 726	*replicate analysis*			19	71.8	0.07	0.08	12.7	0.90	0.08	0.14	0.74	0.06	2.8	4.9	0.01	0.14	5.9	100.3	
					0.6	*0.04*	*0.06*	*0.4*	*0.05*	*0.04*	*0.02*	*0.03*	*0.04*	*0.2*	*0.4*	*0.02*	*0.01*	*0.6*	*0.4*	
PCQ 727			14.7	14	72.3	0.13	0.07	13.3	0.86	0.08	0.13	0.79	0.06	3.1	4.9	0.02	0.16	6.2	102.0	*0.1, tuff =1841 m level at PCQ*
					0.4	*0.02*	*0.04*	*0.2*	*0.05*	*0.02*	*0.01*	*0.01*	*0.03*	*0.3*	*0.3*	*0.03*	*0.01*	*0.4*	*0.2*	
PCQ 728			16.2	16	72.7	0.13	0.07	13.0	0.92	0.09	0.14	0.72	0.06	3.0	5.1	0.04	0.16	5.7	101.8	*0.1, tuff*
					0.5	*0.03*	*0.05*	*0.1*	*0.06*	*0.02*	*0.02*	*0.08*	*0.03*	*0.2*	*0.5*	*0.03*	*0.03*	*1.0*	*0.3*	
PCQ 729			17.0	5	70.9	0.15	0.05	13.8	1.44	0.08	0.19	1.17	0.05	3.2	4.7	0.04	0.17	5.8	101.7	*0.1, tuff =1848 m level at PCQ*
					0.4	*0.04*	*0.04*	*0.2*	*0.04*	*0.02*	*0.02*	*0.05*	*0.04*	*0.3*	*0.6*	*0.01*	*0.02*	*0.5*	*0.3*	
PCQ 729	*mode 2*			4	70.3	0.11	0.03	13.1	1.21	0.09	0.14	0.89	0.06	2.9	5.1	0.03	0.18	6.7	100.7	
					2.5	*0.02*	*0.04*	*0.5*	*0.14*	*0.02*	*0.02*	*0.07*	*0.04*	*0.5*	*0.4*	*0.02*	*0.03*	*1.1*	*1.8*	
PCQ 729	*mode 3*			1	73.2	0.08	0.00	12.3	0.89	0.11	0.10	0.59	0.05	2.6	5.9	0.07	0.14	5.6	101.6	
PCQ 729	*mode 3*			1	72.8	0.07	0.05	12.6	0.85	0.10	0.09	0.62	0.04	2.3	6.0	0.07	0.17	5.7	101.3	
PCQ 729	*mode 3*			1	74.6	0.15	0.01	12.4	0.81	0.04	0.10	0.88	0.09	3.1	4.6	0.05	0.09	4.6	101.5	
PCQ 730			17.6	12	72.1	0.13	0.06	12.9	0.91	0.10	0.13	0.77	0.05	3.1	4.7	0.01	0.13	6.1	101.1	*0.25, tuff with detrital grains*
					0.6	*0.03*	*0.07*	*0.1*	*0.04*	*0.03*	*0.02*	*0.04*	*0.02*	*0.2*	*0.3*	*0.01*	*0.01*	*0.5*	*0.3*	
PCQ 730	*mode 2*			7	74.2	0.14	0.05	11.9	0.72	0.04	0.10	0.81	0.04	2.8	5.1	0.00	0.12	4.6	100.5	
					0.6	*0.03*	*0.05*	*0.1*	*0.05*	*0.02*	*0.02*	*0.03*	*0.03*	*0.3*	*0.4*	*0.01*	*0.03*	*1.0*	*0.4*	
Ash bed with detrital			~20		*not sampled*															*in opposite wall of quebrada*

*Elemental composition of volcanic glass by Electron Probe Microanalysis (cf. Nash, 1992), n=number of shards, for n≥4 average and 1σ standard deviation are reported.

Table A.4: Stratigraphy and composition of volcanic ash beds from San Fernando section #2
(base of section = 27.3234°S, 66.8962°W; total thickness ~50 m, ash beds dip ~15° SSW)

Sample	Lat	Lon	strat	n*	SiO2	TiO2	ZrO2	Al2O3	Fe2O3	MnO	MgO	CaO	BaO	Na2O	K2O	F	Cl	H2O	Total	Comment
	(°S)	(°W)	m																	thickness (m), lithology
PCQ 734	27.3234	66.8962	0.0	12	73.2	0.09	0.05	12.4	0.66	0.07	0.07	1.00	0.11	1.2	5.0	0.03	0.11	6.4	100.5	*lower tuff of triplet*
					0.3	*0.02*	*0.01*	*0.1*	*0.01*	*0.02*	*0.01*	*0.04*	*0.01*	*0.2*	*0.5*	*0.03*	*0.01*	*0.7*	*0.3*	
PCQ 734	*mode 2?*			1	72.1	0.15	0.06	13.1	0.86	0.08	0.12	0.78	0.07	1.0	4.5	0.00	0.13	8.4	101.3	
PCQ 734	*mode 2?*			1	73.1	0.08	0.04	12.4	0.61	0.05	0.08	0.62	0.06	0.9	4.2	0.08	0.08	8.3	100.6	
PCQ 734	*mode 2?*			1	73.3	0.16	0.04	13.1	0.76	0.05	0.08	0.61	0.08	2.1	5.5	0.00	0.14	4.0	99.9	
PCQ 735			3.6		*not analyzed*															*middle tuff of triplet*
PCQ 736			4.6	13	73.3	0.08	0.03	12.4	0.61	0.06	0.08	0.66	0.07	2.7	5.6	0.00	0.08	5.0	100.6	*upper tuff of triplet*
					0.6	*0.03*	*0.04*	*0.2*	*0.04*	*0.02*	*0.02*	*0.03*	*0.03*	*0.4*	*0.4*	*0.00*	*0.01*	*0.9*	*0.3*	
PCQ 736	*mode 2*			5	72.0	0.10	0.03	12.4	0.74	0.05	0.12	0.87	0.04	2.5	5.5	0.00	0.10	6.2	100.8	
					0.5	*0.02*	*0.02*	*0.1*	*0.02*	*0.02*	*0.02*	*0.04*	*0.05*	*0.4*	*0.3*	*0.00*	*0.01*	*0.6*	*0.3*	
PCQ 732	27.3243	66.8970	15.6		*not analyzed*															*0.4, tuff in gray/brown ss*
PCQ 733	27.3243	66.8970	25.0	20	72.8	0.10	0.06	12.4	0.65	0.07	0.07	0.48	0.05	2.4	6.2	0.07	0.13	6.1	101.6	*0.6, tuff in gray/brown ss*
					0.5	*0.03*	*0.05*	*0.2*	*0.10*	*0.02*	*0.02*	*0.07*	*0.06*	*0.3*	*0.3*	*0.02*	*0.01*	*0.6*	*0.3*	
PCQ 731	27.3273	66.8977	~50	5	73.0	0.04	0.05	12.3	0.52	0.14	0.03	0.31	0.02	2.7	6.1		0.09	4.9	100.2	*0.1, tuff, west side of road*
					0.6	*0.05*	*0.06*	*0.4*	*0.11*	*0.06*	*0.01*	*0.06*	*0.02*	*0.3*	*0.4*		*0.03*	*1.0*	*0.4*	
PCQ 731	*mode 2*			7	73.5	0.10	0.11	12.0	0.75	0.07	0.07	0.62	0.04	2.6	5.6		0.12	4.7	100.2	
					1.3	*0.05*	*0.05*	*0.2*	*0.10*	*0.03*	*0.01*	*0.08*	*0.04*	*0.5*	*0.8*		*0.02*	*1.1*	*0.3*	
PCQ 731	*mode 3*			1	71.5	0.31	0.00	12.3	1.46	0.03	0.15	0.73	0.00	2.5	6.2		0.08	4.3	99.5	
PCQ 731	*mode 3*			1	72.3	0.37	0.10	12.0	1.64	0.02	0.19	0.66	0.00	2.3	6.6		0.13	3.9	100.2	

*Elemental composition of volcanic glass by Electron Probe Microanalysis (cf. Nash, 1992), n=number of shards, for n≥4 average and 1σ standard deviation are reported.

Figure A.1: Photographs and geographic locations of sandstone marker beds and volcanic ash beds from Puerta de Corral Quemado. These stratigraphic markers facilitate intergration of the tephrostratigraphy and tooth enamel stable isotope data with the paleosol carbonate data from Latorre *et al*. (1997). Locations were established using the field notes and photographs of J. Quade (University of Arizona). This section was measured on the south side of Río Corral Quemado, and constitutes the principal section to which stable isotope proxy data and volcanic ash chemistry is referenced (Table A.5). The magnetostratigraphic data of Butler *et al*. (1984) were obtained on a stratigraphic section exposed on the north side of Río Corral Quemado, data from this region is presented in Table A.6 and Table A.7.

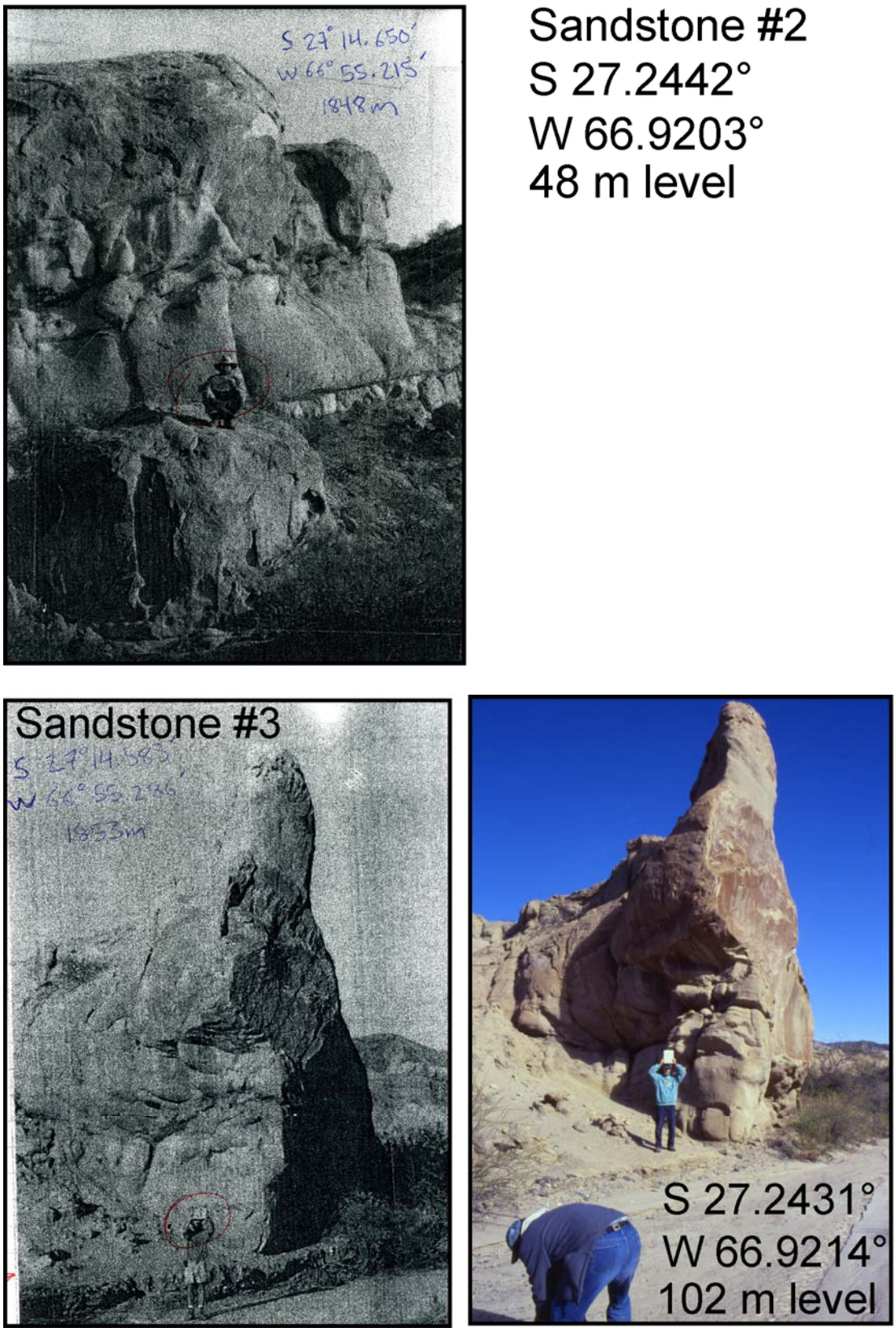

Figure A.1: Sandstone #2 and Sandstone #3, lower section.

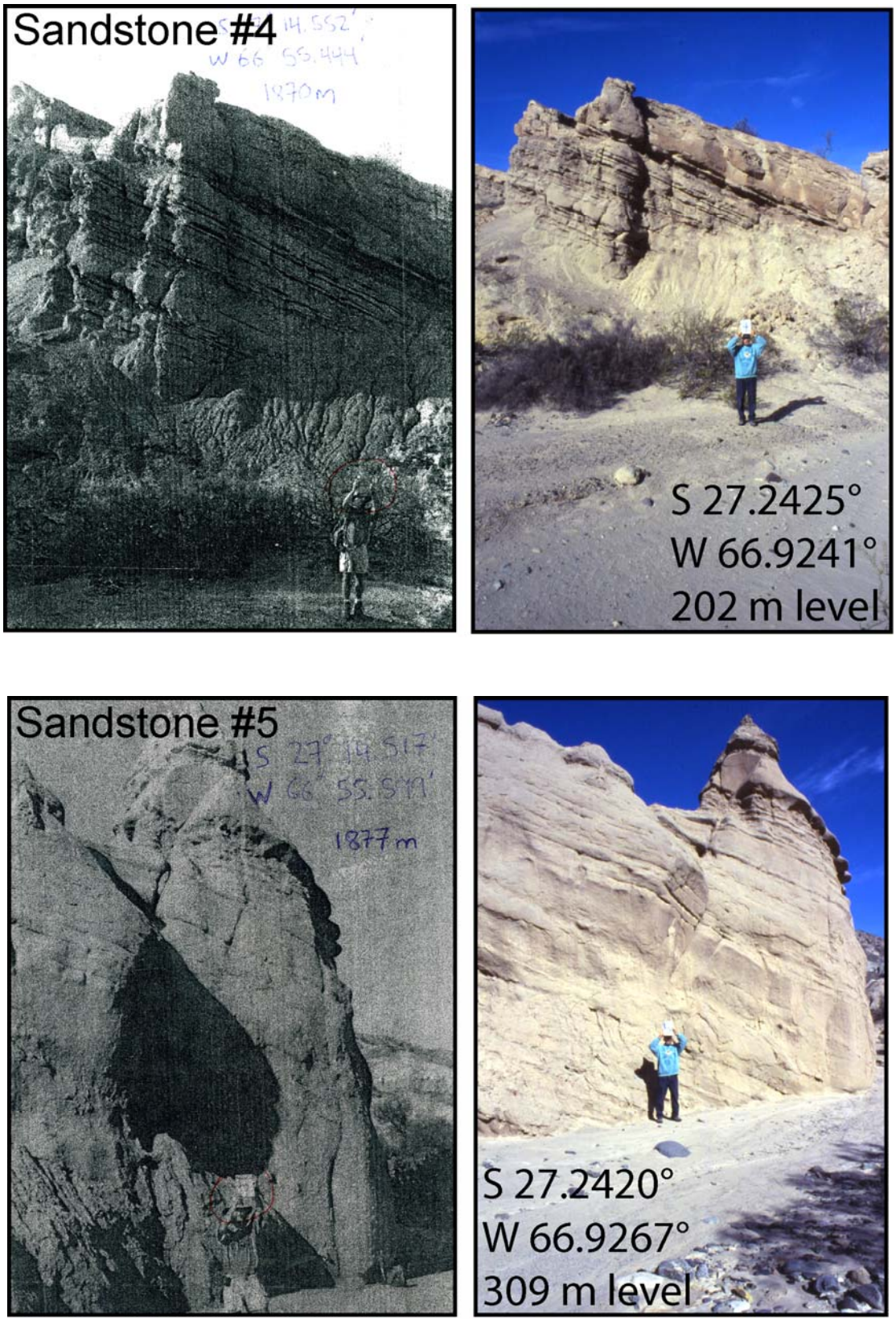

Figure A.1 (*continued*): Sandstone #4 and Sandstone #5, lower section.

Figure A.1 (*continued*): In principal section (**Top**), and Los Barcos section (**bottom**).

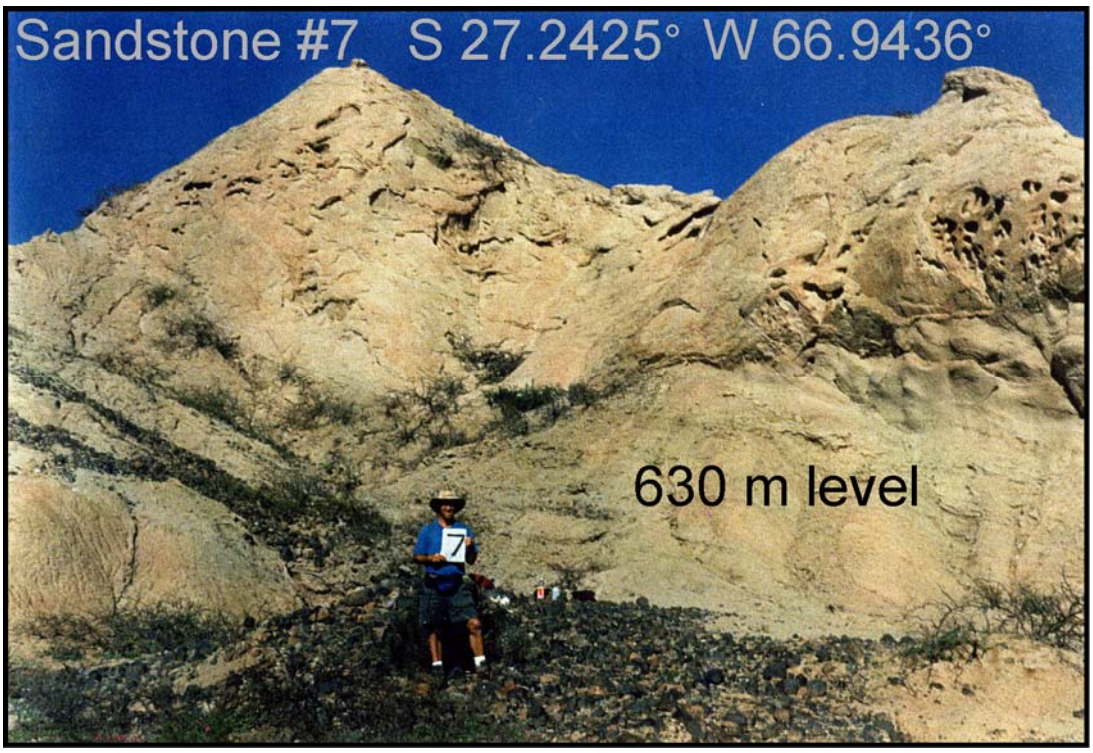

Figure A.1 (*continued*): Sandstone #6 and Sandstone #7, low in the middle section.

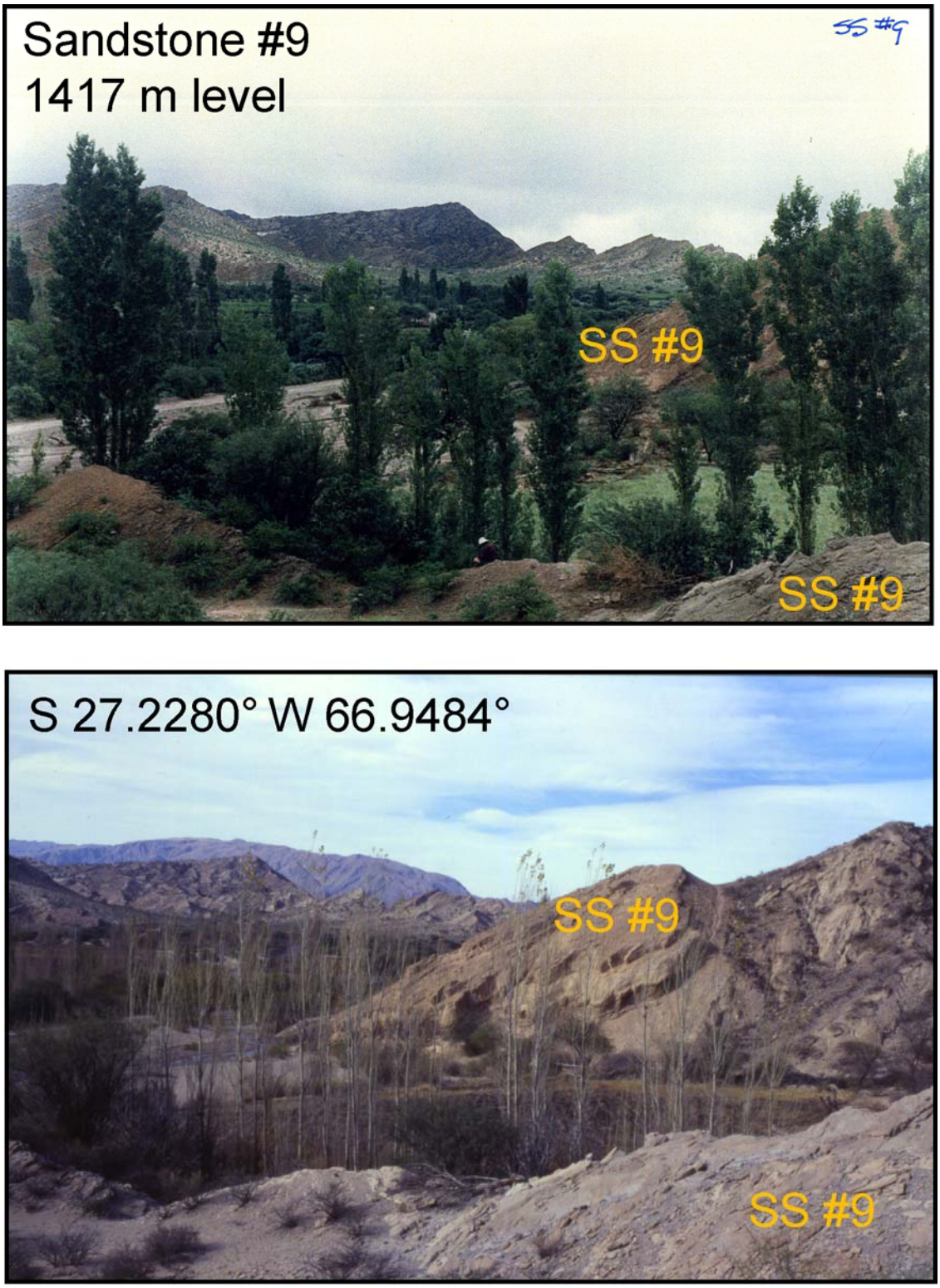

Figure A.1 (*continued*): Sandstone #9 (foreground and intermediate distance), is the transition between the middle and upper parts of the principal section (Table A.5).

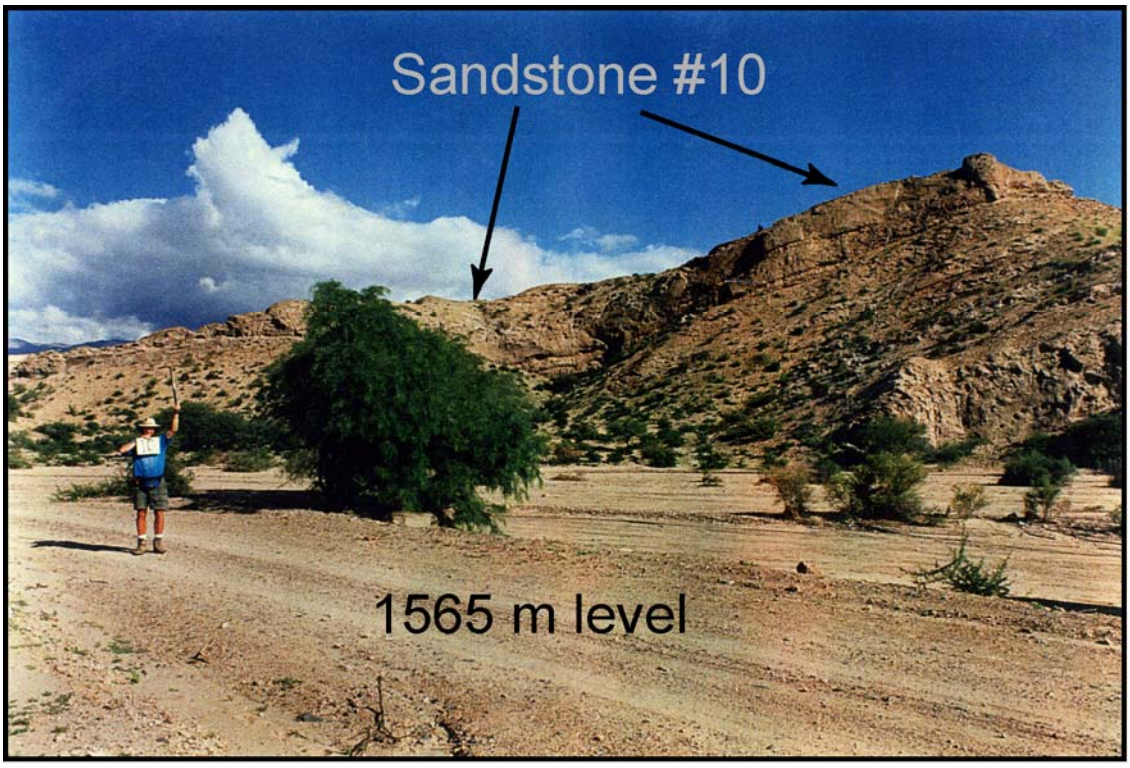

Figure A.1 (*continued*): Sandstone #10, top of the late Miocene sequence of ash beds.

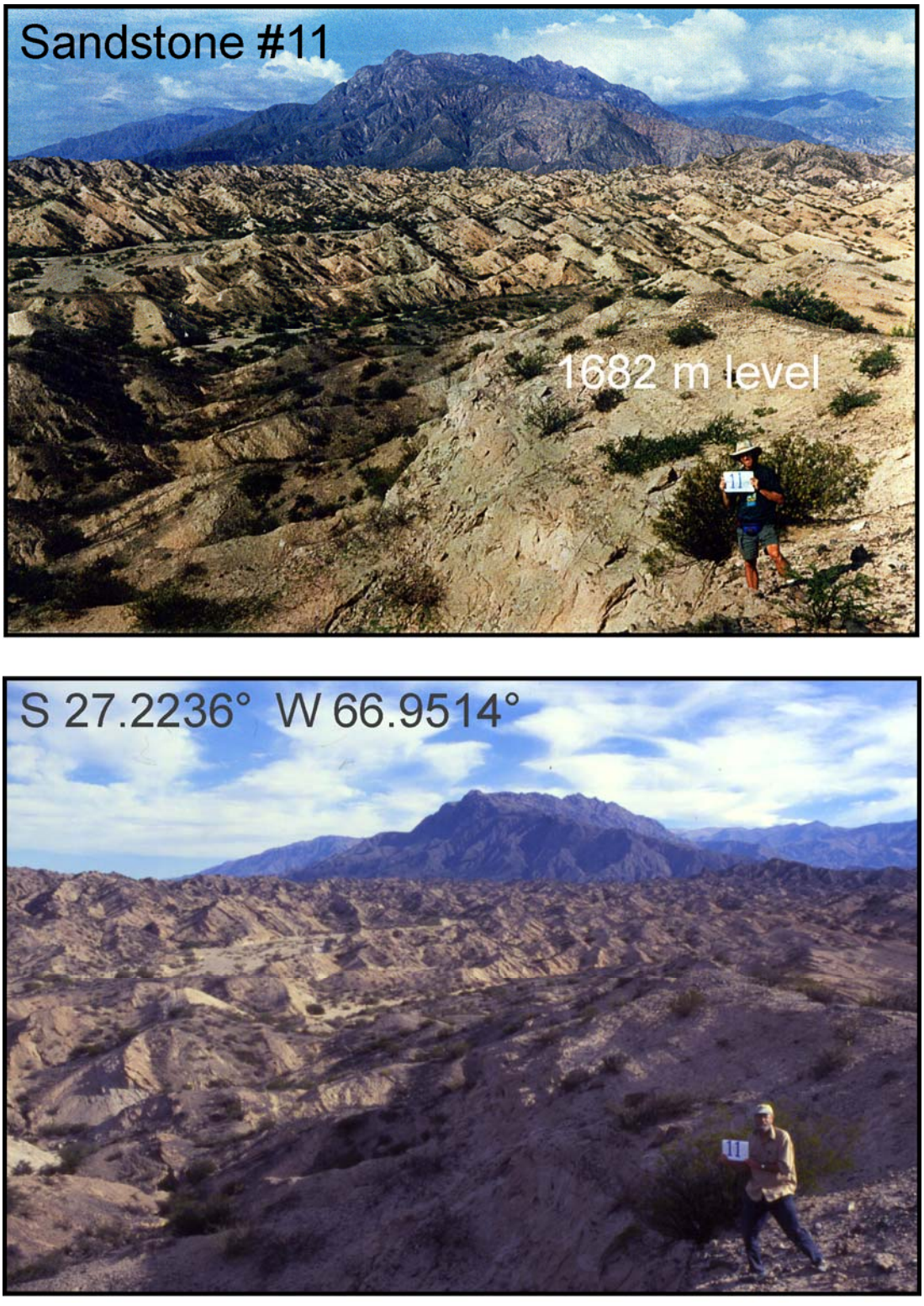

Figure A.1 (*continued*): Sandstone #11, El Durazno in background.

Figure A.1 (*continued*): Sandstone #12.

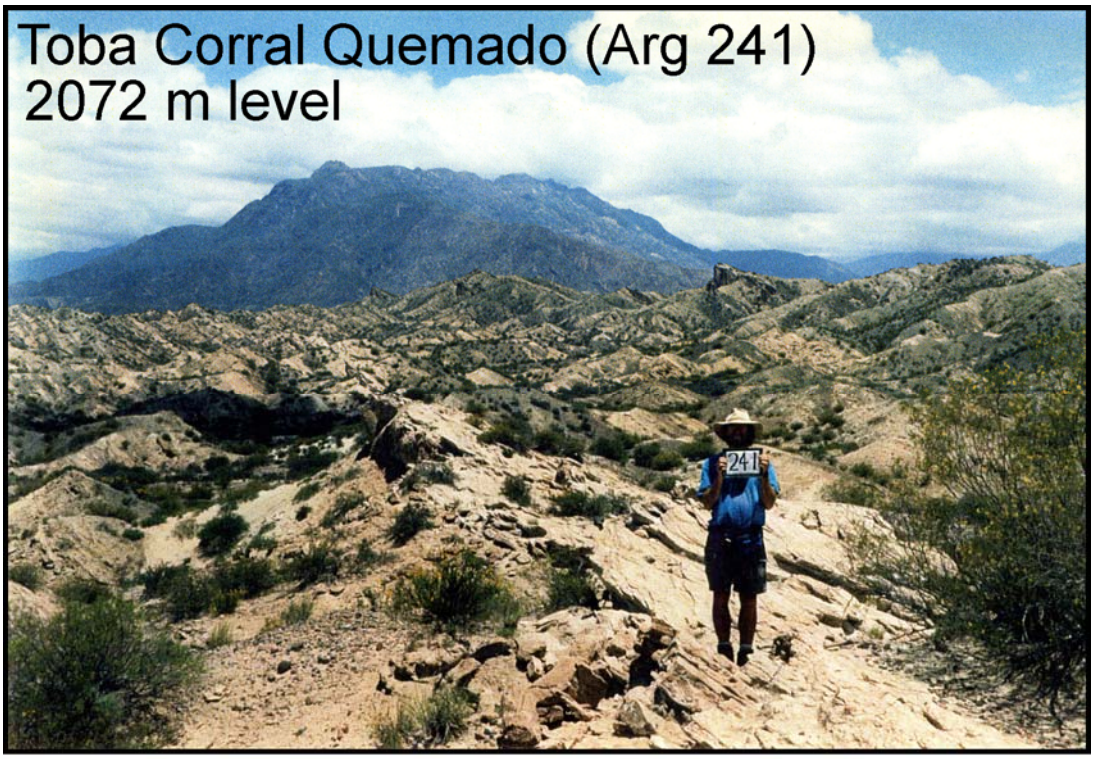

Figure A.1 (*continued*): Toba Corral Quemado (3.66 Ma), El Durazno in background.

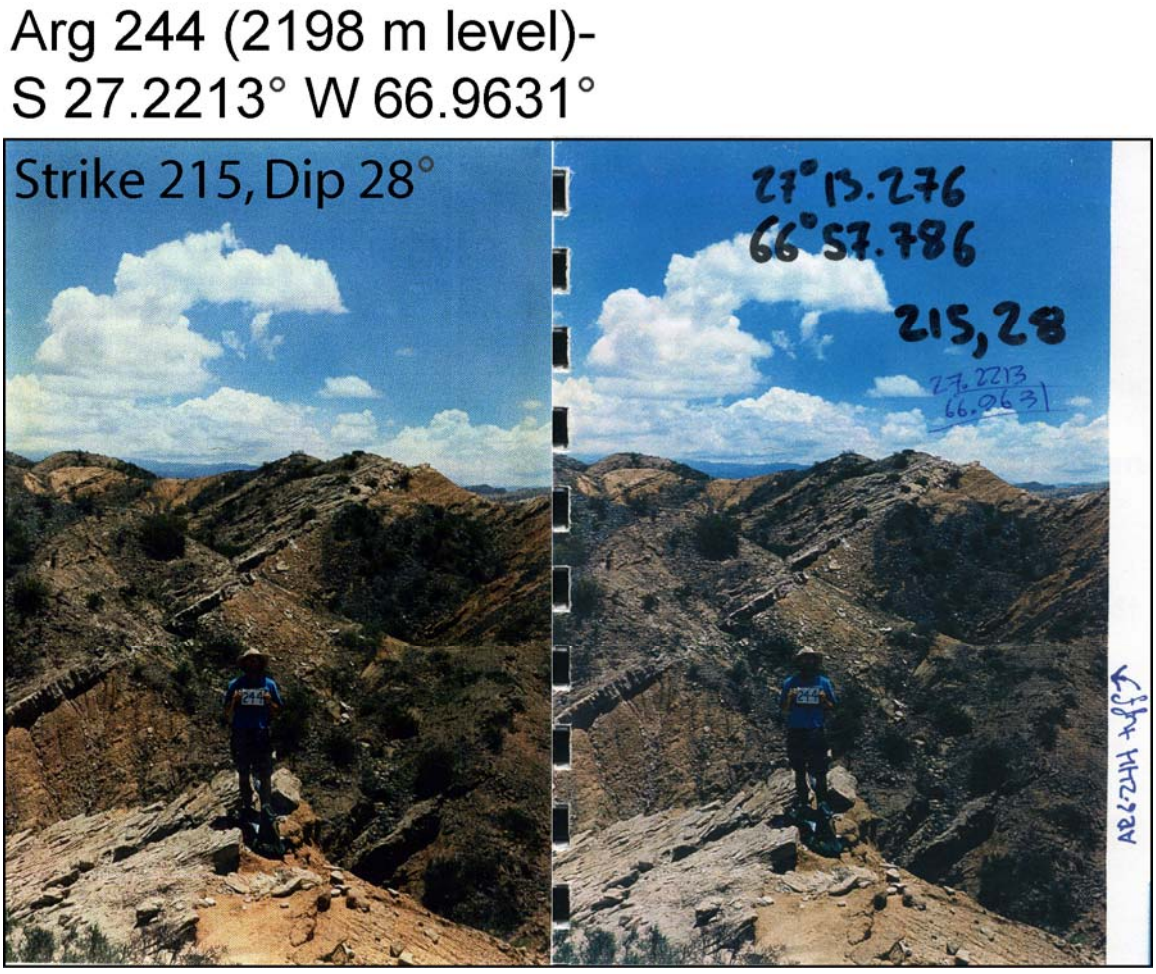

Figure A.1 (*continued*): Volcanic ash bed at 2198 m level, sample Arg 244 is correlative with samples PCQ 578, PCQ 715, and PCQ 805.

Table A.5: Stratigraphy and composition of volcanic ash beds from Puerta de Corral Quemado section
(base of section = 27.2439°S, 66.9189°W; total thickness ~2.5 km)

Sample	Lat	Lon	strat	n*	SiO2	TiO2	ZrO2	Al2O3	Fe2O3	MnO	MgO	CaO	BaO	Na2O	K2O	F	Cl	H2O	Total	Comment
	(°S)	(°W)	m																	thickness (m), lithology
PCQ 514	27.2439	66.9189	5		*not analyzed*															*0.05, tuffaceous siltstone*
PCQ 515	27.2439	66.9189	6		*not analyzed*															*pumice, red igneous cobbles*
SS #2	27.2442	66.9203	48		*coarse green sand, lithic rich, pale green at base, first major sandstone knob in wash.*															*28.5, see Figure A.1*
PCQ 151			100		*not analyzed*															*tuff (?), carbonate rich ledges*
SS #3	27.2431	66.9214	102		*weathers medium brown (varnished), coarse, steep cross beds, pinnacle on south side of wash.*															*16, see Figure A.1*
PCQ 516			115		*not analyzed*															*tuffaceous silt, silicified (?)*
PCQ 123	27.2432	66.9218	120		*not analyzed*															*tuffaceous (?), top of SS #3*
PCQ 124	27.2444	66.9212	120		*not analyzed*															*tuffaceous (?), top of SS #3*
PCQ 517	27.2445	66.9219	139		*not analyzed*															*tuffaceous sand*
PCQ 125	27.2445	66.9219	139		*not analyzed*															*lateral equivalent to PCQ 517*
PCQ 127	27.2478	66.9250	139		*not analyzed*															*lateral equivalent to PCQ 517*
PCQ 128	27.2466	66.9235	139		*not analyzed*															*lateral equivalent to PCQ 517*
Arg 64, Arg 108			140		*not analyzed*															*tuff*
PCQ 541			162		*not analyzed*															*altered tuff, carbonate (?)*
SS #4	27.2425	66.9241	202		*coarse brown ss, crossed bedded at base, stacked paleosols lateral to upper 5 m of sandstone.*															*17, see Figure A.1*
SS #5	27.2420	66.9267	309		*buff, no pebbles, massive sandstone, last major sandstone before wash opens up.*															*25, see Figure A.1*
PCQ 131	27.2453	66.9286	345		*not analyzed*															*upper of two tuffaceous layers*
Arg 100			482		*not analyzed; Toba del Puerto (7.14 ± 0.04 Ma; Latorre et al., 1997), basal white, thinly bedded.*															*9, see Figure A.1*
Arg 101			486		*not analyzed; Toba del Puerto, 7.14 Ma, bedded pumiceous tuff alternating with sandy layers.*															*9, see Figure A.1*
PCQ 518	27.2416	66.9342	580		*not analyzed*															*tuffaceous sand*
SS #6	27.2479	66.9398	588		*coarse, lithic rich sandstone, locally well bedded, paleosol formed on top of deposit (abandoned chan*															*3, see Figure A.1*
Arg 131			595	8	74.6	0.13	0.04	12.9	0.89	0.04	0.11	0.99	0.07	2.3	4.8	0.03	0.13	4.0	100.9	*very localized, in burrows*
					0.5	*0.03*	*0.02*	*0.2*	*0.03*	*0.01*	*0.01*	*0.03*	*0.02*	*0.5*	*0.2*	*0.02*	*0.01*	*1.6*	*1.1*	
Arg 131	*mode 2*			9	74.9	0.16	0.03	13.0	1.02	0.04	0.16	1.10	0.09	2.3	4.8	0.02	0.13	2.8	100.6	
					0.5	*0.03*	*0.01*	*0.2*	*0.03*	*0.01*	*0.01*	*0.03*	*0.03*	*0.4*	*0.2*	*0.02*	*0.02*	*1.5*	*0.8*	
Arg 131	*mode 3*			4	74.4	0.15	0.03	13.3	1.17	0.04	0.19	1.16	0.05	2.9	4.8	0.03	0.14	2.1	100.4	
					0.8	*0.05*	*0.04*	*0.2*	*0.05*	*0.01*	*0.03*	*0.05*	*0.03*	*0.7*	*0.1*	*0.02*	*0.03*	*2.1*	*0.6*	

Table A.5 (*continued*)

Sample	Lat	Lon	strat	n	SiO2	TiO2	ZrO2	Al2O3	Fe2O3	MnO	MgO	CaO	BaO	Na2O	K2O	F	Cl	H2O	Total	Comment
	(°S)	(°W)	m																	thickness (m), lithology
Arg 131	*mode 4*		595	4	73.3	0.29	0.02	13.9	1.56	0.04	0.32	1.41	0.08	2.9	4.8	0.03	0.14	1.0	100.0	
					0.8	*0.03*	*0.02*	*0.2*	*0.06*	*0.01*	*0.03*	*0.09*	*0.04*	*0.6*	*0.1*	*0.04*	*0.01*	*0.8*	*0.7*	
Arg 131	*mode 5*			4	71.2	0.46	0.06	14.6	2.17	0.04	0.49	1.98	0.07	3.0	4.5	0.03	0.13	1.3	100.0	
					0.8	*0.07*	*0.08*	*0.7*	*0.22*	*0.02*	*0.10*	*0.39*	*0.05*	*0.9*	*0.3*	*0.02*	*0.01*	*0.8*	*0.8*	
PCQ 132	27.2451	66.9360	595		*not analyzed*															*0.3, coarse tuff to sandy tuff*
SS #7	27.2425	66.9436	630		*multiple gravel channels at base containing lithic fragments, fining upwards, cross bedded at top.*															*29.2, see Figure A.1*
PCQ 522	27.2425	66.9436	630		*not analyzed*															*welded tuff cobble in SS #7*
PCQ 138	27.2441	66.9468	668		*not analyzed*															*tuff, green w/ slickensides*
PCQ 135	27.2436	66.9477	695		*not analyzed*															tuff
PCQ 133	27.2427	66.9463	708		*not analyzed*															*tuff, discontinuous*
PCQ 134	27.2428	66.9476	746		*not analyzed*															*tuffaceous sand, above clay*
Tuff			818		*not sampled*															*1.5, biotite rich, detrital*
Arg 155			821		*not analyzed*															*thin tuff, biotite rich*
PCQ 136	27.2415	66.9477	821		*not analyzed*															*tuff*
PCQ 139	27.2387	66.9430	821		*not analyzed*															*lateral equivalent of PCQ 136 ?*
PCQ 141	27.2377	66.9422	835		*not analyzed*															*tuff*
PCQ 142	27.2377	66.9422	836		*not analyzed*															*pumice in conglomerate*
Tuff			937		*not sampled*															*2, tuffaceous unit, fine*
PCQ 143	27.2370	66.9458	990		*not analyzed*															*tuff, altered greenish*
PCQ 1045			950±50	20	72.5	0.08	0.04	13.1	0.63	0.03	0.08	0.91	0.02	3.0	4.4		0.10	5.2	100.1	*0.3, grey tuff, biotite-rich base*
					0.4	*0.03*	*0.05*	*0.2*	*0.04*	*0.02*	*0.01*	*0.06*	*0.03*	*0.1*	*0.3*		*0.01*	*0.5*	*0.5*	
PCQ 1046	27.2404	66.9516	975±50	5	72.9	0.08	0.06	12.4	0.71	0.06	0.08	0.66	0.04	2.7	5.4		0.13	5.2	100.3	*0.2, white tuff in gray sand*
					0.9	*0.02*	*0.05*	*0.3*	*0.06*	*0.02*	*0.01*	*0.12*	*0.02*	*0.3*	*1.2*		*0.02*	*1.4*	*0.3*	
PCQ 1046	*mode 2*			1	72.7	0.13	0.03	12.3	0.67	0.07	0.07	0.93	0.08	2.2	6.2		0.12	4.9	100.3	
PCQ 1046	*mode 2*			1	72.7	0.15	0.00	12.4	0.65	0.08	0.10	0.95	0.02	1.5	5.6		0.13	6.6	101.0	
PCQ 1046	*mode 2*			1	72.3	0.12	0.05	12.3	0.68	0.09	0.08	0.99	0.12	1.1	5.4		0.14	6.8	100.1	
Arg 164			1005		*not analyzed*															*tuff, biotite rich, altered*
Tuff			1015		*not sampled*															*tuff, fine white, prominent*

Table A.5 (*continued*)

Sample	Lat	Lon	strat	n	SiO2	TiO2	ZrO2	Al2O3	Fe2O3	MnO	MgO	CaO	BaO	Na2O	K2O	F	Cl	H2O	Total	Comment
	(°S)	(°W)	m																	thickness (m), lithology
PCQ 144	27.2355	66.9458	1015		*not analyzed*															*tuff in base of sandstone #8*
SS #8			1016																	*78, eolian x-beds, no gravel*
Arg 166			1092		*not analyzed*															*green tuff in eolian strata*
PCQ 523	27.2364	66.9488	1095	18	73.7	0.10	0.05	12.1	0.76	0.04	0.08	0.92	0.04	2.1	5.3	0.00	0.14	5.3	100.6	*0.3, tuff base tuffaceous ss*
					0.3	*0.03*	*0.05*	*0.6*	*0.06*	*0.02*	*0.01*	*0.04*	*0.03*	*0.4*	*0.3*	*0.01*	*0.02*	*0.7*	*0.4*	
Tuff			1148		*not sampled*															*1.5, fine white, reworked upper*
Tuff			1152		*not sampled*															*0.7, fine white tuff*
Arg 168			1176		*not analyzed*															*0.3, white tuff, altered*
Arg 167			1180	16	72.5	0.23		12.6	1.22	0.03	0.20	1.04	0.04	2.1	5.1	0.01	0.22	7.0	102.3	*0.3, cs. white tuff, continuous*
					0.4	*0.04*		*0.1*	*0.05*	*0.02*	*0.02*	*0.03*	*0.03*	*0.2*	*0.2*	*0.01*	*0.01*	*0.5*	*0.7*	
Arg 167	*replicate analysis*			15	72.2	0.23	0.07	12.6	1.22	0.04	0.21	1.00	0.04	2.2	5.2		0.22	6.5	101.7	
					0.5	*0.03*	*0.03*	*0.1*	*0.04*	*0.02*	*0.02*	*0.03*	*0.03*	*0.1*	*0.1*		*0.01*	*0.4*	*0.6*	
Tuff			1181		*not sampled*															*0.2, pumice tuff*
Tuff			1182		*not sampled*															*0.3, pumice tuff, fine biotite*
Tuff			1184		*not sampled*															*0.1, fine white tuff*
Tuff			1207		*not sampled*															*0.15, tuff*
Tuff			1229		*not sampled*															*01., tuff*
Tuff			1331		*not sampled*															*0.25, green tuff, altered*
SS #9	27.2280	66.9484	1417		*coarse sandstone, minor gravel, trough cross-bedded, erosional base with numerous rip-up clasts*															*6, see Figure A.1*
Arg 196			1440	19	73.6	0.07		11.9	0.80	0.06	0.05	0.52	0.02	2.0	6.4	0.01	0.12	6.6	102.1	*0.2, white, crystal tuff at base sanidine date (5.64 ± 0.32 Ma)*
					0.3	*0.03*		*0.1*	*0.05*	*0.02*	*0.01*	*0.03*	*0.02*	*0.1*	*0.2*	*0.01*	*0.01*	*0.8*	*0.7*	
Arg 196	*replicate analysis*			21	73.0	0.07	0.07	12.0	0.81	0.05	0.04	0.51	0.03	2.2	6.4		0.12	6.6	101.9	
					0.6	*0.03*	*0.05*	*0.1*	*0.04*	*0.02*	*0.01*	*0.02*	*0.02*	*0.1*	*0.2*		*0.01*	*0.6*	*0.5*	
PCQ 560	27.2278	66.9488	1440	13	72.7	0.07	0.05	12.0	0.81	0.07	0.04	0.49	0.03	2.2	6.4	0.04	0.11	4.3	99.3	*correlative to Arg 196*
					0.5	*0.03*	*0.05*	*0.2*	*0.07*	*0.02*	*0.02*	*0.02*	*0.03*	*0.1*	*0.2*	*0.04*	*0.02*	*0.5*	*0.3*	
PCQ 154	27.2358	66.9571	1465	14	71.9	0.10	0.03	12.2	0.66	0.07	0.06	0.95	0.11	2.1	6.2	0.01	0.13	5.3	99.7	*tuff, weakly bioturbated*
					0.5	*0.05*	*0.04*	*0.4*	*0.05*	*0.03*	*0.02*	*0.02*	*0.04*	*0.1*	*0.1*	*0.02*	*0.02*	*0.6*	*0.3*	
PCQ 561	27.2274	66.9492	1465	11	72.5	0.1	0.0	12.0	0.67	0.06	0.07	0.96	0.09	2.0	6.2	0.01	0.12	4.3	99.3	*0.25, fine white tuff, traceable*
					0.4	*0.0*	*0.1*	*0.3*	*0.05*	*0.03*	*0.02*	*0.05*	*0.04*	*0.1*	*0.1*	*0.01*	*0.02*	*0.4*	*0.4*	

Table A.5 (*continued*)

Sample	Lat	Lon	strat	n	SiO2	TiO2	ZrO2	Al2O3	Fe2O3	MnO	MgO	CaO	BaO	Na2O	K2O	F	Cl	H2O	Total	Comment
	(°S)	(°W)	m																	thickness (m), lithology
PCQ 153	27.2287	66.9504	1472	14	71.3	0.09	0.06	12.6	0.66	0.03	0.08	0.82	0.11	2.2	6.3	0.02	0.10	5.5	99.8	*tuff, silty burrow infillings*
					0.5	*0.05*	*0.06*	*0.2*	*0.06*	*0.03*	*0.02*	*0.06*	*0.03*	*0.2*	*0.2*	*0.03*	*0.01*	*0.5*	*0.2*	
PCQ 562	27.2287	66.9504	1472	9	72.9	0.07	0.02	12.7	0.61	0.03	0.07	0.81	0.11	2.3	6.3	0.03	0.09	5.0	101.0	*0.75, fine tuff, detrital grains*
					0.5	*0.04*	*0.03*	*0.3*	*0.08*	*0.01*	*0.03*	*0.09*	*0.03*	*0.1*	*0.3*	*0.03*	*0.02*	*0.6*	*0.4*	
PCQ 156	27.2338	66.9560	1485±15	13	70.9	0.11	0.04	13.0	0.75	0.05	0.11	1.03	0.08	2.6	5.9	0.00	0.08	5.5	100.0	*tuff, heavily burrowed*
					0.7	*0.04*	*0.04*	*0.3*	*0.06*	*0.04*	*0.03*	*0.04*	*0.04*	*0.3*	*0.4*	*0.00*	*0.01*	*0.6*	*0.3*	
PCQ 157			1485	13	71.6	0.11	0.04	13.4	0.76	0.04	0.09	1.06	0.09	3.2	5.0	0.01	0.08	4.7	100.3	*fine white tuff, clean*
					0.2	*0.04*	*0.06*	*0.3*	*0.06*	*0.03*	*0.02*	*0.04*	*0.03*	*0.4*	*0.6*	*0.02*	*0.01*	*0.3*	*0.3*	
PCQ 563	27.2290	66.9512	1485	10	71.7	0.11	0.07	12.9	0.78	0.04	0.11	1.06	0.08	2.6	5.6	0.02	0.09	4.3	99.4	*0.2, gray, fine, not indurated*
					0.7	*0.04*	*0.07*	*0.2*	*0.05*	*0.03*	*0.02*	*0.03*	*0.03*	*0.5*	*0.7*	*0.03*	*0.01*	*0.4*	*0.4*	
PCQ 158a			1518	16	71.0	0.13	0.03	13.1	0.83	0.07	0.13	0.74	0.07	2.8	5.7	0.01	0.14	5.5	100.2	*pumiceous tuff*
					0.4	*0.05*	*0.03*	*0.5*	*0.06*	*0.03*	*0.02*	*0.03*	*0.04*	*0.4*	*0.4*	*0.03*	*0.02*	*0.5*	*0.5*	
PCQ 158b			1518	16	71.0	0.11	0.04	13.0	0.82	0.07	0.11	0.74	0.07	2.9	5.6	0.01	0.14	5.6	100.1	*1 meter above PCQ 158a*
					0.5	*0.04*	*0.07*	*0.5*	*0.07*	*0.03*	*0.02*	*0.03*	*0.03*	*0.3*	*0.4*	*0.02*	*0.02*	*0.6*	*0.6*	
PCQ 564	27.2288	66.9524	1518	12	71.5	0.13	0.04	12.8	0.82	0.08	0.12	0.73	0.09	2.5	5.8	0.02	0.14	4.8	99.5	*1, pumice/biotite tuff, sandy*
					0.8	*0.05*	*0.04*	*0.2*	*0.04*	*0.02*	*0.02*	*0.03*	*0.07*	*0.5*	*0.5*	*0.02*	*0.02*	*0.7*	*0.4*	
PCQ 159	27.2311	66.9545	1540	12	71.9	0.11	0.04	12.6	0.85	0.07	0.13	0.53	0.07	2.6	6.1	0.01	0.13	5.1	100.1	*glassy tuff, clean*
					0.3	*0.05*	*0.06*	*0.3*	*0.05*	*0.03*	*0.02*	*0.03*	*0.04*	*0.3*	*0.5*	*0.01*	*0.02*	*0.3*	*0.4*	
PCQ 565	27.2253	66.9483	1540	10	72.3	0.13	0.08	12.4	0.82	0.09	0.12	0.53	0.07	2.4	6.1	0.02	0.13	4.4	99.5	*0.2, base of microstrat in sand*
					0.3	*0.05*	*0.06*	*0.2*	*0.04*	*0.03*	*0.02*	*0.02*	*0.05*	*0.3*	*0.5*	*0.03*	*0.01*	*0.6*	*0.3*	
PCQ 1027	27.2309	66.9547	1540	10	71.4	0.14	0.03	12.8	0.81	0.08	0.13	0.51	0.08	2.6	5.8	0.01	0.14	5.5	100.0	*0.45, below gravel interval*
					1.2	*0.07*	*0.03*	*0.2*	*0.05*	*0.02*	*0.02*	*0.02*	*0.04*	*0.3*	*0.4*	*0.01*	*0.01*	*1.0*	*0.6*	
PCQ 1028	27.2309	66.9547	1540	10	71.3	0.12	0.04	12.7	0.83	0.08	0.15	0.56	0.07	2.7	5.7	0.02	0.12	6.0	100.4	*0.05, below gravel interval*
					1.1	*0.05*	*0.03*	*0.3*	*0.08*	*0.04*	*0.02*	*0.05*	*0.03*	*0.3*	*0.4*	*0.03*	*0.01*	*1.2*	*0.4*	
PCQ 1029	27.2295	66.9529	1540	10	70.6	0.12	0.09	12.6	0.77	0.09	0.13	0.50	0.09	2.6	5.7	0.04	0.12	6.6	100.0	*0.1, below gravel interval*
					0.9	*0.05*	*0.07*	*0.3*	*0.07*	*0.03*	*0.02*	*0.02*	*0.05*	*0.3*	*0.6*	*0.05*	*0.02*	*0.9*	*0.5*	
PCQ 1030	27.2295	66.9529	1540-42	4	71.6	0.16	0.02	12.5	0.85	0.09	0.12	0.58	0.05	2.4	6.2	0.03	0.14	5.7	100.4	*0.05, below gravel interval*
					0.5	*0.03*	*0.04*	*0.1*	*0.03*	*0.01*	*0.03*	*0.03*	*0.04*	*0.1*	*0.1*	*0.03*	*0.02*	*0.8*	*0.4*	
PCQ 566	27.2253	66.9483	1541.5	12	71.8	0.15	0.07	12.3	0.93	0.08	0.15	0.57	0.07	2.4	6.1	0.01	0.14	4.7	99.5	*0.2, middle tuff of microstrat*
					0.4	*0.07*	*0.05*	*0.2*	*0.08*	*0.02*	*0.02*	*0.02*	*0.05*	*0.2*	*0.4*	*0.01*	*0.01*	*0.4*	*0.4*	

Table A.5 (*continued*)

Sample	Lat	Lon	strat	n	SiO2	TiO2	ZrO2	Al2O3	Fe2O3	MnO	MgO	CaO	BaO	Na2O	K2O	F	Cl	H2O	Total	Comment
	(°S)	(°W)	m																	thickness (m), lithology
PCQ 567	27.2253	66.9483	1542.5	14	72.7	0.16	0.07	12.1	0.97	0.08	0.15	0.62	0.06	2.5	5.9	0.01	0.13	5.2	100.6	*0.2, base of channel, detrital*
					0.4	*0.04*	*0.05*	*0.3*	*0.08*	*0.02*	*0.02*	*0.04*	*0.03*	*0.2*	*0.3*	*0.01*	*0.01*	*0.5*	*0.3*	
PCQ 567	*mode 2*			4	72.3	0.13	0.05	12.4	0.89	0.06	0.12	0.75	0.07	2.9	5.2	0.00	0.15	5.5	100.5	*sedimentary mixing?*
					0.6	*0.04*	*0.03*	*0.3*	*0.03*	*0.02*	*0.02*	*0.03*	*0.04*	*0.3*	*0.6*	*0.00*	*0.01*	*0.2*	*0.3*	
PCQ 567	*mode 3*			1	70.9	0.20	0.08	12.5	1.33	0.10	0.28	1.08	0.05	3.6	4.2	0.01	0.14	6.0	100.5	*sedimentary mixing?*
PCQ 567	*mode 3*			1	71.3	0.19	0.02	12.2	1.30	0.08	0.26	1.09	0.05	3.3	4.6	0.00	0.15	5.9	100.5	
SS #10	27.2263	66.9494	1565		*brown ss, plane bedded, bank collapse blocks, major cliff former west of road*															*6, see Figure A.1*
PCQ 568	27.2243	66.9504	1635	14	72.2	0.11	0.07	12.7	0.75	0.05	0.11	0.76	0.09	3.0	5.2	0.02	0.08	4.2	99.4	*fine tuff on silt, below sand*
					0.7	*0.05*	*0.06*	*0.2*	*0.04*	*0.02*	*0.02*	*0.05*	*0.04*	*0.3*	*0.5*	*0.03*	*0.01*	*0.4*	*0.4*	
SS #11	27.2236	66.9514	1682		*major cobbly sand, gray but many dark volcanic clasts, last major ss before heading into badlands*															*7, see Figure A.1*
PCQ 569	27.2242	66.9527	1695		*not analyzed*															*0.2, pumice in sand*
Arg 215			1715	14	71.2	0.21		12.6	1.06	0.04	0.18	1.00	0.04	2.2	6.0	0.00	0.18	6.9	101.6	*0.4, biotite pumice tuff*
					0.9	*0.03*		*0.1*	*0.04*	*0.02*	*0.02*	*0.04*	*0.02*	*0.3*	*0.3*	*0.01*	*0.01*	*0.7*	*0.7*	
PCQ 570	27.2239	66.9529	1715	21	71.2	0.19	0.06	12.6	1.06	0.04	0.16	0.93	0.04	2.6	6.0	0.01	0.18	5.8	100.8	*weathers to orange*
					0.6	*0.06*	*0.06*	*0.4*	*0.07*	*0.03*	*0.02*	*0.04*	*0.03*	*0.2*	*0.3*	*0.02*	*0.02*	*0.5*	*0.5*	
PCQ 504	27.2181	66.9502	1730±15	21	73.7	0.20	0.08	11.4	0.86	0.03	0.12	0.59	0.04	2.1	6.4	0.02	0.12	5.0	100.6	*tuff 11a*
					0.6	*0.03*	*0.06*	*0.4*	*0.04*	*0.02*	*0.02*	*0.05*	*0.03*	*0.1*	*0.3*	*0.02*	*0.02*	*0.5*	*0.7*	
PCQ 504	*mode 2*			1	73.1	0.20	0.04	12.0	0.87	0.02	0.11	1.04	0.03	2.3	6.0	0.00	0.12	4.1	100.0	
PCQ 504	*mode 2*			1	72.5	0.16	0.03	11.6	1.04	0.07	0.22	1.05	0.04	2.9	4.7	0.00	0.11	5.8	100.3	
PCQ 505	27.2217	66.9516	1740±20		*not analyzed; see Appendix B for stable isotope data*															*indurated tuff, calcite veins*
PCQ 116	27.2290	66.9610	1775	6	73.2	0.09	0.06	12.3	0.61	0.06	0.06	0.60	0.05	2.4	6.1	0.04	0.10	4.7	100.3	*tuff 11b; mixed with dacite*
					0.5	*0.03*	*0.04*	*0.2*	*0.07*	*0.02*	*0.02*	*0.01*	*0.02*	*0.2*	*0.3*	*0.01*	*0.01*	*0.3*	*0.2*	
PCQ 116	*mode 2*		1775±10	1	72.7	0.28	0.11	12.3	1.46	0.02	0.24	0.57	0.02	2.9	5.4	0.24	0.04	4.3	100.4	*dacite; Figure 1.12a (sample 3)*
PCQ 116	*mode 2*			1	68.5	0.47	0.08	12.7	1.72	0.00	0.27	0.94	0.04	2.9	5.9	0.21	0.10	5.8	99.5	
PCQ 116	*mode 2*			1	68.4	0.42	0.15	12.6	1.74	0.02	0.27	0.97	0.03	2.7	6.0	0.11	0.13	5.7	99.2	
PCQ 116	*mode 2*			1	70.9	0.50	0.12	13.1	1.76	0.01	0.28	1.01	0.01	3.0	5.5	0.16	0.09	4.4	100.8	
PCQ 116	*mode 2*			1	68.6	0.46	0.07	12.9	1.78	0.04	0.28	0.93	0.00	2.9	5.6	0.22	0.10	5.7	99.5	
PCQ 116	*mode 2*			1	69.5	0.48	0.11	13.2	1.79	0.04	0.31	1.02	0.00	3.2	5.5	0.17	0.10	5.1	100.4	
PCQ 116	*mode 2*			1	70.2	0.46	0.12	12.9	1.91	0.03	0.27	0.93	0.06	3.1	5.7	0.17	0.10	4.8	100.7	
PCQ 116	*mode 2*			1	68.9	0.56	0.12	13.3	2.12	0.04	0.39	1.28	0.00	3.2	5.4	0.24	0.11	5.4	100.9	
PCQ 116	*mode 2*			1	67.4	0.49	0.18	13.8	2.38	0.07	0.54	1.64	0.00	3.3	4.9	0.20	0.11	5.0	99.8	

Table A.5 (*continued*)

Sample	Lat	Lon	strat	n	SiO2	TiO2	ZrO2	Al2O3	Fe2O3	MnO	MgO	CaO	BaO	Na2O	K2O	F	Cl	H2O	Total	Comment
	(°S)	(°W)	m																	thickness (m), lithology
PCQ 116	*mode 2*		1775±10	1	67.8	0.58	0.21	13.8	2.63	0.07	0.50	1.62	0.00	3.1	5.3	0.21	0.08	4.7	100.4	
PCQ 116	*mode 2*			1	66.7	0.68	0.05	14.0	2.85	0.11	0.59	1.83	0.03	3.2	4.8	0.18	0.10	5.4	100.4	
PCQ 571	27.2235	66.9546	1775	17	72.1	0.09	0.05	11.8	0.58	0.05	0.06	0.59	0.08	2.1	6.6	0.01	0.10	4.7	98.9	*tuff 11b*
					0.9	*0.05*	*0.07*	*0.2*	*0.07*	*0.03*	*0.02*	*0.02*	*0.04*	*0.1*	*0.1*	*0.01*	*0.01*	*0.7*	*0.5*	
PCQ 1020	27.2235	66.9545	1775	8	72.9	0.07	0.04	12.2	0.53	0.04	0.05	0.59	0.07	2.4	6.0	0.01	0.11	5.4	100.5	*0.05, fine grained biotite tuff*
					0.6	*0.03*	*0.04*	*0.1*	*0.03*	*0.01*	*0.01*	*0.02*	*0.01*	*0.3*	*0.3*	*0.01*	*0.01*	*0.6*	*0.7*	
PCQ 117	27.2325	66.9641	1775±20	20	74.3	0.09	0.06	12.6	0.61	0.06	0.08	0.61	0.04	3.1	5.2	0.01	0.13	3.4	100.3	*see Figure 1.12a (sample 4)*
					1.3	*0.04*	*0.05*	*0.3*	*0.14*	*0.04*	*0.02*	*0.16*	*0.02*	*0.4*	*0.6*	*0.03*	*0.04*	*1.2*	*0.4*	
PCQ 115	27.2325	66.9641	1792	18	72.5	0.11	0.06	12.9	0.66	0.07	0.11	0.61	0.06	2.6	5.8	0.08	0.12	5.2	100.8	*0.2, tuff 11c in fine sands/silts*
					0.4	*0.03*	*0.05*	*0.2*	*0.05*	*0.02*	*0.01*	*0.02*	*0.03*	*0.5*	*0.5*	*0.03*	*0.01*	*0.6*	*0.3*	
PCQ 572	27.2234	66.9548	1792	14	71.6	0.11	0.04	12.7	0.66	0.08	0.10	0.62	0.06	2.2	6.5	0.02	0.12	4.5	99.2	*tuff 11c*
					0.4	*0.03*	*0.04*	*0.2*	*0.04*	*0.03*	*0.02*	*0.02*	*0.05*	*0.4*	*0.3*	*0.03*	*0.02*	*1.0*	*0.4*	
PCQ 1031	27.2241	66.9556	1792	8	71.2	0.13	0.02	12.7	0.64	0.06	0.09	0.61	0.05	2.5	6.0	0.02	0.11	6.4	100.4	*0.6, fine white biotite tuff*
					0.8	*0.04*	*0.02*	*0.1*	*0.05*	*0.02*	*0.01*	*0.03*	*0.04*	*0.3*	*0.4*	*0.02*	*0.02*	*0.6*	*0.5*	
PCQ 500	27.2245	66.9574	1828	17	74.3	0.12	0.07	12.1	0.69	0.04	0.09	0.85	0.07	2.8	5.0	0.02	0.09	5.3	101.5	*tuff in sandstone*
					0.3	*0.04*	*0.07*	*0.2*	*0.08*	*0.03*	*0.02*	*0.03*	*0.04*	*0.3*	*0.4*	*0.03*	*0.01*	*0.5*	*0.2*	
PCQ 502	27.2207	66.9533	1828	15	74.1	0.10	0.05	12.1	0.71	0.04	0.10	0.85	0.05	2.7	5.1	0.03	0.10	5.2	101.3	*thin tuff*
					0.6	*0.05*	*0.06*	*0.2*	*0.05*	*0.03*	*0.02*	*0.03*	*0.04*	*0.2*	*0.3*	*0.04*	*0.01*	*0.5*	*0.4*	
PCQ 1024	27.2259	66.9585	1828	18	73.6	0.11	0.05	12.1	0.72	0.05	0.11	0.83	0.05	3.0	4.6		0.10	5.0	100.3	*plane bedded tuff, black/white*
					0.5	*0.04*	*0.05*	*0.3*	*0.04*	*0.02*	*0.01*	*0.05*	*0.03*	*0.2*	*0.3*		*0.01*	*0.6*	*0.4*	
PCQ 1023	27.2252	66.9583	1830.8	4	73.2	0.13	0.02	12.1	0.76	0.06	0.12	0.86	0.05	2.5	4.7		0.10	5.3	99.9	*0.05, biotite-rich eolian tuff*
					0.4	*0.04*	*0.03*	*0.3*	*0.06*	*0.02*	*0.01*	*0.10*	*0.03*	*1.0*	*0.2*		*0.02*	*1.0*	*0.3*	
PCQ 1023	*mode 2*			7	71.5	0.20	0.07	13.1	1.16	0.05	0.23	1.10	0.03	3.5	4.2		0.11	5.3	100.5	
					0.4	*0.03*	*0.06*	*0.2*	*0.03*	*0.01*	*0.02*	*0.03*	*0.02*	*0.2*	*0.2*		*0.01*	*0.2*	*0.5*	
PCQ 1023	*mode 3*			7	68.6	0.34	0.04	13.8	1.67	0.05	0.41	1.53	0.03	3.7	4.0		0.11	5.4	99.8	
					0.7	*0.07*	*0.04*	*0.4*	*0.28*	*0.02*	*0.09*	*0.22*	*0.03*	*0.2*	*0.1*		*0.01*	*0.6*	*0.8*	
Arg 227			1832	19	71.6	0.19		12.9	1.03	0.05	0.19	1.22	0.05	2.9	4.3	0.01	0.12	6.5	101.1	*tuff of sandstone #12*
					1.1	*0.03*		*0.3*	*0.06*	*0.01*	*0.03*	*0.06*	*0.03*	*0.4*	*0.5*	*0.01*	*0.01*	*1.1*	*0.9*	
Arg 227	*mode 2*			1	73.5	0.18		11.6	0.92	0.04	0.15	0.88	0.04	1.9	5.2	0.01	0.11	7.6	102.0	

Table A.5 (*continued*)

Sample	Lat	Lon	strat	n	SiO2	TiO2	ZrO2	Al2O3	Fe2O3	MnO	MgO	CaO	BaO	Na2O	K2O	F	Cl	H2O	Total	Comment
	(°S)	(°W)	m																	thickness (m), lithology
PCQ 573	27.2226	66.9548	1832	26	71.9	0.16	0.02	13.5	1.03	0.05	0.19	1.20	0.06	3.4	4.1	0.02	0.12	4.9	100.4	*0.2, fine white, see Figure 3.4*
					0.8	*0.04*	*0.05*	*0.4*	*0.05*	*0.03*	*0.02*	*0.06*	*0.03*	*0.2*	*0.3*	*0.03*	*0.01*	*0.6*	*0.3*	
PCQ 573	*mode 2*			1	72.4	0.12	0.00	13.3	0.78	0.05	0.14	0.99	0.05	3.6	4.1	0.04	0.09	4.7	100.3	
PCQ 573	*mode 2*			1	75.1	0.11	0.12	12.7	0.69	0.02	0.10	0.83	0.01	2.4	5.7	0.03	0.12	3.5	101.3	
PCQ 573	*mode 2*			1	73.8	0.13	0.12	11.7	0.72	0.01	0.10	0.82	0.00	2.0	6.2	0.00	0.11	4.0	99.7	
PCQ 574	27.2226	66.9548	1832.2	25	71.7	0.15	0.03	13.3	1.00	0.05	0.18	1.20	0.0	3.1	4.5	0.03	0.12	5.0	100.3	*0.1, coarse gray, see Fig. 3.4*
					0.7	*0.03*	*0.05*	*0.2*	*0.07*	*0.03*	*0.02*	*0.04*	*0.0*	*0.4*	*0.5*	*0.03*	*0.02*	*0.7*	*0.5*	
PCQ 574	*mode 2*			1	72.8	0.13	0.00	12.6	0.84	0.06	0.08	0.92	0.07	2.8	5.0	0.02	0.11	5.0	100.4	
PCQ 574	*mode 2*			1	74.2	0.10	0.00	12.8	0.74	0.07	0.10	0.80	0.04	2.1	6.3	0.00	0.11	3.8	101.2	
PCQ 575	27.2226	66.9548	1832.3	29	73.9	0.11	0.04	12.2	0.73	0.05	0.11	0.83	0.05	2.9	4.8	0.02	0.11	4.5	100.3	*0.3, white, see Figure 3.4*
					0.6	*0.04*	*0.07*	*0.3*	*0.07*	*0.03*	*0.02*	*0.03*	*0.04*	*0.3*	*0.5*	*0.03*	*0.01*	*0.6*	*0.4*	
PCQ 118	27.2318	66.9652	1832.3	19	74.2	0.12	0.06	12.2	0.77	0.05	0.12	0.83	0.06	3.1	4.7	0.03	0.11	4.3	100.5	*tuff in tuffaceous sands/silts*
					0.6	*0.03*	*0.05*	*0.3*	*0.05*	*0.02*	*0.01*	*0.05*	*0.03*	*0.3*	*0.5*	*0.03*	*0.02*	*0.6*	*0.5*	
PCQ 585	27.2161	66.9508	1836	28	73.5	0.13	0.09	12.0	0.77	0.05	0.10	0.81	0.07	3.0	4.6	0.02	0.10	5.4	100.5	*2, tuffaceous sand*
					0.6	*0.05*	*0.06*	*0.1*	*0.05*	*0.03*	*0.02*	*0.05*	*0.04*	*0.3*	*0.4*	*0.02*	*0.02*	*0.7*	*0.3*	*reworked upper tuff of SS #12*
PCQ 585	*mode 2*			1	72.0	0.24	0.19	13.1	1.03	0.13	0.21	1.26	0.04	3.1	4.3	0.00	0.12	5.2	100.9	
PCQ 585	*mode 2*			1	72.3	0.19	0.11	13.1	0.87	0.10	0.22	1.18	0.06	3.0	4.7	0.02	0.15	5.3	101.2	
SS #12	27.2224	66.9548	1838		*major gray ss, laterally variable sheet sand which can be traced for ~5 km, tuffaceous in places*															*7, see Figure A.1*
PCQ 586	27.2161	66.9508	1841	18	72.5	0.14	0.06	13.1	0.88	0.08	0.13	0.78	0.06	1.4	4.2	0.04	0.15	7.2	100.6	*0.5, tuff block in sandstone #12*
					0.6	*0.02*	*0.01*	*0.4*	*0.06*	*0.02*	*0.01*	*0.05*	*0.02*	*0.2*	*0.4*	*0.03*	*0.02*	*0.6*	*1.0*	
PCQ 586	*mode 2*			1	72.0	0.40	0.03	12.9	1.54	0.04	0.21	0.81	0.14	1.4	5.3	0.15	0.09	6.8	101.8	
PCQ 586	*mode 2*			1	72.1	0.45	0.02	13.0	1.55	0.03	0.22	0.85	0.06	1.4	6.1	0.14	0.10	5.6	101.6	
PCQ 587	27.2161	66.9508	1848	6	72.7	0.08	0.06	12.9	0.80	0.08	0.09	0.58	0.07	1.4	5.1	0.05	0.14	6.0	100.1	*0.8, tuffaceous sand*
					1.2	*0.02*	*0.01*	*0.4*	*0.12*	*0.02*	*0.04*	*0.05*	*0.01*	*0.2*	*0.8*	*0.03*	*0.01*	*1.1*	*0.9*	
PCQ 587	*mode 2*			1	72.2	0.12	0.06	13.2	1.08	0.08	0.11	0.75	0.03	1.2	4.1	0.02	0.15	7.5	100.6	
PCQ 587	*mode 2*			1	71.3	0.15	0.08	13.4	1.25	0.10	0.14	0.85	0.08	1.6	5.6	0.06	0.11	5.4	100.1	
PCQ 587	*mode 3*			6	71.3	0.15	0.07	14.0	1.37	0.10	0.18	1.09	0.07	1.5	3.8	0.04	0.15	7.0	101.0	
					0.2	*0.01*	*0.01*	*0.1*	*0.04*	*0.01*	*0.01*	*0.04*	*0.02*	*0.1*	*0.2*	*0.03*	*0.01*	*0.4*	*0.6*	
PCQ 501	27.2245	66.9574	SS #12	5	73.18	0.14	0.03	11.60	0.85	0.05	0.14	0.96	0.04	2.8	4.5	0.00	0.11	5.8	100.2	*tuff in sandstone*
					0.72	*0.02*	*0.06*	*0.47*	*0.07*	*0.01*	*0.02*	*0.11*	*0.03*	*0.2*	*0.4*	*0.00*	*0.00*	*0.5*	*0.3*	

Table A.5 (*continued*)

Sample	Lat	Lon	strat	n	SiO2	TiO2	ZrO2	Al2O3	Fe2O3	MnO	MgO	CaO	BaO	Na2O	K2O	F	Cl	H2O	Total	Comment
	(°S)	(°W)	m																	thickness (m), lithology
PCQ 501	*mode 2*		SS #12	1	71.8	0.16	0.04	11.8	1.12	0.05	0.25	1.09	0.00	3.2	4.1	0.00	0.11	6.5	100.2	
PCQ 501	*mode 2*			1	72.0	0.22	0.00	12.1	1.12	0.02	0.22	1.08	0.01	3.6	3.9	0.00	0.10	5.9	100.3	
PCQ 501	*mode 3*			1	70.3	0.24	0.04	12.5	1.38	0.09	0.30	1.18	0.00	3.3	4.2	0.00	0.11	6.3	100.0	
PCQ 501	*mode 3*			1	69.7	0.23	0.11	13.5	1.48	0.03	0.35	1.42	0.05	2.9	4.6	0.00	0.10	5.7	100.2	
PCQ 501	*mode 4*			1	69.7	0.38	0.13	13.7	1.75	0.05	0.42	1.67	0.00	3.5	4.1	0.00	0.12	5.5	100.9	
PCQ 501	*mode 4*			1	69.6	0.35	0.00	13.1	1.96	0.03	0.48	1.71	0.01	3.5	3.9	0.00	0.10	5.5	100.2	
PCQ 501	*mode 4*			1	66.5	0.45	0.01	13.1	2.32	0.03	0.55	2.00	0.01	3.0	3.9	0.05	0.13	7.1	99.1	
PCQ 508	27.2251	66.9582	SS #12	14	72.9	0.11	0.08	13.0	0.85	0.09	0.10	0.59	0.07	2.9	5.3	0.04	0.15	5.5	101.8	*tuffaceous sand, plane bedded*
					0.5	*0.04*	*0.05*	*0.2*	*0.06*	*0.04*	*0.02*	*0.06*	*0.04*	*0.7*	*0.7*	*0.04*	*0.03*	*0.9*	*0.3*	
PCQ 509	27.2251	66.9582	SS #12	6	72.9	0.09	0.10	12.9	0.77	0.09	0.09	0.54	0.09	3.1	5.3	0.04	0.17	5.1	101.3	*tuff with lithic clasts*
					0.5	*0.04*	*0.05*	*0.2*	*0.09*	*0.05*	*0.03*	*0.07*	*0.05*	*0.4*	*0.6*	*0.04*	*0.02*	*0.7*	*0.3*	
PCQ 509	*mode 2*			4	72.5	0.25	0.09	12.9	1.11	0.06	0.24	1.08	0.06	3.4	4.3	0.05	0.15	5.5	101.6	
					0.1	*0.07*	*0.09*	*0.1*	*0.14*	*0.05*	*0.02*	*0.08*	*0.04*	*0.2*	*0.4*	*0.03*	*0.02*	*0.4*	*0.3*	
PCQ 503	27.2207	66.9533	1852	15	72.7	0.13	0.08	13.0	0.86	0.08	0.12	0.73	0.06	3.0	5.4	0.01	0.13	5.3	101.6	*0.2, tuff*
					1.1	*0.06*	*0.06*	*0.4*	*0.08*	*0.03*	*0.03*	*0.06*	*0.04*	*0.4*	*0.6*	*0.03*	*0.03*	*0.9*	*0.5*	
PCQ 1025	27.2261	66.9594	1853±10	16	71.9	0.10	0.05	12.8	0.79	0.09	0.10	0.56	0.05	3.2	5.0	0.03	0.16	6.3	101.1	*correlate of 508, 509, 587 (?)*
					0.6	*0.04*	*0.03*	*0.2*	*0.04*	*0.02*	*0.02*	*0.04*	*0.03*	*0.5*	*0.6*	*0.03*	*0.01*	*0.4*	*0.6*	
PCQ 1033	27.2324	66.9693	~1950	19	72.2	0.11	0.04	12.7	0.75	0.05	0.09	0.92	0.04	3.1	5.1		0.11	5.3	100.5	*0.4 –1.2, sample pumice*
					0.2	*0.03*	*0.04*	*0.2*	*0.04*	*0.02*	*0.01*	*0.02*	*0.03*	*0.3*	*0.5*		*0.01*	*0.3*	*0.3*	
PCQ 1032	27.2332	66.9714	1998	19	72.7	0.09	0.04	12.0	0.61	0.05	0.06	0.60	0.06	2.6	5.8		0.12	5.6	100.3	*0.3, pumice rich upper*
					0.4	*0.03*	*0.04*	*0.1*	*0.03*	*0.02*	*0.01*	*0.02*	*0.02*	*0.2*	*0.3*		*0.01*	*0.6*	*0.3*	
PCQ 1034	27.2302	66.9682	1998	18	72.8	0.11	0.03	12.2	0.61	0.05	0.06	0.61	0.05	2.7	5.5		0.12	5.5	100.3	*0.75, in gravel, sample pumice*
					0.5	*0.03*	*0.03*	*0.2*	*0.05*	*0.02*	*0.01*	*0.04*	*0.03*	*0.3*	*0.5*		*0.01*	*0.6*	*0.3*	
PCQ 1034	*replicate analysis*			25	73.4	0.11	0.04	12.0	0.64	0.05	0.06	0.63	0.05	2.6	5.5	0.01	0.13	5.6	100.8	*preferred values, see Table 3.5*
					0.4	*0.03*	*0.04*	*0.2*	*0.04*	*0.02*	*0.02*	*0.03*	*0.03*	*0.3*	*0.5*	*0.01*	*0.01*	*0.6*	*0.3*	
PCQ 577	27.2222	66.9605	2055		*not analyzed*															*0.2, tuff on top of sandstone*
PCQ 576	27.2225	66.9608	2062		*not analyzed*															*0.05, pumice tuff below gravel*
PCQ 802	27.2209	66.9600	2062	9	69.5	0.36	0.07	13.4	1.64	0.02	0.33	1.39	0.03	3.1	5.1	0.05	0.13	5.2	100.1	*0.2, pumice tuff below gravel*
					0.6	*0.08*	*0.06*	*0.4*	*0.16*	*0.02*	*0.05*	*0.20*	*0.03*	*0.2*	*0.2*	*0.04*	*0.02*	*0.4*	*0.5*	

Table A.5 (*continued*)

Sample	Lat	Lon	strat	n	SiO2	TiO2	ZrO2	Al2O3	Fe2O3	MnO	MgO	CaO	BaO	Na2O	K2O	F	Cl	H2O	Total	Comment
	(°S)	(°W)	m																	thickness (m), lithology
TCQ			2072		*Toba Corral Quemado (TCQ); soft-sediment deformation at base, cross-bedded throughout*															*14, see Figure A.1*
Arg 241	27.2227	66.9609	2072	17	72.8	0.09		11.9	0.60	0.07	0.06	0.42	0.00	2.6	6.0	0.01	0.16	6.5	101.1	*sanidine date (3.66 ± 0.10 Ma)*
					0.4	*0.03*		*0.1*	*0.04*	*0.02*	*0.02*	*0.02*	*0.01*	*0.3*	*0.6*	*0.01*	*0.01*	*0.6*	*0.5*	
Arg 241	*mode 2*			1	72.9	0.13		11.9	0.77	0.08	0.11	0.55	0.06	2.3	6.2	0.00	0.14	6.0	101.0	
Arg 241	*mode 2*			1	73.2	0.14		12.0	0.84	0.06	0.07	0.58	0.00	2.1	6.5	0.00	0.13	5.4	100.9	
Arg 241	*mode 2*			1	71.1	0.25		12.3	0.85	0.05	0.09	0.65	0.07	1.9	6.4	0.00	0.14	7.9	101.7	
Arg 241	*replicate analysis*			20	73.7	0.11		11.8	0.59	0.07	0.06	0.41	0.01	2.6	5.5	0.02	0.16	6.2	101.3	
					0.3	*0.03*		*0.1*	*0.05*	*0.02*	*0.01*	*0.02*	*0.02*	*0.3*	*0.4*	*0.02*	*0.01*	*1.0*	*0.9*	
Arg 241	*replicate analysis*			15	73.7	0.11	0.03	12.1	0.61	0.08	0.06	0.41	0.01	2.8	5.6	0.02	0.15	4.7	100.4	
					0.4	*0.05*	*0.04*	*0.2*	*0.05*	*0.02*	*0.02*	*0.03*	*0.02*	*0.2*	*0.5*	*0.03*	*0.02*	*0.6*	*0.5*	
PCQ 109a	27.2244	66.9636	2072	20	74.2	0.09	0.05	12.2	0.59	0.07	0.07	0.39	0.00	3.1	5.2	0.05	0.17	4.6	100.6	*very base of TCQ, fine grained*
					0.4	*0.02*	*0.04*	*0.2*	*0.04*	*0.02*	*0.01*	*0.02*	*0.01*	*0.3*	*0.4*	*0.03*	*0.01*	*0.5*	*0.3*	
PCQ 109b	27.2244	66.9636	2073	16	74.4	0.10	0.06	12.1	0.57	0.08	0.07	0.39	0.01	3.3	5.1	0.03	0.16	4.6	101.0	*base TCQ, coarse, indurated*
					0.6	*0.03*	*0.05*	*0.1*	*0.06*	*0.02*	*0.01*	*0.01*	*0.01*	*0.3*	*0.4*	*0.03*	*0.01*	*0.7*	*0.3*	
PCQ 582	27.2217	66.9606	2073	30	73.4	0.09	0.06	12.0	0.60	0.08	0.06	0.41	0.03	3.0	5.3	0.03	0.16	5.4	100.5	*base TCQ*
					0.6	*0.06*	*0.06*	*0.2*	*0.06*	*0.03*	*0.02*	*0.04*	*0.03*	*0.3*	*0.5*	*0.03*	*0.02*	*0.9*	*0.5*	
PCQ 511	27.2100	66.9526	2074	19	74.4	0.10	0.09	12.1	0.60	0.07	0.06	0.40	0.01	2.9	5.5	0.03	0.17	5.1	101.5	*pumice in lower TCQ*
					0.5	*0.04*	*0.07*	*0.2*	*0.05*	*0.04*	*0.02*	*0.02*	*0.02*	*0.4*	*0.5*	*0.04*	*0.02*	*0.7*	*0.3*	
PCQ 583	27.2217	66.9606	2078	30	73.5	0.09	0.08	12.0	0.59	0.09	0.06	0.40	0.01	2.9	5.3	0.02	0.17	5.7	100.9	*middle TCQ*
					0.7	*0.04*	*0.07*	*0.2*	*0.05*	*0.03*	*0.01*	*0.03*	*0.02*	*0.4*	*0.4*	*0.03*	*0.02*	*0.8*	*0.4*	
PCQ 584	27.2217	66.9606	2084	28	73.4	0.11	0.06	11.9	0.61	0.08	0.06	0.40	0.02	3.1	5.1	0.02	0.16	5.4	100.5	*upper TCQ*
					0.8	*0.04*	*0.06*	*0.1*	*0.06*	*0.03*	*0.02*	*0.04*	*0.02*	*0.3*	*0.3*	*0.03*	*0.02*	*0.9*	*0.4*	
PCQ 803	27.2209	66.9600	2096	14	74.8	0.09	0.08	12.3	0.59	0.06	0.06	0.42	0.02	3.0	5.4		0.16	3.6	100.5	*0.05, tuffaceous in fine red ss*
					0.9	*0.04*	*0.05*	*0.2*	*0.11*	*0.04*	*0.02*	*0.07*	*0.03*	*0.4*	*0.6*		*0.03*	*0.8*	*0.6*	*reworked TCQ?*
PCQ 147	27.2220	66.9614	2112		*not analyzed*															*0.2, tuff*
PCQ 804	27.2205	66.9608	2112	15	72.9	0.07	0.09	12.1	0.79	0.06	0.04	0.70	0.03	2.3	6.1	0.02	0.12	4.6	100.0	*0.1, fine-grained glassy tuff*
					0.5	*0.04*	*0.07*	*0.2*	*0.05*	*0.03*	*0.02*	*0.03*	*0.03*	*0.2*	*0.2*	*0.03*	*0.02*	*0.5*	*0.3*	
PCQ 804	*mode 2*			1	72.6	0.12	0.04	12.4	0.89	0.05	0.11	0.94	0.04	2.9	4.8	0.01	0.11	5.3	100.3	
PCQ 804	*mode 2*			1	71.4	0.10	0.13	12.6	1.03	0.09	0.10	0.95	0.02	2.6	5.6	0.04	0.11	4.9	99.5	
PCQ 804	*mode 2*			1	71.6	0.05	0.21	13.1	1.34	0.08	0.17	1.14	0.06	3.3	4.6	0.02	0.13	4.5	100.2	

Table A.5 (*continued*)

Sample	Lat	Lon	strat	n	SiO2	TiO2	ZrO2	Al2O3	Fe2O3	MnO	MgO	CaO	BaO	Na2O	K2O	F	Cl	H2O	Total	Comment
	(°S)	(°W)	m																	thickness (m), lithology
Arg 244	27.2213	66.9631	2198	19	72.5	0.18		12.1	0.95	0.04	0.13	0.76	0.03	2.7	5.4	0.01	0.17	5.9	100.8	*5, see Figure A.1*
					0.6	*0.04*		*0.1*	*0.05*	*0.02*	*0.02*	*0.02*	*0.02*	*0.1*	*0.2*	*0.02*	*0.01*	*0.9*	*0.8*	
Arg 244	*mode 2*			1	72.6	0.18	0.00	12.0	0.75	0.03	0.08	0.39	0.05	2.3	6.8	0.13	0.17	3.6	98.9	
Arg 244	*mode 2*			1	72.7	0.20	0.00	12.4	0.84	0.06	0.12	0.54	0.02	3.0	5.4	0.01	0.18	5.3	100.7	
Arg 244	*replicate analysis*			30	73.4	0.18	0.08	12.1	0.92	0.05	0.12	0.69	0.04	2.6	5.7	0.03	0.18	5.7	101.7	
					0.6	*0.06*	*0.06*	*0.2*	*0.09*	*0.03*	*0.02*	*0.04*	*0.03*	*0.4*	*0.3*	*0.03*	*0.02*	*0.4*	*0.4*	
PCQ 578	27.2212	66.9631	2198	24	72.8	0.17	0.06	12.1	0.97	0.04	0.12	0.72	0.04	2.7	5.6	0.02	0.18	5.4	100.9	*5, sample basal meter*
					0.6	*0.04*	*0.06*	*0.1*	*0.07*	*0.03*	*0.02*	*0.04*	*0.03*	*0.2*	*0.4*	*0.03*	*0.02*	*0.8*	*0.4*	
PCQ 805	27.2200	66.9620	2198	18	73.2	0.18	0.07	12.2	0.91	0.04	0.12	0.71	0.04	2.8	5.4	0.03	0.17	4.3	100.2	*5, upper 4 m reworked*
					0.3	*0.05*	*0.05*	*0.1*	*0.07*	*0.02*	*0.02*	*0.03*	*0.04*	*0.1*	*0.2*	*0.04*	*0.01*	*0.5*	*0.4*	*x-beds indicate flow to NE*
PCQ 148	27.2213	66.9631	2198		*not analyzed*															
PCQ 150	27.2371	66.9777	2198		*not analyzed*															
PCQ 149	27.2249	66.9669	2203		*not analyzed*															*tuffaceous sandstone*
Arg 267			2283	18	74.2	0.07	0.04	12.2	0.65	0.06	0.07	0.84	0.03	3.0	5.1	0.02	0.09	4.3	100.7	*thick white tuff in cliff face*
					0.3	*0.04*	*0.06*	*0.2*	*0.04*	*0.04*	*0.02*	*0.06*	*0.03*	*0.1*	*0.2*	*0.02*	*0.01*	*0.4*	*0.3*	
Arg 267	*replicate analysis*		2283	14	73.9	0.07	0.04	12.1	0.65	0.07	0.07	0.81	0.03	2.7	5.1	0.01	0.10	3.8	99.4	
					0.5	*0.04*	*0.06*	*0.3*	*0.05*	*0.03*	*0.02*	*0.03*	*0.03*	*0.1*	*0.2*	*0.01*	*0.02*	*0.7*	*0.4*	
Arg 267	*mode 2*			1	73.6	0.16	0.12	11.9	0.90	0.10	0.12	0.67	0.02	2.5	5.2	0.00	0.20	4.3	99.7	
Arg 267	*mode 2*			1	73.1	0.09	0.12	11.8	0.97	0.01	0.13	0.72	0.01	2.4	5.3	0.03	0.18	4.8	99.6	
PCQ 579	27.2210	66.9643	2283																	
PCQ 806	27.2209	66.9644	2283	18	73.9	0.09	0.07	12.4	0.66	0.05	0.07	0.84	0.03	3.0	5.1	0.03	0.10	4.0	100.3	*1.5, sandy (lithic) above 30 cm*
					0.3	*0.05*	*0.05*	*0.2*	*0.05*	*0.03*	*0.02*	*0.04*	*0.03*	*0.1*	*0.2*	*0.03*	*0.02*	*0.5*	*0.4*	
PCQ 807	27.2210	66.9649	2317	18	73.8	0.13	0.09	12.5	0.69	0.04	0.08	0.87	0.04	3.1	5.0	0.02	0.11	4.1	100.5	*5, sandy tuff overlain by congl.*
					0.4	*0.04*	*0.07*	*0.2*	*0.05*	*0.02*	*0.02*	*0.04*	*0.03*	*0.2*	*0.2*	*0.03*	*0.02*	*0.4*	*0.4*	
PCQ 512	27.2158	66.9689	>2400	33	74.3	0.06	0.06	12.6	0.48	0.11	0.03	0.51	0.00	3.7	4.7		0.03	5.5	102.1	*cross-bedded clean tuff in ss*
					1.0	*0.03*	*0.05*	*0.2*	*0.04*	*0.03*	*0.02*	*0.05*	*0.01*	*0.3*	*0.4*		*0.02*	*0.9*	*0.7*	*S211 D15; unconformable*
PCQ 512	*replicate analysis*			17	73.9	0.05	0.06	12.5	0.46	0.11	0.03	0.47	0.01	3.7	4.8	0.06	0.03	5.5	101.7	
					0.7	*0.04*	*0.05*	*0.2*	*0.05*	*0.03*	*0.02*	*0.04*	*0.02*	*0.4*	*0.4*	*0.05*	*0.01*	*0.8*	*0.4*	

*Elemental composition of volcanic glass by Electron Probe Microanalysis (cf. Nash, 1992), n=number of shards, for n≥4 average and 1σ standard deviation are reported.

Table A.6: Stratigraphy and composition of volcanic ash beds from Los Barcos section (PCQ)
(base of section = 27.2211°S, 66.9143°W; total thickness ~560 m)

Sample	Lat	Lon	strat	n*	SiO2	TiO2	ZrO2	Al2O3	Fe2O3	MnO	MgO	CaO	BaO	Na2O	K2O	F	Cl	H2O	Total	Comment
	(°S)	(°W)	m																	thickness (m), lithology
PCQ 1015	27.2211	66.9143	2.5		*not analyzed; Toba del Puerto, 7.14 Ma, S215 D30*															*8, sampled basal white portion*
Fossiliferous red clay			130																	*fossil teeth from this interval*
Red/white interbeds; traceable			303																	*2.2, S220 D25*
PCQ 1016	27.2199	66.9223	322	25	73.6	0.10	0.06	12.1	0.66	0.07	0.07	0.48	0.09	3.1	4.3	0.02	0.18	5.5	100.3	*0.05, toba milanesa*
					0.3	*0.05*	*0.07*	*0.1*	*0.06*	*0.03*	*0.02*	*0.03*	*0.03*	*0.1*	*0.5*	*0.03*	*0.02*	*0.6*	*0.3*	
Red bed; traceable			350.2																	*0.8, traceable red band*
PCQ 798	27.2212	66.9251	352.9	5	73.5	0.06	0.05	12.2	0.50	0.11	0.03	0.46	0.01	3.9	4.3	0.01	0.06	4.9	100.0	*1, white lenses in coarse ss*
					1.0	*0.05*	*0.07*	*0.2*	*0.04*	*0.02*	*0.02*	*0.02*	*0.01*	*0.0*	*0.1*	*0.02*	*0.01*	*0.7*	*0.6*	
PCQ 798	*mode 2*			1	73.2	0.06	0.11	12.0	0.56	0.00	0.05	0.67	0.08	3.4	3.8	0.00	0.04	6.0	99.9	
PCQ 798	*mode 2*			1	72.2	0.07	0.03	12.9	0.71	0.07	0.14	0.66	0.02	2.9	3.4	0.00	0.14	8.1	101.2	
PCQ 798	*mode 2*			1	71.9	0.16	0.07	12.6	0.77	0.09	0.09	0.62	0.12	2.9	3.4	0.00	0.16	8.2	101.0	
PCQ 798	*mode 2*			1	72.3	0.12	0.18	12.0	0.72	0.09	0.07	0.46	0.09	3.1	4.4	0.00	0.18	6.3	100.1	
PCQ 800			366.2		*not analyzed*															*thin white bed in corral wall*
PCQ 799			366.9		*not analyzed*															*1.5, pumice at base, x-bedded*
PCQ 801	27.2197	66.9235	370.9		*not analyzed*															*lateral equivalent of PCQ 799*
Tuff	27.2191	66.9227	370.9		*not sampled*															*traced PCQ 799 to this position*
Carbonate ledge			379.6		*not sampled*															*0.2, top of 8.7 m thick gravel*
Tuff			429		*not sampled*															*thin, detrital contamination*
Tuff			517.3		*not sampled*															*0.15, lower piece of doublet*
Tuff			518.9		*not sampled*															*1.5, upper piece of doublet*
Tuff			526.4		*not sampled*															*0.5*
Tuff			529.1		*not sampled*															*1.1*
PCQ 1017	27.2178	66.9233	544.7	23	73.2	0.10	0.07	11.8	0.75	0.04	0.08	0.90	0.04	2.2	5.6	0.02	0.13	5.1	100.0	*0.5*
					0.5	*0.04*	*0.06*	*0.1*	*0.06*	*0.03*	*0.02*	*0.04*	*0.03*	*0.1*	*0.2*	*0.02*	*0.02*	*0.4*	*0.4*	
PCQ 1018	27.2178	66.9233	550.7	26	72.2	0.09	0.07	12.2	0.57	0.05	0.07	0.90	0.08	2.3	5.4	0.02	0.07	5.9	99.9	*0.3, eolian lenses to 1.5 m*
					0.3	*0.04*	*0.05*	*0.2*	*0.06*	*0.02*	*0.02*	*0.03*	*0.03*	*0.1*	*0.1*	*0.03*	*0.01*	*0.5*	*0.3*	

*Elemental composition of volcanic glass by Electron Probe Microanalysis (cf. Nash, 1992), n=number of shards, for n≥4 average and 1σ standard deviation are reported.

Table A.7: Stratigraphy and composition of volcanic ash beds from upper Los Barcos section (PCQ)
(base of section = 27.2199°S, 66.9268°W; total thickness ~1 km)

Sample	Lat	Lon	strat	n*	SiO2	TiO2	ZrO2	Al2O3	Fe2O3	MnO	MgO	CaO	BaO	Na2O	K2O	F	Cl	H2O	Total	Comment
	(°S)	(°W)	m																	thickness (m), lithology
PCQ 737	27.2199	66.9268	0.0		*not analyzed*															*0.2, biotite pumice tuff*
PCQ 738			3.2		*not analyzed*															*1, fine grained tuff*
PCQ 739	27.2184	66.9241	0.0		*not analyzed*															*0.25, reworked tuff*
PCQ 740			3.3		*not analyzed*															*0.1, tuff in eolian strata*
PCQ 741			5.1		*not analyzed*															*0.7, tuff, poorly preserved*
PCQ 742			19.4		*not analyzed*															*0.25, tuff*
PCQ 743			23.5	20	72.9	0.08	0.04	12.3	0.62	0.05	0.08	0.92	0.07	2.2	5.4	0.00	0.07	6.3	101.0	*0.4, tuff, sample coarse base*
					0.2	*0.03*	*0.05*	*0.1*	*0.03*	*0.02*	*0.01*	*0.02*	*0.03*	*0.4*	*0.4*	*0.01*	*0.01*	*0.6*	*0.3*	
PCQ 744	27.2178	66.9238	30.7		*not analyzed*															*0.02, tuff beneath carbonate*
PCQ 745	27.2178	66.9233	32.5	18	72.5	0.09	0.07	12.4	0.62	0.04	0.08	0.90	0.06	2.3	5.3		0.07	6.3	100.6	*0.01, pumice in eolian beds*
					0.4	*0.04*	*0.06*	*0.2*	*0.05*	*0.03*	*0.02*	*0.04*	*0.03*	*0.1*	*0.1*		*0.02*	*0.5*	*0.2*	
PCQ 746			38.7		*not analyzed*															*0.6 tuff/marl?*
PCQ 747	27.2154	66.9247	81.9	9	72.1	0.20	0.08	12.6	1.12	0.06	0.17	0.95	0.06	2.5	5.2	0.04	0.21	5.0	100.2	*0.4, coarse tuff*
					0.3	*0.06*	*0.04*	*0.1*	*0.07*	*0.03*	*0.02*	*0.02*	*0.04*	*0.1*	*0.2*	*0.02*	*0.02*	*0.6*	*0.5*	
PCQ 748			104.3		*not analyzed*															*0.7, fine tuff*
PCQ 749			106.6		*not analyzed*															*0.6, tuff*
PCQ 751	27.2135	66.9263	153.2		*not analyzed*															*0.01 tuff in eolian strata*
PCQ 752			167.6		*not analyzed*															*0.05 tuff*
PCQ 753			184.3		*not analyzed*															*0.01, tuff, poor preservation*
PCQ 754			225.3		*not analyzed*															*0.01, some pumice at base*
PCQ 755			230.2		*not analyzed*															*0.01, tuff*
PCQ 756			237.3		*not analyzed*															*0.05, lower tuff of doublet*
PCQ 757			237.7	6	67.7	0.39	0.09	14.3	2.13	0.06	0.51	2.00	0.00	3.0	3.9	0.04	0.11	6.7	100.8	*0.2 upper tuff of doublet, fluvial*
					1.0	*0.04*	*0.04*	*0.5*	*0.16*	*0.03*	*0.04*	*0.33*	*0.01*	*0.4*	*0.3*	*0.03*	*0.02*	*0.9*	*0.9*	
PCQ 758			238.9		*not analyzed*															*0.01 tuff*
PCQ 759	27.2128	66.9293	241.4	9	71.3	0.10	0.09	13.1	0.88	0.06	0.11	1.17	0.07	3.0	4.4	0.00	0.13	5.8	100.2	*0.1, pumice, fluvial cross beds*
					0.6	*0.04*	*0.06*	*0.1*	*0.04*	*0.03*	*0.01*	*0.04*	*0.03*	*0.1*	*0.2*	*0.00*	*0.01*	*0.4*	*0.3*	

Table A.7 (*continued*)

Sample	Lat	Lon	strat	n	SiO2	TiO2	ZrO2	Al2O3	Fe2O3	MnO	MgO	CaO	BaO	Na2O	K2O	F	Cl	H2O	Total	Comment
	(°S)	(°W)	m																	thickness (m), lithology
PCQ 760			281.0		*not analyzed*															*0.01, fine tuff*
PCQ 761			322.5		*not analyzed*															*0.1, tuff, crystalline at base*
PCQ 762			327.1		*not analyzed*															*0.4, below coarse ss*
PCQ 763			373.1	7	74.6	0.07	0.05	12.5	0.49	0.05	0.04	0.56	0.02	2.6	5.6	0.03	0.06	4.2	100.9	*0.5, white/gray/white interbeds*
					1.8	*0.03*	*0.05*	*0.2*	*0.05*	*0.03*	*0.01*	*0.07*	*0.02*	*0.9*	*1.0*	*0.03*	*0.01*	*2.1*	*0.6*	
PCQ 763	*mode 2*			8	72.8	0.06	0.01	12.4	0.54	0.02	0.05	0.82	0.07	1.8	5.8	0.02	0.07	6.8	101.2	
					0.4	*0.03*	*0.01*	*0.2*	*0.05*	*0.01*	*0.01*	*0.03*	*0.03*	*0.7*	*0.9*	*0.02*	*0.01*	*0.9*	*0.5*	
PCQ 764			386.1		*not analyzed*															*0.15, lenticular tuff, pumiceous*
PCQ 765			396.8		*not analyzed*															*0.05, tuff/marl?*
PCQ 766			397.3		*not analyzed*															*0.05, tuff/marl?*
PCQ 767	27.2112	66.9323	399.1		*not analyzed*															*0.05, tuff*
PCQ 768			409.8		*not analyzed*															*0.08, tuff*
PCQ 769			417.4		*not analyzed*															*0.05, tuff/marl?*
PCQ 770			422.9		*not analyzed*															*0.1, tuff, pumiceous lag deposit*
PCQ 771			423.5		*not analyzed*															*0.05, tuff*
PCQ 1048	27.2154	66.9355	420±5	15	72.3	0.09	0.05	12.0	0.63	0.07	0.07	0.92	0.09	2.1	6.1		0.1	5.5	100.0	*0.05, pumice at base*
					0.6	*0.04*	*0.04*	*0.1*	*0.04*	*0.02*	*0.01*	*0.05*	*0.03*	*0.1*	*0.1*		*0.0*	*0.5*	*0.3*	
PCQ 1048	*mode 2*			1	71.8	0.25	0.09	13.4	0.97	0.03	0.18	1.15	0.02	3.4	4.1		0.12	5.0	100.6	
PCQ 1048	*mode 2*			1	71.6	0.14	0.00	13.2	1.00	0.04	0.17	1.15	0.02	3.2	4.6		0.10	4.8	100.0	
PCQ 1048	*mode 2*			1	72.5	0.13	0.02	13.2	1.01	0.07	0.17	1.20	0.07	0.6	3.9		0.14	7.4	100.4	
PCQ 1049	27.2154	66.9355	420±5	18	72.3	0.10	0.04	12.4	0.66	0.07	0.08	0.95	0.09	2.1	6.0		0.12	5.5	100.3	*0.55, coarse base, biotite*
					0.5	*0.04*	*0.04*	*0.2*	*0.03*	*0.02*	*0.01*	*0.02*	*0.03*	*0.3*	*0.3*		*0.01*	*0.6*	*0.4*	
PCQ 772			428.2	9	71.8	0.09	0.10	12.8	0.80	0.04	0.10	1.00	0.06	2.5	5.5		0.08	5.4	100.3	*0.05, tuff, pumiceous cross bed*
					0.8	*0.07*	*0.08*	*0.3*	*0.07*	*0.02*	*0.02*	*0.10*	*0.03*	*0.5*	*0.6*		*0.02*	*0.5*	*0.4*	
PCQ 772	*mode 2*			1	74.6	0.08	0.00	13.2	0.59	0.15	0.10	0.22	0.00	3.5	4.4		0.12	3.6	100.5	
PCQ 772	*mode 2*			1	75.3	0.04	0.06	13.0	0.66	0.08	0.15	0.52	0.06	3.7	3.9		0.06	3.6	101.1	*potential correlate = PCQ 202*
PCQ 772	*mode 2*			1	74.4	0.13	0.10	12.1	0.57	0.05	0.06	0.58	0.11	2.6	5.8		0.09	3.1	99.7	*potential correlate = PCQ 202*
PCQ 772	*mode 3*			1	68.5	0.27	0.20	14.5	1.55	0.00	0.35	1.62	0.01	3.1	4.3		0.16	5.6	100.2	
PCQ 772	*mode 3*			1	65.3	0.68	0.01	15.0	3.28	0.06	0.88	2.82	0.00	3.5	3.6		0.12	5.9	101.1	

Table A.7 (*continued*)

Sample	Lat	Lon	strat	n	SiO2	TiO2	ZrO2	Al2O3	Fe2O3	MnO	MgO	CaO	BaO	Na2O	K2O	F	Cl	H2O	Total	Comment
	(°S)	(°W)	m																	thickness (m), lithology
PCQ 773			447.1		*not analyzed*															*0.5, tuff/marl?*
PCQ 774			469.0	19	72.4	0.12	0.07	13.0	0.86	0.07	0.13	0.75	0.08	3.0	5.4	0.02	0.14	5.7	101.7	*0.4, coarse pumice tuff*
					0.4	*0.04*	*0.05*	*0.1*	*0.03*	*0.02*	*0.02*	*0.02*	*0.03*	*0.4*	*0.7*	*0.02*	*0.01*	*0.4*	*0.3*	
PCQ 775	27.2106	66.9348	470.4		*not analyzed*															*0.1, fine white tuff; burrowed*
PCQ 776			490.0	20	72.3	0.11	0.07	13.2	0.91	0.10	0.12	0.78	0.05	3.3	4.6	0.04	0.14	6.0	101.7	*0.1, fine tuff, indurated*
					0.3	*0.03*	*0.04*	*0.1*	*0.04*	*0.02*	*0.01*	*0.03*	*0.02*	*0.2*	*0.3*	*0.03*	*0.01*	*0.4*	*0.2*	
PCQ 777	27.2111	66.9372	584.6	20	72.9	0.09	0.04	11.9	0.67	0.07	0.07	1.00	0.02	1.8	6.1	0.00	0.11	5.6	100.5	*0.1, fine tuff grading to pumice*
					0.3	*0.03*	*0.06*	*0.1*	*0.03*	*0.02*	*0.01*	*0.03*	*0.02*	*0.4*	*0.5*	*0.01*	*0.01*	*0.7*	*0.3*	
PCQ 778			595.3	15	72.4	0.14	0.10	12.2	0.75	0.03	0.13	1.02	0.07	2.4	5.3	0.01	0.07	5.1	99.7	*0.15, lenticular pods ~5m wide*
					0.6	*0.05*	*0.06*	*0.2*	*0.07*	*0.03*	*0.02*	*0.10*	*0.03*	*0.4*	*0.6*	*0.02*	*0.01*	*0.5*	*0.6*	
PCQ 779	27.2108	66.9376	615.7		*not analyzed*															*0.5, altered tuff*
PCQ 780			636.2		*not analyzed*															*0.1, altered tuff below gravel*
PCQ 781	27.2211	66.9384	644.9		*not analyzed*															*0.4, fine tuff, not indurated*
PCQ 782	27.2103	66.9408	745.9		*not analyzed*															*0.05, tuff/marl?*
PCQ 784			752.3	17	73.5	0.09	0.04	11.8	0.69	0.05	0.08	0.64	0.06	2.4	5.7	0.00	0.12	5.5	100.7	*0.5, pumice cross beds*
					0.5	*0.03*	*0.05*	*0.1*	*0.04*	*0.02*	*0.01*	*0.06*	*0.04*	*0.4*	*0.6*	*0.00*	*0.02*	*0.8*	*0.4*	
PCQ 784	*mode 2*			1	74.3	0.10	0.00	12.9	0.43	0.03	0.08	0.68	0.05	3.9	4.7	0.00	0.11	3.3	100.6	
PCQ 784	*mode 2*			1	74.3	0.20	0.13	13.0	0.38	0.05	0.08	0.66	0.03	2.8	4.6	0.00	0.12	4.4	100.7	
PCQ 785	27.2102	66.3414	763.3		*not analyzed*															*0.02, tuff, fine biotite, indurated*
PCQ 786			781.3	8	73.5	0.12	0.08	11.9	0.67	0.05	0.07	0.70	0.08	2.4	5.8	0.00	0.13	4.6	100.2	*0.02, pumice in fine-medium ss*
					1.0	*0.05*	*0.07*	*0.3*	*0.05*	*0.02*	*0.02*	*0.11*	*0.04*	*0.5*	*0.7*	*0.00*	*0.03*	*0.9*	*0.4*	
PCQ 786	*mode 2*			1	71.2	0.21	0.06	12.4	0.97	0.08	0.12	0.85	0.05	2.3	5.9	0.00	0.17	6.4	100.6	
PCQ 786	*mode 2*			1	72.1	0.23	0.10	12.1	1.07	0.08	0.12	0.81	0.10	2.4	6.2	0.00	0.19	5.1	100.5	
PCQ 786	*mode 3*			1	70.2	0.26	0.18	12.6	1.15	0.04	0.20	1.01	0.12	2.6	5.9	0.00	0.14	5.1	99.5	
PCQ 786	*mode 3*			1	71.2	0.11	0.00	12.6	1.18	0.01	0.17	1.11	0.02	2.4	5.9	0.00	0.16	5.0	99.7	
PCQ 786	*mode 3*			1	70.3	0.26	0.13	13.2	1.19	0.08	0.24	1.02	0.03	2.8	5.4	0.00	0.17	5.5	100.3	
PCQ 787			791.3		*not analyzed*															*0.05, tuff*
PCQ 788			806.4		*not analyzed*															*0.1, tuff*

Table A.7 (*continued*)

Sample	Lat	Lon	strat	n	SiO2	TiO2	ZrO2	Al2O3	Fe2O3	MnO	MgO	CaO	BaO	Na2O	K2O	F	Cl	H2O	Total	Comment
	(°S)	(°W)	m																	thickness (m), lithology
PCQ 789			809.2	24	71.2	0.23	0.05	13.0	1.26	0.04	0.24	1.13	0.04	2.7	5.6	0.00	0.19	5.1	100.7	*0.3, coarse tuff*
					0.6	*0.03*	*0.04*	*0.2*	*0.06*	*0.02*	*0.02*	*0.03*	*0.03*	*0.4*	*0.4*	*0.01*	*0.02*	*0.5*	*0.6*	
PCQ 789	*mode 2*			1	66.8	0.59	0.36	14.6	2.28	0.02	0.37	2.55	0.04	2.9	5.8	0.00	0.07	3.0	0.0	
PCQ 790			851.5		*not analyzed*															*0.05, lenticular tuff, fine*
PCQ 791	27.2074	66.9409	874.1	15	72.3	0.11	0.07	12.6	0.69	0.07	0.09	0.61	0.06	2.6	5.6		0.12	5.3	100.3	*0.05, fine tuff, burrowed*
					0.8	*0.05*	*0.04*	*0.2*	*0.07*	*0.02*	*0.02*	*0.03*	*0.03*	*0.3*	*0.4*		*0.02*	*0.6*	*0.4*	
PCQ 792	27.2066	66.9416	916.3	20	74.1	0.11	0.07	12.2	0.72	0.04	0.10	0.85	0.06	2.8	4.8	0.01	0.10	5.4	101.3	*0.45, tuff with pumiceous base*
					0.4	*0.02*	*0.05*	*0.5*	*0.04*	*0.02*	*0.01*	*0.03*	*0.03*	*0.2*	*0.4*	*0.01*	*0.01*	*1.0*	*0.7*	
lower tuff of Sandstone #12			*~920.5*																	
PCQ 793	27.2048	66.9408	920.7	11	72.1	0.18	0.11	13.2	1.02	0.04	0.19	1.19	0.05	3.3	3.9		0.12	5.8	101.1	*0.5, tuff, sampled coarse gray*
					0.3	*0.06*	*0.07*	*0.2*	*0.06*	*0.02*	*0.02*	*0.05*	*0.04*	*0.2*	*0.2*		*0.01*	*0.5*	*0.3*	
PCQ 793	*mode 2*			1	73.4	0.10	0.00	11.9	0.76	0.07	0.09	0.79	0.04	2.5	4.7		0.10	6.2	0.0	
PCQ 794	27.1956	66.9371	920.7	17	72.1	0.16	0.07	13.2	0.97	0.06	0.18	1.19	0.06	3.3	4.1	0.02	0.12	5.0	100.4	*0.5, base cross-bedded tuff*
					0.3	*0.05*	*0.05*	*0.2*	*0.06*	*0.03*	*0.02*	*0.03*	*0.04*	*0.2*	*0.4*	*0.03*	*0.01*	*0.4*	*0.4*	
PCQ 794	*mode 2*			1	73.1	0.21	0.09	12.8	0.79	0.07	0.13	1.03	0.06	3.2	4.2	0.08	0.14	4.8	100.6	
PCQ 794	*mode 2*			1	73.2	0.10	0.06	12.5	0.69	0.04	0.17	0.94	0.04	3.3	4.4	0.00	0.12	4.8	100.4	
PCQ 795	27.1933	66.9387	920.7	10	71.3	0.18	0.09	12.9	0.98	0.05	0.18	1.17	0.06	3.0	4.3	0.00	0.11	5.6	99.9	*8.5, tuff, sampled coarse gray*
					0.3	*0.05*	*0.07*	*0.2*	*0.05*	*0.04*	*0.02*	*0.04*	*0.04*	*0.7*	*0.5*	*0.01*	*0.01*	*0.6*	*0.4*	
PCQ 796	27.1929	66.9394	949.4	20	72.1	0.12	0.07	13.3	0.85	0.08	0.13	0.77	0.06	3.3	4.7	0.04	0.14	4.9	100.5	*0.3, tuff*
					0.3	*0.04*	*0.07*	*0.2*	*0.04*	*0.03*	*0.02*	*0.03*	*0.04*	*0.2*	*0.4*	*0.03*	*0.02*	*0.6*	*0.3*	
PCQ 797	27.2044	66.9419	949.4	17	73.6	0.10	0.09	12.5	0.61	0.08	0.09	0.52	0.06	3.1	4.9	0.03	0.13	4.8	100.6	*tuff*
					0.6	*0.04*	*0.07*	*0.2*	*0.05*	*0.03*	*0.02*	*0.02*	*0.05*	*0.4*	*0.5*	*0.03*	*0.02*	*0.8*	*0.4*	
End section			~970																	*Río Corral Quemado*

*Elemental composition of volcanic glass by Electron Probe Microanalysis (cf. Nash, 1992), n=number of shards, for n≥4 average and 1σ standard deviation are reported.

Table A.8: Stratigraphy and composition of volcanic ash beds from upper Río Corral Quemado section (PCQ)
(base of section = 27.1181°S, 66.9275°W; total thickness ~200 m)

Sample	Lat	Lon	strat	n*	SiO2	TiO2	ZrO2	Al2O3	Fe2O3	MnO	MgO	CaO	BaO	Na2O	K2O	F	Cl	H2O	Total	Comment
	(°S)	(°W)	m																	thickness (m), lithology
PCQ 519	27.1140	66.9282	0	29	74.6	0.10	0.08	12.1	0.59	0.07	0.07	0.41	0.02	3.1	5.1	0.02	0.16	5.6	102.0	*4, Toba Corral Quemado*
					0.7	*0.05*	*0.06*	*0.2*	*0.06*	*0.04*	*0.02*	*0.04*	*0.02*	*0.4*	*0.4*	*0.03*	*0.02*	*1.0*	*0.5*	
PCQ 715	27.2178	66.9233	~90	20	73.2	0.19	0.04	11.9	0.95	0.04	0.12	0.72	0.02	2.8	5.3	0.00	0.18	5.5	100.6	*0.1, 10% glass in conglomerate*
					0.3	*0.04*	*0.05*	*0.1*	*0.05*	*0.01*	*0.02*	*0.03*	*0.02*	*0.1*	*0.2*	*0.01*	*0.01*	*0.4*	*0.2*	*(see Figure 1.12c)*
PCQ 716	27.1201	66.9242	~200		*soil carbonate pendant; see appendix B for stable isotope data*															*basalt boulder terrace*

*Elemental composition of volcanic glass by Electron Probe Microanalysis (cf. Nash, 1992), n=number of shards, for n≥4 average and 1σ standard deviation are reported.

Table A.9: Composition of volcanic ash beds between the upper Los Barcos and upper Río Corral Quemado sections (PCQ)
(in flat-lying coarse sandstone and conglomerate; unknown age but likely unconformable with early Pliocene strata underlying)

Sample	Lat	Lon	strat	n*	SiO_2	TiO_2	ZrO_2	Al_2O_3	Fe_2O_3	MnO	MgO	CaO	BaO	Na_2O	K_2O	F	Cl	H_2O	Total	Comment
	(°S)	(°W)	m																	thickness (m), lithology
PCQ 520	27.1712	66.9347		16	73.7	0.13	0.04	11.4	0.76	0.04	0.10	0.80	0.05	2.8	4.8	0.00	0.11	5.7	102.0	*0.2, fine white tuff*
					0.4	*0.04*	*0.06*	*0.5*	*0.04*	*0.02*	*0.02*	*0.05*	*0.03*	*0.3*	*0.5*	*0.01*	*0.01*	*0.5*	*0.5*	
PCQ 521	27.1593	66.9212		16	73.5	0.12	0.05	12.3	0.70	0.03	0.07	0.82	0.03	2.2	5.8	0.01	0.12	4.7	100.4	*2, gray tuff, discontinuous*
					0.5	*0.03*	*0.04*	*0.4*	*0.04*	*0.02*	*0.02*	*0.03*	*0.02*	*0.3*	*0.4*	*0.01*	*0.01*	*0.8*	*0.3*	

*Elemental composition of volcanic glass by Electron Probe Microanalysis (cf. Nash, 1992), n=number of shards, for n≥4 average and 1σ standard deviation are reported.

Table A.10: Composition and approximate stratigraphic positition of volcanic ash beds from BHP 2001 samples (PCQ)
(samples collected in December 2001 by Ben Passey)

Sample	Lat	Lon	strat	n*	SiO2	TiO2	ZrO2	Al2O3	Fe2O3	MnO	MgO	CaO	BaO	Na2O	K2O	F	Cl	H2O	Total	Comment
	(°S)	(°W)	m																	thickness (m), lithology
PCQ 188	27.2199	66.9283	1100±50	14	74.0	0.09	0.07	12.5	0.59	0.06	0.07	0.84	0.05	2.5	5.7	0.00	0.11	3.4	100.0	*eolian sand, ~1% glass*
					0.7	*0.03*	*0.03*	*0.3*	*0.20*	*0.03*	*0.04*	*0.32*	*0.03*	*0.3*	*0.5*	*0.00*	*0.03*	*0.8*	*0.4*	*(see Figure 1.12c)*
PCQ 193	27.2164	66.9265	1200±50	9	72.6	0.19	0.07	12.4	1.02	0.04	0.14	0.82	0.05	2.6	5.4	0.01	0.18	4.4	99.8	*thin tuff in eolian strata*
					0.7	*0.02*	*0.03*	*0.2*	*0.10*	*0.03*	*0.02*	*0.05*	*0.02*	*0.1*	*0.2*	*0.01*	*0.03*	*0.7*	*0.4*	
PCQ 200	27.2109	66.9333	1465±10	6	73.8	0.05		12.5	0.51	0.05	0.04	0.63	0.03	2.6	5.7		0.06	4.2	100.2	*0.1, white tuff*
					0.3	*0.03*		*0.1*	*0.06*	*0.04*	*0.01*	*0.01*	*0.04*	*0.4*	*0.6*		*0.02*	*0.4*	*0.4*	
PCQ 200	*mode 2*		1465	4	72.5	0.11		12.6	0.71	0.02	0.08	1.00	0.10	2.1	5.9		0.10	4.8	99.9	
					1.1	*0.07*		*0.7*	*0.01*	*0.03*	*0.02*	*0.10*	*0.02*	*0.3*	*0.2*		*0.05*	*1.3*	*0.5*	
PCQ 201	27.2109	66.9333	1480±20	5	74.4	0.11		12.6	0.73	0.06	0.11	0.73	0.05	2.8	4.5		0.10	3.7	99.9	*sandy tuff*
					0.8	*0.04*		*0.3*	*0.02*	*0.03*	*0.01*	*0.05*	*0.04*	*1.0*	*0.8*		*0.01*	*1.1*	*0.4*	
PCQ 202	27.2108	66.9342	1500±10	13	73.2	0.10		12.3	0.62	0.06	0.08	0.60	0.06	2.0	5.8		0.09	5.3	100.2	*dark gray*
					0.6	*0.06*		*0.2*	*0.04*	*0.04*	*0.02*	*0.04*	*0.03*	*0.6*	*0.7*		*0.02*	*0.9*	*0.4*	
PCQ 202	*mode 2*			1	72.4	0.10		12.1	0.65	0.05	0.09	0.81	0.09	1.8	6.1		0.09	5.8	100.0	
PCQ 202	*mode 2*			1	73.7	0.08		12.0	0.62	0.05	0.09	0.89	0.00	2.0	5.6		0.11	4.8	100.0	
PCQ 203	27.2108	66.9359	1540±10	5	73.3	0.11		12.4	0.88	0.06	0.11	0.50	0.07	2.2	5.7		0.10	4.6	99.9	*dark gray sandstone*
					0.6	*0.08*		*0.3*	*0.04*	*0.04*	*0.04*	*0.09*	*0.04*	*0.8*	*0.8*		*0.03*	*1.1*	*0.4*	
PCQ 203	*mode 2*		1540±20	5	73.4	0.08		12.2	0.58	0.06	0.07	0.59	0.11	2.1	5.7		0.08	5.1	100.0	*dark gray sandstone*
					0.7	*0.05*		*0.2*	*0.06*	*0.02*	*0.03*	*0.04*	*0.02*	*0.6*	*0.7*		*0.02*	*0.8*	*0.4*	
PCQ 205	27.2121	66.9384	1580±50	9	74.6	0.12		12.5	0.68	0.07	0.09	0.64	0.03	2.4	5.4		0.11	3.7	100.2	*dark gray sandstone*
					0.9	*0.07*		*0.4*	*0.25*	*0.09*	*0.04*	*0.18*	*0.03*	*0.5*	*0.7*		*0.04*	*0.9*	*0.5*	
PCQ 206	27.2132	66.9395	1590±50	9	74.5	0.12		12.3	0.59	0.06	0.07	0.54	0.03	2.3	5.9		0.09	3.6	100.0	*dark gray sandstone*
					1.2	*0.10*		*0.5*	*0.27*	*0.02*	*0.04*	*0.18*	*0.03*	*0.4*	*0.6*		*0.05*	*1.2*	*0.4*	
PCQ 207	27.2117	66.9404	1630±50	11	73.3	0.11		12.4	0.68	0.06	0.11	0.76	0.08	2.4	5.4		0.09	4.6	100.0	*dark gray sandstone*
					1.1	*0.06*		*0.4*	*0.16*	*0.03*	*0.03*	*0.15*	*0.06*	*0.6*	*0.6*		*0.02*	*1.4*	*0.4*	
PCQ 208	27.1380	66.9285	Quat.?	13	75.1	0.07		12.4	0.47	0.10	0.03	0.46	0.01	3.3	4.3		0.06	3.7	100.0	*0.3, white, Buey Muerto ash (?)*
					0.6	*0.04*		*0.2*	*0.04*	*0.03*	*0.02*	*0.03*	*0.01*	*0.1*	*0.2*		*0.01*	*1.0*	*0.3*	
PCQ 210	27.2137	66.9373	2072	16	74.8	0.10		12.0	0.59	0.07	0.06	0.41	0.03	2.5	5.0		0.16	5.3	101.0	*0.1 –0.3, white tuff*
					0.6	*0.05*		*0.2*	*0.07*	*0.03*	*0.02*	*0.03*	*0.02*	*0.4*	*0.4*		*0.02*	*1.0*	*0.4*	

Table A.10 (*continued*)

Sample	Lat	Lon	strat	n	SiO2	TiO2	ZrO2	Al2O3	Fe2O3	MnO	MgO	CaO	BaO	Na2O	K2O	F	Cl	H2O	Total	Comment
	(°S)	(°W)	m																	thickness (m), lithology
PCQ 212	27.1593	66.9212	Quat.?	8	74.5	0.14		11.9	0.67	0.03	0.07	0.81	0.05	2.0	5.5		0.12	5.1	100.9	*2.5, gray tuff in channel*
					0.6	*0.05*		*0.2*	*0.05*	*0.03*	*0.01*	*0.03*	*0.01*	*0.2*	*0.4*		*0.02*	*0.8*	*0.4*	
PCQ 213	27.1711	66.9347	Quat.?	7	75.3	0.15		12.0	0.68	0.05	0.09	0.77	0.05	2.6	4.6		0.10	4.3	100.8	*0.2, fine white tuff*
					0.7	*0.03*		*0.3*	*0.06*	*0.02*	*0.02*	*0.07*	*0.04*	*0.1*	*0.3*		*0.02*	*0.4*	*0.5*	
PCQ 214	27.2019	66.9398	1830±5	12	75.0	0.11		12.0	0.68	0.05	0.09	0.84	0.05	2.5	4.8		0.10	4.2	100.4	*thin, soft sediment deformation*
					0.7	*0.05*		*0.2*	*0.07*	*0.03*	*0.01*	*0.03*	*0.03*	*0.3*	*0.4*		*0.01*	*0.6*	*0.3*	
PCQ 215	27.2137	66.9373	1518	7	73.1	0.12		13.0	0.80	0.07	0.13	0.73	0.05	2.0	6.0		0.13	4.6	100.8	*0.1 –0.3, white tuff*
					0.4	*0.03*		*0.2*	*0.06*	*0.02*	*0.02*	*0.03*	*0.05*	*0.2*	*0.2*		*0.01*	*0.6*	*0.2*	
PCQ 216	27.2149	66.9365	1485	25	73.1	0.11		12.9	0.74	0.04	0.11	1.05	0.08	2.4	5.2		0.08	4.6	100.5	*white tuff, water worked*
					0.7	*0.05*		*0.3*	*0.05*	*0.03*	*0.02*	*0.04*	*0.04*	*0.4*	*0.6*		*0.01*	*0.7*	*0.4*	
PCQ 217	27.2154	66.9357	1465	9	73.9	0.08		12.2	0.66	0.06	0.07	0.97	0.10	1.9	5.9		0.12	4.7	100.6	*0.3, white tuff, continuous*
					0.5	*0.03*		*0.3*	*0.06*	*0.03*	*0.02*	*0.04*	*0.05*	*0.3*	*0.3*		*0.02*	*0.3*	*0.3*	

*Elemental composition of volcanic glass by Electron Probe Microanalysis (cf. Nash, 1992), n=number of shards, for n≥4 average and 1σ standard deviation are reported.
Note: stratigraphic levels reported relative to the section south of Río Corral Quemado (Table A.5 and Latorre et al., 1997).

Table A.11: Stratigraphy and composition of volcanic ash beds at the southern Sierra de Quilmes
(base of section = 26.9864°S, 66.2659°W; total thickness ~50 m)

Sample	Lat	Lon	strat	n*	SiO2	TiO2	ZrO2	Al2O3	Fe2O3	MnO	MgO	CaO	BaO	Na2O	K2O	F	Cl	H2O	Total	Comment
	(°S)	(°W)	m																	thickness (m), lithology
CAT 125	26.2990	66.2669	~35		*see individual analyses in Table A.12*															*biotite-rich crystal tuff*
CAT 126	26.2990	66.2669	>35		*see individual analyses in Table A.12*															*fine tuffaceous sandstone with coarse detrital muscovite*
CAJ 702	26.9859	66.2672	35.5		*not analyzed*															*pumice clast in tuff*
CAJ 703	26.9859	66.2672	39		*see Appendix B for stable isotope data*															*marl*
CAJ 719	26.9848	66.2674	35		*not analyzed*															*1.5, biotite-rich base sampled*
CAJ 720			39.5		*see individual analyses in Table A.12*															*pumice sandstone*
CAJ 721			41		*see individual analyses in Table A.12*															*tuffaceous sandstone with coarse detrital muscovite*
CAJ 722			41.5		*not analyzed*															*tuffaceous sandstone with orange-red biotites*
CAJ 723			43		*see individual analyses in Table A.12*															*0.03, finely laminated, below a carbonate ledge*
southern Quilmes tuff			~35	46	72.8	0.08	0.03	11.9	0.62	0.05	0.05	0.60	0.00	2.1	6.1	0.01	0.14	6.0	100.6	*crystal tuff, laterally continuous*
					0.5	*0.03*	*0.04*	*0.2*	*0.05*	*0.02*	*0.02*	*0.02*	*0.01*	*0.2*	*0.2*	*0.02*	*0.01*	*0.9*	*0.6*	

*Elemental composition of volcanic glass by Electron Probe Microanalysis (cf. Nash, 1992), n=number of shards, for n≥4 average and 1σ standard deviation are reported.

Note: southern Quilmes tuff composition includes analyses highlighted in Table A.12, see Figure 1.12b for possible secondary modes in this stratigraphic sequence.

Table A.12: Composition of individual glass shards from samples at the southern Sierra de Quilmes
(base of section = 26.9864°S, 66.2659°W; total thickness ~50 m)

Sample	Lat	Lon	strat	n*	SiO2	TiO2	ZrO2	Al2O3	Fe2O3	MnO	MgO	CaO	BaO	Na2O	K2O	F	Cl	H2O	Total	Comment
	(°S)	(°W)	m																	thickness (m), lithology
CAT 125			~35	1	73.3	0.09	0.13	12.7	0.54	0.02	0.04	0.60	0.04	2.1	6.2	0.06	0.13	4.7	100.6	
CAT 125				1	72.3	0.09	0.00	11.8	0.54	0.04	0.02	0.56	0.02	2.0	5.9	0.00	0.14	6.6	100.0	
CAT 125				1	72.7	0.08	0.02	11.8	0.55	0.04	0.04	0.60	0.00	2.1	6.3	0.04	0.13	5.8	100.2	
CAT 125				1	73.1	0.13	0.00	12.1	0.56	0.04	0.05	0.61	0.00	1.9	6.1	0.02	0.14	6.0	100.7	
CAT 125				1	72.7	0.08	0.07	11.9	0.57	0.06	0.07	0.60	0.02	2.1	6.2	0.00	0.14	5.8	100.2	
CAT 125				1	71.9	0.08	0.00	11.7	0.58	0.03	0.07	0.61	0.00	2.0	5.7	0.00	0.15	7.7	100.4	
CAT 125				1	73.1	0.08	0.00	11.5	0.58	0.05	0.07	0.60	0.00	2.0	6.2	0.00	0.14	5.8	100.1	
CAT 125				1	72.0	0.05	0.00	11.5	0.58	0.04	0.07	0.63	0.00	1.8	6.0	0.00	0.14	7.5	100.4	
CAT 125				1	72.3	0.07	0.00	11.8	0.59	0.05	0.05	0.61	0.00	2.0	5.9	0.00	0.14	7.3	100.7	
CAT 125				1	72.5	0.06	0.00	11.8	0.61	0.06	0.04	0.58	0.00	1.9	6.0	0.00	0.13	7.0	100.5	
CAT 125				1	71.9	0.07	0.00	11.9	0.61	0.07	0.06	0.58	0.00	2.1	6.3	0.00	0.11	6.6	100.2	
CAT 125				1	72.5	0.08	0.00	11.8	0.61	0.03	0.07	0.59	0.00	2.0	6.1	0.00	0.15	7.0	100.9	
CAT 125				1	73.1	0.12	0.00	11.9	0.61	0.02	0.06	0.58	0.00	2.1	6.0	0.00	0.15	5.9	100.6	
CAT 125				1	72.9	0.10	0.00	12.0	0.61	0.03	0.05	0.62	0.00	2.0	6.1	0.01	0.16	5.7	100.2	
CAT 125				1	72.6	0.07	0.00	12.0	0.62	0.07	0.06	0.61	0.00	2.1	6.2	0.10	0.13	6.1	100.6	
CAT 125				1	73.3	0.12	0.00	11.9	0.62	0.04	0.04	0.59	0.00	2.1	6.1	0.00	0.15	5.5	100.3	
CAT 125				1	72.5	0.06	0.00	11.7	0.62	0.07	0.06	0.59	0.00	1.8	5.9	0.00	0.13	7.3	100.7	
CAT 125				1	72.4	0.06	0.00	11.7	0.62	0.02	0.06	0.60	0.00	2.0	6.2	0.00	0.16	6.4	100.1	
CAT 125				1	72.6	0.07	0.00	11.9	0.62	0.01	0.05	0.59	0.00	1.9	6.2	0.02	0.16	6.3	100.4	
CAT 125				1	72.2	0.06	0.00	11.6	0.62	0.04	0.04	0.59	0.03	2.2	6.1	0.01	0.13	6.7	100.4	
CAT 125				1	72.2	0.11	0.00	11.9	0.63	0.03	0.05	0.58	0.00	1.9	5.9	0.00	0.13	7.2	100.5	
CAT 125				1	72.6	0.11	0.08	11.9	0.63	0.07	0.05	0.58	0.00	2.3	6.1	0.00	0.13	6.3	100.7	
CAT 125				1	72.3	0.07	0.00	11.8	0.64	0.06	0.07	0.62	0.00	2.0	6.0	0.00	0.14	6.8	100.5	
CAT 125				1	72.3	0.12	0.00	11.9	0.65	0.03	0.08	0.60	0.01	1.9	6.0	0.00	0.14	6.9	100.6	
CAT 125				1	73.3	0.14	0.01	12.1	0.65	0.08	0.04	0.59	0.00	2.2	6.1	0.00	0.16	5.4	100.8	
CAT 125				1	72.7	0.10	0.05	12.0	0.66	0.03	0.05	0.63	0.00	2.2	5.9	0.10	0.14	6.1	100.6	
CAT 125				1	72.7	0.15	0.03	11.9	0.66	0.07	0.03	0.58	0.00	2.3	6.2	0.00	0.15	6.0	100.7	
CAT 125				1	72.7	0.06	0.00	11.7	0.67	0.06	0.06	0.62	0.03	2.0	6.0	0.00	0.11	6.4	100.4	
CAT 125				1	72.8	0.11	0.11	11.9	0.69	0.07	0.05	0.60	0.01	2.3	6.1	0.01	0.13	6.1	101.1	
CAT 125				1	72.5	0.14	0.10	11.8	0.72	0.05	0.04	0.57	0.01	2.5	6.1	0.00	0.15	5.6	100.3	
CAT 125				1	72.3	0.10	0.04	11.9	0.73	0.07	0.05	0.58	0.01	2.2	5.8	0.06	0.15	6.2	100.2	
CAT 125				1	72.1	0.15	0.00	12.0	0.83	0.02	0.12	0.70	0.00	2.0	6.0	0.00	0.14	6.2	100.2	
CAT 126			>35	1	74.1	0.13	0.15	13.2	0.33	0.05	0.04	0.24	0.06	2.2	6.8	0.00	0.16	2.4	99.9	
CAT 126				1	75.2	0.11	0.13	12.6	0.33	0.04	0.03	0.58	0.01	2.6	6.4	0.00	0.15	2.6	100.7	

Table A.12: (*continued*)

Sample	Lat	Lon	strat	n*	SiO2	TiO2	ZrO2	Al2O3	Fe2O3	MnO	MgO	CaO	BaO	Na2O	K2O	F	Cl	H2O	Total	Comment
	(°S)	(°W)	m																	thickness (m), lithology
CAT 126				1	73.8	0.06	0.16	13.0	0.53	0.13	0.06	0.28	0.00	2.8	5.8	0.00	0.10	3.2	100.0	
CAT 126				1	74.2	0.04	0.00	12.4	0.54	0.06	0.04	0.61	0.00	2.5	6.3	0.00	0.14	3.2	99.9	
CAT 126				1	73.4	0.05	0.00	12.2	0.59	0.03	0.05	0.59	0.00	2.5	6.3	0.05	0.13	4.5	100.2	
CAT 126				1	74.0	0.07	0.02	12.3	0.59	0.03	0.06	0.61	0.00	2.6	6.2	0.03	0.15	3.3	100.0	
CAT 126				1	72.2	0.04	0.00	12.6	0.62	0.06	0.06	0.81	0.00	2.6	6.0	0.08	0.06	4.9	100.1	
CAT 126				1	73.0	0.07	0.02	11.8	0.66	0.05	0.04	0.57	0.00	2.3	6.4	0.05	0.13	5.3	100.3	
CAT 126				1	72.7	0.05	0.04	12.2	0.67	0.03	0.06	0.73	0.02	2.4	6.2	0.04	0.17	5.1	100.3	
CAT 126				1	72.9	0.11	0.13	12.4	0.68	0.05	0.04	0.75	0.05	2.6	6.1	0.00	0.12	3.8	99.6	
CAT 126				1	72.6	0.07	0.10	12.2	0.69	0.02	0.05	0.78	0.06	2.7	5.9	0.00	0.18	4.9	100.3	
CAT 126				1	73.9	0.10	0.05	12.3	0.73	0.00	0.10	0.75	0.04	2.4	6.1	0.00	0.16	3.7	100.4	
CAT 126				1	73.1	0.15	0.06	12.6	0.74	0.05	0.11	0.80	0.09	2.8	5.6	0.00	0.15	4.0	100.0	
CAT 126				1	73.7	0.11	0.00	12.4	0.80	0.03	0.10	0.79	0.03	1.7	5.2	0.00	0.17	4.4	99.4	
CAT 126				1	74.4	0.05	0.00	12.2	0.88	0.09	0.01	0.50	0.01	2.4	5.8	0.10	0.11	3.7	100.2	
CAT 126				1	72.9	0.20	0.14	11.7	1.05	0.03	0.17	0.74	0.06	2.2	5.7	0.04	0.12	5.4	100.4	
CAT 126				1	72.2	0.22	0.13	11.9	1.25	0.03	0.18	0.84	0.04	2.6	5.0	0.03	0.11	5.6	100.1	
CAT 126				1	72.9	0.34	0.13	11.6	1.46	0.00	0.11	0.48	0.00	2.2	6.3	0.03	0.12	4.7	100.4	
CAJ 720			39.5	1	75.6	0.00	0.14	12.4	0.58	0.01	0.08	0.49	0.00	2.0	5.2	0.00	0.18	3.7	100.4	
CAJ 720				1	72.8	0.00	0.04	11.9	0.59	0.01	0.08	0.63	0.01	2.1	6.2	0.00	0.14	6.3	100.7	
CAJ 720				1	73.5	0.08	0.00	12.0	0.60	0.03	0.05	0.62	0.00	2.1	6.2	0.00	0.14	5.0	100.4	
CAJ 720				1	73.2	0.09	0.15	12.0	0.66	0.00	0.06	0.58	0.00	2.2	6.2	0.00	0.14	5.5	100.7	
CAJ 720				1	73.0	0.08	0.01	11.8	0.67	0.06	0.06	0.58	0.00	2.1	6.2	0.00	0.12	5.9	100.6	
CAJ 720				1	72.5	0.04	0.07	11.6	0.68	0.07	0.06	0.61	0.00	2.1	6.3	0.00	0.13	5.7	99.9	
CAJ 720				1	73.4	0.09	0.00	12.0	0.73	0.02	0.03	0.59	0.00	2.1	6.2	0.00	0.13	4.7	100.0	
CAJ 720				1	73.9	0.13	0.08	12.3	0.73	0.03	0.09	0.77	0.03	2.4	5.5	0.00	0.18	4.5	100.6	
CAJ 720				1	73.7	0.06	0.16	12.2	0.73	0.00	0.07	0.69	0.00	2.0	6.1	0.00	0.16	4.3	100.2	
CAJ 720				1	72.5	0.13	0.07	12.0	0.77	0.04	0.07	0.64	0.00	2.1	6.3	0.00	0.17	5.6	100.3	
CAJ 720				1	72.3	0.04	0.09	12.2	0.80	0.03	0.09	0.84	0.03	2.0	6.1	0.00	0.18	5.9	100.6	
CAJ 720				1	73.5	0.08	0.07	12.3	0.80	0.06	0.13	0.79	0.04	2.6	5.7	0.00	0.18	3.8	100.1	
CAJ 720				1	73.9	0.14	0.13	12.2	0.80	0.07	0.07	1.01	0.07	2.5	5.4	0.00	0.16	3.4	99.8	
CAJ 720				1	73.1	0.17	0.02	12.4	0.81	0.04	0.11	0.78	0.00	2.5	5.8	0.00	0.17	4.1	100.0	
CAJ 720				1	72.8	0.06	0.02	12.2	0.83	0.06	0.08	0.63	0.00	2.2	6.3	0.00	0.12	5.8	101.0	
CAJ 720				1	73.6	0.12	0.03	12.5	0.95	0.05	0.08	0.82	0.05	2.4	5.8	0.00	0.17	3.9	100.4	
CAJ 720				1	74.3	0.24	0.00	11.6	0.99	0.06	0.14	0.69	0.01	2.9	4.7	0.00	0.12	5.0	100.7	
CAJ 720				1	73.0	0.27	0.00	11.8	1.04	0.03	0.16	0.78	0.00	2.3	5.2	0.00	0.09	6.1	100.8	
CAJ 720				1	72.4	0.26	0.12	11.7	1.05	0.03	0.14	0.79	0.06	2.3	5.5	0.00	0.10	6.2	100.7	

Table A.12: (*continued*)

Sample	Lat	Lon	strat	n*	SiO2	TiO2	ZrO2	Al2O3	Fe2O3	MnO	MgO	CaO	BaO	Na2O	K2O	F	Cl	H2O	Total	Comment
	(°S)	(°W)	m																	thickness (m), lithology
CAJ 720				1	72.4	0.14	0.14	11.6	1.12	0.03	0.13	0.79	0.08	2.3	5.2	0.00	0.12	6.6	100.6	
CAJ 720				1	73.1	0.15	0.14	12.0	1.13	0.10	0.15	0.80	0.13	2.2	5.5	0.00	0.11	5.2	100.7	
CAJ 720				1	72.1	0.21	0.10	11.9	1.16	0.07	0.18	0.85	0.02	2.4	5.4	0.00	0.11	6.1	100.6	
CAJ 720				1	72.3	0.24	0.17	11.7	1.20	0.04	0.19	0.79	0.08	2.5	5.1	0.00	0.12	6.0	100.5	
CAJ 720				1	72.5	0.26	0.12	12.1	1.24	0.05	0.21	0.84	0.04	2.1	5.4	0.00	0.11	5.9	100.9	
CAJ 721			41	1	74.8	0.09	0.00	12.1	0.56	0.01	0.06	0.30	0.00	2.3	6.3	0.00	0.16	4.5	101.3	
CAJ 721				**1**	**73.4**	**0.12**	**0.02**	**12.0**	**0.56**	**0.03**	**0.08**	**0.58**	**0.00**	**2.2**	**6.2**	**0.00**	**0.15**	**6.7**	**102.1**	
CAJ 721				**1**	**73.3**	**0.11**	**0.00**	**12.0**	**0.58**	**0.10**	**0.07**	**0.61**	**0.00**	**2.2**	**6.3**	**0.03**	**0.13**	**6.7**	**102.0**	
CAJ 721				**1**	**73.1**	**0.07**	**0.09**	**12.0**	**0.63**	**0.03**	**0.02**	**0.61**	**0.01**	**2.1**	**6.6**	**0.02**	**0.16**	**6.4**	**101.8**	
CAJ 721				1	73.2	0.04	0.00	12.0	0.63	0.05	0.06	0.68	0.00	2.1	6.2	0.00	0.15	6.8	101.9	
CAJ 721				**1**	**73.5**	**0.08**	**0.00**	**11.8**	**0.65**	**0.08**	**0.06**	**0.61**	**0.00**	**2.2**	**6.4**	**0.03**	**0.15**	**6.2**	**101.7**	
CAJ 721				**1**	**73.7**	**0.06**	**0.09**	**12.1**	**0.67**	**0.06**	**0.04**	**0.63**	**0.00**	**2.0**	**6.6**	**0.00**	**0.13**	**6.1**	**102.1**	
CAJ 721				1	73.1	0.11	0.04	12.0	0.72	0.07	0.06	0.67	0.02	2.1	6.3	0.00	0.16	6.9	102.1	
CAJ 721				1	73.3	0.12	0.00	12.4	0.75	0.02	0.08	0.82	0.08	2.5	6.3	0.07	0.17	5.4	101.9	
CAJ 721				1	73.4	0.07	0.04	12.2	0.76	0.06	0.05	0.80	0.02	2.4	6.0	0.05	0.19	5.9	101.9	
CAJ 721				1	73.1	0.11	0.11	12.0	0.79	0.03	0.08	0.76	0.05	2.3	6.1	0.03	0.17	6.6	102.2	
CAJ 721				1	73.0	0.12	0.07	12.5	0.87	0.11	0.07	1.30	0.03	2.6	5.2	0.00	0.16	5.5	101.4	
CAJ 721				1	73.4	0.23	0.10	11.7	1.06	0.02	0.15	0.76	0.04	2.3	5.8	0.00	0.13	6.2	101.9	
CAJ 721				1	73.4	0.30	0.08	11.8	1.09	0.04	0.18	0.76	0.05	2.2	5.8	0.08	0.11	6.7	102.6	
CAJ 721				1	73.1	0.22	0.06	11.9	1.11	0.03	0.17	0.83	0.04	2.6	5.6	0.10	0.11	6.1	101.8	
CAJ 721				1	73.1	0.34	0.03	11.8	1.12	0.01	0.15	0.80	0.00	2.3	5.4	0.03	0.11	6.7	101.9	
CAJ 723			43	1	73.3	0.18	0.06	13.3	0.98	0.02	0.12	0.96	0.11	1.7	4.2	0.04	0.12	6.6	101.8	
CAJ 723				1	74.5	0.45	0.13	11.1	1.35	0.00	0.15	0.52	0.00	2.2	6.0	0.28	0.07	4.6	101.2	

*Elemental composition of volcanic glass by Electron Probe Microanalysis (cf. Nash, 1992), n=number of shards, for n≥4 average and 1σ standard deviation are reported.

Note: **Bolded analyses** are averaged as southern Quilmes tuff in Table A.11, individual shards plotted in Figure 1.12b.

Figure A.2: Composite tephrostratigraphy for sections measured in Vallé Santa Maria. Correlations to Universität Potsdam samples, and potential correlations to Puerta de Corral Quemado (PCQ) section illustrated for reference. The very earliest Pliocene is well constrained by sanidine $^{40}Ar/^{39}Ar$ age of 5.19 Ma for toba rayita amarilla (TRA) obtained on sample ENTR 909, and by a biotite $^{40}Ar/^{39}Ar$ age of 5.20 Ma obtained on Potsdam sample QJ-4. At Quebrada de Jujuy a coarse pumice underlying TRA gives a sanidine $^{40}Ar/^{39}Ar$ age of 5.27 Ma (QDJ 983). Lower and upper age bounds for the sections are not well known. However, if the proposed correlations to PCQ are correct, the total age range of the measured sections is unlikely to exceed 2 Ma.

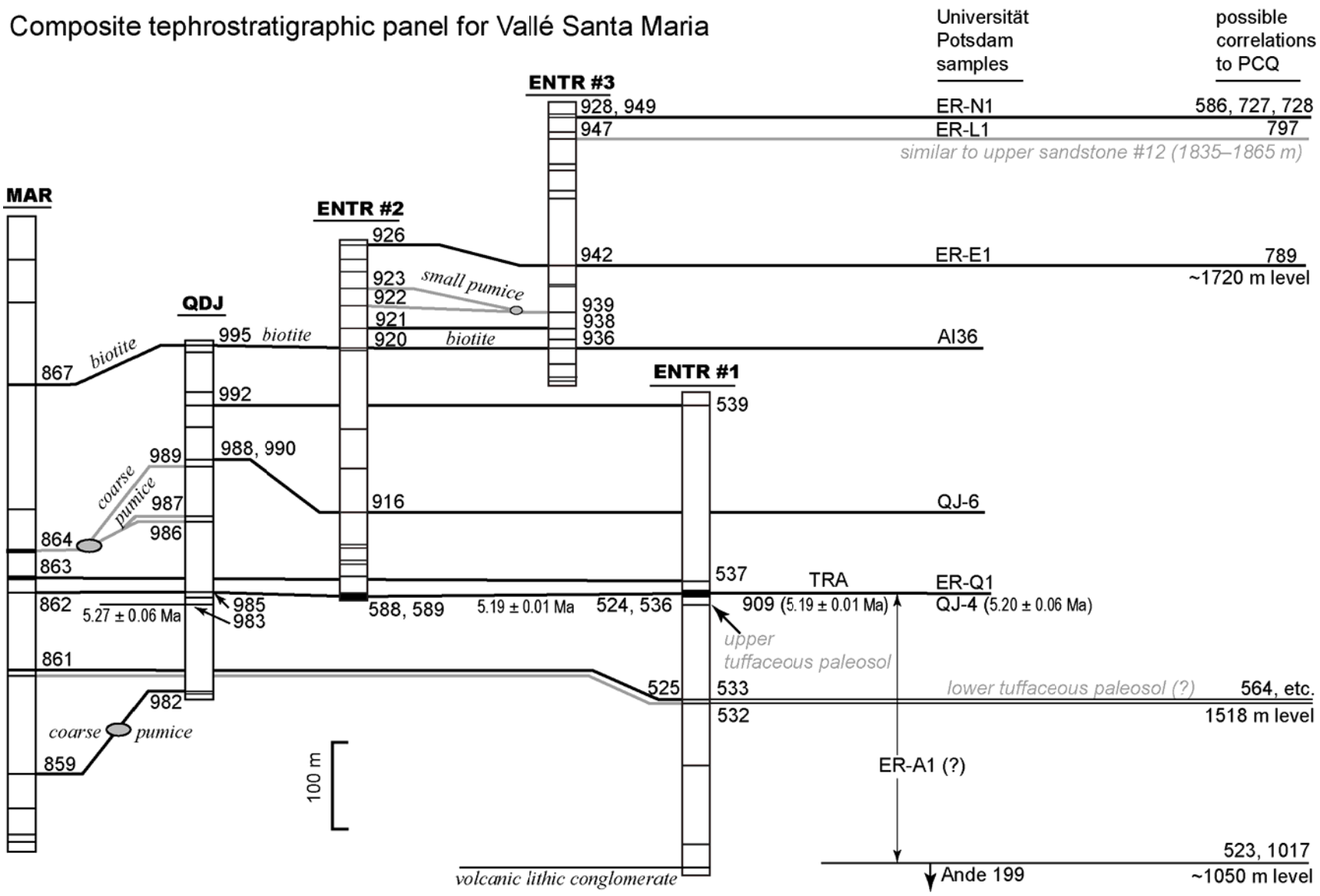
Composite tephrostratigraphic panel for Vallé Santa Maria
Universität Potsdam samples
possible correlations to PCQ
ENTR #3
928, 949
947
ER-N1
586, 727, 728
ER-L1
797
similar to upper sandstone #12 (1835–1865 m)
MAR
ENTR #2
926
942
ER-E1
789
~1720 m level
QDJ
923
small pumice
922
921
920
939
938
936
995
biotite
biotite
biotite
AI36
867
ENTR #1
992
539
989
988, 990
coarse pumice
987
916
QJ-6
986
864
863
537
TRA
ER-Q1
862
5.27 ± 0.06 Ma
985
983
588, 589
5.19 ± 0.01 Ma
524, 536
909 (5.19 ± 0.01 Ma)
QJ-4 (5.20 ± 0.06 Ma)
upper tuffaceous paleosol
861
525
533
lower tuffaceous paleosol (?)
564, etc.
982
532
1518 m level
coarse pumice
859
100 m
ER-A1 (?)
523, 1017
Ande 199
~1050 m level
volcanic lithic conglomerate

Table A.13: Composition and stratigraphic positition of volcanic ash beds from Entre Rios section #1 (ENTR)
(base of section = 26.8526°S, 66.0472°W; total thickness ~600 m)

Sample	Lat	Lon	strat	n*	SiO2	TiO2	ZrO2	Al2O3	Fe2O3	MnO	MgO	CaO	BaO	Na2O	K2O	F	Cl	H2O	Total	Comment
	(°S)	(°W)	m																	thickness (m), lithology
VLC	26.8365	66.0430	0		*north end of traceable bed*															*volcanic lithic conglomerate*
VLC	26.8390	66.0446	0																	*volcanic lithic conglomerate*
VLC	26.8414	66.0449	0																	*volcanic lithic conglomerate*
VLC	26.8447	66.0447	0																	*volcanic lithic conglomerate*
ENTR 527	26.8467	66.0449	0		*not analyzed; sample of rounded volcanic clasts with large amphibole phenocrysts*															*volcanic lithic conglomerate*
VLC	26.8472	66.0454	0																	*volcanic lithic conglomerate*
VLC	26.8489	66.0467	0		*spine between Loma Rica and Pediment* III															*volcanic lithic conglomerate*
VLC	26.8506	66.0467	0																	*volcanic lithic conglomerate*
VLC	26.8526	66.0472	0																	*volcanic lithic conglomerate*
ENTR 528	26.8545	66.0481	0		*not analyzed; fine grained tuffaceous sandstone underlying a channel conglomerate*															*volcanic lithic conglomerate*
VLC	26.8547	66.0486	0		*south end of traceable bed*															*volcanic lithic conglomerate*
ENTR 530	26.8540	66.0465	30	25	74.4	0.13		12.0	0.68	0.08	0.09	0.28		2.7	2.7	0.04	0.16	8.1	101.4	*tuff, laterally discontinuous*
					1.0	*0.03*		*0.2*	*0.03*	*0.02*	*0.02*	*0.02*		*0.3*	*0.2*	*0.01*	*0.01*	*0.9*	*0.6*	
ENTR 531	26.8554	66.0439	120	6	75.0	0.11		11.8	0.73	0.04	0.08	0.92		2.6	2.8	0.03	0.14	6.4	100.6	*0.5, tuff, variably indurated*
					0.5	*0.04*		*0.6*	*0.03*	*0.02*	*0.01*	*0.03*		*0.2*	*0.1*	*0.00*	*0.01*	*0.5*	*0.5*	
ENTR 532	26.8561	66.0415	195.3	29	73.3	0.12		12.9	0.84	0.08	0.13	0.76		2.6	3.6	0.06	0.13	7.5	102.1	*0.75, clean tuff, minor carbonate*
					0.5	*0.04*		*0.1*	*0.04*	*0.02*	*0.02*	*0.02*		*0.2*	*0.3*	*0.01*	*0.01*	*0.9*	*0.6*	
ENTR 533	26.8561	66.0415	200.4	36	72.8	0.13		13.0	0.86	0.08	0.13	0.78		2.3	3.8	0.06	0.15	7.0	101.2	*0.5, burrowed tuff, carbonate*
					0.6	*0.03*		*0.2*	*0.04*	*0.03*	*0.02*	*0.06*		*0.2*	*0.4*	*0.01*	*0.01*	*1.0*	*1.1*	*see Appendix B for isotope data*
ENTR 533	*mode 2*			1	73.7	0.04		13.0	0.51	0.26	0.06	0.59		2.5	3.7	0.02	0.03	6.2	100.6	
ENTR 533	*mode 2*			1	73.2	0.07		13.2	0.48	0.26	0.09	0.66		2.3	3.5	0.04	0.03	6.3	100.1	
ENTR 533	*mode 2*			1	73.4	0.02		13.1	0.47	0.25	0.07	0.64		2.3	3.5	0.03	0.03	8.0	101.8	
ENTR 525	26.8499	66.0413	~200	22	72.9	0.13		12.8	0.83	0.08	0.13	0.75		2.6	3.7	0.06	0.13	7.4	101.5	*0.3, tuff, carbonate cemented*
					0.6	*0.03*		*0.1*	*0.05*	*0.02*	*0.02*	*0.02*		*0.2*	*0.4*	*0.01*	*0.02*	*0.7*	*0.6*	*see Appendix B for isotope data*
ENTR 525	*mode 2*			1	72.8	0.05		13.3	0.56	0.19	0.09	0.75		2.8	3.4	0.04	0.02	7.6	101.6	
ENTR 525	*mode 2*			1	72.1	0.04		13.1	0.39	0.22	0.08	0.65		2.5	3.2	0.04	0.03	8.8	101.2	
ENTR 534	26.8552	66.0366	314.0	34	74.1	0.08		12.2	0.70	0.03	0.05	0.56		2.2	4.2	0.01	0.12	7.8	102.0	*~0.5, see Figure 4.3a*
					0.6	*0.03*		*0.2*	*0.08*	*0.02*	*0.02*	*0.05*		*0.7*	*0.8*	*0.01*	*0.02*	*0.8*	*1.3*	
ENTR 535	26.8552	66.0366	314.8		*not analyzed; see Appendix B for stable isotope data*															*upper tuffaceous paleosol*
ENTR 536	26.8552	66.0366	324.8	13	73.4	0.08		12.4	0.62	0.10	0.07	0.96	0.01	2.0	4.8	0.01	0.09	7.3	101.9	*9, pumice/biotite/feldspar tuff*
					0.4	*0.03*		*0.1*	*0.04*	*0.03*	*0.01*	*0.02*	*0.02*	*0.1*	*0.1*	*0.03*	*0.01*	*0.4*	*0.4*	*Toba Rayita Amarilla (TRA)*

Table A.13 (*continued*)

Sample	Lat	Lon	strat	n	SiO2	TiO2	ZrO2	Al2O3	Fe2O3	MnO	MgO	CaO	BaO	Na2O	K2O	F	Cl	H2O	Total	Comment
	(°S)	(°W)	m																	thickness (m), lithology
ENTR 536	*replicate analysis*			18	73.0	0.07	0.07	12.3	0.60	0.10	0.06	0.93	0.01	2.3	5.0	0.03	0.08	8.0	102.5	*TRA*
					0.6	*0.03*	*0.05*	*0.2*	*0.03*	*0.03*	*0.01*	*0.03*	*0.02*	*0.1*	*0.2*	*0.03*	*0.01*	*1.3*	*0.9*	
ENTR 909	26.8552	66.0366	324.8	5	74.3	0.07	0.08	12.4	0.60	0.11	0.06	0.92	0.00	1.4	5.0	0.03	0.09	5.8	100.9	*TRA, $^{40}Ar/^{39}Ar$ sample*
					0.1	*0.03*	*0.04*	*0.0*	*0.02*	*0.01*	*0.00*	*0.03*	*0.01*	*0.1*	*0.1*	*0.02*	*0.01*	*0.4*	*0.5*	
ENTR 524	26.8506	66.0388	~325	14	73.0	0.08		12.3	0.63	0.12	0.07	0.96	0.01	2.1	5.0	0.03	0.09	8.1	102.4	*TRA, below terrace gravels*
					0.7	*0.03*		*0.2*	*0.04*	*0.02*	*0.01*	*0.03*	*0.03*	*0.2*	*0.2*	*0.01*	*0.01*	*0.7*	*0.4*	
ENTR 537	26.8558	66.0356	343.1	31	73.7	0.10		12.3	0.72	0.08	0.07	1.04	0.05	2.0	5.0	0.01	0.11	7.8	103.0	*0.5, below first Andalhuala Fm. conglomerate*
					0.5	*0.03*		*0.1*	*0.04*	*0.02*	*0.01*	*0.04*	*0.04*	*0.2*	*0.3*	*0.02*	*0.01*	*0.8*	*0.5*	
ENTR 537	*replicate analysis*			23	73.2	0.09	0.05	12.2	0.70	0.08	0.08	1.02	0.04	2.2	5.4		0.11	7.8	103.0	
					0.8	*0.03*	*0.04*	*0.2*	*0.04*	*0.02*	*0.02*	*0.03*	*0.03*	*0.2*	*0.4*		*0.01*	*1.7*	*1.3*	
ENTR 539	26.8631	66.0323	~600	14	73.3	0.08		12.5	0.64	0.07	0.07	0.47	0.02	2.0	6.2	0.04	0.13	6.5	101.8	*1, tuff in coarse sand*
					0.3	*0.02*		*0.1*	*0.04*	*0.02*	*0.02*	*0.03*	*0.03*	*0.1*	*0.2*	*0.04*	*0.01*	*0.8*	*0.6*	

*Elemental composition of volcanic glass by Electron Probe Microanalysis (cf. Nash, 1992), n=number of shards, for n≥4 average and 1σ standard deviation are reported.

Table A.14: Composition and stratigraphic positition of volcanic ash beds from Entre Rios section #2 (ENTR)
(base of section = 26.8236°S, 66.00256°W; total thickness ~500 m)

Sample	Lat	Lon	strat	n*	SiO2	TiO2	ZrO2	Al2O3	Fe2O3	MnO	MgO	CaO	BaO	Na2O	K2O	F	Cl	H2O	Total	Comment
	(°S)	(°W)	m																	thickness (m), lithology
ENTR 588	26.8236	66.0256	0.0	15	73.4	0.08		12.5	0.60	0.11	0.07	0.95	0.02	2.0	3.8	0.01	0.09	8.5	102.0	*9, TRA, see Figure 4.3b*
					0.5	*0.02*		*0.1*	*0.04*	*0.02*	*0.01*	*0.02*	*0.03*	*0.1*	*0.1*	*0.01*	*0.01*	*0.5*	*0.5*	
ENTR 588	*replicate analysis*			16	73.3	0.07	0.04	12.2	0.62	0.10	0.05	0.95	0.01	2.8	3.8	0.04	0.09	7.5	101.6	
					0.8	*0.02*	*0.04*	*0.2*	*0.04*	*0.02*	*0.01*	*0.03*	*0.01*	*0.7*	*0.4*	*0.04*	*0.01*	*2.1*	*1.5*	
ENTR 589	26.8236	66.0256	0.0	8	72.9	0.09		12.3	0.60	0.09	0.05	0.93	0.00	1.9	3.7	0.00	0.09	7.3	100.0	*9, TRA, see Figure 4.3b*
					1.1	*0.03*		*0.1*	*0.03*	*0.03*	*0.01*	*0.04*	*0.00*	*0.3*	*0.1*	*0.01*	*0.01*	*1.0*	*0.5*	
ENTR 589	*replicate analysis*			23	72.7	0.09	0.07	12.1	0.63	0.12	0.06	0.94	0.01	2.8	4.0	0.02	0.09	7.6	101.2	
					0.9	*0.03*	*0.05*	*0.2*	*0.05*	*0.02*	*0.02*	*0.03*	*0.01*	*0.2*	*0.2*	*0.03*	*0.01*	*1.9*	*1.7*	
ENTR 910	26.8239	66.0250	28.5		*not analyzed*															*0.02, tuff above red silt*
ENTR 911	26.8239	66.0250	28.6		*not analyzed*															*0.1, tuffaceous gray mica-rich ss*
ENTR 912	26.8236	66.0248	43.2		*not analyzed*															*coarse pumice in fine gray sand*
ENTR 913			47.8		*not analyzed*															*pumice in sand*
ENTR 914			62.5	12	72.0	0.05	0.04	13.3	0.54	0.14	0.04	1.19	0.01	1.3	3.8	0.08	0.03	7.8	100.4	*0.5, gray tuff, fine white upper*
					0.3	*0.02*	*0.02*	*0.4*	*0.02*	*0.02*	*0.01*	*0.10*	*0.01*	*0.5*	*0.3*	*0.04*	*0.01*	*0.8*	*0.7*	
ENTR 915			63.8	11	73.0	0.05	0.08	13.4	0.53	0.14	0.05	1.19	0.01	2.0	4.6	0.06	0.03	5.3	100.5	*pumice above ENTR 914*
					0.4	*0.02*	*0.02*	*0.1*	*0.02*	*0.02*	*0.01*	*0.04*	*0.01*	*0.2*	*0.3*	*0.02*	*0.01*	*1.0*	*0.4*	
ENTR 916	26.8236	66.0237	107.1	16	73.1	0.10	0.06	12.9	0.73	0.06	0.12	0.88	0.10	1.4	6.4	0.01	0.09	4.2	100.0	*1, gray tuffaceous sandstone*
					0.3	*0.03*	*0.03*	*0.1*	*0.02*	*0.01*	*0.01*	*0.02*	*0.02*	*0.2*	*0.1*	*0.02*	*0.01*	*0.8*	*0.4*	
ENTR 917	26.8241	66.0234	159		*not analyzed*															*0.15, fine white with biotite*
ENTR 918			205		*not analyzed*															*0.15, gray w/ white stripe, biotite*
ENTR 919	26.8253	66.0226	320		*not analyzed*															*0.05, tephra lens*
ENTR 920			321.5	14	74.5	0.09	0.06	12.4	0.61	0.03	0.07	0.82	0.03	1.4	6.5	0.05	0.12	3.6	100.2	*1.5, traceable ash bed*
					0.4	*0.04*	*0.05*	*0.2*	*0.05*	*0.01*	*0.01*	*0.03*	*0.02*	*0.1*	*0.4*	*0.04*	*0.01*	*0.5*	*0.6*	
ENTR 920	*mode 2*			1	74.5	0.06	0.04	12.4	0.57	0.05	0.06	0.49	0.05	1.5	6.2	0.04	0.14	4.3	100.4	
ENTR 920	*mode 2*			1	74.2	0.11	0.02	12.4	0.52	0.04	0.06	0.48	0.00	1.3	6.5	0.02	0.14	4.3	100.1	
ENTR 920	*mode 2*			1	74.6	0.06	0.03	12.4	0.56	0.02	0.07	0.46	0.01	1.5	6.7	0.01	0.12	3.0	99.5	
ENTR 921	26.8254	66.0228	345	17	74.4	0.10	0.06	12.1	0.67	0.05	0.07	0.61	0.08	1.1	6.4	0.02	0.12	4.9	100.8	*1, coarse base, fine white upper*
					0.4	*0.02*	*0.04*	*0.1*	*0.01*	*0.01*	*0.00*	*0.06*	*0.02*	*0.2*	*0.4*	*0.02*	*0.01*	*1.1*	*0.7*	
ENTR 922	26.8251	66.0220	374	4	74.3	0.13	0.05	12.5	0.71	0.07	0.07	0.94	0.04	2.0	6.6	0.00	0.14	3.5	101.0	*pumice in coarse sand*
					1.4	*0.04*	*0.04*	*0.3*	*0.06*	*0.01*	*0.01*	*0.06*	*0.02*	*0.4*	*0.3*	*0.00*	*0.03*	*0.8*	*0.6*	
ENTR 922	*mode 2*			1	75.7	0.10	0.01	13.0	0.25	0.05	0.06	0.95	0.00	2.0	6.6	0.00	0.04	2.6	101.3	

Table A.14 (*continued*)

Sample	Lat	Lon	strat	n	SiO2	TiO2	ZrO2	Al2O3	Fe2O3	MnO	MgO	CaO	BaO	Na2O	K2O	F	Cl	H2O	Total	Comment
	(°S)	(°W)	m																	thickness (m), lithology
ENTR 923	26.8251	66.0216	394	5	74.22	0.10	0.04	12.4	0.29	0.04	0.08	0.90	0.05	1.7	6.7	0.00	0.08	2.6	99.2	*pumice in coarse sand*
					0.4	*0.02*	*0.04*	*0.2*	*0.08*	*0.03*	*0.01*	*0.09*	*0.02*	*0.1*	*0.2*	*0.00*	*0.02*	*0.5*	*0.4*	
ENTR 923	*mode 2*			1	74.7	0.07	0.00	12.8	0.54	0.07	0.09	0.55	0.07	2.6	6.4	0.00	0.09	2.6	100.5	
ENTR 923	*mode 2*			1	73.7	0.19	0.00	12.3	0.66	0.05	0.09	0.60	0.10	2.3	6.3	0.01	0.12	2.9	99.3	
ENTR 923	*mode 2*			1	73.0	0.10	0.03	12.0	0.71	0.04	0.07	0.64	0.07	2.1	6.5	0.00	0.13	4.8	100.2	
ENTR 923	*mode 3*			1	71.0	0.21	0.00	12.3	1.04	0.04	0.17	0.82	0.05	0.6	5.9	0.00	0.18	7.5	99.7	
ENTR 923	*mode 3*			1	71.6	0.13	0.06	12.7	1.01	0.05	0.15	0.84	0.10	2.0	6.9	0.00	0.19	5.0	100.6	
ENTR 923	*mode 3*			1	71.2	0.12	0.01	12.2	0.89	0.05	0.18	0.83	0.03	1.5	6.8	0.00	0.23	5.0	99.0	
ENTR 924	26.8250	66.0215	414		*not analyzed*															*0.6, coarse base, biotite rich*
ENTR 925	26.8250	66.0213	429		*not analyzed*															*0.05, fine white tuff*
ENTR 926	26.8250	66.0212	446	16	71.6	0.21	0.07	13.2	1.30	0.05	0.23	1.17	0.04	1.9	5.9	0.05	0.17	5.8	101.7	*0.45, coarse base, ash fall (?)*
					0.6	*0.11*	*0.09*	*0.3*	*0.14*	*0.06*	*0.03*	*0.05*	*0.03*	*0.2*	*0.5*	*0.05*	*0.03*	*0.8*	*1.2*	
ENTR 926	*mode 2*			1	72.9	0.11	0.19	13.0	1.14	0.01	0.15	0.73	0.02	1.3	5.7	0.00	0.16	5.6	100.9	
ENTR 926	*mode 2*			1	72.9	0.11	0.19	13.0	1.14	0.01	0.15	0.73	0.02	1.3	5.7	0.00	0.16	5.6	100.9	
Pediment deposit			466		*see Appendix B for stable isotope analysis of soil carbonate (ENTR 927)*															*20, top of section*

*Elemental composition of volcanic glass by Electron Probe Microanalysis (cf. Nash, 1992), n=number of shards, for n≥4 average and 1σ standard deviation are reported.

Table A.15: Composition and stratigraphic positition of volcanic ash beds from Entre Rios section #3 (ENTR)
(base of section = 26.8295°S, 66.0233°W; total thickness ~350 m)

Sample	Lat	Lon	strat	n*	SiO2	TiO2	ZrO2	Al2O3	Fe2O3	MnO	MgO	CaO	BaO	Na2O	K2O	F	Cl	H2O	Total	Comment
	(°S)	(°W)	m																	thickness (m), lithology
ENTR 931	26.8295	66.0233	0	12	73.2	0.13	0.04	12.1	0.72	0.02	0.07	0.88	0.06	0.9	5.5	0.04	0.11	6.2	100.0	*thin white biotite tuff lens*
					0.3	*0.02*	*0.03*	*0.1*	*0.03*	*0.01*	*0.02*	*0.03*	*0.02*	*0.3*	*0.2*	*0.03*	*0.02*	*0.5*	*0.5*	
ENTR 932			0.5	13	74.8	0.10	0.09	12.2	0.67	0.03	0.07	0.84	0.06	1.2	6.5	0.04	0.12	4.4	101.1	*1, above gray sand*
					0.3	*0.03*	*0.03*	*0.2*	*0.03*	*0.01*	*0.01*	*0.03*	*0.03*	*0.1*	*0.2*	*0.02*	*0.01*	*0.8*	*0.4*	
ENTR 933	26.8296	66.0232	15.5	10	73.8	0.15	0.07	12.6	0.97	0.06	0.21	1.08	0.08	1.5	5.3	0.01	0.09	3.8	99.7	*0.2, white lens in gray sand*
					0.2	*0.03*	*0.05*	*0.1*	*0.03*	*0.01*	*0.00*	*0.04*	*0.02*	*0.2*	*0.2*	*0.01*	*0.01*	*0.6*	*0.4*	
ENTR 933	*mode 2*			4	73.7	0.05	0.06	13.1	0.41	0.10	0.07	0.46	0.02	1.2	6.5	0.05	0.02	5.2	100.9	
					0.3	*0.01*	*0.04*	*0.1*	*0.04*	*0.00*	*0.00*	*0.09*	*0.01*	*0.1*	*0.3*	*0.01*	*0.01*	*0.8*	*0.5*	
ENTR 934			20	16	74.4	0.10	0.09	12.2	0.69	0.05	0.08	0.65	0.08	1.5	6.2	0.02	0.12	3.7	99.9	*0.3, biotite tuff, coarse base*
					0.9	*0.02*	*0.03*	*0.2*	*0.03*	*0.01*	*0.01*	*0.06*	*0.02*	*0.6*	*0.5*	*0.02*	*0.01*	*1.5*	*0.6*	
ENTR 935			22	25	72.8	0.11	0.06	11.7	0.66	0.05	0.08	0.61	0.07	2.0	6.4	0.01	0.13	5.6	100.2	*0.2, coarse base*
					0.6	*0.04*	*0.05*	*0.1*	*0.05*	*0.03*	*0.02*	*0.02*	*0.04*	*0.5*	*0.7*	*0.02*	*0.02*	*0.7*	*0.3*	
ENTR 936	26.8296	66.0226	41	16	74.7	0.10	0.07	12.3	0.62	0.03	0.07	0.82	0.04	1.4	6.4	0.04	0.12	3.8	100.4	*1, fine white biotite tuff*
					0.3	*0.03*	*0.03*	*0.2*	*0.06*	*0.01*	*0.01*	*0.03*	*0.03*	*0.2*	*0.3*	*0.02*	*0.01*	*0.6*	*0.5*	
ENTR 937			57		*not analyzed*															*0.1, fine white lens*
ENTR 938	26.8295	66.0221	63	25	72.6	0.11	0.05	11.6	0.67	0.05	0.08	0.59	0.07	1.8	6.5	0.02	0.12	5.9	100.1	*0.6, coarse base*
					0.4	*0.05*	*0.06*	*0.1*	*0.05*	*0.03*	*0.01*	*0.02*	*0.04*	*0.2*	*0.3*	*0.03*	*0.02*	*0.5*	*0.2*	
ENTR 939	26.8293	66.0217	83	4	72.2	0.09	0.05	12.4	0.69	0.06	0.07	0.63	0.04	1.8	6.7	0.00	0.15	4.7	99.6	*gravel-sized pumice in sand*
					0.6	*0.02*	*0.04*	*0.1*	*0.06*	*0.02*	*0.01*	*0.02*	*0.03*	*0.2*	*0.1*	*0.00*	*0.02*	*0.4*	*0.3*	
ENTR 939	*mode 2*		83	1	74.3	0.12	0.10	12.1	0.27	0.06	0.08	1.00	0.03	1.8	6.2	0.00	0.08	3.7	99.8	
ENTR 940	26.8298	66.0214	113	16	73.6	0.14	0.08	12.1	1.56	0.05	0.05	0.30	0.02	1.4	2.4	0.16	0.09	9.0	100.9	*1, fine white, below gravel*
					0.2	*0.01*	*0.02*	*0.1*	*0.03*	*0.02*	*0.00*	*0.02*	*0.02*	*0.3*	*0.3*	*0.03*	*0.01*	*0.6*	*0.4*	
ENTR 941			118	16	73.4	0.12	0.05	12.2	0.71	0.04	0.07	0.83	0.04	1.1	5.6	0.05	0.14	5.7	100.0	*0.4, fine white, pumiceous upper*
					0.3	*0.03*	*0.02*	*0.1*	*0.04*	*0.01*	*0.01*	*0.06*	*0.02*	*0.3*	*0.5*	*0.03*	*0.02*	*0.6*	*0.5*	
ENTR 942	26.8299	66.0209	148	4	70.9	0.23	0.05	13.3	1.31	0.05	0.25	1.16	0.06	1.1	5.2	0.02	0.17	6.0	99.8	*0.1, tuff*
					0.2	*0.04*	*0.02*	*0.1*	*0.02*	*0.01*	*0.01*	*0.04*	*0.03*	*0.2*	*0.4*	*0.02*	*0.01*	*0.3*	*0.5*	
ENTR 943	26.8300	66.0201	221	16	73.2	0.14	0.07	12.1	1.57	0.05	0.06	0.29	0.02	1.5	3.3	0.15	0.09	7.3	99.9	*0.3, fine white biotite tuff*
					0.2	*0.02*	*0.01*	*0.1*	*0.03*	*0.01*	*0.01*	*0.02*	*0.02*	*0.3*	*0.4*	*0.03*	*0.01*	*0.5*	*0.4*	
ENTR 944			238	16	73.1	0.13	0.08	12.1	1.56	0.06	0.06	0.30	0.02	1.6	3.6	0.17	0.09	6.6	99.5	*0.02, fine white, burrowed*
					0.2	*0.02*	*0.02*	*0.1*	*0.02*	*0.01*	*0.01*	*0.02*	*0.01*	*0.2*	*0.4*	*0.04*	*0.01*	*0.5*	*0.4*	

Table A.15 (*continued*)

Sample	Lat	Lon	strat	n	SiO2	TiO2	ZrO2	Al2O3	Fe2O3	MnO	MgO	CaO	BaO	Na2O	K2O	F	Cl	H2O	Total	Comment
	(°S)	(°W)	m																	thickness (m), lithology
ENTR 945	26.8305	66.0195	262	10	67.7	0.13	0.04	13.8	1.33	0.10	0.30	2.08	0.04	2.4	4.1	0.00	0.20	6.9	99.1	*1.5, pumiceous lens in sand*
					2.2	*0.04*	*0.04*	*0.3*	*0.12*	*0.02*	*0.05*	*0.08*	*0.03*	*0.6*	*0.3*	*0.01*	*0.06*	*1.4*	*1.1*	
ENTR 945	*mode 2*		262	1	73.4	0.09	0.00	12.7	0.77	0.04	0.10	0.76	0.02	1.7	6.5	0.00	0.23	4.5	100.8	
ENTR 945	*mode 2*		262	1	75.0	0.13	0.11	12.6	0.70	0.03	0.08	0.73	0.05	2.4	5.5	0.00	0.19	3.6	101.1	
ENTR 946			270	3	72.2	0.10	0.08	12.5	0.95	0.11	0.15	1.62	0.06	2.1	5.1	0.00	0.13	4.9	99.9	*0.2, pumiceous lens in sand*
					0.4	*0.09*	*0.12*	*0.0*	*0.05*	*0.04*	*0.01*	*0.02*	*0.07*	*0.1*	*0.3*	*0.00*	*0.02*	*0.5*	*0.2*	
ENTR 946	*mode 2*				73.8	0.05	0.11	12.4	0.54	0.09	0.05	0.25	0.00	2.7	5.3	0.15	0.09	5.1	100.5	
ENTR 946	*mode 2*				73.4	0.10	0.00	12.2	0.53	0.12	0.07	0.31	0.00	2.7	5.4	0.13	0.08	5.9	100.8	
ENTR 947	26.8306	66.0190	293	18	74.6	0.09	0.07	12.4	0.62	0.06	0.07	0.48	0.07	1.6	6.2	0.05	0.13	4.4	100.8	*1.5, tuff*
					0.3	*0.01*	*0.03*	*0.1*	*0.05*	*0.01*	*0.01*	*0.03*	*0.03*	*0.2*	*0.6*	*0.02*	*0.01*	*0.7*	*0.6*	
ENTR 948	26.8308	66.0188	307	6	72.9	0.12	0.05	12.2	0.80	0.04	0.13	1.00	0.05	2.5	5.2	0.00	0.12	4.6	99.7	*2, pumice lenses in sandstone*
					0.9	*0.03*	*0.04*	*0.5*	*0.08*	*0.03*	*0.03*	*0.40*	*0.03*	*0.3*	*0.4*	*0.01*	*0.03*	*0.4*	*0.5*	
ENTR 949	26.8310	66.0185	320	14	72.7	0.13	0.07	13.2	0.87	0.09	0.14	0.78	0.08	1.5	5.5	0.03	0.17	5.1	100.4	*0.3, fine white tuff*
					0.4	*0.03*	*0.04*	*0.1*	*0.02*	*0.02*	*0.01*	*0.03*	*0.02*	*0.2*	*0.7*	*0.02*	*0.01*	*0.9*	*0.5*	
ENTR 949	*mode 2*		320		73.4	0.16	0.04	13.4	0.82	0.08	0.14	0.49	0.07	1.4	6.6	0.05	0.15	3.5	100.3	
ENTR 949	*mode 2*		320		72.9	0.14	0.07	13.4	0.87	0.09	0.13	0.48	0.08	1.6	5.1	0.03	0.17	5.1	100.1	
ENTR 928	26.8314	66.0180	~320	15	73.1	0.13	0.08	13.4	0.88	0.09	0.14	0.80	0.07	1.6	5.5	0.04	0.15	5.3	101.3	*0.4, fine white biotite tuff*
					0.4	*0.03*	*0.03*	*0.1*	*0.02*	*0.01*	*0.01*	*0.03*	*0.02*	*0.2*	*0.8*	*0.02*	*0.01*	*0.8*	*0.5*	
ENTR 950			321	14	73.1	0.09	0.07	11.9	0.71	0.03	0.07	0.78	0.04	2.0	6.3	0.04	0.16	4.4	99.6	*0.25, fine white tuff*
					0.3	*0.05*	*0.06*	*0.1*	*0.09*	*0.02*	*0.02*	*0.08*	*0.03*	*0.2*	*0.4*	*0.04*	*0.02*	*0.4*	*0.3*	
End section	26.8310	66.0181	336		*possible additional ash beds in this interval on the north side of gully*															
Pediment deposit			361																	*25, capping section*

*Elemental composition of volcanic glass by Electron Probe Microanalysis (cf. Nash, 1992), n=number of shards, for n≥4 average and 1σ standard deviation are reported.

Table A.16: Composition and stratigraphic posititon of volcanic ash beds from Quedrada de Jujuy (QDJ)
(base of section = 26.7819°S, 66.0147°W; total thickness ~450 m)

Sample	Lat	Lon	strat	n*	SiO2	TiO2	ZrO2	Al2O3	Fe2O3	MnO	MgO	CaO	BaO	Na2O	K2O	F	Cl	H2O	Total	Comment
	(°S)	(°W)	m																	thickness (m), lithology
QDJ 981	26.7819	66.0147	0	24	71.4	0.15	0.06	13.0	0.96	0.08	0.14	0.82	0.07	3.2	4.0	0.03	0.12	6.3	100.2	*1.5, fine base, coarsens up*
					0.4	*0.05*	*0.05*	*0.1*	*0.06*	*0.02*	*0.02*	*0.03*	*0.04*	*0.1*	*0.2*	*0.03*	*0.01*	*0.5*	*0.4*	
QDJ 982			1.8	10	72.5	0.05	0.07	13.3	0.52	0.14	0.07	0.94	0.03	3.0	4.8	0.00	0.06	4.4	100.0	*0.2, pumice lens*
					0.4	*0.03*	*0.06*	*0.4*	*0.05*	*0.02*	*0.01*	*0.04*	*0.03*	*0.2*	*0.6*	*0.01*	*0.01*	*0.9*	*0.3*	
QDJ 982	*mode 2*			8	71.8	0.13	0.07	13.0	0.94	0.07	0.14	0.81	0.09	3.1	3.9	0.03	0.11	6.1	100.2	
					0.5	*0.05*	*0.06*	*0.1*	*0.06*	*0.05*	*0.02*	*0.03*	*0.04*	*0.1*	*0.1*	*0.02*	*0.01*	*0.5*	*0.4*	
QDJ 983			107	23	72.8	0.05	0.04	13.3	0.47	0.21	0.07	0.68	0.01	2.8	5.4	0.04	0.02	3.8	99.7	*v. coarse pumice, base of sand*
					0.6	*0.03*	*0.05*	*0.1*	*0.05*	*0.04*	*0.02*	*0.03*	*0.02*	*0.2*	*0.4*	*0.03*	*0.01*	*0.3*	*0.5*	
QDJ 984			115	21	72.9	0.05	0.06	13.1	0.50	0.22	0.08	0.59	0.02	2.6	5.8	0.02	0.02	4.0	99.9	*coarse pumice, traceable*
					0.4	*0.03*	*0.06*	*0.1*	*0.06*	*0.04*	*0.02*	*0.04*	*0.02*	*0.3*	*0.5*	*0.02*	*0.01*	*0.4*	*0.2*	
QDJ 985	26.7834	66.0128	124	15	71.3	0.06	0.02	12.9	0.59	0.10	0.05	0.90	0.02	1.9	6.6	0.01	0.09	6.3	100.8	*1.1, pumiceous sand above*
					1.2	*0.05*	*0.03*	*0.3*	*0.05*	*0.03*	*0.02*	*0.03*	*0.02*	*0.1*	*0.2*	*0.01*	*0.02*	*0.8*	*0.7*	
QDJ 986	26.7843	66.0119	208	4	75.3	0.09	0.06	12.5	0.61	0.06	0.08	0.99	0.05	1.6	6.3	0.00	0.12	1.5	99.5	*1, basal pumice lag*
					0.1	*0.02*	*0.05*	*0.0*	*0.05*	*0.02*	*0.00*	*0.03*	*0.01*	*0.2*	*0.5*	*0.00*	*0.01*	*0.3*	*0.4*	
QDJ 986	*mode 2*			1	75.7	0.08	0.08	12.5	0.18	0.04	0.07	0.95	0.07	1.5	6.7	0.00	0.07	1.3	99.3	
QDJ 986	*mode 2*			1	75.7	0.11	0.16	12.5	0.18	0.05	0.07	0.85	0.06	1.6	6.8	0.00	0.04	1.3	99.4	
QDJ 987			214	15	73.3	0.09	0.05	12.6	0.62	0.07	0.07	0.89	0.03	1.6	6.8	0.00	0.13	4.5	100.7	*9, coarse pumice sandstone*
					0.8	*0.03*	*0.06*	*0.5*	*0.10*	*0.03*	*0.01*	*0.04*	*0.03*	*0.2*	*0.2*	*0.01*	*0.02*	*1.0*	*0.5*	
QDJ 989			274	9	71.6	0.10	0.05	12.9	0.66	0.05	0.10	0.80	0.06	1.9	6.9	0.04	0.09	5.6	100.7	*8, coarse pumice sandstone*
					1.4	*0.06*	*0.06*	*0.3*	*0.07*	*0.04*	*0.02*	*0.13*	*0.03*	*0.3*	*0.5*	*0.04*	*0.02*	*1.3*	*0.2*	
QDJ 989	*mode 2*		274	6	73.5	0.09	0.01	12.8	0.23	0.03	0.06	0.85	0.08	1.7	7.1	0.01	0.07	3.9	100.3	
					0.6	*0.03*	*0.02*	*0.4*	*0.06*	*0.03*	*0.02*	*0.10*	*0.05*	*0.3*	*0.3*	*0.02*	*0.02*	*0.3*	*0.3*	
QDJ 988	26.7862	66.0110	283	17	73.1	0.10	0.08	12.8	0.74	0.06	0.11	0.87	0.09	1.4	6.6	0.02	0.09	3.5	99.6	*fine white tuff*
					0.3	*0.04*	*0.03*	*0.1*	*0.02*	*0.01*	*0.01*	*0.03*	*0.02*	*0.2*	*0.2*	*0.01*	*0.01*	*0.8*	*0.6*	
QDJ 990	26.7828	66.0098	283	18	73.2	0.09	0.06	12.9	0.74	0.06	0.12	0.88	0.08	1.3	6.5	0.02	0.10	4.8	100.8	*1, fine white tuff*
					0.3	*0.02*	*0.04*	*0.1*	*0.02*	*0.01*	*0.00*	*0.02*	*0.02*	*0.2*	*0.2*	*0.01*	*0.01*	*1.0*	*0.6*	
QDJ 991	26.7801	66.0100	322	6	74.5	0.13	0.05	12.3	0.24	0.06	0.06	0.93	0.03	1.8	6.9	0.00	0.08	2.7	99.8	*0.3, pumice lens*
					0.2	*0.05*	*0.05*	*0.2*	*0.04*	*0.03*	*0.01*	*0.04*	*0.03*	*0.2*	*0.4*	*0.00*	*0.02*	*0.2*	*0.2*	
QDJ 991	*mode 2*		322	5	74.3	0.08	0.11	12.2	0.71	0.07	0.05	0.82	0.05	2.2	5.9	0.01	0.10	3.4	100.0	
					0.3	*0.04*	*0.10*	*0.2*	*0.18*	*0.03*	*0.03*	*0.19*	*0.06*	*0.7*	*0.6*	*0.02*	*0.02*	*0.3*	*0.1*	

Table A.16 (*continued*)

Sample	Lat	Lon	strat	n	SiO2	TiO2	ZrO2	Al2O3	Fe2O3	MnO	MgO	CaO	BaO	Na2O	K2O	F	Cl	H2O	Total	Comment
	(°S)	(°W)	m																	thickness (m), lithology
QDJ 992	26.7800	66.0097	349	21	73.3	0.09	0.08	12.5	0.59	0.08	0.06	0.44	0.03	1.5	7.6	0.07	0.13	4.2	100.6	*0.4, white tuff, traceable*
					1.1	*0.04*	*0.05*	*0.2*	*0.04*	*0.03*	*0.01*	*0.03*	*0.02*	*0.3*	*0.3*	*0.02*	*0.02*	*0.6*	*0.9*	
QDJ 993			364	11	71.5	0.12	0.06	12.5	0.78	0.03	0.09	0.87	0.07	2.1	6.5	0.04	0.11	5.1	99.7	*0.02, boitite tuff in fine sands*
					0.6	*0.04*	*0.05*	*0.3*	*0.08*	*0.02*	*0.03*	*0.04*	*0.05*	*0.7*	*1.0*	*0.09*	*0.02*	*0.5*	*0.4*	
QDJ 993	*mode 2*			4	71.9	0.03	0.07	12.2	0.52	0.07	0.08	0.39	0.04	1.6	7.5	0.06	0.12	5.4	99.9	
					0.8	*0.06*	*0.10*	*0.2*	*0.03*	*0.04*	*0.02*	*0.02*	*0.04*	*0.2*	*0.1*	*0.05*	*0.01*	*1.0*	*0.2*	
QDJ 993	*mode 3*			1	73.5	0.04	0.00	12.6	0.54	0.00	0.04	0.68	0.00	2.5	6.0	0.00	0.13	3.3	99.3	
QDJ 993	*mode 3*			1	73.7	0.12	0.04	12.9	0.52	0.03	0.03	0.77	0.06	3.0	5.4	0.00	0.12	3.0	99.7	
QDJ 994	26.7800	66.0089	412	14	73.8	0.10	0.05	12.6	0.23	0.06	0.07	0.88	0.03	1.9	6.7	0.01	0.06	4.2	100.7	*0.02, pumice lens*
					0.8	*0.04*	*0.04*	*0.2*	*0.09*	*0.03*	*0.02*	*0.13*	*0.04*	*0.2*	*0.5*	*0.02*	*0.03*	*0.7*	*0.4*	
QDJ 994	*mode 2*			4	73.9	0.11	0.02	12.6	0.65	0.08	0.08	1.01	0.03	2.1	6.1	0.01	0.11	4.1	100.8	
					0.5	*0.03*	*0.03*	*0.2*	*0.08*	*0.03*	*0.01*	*0.03*	*0.02*	*0.4*	*0.5*	*0.01*	*0.03*	*0.5*	*0.1*	
QDJ 995	26.7799	66.0087	420	17	74.9	0.11	0.06	12.2	0.68	0.03	0.07	0.81	0.05	1.3	6.5	0.03	0.12	3.9	100.7	*0.2, fine white biotite tuff*
					0.2	*0.03*	*0.03*	*0.1*	*0.02*	*0.01*	*0.01*	*0.10*	*0.03*	*0.2*	*0.4*	*0.02*	*0.01*	*0.7*	*0.5*	
QDJ 995	*mode 2*			1	75.0	0.07	0.07	12.1	0.61	0.03	0.07	0.60	0.09	1.5	6.6	0.04	0.12	3.3	100.2	
QDJ 995	*mode 2*			1	74.9	0.13	0.09	12.3	0.66	0.04	0.07	0.52	0.06	1.5	6.6	0.03	0.14	2.5	99.5	
QDJ 995	*mode 3*			1	75.0	0.19	0.08	12.7	0.91	0.03	0.14	1.02	0.05	1.9	5.0	0.01	0.12	2.8	100.1	

*Elemental composition of volcanic glass by Electron Probe Microanalysis (cf. Nash, 1992), n=number of shards, for n≥4 average and 1σ standard deviation are reported.

Table A.17: Composition and stratigraphic positition of volcanic ash beds from La Maravilla (MAR)
(base of section = 26.7063°S, 65.9438°W; total thickness >800 m)

Sample	Lat	Lon	strat	n*	SiO2	TiO2	ZrO2	Al2O3	Fe2O3	MnO	MgO	CaO	BaO	Na2O	K2O	F	Cl	H2O	Total	Comment
	(°S)	(°W)	m																	thickness (m), lithology
MAR 856	26.7063	65.9438	0	14	71.8	0.06	0.04	12.7	0.56	0.12	0.08	0.94	0.02	2.8	5.0	0.01	0.07	6.3	100.5	*0.9, pumice in mudstone*
					0.5	*0.04*	*0.04*	*0.4*	*0.07*	*0.05*	*0.01*	*0.10*	*0.03*	*0.2*	*0.2*	*0.02*	*0.03*	*0.9*	*0.5*	
MAR 857	26.7062	65.9437	3.9		*not analyzed*															*2.5, pumiceous sandstone*
MAR 858	26.7064	65.9444	38.4																	*0.6, fine biotite tuff*
MAR 859	26.7063	65.9444	80	10	72.2	0.05	0.04	13.2	0.54	0.15	0.07	0.97	0.01	2.7	5.4	0.00	0.05	5.1	100.4	*coarse pumice at base of ss*
					0.3	*0.03*	*0.04*	*0.4*	*0.03*	*0.02*	*0.01*	*0.02*	*0.01*	*0.1*	*0.2*	*0.01*	*0.01*	*0.5*	*0.3*	
MAR 859	*mode 2*			6	71.5	0.15	0.01	12.9	0.96	0.06	0.15	0.84	0.06	2.6	4.9	0.02	0.11	6.9	101.1	
					0.4	*0.05*	*0.03*	*0.4*	*0.07*	*0.02*	*0.02*	*0.02*	*0.03*	*0.2*	*0.2*	*0.02*	*0.01*	*0.7*	*0.3*	
MAR 860	26.7024	65.9440	~200		*not analyzed*															*0.5, white/gray/white interbeds*
MAR 861			~201	18	71.7	0.13	0.06	11.9	0.82	0.07	0.13	0.75	0.07	2.8	4.8	0.02	0.14	7.1	100.5	*1, white tuff below coarse sand*
					0.3	*0.02*	*0.04*	*0.6*	*0.04*	*0.02*	*0.02*	*0.02*	*0.04*	*0.2*	*0.2*	*0.02*	*0.01*	*0.6*	*0.4*	
MAR 862	26.7010	65.9453	~300	13	72.2	0.07	0.04	11.3	0.60	0.10	0.06	0.89	0.00	1.9	6.2	0.01	0.08	6.9	100.3	*pumiceous tuff*
					0.6	*0.03*	*0.05*	*0.4*	*0.04*	*0.02*	*0.01*	*0.04*	*0.01*	*0.1*	*0.2*	*0.02*	*0.01*	*0.7*	*0.3*	
MAR 863	26.7008	65.9456	~320	12	73.1	0.09	0.05	11.7	0.67	0.08	0.07	1.00	0.02	1.9	6.4	0.00	0.11	5.0	100.2	*>4, coarse pumice tuff*
					0.4	*0.03*	*0.06*	*0.4*	*0.02*	*0.02*	*0.02*	*0.02*	*0.02*	*0.2*	*0.2*	*0.01*	*0.01*	*1.1*	*0.6*	
MAR 863	*mode 2*			1	74.1	0.07	0.09	11.4	0.55	0.09	0.05	1.05	0.05	2.2	6.2	0.00	0.08	3.9	99.9	
MAR 863	*mode 2*			1	71.6	0.10	0.01	12.8	0.55	0.17	0.08	0.97	0.00	2.3	6.3	0.00	0.05	5.2	100.1	
MAR 863	*mode 2*			1	73.6	0.09	0.03	12.2	0.52	0.08	0.05	0.99	0.00	1.7	6.6	0.00	0.11	4.1	100.1	
MAR 863	*mode 3*			1	73.1	0.11	0.02	12.1	0.39	0.06	0.07	0.99	0.05	1.9	6.5	0.00	0.10	4.3	99.6	
MAR 863	*mode 3*			1	73.8	0.10	0.03	12.1	0.26	0.06	0.08	0.96	0.04	1.8	6.5	0.00	0.05	4.0	99.8	
MAR 864	26.7004	65.9458	~350	11	73.7	0.10	0.04	12.0	0.28	0.05	0.06	0.88	0.03	1.8	6.7	0.00	0.08	3.9	99.7	*coarse pumice tuff*
					0.5	*0.03*	*0.05*	*0.6*	*0.07*	*0.02*	*0.01*	*0.08*	*0.02*	*0.1*	*0.1*	*0.00*	*0.02*	*0.6*	*0.4*	
MAR 864	*mode 2*			5	72.9	0.10	0.04	11.8	0.62	0.06	0.08	0.92	0.06	1.8	6.5	0.00	0.11	4.7	99.7	
					0.8	*0.02*	*0.05*	*0.3*	*0.06*	*0.01*	*0.01*	*0.05*	*0.02*	*0.1*	*0.1*	*0.01*	*0.01*	*1.0*	*0.5*	
MAR 865	26.7000	65.9471	~400	6	73.1	0.06	0.02	12.6	0.66	0.06	0.07	1.22	0.04	2.1	6.2	0.02	0.06	4.4	100.5	*>3, coarse pumice tuff*
					0.5	*0.02*	*0.02*	*0.5*	*0.04*	*0.02*	*0.02*	*0.06*	*0.03*	*0.3*	*0.4*	*0.02*	*0.00*	*0.7*	*0.5*	
MAR 866					*not analyzed*															*15 cm pumice in MAR 865*
MAR 867	26.6969	65.9480	~550	17	73.4	0.12	0.06	11.4	0.65	0.03	0.07	0.81	0.03	2.1	6.3	0.02	0.12	5.7	100.7	*0.5, fine white biotite tuff*
					0.3	*0.04*	*0.04*	*0.3*	*0.04*	*0.02*	*0.02*	*0.02*	*0.02*	*0.2*	*0.3*	*0.01*	*0.01*	*0.5*	*0.3*	
MAR 867	*mode 2*			1	73.2	0.12	0.00	12.0	0.51	0.03	0.04	0.76	0.02	2.3	6.4	0.01	0.14	5.4	100.8	
MAR 867	*mode 2*			1	73.1	0.05	0.00	12.1	0.49	0.04	0.04	0.80	0.00	2.1	6.6	0.03	0.11	5.4	100.8	

Table A.17 (*continued*)

Sample	Lat	Lon	strat	n	SiO2	TiO2	ZrO2	Al2O3	Fe2O3	MnO	MgO	CaO	BaO	Na2O	K2O	F	Cl	H2O	Total	Comment
	(°S)	(°W)	m																	thickness (m), lithology
MAR 868	26.6915	65.9481	~700	6	72.2	0.18	0.08	12.1	1.06	0.04	0.14	0.98	0.03	2.0	6.3	0.05	0.21	5.1	100.4	*0.5, in coarse sandstone*
					1.5	*0.08*	*0.06*	*0.5*	*0.33*	*0.02*	*0.09*	*0.24*	*0.03*	*0.5*	*0.8*	*0.04*	*0.04*	*1.0*	*0.5*	
MAR 868	*mode 2*			4	71.4	0.21	0.07	12.3	1.21	0.05	0.20	1.11	0.01	2.1	6.0	0.06	0.22	5.2	100.1	
					0.5	*0.03*	*0.06*	*0.3*	*0.04*	*0.01*	*0.01*	*0.04*	*0.01*	*0.2*	*0.3*	*0.04*	*0.02*	*0.1*	*0.7*	
MAR 868	*mode 3*			1	70.8	0.27	0.00	12.5	1.36	0.06	0.28	1.26	0.01	2.0	6.2	0.09	0.22	5.3	100.2	
MAR 868	*mode 3*			1	69.8	0.30	0.05	12.9	1.51	0.05	0.30	1.37	0.03	2.8	4.9	0.00	0.21	5.7	100.0	
MAR 868	*mode 3*			1	70.5	0.29	0.03	12.4	1.50	0.06	0.31	1.40	0.00	2.7	4.8	0.06	0.20	6.0	100.2	
MAR 868	*mode 4*			1	71.5	0.32	0.07	13.1	1.75	0.06	0.39	1.53	0.00	0.3	3.3	0.14	0.19	8.3	100.9	
MAR 868	*mode 4*			1	69.8	0.36	0.10	12.4	1.72	0.03	0.42	1.51	0.00	2.7	4.9	0.09	0.17	6.0	100.0	

*Elemental composition of volcanic glass by Electron Probe Microanalysis (cf. Nash, 1992), n=number of shards, for n≥4 average and 1σ standard deviation are reported.

Note: Above 100 m stratigraphic levels are estimated using GPS coordinates. Lower part of section strikes N40E and dips 42 to the west, uppermost section dips more steeply

Table A.18: Composition and stratigraphic posititon of volcanic ash beds from El Infiernillo section #1 (INF)
(base of section = 26.7191°S, 65.7967°W; total thickness ~350 m)

Sample	Lat	Lon	strat	n*	SiO2	TiO2	ZrO2	Al2O3	Fe2O3	MnO	MgO	CaO	BaO	Na2O	K2O	F	Cl	H2O	Total	Comment
	(°S)	(°W)	m																	thickness (m), lithology
INF 963	26.7191	65.7963	17		*not analyzed*															*large pumice in brown silts*
INF 964			26		*not analyzed*															*gray sand; S60 D75*
INF 965	26.7197	65.7963	62		*not analyzed*															*pumice bed in sand; S60 D73*
INF 966	26.7198	65.7960	78	6	71.3	0.08	0.02	13.6	0.70	0.09	0.08	1.35	0.09	2.3	5.6	0.01	0.09	5.2	100.5	*0.8, pumice sand; S60 D75*
					0.7	*0.02*	*0.03*	*0.2*	*0.02*	*0.01*	*0.02*	*0.01*	*0.02*	*0.2*	*0.1*	*0.02*	*0.02*	*0.5*	*0.4*	
INF 967	26.7200	65.7960	93	5	70.1	0.03	0.02	14.2	0.77	0.18	0.03	0.21	0.02	2.4	6.3	0.29	0.05	5.7	100.3	*1, 20 cm thick white base; D75*
					1.5	*0.06*	*0.04*	*0.9*	*0.18*	*0.05*	*0.12*	*0.33*	*0.04*	*0.4*	*0.5*	*0.11*	*0.05*	*1.0*	*0.8*	
INF 967	*mode 2*			5	72.7	0.06	0.04	13.1	0.54	0.07	0.05	0.79	0.02	2.6	5.8	0.04	0.06	4.6	100.4	
					0.9	*0.01*	*0.03*	*0.2*	*0.03*	*0.02*	*0.02*	*0.04*	*0.02*	*0.3*	*0.4*	*0.03*	*0.02*	*0.5*	*0.4*	
INF 968	26.7200	65.7956	100	7	71.5	0.17	0.03	11.8	1.02	0.08	0.16	0.82	0.09	1.9	5.9	0.01	0.16	6.1	99.7	*sparse pumice in sand*
					1.7	*0.02*	*0.04*	*0.4*	*0.07*	*0.01*	*0.04*	*0.03*	*0.02*	*0.1*	*0.1*	*0.02*	*0.04*	*1.2*	*0.9*	
INF 968	*mode 2*			4	71.9	0.20	0.02	12.3	0.94	0.09	0.13	1.08	0.09	2.1	5.7	0.01	0.16	5.5	100.2	
					1.6	*0.01*	*0.00*	*0.2*	*0.05*	*0.01*	*0.01*	*0.10*	*0.02*	*0.1*	*0.1*	*0.02*	*0.03*	*1.0*	*0.7*	
Begin conglomerate interbeds			~150																	*S85 D68*
INF 969	26.7209	65.7955	185		*not analyzed*															*blue sand; D55*
INF 970	26.7212	65.7948	220		*not analyzed*															*large pumice clast in blue sand*
INF 973	26.7214	65.7947	230		*not analyzed*															*small pumice in sand*
INF 971	26.7217	65.7946	250		*not analyzed*															*vey thin tuff in coarse sand*
INF 972	26.7221	65.7946	310		*not analyzed*															*0.7, tuff, fining upward*
Congl.	26.7221	65.7947	312																	*10, gravel to boulder sized*
Blue sand			322		*dip ~35 ° to the ESE*															*23, between conglomerate*
Congl.	26.7234	65.7941	350																	*10, gravel to boulder sized*
Congl.	26.7261	65.7943	>350		*flat lying gravel to boulder sized conglomerates, separated by ~10 m of sandstone*															

*Elemental composition of volcanic glass by Electron Probe Microanalysis (cf. Nash, 1992), n=number of shards, for n≥4 average and 1σ standard deviation are reported.

Note: Strike and dip are given such that beds are always dipping to the right.

Table A.19: Composition and stratigraphic positition of volcanic ash beds from El Infiernillo section #2 (INF)
(base of section = 26.7206°S, 65.80073°W; total thickness ~40 m)

Sample	Lat	Lon	strat	n*	SiO2	TiO2	ZrO2	Al2O3	Fe2O3	MnO	MgO	CaO	BaO	Na2O	K2O	F	Cl	H2O	Total	Comment
	(°S)	(°W)	m																	thickness (m), lithology
INF 974			0	15	72.4	0.17	0.08	13.3	0.93	0.06	0.16	0.94	0.08	1.9	4.7	0.07	0.22	7.6	102.6	*1.5, pumiceous sandstone*
					0.5	*0.11*	*0.07*	*0.3*	*0.08*	*0.04*	*0.05*	*0.06*	*0.07*	*0.2*	*0.2*	*0.09*	*0.03*	*0.9*	*1.1*	
INF 974	*mode 2*			7	73.5	0.14	0.05	12.8	0.78	0.10	0.11	0.73	0.06	1.9	5.0	0.08	0.11	7.7	103.1	
					0.9	*0.05*	*0.06*	*0.2*	*0.14*	*0.07*	*0.03*	*0.05*	*0.08*	*0.2*	*0.2*	*0.04*	*0.03*	*1.2*	*1.1*	
INF 974	*mode 3*			1	73.7	0.00	0.06	12.7	0.64	0.03	0.07	0.38	0.03	1.7	5.7	0.01	0.11	7.4	102.4	
INF 974	*mode 3*			1	71.5	0.20	0.00	12.0	0.74	0.00	0.13	0.33	0.00	1.6	5.2	0.00	0.08	9.4	101.0	
INF 974	*mode 3*			1	71.9	0.00	0.09	12.7	0.48	0.15	0.06	0.31	0.00	1.3	5.9	0.03	0.07	9.0	102.0	
INF 975			2	12	72.7	0.05	0.08	12.4	0.53	0.10	0.06	0.29	0.02	2.8	5.3	0.10	0.09	5.8	100.2	*0.3, fine base, coarse upper*
					0.7	*0.05*	*0.06*	*0.1*	*0.06*	*0.04*	*0.02*	*0.03*	*0.03*	*0.3*	*0.2*	*0.04*	*0.01*	*0.8*	*0.2*	
INF 975	*mode 2*			13	72.7	0.09	0.07	12.2	0.65	0.04	0.06	0.68	0.07	2.8	5.2	0.01	0.08	5.5	100.0	
					0.3	*0.04*	*0.05*	*0.1*	*0.08*	*0.03*	*0.01*	*0.06*	*0.05*	*0.1*	*0.1*	*0.01*	*0.02*	*0.6*	*0.3*	
INF976			7.9	22	70.7	0.14	0.05	12.8	0.90	0.06	0.15	0.92	0.08	2.7	4.7	0.02	0.22	6.6	100.0	*0.05, biotite tuff*
					0.3	*0.04*	*0.05*	*0.1*	*0.06*	*0.02*	*0.02*	*0.03*	*0.04*	*0.2*	*0.1*	*0.02*	*0.02*	*0.5*	*0.3*	
INF 977			9.0	12	71.9	0.09	0.05	12.4	0.49	0.11	0.09	0.28	0.02	2.3	5.9	0.00	0.11	6.5	100.2	*0.05, plane-bedded fine pumice*
					0.4	*0.06*	*0.04*	*0.2*	*0.07*	*0.02*	*0.02*	*0.01*	*0.02*	*0.3*	*0.2*	*0.01*	*0.02*	*0.7*	*0.2*	
INF 977	*mode 2*			8	71.7	0.11	0.09	12.5	0.67	0.05	0.11	0.69	0.08	2.7	5.0	0.00	0.09	6.4	100.2	
					0.6	*0.05*	*0.03*	*0.1*	*0.05*	*0.03*	*0.01*	*0.04*	*0.03*	*0.3*	*0.3*	*0.01*	*0.02*	*0.8*	*0.3*	
INF 977	*mode 3*			5	71.0	0.09	0.07	12.7	0.84	0.05	0.12	1.06	0.07	2.9	4.6	0.01	0.19	6.4	100.0	
					0.5	*0.07*	*0.05*	*0.2*	*0.08*	*0.04*	*0.01*	*0.06*	*0.05*	*0.3*	*0.2*	*0.01*	*0.02*	*0.5*	*0.5*	
INF 978			16.2	25	71.5	0.11	0.06	12.5	0.71	0.07	0.10	0.71	0.05	2.5	5.0	0.02	0.09	6.6	100.1	*0.35, vitric tuff*
					0.5	*0.06*	*0.06*	*0.2*	*0.05*	*0.04*	*0.03*	*0.03*	*0.03*	*0.3*	*0.3*	*0.03*	*0.02*	*0.7*	*0.3*	
INF 979			18.7	5	72.9	0.12	0.03	12.8	0.73	0.06	0.10	0.60	0.06	2.8	5.2	0.00	0.08	4.6	100.1	*0.05, fine tuff, indurated*
					0.4	*0.02*	*0.06*	*0.2*	*0.03*	*0.02*	*0.00*	*0.02*	*0.02*	*0.2*	*0.1*	*0.00*	*0.01*	*0.6*	*0.7*	
INF 979	*mode 2*			4	73.8	0.09	0.03	13.4	0.88	0.05	0.38	0.64	0.07	2.7	5.0	0.00	0.10	4.4	101.6	
					0.6	*0.03*	*0.04*	*0.1*	*0.06*	*0.03*	*0.15*	*0.07*	*0.04*	*0.2*	*0.2*	*0.00*	*0.018*	*0.7*	*0.3*	
INF 980			37.2	29	72.6	0.13	0.07	13.2	0.81	0.10	0.12	0.97	0.09	2.0	4.3	0.03	0.12	7.5	102.0	*0.15, tuff*
					0.7	*0.09*	*0.11*	*0.4*	*0.10*	*0.06*	*0.03*	*0.06*	*0.06*	*0.2*	*0.2*	*0.04*	*0.02*	*0.8*	*0.6*	

*Elemental composition of volcanic glass by Electron Probe Microanalysis (cf. Nash, 1992), n=number of shards, for n≥4 average and 1σ standard deviation are reported.

Table A.20: Composition, age, and location of Quaternary ash beds and ignimbrites in northwestern Argentina
(Age data for Puna ignimbrites also presented in this dissertation)

Sample	Lat	Lon	Age	n*	SiO2	TiO2	ZrO2	Al2O3	Fe2O3	MnO	MgO	CaO	BaO	Na2O	K2O	F	Cl	H2O	Total	Comment
	(°S)	(°W)	ka																	thickness (m), lithology
TUC 106	26.9325	65.6755	<5	16	74.7	0.08	0.06	12.8	0.52	0.10	0.05	0.47	0.01	4.0	4.3	0.04	0.06	3.8	0.0	*2, in loess, sample lower part*
					0.5	*0.02*	*0.04*	*0.2*	*0.06*	*0.02*	*0.01*	*0.03*	*0.01*	*0.2*	*0.2*	*0.04*	*0.01*	*0.6*	*0.0*	
ENTR 538	26.8598	66.0338	<5	14	74.6	0.08		12.6	0.53	0.09	0.04	0.50	0.01	3.2	4.5	0.01	0.07	4.2	100.4	*fine, disseminated carbonate*
					0.7	*0.02*		*0.1*	*0.06*	*0.03*	*0.01*	*0.02*	*0.01*	*0.4*	*0.6*	*0.02*	*0.02*	*1.1*	*0.4*	
PCQ 783	27.2102	66.9414	??	1	69.5	0.52	0.02	15.1	2.52	0.06	0.63	2.34	0.02	3.5	4.5	0.01	0.17	1.3	100.2	*pumice biotite ash*
				1	69.9	0.32	0.00	15.9	1.81	0.09	0.55	2.97	0.00	2.7	4.2	0.08	0.11	1.2	99.8	
				1	70.3	0.57	0.00	15.0	2.58	0.10	0.78	2.34	0.00	3.7	4.4	0.04	0.17	0.4	100.3	
				1	71.5	0.37	0.15	14.5	2.30	0.03	0.69	2.16	0.19	3.5	4.6	0.02	0.12	0.2	100.3	
				1	71.6	0.32	0.14	14.6	2.15	0.07	0.63	2.13	0.06	3.6	4.7	0.02	0.14	0.3	100.4	
				1	72.1	0.09	0.08	13.4	1.50	0.01	0.31	1.49	0.00	3.5	4.6	0.00	0.12	2.1	99.2	
PUN 1009	26.5973	67.5019	44	17	74.6	0.11	0.09	12.3	0.29	0.03	0.03	0.13	0.01	3.1	6.6	0.07	0.27	2.8	100.4	*Campo de la Piedra Pómez*
					0.5	*0.06*	*0.06*	*0.5*	*0.04*	*0.03*	*0.01*	*0.01*	*0.01*	*0.1*	*0.1*	*0.03*	*0.03*	*0.5*	*0.4*	
PUN 1009	*mode 2*			1	74.6	0.11	0.06	12.4	0.39	0.03	0.05	0.13	0.00	3.2	6.6	0.09	0.29	2.4	100.5	
	mode 2			1	74.8	0.15	0.04	11.8	0.42	0.02	0.00	0.14	0.00	3.1	6.6	0.10	0.29	3.4	101.0	
	mode 2			1	74.8	0.05	0.00	12.8	0.50	0.02	0.06	0.12	0.03	3.0	6.6	0.11	0.28	1.9	100.2	
	mode 2			1	75.1	0.16	0.05	12.1	0.64	0.04	0.05	0.12	0.01	3.1	6.8	0.07	0.29	1.6	100.2	
	mode 2			1	75.3	0.01	0.24	11.8	0.67	0.07	0.05	0.10	0.04	3.2	6.8	0.10	0.29	1.6	100.5	
	mode 2			1	73.8	0.11	0.23	11.6	0.81	0.02	0.07	0.10	0.02	3.1	6.4	0.08	0.28	3.3	100.2	
	mode 2			1	73.9	0.14	0.11	12.3	0.90	0.07	0.04	0.13	0.00	3.3	6.5	0.05	0.27	3.0	100.7	
PUN 1009	*mode 3*			1	74.6	0.11	0.04	11.4	0.31	0.06	0.00	0.06	0.00	3.1	6.6	0.05	0.27	3.5	100.1	
	mode 3			1	74.1	0.08	0.09	12.0	0.30	0.00	0.02	0.07	0.00	2.9	6.6	0.02	0.26	3.5	99.9	
PUN 1009	*mode 4*			1	73.9	0.08	0.13	11.7	0.29	0.01	0.01	0.43	0.07	2.6	6.8	0.00	0.00	3.4	99.5	
	mode 4			1	74.7	0.08	0.00	12.5	0.28	0.01	0.03	0.39	0.02	2.3	6.7	0.00	0.01	2.6	99.6	
			Ma																	
PUN 1060	25.5528	66.9236	2.06	8	74.0	0.09	0.08	12.5	0.61	0.06	0.06	0.37	0.01	2.8	5.2	0.00	0.18	4.9	100.9	*Cerro Galán ignimbrite*
					0.2	*0.02*	*0.07*	*0.4*	*0.05*	*0.02*	*0.01*	*0.01*	*0.02*	*0.1*	*0.2*	*0.01*	*0.01*	*0.4*	*0.3*	

*Elemental composition of volcanic glass by Electron Probe Microanalysis (cf. Nash, 1992), n=number of shards, for n≥4 average and 1σ standard deviation are reported.

Ages established as follows: TUC 106/ENTR 538 by correlation with Buey Muerto/Alemania ash bed (Hermanns and Schellenberger, 2008); PUN 1009/PUN 1060 from Table A.23

Note: PUN 1060 data derive from the same glass fragment attached to a phenocryst, significantly more chemical variability may exist within the youngest Cerro Galán ignimbrite.

Table A.21: Composition of volcanic ash beds sampled by researchers at Universität Potsdam, Potsdam, Germany
(primary contact for sample information is Dr. Edward Sobel)

Sample	Lat	Lon	strat	n*	SiO2	TiO2	ZrO2	Al2O3	Fe2O3	MnO	MgO	CaO	BaO	Na2O	K2O	F	Cl	H2O	Total	Comment
	(°S)	(°W)	m																	
Fiambalá basin (see Carrapa et al., 2008 for details on stratigraphic position and U-Pb zircon data)																				
001				20	73.2	0.11	0.03	12.2	0.64	0.05	0.05	0.62	0.07	2.8	5.5	0.02	0.12	5.2	100.7	*top Punaschotter Formation*
					0.6	*0.05*	*0.05*	*0.2*	*0.04*	*0.03*	*0.02*	*0.02*	*0.04*	*0.2*	*0.2*	*0.03*	*0.01*	*0.7*	*0.3*	
001	*replicate analysis*			25	73.4	0.11	0.03	11.9	0.65	0.05	0.06	0.63	0.06	2.7	5.4	0.01	0.13	5.8	101.0	
					0.4	*0.03*	*0.05*	*0.1*	*0.04*	*0.02*	*0.01*	*0.02*	*0.03*	*0.2*	*0.2*	*0.02*	*0.01*	*0.8*	*0.3*	
003				19	73.9	0.06	0.03	14.2	0.54	0.24	0.08	0.16	0.00	4.0	4.4	0.02	0.05	3.0	100.6	*top Punaschotter Formation*
					0.3	*0.04*	*0.04*	*0.2*	*0.05*	*0.04*	*0.02*	*0.03*	*0.01*	*0.1*	*0.1*	*0.03*	*0.01*	*0.3*	*0.2*	
006				22	73.3	0.10	0.06	12.6	0.54	0.08	0.08	0.48	0.06	2.5	4.0		0.08	8.0	101.9	*upper Tamberia Formation*
					1.3	*0.03*	*0.05*	*0.3*	*0.11*	*0.02*	*0.02*	*0.08*	*0.03*	*0.5*	*0.5*		*0.01*	*1.4*	*1.0*	
006	*replicate analysis*			24	72.8	0.09	0.08	12.8	0.50	0.08	0.08	0.50	0.06	2.6	3.9		0.07	7.7	101.2	
					1.6	*0.03*	*0.04*	*0.3*	*0.13*	*0.02*	*0.02*	*0.08*	*0.03*	*0.5*	*0.7*		*0.01*	*2.0*	*1.7*	
029				15	72.5	0.07	0.07	13.5	0.70	0.05	0.09	1.22	0.10	2.2	4.2		0.09	4.6	99.3	*Guanchin Formation*
					0.9	*0.04*	*0.04*	*0.3*	*0.05*	*0.02*	*0.03*	*0.05*	*0.03*	*0.4*	*0.3*		*0.01*	*1.1*	*0.7*	
029	*replicate analysis*			15	72.3	0.07	0.05	13.5	0.70	0.05	0.12	1.20	0.09	2.3	4.1		0.10	5.0	99.6	
					0.5	*0.02*	*0.05*	*0.1*	*0.06*	*0.02*	*0.05*	*0.05*	*0.02*	*0.3*	*0.3*		*0.02*	*0.7*	*0.7*	
055				34	73.0	0.09	0.07	12.7	0.58	0.08	0.07	0.44	0.02	2.0	4.8		0.13	5.8	99.7	*Guanchin Formation*
					0.9	*0.03*	*0.05*	*0.1*	*0.04*	*0.02*	*0.02*	*0.02*	*0.03*	*0.3*	*0.2*		*0.01*	*0.9*	*0.6*	
055	*replicate analysis*			25	72.9	0.10	0.08	12.7	0.60	0.07	0.07	0.46	0.02	1.6	4.9		0.14	5.9	99.5	
					0.7	*0.03*	*0.06*	*0.1*	*0.04*	*0.02*	*0.01*	*0.02*	*0.02*	*0.2*	*0.2*		*0.01*	*0.7*	*0.5*	
074				20	73.4	0.12	0.06	12.1	0.63	0.06	0.06	0.63	0.05	3.1	5.1	0.02	0.12	5.3	100.7	*top Punaschotter Formation*
					0.4	*0.05*	*0.06*	*0.2*	*0.05*	*0.04*	*0.02*	*0.02*	*0.03*	*0.2*	*0.3*	*0.03*	*0.01*	*0.6*	*0.3*	
Corral Quemado basin (samples from Dr. Isabelle Coutand, now at Dalhousie University, Halifax, Nova Scotia, Canada; see Chapter 3 for additional details)																				
CQ 22	27.1497	66.9232		25	73.6	0.13	0.07	12.0	0.76	0.05	0.11	0.84	0.06	3.0	4.7		0.11	5.8	101.2	*tuff of SS#12 sequence*
					0.6	*0.02*	*0.05*	*0.1*	*0.03*	*0.02*	*0.02*	*0.03*	*0.03*	*0.3*	*0.5*		*0.01*	*0.5*	*0.3*	
CQ 26	27.1648	66.9105		19	72.0	0.14	0.07	12.5	0.91	0.09	0.16	0.61	0.06	2.9	5.4		0.13	6.6	101.5	*late Miocene sequence*
					0.5	*0.04*	*0.03*	*0.1*	*0.03*	*0.02*	*0.01*	*0.01*	*0.02*	*0.3*	*0.5*		*0.02*	*0.9*	*0.6*	
CQ 26	*replicate analysis*			22	72.5	0.16	0.09	12.5	0.92	0.08	0.16	0.62	0.06	2.8	5.6		0.14	6.4	102.0	
					0.4	*0.02*	*0.05*	*0.1*	*0.04*	*0.02*	*0.02*	*0.03*	*0.03*	*0.3*	*0.5*		*0.02*	*1.0*	*0.6*	
CQ 38	27.1148	66.9283		25	74.4	0.11	0.08	12.1	0.61	0.08	0.06	0.43	0.01	3.1	5.1		0.16	5.0	101.4	*Toba Corral Quemado*
					0.9	*0.04*	*0.05*	*0.2*	*0.07*	*0.02*	*0.01*	*0.05*	*0.02*	*0.4*	*0.5*		*0.02*	*1.6*	*0.7*	

Table A.21 (*continued*)

Sample	Lat	Lon	strat	n	SiO2	TiO2	ZrO2	Al2O3	Fe2O3	MnO	MgO	CaO	BaO	Na2O	K2O	F	Cl	H2O	Total	Comment
	(°S)	(°W)	m																	thickness (m), lithology
Vallé Santa Maria (samples associated with Kleinert and Strecker, 2001)																				
ER-A1				14	72.7	0.06	0.07	12.1	0.57	0.16	0.04	0.31	0.01	1.8	7.3	0.04	0.12	6.6	101.8	
					0.8	*0.03*	*0.04*	*0.2*	*0.05*	*0.04*	*0.01*	*0.05*	*0.02*	*0.4*	*0.4*	*0.07*	*0.02*	*0.8*	*1.1*	
ER-A1	*mode 2*			11	73.0	0.10	0.07	12.1	0.72	0.06	0.07	0.54	0.01	1.6	7.0	0.01	0.16	6.2	101.5	
					0.9	*0.03*	*0.06*	*0.2*	*0.06*	*0.02*	*0.02*	*0.07*	*0.02*	*0.5*	*0.5*	*0.03*	*0.01*	*0.9*	*1.0*	
ER-E1				18	70.5	0.23	0.09	13.0	1.33	0.05	0.26	1.19	0.05	2.2	6.1	0.04	0.18	5.8	101.0	
					0.7	*0.03*	*0.05*	*0.2*	*0.04*	*0.02*	*0.04*	*0.03*	*0.03*	*0.4*	*0.5*	*0.02*	*0.02*	*0.6*	*0.6*	
ER-E1	*mode 2*			1	74.5	0.12	0.00	12.1	0.79	0.01	0.08	0.73	0.04	2.1	5.8	0.08	0.18	3.8	100.3	
				1	74.4	0.15	0.12	12.0	0.77	0.05	0.07	0.70	0.00	1.7	6.7	0.01	0.19	3.3	100.1	
				1	74.2	0.14	0.14	12.1	0.76	0.08	0.07	0.78	0.08	2.4	5.4	0.07	0.14	3.5	99.8	
ER-G1				29	73.0	0.13	0.07	11.9	0.82	0.03	0.10	0.81	0.03	1.9	6.2	0.07	0.18	5.7	100.9	
					0.6	*0.03*	*0.05*	*0.2*	*0.05*	*0.02*	*0.02*	*0.06*	*0.02*	*0.4*	*0.4*	*0.04*	*0.01*	*0.8*	*0.5*	
ER-L1				29	73.6	0.12	0.07	12.2	0.66	0.06	0.07	0.49	0.08	2.4	6.5	0.09	0.14	5.5	101.7	
					0.4	*0.03*	*0.06*	*0.2*	*0.05*	*0.03*	*0.02*	*0.03*	*0.03*	*0.3*	*0.4*	*0.03*	*0.01*	*0.5*	*0.4*	
ER-N1				29	71.9	0.15	0.07	13.0	0.87	0.09	0.14	0.81	0.05	2.7	5.6	0.07	0.16	6.5	102.1	
					0.5	*0.04*	*0.05*	*0.1*	*0.03*	*0.02*	*0.02*	*0.02*	*0.03*	*0.4*	*0.7*	*0.02*	*0.01*	*0.6*	*0.4*	
ER-Q1				14	72.7	0.07	0.07	12.2	0.62	0.11	0.07	0.93	0.01	2.0	5.5	0.06	0.09	6.8	101.2	*Toba Rayita Amarilla*
					0.9	*0.03*	*0.05*	*0.2*	*0.07*	*0.02*	*0.02*	*0.03*	*0.01*	*0.5*	*0.5*	*0.03*	*0.01*	*0.9*	*0.6*	
Ande 199				22	73.2	0.10	0.07	12.1	0.71	0.03	0.07	0.87	0.04	3.4	3.4	0.06	0.15	7.3	101.3	
					1.1	*0.03*	*0.05*	*0.2*	*0.05*	*0.02*	*0.02*	*0.05*	*0.03*	*0.2*	*0.1*	*0.03*	*0.02*	*0.8*	*0.7*	
QJ 4				8	72.6	0.09	0.08	12.1	0.61	0.11	0.06	0.88	0.01	1.8	6.3	0.00	0.09	6.2	100.8	*Toba Rayita Amarilla*
					0.6	*0.02*	*0.04*	*0.1*	*0.04*	*0.02*	*0.01*	*0.04*	*0.01*	*0.1*	*0.2*	*0.00*	*0.01*	*0.3*	*0.8*	
QJ 6				20	71.8	0.09	0.07	12.5	0.74	0.06	0.11	0.87	0.05	1.8	6.9	0.00	0.10	5.9	101.1	
					0.3	*0.03*	*0.03*	*0.1*	*0.03*	*0.02*	*0.01*	*0.02*	*0.03*	*0.2*	*0.2*	*0.01*	*0.01*	*0.5*	*0.3*	
Angastaco basin (see Coutand et al., 2006 for stratigraphic information and U-Pb zircon data)																				
AI29	25.6740	66.0719		20	72.3	0.20	0.07	12.7	1.16	0.03	0.19	1.08	0.02	2.7	4.8	0.09	0.17	5.1	100.5	*upper Palo Pintado Formation*
					0.8	*0.03*	*0.05*	*0.3*	*0.14*	*0.02*	*0.04*	*0.08*	*0.02*	*0.1*	*0.3*	*0.03*	*0.02*	*0.6*	*0.7*	
AI36	25.7015	66.0300		17	73.3	0.11	0.04	12.0	0.72	0.03	0.08	0.84	0.05	2.5	5.6	0.10	0.12	4.7	100.1	*Palo Pintado/San Felipe*
					1.1	*0.03*	*0.05*	*0.2*	*0.07*	*0.01*	*0.03*	*0.05*	*0.04*	*0.1*	*0.2*	*0.03*	*0.02*	*0.6*	*0.6*	
AI37	25.7645	65.9887		15	74.5	0.08	0.07	12.0	0.57	0.03	0.06	0.70	0.00	2.8	5.5	0.02	0.11	4.4	100.8	*Palo Pintado/San Felipe*
					0.6	*0.04*	*0.05*	*0.5*	*0.08*	*0.02*	*0.04*	*0.10*	*0.01*	*0.3*	*0.3*	*0.03*	*0.01*	*0.5*	*0.2*	

*Elemental composition of volcanic glass by Electron Probe Microanalysis (cf. Nash, 1992), n=number of shards, for n≥4 average and 1σ standard deviation are reported.

Table A.22: Trace element data for volcanic glass measured by ICP-MS solution nebulization

Sample		Ba	Ce	Cs	Hf	La	Lu	Nd	Rb	Sm	Sr	Ta	Th	U	Y
		µg/g	µg/g	µg/g	µg/g	µg/g	µg/g	µg/g	µg/g	µg/g	µg/g	µg/g	µg/g	µg/g	µg/g
University of Utah internal glass standard [a]															
MM3	n	23	24	25	26	24	25	24	24	22	21	24	23	25	21
	Avg	**161**	**91**	**3.1**	**3.3**	**47**	**0.38**	**20**	**192**	**3.40**	**35.2**	**2.3**	**22.8**	**5.3**	**17.6**
	1σ	*4*	*5*	*0.2*	*0.5*	*2*	*0.07*	*2*	*5*	*0.08*	*1.2*	*0.2*	*1.0*	*0.3*	*0.6*
	RSD	2.5%	5.3%	7.4%	15%	4.9%	17%	9.0%	2.7%	2.3%	3.4%	10%	4.5%	5.4%	3.3%
Fiambalá basin															
GUA 810		727	65	4	1.7	31	0.18	17	158	3.8	139	1.3	17	4	12
GUA 810		731	58			30		17	153	3.7	142	1.1	17		12
GUA 811		431	32	10		13		12	213		27	2.0	15	8	
GUA 811		433	38	10	1.8	13	0.44	12	229	4.6	27	2.1	16	9	31
GUA 814		640	62	6	1.7	30	0.18	15	172	3.2	85	1.7	20	6	9
FIA 838		665	75	6	1.9	36	0.21	19	183	4.0	143	1.5	23	9	11
FIA 839		660	76	6	2.0	38	0.20	21	183	4.0	131	1.4	24	9	12
FIA 840		662	58			30		19	175	3.9	117	1.3	22		13
FIA 840		654	66	6	1.8	31	0.22	19	182	4.1	113	1.4	24	8	13
FIA 841		609	53	6	2.2	23		14	172	4.3	87	1.5	20	9	10
FIA 841		637	63	6	1.7	29	0.22	17	190	4.0	94	1.3	23	8	13
FIA 842		549	10	9	2.2	3	0.20	2	127	3.1	85	1.4	4	8	4
FIA 843		533	26	8	1.9	11	0.19	7	160	2.9	88	1.5	9	7	13
FIA 846		783	69	6	2.8	35		19	160	3.8	254	0.7	19	5	4
FIA 846		802	76	6	3.0	38		21	173	3.8	262	0.7	21	5	5
FIA 847		109	31			13			232		15	2.1	22		14
FIA 847		114	39	13	1.8	15	0.29	9	249	3.1	13	2.2	23	12	17
001		642	66	6	2.0	30	0.22	19	192	4.1	101	3.2	23	8	14
003		16		26					374		2	8.2		17	
003		19	18	31	1.3	4	0.37	7	511	4.5	2	5.1	17	20	26
055		316	32	10	1.7	10	0.43	10	230	4.1	21	2.4	16	9	31
055		319	28			11			221	4.0	22		14		28
074		609		7	2.2			17	175	4.3	91	1.6	22	9	11
074		634	71	6	1.9	33	0.23	20	208	4.1	98	3.4	25	8	15
Corral Quemado basin															
PCQ 210		107	33	14	1.7	15		10	227		15	2.3	22	11	
PCQ 502		629	72	10	1.8	35	0.25	18	204	3.9	113	2.1	24	9	14
PCQ 511		125	35	11	1.4	16		11	242		17	2.2	22	11	
PCQ 519		114	38	12	1.9	15	0.27	10	250	3.0	15	3.4	24	12	17

Table A.22 (*continued*)

Sample	Ba	Ce	Cs	Hf	La	Lu	Nd	Rb	Sm	Sr	Ta	Th	U	Y
	µg/g	µg/g	µg/g	µg/g	µg/g	µg/g	µg/g	µg/g	µg/g	µg/g	µg/g	µg/g	µg/g	µg/g
Corral Quemado basin														
PCQ 560	338	50	13	1.8	23		16	241	2.9	42	1.4	14	7	
PCQ 560	324	51	12	1.8	24	0.29	18	247	3.0	43	1.6	14	7	
PCQ 564	799	66	3	1.7	30	0.20	19	154	4.3	121	1.2	14	3	13
PCQ 565	801	50	3	1.9	21	0.22	14	166	3.9	81	1.5	13	4	14
PCQ 566	763	63	3	2.2	27	0.23	18	158	4.4	81	1.4	14	3	15
PCQ 573	615	75	7	1.9	38	0.23	19	167	3.7	159	1.3	21	7	13
PCQ 574	649	75	6	2.1	39	0.22	18	156	3.7	191	1.1	17	5	12
PCQ 575	612	74	8	1.6	38	0.23	17	177	3.6	117	1.3	21	7	13
PCQ 578	481	109	18	3.0	52	0.35	30	298	5.8	76	2.4	63	19	18
PCQ 582	204	38		2.0	18		11	234		27	2.4	23	11	
PCQ 583	124	33		1.4	15		10	230		18	1.1	19	9	
PCQ 725	658	80	6	2.5	40		20	159	3.4	185	1.1	20	5	12
PCQ 733	414	31			12			210	4.2	26		14		28
PCQ 733	429	37	9	1.9	13	0.47	12	222	4.7	26	2.2	16	9	30
PCQ 792	610	75	10	1.8	37	0.25	18	203	3.8	124	1.9	24	9	13
PCQ 793	660	65			31		17	136		183		16		10
PCQ 793	666	75	6	2.2	37	0.23	18	156	3.6	179	1.2	19	6	10
PCQ 794	687	77	6	2.3	38	0.24	20	164	3.8	197	1.2	20	6	10
PCQ 794	648	71			37		18	146		195		17		11
PCQ 805	483	105	18	3.0	53	0.36	32	272	5.1	84	2.5	60	19	20
PCQ 805	484	114	18		55	0.35	30	300	5.7	80	2.4	64	18	19
Arg 196	327	55	13	1.9	23	0.34	16	259		39	1.7	14	8	
Arg 196	327	49	13	1.6	23	0.29	17	244	2.8	41	1.5	14	7	22
Arg 227	596		6	2.6			14	120	3.6	193	1.2	15	5	
Arg 227	598		6	2.3			11	107	3.3	233	1.1	12	5	
Arg 227	631	65			35		14	140	3.4	244		17	8	11
Arg 241	182		13					223	3.5	25	2.6			
Arg 241	199	47	12	2.0	20	0.27	12	245	3.2	28	2.6	25	11	17
Arg 241	208	45			20		12	218		28		25		16
Arg 241	208	49	12	1.8	22	0.28	13	240	3.3	27	1.7	26	11	16
Arg 241	214	51	12	1.9	23	0.28	13	244	3.4	29	1.8	26	12	16
Arg 244	453		19	3.7				258	6.0	74	2.5		19	15
Arg 244	483	106	19	3.4	54	0.34	32	276	4.6	84	2.5	61	19	20
CQ 22	609	75	8	1.9	39	0.25	19	183	3.8	114	1.7	22	8	13
CQ 26	791	58	3	2.1	25	0.23	16	162	4.2	87	1.4	14	4	14
CQ 38	152	36			16			240	3.0	19	1.7	23		16
CQ 38	159	39	13	2.0	16	0.29	10	252	3.2	18	2.7	24	12	17

Table A.22 (*continued*)

Sample	Ba	Ce	Cs	Hf	La	Lu	Nd	Rb	Sm	Sr	Ta	Th	U	Y
	µg/g	µg/g	µg/g	µg/g	µg/g	µg/g	µg/g	µg/g	µg/g	µg/g	µg/g	µg/g	µg/g	µg/g
Vallé Santa Maria														
ENTR 532	785	63	3	1.8	27	0.22	18	153	4.4	105	1.8	14	4	12
ENTR 533	734	62	4	1.7	27	0.23	17	166	4.3	111	1.3	14	4	15
ENTR 539	362	32	10	1.8	11	0.44	11	233	4.3	28	2.5	15	9	29
ENTR 909	60	30	26	1.4	14	0.45	7	307	1.8	97	3.0	16	10	18
ENTR 921	651	60	6	1.6	28	0.19	15	198	3.2	83	1.3	20	6	9
ENTR 934	649	61	6	1.6	29	0.18	15	187	3.2	92	1.2	20	6	8
ENTR 935	642	61	6	1.7	28	0.20	14	189	3.2	89	1.3	20	6	8
ENTR 938	646	58	6	1.6	27	0.19	13	186	3.2	88	1.4	19	6	8
ENTR 943	411	89	20	1.6	40	0.16	27	279	5.8	99	1.8	31	10	13
ENTR 944	628	45	11	1.5	18	0.30	14	209	4.1	85	1.7	14	8	21
ENTR 947	674	51	12	1.9	20	0.40	16	222	5.0	40	1.8	17	8	27
ENTR 949	677	71	6	1.7	32	0.33	20	172	4.8	139	1.8	15	4	23
QDJ 983	14	24	20	0.9	9	0.60	7	265	3.7	27	3.6	10	8	41
QDJ 985	66	29	26	1.1	14	0.43	6	313	1.7	92	3.0	16	10	18
QDJ 988	697	64	4	1.6	30	0.17	16	159	3.6	132	1.3	16	4	11
QDJ 992	391	36	10	1.8	12	0.43	11	246	4.5	29	2.0	15	9	29
ER-L1	682	52	12	1.9	20	0.40	16	222	5.1	40	1.8	17	8	27
ER-N1	667	71	6	2.0	33	0.35	21	177	4.9	139	2.1	15	4	25
ER-Q1	49	30	29	1.5	14	0.49	6	310	1.8	76	3.2	17	12	19
QJ-4	66	31	27	1.4	15	0.48	7	298	2.0	94	3.1	16	10	19
QJ-6	726	66	5	1.7	31	0.18	17	164	3.8	139	1.5	17	5	11
El Infiernillo														
INF 975	145	35	16	1.1	13	0.38	14	257	4.4	19	2.3	14	10	29
INF 975	176	42	19	1.3	16	0.46	13	306	5.3	24	2.6	17	12	36
INF 976	671	73	13		41		19	155	3.8	150	0.8	20	9	11
INF 977	365	35	6	2.4	17	0.22	10	166	1.8	72	1.6	12	6	14
INF 978	590	63	5	1.6	32	0.24	20	174	2.6	109	2.2	14	6	

[a]Average, standard deviation, and relative standard deviation (RSD, %) for multiple digestions of the obsidian MM3, n=number of digestions.
For additional information on accuracy and precision of these analyses see Hynek *et al.* (2010).

Table A.23: Summary of $^{40}Ar/^{39}Ar$ laser fusion experiments on eruptive minerals in volcanic ash beds.

(Analyzed at Rare Gas Geochronology Laboratory; University of Wisconsin-Madison)

				Weighted Mean Analysis			Isochron Analysis		
Sample	Experiment	Material	K/Ca total	MSWD	Age (Ma) ± 2 σ	N	$^{40}Ar/^{36}Ar_i$ ± 2 σ	MSWD	Age (Ma) ± 2 σ
FIA 836	UW73C34	plagioclase	0.11	0.78	**3.96 ± 0.09**	14 of 15	369.0 ± 141.8	0.72	3.84 ± 0.23
FIA 840	UW73C33	oligoclase	0.12	0.33	**4.03 ± 0.12**	13 of 14	293.0 ± 22.6	0.36	4.04 ± 0.13
ENTR 909	UW69A01	sanidine	84.58	0.25	**5.19 ± 0.011**	15 of 15	319.4 ± 57.5	0.21	5.19 ± 0.014
QDJ 983	UW69A04	sanidine	104.85	0.95	**5.27 ± 0.009**	13 of 20	303.0 ± 24.8	1.00	5.27 ± 0.010
INF 975	UW73C35	sanidine	69.55	0.50	**9.11 ± 0.03**	15 of 15	310.8 ± 41.2	0.50	9.10 ± 0.03
INF 975	UW73C36	biotite	42.90	0.81	**9.44 ± 0.04**	15 of 15	293.1 ± 17.3	0.87	9.46 ± 0.14
PUN 1009	UW69A02	sanidine	48.66	0.66	**0.044 ± 0.002**	18 of 18	294.7 ± 5.8	0.69	0.044 ± 0.003
PUN 1060	UW69A03	sanidine	65.13	1.27	**2.060 ± 0.004**	15 of 15	301.8 ± 13.5	1.28	2.059 ± 0.005

J-value calculated relative to 28.02 Ma for the Fish Canyon sanidine (Renne *et al*., 1998); details of analyses provided in Table A.24.
N=number of analyses used in weighted mean and isochron analysis.
Age in **bold** is preferred.
For a potential explanation of the sanidine-biotite discordance in INF 975, see Hora *et al*. (2010).

Constants used		Source
Atmospheric argon ratios		
$(^{40}Ar/^{36}Ar)_A$	295.5±0.0	Steiger and Jäger (1977)
$(^{38}Ar/^{36}Ar)_A$	0.1869±0.0001	Nier (1950)
Interfering isotope production ratios		
$(^{40}Ar/^{39}Ar)_K$	0.00086	Singer *et al*. (2004)
$(^{38}Ar/^{39}Ar)_K$	0.01211	Singer *et al*. (2004)
$(^{39}Ar/^{37}Ar)_{Ca}$	0.000673	Singer *et al*. (2004)
$(^{36}Ar/^{37}Ar)_{Ca}$	0.000264	Singer *et al*. (2004)
Decay constants		
$^{40}K\ \lambda_\varepsilon$	(5.81±0.00)E-11 a^{-1}	Steiger and Jäger (1977)
$^{40}K\ \lambda_\beta$	(4.962±0.000)E-10 a^{-1}	Steiger and Jäger (1977)
^{39}Ar	(2.58±0.03)E-03 a^{-1}	Stoenner *et al*. (1965)
^{37}Ar	(5.4300±0.0063)E-02 a^{-1}	Renne and Norman (2001)
$^{36}Cl\ \lambda_\beta$	(2.35±0.02)E-06 a^{-1}	Endt (1998)

Table A.24: Details of $^{40}Ar/^{39}Ar$ laser fusion experiments on eruptive minerals in volcanic ash beds.

(Analyzed at Rare Gas Geochronology Laboratory; University of Wisconsin-Madison - Dr. Brian Jicha, Analyst)

Sample ID File #		Laser Power (%)	^{40}Ar / ^{39}Ar ± 1σ	^{37}Ar / ^{39}Ar ± 1σ	^{36}Ar / ^{39}Ar ± 1σ	F [a] ± 1σ	$^{40}Ar^*$ (%)	^{39}Ar mol x 10^{16}	K/Ca	Apparent Age ± 2σ Ma [b]
FIA 836										
Laser single crystal fusions			plagioclase			J = 0.0005106 ± 0.07% (1σ)[c]				μ = 1.0056 ± 0.02 % (1σ)[d]
BE6713	#	35.0	4.8989 ± 0.0591	3.9048 ± 0.0628	0.0021 ± 0.0009	4.5857 ± 0.2633	93.36	5.15	0.110	4.22 ± 0.48
BE6715	#	35.0	4.6553 ± 0.0230	3.6279 ± 0.0529	0.0025 ± 0.0004	4.1990 ± 0.1308	89.98	9.36	0.118	3.86 ± 0.24
BE6716	#	35.0	4.6644 ± 0.0364	3.7574 ± 0.0523	0.0024 ± 0.0004	4.2530 ± 0.1136	90.95	9.47	0.114	3.91 ± 0.21
BE6718	#	35.0	4.7160 ± 0.0619	4.7001 ± 0.0842	0.0019 ± 0.0010	4.5297 ± 0.2885	95.75	3.98	0.091	4.17 ± 0.53
BE6719	#	35.0	6.0072 ± 0.0623	3.6383 ± 0.0586	0.0072 ± 0.0011	4.1748 ± 0.3284	69.33	5.65	0.118	3.84 ± 0.60
BE6721	#	35.0	4.4196 ± 0.0475	3.9776 ± 0.0693	0.0016 ± 0.0013	4.2770 ± 0.3746	96.51	3.80	0.108	3.94 ± 0.69
BE6722	#	35.0	4.7815 ± 0.0211	3.8698 ± 0.0548	0.0021 ± 0.0008	4.4779 ± 0.2250	93.41	6.14	0.111	4.12 ± 0.41
BE6724	#	35.0	4.5370 ± 0.0280	3.7908 ± 0.0533	0.0023 ± 0.0005	4.1654 ± 0.1590	91.57	7.88	0.113	3.83 ± 0.29
BE6725	#	35.0	5.0142 ± 0.0222	4.0066 ± 0.0582	0.0035 ± 0.0004	4.2960 ± 0.1259	85.45	13.98	0.107	3.95 ± 0.23
BE6727		35.0	64.1731 ± 0.3244	6.6303 ± 0.0981	0.1869 ± 0.0024	9.5143 ± 0.6708	14.76	5.26	0.065	8.74 ± 1.23
BE6728	#	35.0	5.0048 ± 0.0371	5.4955 ± 0.0763	0.0043 ± 0.0005	4.1659 ± 0.1511	82.93	7.59	0.078	3.83 ± 0.28
BE6730	#	35.0	4.6263 ± 0.0401	4.1606 ± 0.0653	0.0022 ± 0.0011	4.3140 ± 0.3291	92.99	4.93	0.103	3.97 ± 0.60
BE6731	#	35.0	5.5134 ± 0.0517	4.2083 ± 0.0647	0.0039 ± 0.0006	4.6966 ± 0.1829	84.95	6.77	0.102	4.32 ± 0.34
BE6733	#	35.0	4.4987 ± 0.0321	3.8422 ± 0.0581	0.0013 ± 0.0009	4.4114 ± 0.2631	97.81	6.21	0.112	4.06 ± 0.48
BE6734	#	35.0	5.0565 ± 0.0588	7.2314 ± 0.1314	0.0034 ± 0.0018	4.6484 ± 0.5288	91.48	3.82	0.059	4.28 ± 0.97
Weighted Mean from 14 of 15 grains:						MSWD 0.78		Weighted Mean age:		**3.96 ± 0.09**
Inverse Isochron from 14 of 15 grains: ^{40}Ar / ^{36}Ar ± 2σ: 369.0 ± 141.8						MSWD 0.72		Isochron age:		**3.84 ± 0.23**

a F is the ratio of radiogenic ^{40}Ar to K-derived ^{39}Ar

b All ages calculated using the decay constants of Steiger and Jäger (λ_{40K} = 5.543 x 10^{-10} yr^{-1}) and corrected for ^{37}Ar and ^{39}Ar decay, half lives of 35.2 days and 269 years, respectively

c J-value calculated relative to 28.02 Ma for the Fish Canyon sanidine (Renne *et al*. 1998)

d μ: mass discrimination per atomic mass unit

\# indicates crystals that have been included in weighted mean and isochron calculations

Table A.24 (*continued*)

Sample ID File #		Laser Power (%)	^{40}Ar / ^{39}Ar ± 1σ	^{37}Ar / ^{39}Ar ± 1σ	^{36}Ar / ^{39}Ar ± 1σ	F [a] ± 1σ	$^{40}Ar^*$ (%)	^{39}Ar mol x 10^{16}	K/Ca	Apparent Age ± 2σ Ma [b]
FIA 840										
Laser single crystal fusions			oligoclase			*J* = 0.0005106 ± 0.07% (1σ)[c]				μ = 1.0056 ± 0.02 % (1σ)[d]
BE6691	#	35.0	4.8068 ± 0.0342	3.3687 ± 0.0517	0.0024 ± 0.0005	4.3667 ± 0.1495	90.64	13.25	0.127	4.02 ± 0.27
BE6692	#	35.0	4.6123 ± 0.0376	3.7935 ± 0.0519	0.0022 ± 0.0008	4.2791 ± 0.2369	92.54	8.75	0.113	3.94 ± 0.44
BE6694	#	35.0	4.8635 ± 0.0422	3.3870 ± 0.0499	0.0018 ± 0.0006	4.6162 ± 0.1924	94.70	9.10	0.127	4.25 ± 0.35
BE6695	#	35.0	4.7004 ± 0.0390	3.3489 ± 0.0495	0.0023 ± 0.0005	4.3053 ± 0.1406	91.39	11.70	0.128	3.96 ± 0.26
BE6697	#	35.0	11.5981 ± 0.0774	6.3033 ± 0.0924	0.0266 ± 0.0009	4.2602 ± 0.2610	36.58	6.04	0.068	3.92 ± 0.48
BE6698		35.0	7.1366 ± 0.0553	3.6017 ± 0.0551	0.0069 ± 0.0007	5.4004 ± 0.2009	75.49	9.46	0.119	4.97 ± 0.37
BE6700	#	35.0	5.4859 ± 0.0766	4.0561 ± 0.0675	0.0050 ± 0.0009	4.3297 ± 0.2837	78.71	5.36	0.106	3.98 ± 0.52
BE6701	#	35.0	5.9011 ± 0.0668	5.4926 ± 0.0864	0.0061 ± 0.0010	4.5565 ± 0.2884	76.93	5.08	0.078	4.19 ± 0.53
BE6703	#	35.0	4.7006 ± 0.0526	3.1051 ± 0.0466	0.0020 ± 0.0007	4.3546 ± 0.2109	92.45	7.65	0.138	4.01 ± 0.39
BE6704	#	35.0	5.9758 ± 0.0803	5.1065 ± 0.0902	0.0060 ± 0.0012	4.6176 ± 0.3649	77.01	5.14	0.084	4.25 ± 0.67
BE6706	#	35.0	4.7811 ± 0.0660	3.4830 ± 0.0552	0.0029 ± 0.0012	4.2078 ± 0.3470	87.80	4.90	0.123	3.87 ± 0.64
BE6707	#	35.0	4.4467 ± 0.0639	2.8609 ± 0.0455	0.0016 ± 0.0009	4.2105 ± 0.2863	94.51	4.97	0.150	3.87 ± 0.53
BE6709	#	35.0	4.6633 ± 0.0591	3.3939 ± 0.0501	0.0015 ± 0.0014	4.4909 ± 0.4122	96.08	4.94	0.126	4.13 ± 0.76
BE6710	#	35.0	5.1032 ± 0.0885	4.3093 ± 0.0782	0.0028 ± 0.0016	4.6309 ± 0.4694	90.48	3.63	0.099	4.26 ± 0.86
Weighted Mean from 13 of 14 grains:						MSWD 0.33			Weighted Mean age:	**4.03 ± 0.12**
Inverse Isochron from 13 of 14 grains: ^{40}Ar / ^{36}Ar ± 2σ: 293.0 ± 22.6						MSWD 0.36			Isochron age:	**4.04 ± 0.13**

a F is the ratio of radiogenic ^{40}Ar to K-derived ^{39}Ar

b All ages calculated using the decay constants of Steiger and Jäger (λ_{40K} = 5.543 x 10^{-10} yr^{-1}) and corrected for ^{37}Ar and ^{39}Ar decay, half lives of 35.2 days and 269 years, respectively

c J-value calculated relative to 28.02 Ma for the Fish Canyon sanidine (Renne *et al*. 1998)

d μ: mass discrimination per atomic mass unit

\# indicates crystals that have been included in weighted mean and isochron calculations

Table A.24 (*continued*)

Sample ID File #		Laser Power (%)	^{40}Ar / ^{39}Ar ± 1σ	^{37}Ar / ^{39}Ar ± 1σ	^{36}Ar / ^{39}Ar ± 1σ	F [a] ± 1σ	$^{40}Ar^*$ (%)	^{39}Ar mol x 10^{16}	K/Ca	Apparent Age ± 2σ Ma [b]
ENTR 909										
Single crystal fusions			sanidine			*J* = 0.0007644 ± 0.08 % (1σ)[c]				μ = 1.0051 ± 0.02 % (1σ)[d]
BE4884	#	35.0	3.8291 ± 0.0063	0.0051 ± 0.0002	0.0002 ± 0.0000	3.7667 ± 0.0115	98.37	7.12	84.130	5.187 ± 0.032
BE4885	#	35.0	3.7863 ± 0.0055	0.0049 ± 0.0001	0.0000 ± 0.0000	3.7717 ± 0.0105	99.61	9.47	87.194	5.194 ± 0.029
BE4887	#	35.0	3.8018 ± 0.0088	0.0049 ± 0.0003	0.0001 ± 0.0000	3.7628 ± 0.0143	98.97	4.32	88.260	5.182 ± 0.039
BE4888	#	35.0	3.7958 ± 0.0073	0.0047 ± 0.0002	0.0001 ± 0.0000	3.7689 ± 0.0154	99.29	4.59	91.473	5.190 ± 0.042
BE4890	#	35.0	3.8029 ± 0.0045	0.0052 ± 0.0001	0.0001 ± 0.0000	3.7733 ± 0.0100	99.22	7.95	83.466	5.196 ± 0.027
BE4891	#	35.0	3.7819 ± 0.0052	0.0047 ± 0.0002	0.0000 ± 0.0000	3.7733 ± 0.0100	99.77	8.42	91.408	5.196 ± 0.028
BE4893	#	35.0	3.7743 ± 0.0061	0.0048 ± 0.0002	0.0000 ± 0.0000	3.7665 ± 0.0115	99.79	6.11	90.252	5.187 ± 0.032
BE4894	#	35.0	3.7931 ± 0.0060	0.0052 ± 0.0002	0.0001 ± 0.0000	3.7700 ± 0.0129	99.39	5.69	82.124	5.192 ± 0.035
BE4896	#	35.0	4.0262 ± 0.0053	0.0055 ± 0.0002	0.0008 ± 0.0001	3.7911 ± 0.0214	94.16	4.91	78.716	5.220 ± 0.059
BE4897	#	35.0	3.8210 ± 0.0052	0.0055 ± 0.0003	0.0002 ± 0.0000	3.7714 ± 0.0125	98.70	5.95	77.484	5.193 ± 0.034
BE4899	#	35.0	3.7797 ± 0.0048	0.0049 ± 0.0001	0.0000 ± 0.0000	3.7683 ± 0.0096	99.70	6.12	87.522	5.189 ± 0.026
BE4900	#	35.0	3.8085 ± 0.0061	0.0050 ± 0.0003	0.0001 ± 0.0001	3.7709 ± 0.0168	99.01	5.39	86.360	5.193 ± 0.046
BE4902	#	35.0	3.7853 ± 0.0039	0.0051 ± 0.0001	0.0001 ± 0.0000	3.7684 ± 0.0064	99.55	10.38	84.715	5.189 ± 0.018
BE4903	#	35.0	3.7972 ± 0.0049	0.0052 ± 0.0002	0.0001 ± 0.0000	3.7800 ± 0.0088	99.55	7.40	82.913	5.205 ± 0.024
BE4905	#	35.0	3.8091 ± 0.0054	0.0052 ± 0.0001	0.0001 ± 0.0000	3.7799 ± 0.0113	99.23	6.18	82.685	5.205 ± 0.031
Weighted Mean from 15 of 15 grains:						MSWD 0.25			Weighted Mean age:	**5.194 ± 0.011**
Inverse Isochron from 15 of 15 grains: ^{40}Ar / ^{36}Ar ± 2σ: 319.4 ± 57.5						MSWD 0.21			Isochron age:	**5.191 ± 0.014**

a F is the ratio of radiogenic ^{40}Ar to K-derived ^{39}Ar

b All ages calculated using the decay constants of Steiger and Jäger ($\lambda_{40K} = 5.543 \times 10^{-10}$ yr^{-1}) and corrected for ^{37}Ar and ^{39}Ar decay, half lives of 35.2 days and 269 years, respectively

c J-value calculated relative to 28.02 Ma for the Fish Canyon sanidine (Renne *et al*. 1998)

d μ: mass discrimination per atomic mass unit

\# indicates crystals that have been included in weighted mean and isochron calculations

Table A.24 (*continued*)

Sample ID File #		Laser Power (%)	^{40}Ar / ^{39}Ar ± 1σ	^{37}Ar / ^{39}Ar ± 1σ	^{36}Ar / ^{39}Ar ± 1σ	F [a] ± 1σ	$^{40}Ar^*$ (%)	^{39}Ar mol x 10^{16}	K/Ca	Apparent Age ± 2σ Ma [b]
QDJ 983										
Single crystal fusions			sanidine			*J* = 0.0007644 ± 0.08 % (1σ)[c]				μ = 1.0051 ± 0.02 % (1σ)[d]
BE4957	#	35.0	3.8420 ± 0.0032	0.0035 ± 0.0001	0.0001 ± 0.0000	3.8253 ± 0.0047	99.56	5.32	121.158	5.268 ± 0.013
BE4958		35.0	3.9667 ± 0.0042	0.0041 ± 0.0001	0.0004 ± 0.0000	3.8615 ± 0.0053	97.35	6.31	105.188	5.317 ± 0.015
BE4960		35.0	3.9133 ± 0.0034	0.0038 ± 0.0001	0.0002 ± 0.0000	3.8517 ± 0.0057	98.42	5.54	114.482	5.304 ± 0.016
BE4961		35.0	3.9092 ± 0.0045	0.0035 ± 0.0001	0.0002 ± 0.0000	3.8479 ± 0.0059	98.43	4.30	121.867	5.299 ± 0.016
BE4963	#	35.0	3.8788 ± 0.0026	0.0042 ± 0.0001	0.0002 ± 0.0000	3.8283 ± 0.0038	98.70	6.33	103.171	5.272 ± 0.011
BE4964	#	35.0	3.8522 ± 0.0023	0.0040 ± 0.0001	0.0001 ± 0.0000	3.8306 ± 0.0041	99.44	7.14	108.025	5.275 ± 0.011
BE4966	#	35.0	3.8796 ± 0.0048	0.0043 ± 0.0001	0.0001 ± 0.0000	3.8401 ± 0.0059	98.98	5.01	100.441	5.288 ± 0.016
BE4967	#	35.0	3.8982 ± 0.0049	0.0039 ± 0.0001	0.0002 ± 0.0000	3.8368 ± 0.0053	98.43	7.03	110.229	5.283 ± 0.015
BE4969	#	35.0	3.9236 ± 0.0052	0.0037 ± 0.0001	0.0003 ± 0.0000	3.8334 ± 0.0067	97.70	4.12	116.406	5.279 ± 0.018
BE4970	#	35.0	3.8550 ± 0.0038	0.0037 ± 0.0001	0.0001 ± 0.0000	3.8338 ± 0.0057	99.45	3.49	116.084	5.279 ± 0.016
BE4972		35.0	3.8597 ± 0.0041	0.0039 ± 0.0001	0.0000 ± 0.0000	3.8541 ± 0.0064	99.86	3.26	111.133	5.307 ± 0.018
BE4973		35.0	4.0743 ± 0.0044	0.0078 ± 0.0002	0.0007 ± 0.0000	3.8741 ± 0.0071	95.08	3.15	54.892	5.335 ± 0.020
BE4975	#	35.0	3.8683 ± 0.0020	0.0052 ± 0.0001	0.0001 ± 0.0000	3.8264 ± 0.0026	98.91	8.66	82.587	5.269 ± 0.007
BE4976	#	35.0	3.8576 ± 0.0063	0.0038 ± 0.0001	0.0001 ± 0.0000	3.8275 ± 0.0067	99.22	7.18	113.036	5.271 ± 0.018
BE4978	#	35.0	3.8456 ± 0.0029	0.0037 ± 0.0001	0.0000 ± 0.0000	3.8356 ± 0.0041	99.74	5.32	116.246	5.282 ± 0.011
BE4979		35.0	3.8717 ± 0.0031	0.0055 ± 0.0001	0.0001 ± 0.0000	3.8542 ± 0.0046	99.55	4.27	77.773	5.307 ± 0.013
BE4981		35.0	3.8830 ± 0.0033	0.0043 ± 0.0001	0.0001 ± 0.0000	3.8634 ± 0.0056	99.50	3.85	99.740	5.320 ± 0.015
BE4982	#	35.0	3.9474 ± 0.0049	0.0037 ± 0.0001	0.0004 ± 0.0000	3.8307 ± 0.0083	97.04	2.44	115.136	5.275 ± 0.023
BE4984	#	35.0	3.8851 ± 0.0033	0.0043 ± 0.0001	0.0002 ± 0.0000	3.8364 ± 0.0071	98.75	4.24	101.007	5.283 ± 0.020
BE4985	#	35.0	4.0048 ± 0.0054	0.0036 ± 0.0001	0.0006 ± 0.0000	3.8344 ± 0.0074	95.74	3.04	118.971	5.280 ± 0.020
Weighted Mean from 13 of 20 grains:						MSWD 0.95			Weighted Mean age:	**5.275 ± 0.009**
Inverse Isochron from 13 of 20 grains: ^{40}Ar / ^{36}Ar ± 2σ: 303.0 ± 24.8						MSWD 1.00			Isochron age:	**5.273 ± 0.010**

a F is the ratio of radiogenic ^{40}Ar to K-derived ^{39}Ar

b All ages calculated using the decay constants of Steiger and Jäger (λ_{40K} = 5.543 x 10^{-10} yr^{-1}) and corrected for ^{37}Ar and ^{39}Ar decay, half lives of 35.2 days and 269 years, respectively

c J-value calculated relative to 28.02 Ma for the Fish Canyon sanidine (Renne *et al*. 1998)

d μ: mass discrimination per atomic mass unit

\# indicates crystals that have been included in weighted mean and isochron calculations

Table A.24 (*continued*)

Sample ID File #	Laser Power (%)	^{40}Ar / ^{39}Ar ± 1σ	^{37}Ar / ^{39}Ar ± 1σ	^{36}Ar / ^{39}Ar ± 1σ	F [a] ± 1σ	$^{40}Ar^*$ (%)	^{39}Ar mol x 10^{16}	K/Ca	Apparent Age ± 2σ Ma [b]
INF 975									
Laser single crystal fusions		sanidine			*J* = 0.0005106 ± 0.07% (1σ)[c]				μ = 1.0056 ± 0.02 % (1σ)[d]
BE6713	# 35.0	9.9594 ± 0.0277	0.0062 ± 0.0006	0.0003 ± 0.0001	9.8692 ± 0.0468	99.09	7.73	69.837	9.07 ± 0.09
BE6715	# 35.0	9.9535 ± 0.0206	0.0065 ± 0.0006	0.0002 ± 0.0002	9.9036 ± 0.0627	99.50	5.00	66.506	9.10 ± 0.11
BE6716	# 35.0	10.1231 ± 0.0343	0.0067 ± 0.0009	0.0007 ± 0.0003	9.9110 ± 0.0860	97.90	3.66	64.079	9.11 ± 0.16
BE6718	# 35.0	9.9379 ± 0.0225	0.0057 ± 0.0008	0.0001 ± 0.0001	9.9128 ± 0.0440	99.75	7.69	75.770	9.11 ± 0.08
BE6719	# 35.0	10.0123 ± 0.0180	0.0065 ± 0.0006	0.0003 ± 0.0001	9.9319 ± 0.0330	99.20	9.96	66.533	9.13 ± 0.06
BE6721	# 35.0	9.9115 ± 0.0216	0.0067 ± 0.0007	0.0000 ± 0.0001	9.9091 ± 0.0406	99.98	7.77	64.232	9.10 ± 0.07
BE6722	# 35.0	9.9471 ± 0.0215	0.0058 ± 0.0007	0.0000 ± 0.0001	9.9376 ± 0.0394	99.90	7.60	74.212	9.13 ± 0.07
BE6724	# 35.0	9.8704 ± 0.0323	0.0071 ± 0.0011	0.0000 ± 0.0002	9.8644 ± 0.0770	99.94	4.03	60.406	9.06 ± 0.14
BE6725	# 35.0	10.2731 ± 0.0381	0.0060 ± 0.0004	0.0012 ± 0.0001	9.9236 ± 0.0472	96.60	11.99	71.214	9.12 ± 0.09
BE6727	# 35.0	11.0462 ± 0.0367	0.0067 ± 0.0009	0.0038 ± 0.0002	9.9324 ± 0.0773	89.92	4.74	63.940	9.13 ± 0.14
BE6728	# 35.0	10.0376 ± 0.0246	0.0053 ± 0.0005	0.0003 ± 0.0002	9.9344 ± 0.0556	98.97	5.62	81.030	9.13 ± 0.10
BE6730	# 35.0	9.9926 ± 0.0322	0.0067 ± 0.0007	0.0000 ± 0.0002	9.9778 ± 0.0761	99.85	4.05	64.333	9.17 ± 0.14
BE6731	# 35.0	9.8626 ± 0.0243	0.0062 ± 0.0007	0.0000 ± 0.0002	9.8560 ± 0.0587	99.93	5.84	69.012	9.06 ± 0.11
BE6733	# 35.0	9.8519 ± 0.0230	0.0063 ± 0.0006	0.0001 ± 0.0002	9.8125 ± 0.0563	99.60	5.62	67.813	9.02 ± 0.10
BE6734	# 35.0	9.9370 ± 0.0343	0.0059 ± 0.0008	0.0001 ± 0.0001	9.9148 ± 0.0451	99.78	8.70	73.429	9.11 ± 0.08
Weighted Mean from 15 of 15 grains:					MSWD 0.50			Weighted Mean age:	**9.11 ± 0.03**
Inverse Isochron from 15 of 15 grains:		^{40}Ar / ^{36}Ar ± 2σ: 310.8 ± 41.2			MSWD 0.50			Isochron age:	**9.10 ± 0.03**

a F is the ratio of radiogenic ^{40}Ar to K-derived ^{39}Ar

b All ages calculated using the decay constants of Steiger and Jäger ($\lambda_{40K} = 5.543 \times 10^{-10}$ yr^{-1}) and corrected for ^{37}Ar and ^{39}Ar decay, half lives of 35.2 days and 269 years, respectively

c J-value calculated relative to 28.02 Ma for the Fish Canyon sanidine (Renne *et al*. 1998)

d μ: mass discrimination per atomic mass unit

\# indicates crystals that have been included in weighted mean and isochron calculations

Table A.24 (*continued*)

Sample ID File #	Laser Power (%)	^{40}Ar / ^{39}Ar ± 1σ	^{37}Ar / ^{39}Ar ± 1σ	^{36}Ar / ^{39}Ar ± 1σ	F [a] ± 1σ	$^{40}Ar^*$ (%)	^{39}Ar mol x 10^{16}	K/Ca	Apparent Age ± 2σ Ma [b]
INF 975									
Laser single crystal fusions		biotite			*J* = 0.0005106 ± 0.07% (1σ)[c]				μ = 1.0056 ± 0.02 % (1σ)[d]
BE6760	# 35.0	13.0617 ± 0.0460	0.0029 ± 0.0007	0.0097 ± 0.0003	10.1863 ± 0.0931	77.99	9.62	148.996	9.36 ± 0.17
BE6761	# 35.0	12.5652 ± 0.0335	0.0107 ± 0.0006	0.0075 ± 0.0001	10.3455 ± 0.0442	82.33	16.79	40.080	9.50 ± 0.08
BE6763	# 35.0	12.6125 ± 0.0414	0.0341 ± 0.0006	0.0080 ± 0.0001	10.2565 ± 0.0438	81.32	18.31	12.594	9.42 ± 0.08
BE6764	# 35.0	12.6810 ± 0.0657	0.0060 ± 0.0017	0.0082 ± 0.0004	10.2706 ± 0.1217	80.99	4.32	71.993	9.44 ± 0.22
BE6766	# 35.0	13.1532 ± 0.0507	0.0295 ± 0.0009	0.0098 ± 0.0003	10.2707 ± 0.0902	78.08	8.15	14.599	9.44 ± 0.17
BE6767	# 35.0	12.9638 ± 0.0430	0.0195 ± 0.0009	0.0091 ± 0.0002	10.2688 ± 0.0696	79.21	8.42	22.064	9.43 ± 0.13
BE6769	# 35.0	13.3396 ± 0.0549	0.0118 ± 0.0014	0.0109 ± 0.0002	10.1083 ± 0.0865	75.78	5.18	36.437	9.29 ± 0.16
BE6770	# 35.0	13.1361 ± 0.0857	0.0971 ± 0.0018	0.0101 ± 0.0003	10.1544 ± 0.1181	77.30	7.03	4.429	9.33 ± 0.22
BE6772	# 35.0	11.3376 ± 0.0742	0.0071 ± 0.0021	0.0034 ± 0.0003	10.3411 ± 0.1139	91.21	4.13	60.686	9.50 ± 0.21
BE6773	# 35.0	12.1037 ± 0.0791	0.0540 ± 0.0035	0.0059 ± 0.0005	10.3545 ± 0.1762	85.55	3.47	7.963	9.51 ± 0.32
BE6775	# 35.0	14.2985 ± 0.0825	0.0034 ± 0.0017	0.0135 ± 0.0003	10.3158 ± 0.1193	72.15	4.02	127.692	9.48 ± 0.22
BE6776	# 35.0	16.0975 ± 0.0764	0.0404 ± 0.0014	0.0192 ± 0.0004	10.4185 ± 0.1409	64.72	5.12	10.641	9.57 ± 0.26
BE6778	# 35.0	13.0673 ± 0.1910	0.0628 ± 0.0054	0.0082 ± 0.0013	10.6340 ± 0.4139	81.38	1.44	6.844	9.77 ± 0.76
BE6779	# 35.0	10.6443 ± 0.1319	-0.0020 ± 0.0028	0.0010 ± 0.0005	10.3359 ± 0.2066	97.10	2.12	6.934	9.50 ± 0.38
BE6781	# 35.0	11.7424 ± 0.1421	0.0033 ± 0.0035	0.0056 ± 0.0008	10.0963 ± 0.2677	85.98	1.90	130.217	9.28 ± 0.49
Weighted Mean from 15 of 15 grains:					MSWD 0.81			Weighted Mean age:	**9.44 ± 0.04**
Inverse Isochron from 15 of 15 grains:		^{40}Ar / ^{36}Ar ± 2σ:	293.1 ± 17.3		MSWD 0.87			Isochron age:	**9.46 ± 0.14**

a F is the ratio of radiogenic ^{40}Ar to K-derived ^{39}Ar

b All ages calculated using the decay constants of Steiger and Jäger ($\lambda_{40K} = 5.543 \times 10^{-10}$ yr^{-1}) and corrected for ^{37}Ar and ^{39}Ar decay, half lives of 35.2 days and 269 years, respectively

c J-value calculated relative to 28.02 Ma for the Fish Canyon sanidine (Renne *et al*. 1998)

d μ: mass discrimination per atomic mass unit

\# indicates crystals that have been included in weighted mean and isochron calculations

Table A.24 (*continued*)

Sample ID File #		Laser Power (%)	^{40}Ar / ^{39}Ar ± 1σ	^{37}Ar / ^{39}Ar ± 1σ	^{36}Ar / ^{39}Ar ± 1σ	F [a] ± 1σ	$^{40}Ar^*$ (%)	^{39}Ar mol x 10^{16}	K/Ca	Apparent Age ± 2σ Ma [b]
PUN 1009										
Single crystal fusions			sanidine			*J* = 0.0007644 ± 0.08 % (1σ)[c]				μ = 1.0051 ± 0.02 % (1σ)[d]
BE4907	#	35.0	0.0811 ± 0.0002	0.0078 ± 0.0001	0.0002 ± 0.0000	0.0312 ± 0.0040	38.41	5.79	55.398	0.043 ± 0.011
BE4908	#	35.0	0.2107 ± 0.0004	0.0084 ± 0.0001	0.0006 ± 0.0000	0.0353 ± 0.0033	16.75	7.02	50.986	0.049 ± 0.009
BE4910	#	35.0	0.0622 ± 0.0003	0.0079 ± 0.0001	0.0001 ± 0.0000	0.0321 ± 0.0030	51.64	5.20	54.443	0.044 ± 0.008
BE4911	#	35.0	0.0664 ± 0.0002	0.0109 ± 0.0001	0.0001 ± 0.0000	0.0279 ± 0.0031	42.01	5.51	39.484	0.038 ± 0.008
BE4913	#	35.0	0.0537 ± 0.0002	0.0103 ± 0.0001	0.0001 ± 0.0000	0.0334 ± 0.0023	62.14	7.33	41.866	0.046 ± 0.006
BE4914	#	35.0	0.0886 ± 0.0003	0.0102 ± 0.0001	0.0002 ± 0.0000	0.0297 ± 0.0035	33.55	6.11	42.196	0.041 ± 0.010
BE4916	#	35.0	0.0736 ± 0.0003	0.0085 ± 0.0001	0.0002 ± 0.0000	0.0280 ± 0.0043	38.04	3.95	50.448	0.039 ± 0.012
BE4917	#	35.0	0.3995 ± 0.0006	0.0076 ± 0.0001	0.0013 ± 0.0000	0.0280 ± 0.0038	7.01	6.41	56.628	0.039 ± 0.011
BE4919	#	35.0	0.1133 ± 0.0003	0.0088 ± 0.0001	0.0003 ± 0.0000	0.0338 ± 0.0040	29.88	4.38	49.053	0.047 ± 0.011
BE4920	#	35.0	0.0879 ± 0.0003	0.0072 ± 0.0001	0.0002 ± 0.0000	0.0244 ± 0.0050	27.76	4.96	59.900	0.034 ± 0.014
BE4922	#	35.0	0.1621 ± 0.0004	0.0090 ± 0.0001	0.0004 ± 0.0000	0.0328 ± 0.0044	20.22	3.87	47.945	0.045 ± 0.012
BE4923	#	35.0	0.0990 ± 0.0004	0.0079 ± 0.0002	0.0002 ± 0.0000	0.0287 ± 0.0076	29.00	3.09	54.650	0.040 ± 0.021
BE4925	#	35.0	0.0678 ± 0.0004	0.0095 ± 0.0001	0.0001 ± 0.0000	0.0318 ± 0.0058	46.92	3.22	45.187	0.044 ± 0.016
BE4926	#	35.0	0.1304 ± 0.0004	0.0085 ± 0.0002	0.0003 ± 0.0000	0.0276 ± 0.0067	21.14	2.92	50.539	0.038 ± 0.019
BE4928	#	35.0	0.0697 ± 0.0002	0.0094 ± 0.0002	0.0001 ± 0.0000	0.0357 ± 0.0028	51.27	6.36	45.569	0.049 ± 0.008
BE4929	#	35.0	0.0570 ± 0.0002	0.0085 ± 0.0001	0.0001 ± 0.0000	0.0333 ± 0.0035	58.35	5.37	50.347	0.046 ± 0.010
BE4931	#	35.0	0.1688 ± 0.0002	0.0083 ± 0.0001	0.0005 ± 0.0000	0.0334 ± 0.0022	19.78	11.84	51.913	0.046 ± 0.006
BE4932	#	35.0	0.2151 ± 0.0003	0.0078 ± 0.0001	0.0006 ± 0.0000	0.0323 ± 0.0030	15.03	6.67	55.277	0.045 ± 0.008
Weighted Mean from 18 of 18 grains:						MSWD 0.66			Weighted Mean age:	**0.044 ± 0.002**
Inverse Isochron from 18 of 18 grains: ^{40}Ar / ^{36}Ar ± 2σ: 294.7 ± 5.8						MSWD 0.69			Isochron age:	**0.044 ± 0.003**

a F is the ratio of radiogenic ^{40}Ar to K-derived ^{39}Ar

b All ages calculated using the decay constants of Steiger and Jäger (λ_{40K} = 5.543 x 10^{-10} yr^{-1}) and corrected for ^{37}Ar and ^{39}Ar decay, half lives of 35.2 days and 269 years, respectively

c J-value calculated relative to 28.02 Ma for the Fish Canyon sanidine (Renne *et al*. 1998)

d μ: mass discrimination per atomic mass unit

\# indicates crystals that have been included in weighted mean and isochron calculations

Table A.24 (*continued*)

Sample ID File #		Laser Power (%)	^{40}Ar / ^{39}Ar ± 1σ	^{37}Ar / ^{39}Ar ± 1σ	^{36}Ar / ^{39}Ar ± 1σ	F [a] ± 1σ	$^{40}Ar^*$ (%)	^{39}Ar mol x 10^{16}	K/Ca	Apparent Age ± 2σ Ma [b]
PUN 1060										
Single crystal fusions			sanidine			*J* = 0.0007644 ± 0.08 % (1σ)[c]				μ = 1.0051 ± 0.02 % (1σ)[d]
BE4934	#	35.0	1.5594 ± 0.0013	0.0051 ± 0.0001	0.0002 ± 0.0000	1.4923 ± 0.0029	95.70	5.81	83.528	2.057 ± 0.008
BE4935	#	35.0	1.5067 ± 0.0024	0.0052 ± 0.0001	0.0000 ± 0.0000	1.4955 ± 0.0034	99.26	6.33	82.035	2.061 ± 0.009
BE4937	#	35.0	1.5297 ± 0.0019	0.0051 ± 0.0001	0.0001 ± 0.0000	1.4995 ± 0.0045	98.03	4.24	84.823	2.067 ± 0.013
BE4938	#	35.0	1.5119 ± 0.0012	0.0061 ± 0.0001	0.0001 ± 0.0000	1.4903 ± 0.0027	98.57	6.11	70.556	2.054 ± 0.007
BE4940	#	35.0	1.5098 ± 0.0011	0.0050 ± 0.0001	0.0001 ± 0.0000	1.4933 ± 0.0029	98.91	6.54	85.931	2.058 ± 0.008
BE4941	#	35.0	1.5334 ± 0.0019	0.0085 ± 0.0001	0.0001 ± 0.0000	1.4933 ± 0.0027	97.39	7.05	50.660	2.058 ± 0.007
BE4943	#	35.0	1.5116 ± 0.0010	0.0056 ± 0.0001	0.0001 ± 0.0000	1.4938 ± 0.0024	98.82	6.10	76.614	2.059 ± 0.007
BE4944	#	35.0	1.5204 ± 0.0014	0.0055 ± 0.0001	0.0001 ± 0.0000	1.4965 ± 0.0025	98.43	7.95	77.711	2.063 ± 0.007
BE4946	#	35.0	1.5067 ± 0.0012	0.0057 ± 0.0001	0.0000 ± 0.0000	1.4930 ± 0.0023	99.09	7.35	75.246	2.058 ± 0.006
BE4947	#	35.0	1.5201 ± 0.0014	0.0057 ± 0.0001	0.0001 ± 0.0000	1.5022 ± 0.0035	98.82	8.14	75.051	2.070 ± 0.010
BE4949	#	35.0	1.6512 ± 0.0020	0.0059 ± 0.0001	0.0005 ± 0.0000	1.4964 ± 0.0028	90.63	7.17	72.667	2.062 ± 0.008
BE4950	#	35.0	1.5144 ± 0.0020	0.0056 ± 0.0001	0.0001 ± 0.0000	1.4973 ± 0.0026	98.87	7.29	76.459	2.064 ± 0.007
BE4952	#	35.0	1.5054 ± 0.0011	0.0057 ± 0.0001	0.0000 ± 0.0000	1.4919 ± 0.0023	99.10	7.34	76.002	2.056 ± 0.006
BE4953	#	35.0	1.5484 ± 0.0014	0.0118 ± 0.0002	0.0002 ± 0.0000	1.4952 ± 0.0042	96.57	4.42	36.451	2.061 ± 0.012
BE4955	#	35.0	1.5506 ± 0.0013	0.0055 ± 0.0001	0.0002 ± 0.0000	1.4991 ± 0.0021	96.68	8.16	77.878	2.066 ± 0.006
Weighted Mean from 15 of 15 grains:						MSWD 1.27			Weighted Mean age:	**2.060 ± 0.004**
Inverse Isochron from 15 of 15 grains: ^{40}Ar / ^{36}Ar ± 2σ: 301.8 ± 13.5						MSWD 1.28			Isochron age:	**2.059 ± 0.005**

a F is the ratio of radiogenic ^{40}Ar to K-derived ^{39}Ar

b All ages calculated using the decay constants of Steiger and Jäger ($\lambda_{40K} = 5.543 \times 10^{-10}$ yr^{-1}) and corrected for ^{37}Ar and ^{39}Ar decay, half lives of 35.2 days and 269 years, respectively

c J-value calculated relative to 28.02 Ma for the Fish Canyon sanidine (Renne *et al*. 1998)

d μ: mass discrimination per atomic mass unit

\# indicates crystals that have been included in weighted mean and isochron calculations

APPENDIX B

STABLE ISOTOPE DATA

Introduction

The stable isotope composition was measured for a variety of sample materials in the laboratory of Dr. Thure Cerling, Department of Biology, University of Utah. Several samples sets representing modern, Quaternary, and Mio-Pliocene environments were analyzed. Surface, ground, and tap water samples are reported in Table B.1. Analyses of carbonate from modern environments, as well as pedogenic carbonate from geomorphic surfaces and paleosol and diagenetic carbonate from stratified sections are presented in Tables B.2 through B.4. These tables are organized by sedimentary basin, from south to north. Table B.5 presents data from modern and fossil tooth enamel, the vast majority of this data is from the Corral Quemado basin.

All carbonate isotopic data was produced using an autosampler connected to a common acid bath (Finnigan Carboflo) and inlet to the mass spectrometer via dual inlet. The common acid bath (100% phosphoric acid) was kept at 90 ± 1°C, and sample $\delta^{18}O$ values were calculated using acid fractionation factors described in Swart *et al*. (1991) and Passey *et al*. (2007). Laser ablation methods are presented in Passey and Cerling (2006). Further details can be found in Chapter 2.

Table B.1: Surface, ground, and tap water stable isotope data; Catamarca and Tucuman Provinces, Argentina

ID	Date	Type	Latitude	Longitude	Elevation	$\delta^{18}O$[a]	$\delta^{2}H$[b]	Comments
			°S	°W	m	SMOW	SMOW	
TUC-118	11-Dec-01	Stream	27.0436	65.6689	1000	-6.6		Río de los Sosa tributary
TUC-119	11-Dec-01	River	26.96	65.66	1800	-4.2		Río de los Sosa[c]
TUC-120	11-Dec-01	Stream	26.96	65.66	1800	-6.6		Río de los Sosa tributary
TUC-121	11-Dec-01	Stream	26.7990	65.7241	2600	-5.0		Río Tafí del Valle tributary
CAT-174	16-Dec-01	River	27.2566	66.8604	1780	-3.5		Río Belén tributary
CAT-175	16-Dec-01	River	27.19	66.76	1970	-5.2		Río Belén tributary
TUC-102	4-Jun-02	River	27.093	65.559	390	-4.6		Río Cerda
TUC-103	4-Jun-02	Stream	27.0490	65.6691	980	-4.1		Río de los Sosa tributary
TUC-104	4-Jun-02	Stream	27.0315	65.6572	1120	-4.3		Río de los Sosa tributary
TUC-105	4-Jun-02	Stream	26.9757	65.6608	1620	-2.0		Río de los Sosa[c]
CAT-107	4-Jun-02	River	27.1945	66.7633	1960	-4.7		Río Belén tributary
PCQ-129	14-Jun-02	Spring	27.2512	66.9347	1840	-6.2		Spring from cliff below Toba del Pue
4750	28-Mar-07	Tap water	26.8284	65.1993	440	-3.0	-20	Tucumán tap water
4751	13-Apr-07	Tap water	27.1443	66.9447	2090	-10.0	-79	Corral Quemado tap water

[a]Samples with only $\delta^{18}O$ values were analyzed by CO_2 equilibration, estimated uncertainty ~0.2‰ (1σ).

[b]Samples with $\delta^{18}O$ and $\delta^{2}H$ values analyzed by TCEA, respective estimated uncertainties are 0.2‰ and 1.5‰ (1σ).

[c]Sampled downstream of a reservoir, $\delta^{18}O$ value likely enriched due to evaporation.

Table B.2: Paleosol carbonate stable isotope data from Fiambalá basin; Catamarca Province, Argentina

Sample ID	Material	Latitude °S	Longitude °W	Thickness m [a]	$\delta^{13}C$ PDB	$\delta^{18}O$ PDB	Comments
FIA 827	amalgamated powder	27.6363	67.6894	171	**-6.4**	**-4.3**	5 analyses; nodules 3–7 amalgamated
1 σ	n=5				***0.1***	***0.2***	
FIA 827	paleosol carbonate nodule				-4.9	-3.9	nodule 1; amalgamated
FIA 827	paleosol carbonate nodule				-5.7	-4.5	nodule 2; subsample 1
FIA 827	paleosol carbonate nodule				-6.5	-4.8	nodule 2; subsample 2
FIA 827	paleosol carbonate nodule				-6.9	-5.2	nodule 3; subsample 1
FIA 827	paleosol carbonate nodule				-6.3	-5.1	nodule 3; subsample 2
FIA 827	paleosol carbonate nodule				-6.6	-6.6	nodule 4; subsample 1
FIA 827	paleosol carbonate nodule				-6.6	-5.7	nodule 4; subsample 2
FIA 827	paleosol carbonate nodule				-6.8	-3.9	nodule 5; amalgamated
FIA 827	paleosol carbonate nodule				-6.8	-3.8	nodule 6; amalgamated
FIA 827	paleosol carbonate nodule				-6.4	-6.4	nodule 7; amalgamated
FIA 827	*all nodule analyses; n=10*				*-6.4*	*-5.0*	
1 σ					*0.6*	*1.0*	
FIA 829	amalgamated powder	27.6365	67.6894	184	**-5.7**	**-3.4**	5 analyses; nodules 4–7 amalgamated
1 σ	n=5				***0.3***	***0.2***	
FIA 829	paleosol carbonate nodule				-5.1	-4.5	nodule 1; amalgamated
FIA 829	paleosol carbonate nodule				-6.3	-5.4	nodule 2; amalgamated
FIA 829	paleosol carbonate nodule				-5.9	-5.2	nodule 3; amalgamated
FIA 829	paleosol carbonate nodule				-6.2	-5.5	nodule 4; subsample
FIA 829	paleosol carbonate nodule				-5.5	-2.6	nodule 5; subsample
FIA 829	paleosol carbonate nodule				-5.3	-1.4	nodule 6; subsample 1
FIA 829	paleosol carbonate nodule				-5.2	-4.3	nodule 6; subsample 2
FIA 829	paleosol carbonate nodule				-5.6	-3.7	nodule 7; subsample 1
FIA 829	paleosol carbonate nodule				-5.3	-3.2	nodule 7; subsample 2
FIA 829	*all nodule analyses; n=9*				*-5.6*	*-4.0*	
1 σ					*0.4*	*1.4*	

Table B.2: (*continued*)

Sample ID	Material	Latitude °S	Longitude °W	Thickness m [a]	$\delta^{13}C$ PDB	$\delta^{18}O$ PDB	Comments
FIA 831	amalgamated powder	27.6365	67.6894	186	**-1.9**	**-3.9**	5 analyses; nodules 2–6 amalgamated
1 σ	n=5				***0.2***	***0.2***	
FIA 831	paleosol carbonate nodule				-3.7	-4.1	nodule 1; subsample 1
FIA 831	paleosol carbonate nodule				-3.8	-2.6	nodule 1; subsample 2
FIA 831	paleosol carbonate nodule				-1.0	-4.1	nodule 2; subsample
FIA 831	paleosol carbonate nodule				-2.0	-5.4	nodule 3; subsample
FIA 831	paleosol carbonate nodule				-1.8	-4.0	nodule 2/3; amalgamated
FIA 831	paleosol carbonate nodule				-0.9	-4.2	nodule 4; subsample 1
FIA 831	paleosol carbonate nodule				-0.4	-3.9	nodule 4; subsample 2
FIA 831	paleosol carbonate nodule				-4.8	-4.0	nodule 5; subsample 1
FIA 831	paleosol carbonate nodule				-0.6	-4.0	nodule 5; subsample 2
FIA 831	paleosol carbonate nodule				-1.2	-3.8	nodule 6; subsample
FIA 831	*all nodule analyses; n=10*				*-2.0*	*-4.0*	
1 σ					*1.6*	*0.7*	

Note: Analytical methods are discussed in Chapter 2 , sampling strategy and results are discussed in Chapter 4.

[a]Stratigraphic height above the base of the section as defined in Table A.1.

Table B.3: Carbonate stable isotope data from Corral Quemado basin; Catamarca Province, Argentina

Sample ID	Material	Latitude °S	Longitude °W	Thickness m [a]	$\delta^{13}C$ PDB	$\delta^{18}O$ PDB	Comments
PCQ 709	terrestrial snail shell	27.2110	66.9307	modern	-4.1	-3.5	shells collected on ridge; single shell analyzed
PCQ 709	terrestrial snail shell				-3.1	-1.8	shells collected on ridge; single shell analyzed
PCQ 709	terrestrial snail shell				-5.1	1.2	shells collected on ridge; single shell analyzed
PCQ 1038	vesicular A horizon	27.2364	66.9327	Quaternary	-0.1	2.6	5 cm depth, beneath desert pavement
PCQ 1039	loess	27.2364	66.9327	Quaternary	-5.1	-0.3	25 cm depth (total thickness may be >1 m)
PCQ 1039	loess				-4.6	-0.8	25 cm depth (total thickness may be >1 m)
PCQ 1039	loess				-3.9	-1.0	25 cm depth (total thickness may be >1 m)
PCQ 716a-1	carbonate pendant	27.1201	66.9242	Quaternary?	-2.7	-2.3	outermost lamination
PCQ 716a-2	carbonate pendant				-2.5	-2.4	outer lamination
PCQ 716a-2	carbonate pendant				-2.5	-2.5	outer lamination
PCQ 716a-3	carbonate pendant				-1.8	-2.7	outer tan lamination
PCQ 716a-3	carbonate pendant				-1.9	-2.5	outer tan lamination
PCQ 716a-4	carbonate pendant				-2.1	-2.4	inner tan lamination
PCQ 716a-5	carbonate pendant				-2.5	-1.9	powdery white coat on outside of pendant
PCQ 521	disseminated carbonate	27.1593	66.9212	Quaternary?	-4.8	-5.1	tuff; diagenetic; <125 μm fraction analyzed
PCQ 521	disseminated carbonate				-4.3	-5.2	tuff; diagenetic; <125 μm fraction analyzed
PCQ 730	disseminated carbonate	27.3421	66.9076	≥ 1850	-6.1	-6.0	tuff; diagenetic
PCQ 730	disseminated carbonate				-6.0	-6.0	tuff; diagenetic
PCQ 505	calcite vein	27.2217	66.9516	1764	-3.0	-4.5	tuff; diagenetic
PCQ 505	calcite vein				-2.0	-4.6	tuff; diagenetic
PCQ 505	calcite vein				-5.3	-5.5	tuff; diagenetic
PCQ 505	calcite vein				-6.3	-5.0	tuff; diagenetic
PCQ 505	disseminated carbonate				-7.2	-5.0	tuff; diagenetic; <125 μm fraction analyzed
PCQ 505	disseminated carbonate				-7.2	-5.0	tuff; diagenetic; <125 μm fraction analyzed
PCQ 731	disseminated carbonate	27.3273	66.89777	1500±35	-3.8	-5.4	tuff; diagenetic
PCQ 731	disseminated carbonate				-6.3	-5.4	tuff; diagenetic
PCQ 731	disseminated carbonate				-6.7	-6.2	tuff; diagenetic
PCQ 731	disseminated carbonate				-6.7	-6.3	tuff; diagenetic
PCQ 202	micrite nodule	27.2108	66.9342	1500±10	-4.8	-10.5	in Mio-Pliocene sandstone (recent carbonate)
PCQ 732	disseminated carbonate	27.3243	66.8970	1480±15	-6.6	-5.6	tuff; diagenetic
PCQ 732	disseminated carbonate				-6.4	-5.5	tuff; diagenetic
PCQ 736	disseminated carbonate	27.3234	66.8962	1475±10	-6.5	-5.7	tuff; diagenetic
PCQ 736	disseminated carbonate				-6.5	-5.5	tuff; diagenetic
PCQ 219[b]	paleosol carbonate nodule	27.2154	66.9355	1462	-6.0	-5.8	2 m thick paleosol; leached matrix, 1.6 m depth
PCQ 219[b]	paleosol carbonate nodule				-6.0	-5.7	2 m thick paleosol; leached matrix, 1.6 m depth
PCQ 219[b]	paleosol carbonate nodule				-6.6	-5.8	2 m thick paleosol; leached matrix, 1.0 m depth

Table B.3: (*continued*)

Sample ID	Material	Latitude °S	Longitude °W	Thickness m [a]	$\delta^{13}C$ PDB	$\delta^{18}O$ PDB	Comments
PCQ 742	disseminated carbonate	27.218	66.924	1030±20	-4.1	-5.4	tuff; diagenetic
PCQ 742	disseminated carbonate				-4.3	-5.8	tuff; diagenetic
PCQ 188	disseminated carbonate	27.2219	66.9300	1000	-5.5	-5.9	clastic dike, carbonate cemented
PCQ 187	disseminated carbonate	27.2242	66.9327	950	-2.3	-5.9	clastic dike, carbonate cemented
PCQ 706	micritic carbonate coating	27.2221	66.9286	~900	-1.9	-7.4	vertical fractures in sandstone with modern roots
PCQ 706	micritic carbonate coating				-2.0	-7.8	vertical fractures in sandstone with modern roots
PCQ 183	disseminated carbonate	27.2221	66.9286	~900	-4.7	-7.9	recent soil micrite in eolian sandstones
PCQ 183	disseminated carbonate				-3.4	-7.7	recent soil micrite in eolian sandstones
PCQ 183	disseminated carbonate				-3.0	-8.3	recent soil micrite in eolian sandstones
PCQ 183	micritic rootlet				-3.8	-7.4	recent soil micrite in eolian sandstones
PCQ 183	micritic rootlet				-3.2	-8.2	recent soil micrite in eolian sandstones
PCQ 183	calcite vein				-2.9	-9.5	vein in micrite rootlet (recent to modern)
PCQ 183	calcite vein				-3.6	-8.7	vein in micrite rootlet (recent to modern)
PCQ 183	calcite vein				-3.4	-9.0	vein in micrite rootlet (recent to modern)
PCQ 183	calcite vein				-3.2	-9.1	vein in micrite rootlet (recent to modern)
Arg 148	calcite			629	-9.4	-9.6	yellow crystal growing in maxillary bone
Arg 148	calcite				-9.0	-9.2	yellow crystal growing in maxillary bone
PCQ 518	disseminated carbonate	27.2416	66.9342	530	-4.5	-5.8	tuffaceous sand matrix; <125 µm fraction analyzed
PCQ 518	disseminated carbonate				-4.2	-5.4	tuffaceous sand matrix; <125 µm fraction analyzed
PCQ 553.1	disseminated carbonate	27.2430	66.9213	162	-7.9	-6.3	in fine grained strata; associated with calcite veins
PCQ 553.1	disseminated carbonate				-8.5	-6.3	in fine grained strata; associated with calcite veins
PCQ 553.1	calcite vein				-8.2	-11.8	clear crystal
PCQ 553.1	calcite vein				-8.3	-11.6	clear crystal
PCQ 553.1	calcite vein				-8.3	-11.6	clear crystal
PCQ 553.1	calcite vein				-5.7	-8.8	clear crystal
PCQ 553.1	calcite vein				-8.5	-9.5	yellow crystal
PCQ 553.1	calcite vein				-8.7	-11.5	yellow crystal
PCQ 553.2	calcite vein				-8.5	-10.9	clear crystal
PCQ 553.2	calcite vein				-8.4	-10.8	clear crystal
PCQ 553.2	calcite vein				-8.3	-11.6	clear crystal

Note: Analytical methods are discussed in Chapter 2.

[a]Stratigraphic height above the base of the section as defined in Table 2.1 and Table A.5.

[b]Paleosol associated with Mesothere Notoungulate sample Arg2001-50.

Table B.4: Stable isotope data from Vallé Santa Maria and adjacent localities; Catamarca and Tucuman Provinces, Argentina

Sample ID	Material	Latitude °S	Longitude °W	Thickness m [a]	$\delta^{13}C$ PDB	$\delta^{18}O$ PDB	Comments
ENTR 929	terrestrial snail shell	26.8318	66.0171	modern	-4.6	0.2	collected on ridge below pediment
ENTR 929	terrestrial snail shell				-4.7	2.1	collected on ridge below pediment
ENTR 929	terrestrial snail shell				-4.1	0.7	collected on ridge below pediment
ENTR 538	disseminated carbonate	26.8598	66.0338	Holocene	-4.3	-2.5	unconsolidated tuff; diagenetic (see Table A.20)
ENTR 538	disseminated carbonate				-3.5	-2.7	unconsolidated tuff; diagenetic (see Table A.20)
TUC 908	soil carbonate, nodular	26.7262	65.8247	recent	-7.4	-2.0	sampled 70 cm below surface
TUC 908	soil carbonate, nodular				-7.2	-2.0	sampled 70 cm below surface
TUC 908	soil carbonate, nodular				-7.1	-2.2	sampled 70 cm below surface
TUC 908	soil carbonate, nodular				-7.9	-2.5	sampled 70 cm below surface
ENTR 927	carbonate pendant	26.8252	66.0209	Quaternary	-2.0	2.8	powdery white coat on outside of pendant
ENTR 927	carbonate pendant				-2.8	-0.3	inner tan lamination (see Table A.16)
ENTR 927	carbonate pendant				-2.8	-0.3	inner tan lamination (see Table A.16)
ENTR 534	tuffaceous paleosol	26.8552	66.0366	314	-2.3	-7.7	upper tuffaceous paleosol; >250 µm fraction
ENTR 534	tuffaceous paleosol				-2.8	-8.0	upper tuffaceous paleosol; 125–250 µm
ENTR 534	tuffaceous paleosol				-2.8	-7.8	upper tuffaceous paleosol; 125–250 µm fraction
ENTR 534	tuffaceous paleosol				-2.9	-7.8	upper tuffaceous paleosol; 125–250 µm fraction
ENTR 534	tuffaceous paleosol				-3.0	-8.0	upper tuffaceous paleosol; <125 µm fraction
ENTR 534	tuffaceous paleosol				-2.9	-8.4	upper tuffaceous paleosol; <125 µm fraction
ENTR 533	calcareous tuff, paleosoil?	26.8554	66.0439	200.4	-3.3	-6.7	lower tuffaceous paleosol; <125 µm fraction
ENTR 533	calcareous tuff, paleosoil?				-3.1	-6.1	lower tuffaceous paleosol; <125 µm fraction
ENTR 525	calcareous tuff, paleosol?	26.8499	66.0413	~200	-2.7	-7.0	lower tuffaceous paleosol; <125 µm fraction
ENTR 525	calcareous tuff, paleosol?				-2.5	-6.9	lower tuffaceous paleosol; <125 µm fraction
CAJ 703	marl	26.9859	66.2672	< ~5.5 Ma	-6.6	-6.1	paludal carbonate (?), see Table A.11
CAJ 703	marl				-6.6	-6.3	paludal carbonate (?), see Table A.11

Note: Analytical methods are discussed in Chapter 2.

[a]Stratigraphic height above the base of the section as defined in Table A.13.

Table B.5: Tooth enamel stable isotope data from Corral Quemado basin, Catamarca Province, Argentina

Sample ID	Order	Family	Taxon	Tooth pos. [a]	Tooth mm [b]	Lat. °S	Lon. °W	Thick. m [c]	$\delta^{13}C$ PDB	$\delta^{18}O_{cvn}$ PDB	$\delta^{18}O_{las}$ PDB
Modern Tooth Enamel											
Arg2001-TUC122	Perissodactyla	Equidae	*Equus Caballus*	M3	0.0	26.7842	65.7292		-12.4	-4.8	
Arg2001-TUC122 (nt) [d]	Perissodactyla	Equidae	*Equus Caballus*	M3	medial	26.7842	65.7292		-11.9	-3.7	
Arg2001-TUC122 (tr)	Perissodactyla	Equidae	*Equus Caballus*	M3	medial	26.7842	65.7292		-12.3	-3.5	
Arg2001-PCQ131 (nt)	Perissodactyla	Equidae	*Equus Caballus*	m		27.10	66.82		-8.6	-3.8	
Arg2001-PCQ131 (tr)	Perissodactyla	Equidae	*Equus Caballus*	m		27.10	66.82		-8.8	-2.7	
Arg2001-300 (nt)	Perissodactyla	Equidae	*Equus Caballus*			27.2233	66.9118		-1.8	-0.8	
Arg2001-300 (tr)	Perissodactyla	Equidae	*Equus Caballus*			27.2233	66.9118		-1.6	0.3	
Arg2002-PCQ112	Perissodactyla	Equidae	*Equus Caballus*	M3		27.2259	66.9494		-7.7	-2.1	
Arg2002-PCQ112	Perissodactyla	Equidae	*Equus Caballus*	rM2	0.0	27.2259	66.9494		-7.8	-1.2	
Arg2002-PCQ112	Perissodactyla	Equidae	*Equus Caballus*	rM2	12.5	27.2259	66.9494		-7.3	-1.7	
Arg2002-PCQ112	Perissodactyla	Equidae	*Equus Caballus*	rM2	26.8	27.2259	66.9494		-8.1	-2.7	
Arg2002-PCQ161	Perissodactyla	Equidae	*Equus Caballus*	lm2		27.2257	66.9519		-7.0	-1.2	
Arg002-PCQ162	Perissodactyla	Equidae	*Equus Caballus*	lm2		27.2287	66.9540		-5.9	-2.9	
Arg2001-AND131	Artiodactyla	Bovidae	*Capra*						-10.7	1.0	
Arg2001-PCQ172 (nt)	Artiodactyla	Bovidae	*Capra*	M		27.2194	66.9201		-10.7	1.6	
Arg2001-PCQ172 (tr)	Artiodactyla	Bovidae	*Capra*	M		27.2194	66.9201		-10.9	2.5	
Arg2001-PCQ136 (nt)	Artiodactyla	Bovidae	*Capra*	m3					-5.6	5.0	
Arg2001-PCQ136 (tr)	Artiodactyla	Bovidae	*Capra*	m3					-5.8	5.5	
Arg2001-PCQ137 (nt)	Artiodactyla	Bovidae	*Capra*	M					-6.0	5.4	
Arg2001-PCQ137 (tr)	Artiodactyla	Bovidae	*Capra*	M					-6.5	7.1	
Arg2001-PCQ180 (nt)	Artiodactyla	Bovidae	*Capra*	M3		27.2207	66.9251		-5.6	-0.8	
Arg2001-PCQ180 (tr)	Artiodactyla	Bovidae	*Capra*	M3		27.2207	66.9251		-6.0	1.1	
Arg2001-PCQ182	Artiodactyla	Bovidae	*Capra*	m2		27.2222	66.9286		-7.1	-0.9	
Arg2001-PCQ182	Artiodactyla	Bovidae	*Capra*	m2		27.2222	66.9286		-7.1	0.5	
Arg2002-PCQ137	Artiodactyla	Bovidae	*Capra*	M3		27.2395	66.9503		-5.6	2.2	
Arg2002-PCQ137	Artiodactyla	Bovidae	*Capra*	M2	30.0	27.2395	66.9503		-6.7	5.6	
Arg2002-PCQ137	Artiodactyla	Bovidae	*Capra*	M2	20.5	27.2395	66.9503		-6.4	1.9	
Arg2002-PCQ137	Artiodactyla	Bovidae	*Capra*	M2	11.0	27.2395	66.9503		-5.2	3.8	
Arg2007-PUN1010	Artiodactyla	Camelidae	*Vicugna vicugna*	M2	0.5	26.5127	67.4092		-9.3	3.7	
Arg2007-PUN1010	Artiodactyla	Camelidae	*Vicugna vicugna*	M3	0.5	26.5127	67.4092		-9.1	3.4	
Arg2007-PUN1010	Artiodactyla	Camelidae	*Vicugna vicugna*	M3	4.0	26.5127	67.4092		-9.1	3.5	

Table B.5: (*continued*)

Sample ID	Order	Family	Taxon	Tooth pos. [a]	Tooth mm [b]	Lat. °S	Lon. °W	Thick. m [c]	$\delta^{13}C$ PDB	$\delta^{18}Ocvn$ PDB	$\delta^{18}Olas$ PDB
Modern Tooth Enamel											
Arg2001-PCQ134 (nt)	Rodentia								-9.8	6.4	
Arg2001-PCQ134 (tr)	Rodentia								-10.2	7.8	
Arg2001-PCQ171	Rodentia			molar		27.2194	66.9201		-10.2	-0.1	
Arg2001-PCQ195 C	Rodentia					27.2149	66.9265		-6.8	-0.7	
Arg2001-PCQ195	Rodentia			incisor	3.5–4.0	27.2149	66.9265		-8.0	0.5	
Arg2001-PCQ195	Rodentia			incisor	8.0–12.5	27.2149	66.9265		-7.3	0.3	
Arg2001-PCQ195	Rodentia			incisor	15–18	27.2149	66.9265		-6.1	-0.3	
Arg-112-1 [e]	Lagomorpha	Leporidae	*Lepus europaeus*						-13.4	2.4	
Arg-112-1 [e]	Lagomorpha	Leporidae	*Lepus europaeus*						-13.7	2.1	
Arg2001-PCQ178 (nt)	Carnivora	Canidae	*C. l. familiaris*			27.2207	66.9251		-10.3	-3.7	
Arg2001-PCQ178 (tr)	Carnivora	Canidae	*C. l. familiaris*			27.2207	66.9251		-10.5	-2.9	
Arg2001-PCQ192 C	Carnivora	Canidae	*Vulpes*			27.2175	66.9268		-11.8	-0.1	
Arg2001-PCQ209	Carnivora	Canidae	*C. l. familiaris*						-10.1	-3.3	
Arg2001-AND130 T [f]	Xenarthra		Cingulata indet.	tooth		27.2196	66.4164		-10.7	1.5	
Arg2001-AND130 P [f]	Xenarthra		Cingulata indet.	carapace (bone apatite)		27.2196	66.4164		-10.4	0.0	
Fossil Tooth Enamel											
Arg-246	Notoungulata	Hegetotheriidae	*Paedotherium sp.*	molar				2215	-0.9	4.6	
Arg-246 scan 1	Notoungulata	Hegetotheriidae	*Paedotherium sp.*	molar	1.5			2215	-6.5		-8.2
Arg-246 scan 2	Notoungulata	Hegetotheriidae	*Paedotherium sp.*	molar	2.2			2215	-6.1		-7.5
Arg-246 scan 3	Notoungulata	Hegetotheriidae	*Paedotherium sp.*	molar	2.8			2215	-5.8		-7.5
Arg-246 scan 4	Notoungulata	Hegetotheriidae	*Paedotherium sp.*	molar	3.3			2215	-5.6		-7.3
Arg-246 scan 5	Notoungulata	Hegetotheriidae	*Paedotherium sp.*	molar	3.8			2215	-6.0		-7.5
Arg-246 scan 6	Notoungulata	Hegetotheriidae	*Paedotherium sp.*	molar	4.1			2215	-6.3		-7.6
Arg-246 scan 7	Notoungulata	Hegetotheriidae	*Paedotherium sp.*	molar	5.7			2215	-4.3		-6.7
Arg-246 scan 8	Notoungulata	Hegetotheriidae	*Paedotherium sp.*	molar	6.6			2215	-2.0		-6.1
Arg-246 scan 9	Notoungulata	Hegetotheriidae	*Paedotherium sp.*	molar	8.5			2215	-4.3		-6.6
Arg-246 scan 10	Notoungulata	Hegetotheriidae	*Paedotherium sp.*	molar	7.2			2215	-1.8		-5.8
Arg-246 scan 11	Notoungulata	Hegetotheriidae	*Paedotherium sp.*	molar	6.0			2215	-3.7		-6.7
Arg-246 scan 12	Notoungulata	Hegetotheriidae	*Paedotherium sp.*	molar	4.9			2215	-6.2		-7.3

Table B.5: (*continued*)

Sample ID	Order	Family	Taxon	Tooth pos. [a]	Tooth mm [b]	Lat. °S	Lon. °W	Thick. m [c]	$\delta^{13}C$ PDB	$\delta^{18}O_{cvn}$ PDB	$\delta^{18}O_{las}$ PDB
Arg-246 scan 13	Notoungulata	Hegetotheriidae	*Paedotherium sp.*	molar	7.5			2215	-2.5		-6.1
Arg-290	Rodentia	Caviidae		rm2	distal			2175	-3.9	-3.5	
Arg2002-18 scan 1	Rodentia			incisor		27.2343	66.9734	2135	-13.5		-7.6
Arg2002-18 scan 2	Rodentia			incisor		27.2343	66.9734	2135	-12.5		-8.0
Arg-269	Rodentia	Caviidae		molar	medial			2120	1.1	-1.2	
Arg-289 scan 3	Rodentia	Octodontidae		molar	1.5			2120	-8.2		-9.8
Arg-289 scan 4	Rodentia	Octodontidae		molar	1.0			2120	-7.1		-9.5
Arg-272	Rodentia	Caviidae		molar				2100	-7.6	1.6	
Arg2002-31	Rodentia	Ctenomyidae		incisor		27.2332	66.9726	2100	-7.8		-7.9
Arg2002-31	Rodentia	Ctenomyidae		incisor		27.2332	66.9726	2100	-7.5		-7.8
Arg2002-31	Rodentia	Ctenomyidae		incisor		27.2332	66.9726	2100	-8.9		-9.3
Arg2002-22 red [f]	Rodentia			incisor		27.2332	66.9714	2067	-7.4	-3.3	
Arg2002-22 en	Rodentia			incisor		27.2332	66.9714	2067	-7.9	-0.2	
Arg2002-22 scan 1	Rodentia			incisor	7.5	27.2332	66.9714	2067	-10.9		-10.2
Arg2002-22 scan 2	Rodentia			incisor	6.8	27.2332	66.9714	2067	-10.9		-10.4
Arg2002-22 scan 3	Rodentia			incisor	5.5	27.2332	66.9714	2067	-7.8		-6.9
Arg2002-22 scan 7	Rodentia			incisor	2.0	27.2332	66.9714	2067	-10.3		-9.7
Arg2002-22 scan 8	Rodentia			incisor	1.0	27.2332	66.9714	2067	-10.9		-10.2
Arg2002-22 scan 9	Rodentia			incisor	7.2	27.2332	66.9714	2067	-11.1		-10.4
Arg2002-22 scan 10	Rodentia			incisor	6.5	27.2332	66.9714	2067	-11.8		-11.7
Arg2002-20 scan 1	Rodentia			incisor		27.2335	66.9718	2053	-10.8		-13.1
Arg2002-20 scan 2	Rodentia			incisor		27.2335	66.9718	2053	-9.7		-12.2
Arg2002-21	Rodentia			incisor		27.2322	66.9707	2041	-9.2	-1.7	
Arg2002-21 scan 1	Rodentia			incisor	1.8	27.2322	66.9707	2041	-8.9		-7.9
Arg2002-21 scan 2	Rodentia			incisor	2.3	27.2322	66.9707	2041	-9.5		-8.0
Arg2002-21 scan 3	Rodentia			incisor	2.5	27.2322	66.9707	2041	-10.7		-11.0
Arg2002-21 scan 5	Rodentia			incisor	1.8–2.3	27.2322	66.9707	2041	-8.7		-7.3
Arg2002-17 scan 9	Rodentia			incisor	0.5	27.2302	66.9682	2017	0.3		-8.7
Arg2002-17 scan 1	Rodentia			incisor	1.1	27.2302	66.9682	2017	2.8		-5.2
Arg2002-17 scan 2	Rodentia			incisor	1.8	27.2302	66.9682	2017	0.2		-9.0
Arg2002-17 scan 3	Rodentia			incisor	2.2	27.2302	66.9682	2017	1.8		-6.7
Arg2002-17 scan 4	Rodentia			incisor	2.8	27.2302	66.9682	2017	1.0		-7.6

Table B.5: (*continued*)

Sample ID	Order	Family	Taxon	Tooth pos. [a]	Tooth mm [b]	Lat. °S	Lon. °W	Thick. m [c]	$\delta^{13}C$ PDB	$\delta^{18}O_{cvn}$ PDB	$\delta^{18}O_{las}$ PDB
Arg2002-17 scan 5	Rodentia			incisor	3.2	27.2302	66.9682	2017	0.5		-8.4
Arg2002-17 scan 6	Rodentia			incisor	3.8	27.2302	66.9682	2017	1.2		-7.4
Arg2002-17 scan 7	Rodentia			incisor	4.2	27.2302	66.9682	2017	-0.7		-9.4
Arg2002-17 scan 8	Rodentia			incisor	4.4	27.2302	66.9682	2017	-0.1		-7.3
Arg2002-16 scan 1	Rodentia	Octodontidae		molar		27.2326	66.9684	1921	-10.9		-5.9
Arg2002-16 scan 2	Rodentia	Octodontidae		molar		27.2326	66.9684	1921	-10.4		-5.8
Arg2002-16 scan 3	Rodentia	Octodontidae		molar		27.2326	66.9684	1921	-13.6		-6.2
Arg2002-15 scan 1	Rodentia			m		27.2326	66.9684	1921	-10.3		-7.5
Arg2002-1-b	Notoungulata	Mesotheriidae		incisor	1.0	27.2252	66.9583	1833	-2.3	-3.3	
Arg2002-1-a	Notoungulata	Mesotheriidae		incisor	3.5	27.2252	66.9583	1833	-1.7	-3.2	
Arg2002-1-0	Notoungulata	Mesotheriidae		incisor	6.5	27.2252	66.9583	1833	-1.3	-3.7	
Arg2002-1-1	Notoungulata	Mesotheriidae		incisor	10.0	27.2252	66.9583	1833	-1.5	-4.1	
Arg2002-1-2	Notoungulata	Mesotheriidae		incisor	12.5	27.2252	66.9583	1833	-1.5	-4.6	
Arg2002-1-3	Notoungulata	Mesotheriidae		incisor	14.0	27.2252	66.9583	1833	-1.6	-4.7	
Arg2002-1-4	Notoungulata	Mesotheriidae		incisor	15.5	27.2252	66.9583	1833	-1.7	-4.5	
Arg2002-1-5	Notoungulata	Mesotheriidae		incisor	17.3	27.2252	66.9583	1833	-1.9	-4.6	
Arg2002-1-6	Notoungulata	Mesotheriidae		incisor	19.0	27.2252	66.9583	1833	-2.2	-4.7	
Arg2002-1-7	Notoungulata	Mesotheriidae		incisor	21.0	27.2252	66.9583	1833	-2.3	-4.3	
Arg2002-1-8	Notoungulata	Mesotheriidae		incisor	23.0	27.2252	66.9583	1833	-2.8	-4.2	
Arg-110 scan 1	Rodentia	Octodontidae	*Propithanotomys intermedius*	incisor	9.7			1813	-8.4		-10.0
Arg-110 scan 2	Rodentia	Octodontidae	*Propithanotomys intermedius*	incisor	9.1			1813	-8.6		-10.3
Arg-110 scan 3	Rodentia	Octodontidae	*Propithanotomys intermedius*	incisor	8.1			1813	-8.9		-10.2
Arg2002-13	Rodentia			i		27.2239	66.9560	1788	-9.2		-8.1
Arg2002-13	Rodentia			i		27.2239	66.9560	1788	-9.2		-8.5
Arg2002-11 scan 1	Rodentia			incisor	6.5	27.2239	66.9559	1788	-14.1		-1.5
Arg2002-11 scan 2	Rodentia			incisor	5.4	27.2239	66.9559	1788	-13.0		-1.7
Arg2002-11 scan 3	Rodentia			incisor	4.3	27.2239	66.9559	1788	-12.9		-1.0
Arg2002-11 scan 4	Rodentia			incisor	3.9	27.2239	66.9559	1788	-13.6		-3.7
Arg2002-11 scan 8	Rodentia			incisor	7.6	27.2239	66.9559	1788	-15.6		-1.4
Arg2002-28 en	Notoungulata					27.2239	66.9538	1753	-8.6	-1.7	
Arg2002-28 dent [f]	Notoungulata					27.2239	66.9538	1753	-8.5	-4.2	
Arg2002-28-1/8/05.1	Notoungulata					27.2239	66.9538	1753	-8.7	-3.1	

Table B.5: (*continued*)

Sample ID	Order	Family	Taxon	Tooth pos. [a]	Tooth mm [b]	Lat. °S	Lon. °W	Thick. m [c]	$\delta^{13}C$ PDB	$\delta^{18}O_{cvn}$ PDB	$\delta^{18}O_{las}$ PDB
Arg2002-28-1/8/05.1	Notoungulata					27.2239	66.9538	1753	-8.5	-1.8	
Arg2002-28-11/13/05.1	Notoungulata					27.2239	66.9538	1753	-8.9	-3.2	
Arg2002-28-11/18/05.1	Notoungulata					27.2239	66.9538	1753	-9.5	-2.9	
Arg2002-28 scan 1	Notoungulata					27.2239	66.9538	1753	-7.7		-8.1
Arg2002-28 scan 2	Notoungulata					27.2239	66.9538	1753	-7.9		-7.9
Arg2002-28 scan 3	Notoungulata					27.2239	66.9538	1753	-8.3		-8.1
Arg2002-27-1/8/05.1 red	Rodentia			incisor		27.2241	66.9529	1710	-9.4	-2.1	
Arg2002-27-1/8/05.2 en	Rodentia			incisor		27.2241	66.9529	1710	-9.8	-0.6	
Arg2002-27-11/13/05.1	Rodentia			incisor		27.2241	66.9529	1710	-10.3	0.5	
Arg2002-27-11/18/05.1	Rodentia			incisor		27.2241	66.9529	1710	-10.4	0.6	
Arg-213	Rodentia	Octodontidae	*Pithanotomys columnaris*	incisor	distal			1703	-6.4	-0.4	
Arg2002-2	Notoungulata	Hegetotheriidae	Pachyrukhinae	fragment		27.2290	66.9529	1561	-1.8	-1.8	
Arg2002-2 scan 1	Notoungulata	Hegetotheriidae	Pachyrukhinae		1.1	27.2290	66.9529	1561	-5.3		-10.7
Arg2002-2 scan 2	Notoungulata	Hegetotheriidae	Pachyrukhinae		2.1	27.2290	66.9529	1561	0.2		-9.4
Arg2002-2 scan 3	Notoungulata	Hegetotheriidae	Pachyrukhinae		1.6	27.2290	66.9529	1561	-0.6		-9.3
Arg2002-2 scan 4	Notoungulata	Hegetotheriidae	Pachyrukhinae		3.3	27.2290	66.9529	1561	-1.8		-9.1
Arg2002-2 scan 5	Notoungulata	Hegetotheriidae	Pachyrukhinae		4.4	27.2290	66.9529	1561	-1.3		-9.1
Arg2002-2 scan 6	Notoungulata	Hegetotheriidae	Pachyrukhinae		4.8	27.2290	66.9529	1561	-1.3		-9.0
Arg2002-2 scan 7	Notoungulata	Hegetotheriidae	Pachyrukhinae		6.3	27.2290	66.9529	1561	-1.4		-8.8
Arg2002-2 scan 8	Notoungulata	Hegetotheriidae	Pachyrukhinae		7.6	27.2290	66.9529	1561	-3.4		-8.6
Arg2002-2 scan 9	Notoungulata	Hegetotheriidae	Pachyrukhinae		0.5	27.2290	66.9529	1561	-2.3		-10.0
Arg-208a	Rodentia	Octodontidae	*Pseudoplataeomys*	incisor	medial			1561	-4.5	-2.5	
Arg-208b	Rodentia	Chinchillidae		rm1	medial			1561	-5.7	-3.7	
Arg-208b	Rodentia	Chinchillidae		rm1	distal			1561	-8.3	-0.3	
Arg2002-5 scan 1	Rodentia	Octodontidae		incisor	4.2	27.2309	66.9551	1550	-6.7		-6.4
Arg2002-5 scan 2	Rodentia	Octodontidae		incisor	4.8	27.2309	66.9551	1550	-7.7		-8.2
Arg2002-5 scan 3	Rodentia	Octodontidae		incisor	5.4	27.2309	66.9551	1550	-8.5		-7.8
Arg2002-5 scan 4	Rodentia	Octodontidae		incisor	5.8	27.2309	66.9551	1550	-7.3		-7.6
Arg2002-5 scan 5	Rodentia	Octodontidae		incisor	2.6	27.2309	66.9551	1550	-7.4		-7.1
Arg2002-5 scan 6	Rodentia	Octodontidae		incisor	-	27.2309	66.9551	1550	-8.2		-7.8
Arg2002-4 scan 1	Rodentia	Octodontidae		incisor	2.0–2.3	27.2309	66.9551	1550	-9.7		-8.0
Arg2002-4 scan 2	Rodentia	Octodontidae		incisor	2.8	27.2309	66.9551	1550	-10.7		-9.1

Table B.5: (*continued*)

Sample ID	Order	Family	Taxon	Tooth pos. [a]	Tooth mm [b]	Lat. °S	Lon. °W	Thick. m [c]	$\delta^{13}C$ PDB	$\delta^{18}O_{cvn}$ PDB	$\delta^{18}O_{las}$ PDB
Arg2002-7-5/13/05.1	Rodentia			incisor		27.2295	66.9533	1538	-5.1	-0.3	
Arg2002-7-11/13/05.1	Rodentia			incisor		27.2295	66.9533	1538	-5.9	-1.0	
Arg2002-7 scan 1	Rodentia			incisor		27.2295	66.9533	1538	-6.5		-4.4
Arg2002-7 scan 2	Rodentia			incisor		27.2295	66.9533	1538	-5.5		-4.3
Arg2002-7 scan 3	Rodentia			incisor		27.2295	66.9533	1538	-9.8		-4.7
Arg2002-29 scan 1	Rodentia	Octodontidae		molar		27.2290	66.9530	1535	-5.1		-7.4
Arg2002-29 scan 2	Rodentia	Octodontidae		molar		27.2290	66.9530	1535	-4.6		-7.8
Arg2002-29 scan 3	Rodentia	Octodontidae		molar		27.2290	66.9530	1535	-7.2		-8.4
Arg2002-26-5/13/05.1	Rodentia			incisor		27.2291	66.9529	1533	-3.0	-1.7	
Arg2002-26-11/13/05.1	Rodentia			incisor		27.2291	66.9529	1533	-2.7	-0.3	
Arg2002-26-11/13/05.2	Rodentia			incisor		27.2291	66.9529	1533	-2.9	-1.2	
Arg2002-26-11/18/05.1	Rodentia			incisor		27.2291	66.9529	1533	-2.9	-0.4	
Arg2002-26 scan 1	Rodentia			incisor		27.2291	66.9529	1533	-4.6		-5.9
Arg2002-26 scan 2	Rodentia			incisor		27.2291	66.9529	1533	-6.1		-5.7
Arg2002-26 scan 3	Rodentia			incisor		27.2291	66.9529	1533	-4.6		-5.7
Arg2002-26 scan 1	Rodentia			incisor		27.2291	66.9529	1533	-2.7		-4.7
Arg2002-26 scan 2	Rodentia			incisor		27.2291	66.9529	1533	-4.5		-4.6
Arg-200 scan 1	Rodentia	Octodontidae		incisor	1.5			1511	-6.6		-11.9
Arg-200 scan 2	Rodentia	Octodontidae		incisor	3.1			1511	-7.5		-13.3
Arg-200 scan 3	Rodentia	Octodontidae		incisor	4.5			1511	-6.7		-12.8
Arg-200 scan 4	Rodentia	Octodontidae		incisor	6.0			1511	-6.8		-11.9
Arg-200 scan 5	Rodentia	Octodontidae		incisor	7.3			1511	-6.3		-11.3
Arg2002-9-5/13/05.1	Rodentia			i		27.2315	66.9554	1484	-6.7	-4.2	
Arg2002-9-11/13/05.1	Rodentia			i		27.2315	66.9554	1484	-7.0	-3.7	
Arg2002-9-11/13/05.2	Rodentia			i		27.2315	66.9554	1484	-6.0	-4.3	
Arg2002-9-11/18/05.1	Rodentia			i		27.2315	66.9554	1484	-6.3	-3.1	
Arg2002-9 scan 1	Rodentia			i		27.2315	66.9554	1484	-6.9		-9.8
Arg2002-9 scan 2	Rodentia			i		27.2315	66.9554	1484	-7.4		-9.1
Arg2002-9 scan 3	Rodentia			i		27.2315	66.9554	1484	-7.2		-8.4
Arg2001-50-1,2	Notoungulata	Mesotheriidae		molar	22.0	27.2154	66.9355	1462	0.1	-1.5	
Arg2001-50-3	Notoungulata	Mesotheriidae		molar	16.0	27.2154	66.9355	1462	-0.4	-1.7	
Arg2001-50-4	Notoungulata	Mesotheriidae		molar	12.0	27.2154	66.9355	1462	-0.2	-1.9	

Table B.5: (*continued*)

Sample ID	Order	Family	Taxon	Tooth pos. [a]	Tooth mm [b]	Lat. °S	Lon. °W	Thick. m [c]	$\delta^{13}C$ PDB	$\delta^{18}O_{cvn}$ PDB	$\delta^{18}O_{las}$ PDB
Arg2001-50-5	Notoungulata	Mesotheriidae		molar	8.0	27.2154	66.9355	1462	0.1	-1.8	
Arg2001-50-6	Notoungulata	Mesotheriidae		molar	4.0	27.2154	66.9355	1462	-0.3	-2.2	
Arg-248	Rodentia			incisor	proximal			1439	-8.6	0.2	
Arg-248	Rodentia			incisor	medial			1439	-9.7	0.9	
Arg-249	Notoungulata	Hegetotheriidae		rm3				1437	-3.6	-0.5	
Arg2001-44	Rodentia					27.2127	66.9293	1400	-5.0	-2.7	
Arg-194	Rodentia	Chinchillidae		m3	medial			1370	-6.9	-3.6	
Arg-173 scan 1	Rodentia			incisor	8.4			1239	-3.8		-10.6
Arg-173 scan 2	Rodentia			incisor	7.5			1239	-8.4		-7.2
Arg-173 scan 3	Rodentia			incisor	6.5			1239	-7.9		-6.7
Arg-173 scan 4	Rodentia			incisor	5.6			1239	-6.5		-6.5
Arg2002-23-1/8/05.1	Rodentia			incisor		27.2405	66.9515	1010	-8.6	-3.4	
Arg2002-23 scan 1	Rodentia			incisor		27.2405	66.9515	1010	-9.6		-10.1
Arg2002-24-1/8/05.1	Notoungulata					27.2411	66.9507	944	-8.9	-1.7	
Arg2002-24 scan 1	Notoungulata					27.2411	66.9507	944	-8.8		-7.4
Arg2002-24 scan 2	Notoungulata					27.2411	66.9507	944	-8.6		-7.4
Arg2002-24 scan 3	Notoungulata					27.2411	66.9507	944	-8.7		-7.3
Arg2002-24 scan 4	Notoungulata					27.2411	66.9507	944	-9.2		-7.3
Arg-154a (nt)	Rodentia	Chinchillidae		M				826	-9.3	-2.6	
Arg-154a (nt)	Rodentia	Chinchillidae		M				826	-9.1	-2.5	
Arg-154a (tr)	Rodentia	Chinchillidae		M				826	-9.6	-1.8	
Arg-154b	Rodentia	Chinchillidae		M	2.0–4.5			826	-6.5	-2.3	
Arg-154b	Rodentia	Chinchillidae		M	8.0–10.5			826	-7.9	-2.8	
Arg-154c	Rodentia	Chinchillidae		M	medial			826	-6.8	-3.2	
Arg-154c	Rodentia	Chinchillidae		M	0.5–4.5			826	-8.6	-3.5	
Arg2002-25	Rodentia	Chinchillidae		incisor		27.2466	66.9560	800	-9.2	-5.8	
Arg2002-25 scan 1	Rodentia	Chinchillidae	*Lagostomus sp.*	incisor	0.5	27.2466	66.9560	800	-10.7		-11.2
Arg2002-25 scan 2	Rodentia	Chinchillidae	*Lagostomus sp.*	incisor	1.2	27.2466	66.9560	800	-11.5		-11.3
Arg2002-25 scan 3	Rodentia	Chinchillidae	*Lagostomus sp.*	incisor	1.9	27.2466	66.9560	800	-11.4		-11.2
Arg2002-25 scan 4	Rodentia	Chinchillidae	*Lagostomus sp.*	incisor	2.5	27.2466	66.9560	800	-11.5		-11.1
Arg2002-25 scan 5	Rodentia	Chinchillidae	*Lagostomus sp.*	incisor	3.1	27.2466	66.9560	800	-11.9		-10.8
Arg2002-25 scan 6	Rodentia	Chinchillidae	*Lagostomus sp.*	incisor	4.0	27.2466	66.9560	800	-11.8		-10.4

Table B.5: (*continued*)

Sample ID	Order	Family	Taxon	Tooth pos. [a]	Tooth mm [b]	Lat. °S	Lon. °W	Thick. m [c]	$\delta^{13}C$ PDB	$\delta^{18}O_{cvn}$ PDB	$\delta^{18}O_{las}$ PDB
Arg2002-25 scan 7	Rodentia	Chinchillidae	*Lagostomus sp.*	incisor	5.0	27.2466	66.9560	800	-11.4		-10.2
Arg2002-25 scan 8	Rodentia	Chinchillidae	*Lagostomus sp.*	incisor	6.2	27.2466	66.9560	800	-11.2		-10.0
Arg2002-25 scan 9	Rodentia	Chinchillidae	*Lagostomus sp.*	incisor	6.9	27.2466	66.9560	800	-11.0		-9.8
Arg2002-25 scan 10	Rodentia	Chinchillidae	*Lagostomus sp.*	incisor	8.2	27.2466	66.9560	800	-11.1		-9.9
Arg2002-42 scan 1	Rodentia			incisor		27.2467	66.9562	800	-9.9		-5.8
Arg2002-42 scan 2	Rodentia			incisor		27.2467	66.9562	800	-8.7		-5.1
Arg2002-42 scan 3	Rodentia			incisor		27.2467	66.9562	800	-8.6		-5.8
Arg2002-42 scan 4	Rodentia			incisor		27.2467	66.9562	800	-10.3		-8.4
Arg2001-24	indet.					27.2183	66.9184	790	-6.3	0.1	
Arg-152	Rodentia							760	-11.4	4.2	
Arg-152a	Rodentia			incisor				760	-9.2	0.6	
Arg-152b	Rodentia	Caviidae		molar	medial			760	-9.8	-1.5	
Arg-152b	Rodentia	Caviidae		molar	medial			760	-10.1	-0.2	
Arg-152c	Rodentia	Chinchillidae		molar	medial			760	-7.9	-3.1	
Arg2001-21 (nt)	Rodentia			molar		27.2194	66.9171	720	-3.9	-3.8	
Arg2001-21 (tr)	Rodentia			molar		27.2194	66.9171	720	-3.3	-1.9	
Arg2002-19 scan 1	Rodentia			incisor	3.0	27.2422	66.9452	692	-10.2		-10.5
Arg2002-19 scan 2	Rodentia			incisor	3.7	27.2422	66.9452	692	-10.3		-10.2
Arg2002-19 scan 3	Rodentia			incisor	4.4	27.2422	66.9452	692	-10.5		-10.3
Arg2002-19 scan 4	Rodentia			incisor	5.1	27.2422	66.9452	692	-11.6		-10.3
Arg2002-19 scan 5	Rodentia			incisor	5.7	27.2422	66.9452	692	-11.3		-9.9
Arg2002-19 scan 6	Rodentia			incisor	6.5	27.2422	66.9452	692	-12.4		-10.0
Arg2002-19 scan 7	Rodentia			incisor	7.3	27.2422	66.9452	692	-12.9		-10.0
Arg2002-19 scan 8	Rodentia			incisor	8.0	27.2422	66.9452	692	-13.3		-10.1
Arg2002-19 scan 9	Rodentia			incisor	8.7	27.2422	66.9452	692	-13.6		-10.1
Arg2002-19 scan 10	Rodentia			incisor	2.5	27.2422	66.9452	692	-10.5		-10.4
Arg2002-19 scan 11	Rodentia			incisor	0.8	27.2422	66.9452	692	-10.7		-10.2
Arg2001-22 (nt)	indet.					27.2194	66.9166	670	-10.2	-0.9	
Arg2001-22 (tr)	indet.					27.2194	66.9166	670	-10.7	0.2	
Arg2001-34 (nt)	Notoungulata					27.2202	66.9177	670	-6.0	-0.1	
Arg2001-34 (tr)	Notoungulata					27.2202	66.9177	670	-6.8	1.1	
Arg-148	Rodentia							629	-3.7	-3.6	

Table B.5: (*continued*)

Sample ID	Order	Family	Taxon	Tooth pos. [a]	Tooth mm [b]	Lat. °S	Lon. °W	Thick. m [c]	$\delta^{13}C$ PDB	$\delta^{18}O_{cvn}$ PDB	$\delta^{18}O_{las}$ PDB
Arg-148	Rodentia							629	-3.9	-3.7	
Arg2001-23a-a	indet.			fragment		27.2209	66.9169	628	-8.1	-0.7	
Arg2001-23a-b	indet.			fragment		27.2209	66.9169	628	-7.0	-0.6	
Arg2001-23a-c	indet.			fragment		27.2209	66.9169	628	-8.1	0.0	
ARG2007-PCQ707	indet.			molar	10.0	27.2193	66.9163	616	-7.8	0.2	
ARG2007-PCQ707	indet.			molar	30.0	27.2193	66.9163	616	-7.6	0.5	
Arg2001-12	Rodentia	Hydrochoeridae		incisor		27.2200	66.9164	614	-9.1	-3.5	
Arg2001-9	Notoungulata	Mesotheriidae				27.2199	66.9163	614	-8.5	-3.9	
Arg-136 scan 1	Notoungulata	Hegetotheriidae		rm3	1.8			604	-12.1		-10.2
Arg-136 scan 2	Notoungulata	Hegetotheriidae		rm3	1.3			604	-11.9		-10.6
Arg2002-50 scan 1	Notoungulata					27.2428	66.9428	600	-11.7		-11.4
Arg-133 n	Notoungulata	Hegetotheriidae		molar	0.5			591	-9.7	-4.6	
Arg-133 n	Notoungulata	Hegetotheriidae		molar	4.9			591	-9.6	-4.2	
Arg-133 n	Notoungulata	Hegetotheriidae		molar	7.2			591	-9.6	-4.1	
Arg-133 r	Rodentia	Echimyidae		incisor	medial			591	-10.4	-4.7	
Arg-132	Rodentia	Echimyidae		rm3	distal			591	-10.5	-4.2	
Arg-132 scan 1	Rodentia	Echimyidae		lm1	0.8			591	-11.6		-9.7
Arg-132 scan 2	Rodentia	Echimyidae		lm1	1.5			591	-11.3		-10.6
Arg-125a	Rodentia	Echimyidae		lm3	distal			591	-11.6	-4.4	
Arg-141	Rodentia	Chinchillidae	*Lagostomopsis sp.*	molar	medial			591	-9.4	-7.5	
Arg-123 (nt)	Notoungulata	Toxodontidae	*Xotodon sp.*	molar				580	-4.9	-0.5	
Arg-123 (nt)	Notoungulata	Toxodontidae	*Xotodon sp.*	molar				580	-4.9	0.5	
Arg-123 (tr)	Notoungulata	Toxodontidae	*Xotodon sp.*	molar				580	-4.9	0.2	
Arg-129	Notoungulata	Mesotheriidae	*Pseudotypotherium sp.*	molar				580	-8.7	0.8	
Arg-129-1 (nt)	Notoungulata	Mesotheriidae	*Pseudotypotherium sp.*	M1				580	-8.3	-1.3	
Arg-129-1 (tr)	Notoungulata	Mesotheriidae	*Pseudotypotherium sp.*	M1				580	-8.4	-1.4	
Arg-129-2	Notoungulata	Mesotheriidae	*Pseudotypotherium sp.*	M2				580	-8.8	-1.7	
Arg-129-3 (nt)	Notoungulata	Mesotheriidae	*Pseudotypotherium sp.*	M3				580	-8.8	0.6	
Arg-129-3 (tr)	Notoungulata	Mesotheriidae	*Pseudotypotherium sp.*	M3				580	-9.1	1.6	
Arg-121-p	Notoungulata	Mesotheriidae	*Pseudotypotherium sp.*	molar				577	-9.1	-2.5	
Arg-121-t (nt)	Notoungulata	Toxodontidae		molar				577	-9.2	-4.5	
Arg-121-t (tr)	Notoungulata	Toxodontidae		molar	distal			577	-9.5	-2.3	

Table B.5: (*continued*)

Sample ID	Order	Family	Taxon	Tooth pos. [a]	Tooth mm [b]	Lat. °S	Lon. °W	Thick. m [c]	$\delta^{13}C$ PDB	$\delta^{18}O_{cvn}$ PDB	$\delta^{18}O_{las}$ PDB
Arg-121 cementum.1 [f]	Notoungulata	Mesotheriidae		M	16–23			577	-8.5	-4.5	
Arg-121 cementum.1 [f]	Notoungulata	Mesotheriidae		M	16–23			577	-8.6	-4.6	
Arg-121 cementum.1 [f]	Notoungulata	Mesotheriidae		M	16–23			577	-8.6	-6.0	
Arg-121 cementum.2 [f]	Notoungulata	Mesotheriidae		M	16–23			577	-8.5	-6.1	
Arg-121 cementum.2 [f]	Notoungulata	Mesotheriidae		M	16–23			577	-8.5	-6.0	
Arg-121 (nt.1)	Notoungulata	Mesotheriidae		M	16–23			577	-9.9	-5.5	
Arg-121 (nt.1)	Notoungulata	Mesotheriidae		M	16–23			577	-9.9	-5.5	
Arg-121 (nt.1)	Notoungulata	Mesotheriidae		M	16–23			577	-9.9	-5.5	
Arg-121 (tr.1)	Notoungulata	Mesotheriidae		M	16–23			577	-9.9	-4.8	
Arg-121 (tr.1)	Notoungulata	Mesotheriidae		M	16–23			577	-9.9	-4.2	
Arg-121	Notoungulata	Mesotheriidae		M	0.5			577	-10.5	-4.4	
Arg-121	Notoungulata	Mesotheriidae		M	1.4			577	-10.4	-5.3	
Arg-121	Notoungulata	Mesotheriidae		M	2.3			577	-10.6	-5.3	
Arg-121	Notoungulata	Mesotheriidae		M	3.4			577	-10.8	-5.8	
Arg-121	Notoungulata	Mesotheriidae		M	4.5			577	-10.8	-5.7	
Arg-121	Notoungulata	Mesotheriidae		M	5.5			577	-11.0	-6.2	
Arg-121	Notoungulata	Mesotheriidae		M	7.6			577	-10.6	-6.8	
Arg-121	Notoungulata	Mesotheriidae		M	8.3			577	-10.4	-7.1	
Arg-121	Notoungulata	Mesotheriidae		M	9.3			577	-10.4	-7.4	
Arg-121	Notoungulata	Mesotheriidae		M	11.0			577	-10.1	-8.0	
Arg-121	Notoungulata	Mesotheriidae		M	16.1			577	-9.8	-7.5	
Arg-121	Notoungulata	Mesotheriidae		M	16.7			577	-9.7	-7.0	
Arg-121	Notoungulata	Mesotheriidae		M	17.7			577	-9.7	-6.8	
Arg-121	Notoungulata	Mesotheriidae		M	18.6			577	-9.7	-5.9	
Arg-121	Notoungulata	Mesotheriidae		M	19.7			577	-9.7	-5.5	
Arg-121	Notoungulata	Mesotheriidae		M	20.8			577	-9.8	-5.2	
Arg-121	Notoungulata	Mesotheriidae		M	21.8			577	-10.1	-4.9	
Arg-121	Notoungulata	Mesotheriidae		M	23.1			577	-10.0	-4.8	
Arg-121	Notoungulata	Mesotheriidae		M	32.2			577	-9.9	-4.3	
Arg-121	Notoungulata	Mesotheriidae		M	33.0			577	-9.9	-4.3	
Arg-121	Notoungulata	Mesotheriidae		M	33.9			577	-9.9	-4.1	
Arg-121	Notoungulata	Mesotheriidae		M	34.5			577	-9.7	-4.5	

Table B.5: (*continued*)

Sample ID	Order	Family	Taxon	Tooth pos. [a]	Tooth mm [b]	Lat. °S	Lon. °W	Thick. m [c]	$\delta^{13}C$ PDB	$\delta^{18}O_{cvn}$ PDB	$\delta^{18}O_{las}$ PDB
Arg-121	Notoungulata	Mesotheriidae		M	36.0			577	-9.8	-4.8	
Arg-121	Notoungulata	Mesotheriidae		M	36.9			577	-9.9	-4.3	
Arg-121	Notoungulata	Mesotheriidae		M	37.7			577	-9.9	-4.6	
Arg-121	Notoungulata	Mesotheriidae		M	38.6			577	-10.0	-5.0	
Arg-121	Notoungulata	Mesotheriidae		M	39.6			577	-9.8	-4.7	
Arg-121	Notoungulata	Mesotheriidae		M	40.3			577	-9.8	-4.7	
Arg-121	Notoungulata	Mesotheriidae		M	41.2			577	-10.0	-4.8	
Arg-121	Notoungulata	Mesotheriidae		M	12.7			577	-10.2	-7.8	
Arg-121	Notoungulata	Mesotheriidae		M	14.8			577	-9.8	-7.5	
Arg-121	Notoungulata	Mesotheriidae		M	15.7			577	-10.0	-7.6	
Arg-121	Notoungulata	Mesotheriidae		M	24.1			577	-10.3	-4.2	
Arg-121	Notoungulata	Mesotheriidae		M	24.9			577	-10.0	-4.5	
Arg-121	Notoungulata	Mesotheriidae		M	26.3			577	-9.7	-4.7	
Arg-121	Notoungulata	Mesotheriidae		M	27.9			577	-9.9	-4.3	
Arg-121	Notoungulata	Mesotheriidae		M	29.0			577	-10.0	-4.0	
Arg-121	Notoungulata	Mesotheriidae		M	30.5			577	-9.9	-4.5	
Arg-139	indet.			molar				577	-10.0	-4.7	
Arg-291 bhp	Rodentia	Caviidae		molar				558	-9.5	-0.5	
Arg-291 bhp	Rodentia	Caviidae		molar				558	-9.4	-0.3	
Arg-292	Notoungulata	Toxodontidae		molar	0–2.7			555	-8.0	-4.2	
Arg-292	Notoungulata	Toxodontidae		fragment	4.0			555	-8.6	-3.6	
Arg-292	Notoungulata	Toxodontidae		fragment	4.5–7.4			555	-8.9	-3.2	
Arg-292	Notoungulata	Toxodontidae		fragment	8.9			555	-8.6	-3.7	
Arg-292 cementum [f]	Notoungulata	Toxodontidae						555	-8.0	-4.7	
Arg-292 cementum [f]	Notoungulata	Toxodontidae						555	-7.5	-4.7	
Arg-127	Rodentia			m3				555	-7.6	-1.0	
Arg-293 (nt)	Notoungulata	Toxodontidae		fragment				515	-9.4	-3.0	
Arg-293 (tr)	Notoungulata	Toxodontidae		fragment				515	-9.0	-2.4	
Arg-298	Notoungulata	Hegetotheriidae		molar	distal			474	-7.2	-5.1	
Arg-278a	Rodentia	Dinomyidae		molar	prox			470	-10.0	-4.7	
Arg-278b	Notoungulata	Hegetotheriidae		rm3	distal			470	-8.8	-4.2	
Arg-278b cementum [f]	Notoungulata	Hegetotheriidae		rm3				470	-9.7	-5.5	

Table B.5: (*continued*)

Sample ID	Order	Family	Taxon	Tooth pos. [a]	Tooth mm [b]	Lat. °S	Lon. °W	Thick. m [c]	$\delta^{13}C$ PDB	$\delta^{18}O_{cvn}$ PDB	$\delta^{18}O_{las}$ PDB
Arg-280-1 dentin [f]	Litopterna	Brachytherium?						470	-8.6	-4.6	
Arg-280-1 en	Litopterna	Brachytherium?						470	-10.3	-1.7	
Arg-280-2 dentin [f]	Notoungulata							470	-8.3	-5.3	
Arg-280-2 en	Notoungulata							470	-8.9	0.1	
Arg-280-51	indet.							470	-10.1	-2.2	
Arg-274	Rodentia	Dinomyidae		molar	2.3–4.0			463	-9.2	-5.0	
Arg-274	Rodentia	Dinomyidae		molar	5.5–8.0			463	-10.6	-5.7	
Arg-274	Rodentia	Dinomyidae		molar	10.0–12.5			463	-9.9	-3.0	
Arg-297 (nt)	Rodentia	Dinomyidae		molar	distal			452	-10.7	-1.2	
Arg-297 (tr)	Rodentia	Dinomyidae		molar	distal			452	-10.9	-0.4	
Arg-297	Notoungulata		Typotheria	incisor	1.2			452	-10.7	-6.6	
Arg-297	Notoungulata		Typotheria	incisor	2.5			452	-11.2	-7.0	
Arg-297	Notoungulata		Typotheria	incisor	4.2			452	-10.9	-6.6	
Arg-297	Notoungulata		Typotheria	incisor	5.9			452	-10.9	-7.0	
Arg-297	Notoungulata		Typotheria	incisor	7.0			452	-11.1	-7.1	
Arg-297	Notoungulata		Typotheria	incisor	8.1			452	-11.2	-7.1	
Arg-297	Notoungulata		Typotheria	incisor	10.0			452	-10.9	-5.7	
Arg-297	Notoungulata		Typotheria	incisor	11.4			452	-11.0	-6.1	
Arg-297	Notoungulata		Typotheria	incisor	13.3			452	-11.3	-6.2	
Arg-297	Notoungulata		Typotheria	incisor	14.0			452	-10.9	-6.1	
Arg-297	Notoungulata		Typotheria	incisor	15.4			452	-10.9	-5.8	
Arg-297	Notoungulata		Typotheria	incisor	16.7			452	-10.7	-5.6	
Arg-297	Notoungulata		Typotheria	incisor	17.8			452	-10.6	-5.4	
Arg2002-46 scan 1	Rodentia	Caviidae		molar		27.2465	66.9286	360	-13.1		-6.7
Arg2002-46 scan 2	Rodentia	Caviidae		molar		27.2465	66.9286	360	-13.1		-7.3
Arg2002-46	Rodentia	Caviidae		molar		27.2465	66.9286	360	-9.7	-6.9	
Arg-103	Rodentia	Caviidae		molar				350	-3.7	-2.0	
Arg-103 scan 1	Rodentia	Caviidae		molar	4.6			350	-6.8		-8.7
Arg-103 scan 2	Rodentia	Caviidae		molar	4.5			350	-6.2		-8.9
Arg-103 scan 3	Rodentia	Caviidae		molar	3.3			350	-5.8		-8.8
Arg-103 scan 4	Rodentia	Caviidae		molar	1.6			350	-6.7		-9.2
Arg-103 scan 5	Rodentia	Caviidae		molar	0.8			350	-7.0		-8.9

Table B.5: (*continued*)

Sample ID	Order	Family	Taxon	Tooth pos. [a]	Tooth mm [b]	Lat. °S	Lon. °W	Thick. m [c]	$\delta^{13}C$ PDB	$\delta^{18}O_{cvn}$ PDB	$\delta^{18}O_{las}$ PDB
Arg-103 scan 6	Rodentia	Caviidae		molar	2.4			350	-6.4		-8.3
Arg2002-57	Rodentia			incisor		27.2452	66.9289	340	-11.3		-4.3
Arg2002-57	Rodentia			incisor		27.2452	66.9289	340	-11.7		-4.2
Arg2002-57	Rodentia			incisor		27.2452	66.9289	340	-11.8		-3.7
Arg2002-60a	Rodentia			m		27.2417	66.9265	310	-10.4	-3.9	
Arg2002-60b	Rodentia			m		27.2417	66.9265	310	-10.1	-4.0	
Arg-46	Rodentia	Caviidae		m1				291	-8.4	-4.9	
Arg-50 dent [f]	Xenartha indet.			m	distal			290	-7.2	-4.3	
Arg-49	Rodentia	Dinomyidae		incisor	0.6			290	-10.3	-4.8	
Arg-49	Rodentia	Dinomyidae		incisor	1.7			290	-10.0	-4.5	
Arg-49	Rodentia	Dinomyidae		incisor	2.9			290	-10.3	-4.4	
Arg-49	Rodentia	Dinomyidae		incisor	3.8			290	-10.5	-4.7	
Arg-49	Rodentia	Dinomyidae		incisor	4.9			290	-10.3	-5.1	
Arg-49	Rodentia	Dinomyidae		incisor	5.8			290	-9.4	-4.3	
Arg-49	Rodentia	Dinomyidae		incisor	6.8			290	-10.3	-4.9	
Arg-49	Rodentia	Dinomyidae		incisor	7.8			290	-10.0	-5.3	
Arg-49	Rodentia	Dinomyidae		incisor	8.7			290	-10.4	-4.8	
Arg-49	Rodentia	Dinomyidae		incisor	9.9			290	-9.7	-5.0	
Arg-49	Rodentia	Dinomyidae		incisor	11.2			290	-10.1	-4.9	
Arg-49	Rodentia	Dinomyidae		incisor	12.3			290	-10.1	-4.6	
Arg-49	Rodentia	Dinomyidae		incisor	13.4			290	-9.9	-5.5	
Arg-49	Rodentia	Dinomyidae		incisor	14.3			290	-9.6	-5.7	
Arg-49	Rodentia	Dinomyidae		incisor	15.3			290	-9.4	-5.2	
Arg2002-37 scan 1	Rodentia					27.2429	66.9262	286	-9.5		-9.3
Arg2002-37 scan 2	Rodentia					27.2429	66.9262	286	-9.6		-10.4
Arg2002-37 scan 3	Rodentia					27.2429	66.9262	286	-9.8		-11.0
Arg2002-37 scan 4	Rodentia					27.2429	66.9262	286	-9.5		-9.7
Arg-45	indet.			molar				278	-8.0	-1.0	
Arg2002-54 scan 1	Rodentia			incisor		27.2425	66.9259	274	-13.5		-8.6
Arg2002-54 scan 2	Rodentia			incisor		27.2425	66.9259	274	-13.6		-8.3
Arg2002-54 scan 3	Rodentia			incisor		27.2425	66.9259	274	-12.7		-8.4
Arg2002-47 scan 1	Rodentia	Caviidae		molar		27.2424	66.9255	270	-8.2		-10.2

Table B.5: (*continued*)

Sample ID	Order	Family	Taxon	Tooth pos. [a]	Tooth mm [b]	Lat. °S	Lon. °W	Thick. m [c]	$\delta^{13}C$ PDB	$\delta^{18}O_{cvn}$ PDB	$\delta^{18}O_{las}$ PDB
Arg2002-47 scan 2	Rodentia	Caviidae		molar		27.2424	66.9255	270	-9.1		-10.1
Arg2002-47 scan 3	Rodentia	Caviidae		molar		27.2424	66.9255	270	-10.7		-11.7
Arg2002-43 scan 1	Notoungulata	Hegetotheriidae				27.2426	66.9256	270	-9.0		-8.6
Arg2002-43 scan 2	Notoungulata	Hegetotheriidae				27.2426	66.9256	270	-8.4		-9.4
Arg2002-32-5/13/05.1	Rodentia	Octodontidae		incisor		27.2422	66.9255	270	-10.8	-3.9	
Arg2002-32-11/13/05.1	Rodentia	Octodontidae		incisor		27.2422	66.9255	270	-11.4	-1.7	
Arg2002-32-11/18/05.1	Rodentia	Octodontidae		incisor		27.2422	66.9255	270	-12.0	-0.5	
Arg2002-32 scan 1	Rodentia	Octodontidae		incisor		27.2422	66.9255	270	-12.6		-8.1
Arg2002-32 scan 2	Rodentia	Octodontidae		incisor		27.2422	66.9255	270	-11.7		-7.6
Arg2002-32 scan 3	Rodentia	Octodontidae		incisor		27.2422	66.9255	270	-11.3		-6.9
Arg2002-32 scan 4	Rodentia	Octodontidae		incisor		27.2422	66.9255	270	-11.7		-6.3
Arg2002-32 scan 5	Rodentia	Octodontidae		incisor		27.2422	66.9255	270	-10.0		-9.2
Arg-91	Rodentia	Caviidae		m	3.3			258	-9.5	-5.6	
Arg-73	Notoungulata			molar				253	-5.7	-3.9	
Arg-47	Rodentia	Caviidae		rm3	distal			253	-9.6	-5.5	
Arg-47	Rodentia	Caviidae		lm3	distal			253	-8.6	-3.4	
Arg-47	Rodentia	Caviidae		lm3	distal			253	-8.4	-5.3	
Arg-72 scan 1	Rodentia	Caviidae		molar	4.1			252	-11.1		-13.8
Arg-72 scan 2	Rodentia	Caviidae		molar	3.1			252	-11.2		-14.5
Arg-72 scan 3	Rodentia	Caviidae		molar	2.6			252	-11.4		-14.8
Arg-72 scan 4	Rodentia	Caviidae		molar	1.1			252	-11.6		-13.5
Arg-104 sah	Rodentia	Chinchillidae	*Lagostomus sp.*	rm2				250	-7.3	-4.7	
Arg-104 bhp	Rodentia	Chinchillidae	*Lagostomus sp.*	rm2				250	-6.0	-4.7	
Arg-106	Rodentia	Caviidae		molar				250	-5.6	-1.4	
Arg-106 scan 1	Rodentia	Caviidae		molar	2.8			250	-8.6		-8.8
Arg-106 scan 2	Rodentia	Caviidae		molar	2.1			250	-8.9		-9.2
Arg-106 scan 3	Rodentia	Caviidae		molar	1.4			250	-8.8		-9.3
Arg-84 dent	Xenartha	Megatheriidae						250	-9.7	-5.3	
Arg-82 bhp	Rodentia	Dinomyidae	*Tetrastylus sp.*	m	16.0			250	-8.5	-3.5	
Arg-82 bhp	Rodentia	Dinomyidae	*Tetrastylus sp.*	m	16.0			250	-8.8	-5.6	
Arg-82 bulk (nt.1)	Rodentia	Dinomyidae	*Tetrastylus sp.*	incisor				250	-9.4	-4.6	
Arg-82 bulk (tr.1)	Rodentia	Dinomyidae	*Tetrastylus sp.*	incisor				250	-9.6	-3.8	

Table B.5: (*continued*)

Sample ID	Order	Family	Taxon	Tooth pos. [a]	Tooth mm [b]	Lat. °S	Lon. °W	Thick. m [c]	$\delta^{13}C$ PDB	$\delta^{18}O$cvn PDB	$\delta^{18}O$las PDB
Arg-82 bulk (tr.1)	Rodentia	Dinomyidae	*Tetrastylus sp.*	incisor				250	-9.4	-4.1	
Arg-82.las.bulk	Rodentia	Dinomyidae	*Tetrastylus sp.*	incisor				250	-8.7	-6.6	
Arg-82.las.1	Rodentia	Dinomyidae	*Tetrastylus sp.*	incisor				250	-10.5	-5.9	
Arg-82.las.1	Rodentia	Dinomyidae	*Tetrastylus sp.*	incisor				250	-10.6	-5.9	
Arg-82.las.1	Rodentia	Dinomyidae	*Tetrastylus sp.*	incisor				250	-10.6	-6.0	
Arg-82.las.2	Rodentia	Dinomyidae	*Tetrastylus sp.*	incisor				250	-10.6	-6.2	
Arg-82.las.3	Rodentia	Dinomyidae	*Tetrastylus sp.*	incisor				250	-8.5	-7.1	
Arg-82	Rodentia	Dinomyidae	*Tetrastylus sp.*	incisor	0.8			250	-8.6	-5.0	
Arg-82	Rodentia	Dinomyidae	*Tetrastylus sp.*	incisor	2.2			250	-8.8	-5.4	
Arg-82	Rodentia	Dinomyidae	*Tetrastylus sp.*	incisor	3.6			250	-10.2	-6.7	
Arg-82	Rodentia	Dinomyidae	*Tetrastylus sp.*	incisor	4.8			250	-10.5	-6.6	
Arg-82	Rodentia	Dinomyidae	*Tetrastylus sp.*	incisor	6.5			250	-10.3	-5.4	
Arg-82	Rodentia	Dinomyidae	*Tetrastylus sp.*	incisor	8.6			250	-10.4	-6.5	
Arg-82	Rodentia	Dinomyidae	*Tetrastylus sp.*	incisor	10.1			250	-10.5	-6.4	
Arg-82	Rodentia	Dinomyidae	*Tetrastylus sp.*	incisor	12.4			250	-10.2	-6.4	
Arg-82	Rodentia	Dinomyidae	*Tetrastylus sp.*	incisor	14.3			250	-9.6	-6.4	
Arg-82	Rodentia	Dinomyidae	*Tetrastylus sp.*	incisor	15.8			250	-10.1	-5.8	
Arg-82	Rodentia	Dinomyidae	*Tetrastylus sp.*	incisor	17.4			250	-10.1	-4.6	
Arg-82	Rodentia	Dinomyidae	*Tetrastylus sp.*	incisor	18.9			250	-10.1	-4.6	
Arg2002-58	Rodentia	Chinchillidae		molar		27.2432	66.925	230	-9.0		-6.7
Arg2002-58	Rodentia	Chinchillidae		molar		27.2432	66.925	230	-10.3		-6.2
Arg2002-58	Rodentia	Chinchillidae		molar		27.2432	66.925	230	-9.2		-6.8
Arg2002-53-5/13/05.1	Notoungulata			molar		27.2426	66.9256	230	-11.4	4.8	
Arg2002-53-11/13/05.1	Notoungulata			molar		27.2426	66.9256	230	-9.9	0.6	
Arg2002-53-11/18/05.1	Notoungulata			molar		27.2426	66.9256	230	-10.6	2.9	
Arg2002-53 scan 2	Notoungulata			molar		27.2426	66.9256	230	-10.5		0.5
Arg2002-53 scan 3	Notoungulata			molar		27.2426	66.9256	230	-11.1		1.7
Arg2002-53 scan 4	Notoungulata			molar		27.2426	66.9256	230	-11.3		1.0
Arg2002-44a	Rodentia	Chinchillidae	*Lagostomus sp.*	incisor		27.2444	66.9243	220	-9.8	-2.3	
Arg2002-44b	Rodentia	Chinchillidae	*Lagostomus sp.*	molar		27.2444	66.9243	220	-9.8	-3.9	
Arg2002-33-5/13/05.1	Rodentia			fragment		27.2444	66.9243	220	-10.4	-6.4	
Arg2002-33-5/13/05.2	Rodentia			fragment		27.2444	66.9243	220	-10.6	-5.2	

Table B.5: (*continued*)

Sample ID	Order	Family	Taxon	Tooth pos. [a]	Tooth mm [b]	Lat. °S	Lon. °W	Thick. m [c]	$\delta^{13}C$ PDB	$\delta^{18}O_{cvn}$ PDB	$\delta^{18}O_{las}$ PDB
Arg2002-33-11/13/05.1	Rodentia			fragment		27.2444	66.9243	220	-9.9	-6.0	
Arg2002-33-11/13/05.2	Rodentia			fragment		27.2444	66.9243	220	-10.0	-6.0	
Arg2002-33-11/18/05.1	Rodentia			fragment		27.2444	66.9243	220	-10.3	-5.5	
Arg2002-33-11/18/05.2	Rodentia			fragment		27.2444	66.9243	220	-10.4	-5.7	
Arg2002-33 scan 1	Rodentia			fragment		27.2444	66.9243	220	-10.4		-10.3
Arg2002-33 scan 2	Rodentia			fragment		27.2444	66.9243	220	-10.0		-10.7
Arg2002-33 scan 1	Rodentia			fragment		27.2444	66.9243	220	-10.8		-11.2
Arg2002-33 scan 2	Rodentia			fragment		27.2444	66.9243	220	-10.3		-11.0
Arg2002-33 scan 3	Rodentia			fragment		27.2444	66.9243	220	-10.8		-10.8
Arg2002-33 scan 4	Rodentia			fragment		27.2444	66.9243	220	-10.7		-10.7
Arg2002-33 scan 5	Rodentia			fragment		27.2444	66.9243	220	-10.7		-11.1
Arg-77	indet.							182	-8.3	-6.7	
Arg2001-CH126	Rodentia					27.2130	66.9022	182	-9.4	-4.1	
Arg2001-CH126	Rodentia					27.2130	66.9022	182	-9.5	-4.2	
Arg-63	Notoungulata			molar				132	-8.5	0.7	
Arg-063a-1 (1hr) [e]	Notoungulata							132	-8.9	1.2	
Arg-063a-1 (6hr) [e]	Notoungulata							132	-8.6	1.4	
Arg-063a-1 [e]	Notoungulata							132	-8.9	1.0	
Arg-063b-1 dent [e, f]	Notoungulata							132	-8.6	-4.0	
Arg2002-34 [f]	Xenarthra	Dasypodidae				27.2430	66.9222	125	-8.9	1.1	
Arg2002-35	Rodentia			incisor		27.2430	66.9222	125	-8.1	-2.7	
Arg-62-1	indet.			fragment				123	-5.3	1.1	
Arg-62-2	indet.			fragment				123	-11.8	-1.8	
Arg-68a	indet.							120	-8.8	0.9	
Arg-68b	Rodentia	Caviidae						120	-10.4	-2.9	
Arg2002-36	Rodentia	Chichillidae		incisor	prox	27.2434	66.9219	115	-10.4	-2.8	
Arg2002-36	Rodentia	Chichillidae		incisor	med	27.2434	66.9219	115	-10.3	-2.4	
Arg2001-TUC110-1 [g]	Notoungulata	Toxodontidae		i3	22.4	27.10	66.82	~250	-6.4	-4.0	
Arg2001-TUC110-2 [g]	Notoungulata	Toxodontidae		i3	16.8	27.10	66.82	~250	-6.2	-4.7	
Arg2001-TUC110-3 [g]	Notoungulata	Toxodontidae		i3	11.2	27.10	66.82	~250	-6.4	-4.9	
Arg2001-TUC110-4 [g]	Notoungulata	Toxodontidae		i3	5.6	27.10	66.82	~250	-7.1	-4.4	
Arg2001-TUC111 [g]	Litopterna	Proterotheriidae	*Diadiaphorus sp.*	lM3		27.10	66.82	~250	-7.9	-3.1	

Table B.5: (*continued*)

Sample ID	Order	Family	Taxon	Tooth pos. [a]	Tooth mm [b]	Lat. °S	Lon. °W	Thick. m [c]	$\delta^{13}C$ PDB	$\delta^{18}Ocvn$ PDB	$\delta^{18}Olas$ PDB
Arg2001-TUC112-1 [g]	Rodentia	Dinomyidae		incisor	proximal			~250	-7.8	-4.4	
Arg2001-TUC112-2 [g]	Rodentia	Dinomyidae		incisor	medial			~250	-7.4	-3.2	
Arg2001-TUC112-3 [g]	Rodentia	Dinomyidae		incisor	distal			~250	-7.4	-2.8	
Arg2001-TUC113 [g]	Rodentia			incisor				~250	-9.6	-4.1	
Arg2001-TUC114 [g]	Rodentia			molar				~250	-8.7	-4.4	
Arg2001-TUC115a [g]	Rodentia			molar				~250	-9.5	-5.1	
Arg2001-TUC115b [g]	Rodentia			molar				~250	-8.9	-4.0	
Arg2001-TUC116a [g]	indet.			molar				~250	-8.9	-4.5	
Arg2001-TUC116b [g]	indet.			molar				~250	-9.8	-5.2	
Arg2001-TUC116c [g]	indet.			incisor				~250	-10.2	-5.2	
Arg2001-TUC116d [g]	indet.			incisor				~250	-11.0	-4.7	

Note: Analytical methods are discussed in Chapter 2.

[a] Tooth position specified as follows: r, right; l, left; m, molar; i, incisor where upper and lowercase latters refer to the maxillar and mandibular teeth, r
Isolated, but identifiable teeth with unknown position are not abbreviated.

[b] Measured as distance from the cervical margin.

[c] Stratigraphic height above the base of the section as defined in Table 2.1 and Table A.5.

[d] Enamel powders for which treated (tr) and not treated (nt) comparisons were conducted; samples without notation were not treated prior to analysis

[e] Data previously reported in Latorre et al., 1997; $\delta^{18}O$ values recalculated using the equations presented in Passey et al. (2007).

[f] Not tooth enamel, excluded from all paleocologic analyses.

[g] Sampled at Insituto Miguel Lillo (Universidad Nacional de Tucumán); stratigraphic level approximate. Provenance documented as Chiquimil Forma
Data included in Figure 2.4 and Table 2.2, but excluded from stratigraphic analysis for Figure 2.8.

REFERENCES

Allen, P.A., Allen, J.R., 2005. Basin Analysis: Principles and Applications. Blackwell Publishing, Oxford, UK, 2nd edition, 549 pp.

Allmendinger, R.W., 1986. Tectonic development, southeastern border of the Puna Plateau, northwestern Argentine Andes. Geological Society of America Bulletin 97, 1070–1082.

Allmendinger, R.W., Gubbels, T., 1996. Pure and simple shear plateau uplift, Altiplano-Puna, Argentina and Bolivia. Tectonophysics 259, 1–13.

Allmendinger, R.W., Ramos, V.A., Jordan, T.E., Palma, M., Isacks, B.L., 1983. Paleogeography and Andean structural geometry, northwest Argentina. Tectonics 2, 1–16.

Allmendinger, R.W., Jordan, T.E., Kay, S.M., Isacks, B.L., 1997. The evolution of the Altiplano-Puna plateau of the central Andes. Annual Review of Earth and Planetary Sciences 25, 747–787.

Alonso, R.N., Jordan, T.E., Tabbutt, K.T., Vandervoort, D.S., 1991. Giant evaporite belts of the Neogene central Andes. Geology 19, 401–404.

Amundson, R., Chadwick, O., Kendall, C., Wang, Y., DeNiro, M., 1996. Isotopic evidence for shifts in atmospheric circulation patterns during the late Quaternary in mid-North America. Geology 24, 23–26.

Arnosio, M., Becchio, R., Viramonte, J., Groppelli, J., Norini, G., Corazzato, C., 2005. Geología del Complejo Volcánico Cerro Blanco (26° 45′ S – 67° 45′ W), Puna Austral. Proceedings of the XVI Congreso Geológico Argentino 1, 851–855.

Arnosio, M., Becchio, R., Viramonte, J.G., de Silva, S., Viramonte, J.M., 2008. Geochronologia e isotopia del complejo volcanico Cerro Blanco: Un sistema de calderas cuaternario (73–12 ka) en los Andes Centrales del Sur. Proceedings of the XVII Congreso Geológico Argentino 1, 134–135.

Balasse, M., 2002. Reconstructing dietary and environmental history from enamel isotopic analysis: Time resolution of intra-tooth sequential sampling. International Journal of Osteoarchaeology 12, 155–165.

Bangs N.L., Cande S.C., 1997. Episodic development of a convergent margin inferred from structures and processes along the southern Chile margin. Tectonics 16, 489–503

Banner, J.L., Hanson, G.N., 1990. Calculation of simultaneous isotopic and trace element variations during rock-water interaction with applications to carbonate diagenesis. Geochimica Cosmochima Acta 54, 3123–3137.

Barnes, J.B., Ehlers, T.A., 2009. End member models for Andean Plateau uplift. Earth-Science Reviews 97, 117–144.

Beck, S.L., Zandt, G., 2002. The nature of orogenic crust in the central Andes. Journal of Geophysical Research 107, B10, 2230.

Beck, S., Zandt, G., Myers, S., Wallace, T., Silver, R., Drake, L., 1996. Crustal-thickness variations in the central Andes. Geology 24, 407–410.

Behrensmeyer, A.K., Quade, J., Cerling, T.E., Kappelman, J., Khan, I.I., Copeland, P., Roe, L., Hicks, J., Stubblefield, P., Willis, B.J., Latorre, C., 2007. The structure and rate of late Miocene expansion of C_4 plants: Evidence from lateral variation in stable isotopes in paleosols of the Siwalik Group, northern Pakistan. Geological Society of America Bulletin 119, 1486–1505.

Bershaw, J., Garzione, C.N., Higgins, P., MacFadden, B.J., Anaya, F., Alvarenga, H., 2010. Spatial-temporal changes in Andean plateau climate and elevation from stable isotopes of mammal teeth. Earth and Planetary Science Letters 289, 530–538.

Black, C.C., Osmond, C.B., 2003. Crassulacean acid metabolism photosynthesis: 'working the night shift'. Photosynthesis Research 76, 329–341.

Bookhagen, B., Strecker, M.R., 2008, Orographic barriers, high-resolution TRMM rainfall, and relief variations along the eastern Andes: Geophysical Research Letters 35, L06403.

Bossi, G.E., Villanueva García, A., Carrión, M.H., Palma, R.M., Díaz, J.I., 1984. El Grupo Santa Maria en la Quebrada de Amaicha (depto. Tafí, provincia de Tucumán. IX Congreso Geológico Argentino, Bariloche, Argentina, Actas I, 124–141.

Bossi, G.E., Gariloff, I.J.C., Esteban, G., 1998. Terciario: Estratigrafía, bioestratigrafía y paleogeografía in Gianfrancisco et al., eds, Geología de Tucumán. Tucumán, Argentina, Colegio de Graduados en Ciencias Geológicas de Tucumán, p. 87–108.

Bowen, G.J., Beerling, D.J., Koch, P.L., Zachos, J.C., Quattlebaum, T., 2005. A humid climate state during the Palaeocene/Eocene thermal maximum. Nature 432, 495–499.

Breecker, D.O., Sharp, Z.D., McFadden, L.D., 2009. Seasonal bias in the formation and stable isotopic composition of pedogenic carbonate in modern soils from central New Mexico, USA. Geological Society of America Bulletin 121, 630–640.

Butler, R.F., Marshall, L.G., Drake, R.E. , Curtis, G.H., 1984. Magnetic polarity stratigraphy and ^{40}K-^{40}Ar dating of late Miocene and early Pliocene continental deposits, Catamarca Province, NW Argentina. Journal of Geology 92, 623–636.

Bywater-Reyes, S. V., 2009. Tectonic and climatic evolution of the Angastaco basin (25°-26°S, Eastern Cordillera, NW Argentina. M.S. thesis, Department of Geology and Geophysics, University of Wyoming, 155 pp.

Bywater-Reyes, S., Carrapa, B., Clementz, M., Schoenbohm, L., 2010. Effect of late Cenozoic aridification on sedimentation in the Eastern Cordillera of northwest Argentina (Angastaco basin). Geology 38, 235–238.

Cabido, M., Ateca, N., Astegiano, M.E., Anton, A.M., 1997. Distribution of C_3 and C_4 grasses along an altitudinal gradient in Central Argentina. Journal of Biogeography, 24, 197–204.

Carlier, G., Lorand, J.P., Liégeois, J.P., Fornari, M., Soler, P., Carlotto, V., Cárdenas, J., 2005. Potassic-ultrapotassic mafic rocks delineate two lithospheric mantle blocks beneath the southern Peruvian Altiplano. Geology 33, 601–604.

Carrapa, B., Adelman, D, Hilley, G.E., Mortimer, E., Sobel, E.R., Strecker, M.R., 2005. Oligocene range uplift and development of plateau morphology in the southern central Andes. Tectonics 24,TC4011, doi:10.1029/2004TC001762.

Carrapa, B., Strecker, M.R., Sobel, E.R., 2006. Cenozoic orogenic growth in the Central Andes: Evidence from sedimentary rock provenance and apatite fission track thermochronology in the Fiambalá Basin, southernmost Puna Plateau margin (NW Argentina). Earth and Planetary Science Letters 247, 82–100.

Carrapa, B., Hauer, J., Schoenbohm, L., Strecker, M.R., Schmitt, A.K., Villanueva, A., Gomez, J.S., 2008. Dynamics of deformation and sedimentation in the northern Sierras Pampeanas: An integrated study of the Neogene Fiambalá basin, NW Argentina. Geological Society of America Bulletin 120, 1518–1543.

Carrapa. B., Trimble, J.D., Stockli, D.F., in press. Patterns and timing of exhumation and deformation in the Eastern Cordillera of NW Argentina revealed by (U-Th)/He thermochronology. Tectonics, doi:10.1029/2010TC002707.

Carroll, A.R., Chetel, L.M., Smith, M.E., 2006. Feast to famine: Sediment supply control on Laramide basin fill. Geology 34, 197–200.

Cerling, T.E., 1984. The stable isotopic composition of modern soil carbonate and its relationship to climate. Earth and Planetary Science Letters 71, 229–240.

Cerling, T.E., 1992. Development of grasslands and savannas in East Africa during the Neogene. Palaeogeography Palaeoclimatology Palaeoecology. 97, 241–247.

Cerling, T.E., Quade, J., 1993. Stable carbon and oxygen isotopes in soil carbonates. In: Swart, P.K., Lohmann, K.C., McKenzie, J.A., Savin, S. (Eds.), Climate Change in Continental Isotopic Records Monograph 78. American Geophysical Union, Washington D.C., pp. 217–231.

Cerling, T.E., Harris, J.M., 1999. Carbon isotope fractionation between diet and bioapatite in ungulate mammals and implications for ecological and paleoecological studies. Oecologia 120, 347–363.

Cerling, T.E., Quade, J., Wang, Y, Bowman, J.R., 1989. Carbon isotopes in soils and palaeosols as paleoecologic indicators. Nature 341, 138–139.

Cerling, T.E., Solomon, D.K., Quade, J., Bowman, J.R., 1991. On the isotopic composition of carbon in soil carbon dioxide. Geochimica Cosmochima Acta 55, 3403–3406.

Cerling, T.E., Harris, J.M., MacFadden, B.J., Leakey, M.G., Quade, J., Eisenmann, V., Ehleringer, J.R., 1997. Global vegetation change through the Miocene/Pliocene boundary. Nature 389, 153–158.

Cerling, T.E., Harris, J.M., Leakey, M.G., Passey, B.H., Levin, N.E., 2010. Stable carbon and oxygen isotopes in East African mammals: modern and fossil. In: Werdelin, L. and Sanders W. (Eds.), Cenozoic Mammals of East Africa. University of California Press, Berkeley, pp. 941–952. ISBN 978-0-520-25721-4.

Chmielowski, J., Zandt, G., Haberland, C., 1999. The Central Andean Altiplano-Puna Magma Body. Geophysical Research Letters 26, 783–786.

Clyde, W. C., Sheldon, N. D., Koch, P. L., Gunnell, G. F., Bartels, W. S. 2001. Linking the Wasatchian-Bridgerian boundary to the Global Cenozoic Climate Optimum: new magnetostratigraphic and isotopic results from South Pass, Wyoming. Palaeogeography Palaeoclimatology Palaeoecology 167, 175–199.

Coira, B., Kay, S.M., Viramonte, J. 1993. Upper Cenozoic magmatic evolution of the Argentine Puna—A model for changing subduction geometry. International Geology Review 35, 677–720.

Coughlin, T.J., O'Sullivan, P.B., Kohn, B.P., Holcombe, R.J., 1998. Apatite fission-track thermochronology of the Sierras Pampeanas, central western Argentina: Implications of the mechanism of plateau uplift in the Andes. Geology 26, 999–1002.

Coutand, I., Carrapa, B., Deeken, A., Schmitt, A.K., Sobel, E.R., Strecker, M.R., 2006. Propagation of orographic barriers along an active range front: insights from sandstone petrography and detrital apatite fission-track thermochronology in the intramontane Angastaco basin, NW Argentina. Basin Research 18, 1–26.

Croft, D.A., Flynn, J.J., Wyss, A.R., 2004. Notoungulata and Litopterna of the early Miocene Chucal Fauna, northern Chile. Fieldiana Geology 50, 1–52.

Dansgaard, W., 1964. Stable isotopes in precipitation. Tellus XVI, 436–468.

Davidson, G.R., 1995. The stable isotopic composition and measurement of soil CO_2. Geochimica Cosmochima Acta 59, 2485–2489.

Davidson, J.P., de Silva, S.L., 1992. Volcanic rocks from the Bolivian Altiplano : Insights into crustal structure, contamination, and magma genesis in the central Andes. Geology 20, 1127–1130.

de Silva, S.L., 2010. The largest wind ripples on Earth: Comment. Geology, doi: 10.1130/G30780C.1.

de Silva, S.L., Francis, P.W., 1991. Volcanoes of the Central Andes. Berlin, Springer Verlag, 216 pp.

de Silva, S.L., Bailey, J.E., Mandt, K.E., Viramonte, J.M., 2010. Yardangs in terrestrial ignimbrites: Synergistic remote and field observations on Earth with applications to Mars. Planetary and Space Science 58, 459–471.

Deeken, A., Sobel, E.R., Coutand, I., Haschke, M., Riller, U., Strecker, M.R., 2006. Development of the southern Eastern Cordillera, NW Argentina, constrained by apatite fission track thermochronology: From early Cretaceous extension to middle Miocene shortening. Tectonics 25, TC6003.

Dettman, D.L., Kohn, M.J., Quade, J., Ryerson, F.J., Ojha, T.P., Hamidullah, S., 2001. Seasonal stable isotope evidence for a strong Asian monsoon throughout the past 10.7 m.y. Geology 29, 31–34.

Dodd, A.N., Borland, A.M., Haslam, R.P., Griffiths, H., Maxwell, K., 2002. Crassulacean acid metabolism: plastic, fantastic. Journal of Experimental Botany 53, 569–580.

Drew, S.T., Ducea, M.N., Schoenbohm, L.M., 2009. Mafic volcanism on the Puna Plateau, NW Argentina: Implications for lithospheric composition and evolution with an emphasis on lithospheric foundering. Lithosphere 1, 305–318.

Ehleringer, J.R., Cerling, T.E., Helliker, B.R., 1997. C_4 photosynthesis, atmospheric CO_2, and climate. Oecologia 112, 285–299.

Ehlers, T.A., Poulsen, C.J., 2009. Influence of Andean uplift on climate and paleoaltimetry estimates. Earth and Planetary Science Letters 281, 238–248.

Endt, P.M., 1998. Supplement to energy levels of A = 21-44 nuclei (VII). Nuclear Physics A 633, 1–220.page 253.

English, N. T., 2008. Stable isotopes in the spines of columnar cactus: A new proxy for climate and ecophysiological research. (Ph.D. dissertation, University of Arizona), 213 pp.

Farquhar, G.D., Ehleringer, J.R., Hubick, K.T., 1989. Carbon isotope discrimination and photsynthesis. Annual Review of Plant Physiology and Plant Molecular Biology 40, 503-37.

Flynn, J. J., Swisher, C. C., 1995. Cenozoic South American land mammal ages: correlation to global geochronologies. Geochronology, Time Scales and Global Stratigraphic Correlation. SEPM Special Publication 54, 317–333.

Francis, P.W., Hammill, M., Kretzschmar, G.A., Thorpe, R.S., 1978. The Cerro Galan Caldera, North-west Argentina and its tectonic setting. Nature 274, 749–751.

Francis, P.W., O'Callaghan, L., Kretzschmar, G.A., Thorpe, R.S., Sparks, R.S.J., Page, R.N., de Barrio, R.E., Gillou, G., Gonzalez, O.E., 1983. The Cerro Galan ignimbrite. Nature 301, 51–53.

Francis, P.W., Sparks, R.S.J., Hawkesworth, C.J., Thorpe, R.S., Pyle, D.M., Tait, S.R., Mantovani, M.S., McDermott, F., 1989. Petrology and geochemistry of volcanic rocks of the Cerro Galan caldera, northwest Argentina. Geological Magazine 126, 515–547.

Fox, D.L., Koch, P.L., 2004. Carbon and oxygen isotopic variability in Neogene paleosol carbonates: constraints on the evolution of the C_4 grasslands of the Great Plains, USA. Palaeogeography, Palaeoclimatology, Palaeoecology 207, 305–329.

Friedman, I., O'Neil, J.R., 1977. Compilation of stable isotope fractionation factors of geochemical interest, in: M. Fleischer (Ed.), Data of Geochemistry, Professional Paper 440, US Geological Survey, Washington, DC.

Froidevaux, C., Isacks, B.L., 1984. The mechanical state of the lithosphere in the Altiplano-Puna segment of the Andes. Earth and Planetary Science Letters 71, 305–314.

Gaiero, D.M., 2007. Dust provenance in Antarctic ice during glacial periods: From where in southern South America? Geophysical Research Letters 34, L177707.

Galewsky, J., 2009a. Rain shadow development during the growth of mountain ranges: An atmospheric dynamics perspective. Journal of Geophysical Research 114, F01018.

Galewsky, J., 2009b. Orographic precipitation isotopic ratios in stratified atmospheric flows: Implications for paleoelevation studies. Geology 37, 791–794.

Garzione, C.N., Molnar, P., Libarkin, J.C., MacFadden, B.J., 2006. Rapid late Miocene rise of the Bolivian Altiplano: Evidence for removal of mantle lithosphere. Earth and Planetary Science Letters 241, 543–556.

Garzione, C.N., Hoke, G.D., Libarkin, J.C., Withers, S., MacFadden, B., Eiler, J., Ghosh, P., Mulch, A., 2008. Rise of the Andes. Science 320, 1304–1307.

Gat, J.R., 1996. Oxygen and hydrogen isotopes in the hydrologic cycle. Annual Review of Earth and Planetary Science 24, 225–262.

Ghosh, P., Garzione, C.N., Eiler, J.M., 2006. Rapid Uplift of the Altiplano Revealed Through ^{13}C-^{18}O Bonds in Paleosol Carbonates. Science 311, 511–515.

Gioncada, A., Vezzoli, L., Mazzuoli, R., Omarini, R., Nonnotte, P., Guillou, H., 2010. Pliocene intraplate-type volcanism in the Andean foreland at 25°10′S, 64°40′W (NW Argentina): Implications for magmatic and structural evolution of the Central Andes. Lithosphere 2, 153–171.

Godfrey, L.V., Jordan, T.E., Lowenstein, T.K., Alonso, R.L., 2003. Stable isotope constraints on the transport of water to the Andes between 22 and 26 S during the last glacial cycle. Palaeogeography, Palaeoclimatology, Palaeoecology 194, 299–317.

Gradstein, F., Ogg, J.G., Smith, A.G., eds., 2004. A Geologic Time scale 2004. Cambridge University Press, 610 pp.

Greene, L. 1995. Eolian Landforms in the Central Andes: Implications for the Long Term Stability of Atmospheric Circulation. M.S. Thesis, Cornell University, Ithaca, NY 62 pp.

Grier, M.E., Salfity, J.A., Allmendinger, R.W., 1991. Andean reactivation of the Cretaceous Salta rift, northwestern Argentina. Journal of South American Earth Sciences 4, 351–372.

Griffiths, H., Cousins, A.B., Badgeer, M.R., von Caemmerer, S., 2007. Discrimination in the Dark. Resolving the Interplay between Metabolic and Physical Constraints to Phosphoenolpyruvate Carboxylase Activity during the Crassulacean Acid Metabolism Cycle. Plant Physiology 143, 1055–1067.

Gubbels, T.L., Isacks, B.L., Farrar, E., 1993. High-level surfaces, plateau uplift, and foreland development, Bolivian central Andes. Geology 21, 695–698.

Hain, M.P., Strecker, M.R., Bookhagen, B., Alonso, R.N., Pingel, H., Schmitt, A.K., in press. Neogene to Quaternary broken-foreland deformation and sedimentation dynamics in the Andes of NW Argentina (25°S). Tectonics, doi:10.1029/2010TC002703.

Haselton, K., Hilley, G., Strecker, M.R., 2002. Average Pleistocene climatic pattern in the southern Central Andes: Controls on mountain glaciation and paleoclimate implications. Journal of Geology 110, 211–226.

Helliker, B.R., Ehleringer, J.R., 2000. Establishing a grassland signature in veins: ^{18}O in the leaf water of C_3 and C_4 grasses. Proceedings of the National Academy of Science 97, 7894–789.

Hermanns, R.L., Schellenberger, A., 2008. Quaternary tephrochronology helps define conditioning factors and triggering mechanisms of rock avalanches in NW Argentina. Quaternary International 178, 261–275.

Hernandez, R.M., Jordan, T.E., Dalenz Farjat, A., Echavarría, L., Idleman, B.D., Reynolds, J.H., 2005. Age, distribution, tectonics, and eustatic controls of the Paranese and Carribean marine transgressions in southern Bolivia and Argentina. Journal of South American Earth Sciences 19, 495–512.

Hilley, G.E., Strecker, M.R., 2005. Processes of oscillatory basin infilling and excavation in a tectonically active orogen: Quebrada del Toro Basin, NW Argentina. Geological Society of America 117, 887–901.

Hindle, D., Kley, J., Oncken, O., Sobolev, S., 2005. Crustal blance and crustal flux from shortening estimates in the Central Andes. Earth and Planetary Science Letters 230, 113–124.

Hoke, G.D., Garzione, C. N., 2008. Paleosurfaces, paleoelevation, and the mechanisms for the late Miocene topographic development of the Altiplano plateau. Earth and Planetary Science Letters 271, 192–201.

Houston, J., Hartley, A.J., 2003. The Central Andean west-slope rainshadow and its potential contribution to the origin of hyper-aridity in the Atacama Desert. International Journal of Climatology 23, 1453–1464.

Huang, Y., Clemens, S.C., Liu, W., Wang, Yi, Prell, W., 2007. Large-scale hydrologic change drove the late Miocene C_4 plant expansion in the Himalayan foreland and Arabian Peninsula. Geology 35, 531–534.

Hunt, J.B., Hill, P.G., 2001. Tephrological implications of beam size—sample-size effects in electron microprobe analysis of glass shards. Journal of Quaternary Science 16, 105–117.

Husson, L., Sempere, T., 2003. Thickening the Altiplano crust by gravity-driven crustal channel flow. Geophysical Research Letters 30, 1243.

Hynek, S.A., Marchetti, D.W., Fernandez, D.P., Cerling, T.E., 2010. Composition, pre-eruptive zonation, and geochronologic significance of the ~ 450 ka Diamante Tuff, Andean Cordillera (34°S), Argentina. Quaternary Geochronology 5, 591–601.

Hynek, S.A., Brown, F.H., Fernandez, D.P., 2011. A rapid method for handpicking potassium rich feldspar from silicic tephra. Quaternary Geochronology 6, 285–288.

Insel, N., Poulsen, C.J., Ehlers, T.A., 2009. Influence of the Andes Mountains on South American moisture transport, convection, and precipitation. Climate Dynamics, doi:10.1007/s00382-009-0637-1.

Isacks, B.L., 1988. Uplift of the central Andean plateau and bending of the Bolivian orocline. Journal of Geophysical Research 93, 3211–3231.

Izett, G.A., 1981. Volcanic Ash Beds: Recorders of Upper Cenozoic Silicic Pyroclastic Volcanism in the Western United States. Journal of Geophysical Research 86, 10200–10222.

Jordan, T.E., Allmendinger, R.W., 1986. The Sierras Pampeanas of Argentina: A modern analogue of Rocky Mountain foreland deformation. American Journal of Science 286, 737–764.

Jordan, T.E., Isacks, B.L., Allmendinger, R.W., Brewer, J.A., Ramos, V.A., Ando, C.J., 1983, Andean tectonics related to geometry of subducted Nazca plate: Geological Society of America Bulletin 94, 341–361.

Jourdan, F., Renne, P.R., 2007. Age calibration of the Fish Canyon sanidine $^{40}Ar/^{39}Ar$ dating standard using primary K-Ar standards. Geochimica et Cosmochimica Acta 71, 387–402.

Kay, R.W., Kay, S.M., 1993. Delamination and delamination magmatism. Tectonophysics 219, 177–189.

Kay, S.M., Coira, B., 2009. Shallowing and steepening subduction zones, continental lithospheric loss, magmatism, and crustal flow under the Central Andean Altiplano-Puna Plateau. In: Kay, S.M., Ramos, V.A., Dickinson, W.R. (Eds.), Backbone of the Americas: Shallow Subduction, Plateau Uplift, and Ridge and Terrane Collision. GSA Memoir 204, Boulder, pp. 229–259.

Kay, S.M., Coira, B., Viramonte, J., 1994. Young mafic back arc volcanic rocks as indicators of continental lithospheric delamination beneath the Argentine Puna plateau, central Andes. Journal of Geophysical Research 99, 24,323–24,339.

Kay, S.M., Coira, B.L., Caffe, P.J., Chen, C-H, 2010. Regional chemical diversity, crustal and mantle sources and evolution of central Andean Puna plateau ignimbrites. Journal of Volcanology and Geothermal Research 198, 81–111.

Kay, S.M., Coira, B., Worner, G., Kay, R.W., Singer, B.S., in press. Geochemical, isotopic and single crystal $^{40}Ar/^{39}Ar$ age constraints on the evolution of the Cerro Galan ignimbrites. Bulletin of Volcanology. doi: 10.1007/s00445-010-0410-7.

Kleinert, K., Strecker, M.R., 2001. Climate change in response to orographic barrier uplift: Paleosol and stable isotope evidence from the late Neogene Santa María basin, northwestern Argentina. Geological Society of America Bulletin 113, 728–742.

Kley, J., Monaldi, C.R., 2002. Tectonic inversion in the Santa Barbara System of the central Andean foreland thrust belt, northwestern Argentina. Tectonics 21, 1061.

Koch, P.L., 1998. Isotopic reconstruction of past continental environments. Annual Review of Earth and Planetary Science 26, 573–613.

Koch, P.L., Fisher, D.C., Dettman, D, 1989. Oxygen isotope variation in the tusks of extinct proboscideans: a measure of season of death and seasonality. Geology 17, 515–519.

Koch, P.L., Clyde, W.C., Hepple, R.P., Fogel, M.L., Wing, S.L., Zachos, J.C., 2003. Carbon and oxygen isotope records from paleosols spanning the Paleocene-Eocene boundary, Bighorn Basin, Wyoming in Wing, S.L., Gingerich, P.D., Schmitz, B., and Thomas, E., eds., Causes and Consequences of Globally Warm Climates in the Early Paleogene: Boulder, Colorado, Geological Society of America Special Paper 369, 49–64.

Kohn, M.J., Welker, J.M., 2005. On the temperature correlation of $\delta^{18}O$ in modern precipitation. Earth and Planetary Science Letters 231, 87–96.

Kohn, M.J., 2010. Carbon isotope compositions of terrestrial C3 plants as indicators of (paleo)ecology and (paleo)climate. Proceedings of the National Academy of Sciences 107, 19691–19695.

Kraemer, B., Adelmann, D., Alten, M., Schnurr, W., Erpenstein, K., Kiefer, E., van den Bogaard, P., Görler, K., 1999. Incorporation of the Paleogene foreland into the Neogene Puna plateau: The Salar de Antofalla area, NW Argentina. Journal of South American Earth Sciences 12, 157–182.

Kuiper, K.F., Deino, A., Hilgen, F.J., Krijgsman, W., Renne, P.R., Wijbrans, J.R., 2008. Synchronizing Rock Clocks of Earth History. Science 320, 500–504.

Lamb, S., Davis, P., 2003. Cenozoic climate change as a possible cause for the rise of the Andes. Nature 425, 792–797.

Latorre, C., Quade, J., McIntosh, W.C., 1997. The expansion of C_4 grasses and global change in the late Miocene: Stable isotope evidence from the Americas. Earth and Planetary Science Letters 146, 83–96.

Le Bas, M.J., Le Maitre, R.W, Streckeisen, A., Zanettin, B., 1986. A chemical classification of volcanic rocks on the total alkali−silica diagram. Journal of Petrology 27, 745–750.

Leier, A., Quade, J., DeCelles, P., Kapp, P., 2009. Stable isotopic results from paleosol carbonate in South Asia: Paleoenvironmental reconstructions and selective alteration. Earth and Planetary Science Letters 272, 242–254.

Levin, N.E., Quade, J., Simpson, S.W., Semaw, S., Rogers, M., 2004. Isotopic evidence for Plio-Pleistocene environmental change at Gona, Ethiopia. Earth and Planetary Science Letters 219, 93–110.

Levin, N.E., Cerling, T.E., Passey, B.H., Harris, J.H., Ehleringer, J.R., 2006. A stable isotope aridity index for terrestrial environments. Proceedings of the National Academy of Science 103, 11201–11205.

Levin, N.E., Simpson, S.W., Quade, J., Cerling T.E., Frost, S.R., 2008. Herbivore enamel carbon isotopic composition and the environmental context of Ardipithecus at Gona, Ethiopia, in: Quade J., Wynn J.G. (eds.), The Geology of Early Humans in the Horn of Africa. Geological Society of America Special Paper 446, 215–234.

Levin, N.E., Brown, F.H., Beherensmeyer, A.K., Bobe, R., Cerling, T.E., in review. Paleosol carbonates from the Omo Group: isotopic records of local and regional environmental change in East Africa. Palaeogeography, Palaeoclimatology, Palaeoecology.

MacFadden, B.J., 2005. Diet and habitat of toxodont megaherbivores (Mammalia, Notoungulata) from the late Quaternary of South and Central America. Quaternary Research 64, 113–124.

Marrett R., Strecker, M.R., 2000. Response of intracontinental deformation in the central Andes to late Cenozoic reorganization of South American Plate motions. Tectonics 19, 452–467.

Marshall, L.G., Patterson, B., 1981. Geology and geochronology of the mammal-bearing Tertiary of the Valle de Santa María and Río Corral Quemado. Fieldiana Geology 9, 1–80.

Marshall, L.G., Butler, R.F., Drake, R.E., Curtis, G.H., Tedford, R.H., 1979. Calibration of the Great American Interchange. Science 204, 272–279.

Masek, J.G., Isacks, B.L., Gubbels, T.L., Fielding, E.J., 1994. Erosion and tectonics at the margins of continental plateaus. Journal of Geophysical Research, Solid Earth 99, 13941–13956.

McDougall, I., Maier, R., Sutherland-Hawkes, P., Gleadow, A.J.W., 1980. K-Ar age estimate for the KBS Tuff, East Turkana, Kenya. Nature 284, 230–234.

McDowell, F.W., 1983. K-Ar dating: Incomplete extraction of radiogenic argon from alkali feldspar. Chemical Geology 41, 119–126.

McFadden, L.D., Wells, S.G. and Jercinovich, M.J., 1987. Influences of eolian and pedogenic processes on the origin and evolution of desert pavements. Geology 15, 504–508.

McFadden, L.D., McDonald, E.V., Wells, S.G., Anderson, K., Quade, J., Forman, S.L., 1998. The vesicular layer and carbonate collars of desert soils and pavements: formation, age, and relation to climate change. Geomorphology 24, 101–145.

McGlashan, N., Brown, L., Kay, S., 2008. Crustal thickness in the central Andes from teleseismically recorded depth phase precursors. Geophysical Journal International 175, 1013–1022.

McPherson, H.M., 2008. Climate and Tectonic Controls on sedimentation and deformation in the Fiambalá basin of the southern Puna plateau, northwest Argentina. M.S. Thesis, The Ohio State University, 91 pp.

Milana, J.P., 2009. The largest wind ripples on Earth? Geology 37, 343–346.

Milana, J.P., Forman, S., Kröhling, D., 2010. The largest wind ripples on Earth: Reply. Geology, doi: 10.1130/G31354Y.1.

Min, K., Mundil, R., Renne, P.R., Ludwig, K.R., 2000. A test for systematic errors in $^{40}Ar/^{39}Ar$ geochronology through comparison with U/Pb analysis of a 1.1-Ga rhyolite. Geochimica et Cosmochimica Acta 64, 73–98.

Molnar, P., England, P., 1990. Late Cenozoic uplift of mountain ranges and global climate change: chicken or egg? Nature 346, 29–34.

Molnar, P., Houseman, G.A., 2004. The effects of buoyant crust on the gravitational instability of thickened mantle lithosphere at zones of intracontinental convergence. Geophysical Journal International 158, 1134–1150.

Montgomery, D.R., Balco, G., Willett, S.D., 2001. Climate, tectonics, and the morphology of the Andes. Geology 29, 579–582.

Mortimer, E., Carrapa, B., Coutand, I., Schoenbohm, L., Sobel, E.R., Gomes, J.S., Strecker, M.R., 2007. Fragmentation of a foreland basin in response to out-of-sequence basement uplifts and structural reactivation: El Cajon-Campo del Arenal basin, NW Argentina. Geological Society of America Bulletin 119, 637–653.

Mosolf, J.G., Horton, B.K., Heizler, M.T., Matos, R., in press. Unroofing the core of the central Andean fold-thrust belt during focused late Miocene exhumation: evidence from the Tipuani-Mapiri wedge-top basin, Bolivia. Basin Research doi:10.1111/j.1365-2117.2010.00491.x

Mulch, A., Uba, C.E., Strecker, M.R., Schoenberg, R., Chamberlain, C.P., 2010. Late Miocene climate variability and surface elevation in the central Andes. Earth and Planetary Science Letters 290, 173–182.

Mundil, R., Renne, P.R., Min, K.K., Ludwig, K.R., 2006. Resolvable miscalibration of the $^{40}Ar/^{39}Ar$ geochronometer (Abstract). *Eos Transactions AGU*, **87***(52)*, *Fall Meeting Supplement*, Abstract V21A-0543.

Muruaga, C.M., 2001. Estratigrafía y desarollo tectosedimentario de los sedimentos terciarios en los alrededores de la Sierra de Hualfín, borde suroriental de la Puna, Catamarca, Argentina. Asociación Argentina de Sedimentología 8 (1), 27–50.

Nash, W.P., 1992. Analysis of oxygen with the electron microprobe: Application to hydrous glass shards and minerals. American Mineralogist 77, 453–457.

Nash, B.P., Perkins, M.E., Christensen, J.N., Lee, D-C.,Halliday, A.N., 2006. The Yellowstone hotspot in space and time: Nd and Hf isotopes in silicic magmas. Earth and Planetary Science Letters 247, 143–156.

Nielsen, C.H., Sigurdsson, H., 1981. Quantitative methods for electron microprobe analysis of sodium in natural and synthetic glasses. American Mineralogist 66, 547–552.

Nier, A.O., 1950. A redetermination of the relative abundances of the isotopes of carbon, nitrogen, oxygen, argon, and potassium. Physical Reviews 77, 789–793.

Oncken, O., ANCORP Working Group, 2003. Seismic imaging of a convergent continental margin and plateau in the central Andes (Andean Continental Research Project 1996 (ANCORP'96)). Journal of Geophysical Research 108, B7, 2328.

Pagani, M., Freeman, K.H., Arthur, M.A., 1999. Late Miocene atmospheric CO_2 concentrations and the expansion of C_4 grasses. Science 285, 876–879.

Pagani, M., Liu, Z., LaRiviera, J., Ravelo, A.C., 2010. High climate sensitivity to atmospheric carbon dioxide for the past 5 million years. Nature Geoscience 3, 27–30.

Passey, B.H., Cerling, T.E., 2002. Tooth enamel mineralization in ungulates: implications for recovering a primary isotopic time-series. Geochimica Cosmochimica Acta 66, 3225–3234.

Passey, B.H., Cerling, T.E., 2006. In situ stable isotope analysis ($\delta^{13}C$, $\delta^{18}O$) of very small teeth using laser ablation GC/IRMS. Chemical Geology 235, 238–249.

Passey, B.H., Cerling, T.E., Perkins, M.E., Voorhies, M.R., Harris, J.M., Tucker, S.T., 2002. Environmental change in the Great Plains: an isotopic record from fossil horses. Journal of Geology 110, 123–140.

Passey, B.H., Cerling, T.E., Schuster, G.T., Robinson, T.F., Roeder, B.L., Krueger, S.K., 2005a. Inverse methods for estimating primary input signals from time-averaged isotope profiles. Geochimica et Cosmochimica Acta 69, 4101–4116.

Passey, B.H., Robinson, T.F., Ayliffe, L.K., Cerling, T.E., Sponheimer, M., Dearing, D., Roeder, B.L., Ehleringer, J.R., 2005b. Carbon isotope fractionation between diet, breath CO_2, and bioapatite in different mammals. Journal of Archeological Science 32, 1459–1470.

Passey, B.H., Cerling, T.E., Levin, N.E., 2007. Temperature dependence of oxygen isotope acid fractionation for modern and fossil tooth enamels. Rapid Communication in Mass Spectrometry 21, 2853–2859.

Passey, B.H., Ayliffe, L.K., Kaakinen, A., Zhang, Z., Eronen, J.T., Zhu, Y., Zhou, L., Cerling, T.E., Fortelius, M., 2009. Strengthened East Asian summer monsoons during a period of high-latitude warmth? Isotopic evidence from Mio-Pliocene fossil mammals and soil carbonates from northern China. Earth and Planetary Science Letters 277, 443–452.

Penck, W., 1920. Der Südrand der Puna de Atacama (NW-Argentinien). Abhandlungen Mathematisch-Physikalische Klasse de Sächsischen Akademie der Wissenschaften 37, 420 pp.

Perkins, M.E., Nash, B.P., 2002. Explosive silicic volcanism of the Yellowstone hotspot: The ash fall tuff record. Geological Society of America Bulletin 114, 367–381.

Perkins, M.E., Nash, W.P., Brown, F.H., Fleck, R.J., 1995. Fallout tuffs of Trapper Creek, Idaho – A record of Miocene explosive volcanism in the Snake River Plain volcanic province. Geological Society of America Bulletin 107, 1484–1506.

Perkins, M.E., Brown, F.H., Nash, W.P., McIntosh, W., Williams, S.K., 1998. Sequence, age, and source of silicic fallout tuffs in middle to late Miocene basins of the northern Basin and Range province. Geological Society of America Bulletin 110, 344–360.

Pilger, R.H., 1981. Plate reconstructions, aseismic ridges, and low-angle subduction beneath the Andes. Geological Society of America Bulletin 92, 448–456.

Placzek, C., Quade, J., Patchett, P.J., 2006. Geochronology and stratigraphy of late Pleistocene lake cycles on the southern Bolivian Altiplano: Implications for causes of tropical climate change. Geological Society of America Bulletin 118, 515–532.

Podelsak, D.W., Torregrossa, A., Ehleringer, J.R., Dearing, M.D., Passey, B.H., Cerling, T.E., 2008. Turnover of oxygen and hydrogen isotopes in the body water, CO_2, hair, and enamel of a small mammal. Geochimica Cosmochimica Acta 72, 19–35.

Pope, D.C., Willett, S.D., 1998. Thermal-mechanical model for crustal thickening in the central Andes driven by ablative subduction. Geology 26, 511–514.

Pritchard, M.E., Simons, M., 2002. A satellite geodetic survey of large-scale deformation of volcanic centres in the central Andes. Nature 418, 167–171.

Pritchard, M.E., Simons, M., 2004. An InSAR-based survey of volcanic deformation in the central Andes. Geochemistry, Geophysics, Geosystems 5, Q02002.

Quade, J., Cerling, T.E., 1995. Expansion of C_4 grasses in the late Miocene of northern Pakistan: Evidence from stable isotopes in paleosols. Palaeogeography, Palaeoclimatology, Palaeoecology 115, 91–116.

Quade, J., Cerling, T.E., Bowman, J.R., 1989. Systematic variations in the carbon and oxygen isotopic composition of pedogenic carbonate along elevation transects in the southern Great Basin, United States. Geological Society of America Bulletin 101, 464–475.

Quade, J., Cater, J.M.L., Ojha, T.P., Adam J., Harrison, T.M., 1995. Late Miocene environmental change in Nepal and the northern Indian subcontinent: stable isotopic evidence from paleosols. Geological Society of America Bulletin 107, 1381–1397.

Quade, J., Garzione, C., Eiler, J., 2007. Paleoelevation Reconstruction using Pedogenic Carbonates. Reviews in Mineralogy and Geochemistry 66, 53–87.

Ramos, V.A., Alonso, R.N., 1995. El Mar Paranese en la provincia de Jujuy. Revista del Instituto de Geología y Minería 10, 73–80.

Renne, P.R., Norman, E.B., 2001. Determination of the half-life of ^{37}Ar by mass spectrometry. Physical Review C 63, 047302, 3 pp.

Renne, P.R., Swisher, C.C., Deino, A.L., Karner, D.B., Owens, T.L., DePaolo, D.J., 1998. Intercalibration of standards, absolute ages and uncertainties in $^{40}Ar/^{39}Ar$ dating. Chemical Geology 145, 117–152.

Renne, P.R., Mundil, R., Balco, G.,Min, K., Ludwig, K.R., 2010. Joint determination of ^{40}K decay constants and $^{40}Ar^*/^{40}K$ for the Fish Canyon sanidine standard, and improved accuracy for $^{40}Ar/^{39}Ar$ geochronology. Geochimica et Cosmochimica Acta 74, 5349–5367.

Riller, U., Petrinovic, I., Ramelow, J., Strecker, M., Oncken, O., 2001. Late Cenozoic tectonism, collapse caldera and plateau formation in the central Andes. Earth and Planetary Science Letters 188, 299–311.

Risse, A., Trumbull, R.B., Coira, B., Kay, S.M., van den Bogaard, P., 2008. $^{40}Ar/^{39}Ar$ geochronology of mafic volcanism in the back-arc region of the southern Puna plateau, Argentina. Journal of South American Earth Sciences 26, 1–15.

Romanek, C.S., Grossman, E.L., Morse, J.W., 1992. Carbon isotopic fractionation in synthetic aragonite and calcite: effects of temperature and precipitation rate. Geochimica Cosmochimica Acta 56, 419–430.

Rozanski, K., Araguas-Araguas, L., Gonfiantini, R., 1993. Isotopic patterns in modern global precipitation. In: Swart, P.K., Lohmann, K.C., McKenzie, J.A., Savin, S. (Eds.), Climate Change in Continental Isotopic Records Monograph 78. American Geophysical Union, Washington D.C., pp. 1–36.

Salisbury, M.J., Jicha, B.R., de Silva, S.L., Singer, B.S., Jiménez, N.C., Ort, M.H., 2011. $^{40}Ar/^{39}Ar$ chronostratigraphy of Altiplano-Puna volcanic complex ignimbrites reveals the development of a major magmatic province. Geological Society of America Bulletin 123, 821–840.

Sarna-Wojcicki, A.M., Morrison, S.D., Meyer, C.E., Hillhouse, J.W., 1987. Correlation of upper Cenozoic tephra layers between sediments of the western United States and eastern Pacific Ocean and comparison with biostratigraphic and magentostratigraphic data. Geological Society of America Bulletin 98, 207–223.

Schnurr, W. B. W., Trumbull, R. B., Clavero, J., Hahne, K., Siebel, W., Gardeweg, M., 2007. Twenty-five million years of felsic magmatism in the southern Central Volcanic Zone of the Andes: geochemistry and magma genesis of ignimbrites from 25–27°S, 67–72°W. Journal of Volcanology and Geothermal Research 166, 17–46.

Schoenbohm, L.M., Strecker, M.R., 2009. Normal Faulting along the southern margin of the Puna Plateau, northwest Argentina. Tectonics 28, TC5008.

Seki, O., Foster, G.L., Schmidt, D.N., Mackensen, A., Kawamura, K., Pancost, R.D., 2010. Alkenone and boron-based Pliocene pCO_2 records. Earth and Planetary Science Letters 292, 201–211.

Siebel, W., Schnurr, W.B.W., Hahne, K., Kraemer, B., Trumbull, R.B., van den Bogaard, P., Emmermann, R., 2001. Geochemistry and isotope systematics of small- to medium-volume Neogene–Quaternary ignimbrites in the southern central Andes: evidence for derivation from andesitic magma sources. Chemical Geology 171, 213–237.

Siewert, S.E., Singer, B.S., Condon, D., Obradovich, J.D., Sagemen, B.B., Meyers, S.R., Jicha, B.R., Sawyer, D.A., 2010. $^{40}Ar/^{39}Ar$ and U-Pb dating of the Cretaceous Niobrara Formation. Geological Society of America Abstracts with Programs 42, p. 394.

Simpson, G. G., 1980, Splendid Isolation: The curious history of South American mammals. New Haven: Yale University Press, 1980; 266 pp.

Singer, B.S. Ackert, R.P., Guillou, H., 2004. $^{40}Ar/^{39}Ar$ and K-Ar chronology of Pleistocene glaciations in Patagonia. Geological Society of America Bulletin 116, 434–450.

Smith, M.E., Chamberlain, K.R., Singer, B.S., Carroll, A.R., 2010. Eocene clocks agree: Coeval $^{40}Ar/^{39}Ar$, U-Pb and astronomical ages for the Green River Formation. Geology 38, 527–530.

Smith, R.B., Evans, J.P., 2007. Orographic Precipitation and Water Vapor Fractionation over the Southern Andes. Journal of Hydrometeorology 8, 3–19.

Smith, R.B., Barstad, I., Bonneau, L., 2005. Orographic Precipitation and Oregon's Climate Transition. Journal of the Atmospheric Sciences 62, 177–191.

Sobel, E.R., Strecker, M.R., 2003. Uplift, exhumation and precipitation: tectonic and climatic control of Late Cenozoic landscape evolution in the northern Sierras Pampeanas, Argentina. Basin Res. 15, 431–451.

Sobel, E.R., Hilley, G.E., Strecker, M.R., 2003. Formation of internally drained contractional basins by aridity-limited bedrock incision. Journal of Geophysical Research 108, B7, 2344.

Spell, T.L., McDougall, I., 2003. Characterization and calibration of $^{40}Ar/^{39}Ar$ dating standards. Chemical Geology 198, 189–211.

Starck, D., Anzotegui, L.M., 2001. The late Miocene climatic change – Persistence of a climatic signal through the orogenic stratigraphic record in northwestern Argentina. Journal of South American Earth Sciences 14, 763–774.

Steiger. R.H., Jäger, E., 1977. Subcommission on Geochronology: Convention on the use of decay constants in geo- and cosmochronology. Earth and Planetary Science Letters 36, 359–362.

Stoenner, R.W., Schaeffer, O.A., Katcoff, S., 1965. Half-lives of argon-37, argon-39, and argon-42. Science 148, 1325–1328.

Strecker, M.R., Cerveny, P., Bloom, A.L., Malizia, D., 1989. Late Cenozoic tectonism and landscape development in the foreland of the Andes: northern Sierras Pampeanas (26°–28°S), Argentina. Tectonics 8, 517–534.

Strecker, M.R., Alonso, R.N., Bookhagen, B., Carrapa, B., Hilley, G.E., Sobel, E.R., Trauth, M.H., 2007a. Tectonics and Climate of the Southern Central Andes. Annual Review of Earth and Planetary Sciences 35, 747–787.

Strecker, M.R., Mulch, A., Uba, C., Schmitt, A.K., Chamberlain, C.P., 2007b. Tectonics, Climate, and Surface Processes of the Southern Central Andes: Insights from Stable C isotopes and Sedimentary Environments. Abstract AGU Fall Meeting, San Francisco.

Strecker, M.R., Alonso, R., Bookhagen, B., Carrapa, B., Coutand, I., Hain, M.P., Hilley, G.E., Mortimer, E., Schoenbohm, L., Sobel, E.R., 2009. Does the topographic distribution of the central Andean Puna Plateau result from climatic or geodynamic processes? Geology 37, 643–646.

Swart, P.K., Burns, S.J., Leder, J.J., 1991. Fractionation of the stable isotopes of oxygen and carbon in carbon dioxide during the reaction of calcite with phosphoric acid as a function of temperature and technique. Chemical Geology 86, 89–96.

Tassara, A., Gotze, H-J., Schmidt, S., Hackney, R., 2006. Three-dimensional density model of the Nazca plate and the Andean continental margin. Journal of Geophysical Research 111, B09404.

Tipple, B.J., Pagani, M., 2007. The early origins of terrestrial C_4 photosynthesis. Annual Review of Earth and Planetary Science 35, 435–461.

Tipple, B.J. Meyers, S.R., Pagani, M, 2010. The carbon isotope ratio of Cenozoic CO_2: a comparative evaluation of available geochemical proxies. Paleoceanography. doi:10.1029/2009PA001851.

Tripati, A.K., Roberts, C.D., Eagle, R.A., 2009. Coupling of CO_2 and Ice Sheet stability over major climate transitions of the last 20 million years. Science 326, 1394–1397.

Trumbull, R.B., Riller, U., Oncken, O., Scheuber, E., Munier, K., Hongn, F., 2006. The Time-Space Distribution of Cenozoic Volcanism in the South-Central Andes: a new Data Compilation and Some Tectonic Implications. In: Oncken, O., Chong, G.,

Franz, G., Giese, P., Götze, H-J., Ramos, V.A., Strecker, M.R., Wigger, P. (Eds.), The Andes - Active Subduction Orogeny. Frontiers in Earth Sciences, vol. 1 Springer, Berlin, pp. 29–43.

Uba, C.E., Strecker, M.R., Schmitt, A.K., 2007. Increased sediment accumulation rates and climatic forcing in the central Andes during the late Miocene. Geology 35, 979–982.

Uba, C.E., Hasler, C-A., Buatois, L.A., Schmitt, A.K., Plessen, B., 2009. Isotopic, paleotontologic, and ichnologic evidence for late Miocene pulses of marine incursions in the central Andes. Geology 37, 827–830.

Van Couvering, J.A., Castradori, D., Cita, M.B., Hilgen, F.J., Rio, D., 2000. The base of the Zanclean Stage and of the Pliocene Series. Episodes 23, 179–187.

Vandervoort, D.S., Jordan, T.E., Zeitler, P.K., Alonso, R.N., 1995. Chronology of internal drainage development and uplift, southern Puna plateau, Argentine central Andes. Geology 23, 145–148.

Vila, B.L., Roig, V.G., 1992. Diurnal movements, family groups and alertness of vicuña (*Vicugna vicugna*), during the late dry season in Laguna Blanca Reserve (Catamarca, Argentina). Small Ruminate Research 7, 289–297.

von Huene, R., Ranero, C.R., 2009. Neogene collision and deformation of convergent margins along the backbone of the Americas. In: Kay, S.M., Ramos, V.A., Dickinson, W.R. (Eds.), Backbone of the Americas: Shallow Subduction, Plateau Uplift, and Ridge and Terrane Collision. GSA Memoir 204, Boulder, pp. 67–83.

Wang, Y., Cerling, T.E., 1994. A model of fossil tooth and bone diagenesis: implications for paleodiet reconstruction from stable isotopes. Palaeogeography, Palaeoclimatology, Palaeoecology 107, 281–289.

Wang, Y., Cerling, T.E., MacFadden, B.J., 1994. Fossil horses and carbon isotopes : new evidence for Cenozoic dietary, habitat, and ecosystem changes in North America. Palaeogeography, Palaeoclimatology, Palaeoecology 107, 269–269.

Webb, S.D., 1991. Ecogeography and the Great American Interchange. Paleobiology 17, 266-280.

Webb, S.D., 2006. The Great American Biotic Interchange: Patterns and Processes. Annals of the Missouri Botanical Garden 93, 245–257.

Willbold, M., Jochum, K.P., 2005. Multi-element isotope dilution sector field ICP-MS: A precise technique for the analysis of geological materials and its application to geological reference materials. Geostandards and Geoanalytical Research 29, 63–82.

Wilson, C.J.N., Hildreth, W., 1997. The Bishop Tuff: New insights from eruptive stratigraphy. Journal of Geology 105, 407–439.

WMO. 1975. Climatic Atlas of South America. Geneva, World Meteorological Organization, 28 pp.

Yuan, X., Sobolev, S., Kind, R., 2002. Moho topography in the central Andes and its geodynamic implications. Earth and Planetary Science Letters 199, 389–402.

Zazzo, A., Lecuyer, C., Sheppard, S.M.F., Grandjean, P., Mariotti, A., 2004. Diagenesis and the reconstruction of paleoenvironments: a method to restore original $\delta^{18}O$ values of carbonate and phosphate from fossil tooth enamel. Geochimica Cosmochimica Acta 68, 2245–2258.